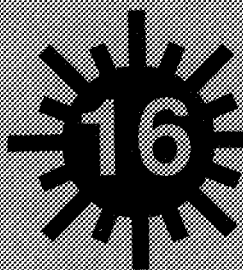


NASA Conference Publication 3158
Part 2

Sixteenth International Laser Radar Conference



(NASA-CP-3158-Pt-2) SIXTEENTH
INTERNATIONAL LASER RADAR
CONFERENCE, PART 2 (NASA) 361 p

N92-31013
--THRU--
N92-31106
Unclas

H1/35 0104734

*Abstracts of papers presented
at a conference and held at the
Massachusetts Institute of Technology
Cambridge, Massachusetts
July 20-24, 1992*

AMS

USAF

OSA

NASA

*NASA Conference Publication 3158
Part 2*

Sixteenth International Laser Radar Conference

*Edited by
M. P. McCormick
NASA Langley Research Center
Hampton, Virginia*

Abstracts of papers presented at a conference
sponsored by the United States Air Force Office
of Scientific Research, NASA Langley Research
Center, the United States Air Force Phillips
Laboratory, the American Meteorological Society,
and the Optical Society of America, and held at the
Massachusetts Institute of Technology
Cambridge, Massachusetts
July 20-24, 1992

NASA

National Aeronautics and
Space Administration
Office of Management
Scientific and Technical
Information Program

1992

Preface

Abstracts of papers presented at the Sixteenth International Laser Radar Conference (ILRC), held on the campus of the Massachusetts Institute of Technology in Cambridge, Massachusetts, July 20-24, 1992, are contained in this publication. These conferences, held biennially, bring together an interdisciplinary group of scientists working in the field of laser remote sensing as applied to the atmosphere, earth and oceans. At the 16th ILRC, 100 oral papers and 95 poster papers were presented during 16 sessions. Topics covered include: the worldwide measurements of aerosols produced from the June 1991 eruption of the Pinatubo volcano; the role of lidars in global change research, including long-term stratospheric ozone measurements and the Network for the Detection of Stratospheric Change (NDSC); measurements from space by the Laser Atmospheric Winds Sensor (LAWS) and the Lidar In-space Technology Experiment (LITE); stratospheric and mesospheric temperature and wind measurements; mesospheric sodium and ion measurements; cloud measurements, including the Experimental Cloud Lidar Pilot Study (ECLIPS); laser imaging and ranging; tropospheric water vapor and aerosol measurements; and, the description of new systems and facilities. Although no abstracts are included herein, a NASA-sponsored special session on 2 μ m solid state doppler lidar technology for remote sensing of winds took place also.

The conference was held under the auspices of the International Coordination group for Laser Atmospheric Studies (ICLAS) of the International Radiation Commission, International Association of Meteorology and Atmospheric Physics. ICLAS is the parent organization for these ILRC's which are held during even years. Through the cooperation of many societies and organizations, national lidar conferences and conferences/workshops associated with specific or related aspects of lidar research are held during odd years. The conference was co-sponsored by the U.S. Air Force Phillips Laboratory, U. S. Air Force Office of Scientific Research, NASA, the American Meteorological Society, and the Optical Society of America. The 16th ILRC was organized under the leadership of Robert A. McClatchey (General Chairman), R. Earl Good (Technical Program Chairman), and Gilbert Davidson (Local Organizing Committee Chairman). They are to be commended for the excellent venue and selection of scientific papers.

This volume was prepared for publication through the efforts of the staff of the Research Information and Applications Division, NASA Langley Research Center. Special thanks go to Natalie Bennett of PhotoMetrics and Gayle Fitzgerald, Marie Seamon and Trish Ezekiel of the MIT Conference Services Office for attending to the diverse tasks required for the success of this conference.

The use of trade names or manufacturers' names in this publication does not constitute endorsement, either expressed or implied, by the National Aeronautics and Space Administration.

M. Patrick McCormick
Chairman, International Coordination
Group for Laser Atmospheric Studies
International Radiation Commission

Robert A. McClatchey, General Chairman
Phillips Laboratory

Technical Program Committee

R. Earl Good, Program Chairman
Phillips Laboratory

Steven B. Alejandro
Phillips Laboratory

Allan I. Carswell
York University, Canada

Marie-Lise Chanin
CNRS, France

Edwin W. Floranta
University of Wisconsin

R. Michael Hardesty
NOAA

Dennis K. Killinger
University of South Florida

M. Patrick McCormick
NASA Langley Research Center

Harvey Melfi
NASA Goddard Space Flight Center

Norman Menyuk
MIT Lincoln Laboratory (ret.)

John W. Meriwether
Phillips Laboratory

C. Martin Platt
CSIRO, Australia

Ronald G. Prinn
Massachusetts Institute of Technology

Wolfgang Renger
DLR, Germany

Duane D. Smith
Kaman Aerospace Corporation

J. William Snow
Phillips Laboratory

Nobuo Takeuchi
Chiba University, Japan

Vladimir E. Zuev
Institute of Atmospheric Optics, Russia

Local Organizing Committee

Gilbert Davidson, Chairman
PhotoMetrics, Inc.

Donald E. Bedo
Phillips Laboratory

Phan D. Dao
Phillips Laboratory

Paul L. Kelley
MIT Lincoln Laboratory

LTC George G. Koenig
Phillips Laboratory

ICLAS MEMBERSHIP

Dr. Al Carswell
York University
Dept. of Physics & CRESS
4700 Keele St.
North York Ontario
M3J 1P3 CANADA

Professor Giorgio Fiocco
Dipto di Fisica
Citta Universitaria
Pizzale Aldo Moro #2
00185-Roma
ITALY

Dr. Pierre H. Flamant
Laboratoire de Meteorologie
Dynamique du CNRS
Ecole Polytechnique
91128 Palaiseau
FRANCE

Dr. R. Michael Hardesty
NOAA/ERL Propagation Laboratory
U. S. Department of Commerce
325 Broadway
Boulder, CO 80303

Dr. Benjamin M. Herman
School of Atmospheric Sciences
University of Arizona
Tucson, AZ 85721

Dr. M. Patrick McCormick
NASA Langley Research Center
Mail Stop 475
Hampton, VA 23665-5225

Dr. Gerard Megie
Service d'Aeronomie CNRS
BP n° 3
91371 Verrieres Le Buisson
FRANCE

Dr. S. Harvey Melfi
NASA Goddard Space Flight Center
Mail Code 917.0
Greenbelt, MD 20771

Dr. C. M. R. Platt
CSIRO
Div. of Atmos. Physics
Aspendale, Victoria
AUSTRALIA

Dr. Wolfgang Renger
DLR Institut für Physik der
Atmosphäre
D-8031 Oberpfaffenhofen
GERMANY

Dr. Leopoldo Stefanutti
Ist. di Ricerca sulle Onde
Elettro Magnetiche of CNR
Via Panciatichi 64
Firenze 50127
ITALY

Dr. Lance Thomas
Department of Physics
Univ. of College of Wales
Penglais, Aberystwyth
Dyfed SY23 3BZ
UNITED KINGDOM

Dr. Christian Werner
Ins. of Atmos. Physics
German Aerospace Estab.
D8031 Oberpfaffenhoffen
GERMANY

Dr. V. E. Zuev
Instit. of Atmos. Optics
1 Akademichesky Av.
Tomsk 634055
RUSSIA

Dr. Takao Kobayashi
Dept. of Electronics
Fukui University 3-9-1
Bunkyo Fukui 910
JAPAN

AGENDA

16TH INTERNATIONAL LASER RADAR CONFERENCE

Monday, 20 July 1992

PART 1*

8:30 OPENING CEREMONIES

8:45 Thirty Years of Optical Radar Work: Reminiscences and Perspectives
Giorgio Fiocco

9:30-11:45 SESSION A: Volcanic (Mt. Pinatubo) Dust Layer Measurements

Session Chair:
Allan Carswell

9:30 A1 (Invited) Long Term Stratospheric Aerosol Lidar Measurements in Kyushu 1
Motow Fujiwara

10:00-10:30 COFFEE BREAK

10:30 A2 Southern Hemisphere Lidar Measurements of the Aerosol Clouds from Mt.
Pinatubo and Mt. Hudson 3
Stuart A. Young, Peter J. Manson, and Graeme R. Patterson

10:45 A3 Stratospheric Backscatter, Extinction, and Lidar Ratio Profiling After the Mt.
Pinatubo Eruptions 7
*Albert Ansmann, Christoph Schulze, Ulla Wandinger, Claus Weitkamp, and
Walfried Michaelis*

11:00 A4 Measurements of Stratospheric Pinatubo Aerosol Extinction Profiles by a
Raman Lidar 11
Makoto Abo and Chikao Nagasawa

11:15 A5 Raman Lidar Measurements of Pinatubo Aerosols Over Southeastern Kansas
During November-December 1991 13
R. A. Ferrare, S. H. Melfi, D. N. Whiteman, and K. D. Evans

11:30 A6 Lidar Observations of Stratospheric Aerosol Layer After the Mt. Pinatubo
Volcanic Eruption 17
Tomohiro Nagai, Osamu Uchino, and Toshifumi Fujimoto

11:45-1:15 LUNCH

1:15-4:30 SESSION B: Global Change/Ozone Measurements

Session Chairs:
Paul Kelley
Ronald Prinn

*Part 1 is presented under separate cover.

1:15	B1	(Invited) The Role of LIDARs in Global Change Research <i>Ronald G. Prinn</i>	21
1:45	B2	Interpretation of DIAL Measurements of Lower Stratospheric Ozone in Regions with Pinatubo <i>William B. Grant, Edward V. Browell, Marta A. Fenn, Carolyn F. Butler, Vincent G. Brackett, Robert E. Veiga, Shane D. Mayor, Jack Fishman, D. Nganga, A. Minga, B. Cros, and Larry L. Stowe</i>	23
2:00	B3	Correcting for Interference of Mt. Pinatubo Aerosols on DIAL Measurements of Stratospheric Ozone <i>W. Steinbrecht and A. I. Carswell</i>	27
2:15	B4	A New Raman DIAL Technique for Measuring Stratospheric Ozone in the Presence of Volcanic Aerosols <i>Upendra N. Singh, Thomas J. McGee, Michael Gross, William S. Heaps, and Richard Ferrare</i>	31
2:30	B5	The JPL Table Mountain and Mauna Loa Stratospheric Ozone LIDARs <i>I. Stuart McDermid</i>	35
2:45-3:15		COFFEE BREAK	
3:15	B6	The NDSC Primary Site at the Observatoire de Haute-Provence: Ozone and Aerosols Observations (1986-1992) <i>G. Mégie, S. Godin, G. Ancellet, M. Beekmann, and A. M. Lacoste</i>	39
3:30	B7	Lidar Atmosphere Observatory in the Canadian Arctic <i>Arkady Ulitsky, Tin-Yu Wang, Martin Flood, and Brent Smith</i>	43
3:45	B8	Observation of Stratospheric Ozone with NIES Lidar System in Tsukuba, Japan <i>H. Nakane, S. Hayashida, Y. Sasano, N. Sugimoto, I. Matsui, and A. Minato</i>	45
4:00	B9	Observations of Ozone-Aerosol Correlated Behavior in the Lower Stratosphere During the EASOE Campaign <i>P. Di Girolamo, M. Cacciani, A. di Sarra, G. Fiocco, D. Fud, T. S. Joergensen, B. Knudsen, and N. Larsen</i>	49
4:15	B10	First Results from TROLIX '91: An Intercomparison of Tropospheric Ozone LIDARs <i>A. Apituley, J. Bösenberg, G. Ancellet, H. Edner, B. Galle, J. B. Bergwerff, G. von Cossart, J. Fiedler, C. N. de Jonge, J. Mellquist, V. Mitev, T. Schaberl, G. Sonnemann, J. Spakman, D. P. J. Swart, and E. Wallinder</i>	53

4:30-5:15

SESSION C: GLOBE

Session Chair:

Nobuo Takeuchi

4:30	C1	Global Backscatter Experiment (GLOBE) Results: Aerosol Backscatter Global Distribution and Wavelength Dependence <i>David A. Bowdle</i>	57
4:45	C2	The Global Backscatter Experiment Airborne Pulsed Lidar Measurements <i>James D. Spinhirne, S. Chudamani, Robert T. Menzies, and David M. Tratt</i>	61
5:00	C3	Multi-Wavelength Airborne Lidar Intercomparisons of Aerosol and CIRRUS Backscatter over the Pacific Ocean <i>Robert T. Menzies, David M. Tratt, James D. Spinhirne, and S. Chudamani</i>	63

5:15-7:00

SESSION D: POSTER PARTY #1

D1	Airborne Lidar Observations of the Stratosphere After the Pinatubo Eruption .. <i>David M. Winker, Mary T. Osborn, and Robert J. DeCoursey</i>	67
D2	Multiwavelength Measurements of the Stratospheric Aerosol Layer Made at Hampton, Virginia (37N, 76W) <i>G. S. Kent, G. M. Hansen, and K. M. Stevens</i>	71
D3	Three-Wavelength Lidar Measurements of Pinatubo Aerosol and its Optical Properties <i>Y. Sasano, I. Matsui, and S. Hayashida</i>	75
D4	Lidar Observations of the Pinatubo Stratospheric Aerosol Cloud Over Frascati, Italy <i>Fernando Congeduti, Alberto Adriani, Gian Paolo Gobbi, and Sante Centurioni</i>	79
D5	L625 Lidar Measurements of Pinatubo Volcanic Cloud at Hefei <i>Huanling Hu and Jun Zhou</i>	83
D6	Two Wavelength Measurements of the Pinatubo Aerosol above Toronto, Canada <i>W. Steinbrecht, D. Donovan, and A. I. Carswell</i>	87
D7	Lidar Observations of the Pinatubo Volcanic Cloud Over Hampton, Virginia .. <i>M. T. Osborn, D. M. Winker, D. C. Woods, and R. J. DeCoursey</i>	91

D8	Ozone Measurements with the U.S. EPA UV-DIAL: Preliminary Results	95
	<i>H. Moosmüller, D. Diebel, D. H. Bundy, M. P. Bristow, R. J. Alvarez II, V. A. Kovalev, C. M. Edmonds, R. M. Turner, and J. L. McElroy</i>	
D9	Lidar Development for the Atmospheric Radiation Measurement (ARM) Program	99
	<i>J. Griffin and M. Lapp</i>	
D10	Lidar Measurements of Stratospheric Ozone, Temperature and Aerosol During 1992 UARS Correlative Measurement Campaign	103
	<i>Thomas J. McGee, Upendra N. Singh, Michael Gross, William S. Heaps, and Richard Ferrare</i>	
D11	Airborne DIAL Remote Sensing of the Arctic Ozone Layer	107
	<i>Martin Wirth, Wolfgang Renger, and Gerhard Ehret</i>	
D12	Lidar Measurements of Stratospheric Ozone at Hohenpeissenberg -An Improved Evaluation Method-	109
	<i>W. Vandersee, F. Schönenborn, and H. Claude</i>	
D13	A Multi-Wavelength Ozone Lidar for the EASOE Experiment	113
	<i>S. Godin, G. Ancellet, C. David, J. Porteneuve, C. Leroy, V. Mitev, Y. Emery, C. Flesia, V. Rizi, G. Visconti, and L. Stefanutti</i>	
D14	Correction of DIAL Stratospheric Ozone Measurements in the Presence of Pinatubo Aerosols	117
	<i>Marta A. Fenn, Syed Ismail, Edward V. Browell, and Carolyn F. Butler</i>	
D15	The Laser Atmospheric Wind Sounder (LAWS) Preliminary Error Budget and Performance Estimate	121
	<i>David L. Kenyon and Kent Anderson</i>	
D16	Lag Angle Compensation in a Space Borne Scanning Lidar	125
	<i>A. B. Wissinger</i>	
D17	Lidar In-Space Technology Experiment (LITE) Electronics Overview	129
	<i>Michael P. Blythe, Richard H. Couch, Carroll W. Rowland, Wayne L. Kitchen, Curtis P. Regan, Michael R. Koch, Charles W. Antill, William T. Stevens, Courtney H. Rollins, Edward H. Kist, David M. Rosenbaum, Ruben W. Remus, and Clayton P. Turner</i>	
D18	Laser Transmitter Module (LTM) for LITE	133
	<i>John Chang, Marc Cimolino, Edmond Joe, Mulgeta Petros, Karl Reithmaier, Ray Thompson, and Ron Villane</i>	

D19	Intercomparisons of Lidar Backscatter Measurements and In-Situ Data from GLOBE	137
	<i>S. Chudamani and James D. Spinhirne</i>	
D20	Simulation of the Performances of WIND an Airborne CO ₂ Lidar	141
	<i>D. Oh, A. Dabas, F. Lieutaud, C. Loth, and P. H. Flamant</i>	
D21	Sampling and Representativeness for a Spaceborne Wind Lidar	145
	<i>F. Lieutaud, A. Dabas, P. H. Flamant, G. Seze, and Ph. Courtier</i>	
D22	Laboratory Velocimeter Measurements Using the Edge Technique	149
	<i>Bruce M. Gentry and C. Laurence Korb</i>	
D23	Identification of Critical Design Points for the EAP of a Space-Based Doppler Lidar Wind Sounder	153
	<i>G. D. Emmitt and S. A. Wood</i>	
D24	Wind Profiles Derived from Volume Imaging Lidar Data: Enhancements to the Algorithm and Comparisons with In-situ Observations	157
	<i>A. K. Piironen and E. W. Eloranta</i>	
D25	Measurements of Wind Divergence with Volume Imaging Lidar	161
	<i>P. W. Young and E. W. Eloranta</i>	
D26	DIAL Mapping of Atmospheric Atomic Mercury of Geophysical Origin	165
	<i>H. Edner, P. Ragnarson, S. Svanberg, and E. Wallinder</i>	
D27	Lidar Tracking of Multiple Fluorescent Tracers: Method and Field Test	169
	<i>Wynn L. Eberhard and Ron J. Willis</i>	
D28	Lidar Monitoring of Mexico City's Atmosphere During High Air Pollution Episodes	173
	<i>C. R. Quick, Jr., F. L. Archuleta, D. E. Hof, R. R. Karl, Jr., J. J. Tice, W. E. Eichinger, D. B. Holtkamp, and L. Tellier</i>	
D29	Lab-Scale Lidar Sensing of Diesel Engines Exhausts	177
	<i>A. Borghese</i>	
D30	Infrared Pulse-Laser Long-Path Absorption Measurement of Carbon Dioxide Using a Raman-Shifted Dye Laser	181
	<i>Atsuchi Minato, Nobuo Sugimoto, and Yasuhiro Sasano</i>	
D31	Transportable Lidar for the Measurement of Ozone Concentration and Flux Profiles in the Lower Troposphere	185
	<i>Yanzeng Zhao, James N. Howell, and R. Michael Hardesty</i>	

D32	Remote Detection of Biological Particles and Chemical Plumes Using UV Fluorescence Lidar	189
	<i>J. J. Tjee, D. E. Hof, R. R. Karl, R. J. Martinez, C. R. Quick, D. I. Cooper, W. E. Eichinger, and D. B. Holtkamp</i>	
D33	Signal Quality Influence on Averaging Procedure for DIAL Pollution Monitoring	193
	<i>S. Egert</i>	
D34	Extraction of Aerosol and Rayleigh Components from Doppler Lidar Return Signal	195
	<i>John E. Barnes, Ken W. Fischer, Vincent J. Abreu, and Wilbert R. Skinner</i>	
D35	Application of Laser Imaging for Bio/Geophysical Studies	199
	<i>J. R. Hummel, S. M. Goltz, N. L. DePiero, D. P. DeGloria, and F. M. Pagliughi</i>	
D36	ARCLITE: The Arctic Lidar Technology Facility at Søndre Strømfjord, Greenland	201
	<i>J. P. Thayer</i>	
D37	Rotational Raman Lidar for Lower Tropospheric Temperature Profiling	205
	<i>Takao Kobayashi, Takunori Taira, Takanobu Yamamoto, Akihiro Hori, and Toshinobu Kitada</i>	
D38	One Year of Rayleigh Lidar Measurements at Toronto	209
	<i>James A. Whiteway and Allan I. Carswell</i>	
D39	Lidar Observations of Aerosol and Temperature Stratification over Urban area During the Formation of a Stable Atmospheric PBL	213
	<i>I. Kolev, O. Parvanov, B. Kaprielov, V. Mitev, V. Simeonov, and I. Grigorov</i>	
D40	A Comparison Between Raman Lidar and Conventional Contact Measurements of Atmospheric Temperature	217
	<i>V. M. Mitev, V. B. Simeonov, and I. V. Grigorov</i>	
D41	Efficiencies of Rotational Raman, and Rayleigh Techniques for Laser Remote Sensing of the Atmospheric Temperature	221
	<i>I. D. Ivanova, L. L. Gurdev, and V. M. Mitev</i>	
D42	Lidar Investigation of Aerosol Pollution Distribution Near a Coal Power Plant ..	225
	<i>Ts. Mitsev and G. Kolarov</i>	
D43	Laser Remote Sensing of Pollution on Water Surfaces	229
	<i>A. F. Bunkin and A. I. Surovegin</i>	
D44	Correlation Analysis of Wind Lidar Data	233
	<i>R. P. Avramova</i>	

D45	A Developing Multiple-Wavelength Lidar for Detecting Mainly Ozone and Aerosol Distributions in the Stratosphere	237
	<i>Zheng Siping, Qiu Jinhuan, Wang Shufang, Huang Qirong, Wang Wenming, and Wu Shaoming</i>	
D46	An Extension of the Raman-Lidar Technique to Measure the Velocity and Temperature of the Atmospheric Emission Jets from Stacks	239
	<i>Yu. F. Arshinov, S. M. Bobrovnikov, V. K. Shumskii, A. G. Popov, and I. B. Serikov</i>	
D47	Lidar Observations of Stratospheric Clouds After Volcanic Eruption of Pinatubo	243
	<i>Sun Jinhui, Qiu Jinhuan, Xia Qilin, and Zhang Jinding</i>	
D48	In Vivo and In Vitro Chlorophyll-a and Pheophytin-a Concentration Measurements by Laser Fluorometry	247
	<i>A. A. Demidov, E. V. Baulin, and E. A. Chernyavskaya</i>	

8:30-10:15	SESSION E: LAWS/LITE		
	Session Chairs:		
	<i>Donald Bedo</i>		
	<i>William Vickery</i>		
8:30	E1	Science Goals and Mission Objectives of NASA's Laser Atmospheric Wind Sounder Program	251
		<i>Wayman E. Baker</i>	
8:45	E2	The Laser Atmospheric Wind Sounder (LAWS) Phase II Preliminary System Design	257
		<i>John C. Petheram, David L Kenyon, Alan B. Wissinger, and T. Rhidian Lawrence</i>	
9:00	E3	The Laser Atmospheric Wind Sounder (LAWS) Phase II Preliminary Laser Design	261
		<i>T. Rhidian Lawrence, Albert L. Pindroh, Mark S. Bowers, Terence E. DeHart, Kenneth F. McDonald, Ananda Cousins, and Stephen E. Moody</i>	
9:15	E4	G. E.'s Mobile, Coherent Doppler Lidar Test/Evaluation Facilities	265
		<i>J. T. Sroga, J. W. Scott, S. C. Kiernan, F. J. Weaver, J. E. Trotta, J. C. Petheram</i>	
9:30	E5	e-Beam Sustained Laser Technology for Space-Based Doppler Wind Lidar	269
		<i>M. J. Brown, W. Holman, R. J. Robinson, P. M. Schwarzenberger, I. M. Smith, S. Wallace, M. R. Harris, D. V. Willetts, and S. C. Kurzius</i>	
9:45-10:15	COFFEE BREAK		
10:15	E6	(Invited) The Lidar In-Space Technology Experiment (LITE)	273
		<i>M. Patrick McCormick</i>	
10:45	E7	System Testing and Performance Characterization of the LITE Laser Transmitter Module at NASA	277
		<i>Marc C. Cimolino and Mulugeta Petros</i>	
11:00	E8	Mechanical and Thermal Issues in the Development of a Spaceborne Lidar System	281
		<i>Joseph F. DeLorme</i>	
11:15-12:15	SESSION F: Stratospheric Measurements		
	Session Chair:		
	<i>Dennis Killinger</i>		

Tuesday, 21 July 1992

11:15	F1	Lidar Measurements of Aerosol and Ozone Distributions During the 1992 Airborne Arctic Stratospheric Expedition	285
		<i>E. V. Browell, C. F. Butler, M. A. Fenn, W. B. Grant, and A. F. Carter</i>	
11:30	F2	Airborne Lidar Measurements of Stratospheric Aerosols During the European Arctic Stratospheric Ozone Experiment (EASOE)	289
		<i>Wolfgang Renger, Gerhard Ehret, Peter Moerl, and Martin Wirth</i>	
11:45	F3	Aerosols and Polar Stratospheric Clouds Measurements During the EASOE Campaign	291
		<i>D. Haner, S. Godin, G. Mégie, C. David, and V. Mitev</i>	
12:00	F4	Lidar Observations of Polar Stratospheric Clouds and Stratospheric Temperatures at the South Pole	293
		<i>Richard L. Collins, Kenneth P. Bowman, and Chester S. Gardner</i>	

Tuesday Afternoon and Evening—Optional Activities

NASA has scheduled a special session on:

2 μ m Solid State Doppler Lidar Technology for Remote Sensing of Winds

The session will be held in Huntington Hall (Room 10-250) from 1:30-5:00 p.m. on Tuesday, and is open to all interested conference attendees.

8:30-2:00

SESSION G: Sodium, the Mesosphere, and the Middle Atmosphere

Session Chairs:

Marie-Lise Chanin

Phan Dao

8:30	G1	(Invited) Development of Mesospheric Sodium Laser Beacon for Atmospheric Adaptive Optics	297
		<i>T. H. Jeys</i>	
9:00	G2	Characterization of Artificial Guidestars Generated in the Mesospheric Sodium Layer	301
		<i>M. P. Jelonek, R. Q. Fugate, W. J. Lange, A. C. Slavin, R. E. Ruane, and R. A. Cleis</i>	
9:15	G3	Optical Pumping of Mesospheric Sodium: A New Measurement Capability ...	305
		<i>R. M. Heinrichs, T. H. Jeys, K. F. Wall, J. Korn, and T. C. Hotaling</i>	
9:30	G4	Lidar Probing of the Mesosphere: Simultaneous Observations of Sporadic Sodium and Ion Formations, Calcium Ion Layers, Neutral Temperature and Winds	309
		<i>Timothy J. Kane, Jun Qian, Daniel R. Scherrer, Daniel C. Senft, W. Matthew Pfenninger, George C. Papen, and Chester S. Gardner</i>	
9:45	G5	Lidar Measurements of Metallic Species in Mesopause Region	313
		<i>Chikao Nagasawa and Makoto Abo</i>	
10:00-10:30		COFFEE BREAK	
10:30	G6	Narrowband Lidar System for Measurement of Upper Mesosphere Temperatures and Winds	315
		<i>Daniel R. Scherrer, William M. Pfenninger, Daniel C. Senft, George C. Papen, and Chester C. Gardner</i>	
10:45	G7	Error Analysis of Wind Measurements for the University of Illinois Sodium Doppler Temperature System	317
		<i>W. Matthew Pfenninger and George C. Papen</i>	
11:00	G8	Sodium Doppler Temperature Lidar Observations of the Mesopause Region Temperature and Wind Structure	321
		<i>Daniel C. Senft, Daniel R. Scherrer, and Chester S. Gardner</i>	
11:15	G9	Airborne Sodium and Rayleigh Lidar Observations from ALOHA-90	325
		<i>Chris A. Hostetler and Chester S. Gardner</i>	

11:30	G10	Rayleigh/Raman Greenland Lidar Observations of Atmospheric Temperature During a Major Arctic Stratospheric Warming Event	329
		<i>John W. Meriwether, Robert Farley, Ross McNutt, Phan D. Dao, Warren P. Moskowitz, and Gilbert Davidson</i>	
11:45	G11	Elastic and Raman Lidar Temperature Measurements from Poker Flat, Alaska During February 1992	333
		<i>Michael Burka, Phan Dao, Gilbert Davidson, Robert Farley, John Meriwether, and Alex Wilson</i>	
12:00-1:15		LUNCH	
1:15	G12	(Invited) Rayleigh/Raman Lidars: Intercomparisons and Validation	337
		<i>Marie-Lise Chanin</i>	
1:45	G13	Wind Measurements from 15 to 50 KM with a Doppler Rayleigh Lidar	341
		<i>A. Garnier and M. L. Chanin</i>	
2:00-4:15		SESSION H: Clouds	
		Session Chairs:	
		<i>G. G. Koenig</i>	
		<i>Martin Platt</i>	
2:00	H1	Lidar Studies of Extinction in Clouds in the ECLIPS Project	345
		<i>C. M. R. Platt</i>	
2:15	H2	Lidar Studies of Clouds at Toronto During the ECLIPS Program	349
		<i>S. R. Pal, A. I. Carswell, A. Y. Fong, I. Pribluda, and W. Steinbrecht</i>	
2:30	H3	Adaptation of the University of Wisconsin High Spectral Resolution Lidar for Polarization and Multiple Scattering Measurements	353
		<i>E. W. Eloranta and P. K. Piironen</i>	
2:45	H4	Polarization Lidar Liquid Cloud Detection Algorithm for Winter Mountain Storms	357
		<i>Kenneth Sassen and Hongjie Zhao</i>	
3:00-3:15		COFFEE BREAK	
3:15	H5	Measurement of Mean or Effective Radius of Cloud Drop Size Distributions with a 10.6- μ m Wavelength Lidar	361
		<i>Wynn L. Eberhard</i>	

Wednesday, 22 July 1992

3:30	H6	Observations of CIRRUS Clouds over the Pacific Region by the NASA Multiwavelength Lidar System <i>Syed Ismail, Edward V. Browell, Marta A. Fenn, and Greg D. Nowicki</i>	365
3:35	H7	Diode - Pumped Nd: YAG Lidar for Airborne Cloud Measurements <i>A. Mehnert, Th. Halldorsson, H. Herrmann, R. Håring, W. Krichbaumer, J. Streicher, and Ch. Werner</i>	369
4:00	H8	Remote Sensing by Spaceborne Lidar Aided by Surface Returns <i>J. A. Reagan and T. W. Cooley</i>	373
4:15	H9	NWP Impact of Cloud Top and Boundary Layer Winds from a Satellite Borne Lidar: An Observing System Simulation Experiment <i>R. G. Isaacs, C. Grassotti, R. N. Hoffman, M. Mickelson, T. Nehr Korn, and J. -F. Louis</i>	377
4:30-5:30		Open Meeting of ICLAS	
7:00		BANQUET	

PART 2

8:30-12:00	SESSION I: Winds (Systems and Measurements)	
	Session Chairs: <i>Steven Alejandro</i> <i>William Snow</i>	
8:30	I1	Boundary Layer Structure over the Ocean Observed by Leandre During a Tramontane Event 381 <i>C. Flamant, J. Pelon, P. Flamant, and P. Durand</i>
8:45	I2	Low-Level Atmospheric Flows Studied by Pulsed Doppler Lidar 385 <i>Robert M. Banta, Lisa D. Olivier, and R. Michael Hardesty</i>
9:00	I3	On the Existence of Convectively Produced Gravity Waves 389 <i>Stephen P. Palm and S. H. Melfi</i>
9:15	I4	Doppler Lidar Wind Measurement with the Edge Technique 393 <i>C. Laurence Korb and Bruce M. Gentry</i>
9:30	I5	Tropospheric and Stratospheric Wind Profiling with a Direct Detection Doppler Lidar 397 <i>Vincent J. Abreu, John E. Barnes, Ken W. Fischer, Wilbert R. Skinner, and Matt J. McGill</i>
9:45	I6	Atmospheric Wind Sensing with a 1 and 2 μm Coherent Lidar 401 <i>R. Milton Huffaker and Sammy W. Henderson</i>
10:00-10:30	COFFEE BREAK	
10:30	I7	Design of a Near-IR Coherent Lidar for High Spatial and Velocity Resolution Wind Measurement 405 <i>Christian J. Grund and Madison J. Post</i>
10:45	I8	Boundary Layer Monitoring with a Compact Pulsed CO ₂ Doppler Lidar 409 <i>Guy N. Pearson</i>
11:00	I9	A Compact High Repetition Rate CO ₂ Coherent Doppler Lidar 413 <i>S. Alejandro, R. Frelin, B. Dix, and P. J. McNicholl</i>
11:15	I10	Simplified Signal Processing for an Airborne CO ₂ Doppler Lidar 417 <i>R. L. Schwiesow and M. P. Spowart</i>
11:45	I11	Phase Noise in Pulsed Doppler Lidar and Limitations on Achievable Single-Shot Velocity Accuracy 421 <i>P. McNicholl and S. Alejandro</i>

12:00	I12	A Comparison of Ultra-Sensitive Coherent Detection (USCD) and Heterodyne Detection for a Wind Sensing Application	425
		<i>Sherwin Amimoto, Rolf Gross, Bob Lacy, Lissa Garman-DuValle, and Tom Good</i>	
12:00-1:30		LUNCH	
1:30-3:00		SESSION J: Laser Imaging and Ranging	
		Session Chair: <i>Duane Smith</i>	
1:30	J1	(Invited) Diversity Imaging Techniques in Lidar	429
		<i>K. I. Schultz</i>	
2:00	J2	A Range-Resolved Bistatic Lidar Using a High-Sensitive CCD Camera	431
		<i>K. Yamaguchi, A. Nomura, Y. Saito, and T. Kano</i>	
2:15	J3	Fluorescence Lidar Multi-Color Imaging of Vegetation	433
		<i>J. Johansson, E. Wallinder, H. Edner, and S. Svanberg</i>	
2:30	J4	A Geodetic Laser Radar Rangefinder with 10^{-7} Resolution	437
		<i>Y. Mizushima, M. Takeichi, Y. Warashima, A. Takeshima, I. Ogawa, and K. Ichie</i>	
2:45	J5	Altimetry and Lidar Using AlGaAs Lasers Modulated with Pseudo-Random Codes	441
		<i>James B. Abshire, Jonathan A. R. Rall, and Serdar S. Manizade</i>	
3:00-3:15		COFFEE BREAK	
3:15-5:00		SESSION K: Multiple Scattering	
		Session Chair: <i>Michael Hardesty</i>	
3:15	K1	(Invited) Multiple Scattering Technique Lidar	447
		<i>Luc R. Bissonnette</i>	
3:45	K2	Multiple Scattering Effects on Spaceborne Lidar	451
		<i>David M. Winker and Lamont R. Poole</i>	
4:00	K3	Measurement of Multiple Scattering Effects with a Polarization Raman Elastic-Backscatter Lidar	455
		<i>Ulla Wandinger, Albert Ansmann, Claus Weitkamp, and Walfried Michaelis</i>	

4:15	K4	Determining Water Cloud Particle Sizes from Lidar Depolarization Measurements and Time Dependent Multiple Scattering Calculations	459
		<i>R. C. Garner and G. G. Koenig</i>	
4:30	K5	Multiple Scattering Lidar Returns from Stratus Clouds	463
		<i>D. L. Hutt and L. R. Bissonnette</i>	
4:45	K6	Analytical Multiple Scattering Correction to the Mie Theory: Application to the Analysis of the Lidar Signal	467
		<i>C. Flesia and P. Schwendimann</i>	
5:00-7:00	SESSION L: POSTER PARTY #2		
	L1	Airborne Lidar and Radiometric Observations of PBL-and Low Clouds	471
		<i>P. H. Flamant, R. Valentin, and J. Pelon</i>	
	L2	ECLIPS at LMD: Preliminary Results of Phase 2	475
		<i>R. Valentin, L. Menenger, S. Elouragini, P. H. Flamant, and J. Pelon</i>	
	L3	The 2nd Phase of the LEANDRE Program: Water-Vapor DIAL Measurement .	479
		<i>P. Quaglia, D. Bruneau, and J. Pelon</i>	
	L4	Advanced Raman Water Vapor Lidar	483
		<i>David N. Whiteman, S. Harvey melfi, Richard A. Ferrare, Keith A. Evans, Luis Ramos-Izquierdo, O. Glenn Staley, Raymond W. DiSilvestre, Inna Gorin, Kenneth R. Kirks, William A. Mamakos, Lewis S. Wan, Nita W. Walsh, James M. Marsh, and Richard L. Aldridge</i>	
	L5	Water Vapor Variance Measurements Using a Raman Lidar	485
		<i>K. Evans, S. H. Melfi, R. Ferrare, and D. Whiteman</i>	
	L6	Airborne Remote Sensing of Tropospheric Water Vapor Using a Near Infrared DIAL System	489
		<i>G. Ehret, C. Kiemle, W. Renger, and G. Simmet</i>	
	L7	Trial of a Slant Visual Range Measuring Device	493
		<i>J. Streicher, C. Munkel, and H. Borchardt</i>	
	L8	Lidar Depolarization by Nonspherical Particles: Potential of Combined Depolarization/Backscattering Measurements for PSC's Characteristics	497
		<i>C. Flesia, A. Mugnai, L. de Schoulepnikoff, and L. Stefanutti</i>	
	L9	Coherent CO ₂ Lidar: A Superior System for Observing Clouds?	501
		<i>Wynn L. Eberhard and R. Michael Hardesty</i>	
	L10	Measurements of Aerosol Profiles Using High-Spectral-Resolution Rayleigh-Mie Lidar	505
		<i>D. A. Krueger, R. J. Alvarez, II, L. M. Caldwell, and C. Y. She</i>	
	L11	Laboratory Scaled Simulation of Lidar Cloud Sounding Experiments	509
		<i>G. Zaccanti, P. Bruscazioni, M. Guriolo, and P. Sansoni</i>	

L12	An Alexandrite Regenerative Amplifier for Water Vapor and Temperature Measurements	513
	<i>P. -Y. Thro, J. Bösenberg, and V. Wulfmeyer</i>	
L13	Wavemeter Measurements of Frequency Stability of an Injection Seeded Alexandrite Laser for Pressure and Temperature Lidar	517
	<i>C. R. Prasad, G. K. Schwemmer, and C. L. Korb</i>	
L14	Conically Scanned Lidar Telescopes Using Holographic Optical Elements	521
	<i>Geary K. Schwemmer and Thomas D. Wilkerson</i>	
L15	Optics of the Ozone Lidar ELSA	525
	<i>J. Porteneuve</i>	
L16	Interferometers Adaptations to Lidars	529
	<i>J. Porteneuve</i>	
L17	An Ultra-Sensitive Coherent Detector Capable of Single Photon Detection for LIDAR Applications	533
	<i>Sherwin Amimoto, Rolf Gross, Bob Lacy, Lissa Garman-DuValle, and Tom Good</i>	
L18	A High Speed Signal Processing System for A Diode-Pumped YAG Lidar	537
	<i>H. Okumura, T. Sugita, H. Matsumoto, N. Takeuchi, and S. Kuwashima</i>	
L19	Pulsed Laser Spectral Measurement Using a Fabry-Perot Interferometer: Limits to Resolution	541
	<i>Anthony Notari and Bruce M. Gentry</i>	
L20	Tunable Electro-Optic Modulators for Lidar Systems and Atmospheric Applications	545
	<i>R. S. Eng, N. W. Harris, C. L. Summers, and B. Lax</i>	
L21	Injection Seeded Single Mode Alexandrite Ring Laser for Lidar Applications ..	549
	<i>H. Sang Lee and Anthony Notari</i>	
L22	Tm,Ho:YAG Laser with Tunable Range of 2.08-2.12 μm and its Applications to Spectroscopy	553
	<i>Kazuhiro Asai and Toshikazu Itabe</i>	
L23	Theoretical Simulation of a 2 μm Airborne Solid State Laser Anemometer	555
	<i>Béatrice Imbert and Jean-Pierre Cariou</i>	
L24	Comparison of Eye-Safe Solid State Laser Dial with Passive Gas Filter Correlation Measurements from Aircraft and Spacecraft	559
	<i>Robert V. Hess, Leo D. Staton, H. Andrew Wallio, and Liang-Guo Wang</i>	

L25	Lidar Multiple Scattering: Dependence on Atmospheric Parameters	563
	<i>Matthias Weigner</i>	
L26	Verification Measurement of a Polarization Raman Elastic-Backscatter Lidar ..	567
	<i>Christoph Schulze, Ulla Wandinger, Albert Ansmann, Claus Weitkamp, and Walfried Michaelis</i>	
L27	Time and Polarization Dependent Double Scattering Calculations of Lidar Returns from Water Clouds	571
	<i>R. C. Garner</i>	
L28	Multiple Scattering Wavelength Dependent Backscattering of Kaolin Dust in the I. R.: Measurements and Theory	575
	<i>Avishai Ben-David</i>	
L29	Aureole Lidar: Design, Operation, and Comparison with In-Situ Measurements.	579
	<i>William P. Hooper and D. R. Jensen</i>	
L30	Effect of Atmospheric Extinction on Laser Rangefinder Performance at 1.54 and 10.6 μm	581
	<i>D. L. Hutt, J. -M. Thériault, V. Larochelle, and D. Bonnier</i>	
L31	A Study of Atmospheric Optical Scattering Parameters at 1.5 and 2 Micron Region for Solid State Doppler Lidar Applications	585
	<i>Eli Margalit, Farzin Amzajerdian, Rodney Benoist, and Richard Dubinsky</i>	
L32	A Cable Detection Lidar System for Helicopters	589
	<i>Benoist Grossmann, Alain Capbern, Martin Defour, and Rémi Fertala</i>	
L33	Lidar Analysis Techniques for Use in the Atmospheric Boundary Layer	593
	<i>William E. Eichinger, Daniel I. Cooper, Doug Hof, David Holtkamp, Robert Quick, Jr., Joe Tice, and Robert Karl</i>	
L34	Correction for Nonlinear Photon Counting Effects in Lidar Systems	597
	<i>D. P. Donovan, J. A. Whiteway, and A. I. Carswell</i>	
L35	High Background Photon Counting Lidar	601
	<i>W. J. Lentz</i>	
L36	Development of a Raman Lidar Simulation Tool	605
	<i>R. J. Grasso and J. R. Hummel</i>	
L37	A Variable Phase Function Approach for the Inversion of Lidar Return Signals .	607
	<i>V. A. Kovalev and H. Moosmüller</i>	

L38	A Comparison of Lidar Inversion Methods for CIRRUS Applications	611
	<i>Salem Elouragini and Pierre H. Flamant</i>	
L39	Time and Wavelength Domain Algorithms for Chemical Analysis by Laser Radar	613
	<i>David L. Rosen and James B. Gillespie</i>	
L40	Lidar Receivers for Picosecond Remote Sensing	617
	<i>D. V. Stoyanov and T. N. Dreischuh</i>	
L41	Acousto-Optic Filtering of Lidar Signals	621
	<i>G. Kolarov, A. Deleva, and Ts. Mitsev</i>	
L42	Ground-Based Doppler Lidar of Increased Laser Instability: Conception and Design	625
	<i>D. V. Stoyanov, B. M. Bratanov, V. N. Naboko, and M. D. Angelova</i>	
L43	Analytical Estimates of the PP-Algorithm at Low Number of Doppler Periods Per Pulse Length	629
	<i>M. D. Angelova, E. V. Stoykova, and D. V. Stoyanov</i>	
L44	A Considerable Effect of Stratospheric Aerosol on Lidar-Detected Ozone Profile and a Three-Wavelength Inversion Technique for Both Ozone and Aerosol	633
	<i>Qiu Jinhuan</i>	
L45	High-Resolution Processing of Long-Pulse-Lidar Data	637
	<i>L. L. Gurdev, T. N. Dreischuh, and D. V. Stoyanov</i>	
L46	Lidar Measurements of Cloud Extinction Coefficient Distribution and its Forward Scattering Phase Function According to Multiply Scattered Lidar Returns	641
	<i>Qiu Jinhuan and Huang Qirong</i>	
L47	Measurements of the Backscattering Phase Matrices of Crystal Clouds with a Polarization Lidar	643
	<i>B. V. Kaul, A. L. Kuznetsov, and E. R. Polovtseva</i>	

8:30-10:00 **SESSION M: Systems and Facilities**

Session Chair:
Richard Schotland

8:30	M1	(Invited) Measurement Capabilities of Giant Lidars for Middle and Upper Atmospheric Applications <i>Chester S. Gardner</i>	647
9:00	M2	Lidar Sounding of Ozone and Aerosols <i>V. E. Zuev</i>	649
9:15	M3	Atmospheric Measurements Using the LAMP Lidar During the LADIMAS Campaign <i>C. R. Philbrick, D. B. Lysak, T. D. Stevens, P. A. T. Haris, and Y. -C. Rau</i>	651
9:30	M4	Lidar Measurements Using Large Liquid Mirror Telescopes <i>R. J. Sica, S. Sargoytchev, S. Flatt, E. Borra, and L. Girard</i>	655
9:45	M5	Spectroscopic Method for Earth-Satellite-Earth Laser Long-Path Absorption Measurements Using Retroreflector In Space (RIS) <i>Nobuo Sugimoto, Atsuchi Minato and Yasuhiro Sasano</i>	659

10:00-10:30 **COFFEE BREAK**

10:30-12:00 **SESSION N: Water Vapor Measurements**

Session Chair:
Wolfgang Renger

10:30	N1	Raman Lidar Measurements of Water Vapor and Aerosol/Clouds During the FIRE/SPECTRE Field Campaign <i>S. H. Melfi, D. Whiteman, R. Ferrare, K. Evans, J. E. M. Goldsmith, M. Lapp, and S. E. Bisson</i>	663
10:45	N2	Performance Modeling of Daytime Raman Lidar Systems for Profiling Atmospheric Water Vapor <i>J. E. M. Goldsmith and Richard A. Ferrare</i>	667
11:00	N3	BELINDA: Broadband Emission Lidar with Narrowband Determination of Absorption - A New Concept for Measuring Water Vapor and Temperature Profiles <i>F. A. Theopold, C. Weitkamp, and W. Michaelis</i>	671
11:15	N4	DIAL Simulations for Satellite Water Vapor Profile Measurements within the BEST Project <i>P. Chazette, J. Pelon, and G. Megie</i>	675

11:30	N5	Airborne Water Vapor DIAL Research: System Development and Field Measurements <i>Noah S. Higdon, Edward V. Browell, Patrick Ponsardin, Thomas H. Chyba, Benoist E. Grossmann, Carolyn F. Butler, Marta A. Fenn, Shane D. Mayor, Syed Ismail, and William B. Grant</i>	679
11:45	N6	Alexandrite Lidar for the Atmospheric Water Vapor Detection and Development of Powerful Tunable Sources in IR <i>M. Uchiuni, M. Maeda, K. Muraoka, and O. Uchino</i>	683
12:00-1:30	LUNCH		
1:30-3:15	SESSION O: Devices and Techniques		
	Session Chair: <i>Norman Menyuk</i>		
1:30	O1	(Invited) Emerging Solid-State Laser Technology for LIDAR/DIAL Remote Sensing <i>Dennis Killinger</i>	687
2:00	O2	Coherent Summation of Spatially Distorted Doppler Lidar Signals Using a Two-Dimensional Heterodyne Detector Array <i>Kin Pui Chan and Dennis K. Killinger</i>	689
2:15	O3	The Role of Laser Coherence in Long-Range Vibration Measurements <i>R. S. Eng, C. Freed, R. H. Kingston, K. I. Schultz, A. L. Kachelmyer, and W. E. Keicher</i>	691
2:30	O4	A Portable Lidar Using a Diode-Pumped YAG Laser <i>N. Takeuchi, H. Okumura, T. Sugita, H. Matsumoto, and S. Yamaguchi</i>	695
2:45	O5	Investigations on Atomic-Vapor-Filter High-Spectral-Resolution Lidar for Temperature Measurements <i>E. Voss and C. Weitkamp</i>	699
3:00	O6	HgCdTe Photomixers for CO ₂ Laser Radar Systems <i>Peter R. Bratt</i>	703
3:15-3:30	COFFEE BREAK		
3:30-5:00	SESSION P: Tropospheric Measurements		
	Session Chair: <i>Harvey Melfi</i>		
3:30	P1	Airborne Lidar Mapping of Vertical Ozone Distributions in Support of the 1990 Clean Air Act Amendments <i>Edward E. Uthe, Norman B. Nielsen, and John M. Livingston</i>	707

Friday, 24 July 1992

3:45	P2	Measurements of Fugitive Hydrocarbon Emissions with a Tunable Infrared DIAL	711
		<i>M. J. T. Milton, P. T. Woods, B. W. Jolliffe, N. R. W. Swann, and R. A. Robinson</i>	
4:00	P3	The ENEA CO ₂ LIDAR/DIAL Station Activity in a Tropospheric Remote Sensing Program	715
		<i>R. Barbini, F. Colao, A. Palucci, and S. Ribezzo</i>	
4:15	P4	Lidar Observation of Marine Mixed Layer	719
		<i>Susumu Yamagishi, Hiroshi Yamanouchi, and Masayuki Tsuchiya</i>	
4:30	P5	Aerosol Extinction Measurements with CO ₂ -Lidar	723
		<i>Arne Hågård and Rolf Persson</i>	
4:45	P6	Dense Fog on the Highway Visual Range Monitoring in Cars?	727
		<i>W. Hahn, W. Krichbaumer, J. Streicher, and Ch. Werner</i>	
5:00		ADJOURN	

THIRTY YEARS OF OPTICAL RADAR WORK:
REMINISCENCES AND PERSPECTIVES

Giorgio Fiocco
University of Rome "La Sapienza"

The work carried out at MIT between 1962 and 1969 towards the development of lidar and the subsequent evolution of some of those ideas will be outlined, starting from the successful experiments to obtain lunar echoes (Smullin & Fiocco 1962). For the purpose of studying the atmosphere several concepts appeared feasible. Some were demonstrated or studied to a certain depth: the basic measurement of the molecular and aerosol cross sections, the Raman technique, Doppler retrievals by either heterodyning or interferometric techniques of wind velocity, temperature and aerosol to molecules ratio, and feedback controlled telescopes to achieve large gains. Some geophysical results were also produced. Long series of observations of the stratospheric aerosol in the aftermath of the Mt. Agung eruption were carried out in 1964 and 1965. In 1964 and 1966, lidars were deployed in Sweden, Alaska and Norway, in attempts to detect stratospheric and noctilucent clouds. Much of the activity, however, had to be dedicated to the solution of new and sometimes unexpected technical problems, both in the hardware and in the software; and a large share of the credit for those projects that were successful, should be given to a few brave and hard-working graduate students of the time, particularly to Gerald Grams and Bart De Wolf. Many other groups had in the meanwhile progressively become active, all over the world. In perspective, continued support has been a key to success.

After a jump of more than 20 years, some new ideas and recent developments will be discussed. Among those, observations in the polar regions regarding ozone-aerosol interactions will be shown and compared with earlier work.

Keynote Speaker

**BOUNDARY LAYER STRUCTURE OVER THE OCEAN OBSERVED BY
LEANDRE 1 DURING A TRAMONTANE EVENT**

C. FLAMANT, J. PELON

Service d'Aéronomie du CNRS, Université Paris 6, T15 E5 B102, 4 Place Jussieu, 75252
Paris cedex 05,

P. FLAMANT

Laboratoire de Météorologie Dynamique du CNRS, Ecole Polytechnique, 91128 Palaiseau,
P. DURANDLaboratoire d'Aérodynamique, Université Paul Sabatier, 118 rte de Narbonne, 31062 Toulouse,
FRANCE

A new airborne backscatter lidar, has been developed by CNRS (Service d'Aéronomie, (SA) Laboratoire de Météorologie Dynamique (LMD) and the Institut des Sciences de l'Univers) in the frame of the LEANDRE research programme. It has been qualified on board the ARAT in autumn 1989 and spring 1990 and was involved in its first cooperative campaign during PYREX in October and November 1990. During this campaign, lidar observations of the perturbations induced on tropospheric flow and boundary layer structure were performed, and results will be presented.

The PYRENEES EXperiment was proposed by the French and Spanish Meteorological Services, Electricité de France and several CNRS laboratories (CRPE, LA, LMD, OPGC, SA). Its main objectives were to determine momentum budget and improve model representativeness for a 2D mountain flow perturbation (1). Cases analyzed during PYREX were thus related to perturbations of the atmospheric flow above the Pyrenees and induced flows around these mountains. A large number of experiments were performed, for synoptic situation description (meteorological radiosoundings, constant level balloons) and local flow analysis (aircrafts, radars, sodars). For a first time in such an experiment, a lidar has been flown on a research aircraft to perform altitude resolved observations of these perturbations, and we will present here results obtained for deflected flow structure.

In the presence of a synoptic northerly flow, part of it is deflected to the east by the Pyrenees, and accelerated over the Méditerranée by the mountain surroundings. In this case, a low level wind is generated (the Tramontane) bringing cold and dry air over the Mediterranean sea. As the sea is still at warm temperature in November (around 17 °), an Internal Marine Boundary Layer rapidly grows over the first tens of kilometers and stabilizes at about 1 km depth, corresponding to an altitude just below the Lifting Condensation Level. The whole MABL is characterized by highly turbulent motions bringing large humid particles from the surface up to its top. The lidar signal due to scattering by these particles is then representative of the turbulent kinetic energy in this layer. Observations have been performed on three main axes longitudinally and latitudinally orientated (see figure 1). Lidar measurements have been made on these flight tracks between points J1 and J4, at high level (3200 m) for nadir observation, and low level (450 m) for zenith and in situ measurements. A second Aircraft (Merlin IV from Meteo France) was performing in-situ measurements on the same tracks at 37 m and 940 m asl.

Results reported on figure 2 are relative to the southern part of the flow in a region where the MABL is well developed. Measurements have been obtained during cross wind tracks J3-J4 (see figure 1) performed during IOP 6. This leg corresponds to the weakening of the Tramontane near the shore due to mountain shielding. On the upper part (a) of the figure is represented the lidar MABL observation from the ARAT flying at an altitude of 3.2 km between 13.01 and 13.10 GMT. On the lower part (b) is shown moisture detrended series obtained at the top of the MABL by the Merlin IV.

Figure 2 clearly shows two regions, east and west of a longitude of 3.55 degrees. In the first part the signal measured by the lidar is quite intense, with condensation forming at the top of the MABL, represented as white regions. These are associated with vertical structures indicating the presence of organized motions. They correspond to cell size of about 3 km, giving a ratio of about 3, consistent with previous observations (see 2 for example). These structures are still observed in the second part of figure 2.a but with lower intensity as shown by the oscillation of the first black isocontour line. On figure 2.b, the series also show periodic modulation in the MABL moisture, which is a very good tracer of these motions as previously observed (2). Fluctuations of the water vapor mixing ratio in the entrainment zone are in good agreement with lidar structure observations although there is a time difference of about 45 mn between both measurements. Moisture registered at 940 m asl shows that this altitude is clearly within the entrainment zone east of 3.55 E, as evidenced by its large modulation, whereas it is above the MABL top for longitudes west of this point, which is consistent with the fact that the turbulent internal MABL height decreases as observed by lidar.

Effectively west of 3.50 E in longitude, the intensity of the wind is rapidly decreasing due to shielding by the Pyrenees (fig. 1). As a consequence, the surface fluxes decrease very rapidly, which can be materialized by the parabolic decrease of the MABL top as represented by the first black isocontour line. The second black isocontour, which height increases close to the mountain, appears to be related to a higher synoptic inversion as shown by the ARAT descent sounding.

Further analysis will be presented at the conference.

References

- (1) Bougeault P., A. Jansa Clar, B. Benech, B. Carissimo, J. Pelon, E. Richard, Momentum Budget over the Pyrénées : The PYREX experiment, Bull. Amer. Met. Soc., 71, 6, 806, 1990.
- (2) Melfi S. H., J. D. Spinhirne, S. H. Chou, S. P. Palm, Lidar observations of vertically organized convection in the planetary boundary layer over the ocean, J. Clim. Appl. Meteor., 24, 8, 806, 1985.

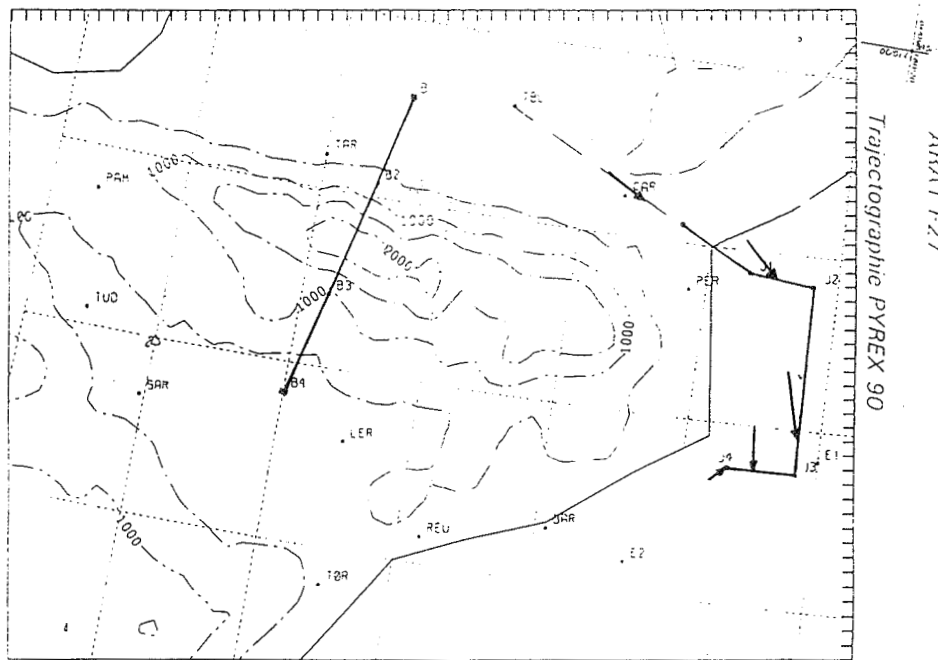


Figure 1 : ARAT and Merlin IV flight tracks and principal along track wind directions. The isocontours give the average mountain height.

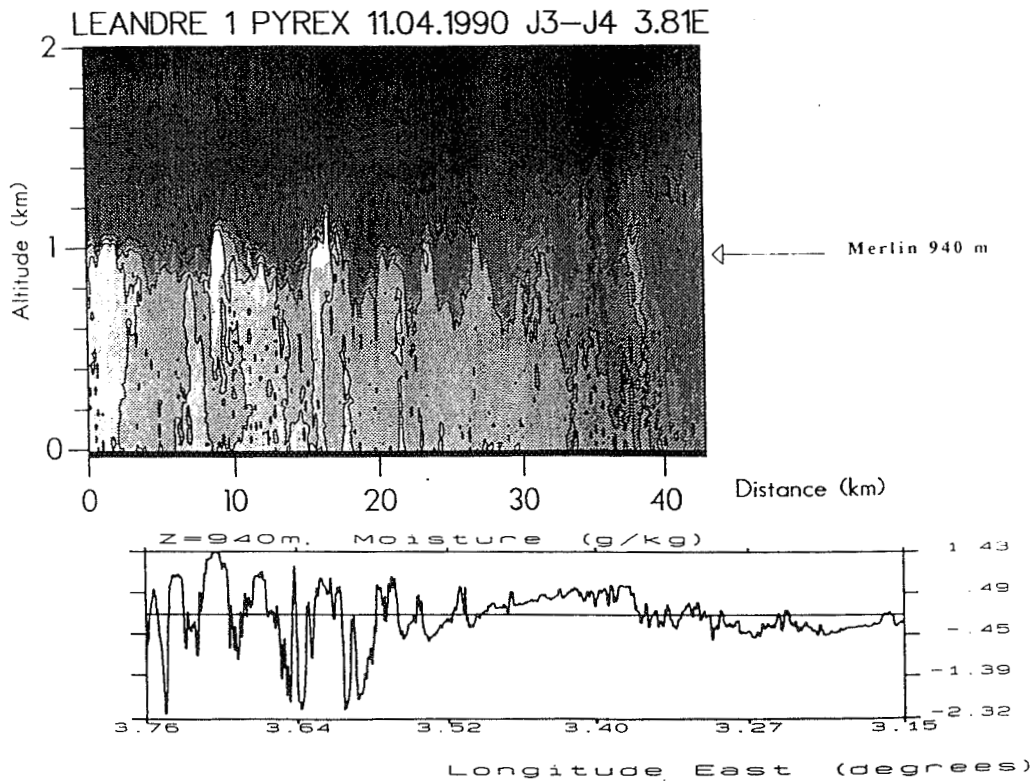


Figure 2 : Lidar and in-situ moisture measurements along east to west flight track J3-J4 as a function, of distance or decimal longitude. On the upper part (a) is represented the lidar MABL observation from the ARAT flying at an altitude of 3.2 km. On the lower part (b) is

Low-Level Atmospheric Flows Studied by Pulsed Doppler Lidar

Robert M. Banta, Lisa D. Olivier, and R. Michael Hardesty

NOAA/ERL Wave Propagation Laboratory
325 Broadway
Boulder CO 80303-3328

A pulsed Doppler lidar gains a tremendous advantage in studying atmospheric flows when it has the ability to scan. The Wave Propagation Laboratory (WPL) has been operating a scanning, 10.59 μm CO₂ system for over 10 years. During this time it has been used to study many phenomena including flow in mountain valleys, low-level flow leading to thunderstorm formation, and the structure of dry-line fronts. Recently the WPL lidar has been a featured instrument in several investigations of mesoscale wind fields in the lowest 3-4 km of the atmosphere. These include four experiments that will be discussed in this paper: a study on the initiation and growth of the sea breeze off the coast of California, a study of the smoke column of a prescribed forest fire, a study of the nighttime flow over the complex terrain near Rocky Flats, Colorado, as it affects the dispersion of atmospheric contaminants, and a study of the wind flow in the Grand Canyon. We have analyzed much data from each of these experiments, and we have found that the lidar provides new insight into the structure of these flows. Many of these studies took place in rugged or mountainous terrain, thus using one of the major benefits of the lidar: the narrow, 90 μrad beam of the lidar makes it an ideal instrument for studying flow close to topography.

Monterey Bay Sea Breeze

The sea breeze along the northern and central California coast is different from the sea breeze in many other parts of the world. Current understanding of the structure of the sea breeze is based largely on observations in these other regions. Main differences include very cold waters off the coast, mountain ranges just inland, and a very hot interior valley to the east of these mountains in central California. The cold waters produce a very stable temperature profile in the atmospheric boundary layer (ABL), and suppress vertical motions in the flow near the ground.

A major aspect of current understanding of sea-breeze structure is the presence of a compensatory return-flow layer blowing back out to sea above the sea breeze. Although many studies of sea-breeze structure have described the return flow as "difficult to find," they have been reluctant to conclude that the return flow was not there.

In the Monterey Bay study, the Doppler lidar performed range-height scans to observe the region above the sea breeze in the morning and early afternoon on several days (Banta et al. 1992). The scans produced vertical slices of Doppler wind data perpendicular to the coastline. In this plane the Doppler velocities represent the onshore and offshore component of the flow. The sea breeze layer was clearly observed to begin as a very shallow layer of less than 50 m height at the coast and to grow horizontally and vertically as the day proceeded.

No return flow was observed by the lidar. The significance of this is that the return current aloft, which was supposed to be "required" by theory for mass balance, is actually required only in a closed system where mass compensation must be local. In an open system such as the atmosphere, a return flow, though sometimes observed, is not required. Lidar range-height scans provide fine-scale measurements of layers in the atmosphere. These measurements allowed us to conclude with confidence that the return flow was absent in the Monterey Bay sea breeze observations.

Prescribed Forest Fire in Battersby Township, Ontario, Canada

The interior of the vertical column of hot gases over a large fire, called the convection column by fire scientists, is a very difficult region in which to obtain observations. Such observations are important, however, for understanding and improving predictions of fire behavior. Vertical velocity in the column, rotation of the column, and wind flow into the base of the column are some of the measurements needed for numerical fire-prediction models.

To test the feasibility of using CO₂ Doppler lidar to study fires, we observed a prescribed forest fire in northern Ontario, Canada (Banta et al. 1992). The lidar performed very well. Horizontal scans of Doppler velocity through the base of the nearly vertical convection column showed convergent flow into the base of the column and column rotation that was independently observed by time lapse video recordings. Vertical slices of Doppler winds through the convection column were analyzed to determine vertical updraft speeds and flow streamlines in and near the column. Figure 1 is a streamline and flow vector analysis. Because of the symmetry of the convection column we were able to estimate peak updraft speeds of 15 m s⁻¹, 24 m s⁻¹, and 10 m s⁻¹ at three different times during the fire.

Mountain Drainage Winds at Rocky Flats, Colorado

The Rocky Flats plant northwest of Denver, Colorado, uses hazardous materials in manufacturing plutonium devices. Because of the risk of accidental releases into the atmosphere, it is crucial to have atmospheric transport models that can predict the spread of such materials. A wintertime atmospheric measurement program, including tracer releases and surface-wind and wind-profile measurements, was carried out in conjunction with the Department of Energy's Atmospheric Studies in Complex Terrain (ASCOT) program. The purposes of the experiment were (1) to provide a wind and tracer data set to verify the Rocky Flats and other atmospheric transport models and (2) to study the meteorology of cold-air drainage flow as it exits canyons and moves onto adjacent plains.

Rocky Flats is located on the plains about 10 km east of the Front Range. Two canyons, Eldorado Canyon 10 km to the west-northwest and Coal Creek Canyon 10 km to the west-southwest, empty onto the plains in the vicinity of Rocky Flats. We suspected that Coal Creek Canyon would have the major influence on flow over Rocky Flats.

WPL's Doppler lidar scanned the region along the foothills and over Rocky Flats from a site just northeast of Rocky Flats. The lidar provided vertical profiles of the horizontal wind, vertical slices of the flow field, and three-dimensional, high-resolution volumes of the flow field between Rocky Flats and the mountains.

We analyzed data from a night (February 5, 1991) with light winds aloft in order to study the effects of thermally forced flows, i.e., downslope and downvalley flows that are forced by cooling at the Earth's surface. Lidar measurements of the wind field between the Front Range and Rocky Flats indicated a major unexpected contribution from Eldorado Canyon. Since the major flow was expected from Coal Creek Canyon, the Eldorado Canyon flow was not well sampled in the data from the other instruments. The scanning capability of the lidar allowed the flow from Eldorado Canyon to be studied even though the experiment had not been set up to investigate this flow.

The lidar data documented the space and time scales of the small-scale flow systems that affected the transport of atmospheric contaminants over Rocky Flats on this night. The drainage jet that streamed out of Eldorado Canyon was 2-3 km wide and changed significantly over time periods of a half hour. The flow from Coal Creek Canyon also changed considerably over time. The lidar documented the complex series of events involving the strengthening and dissipating of the canyon flows at different times. Even the orientation of the flow from Eldorado Canyon changed with time (flow to the southeast and then to the east). These findings have important implications for designing a meteorological measurement program in complex terrain. Instrumentation that is spaced more than 1-2 km apart may miss important phenomena, and similarly, data that are taken at intervals of greater than 20-30 min may

miss important stages in the evolution of small-scale flows.

Such results are also important in providing wind data to be used in atmospheric dispersion models. If important features of the flow are undersampled and therefore absent in the wind data set, then the predicted transport could be considerably in error. In future studies we shall attempt to assess the potential seriousness of these errors by comparing predictions of tracer concentrations using surface and radiosonde wind data with and without lidar data.

Flow in the Bottom of the Grand Canyon

WPL deployed the Doppler lidar to the south rim of the Grand Canyon to look north toward Marble Canyon, where the Colorado River gorge opens into the Grand Canyon. The main objective of this experiment was to find out whether visibility in the Grand Canyon would improve if a coal-burning power plant at Page, Arizona (about 50 mi north of the canyon), reduced its emissions. The lidar scanned into the canyon and observed the along-canyon flow to the north. The instrument also scanned into the canyon to the northwest, where it detected cross-canyon flow that was often opposite in direction to the flow at rimtop, and it scanned above the rim to the northeast, where it monitored the buildup of haze over the Painted Desert. Data from two periods, late January and early March, have been analyzed intensively and integrated with other remote sensing (UHF profiler) and conventional (tethersonde) data taken by WPL, as well as upper-air and surface-station data taken by other groups. During early March, the synoptic winds were very light for over a week. The lidar found a jet of northerly (down-canyon) flow in the bottom of the canyon (Banta et al. 1991a, 1991b). The jet intensified at night and weakened or reversed during the day, indicating that it was forced by nighttime cooling at the Earth's surface.

The Doppler lidar has documented the complete three-dimensional structure and time dependence of flow in the Grand Canyon during an intensive observation period, a feat that would have been extremely difficult and costly in this rugged and inaccessible environment with conventional instrumentation. During early March, evidence of the plume from the power plant was detected at the Grand Canyon one morning. The light winds measured outside the canyon during the previous night were not persistent enough from a northeasterly direction to explain the transport. During this night, however, the lidar observed a steady flow of 3 m s^{-1} down the canyon. These measurements show that along-canyon transport was a possible mechanism for moving material from the vicinity of Page into the Grand Canyon, although further measurements would be required to prove this. Without the lidar's ability to scan down into otherwise inaccessible reaches of the canyon, this important piece of information would be missing.

Conclusions

Pulsed Doppler lidar has proved to be a valuable tool for studying atmospheric flows over complex terrain and in inaccessible places. Kinematic fields revealed by the lidar provide valuable insight into the physical mechanisms that drive the flows. An important application of the fine-resolution data that can be obtained from the lidar is in the initiation and verification of sophisticated dynamic numerical models of atmospheric flows. These models have also been an important tool for studying the dynamics of flows, but fine-resolution observations to compare with their fine-resolution predicted fields have been lacking. Doppler lidar data will certainly be able to fill this void.

References

Banta, R. M., and L.D. Olivier, 1991: Doppler lidar observations of air flow in the Grand Canyon. *Papers from the 84th Annual Meeting. Volume 2, Atmospheric Monitoring and Measurement*. 16-21 June 1991, Vancouver, British Columbia. Air and Waste Management Association, Pittsburgh PA.

Banta, R.M., L.D. Olivier, and W.D. Neff, 1991: Flow in the Grand Canyon and other valleys as revealed by Doppler lidar. *Preprint Volume, 7th Joint Conference on Applications of Air Pollution Meteorology with AWMA*, New Orleans LA, 14-18 January. American Meteorological Society, Boston, MA, J210-J213.

Banta, R.M., L.D. Olivier, E.T. Holloway, R.A. Kropfli, B.W. Bartram, R.E. Cupp, and M.J. Post, 1992: Smoke column observations from two forest fires using Doppler lidar and Doppler radar. *J. Appl. Meteor.*, **30**, accepted for publication.

Banta, R.M., L.D. Olivier, and D.H. Levinson, 1992: Evolution of the Monterey sea-breeze layer as observed by pulsed Doppler lidar. *J. Atmos. Sci.*, submitted for publication.

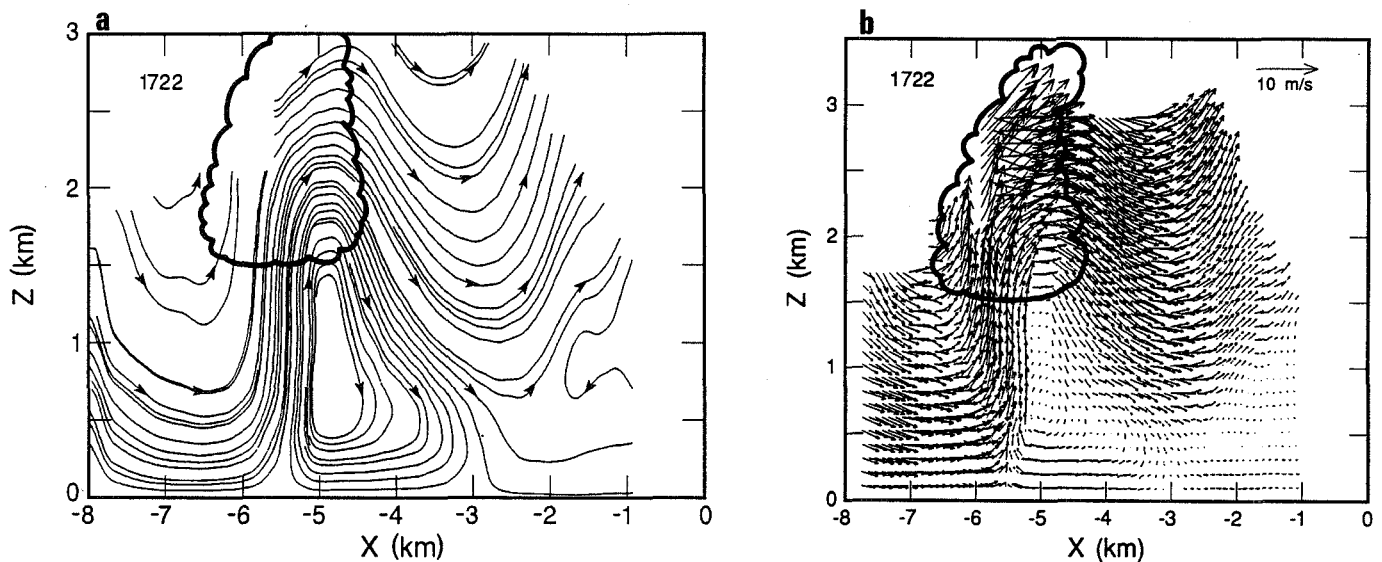


Figure 1: Vertical cross-section of the u_r and w components of the wind along the 223.4° azimuth radial. The lidar was located at (0,0). Lidar-measured radial velocity was transformed from polar coordinates to a 50 m by 50 m Cartesian grid. Assuming the cross-beam divergence was zero, the w component of the wind was calculated by continuity. The bold line indicates the estimated position of a capping cumulus cloud. (a) Streamlines. (b) Vectors.

On the Existence of Convectively Produced Gravity Waves.

Stephen P. Palm
Science Systems and Applications Inc.
Lanham, Maryland 20706
301-286-4277

S. H. Melfi
Laboratory for Atmospheres, Code 917
Goddard Space Flight Center
Greenbelt, Maryland 20771
301-286-6348

I Introduction

During the winter of 1990 NASA/Goddard collaborated with NCAR and NASA/Langley to study a phenomenon known as convection waves. Previous research on this subject has indicated that under the proper conditions, convective cells within a heated boundary layer can act as obstructions to the flow in the free troposphere and produce gravity waves. This conclusion was based, in large part, on the experiences of glider pilots who would often find that after soaring up through cumulus clouds, they could continue their ascent to heights that greatly exceeded the depth of the convective layer. Since strong convective motions do not in general exist above the Planetary Boundary Layer (PBL), how is it that the glider pilots can penetrate through the capping stable layer and continue to experience lift? The most probable answer to this question is that the glider pilots were soaring through gravity waves produced by the convection below.

Convection waves are an exact analogy to the more well known mountain lee waves, where the convective cell replaces the mountain. However, for a convective cell to act as an obstruction to the flow, there must be a substantial difference in momentum between the flow in the PBL and that of the free troposphere above. Therefore, only when substantial windshear exists between the two layers would one expect to find convection waves. Because lee waves can extract energy from the general circulation and because convection waves may exist in great numbers, it follows that the later may play an important role in general circulation energetics as well. Kuettner et al (1987) conducted an experiment to verify the existence and investigate the nature of convection waves. By correlating vertical velocity measurements with radiometer data, they were able to show a relationship between the occurrence of cumulus clouds at the top of the convective layer and gravity waves a few km above the clouds. However, they lacked the instrumentation necessary to definitively link the presence of the gravity waves in the troposphere to individual convective cells in the PBL.

II Experiment Design

In January of 1990, the Convective Waves Experiment (COWEX) was organized as a follow up study to address the still unanswered questions about these waves. Three research aircraft were utilized including the NASA Electra which carried the Boundary Layer Lidar System (BLLS) and a gustprobe system. The BLLS is ideally suited for the investigation of convection waves since it can provide a unique cross sectional snapshot of the vertical structure of atmospheric aerosol from just below the plane to the ground. The two other NCAR aircraft provided additional gustprobe measurements and vertical profiles of temperature and moisture. Figure 1 is a GOES image of the experiment area on 17 February, 1990 with the flight

tracks of the NASA Electra superimposed. The winds in the PBL were from the north at 10-12 m/s and the winds in the lower troposphere were from the west-northwest at 15-18 m/s. This produces a shear vector which is very nearly alligned along the southwest to northeast flight segments (BC, DE and FG).

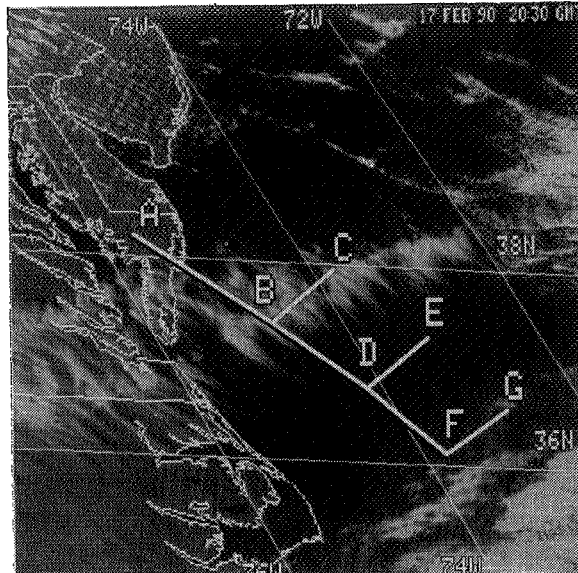


Figure 1. A GOES eye view of the COWEX area on 17 Feb 1990, at 20:30 GMT showing the aircraft flight pattern.

The design of COWEX called for the research aircraft to be deployed during cold air outbreaks so that a well defined convective layer would exist over the warmer ocean water and vertical windshear would also be present. The most desirable conditions were that of cloud streets which frequently occur off the mid Atlantic coast during wintertime cold air outbreaks. The winter of 1990 was unseasonably warm for the eastern half of the US and, unfortunately, no cloud street formation occurred during the 6 weeks allotted for COWEX.

III Lidar Data

Figure 2 shows BLLS normalized backscatter data acquired during COWEX displayed in a black and white image format where the largest return signal is shown as white. The signal then decreases through shades of grey such that the smallest value is dark grey or black. Clearly seen in the figure is the convective layer below about 800 m with a well defined gravity wave above it between 1200 and 2000 m. This exciting image vividly shows, for the first time, a gravity wave above a convective layer which is obviously correlated with the convective activity below. These data were taken along flight segment ED at about 21:58 GMT. To verify that the undulating layer above the PBL in figure 2 is indeed a gravity wave, we plotted the height of the uppermost aerosol layer detected by the lidar with the vertical velocity measured simultaneously by the gustprobe onboard the Electra flying along ED at 2600 m. Figure 3 shows the undulation in the uppermost aerosol layer (1600 m above the ground) at about 86 km into the flight line and also shows the peak in vertical velocity occurring at about 88 km. The relative motion of the layer above the PBL is from right to left in the figure. Therefore, one would expect the maximum vertical velocity to be seen on the upwind side of this perturbation. Moreover, if it is a

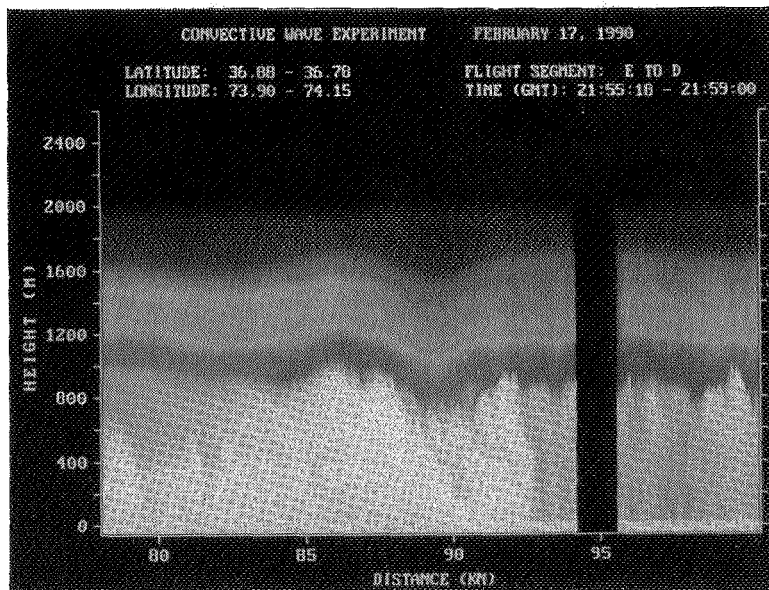


Figure 2. Lidar backscatter return, in image form for a portion of flight segment ED.

gravity wave and it had no tilt in the vertical then one would expect the vertical velocity measured a kilometer above to be exactly 90 degrees out of phase with the aerosol layer height. This is precisely what is seen in figure 3. About an hour later, the Electra again passed over the same region, this time flying about a kilometer higher (3700 m). Figure 4 now shows a more well developed wave structure with 3 complete wavelengths evident. Also, notice the relationship of the convection in the PBL to the gravity wave above. Normally, the dominate scale of the convective cells is between 2-4 times the PBL depth, in this case 1.6-3.2 km. These scales are

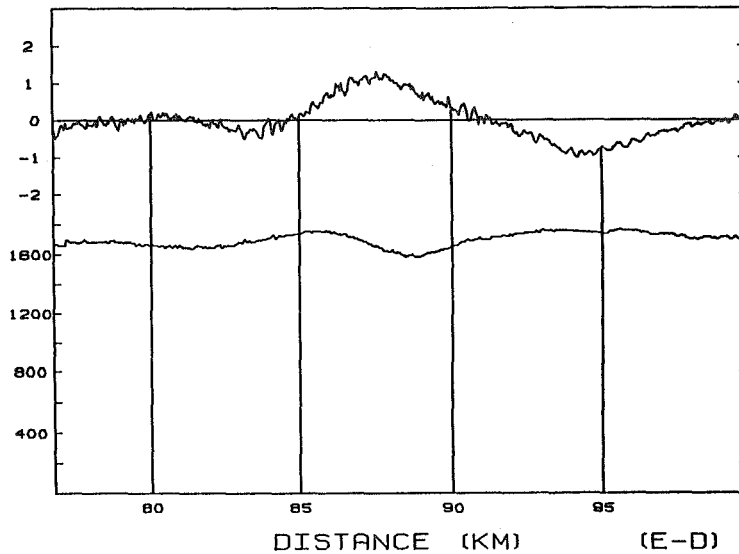


Figure 3. Gustprobe measured vertical velocity (m/s) at 2600 m and lidar derived aerosol layer height (m) for the data segment shown in figure 2.

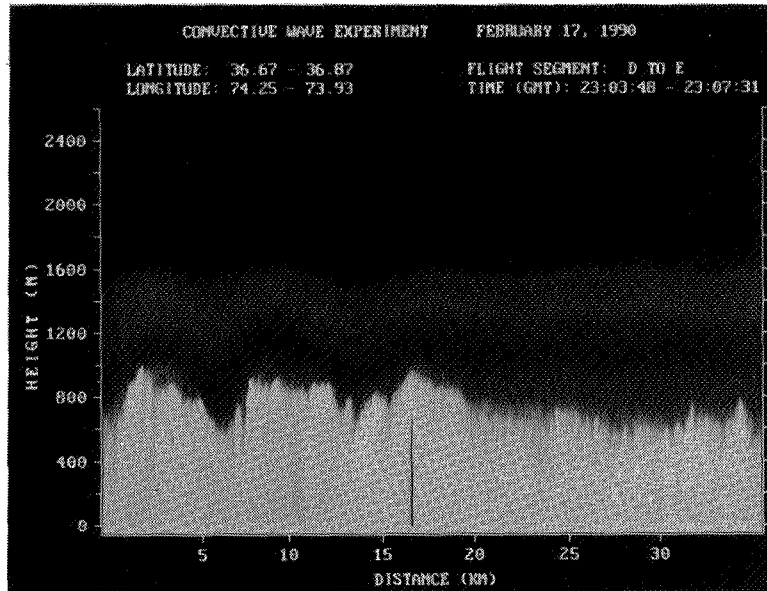


Figure 4. Same as figure 2, except for flight segment DE.

indeed seen in the data, but they tend to be organized into another, larger scale which corresponds exactly to the wavelength of the gravity wave (6-7 km). This indicates that the gravity wave has an organizing influence on the convection within the PBL. Interestingly, we did not measure a strong signal in the vertical velocity above the waves in figure 4. We believe the reason for this is that the waves are trapped by an almost neutral layer between 2000 and 2400 m. Above this layer, the wave energy decays exponentially and at 3.7 km, the vertical velocity amplitude is undetectable. However, when we fly at a lower altitude, as we had on segment ED, the vertical velocity signal is still strong enough to measure.

IV Summary and Conclusion

The BLLS together with the gustprobe system onboard the NASA Electra has acquired a unique data set which, for the first time, clearly depicts a gravity wave above a convectively driven PBL. In addition, we believe the data show the development of a trapped gravity wave over a period of about an hour. If this is the case, it would certainly be the first time such a process has ever been seen in the atmosphere. We also conclude that the gravity wave, while being initiated by the convection in the PBL, ultimately acts to organize and control convective scales in the PBL.

V Reference

Kuettner, J.P., P.A. Hildebrand and T.L. Clark, 1987, Convection waves: Observations of gravity wave systems over convectively active boundary layers. Q.J.R. Meteorol. Soc. 113, pp. 445-467.

Acknowledgements

The authors would like to recognize the co-investigators in the COWEX project, without whom these measurements would not have been possible: Dr. Reinout Boers, presently with CSIRO, Mordialloc, Australia; Dr John Ritter, NASA/Langley research center; Dr. Joachim Kuettner at NCAR, Boulder, Colorado and Dr Robert Grossman, also with NCAR.

Doppler Lidar Wind Measurement with the Edge Technique

C. Laurence Korb and Bruce M. Gentry

NASA/Goddard Space Flight Center
Laboratory for Atmospheres
Code 917
Greenbelt, MD 20771

(301) 286-6233

(301) 286-6842

The edge technique is a new and powerful method for measuring small frequency shifts. Range resolved lidar measurements of winds can be made with high accuracy and high vertical resolution using the edge technique to measure the Doppler shift of an atmospheric backscattered signal from a pulsed laser. The edge technique can be used at near-infrared or visible wavelengths using well developed solid state lasers and detectors with various edge filters.

In the edge technique, the laser frequency is located on the steep slope of the spectral response function of a high resolution optical filter. Due to the steep slope of the edge, very small frequency shifts cause large changes in measured signal. The frequency of the outgoing laser pulse is determined by measuring its location on the edge of the filter. This is accomplished by sending a small portion of the beam to the edge detection setup (see Figure 1) where the incoming light is split into two channels - an edge filter and an energy monitor channel. The energy monitor signal is used to normalize the edge filter signal for magnitude. The laser return backscattered from the atmosphere is collected by a telescope and directed through the edge detection setup to determine its frequency (location on the edge) in a similar manner for each range element. The Doppler shift, and thus the wind, is determined from a differential measurement of the frequency of the outgoing laser pulse and the frequency of the laser return backscattered from the atmosphere.

The differential frequency technique which is used to measure the Doppler shift renders the measurement insensitive to laser and filter frequency jitter and drift. The Doppler shift can be measured to an accuracy that is of the order of one hundred times better than the spectral bandwidth of the measurement. The edge measurement is also insensitive to the spectral width of the laser provided the width is smaller than the characteristic width of the edge filter¹. We have demonstrated these characteristics with recent laboratory measurements at an accuracy level of 10 to 20 cm/sec. The relatively broad laser spectral width that can be used with the edge technique permits a proportionately shorter (100 times) transform limited temporal pulse width and a corresponding improvement in range (vertical) resolution. A lidar system utilizing the edge technique in the visible and near infrared would obtain orders of magnitude larger signal than in the thermal infrared. For a system working at ultraviolet wavelengths, the Rayleigh backscatter would provide an even larger signal.

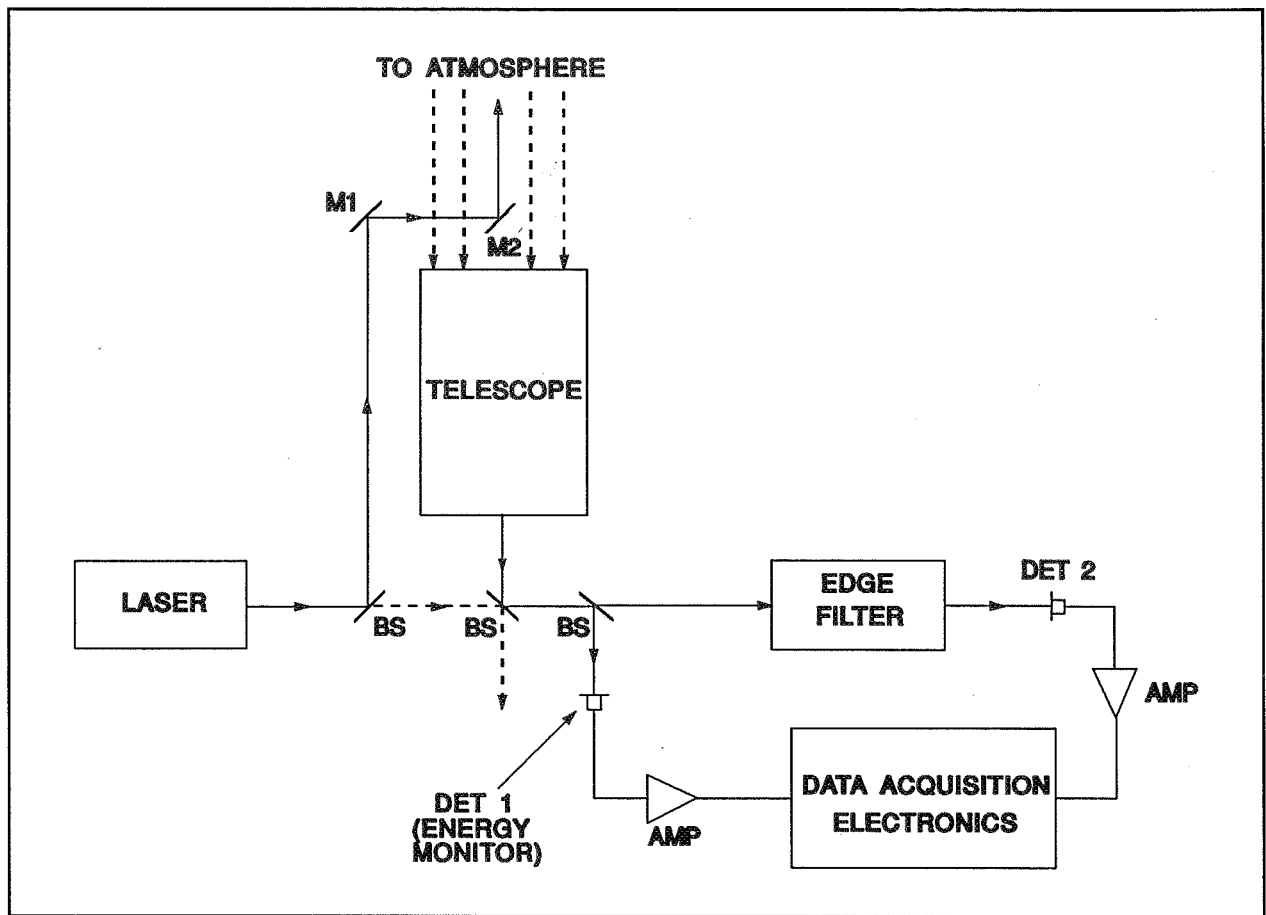


Figure 1 - Block diagram of the optical layout for a lidar using the edge technique.

We have conducted simulations of the performance of an edge lidar system using an injection seeded pulsed Nd:YAG laser at $1.06 \mu\text{m}$. The central fringe of a Fabry-Perot etalon is used as a high resolution edge filter to measure the shift of the aerosol return. The edge technique does not require a spectral scan since the edge filter is used as a static spectral filter which allows the laser energy to be used on that portion of the edge which has high sensitivity to the Doppler shift. We define the sensitivity as the fractional change in signal as observed by the edge filter for a velocity of 1 m/sec. For a high resolution etalon with a spectral width of 0.0033 cm^{-1} (FWHH), the sensitivity is 4% near the etalon half-width. The physical significance of the sensitivity is that if a 1% measurement of the normalized edge filter signal is made, the corresponding velocity accuracy is 25 cm/sec.

The error ϵ in the line of sight wind velocity at a given position on the edge can be found from the sensitivity (θ) and the signal to noise (S/N) for the differential edge measurement as $\epsilon = 1/(S/N * \theta)$. The signals backscattered from the atmosphere were calculated for a ground-based upward viewing lidar system utilizing a Nd:YAG laser at $1.06 \mu\text{m}$ with a pulse energy of 0.8 J per pulse, a telescope with a diameter of 0.4 m, an etalon with a spectral width of 0.0033 cm^{-1} (FWHH), and avalanche photodiode detectors

with quantum efficiency of 0.4. The simulations are for the AFGL clear air aerosol model. The outgoing laser frequency is located near the half-width of the etalon fringe where the sensitivity is a maximum (4%/(m/sec)).

The error in the horizontal component of the wind for an elevation angle of 50 degrees is shown as a function of range (altitude) in Figure 2. The velocity errors are shown for measurements with the Doppler shifted laser frequency located on the edge at 0.5, 1.0, and 2.0 etalon half widths (HWHH) from the center of the etalon fringe. Optimum accuracy is obtained at the half width (x=1) as expected for a high resolution laser. We note that x=1 corresponds to the case of low wind velocities. For a 100m vertical resolution and a 100 shot average, an accuracy of better than 0.5 m/sec is obtained from the ground to an altitude of nearly 20 km.

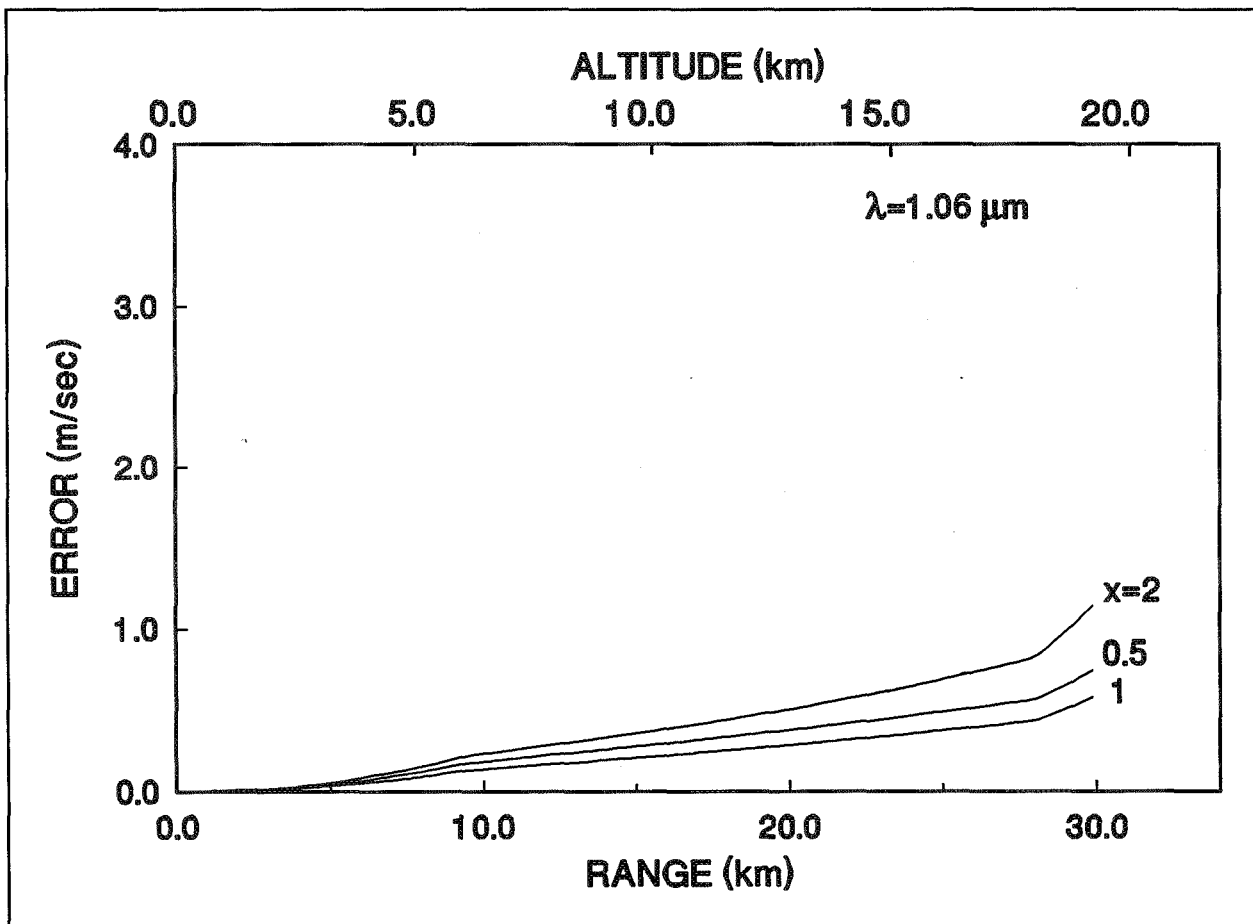


Figure 2 - Errors in the horizontal wind velocity at 1.06 μm for a 100 m vertical resolution and a 100 shot average for the laser frequency at various locations on the edge of an etalon fringe with a width of 0.0033cm^{-1} .

For studies of winds in the lower atmosphere even higher vertical resolution and accuracy can be obtained. Figure 3 shows simulations of errors for measurement of the

vertical component of the wind in the boundary layer. For a vertical resolution of 20 m and a 2 shot average, an accuracy of better than 15 cm/sec is obtained for a measurement near the half-width.

This represents a powerful new capability which could be used to directly observe winds with very high spatial resolution (20 m) and accuracy (15 cm/sec) which will allow studies of turbulent motion and convective processes in the lower atmosphere. We are currently building such a system. In addition, the edge technique could be utilized for satellite wind measurements using an injection-seeded Nd:YAG laser at $1.06 \mu\text{m}$ with a 1 km vertical resolution and an accuracy of 1 m/sec in the troposphere.

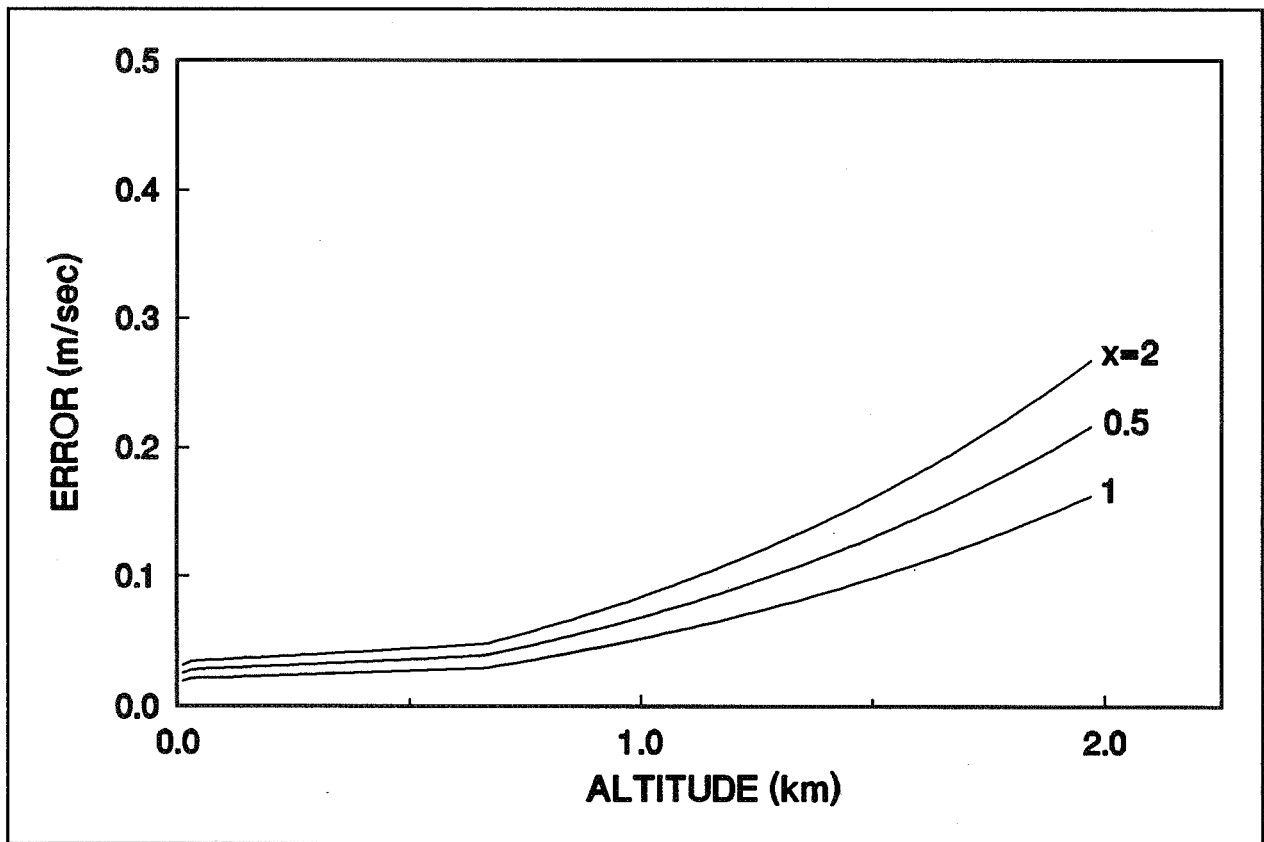


Figure 3 - Errors in the vertical wind velocity at $1.06 \mu\text{m}$ for a 20 m vertical resolution and a 2 shot average for the laser frequency at various locations on the edge of an etalon fringe with a width of 0.0033cm^{-1} .

REFERENCES

1. Korb, C. L., B. M. Gentry, and C. Y. Weng, "The Edge Technique - Theory and application to the lidar measurement of atmospheric winds", accepted for publication in *Appl. Opt.*.

TROPOSPHERIC AND STRATOSPHERIC WIND PROFILING WITH A DIRECT DETECTION DOPPLER LIDAR

Vincent J. Abreu, John E. Barnes, Ken W. Fischer,
Wilbert R. Skinner, Matt J. McGill

Department of Atmospheric, Oceanic and Space Sciences
Space Physics Research Laboratory
The University of Michigan
Ann Arbor, Michigan 48109-2143

The Space Physics Research Laboratory at the University of Michigan has been operating a direct detection, high resolution Doppler Lidar (HRDL) to measure winds in the boundary layer, free troposphere and lower stratosphere. A direct detection Doppler lidar measures the Doppler shift of the aerosol or Rayleigh backscattered signal, from which the wind velocity vector can be retrieved (Benedetti-Michelangeli et al., 1972, 1974; Chanin et al., 1989; Abreu et al., 1992). The system components are shown in Fig. 1.

The transmitting system is a Continuum NY-60 Nd:YAG laser frequency doubled to a wavelength of 532 nm. The laser is injection seeded for single line mode operation yielding a linewidth of 0.0045 cm^{-1} (135 MHz) with excellent shot-to-shot frequency stability. The laser produces 60 mJ pulses and operates at a 50 Hz repetition rate for an effective output power of 3.0 W. The beam is expanded to 1 cm diameter and the divergence half angle set to 0.5 mrad using a telephoto pair of lenses near the output aperture of the laser head. Expanding the beam also prevents damage to the beam steering optics. The outgoing beam is brought coaxial with the telescope axis using a system of high-power laser mirrors. The laser is fired coaxial with the telescope in the "monostatic" configuration to make the system easier to align. Final beam direction is controlled by a mirror scanning system which, through computer control, permits viewing geometries from zenith to horizon at all azimuth angles.

The front end of the receiving system comprises the same mirror scanning system as is used for the transmitting portion of the system in order to coalign the transmitted and backscattered beams. The backscattered

signal is received by an Odyssey 2, 44.5 cm, f/4.5, Newtonian Astronomical telescope. From the telescope, the light passes through a optical fiber bundle which provides a more uniform illumination of the system. The beam is then expanded and collimated, filtered for daylight with a solid etalon Daystar filter and low resolution etalon using a telephoto lens pair. The daylight filtering capability can be removed for maximum efficiency during nighttime operation. The light is then fed into the high resolution Fabry-Perot which has a spacing of 10 cm. and a diameter of 9.6 cm.

The ring pattern from the Fabry-Perot etalon is projected by a telephoto lens pair onto the Image Plane Detector (Killeen et al., 1983). The IPD anode geometry is matched to the ring pattern produced by the Fabry-Perot etalon, and the IPD effectively carries out a wavelength scan of the backscattered signal. The detector is composed of thirty-two concentric ring anodes, each having equal areas, such that the spatial scan is linear in wavelength. At this time only the central twelve anodes are used. The amplification of an arriving photon is accomplished by a micro-channel plate biased with respect to the anodes. Photons are counted on each of the twelve anodes simultaneously. The array of anodes is 4.0 cm in diameter and the detector is cooled to -10 C to reduce thermal noise. To prevent the detector from becoming saturated by the intense low-altitude return signal when the laser fires, the photocathode voltage is lowered to reduce the number of photoelectrons incident on the microchannel plate, thus effectively reducing the quantum efficiency. The detector is switched to the nominal voltage 10 μ sec after the laser has fired to record high altitude data at full sensitivity. A fraction of the Fabry-Perot's free spectral range can be projected onto the detector. This is equivalent to reducing the width of the detector rings and consequently improves the accuracy with which the wind can be measured (Hays et al., 1984). The fraction can be adjusted to minimize the wind error or optimize aerosol measurements.

The analysis procedure consists of determining the peak position of a spectrum measured for a given altitude and direction. The difference between this peak position and the unshifted reference laser line determines the component of the wind speed. The analysis will show that Doppler shifts can be measured which are much smaller than a single channel.

A description of the University of Michigan's Doppler lidar is given with examples of wind profiles for the boundary layer, free troposphere and

and for the lower stratosphere. The system provides a reliable method of remotely measuring the wind. The wind error is smallest in regions of high aerosols. The system also produces aerosol extinction profiles versus altitude which can be determined by the shape of the spectra. The aerosol analysis is being presented at this conference in another paper (Barnes et al).

The system has been installed in a trailer so that measurements can be made for field campaigns. Winds and aerosol data are available immediately at the site for use in forecasting.

References

- Abreu, V. J., J. E. Barnes, and P. B. Hays, 1992: Observations of Winds with an Incoherent Lidar Detector. *Applied Optics*, accepted for publication.
- Benedetti-Michelangeli, G., F. Congedati, and G. Fiocco, 1986: Measurement of aerosol motion and wind velocity in the lower troposphere by Doppler optical lidar. *J. Atmos. Sci.*, **29**, 906-910.
- Benedetti-Michelangeli, G., F. Congedati, and G. Fiocco, 1974: Determination of vertical eddy diffusion parameters by Doppler optical radar. *Atmos. Environ.*, **8**, 793-799.
- Chanin, M. L., A. Garnier, A. Hautecorne, and J. Porteneuve, 1989: A Doppler Lidar for Measuring Winds in the Middle Atmosphere. *J. Geophys. Res.* **16**, 1273-1276.
- Hays, P. B., V. J. Abreu, J. Stroga and A. Rosenberg, 1984: Analysis of a 0.5 micron spaceborne wind sensor. *Proceedings of Conference on Satellite Meteorology/Remote Sensing and Applications*, Clearwater Beach, FL, June 25-29, 266-271.
- Killeen, T. L., B. C. Kennedy, P. B. Hays, D. A. Symanow, and D. H. Ceckowski, 1983: Image plane detector for the Dynamics Explorer Fabry-Perot interferometer. *Appl. Opt.*, **22**, 3503-3517.

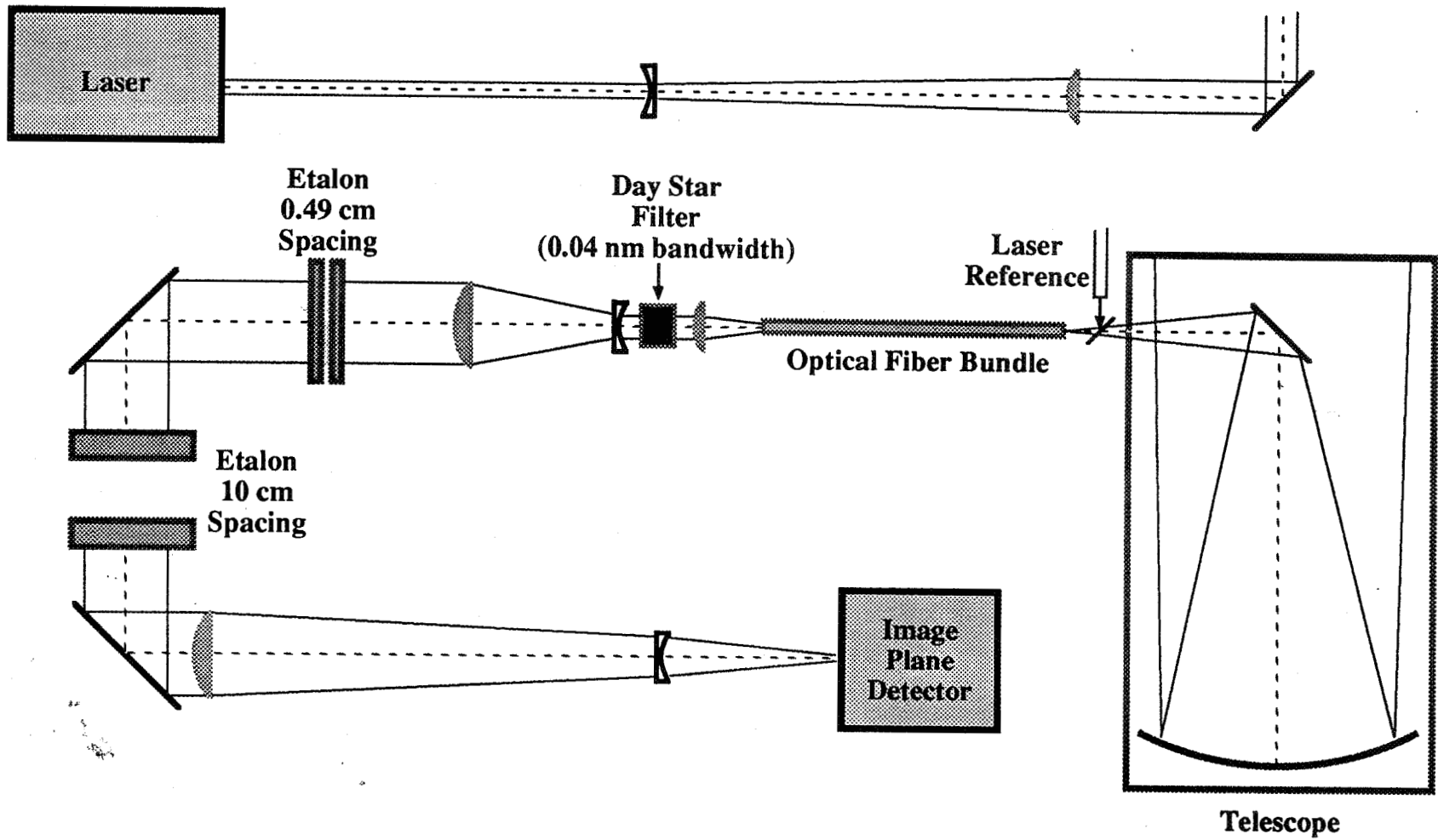


FIGURE 1. University of Michigan High Resolution Doppler Lidar

ATMOSPHERIC WIND SENSING WITH A
1 AND 2 μm COHERENT LIDAR

R. Milton Huffaker
Sammy W. Henderson
Coherent Technologies, Inc.
Boulder, Colorado

Background

The majority of coherent lidar remote sensing performed to date has utilized CO_2 gas laser technology at wavelengths of 9-11 μm . However, the use of rapidly developing solid-state laser technology and their shorter wavelengths offers many potential advantages. These advantages include low mass, small size, long shelf and operating lifetimes, the absence of consumables, and in many cases, increased atmospheric transmission. The shorter wavelengths of solid-state lasers allow velocity measurements having better range resolution for equivalent wind velocity resolution. Coherent Technologies, Inc. has developed a 1.06 and 2.1 μm coherent lidar system for remote wind field measurements.

Nd:YAG 1.06 μm Coherent Lidar

The 1.06 μm solid-state coherent lidar at CTI developed under funding from the U.S. Air Force, utilizes a diode-pumped CW master oscillator and a high gain multiple-pass flashlamp-pumped Nd:YAG slab amplifier. A photograph of the 1.06 μm coherent lidar transceiver is shown in Figure 1. Under NASA funding, additional amplifiers were added to increase the output energy from 200 mJ/pulse to 1 J/pulse.

Our numerical lidar simulation codes have been used to predict that this level of energy should allow ground-based measurement of atmospheric winds to altitudes of 20 km. The high energy system was taken to Cape Canaveral in September, 1991 for wind profile measurement during the launch and landing period of the space shuttle. An example of the wind profiling capability is shown in Figure 2. The figure shows the wind speed and direction vs altitude as measured by the ground-based 1.06 μm coherent lidar system compared to that measured by a rawinsonde launched 20 km distance from the lidar. The horizontal wind speed was measured with the lidar system by scanning the beam in an upward-pointing Velocity Azimuth Display (VAD) conical scan with the code half-angle being 10° . The agreement between the coherent lidar and the rawinsonde is excellent up to ~ 26 km in altitude.

Cr,Tm,Ho:YAG 2.09 μm Flashlamp-Pumped Coherent Lidar

CTI demonstrated the first working coherent lidar using Tm,Ho:YAG lasers operating at the eyesafe wavelength of 2.09 μm . This system utilizes a diode-pumped master oscillator and a flashlamp-pumped slave oscillator. The system is in the injection-seeded configuration with the master oscillator used to injection seed the slave oscillator, driving it into single-longitudinal-mode operation. The detector used in this system operates at room temperature and has a quantum efficiency of $\sim 70\%$.

The system has demonstrated accurate velocity and range measuring capability during preliminary field tests. Results to date include horizontal atmospheric wind measurements to 30 km, vertical atmospheric aerosol returns to 10 km, near-horizontal cloud returns to 100 km, and hard target (mountainside) returns from 145 km. All these returns were obtained with a transmitted pulse energy at 2.09 μm of only ~ 20 mJ. The long range cloud and mountainside returns indicate very high atmospheric transmission of 2.09 μm .

The high SNR velocity accuracy of this system is ~ 11 cm/s even though the transmitted pulse length is only ~ 200 ns. Figure 3 shows an interesting example of atmospheric wind measured with the 2.09 μm lidar system. The lidar beam was aimed approximately horizontal, and the beam terminated on a mountainside located 16.5 km from the coherent lidar. The gust front seen in the figure was felt at the lidar location 10-15 minutes after the data was taken. Note the estimated radial velocity of 0 m/s at 16.5 km (the location of the mountainside). Beyond the mountainside the velocity estimates experience large fluctuations due to the lack of signal.

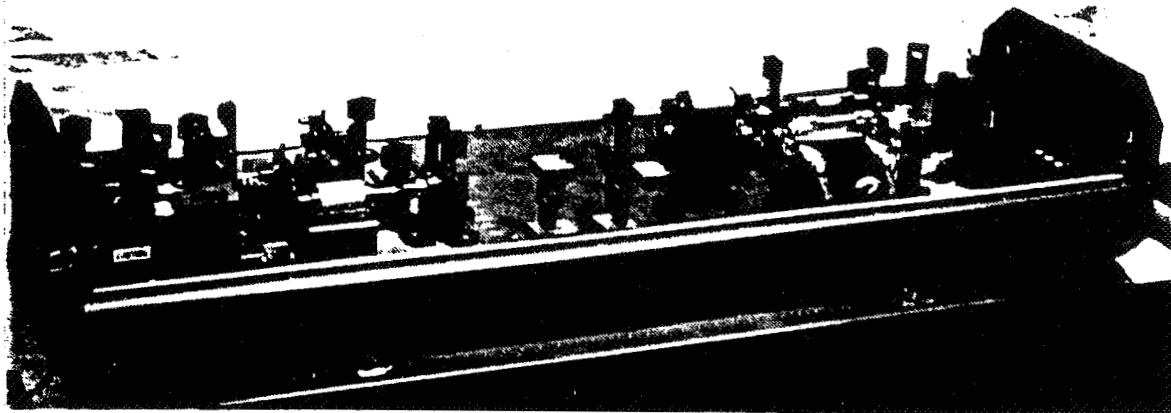


Figure 1 Nd:YAG 1.06 μm Coherent Laser Radar Transceiver

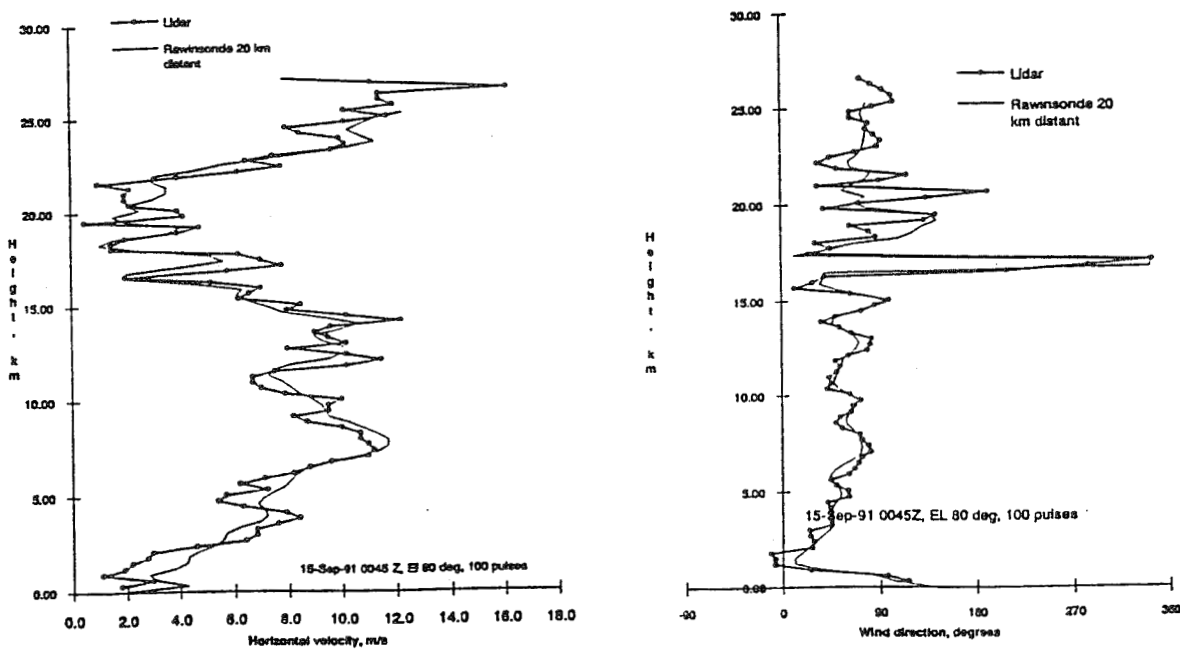


Figure 2 Wind Profiling Capability of the 1-J 1.06 μm Coherent Laser Radar

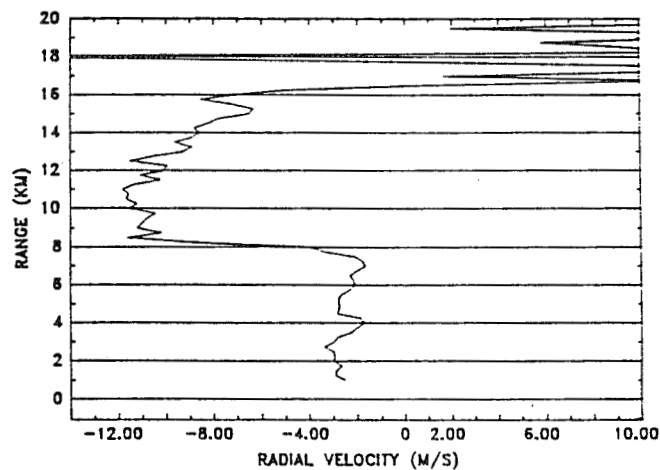


Figure 3 Winds Measured with the Tm, Ho:YAG Lidar Showing a Strong Gust Front

Design of a Near-IR Coherent Lidar for High Spatial and Velocity Resolution Wind Measurement

Christian J. Grund and Madison J. Post
 NOAA/ERL Wave Propagation Laboratory
 325 Broadway, Boulder, CO 80303
 (303) 497 - 6870

I. Introduction and Background

Weather and climate are largely shaped by the exchange of heat, moisture, and momentum between earth's surface and the atmosphere. Air quality and global climate studies depend on knowledge of the sources, sinks, and turbulent exchange processes for greenhouse gasses and pollutants in the atmosphere. Much of our present knowledge of these processes is based on measurement of the fluxes of these quantities carried out using in situ sensors on aircraft and supported by towers and tethered balloons and by radar, sodar, and lidar remote sensors. Recently, large eddy simulation models (Moeng and Wyngaard, 1988) have added significantly to the understanding of these exchange processes. Significant improvements in the spatial, temporal, and velocity resolution of current measurement techniques for determining wind and species concentration fluctuations will result in a better understanding of these processes and provide adequate data sets from which to test improved theories and models of turbulent transfer. Remote flux measurement instruments using, for example, eddy correlation techniques could fulfill these measurement needs.

Since 1981, a CO₂ coherent lidar system operating in the 9-11 μm region has provided wind measurements with 0.6 m/s accuracy at 450 m range resolution (Post and Cupp, 1990). Shortening the pulse length to provide 60 m resolution results in wind measurements accurate to ~ 2.2 m/s. Poor frequency estimation during the gain-switched spike and frequency chirp throughout the pulse are believed to be responsible for this limitation. System weight (~ 3000 kg), size (~ 9 m³), and power consumption (~ 7 kW without display and computer) limit deployment to sites accessible by semi-trailer. Also, water vapor continuum near 10 μm limits range under humid conditions, and small ambient aerosol size parameter reduces sensitivity in the upper troposphere.

Consequently, a coherent Doppler lidar based on a CW diode-pumped, injection seeded, Th:YAG laser operating at ~ 2.02 μm is currently under development. This system is optimized for measurements of boundary layer winds with high spatial, temporal, and velocity resolution. Initially the system will be run alongside a new high repetition rate (5-10 kHz) CO₂ mini-MOPA Doppler lidar (Pearson, et al, 1990) which will provide simultaneous range-resolved DIAL water vapor measurements. Water vapor DIAL operation of the 2 μm system is being considered as a future option.

II. Design trades

The operating wavelength region was chosen for several reasons. For a given wind velocity, V , the Doppler frequency shift, Δf_{Dop} , is inversely proportional to the laser wavelength ($\Delta f_{\text{Dop}} = 2V / \lambda$), while the Fourier transform width of a fixed pulse length, τ_p , is constant with wavelength ($\Delta f_p = 1 / 2\pi\tau_p$). This suggests operation at a shorter wavelength facilitates improved velocity estimates with greater range resolution. Because routine field operations in conjunction with aircraft are anticipated, the system requires complete eye-safety at the transmitted energy density ($\sim 6 \times 10^{-5}$ J/cm²), suggesting operation at wavelengths longer than 1.4 μm . Eye-safe UV wavelengths are not suitable because the requirement on optics quality for coherent detection become severe, background skylight can pose some additional noise problems, and loss of coherence in the beam due to propagation through moderate turbulence would cause severe reductions in signal to noise under average boundary layer conditions. Because the maximum range required exceeds 10 km, operation at a wavelength where the one way atmospheric absorption < 0.04 km⁻¹ is advisable, suggesting the 1.5 - 1.7 μm or 2.0 - 2.3 μm regions (see Fig. 1).

Diode-pumping was chosen because of the moderately high repetition rate (> 200 Hz) required to facilitate speckle noise reduction by averaging and to implement rapid volume and sector scans, while minimizing the cooling requirements on the laser crystal. High heat removal capacity would demand large water flows that could cause troublesome cavity vibration leading to frequency jitter.

Th:YAG was chosen as a laser material for several reasons. The solid state nature of the medium and the efficient diode pumping capability lend themselves to a robust and stable system design. Injection seeded, Q-switched lasers and transmitters for coherent lidar systems have been demonstrated using this and similar materials (Kane et al., 1990; Henderson et al., 1991). Th:YAG was chosen over Th,Ho:YAG primarily because the latter system requires significant cooling to achieve good efficiencies. Although cooling improves the efficiency of Th:YAG, it is capable of reasonably good room temperature operation, a consideration for field operation under adverse environmental conditions.

Injection seeding was chosen over a master-oscillator power-amplifier design because diode-pumped Th:YAG produces a relatively low gain system.

III. Anticipated Specifications

Radial velocity measurement range:	≤ 1 cm/s to ≥ 50 m/s
Velocity measurement accuracy:	± 0.5 cm/s (averaging applied)
Measurement range:	≥ 10 km
Range resolution:	≤ 30 m
Pulse repetition frequency:	100-300 Hz
Operating wavelength:	~ 2.02 μ m, Th:YAG
Transmitted pulse energy:	10-20 mJ

The lower extreme for wind speed measurement will allow direct observations of subsidence and divergence from aerosol backscatter in relatively clear air and of ice crystal fall speeds in cirrus. With the anticipated frequency purity and stability of this system, we expect to achieve the specified velocity resolution by incoherent accumulation (~ 625 profiles or ~ 3.2 seconds at 200 Hz, and 0 dB wide-band SNR per shot. See Rye and Hardesty (1992) for estimation procedure). It appears the required atmospheric transparency can be reached at 2.0218 μ m and potential future DIAL operations can be conducted near the water vapor line at 2.02165 μ m (see Fig. 2). The operational wavelength will be set and maintained with a commercial wavemeter based on a Michelson interferometer.

IV. Preliminary Design

Figure 3 shows a schematic of the preliminary design for the 2 μ m coherent lidar system. Two samples of light from a narrow-bandwidth frequency-stable CW reference oscillator (RO) are split from the main RO beam by a holographic beamsplitter. The samples provide input for the wavemeter and a local oscillator signal for the output pulse frequency detector (D2). The RO is a reentrant-cavity single 785 nm diode-pumped temperature-stabilized Th:YAG laser containing two solid etalons to insure single frequency operation over a wide tuning range (Coherent Technologies Inc., Boulder, CO). It is specified to produce > 100 mW with 10 kHz bandwidth over 2.01 - 2.024 μ m. The main RO beam passes to a 95% reflecting beam splitter through a variable attenuator. The majority of the RO beam power is then used for injection seeding the slave oscillator after passing through a Faraday isolator and undergoing a ~ 100 Mhz frequency shift in an acousto-optic modulator. In this configuration, seed light is injected into the slave laser cavity through the cavity output coupler ($\sim 5\%$) via another holographic diffraction grating. Other more efficient and less costly injection methods are under consideration.

The slave oscillator is a plano-concave design with the output mirror supported by a piezo-electric translator (PZT) and the rear mirror ground onto the 4 mm diameter, 13 mm long, 3% doped Th:YAG rod. The rod is encased in an Al (possibly Cu) block which contains 2 TE coolers. The TE coolers will have heat removed by a moderate chilled water flow. The spherical rod end has a dielectric coating producing high reflection at 2.02 μ m and high transmission at the pump wavelength

of 785 nm. Initially, the spherical end mirror will be a discrete component to allow experimentation with cavity parameters.

The rod is pumped from both ends through dichroic reflectors from two 400 μm diameter optical fibers each delivering 10 W of CW optical power into a 0.22 NA cone. Each half of the pump assembly contains five 3 W 785 nm room temperature diode lasers, optics to shape the beams and efficiently couple into the fiber, and cooling for the diodes (Lightwave Electronics Inc., Mountain View, CA). The optical quality of the pump beam dictates a 1.53 mm diameter mode volume in the crystal (Fan and Sanchez, 1990). The cavity length is ~ 600 mm and contains an etalon to allow operation near 2.02 μm (not at the peak of the fluorescence curve). An AO Q-switch will provide pulsed operation with a ~ 200 ns pulse width.

A sample of the output from the slave oscillator is sent to a pulse energy monitor and to a fast detector (D3). The main slave oscillator output beam is reflected by a polarizing beamsplitter through a $\lambda/4$ waveplate into an 8" diameter off-axis parabola-parabola (Mersenne) telescope. The $\lambda/4$ waveplate causes circularly polarized light to be transmitted. Light backscattered from atmospheric aerosols is largely converted to the opposite circular polarization (depolarization by non-spherical aerosols and ice particles causes some ellipticity) and collected by the same telescope. The $\lambda/4$ waveplate converts the receiver beam to the linear polarization perpendicular to the transmitter beam polarization. The receiver beam passes through the beamsplitter and on to a $\lambda/2$ waveplate, where the polarization is rotated to match the RO and reflected into the signal detector D1 where it is mixed with the RO CW signal. The heterodyne signal from D1 is amplified and sent to a complex demodulator where it is normalized by the transmitted pulse frequency and separated into inphase and quadrature components. The baseband signals are subsequently digitized (~ 100 MHz), normalized to the transmitted pulse frequency, and recorded as a function of time from pulse transmission (range).

Several methods are available to insure injection-seeded operation of the slave oscillator. Between pulses, the cavity length is dithered by the PZT while the output of D3 is monitored for peak response (i.e. resonance) to the injected seed light. A hill-climbing algorithm maintains this resonance. During pulse generation, the time between Q-switch deactivation and output pulse generation is monitored using D3. The Q-switch build-up time is shortest for seeded operation because the oscillation builds up out of the injected photons for which the cavity is resonant. Also, an output from the complex demodulator provides a direct estimate of the offset frequency between the RO and outgoing pulse. All of these inputs will be analyzed in a processor to derive appropriate drive signals for the PZT controlling the slave oscillator cavity length.

Delivery of the reference oscillator and pump assembly are expected by August, 1992. We hope to be on the air in a preliminary configuration by December of this year.

References

- Anderson, G.P., S.A. Clough, F.X. Kneizys, J.H. Chetwynd, and E.P. Shettle, "AFGL Atmospheric Constituent Profiles (0-120 km)," AFGL-TR-86-0110 (1986).
- Fan, T.Y., and A. Sanchez, "Pump source requirements for end-pumped lasers," IEEE J. Quant. Electr., 26, 311-316 (1990).
- Henderson, S.W., C.P. Hale, J.R. Magee, M.J. Kavaya, and A.V. Huffaker, "Eye-safe coherent laser radar system at 2.1 μm using Th,Ho:YAG lasers," Opt. Lett. 16, 39-44 (1991).
- Kane, T.J., T.S. Kubo, and R.W. Wallace, "Diode-pumped Eye-Safe Coherent Laser Transmitter," final report, Geophysics Lab. GL-TR-90-0316 (GL/OPA, Hanscom AFB, MA 01731-5000) (1990).
- Moeng, C.H., and J.C. Wyngaard, "Spectral analysis of large-eddy simulations of the convective boundary layer," J.Atmos.Sci. 45, 3573-3587 (1988).
- Pearson, G.N., B.J. Rye, and R.M. Hardesty, "Design of a high repetition rate CO2 Doppler lidar for atmospheric monitoring," SPIE 22, Laser Radar V, 142-153 (1990).
- Post, M.J., and R.E. Cupp, "Optimizing a pulsed Doppler lidar", Appl. Opt. 29, 4145-4158 (1990).
- Rye, B.J., and R.M. Hardesty, "Incoherent accumulation and the Cramer-Rao lower bound for discrete spectral peak estimators in Doppler lidar," IEEE Trans. on Geosci. and Rem. Sens., in review (1992, possibly Jan. 1993 special issue).

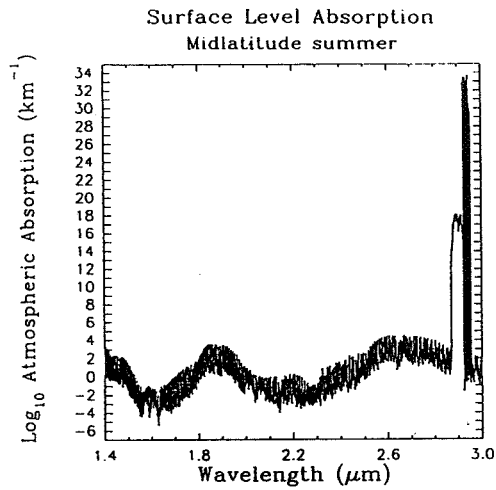


Fig. 1 Near IR atmospheric absorption using all species in the GL HITRAN data base applied to the midlatitude summer model in Anderson, et al, 1986.

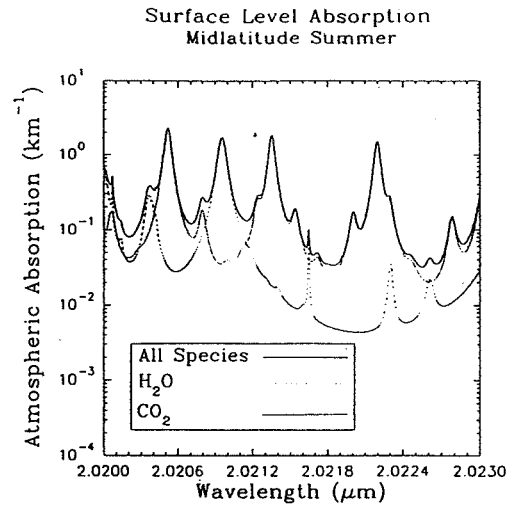


Fig. 2 Expanded view of the atmospheric absorption near the Th:YAG laser wavelength.

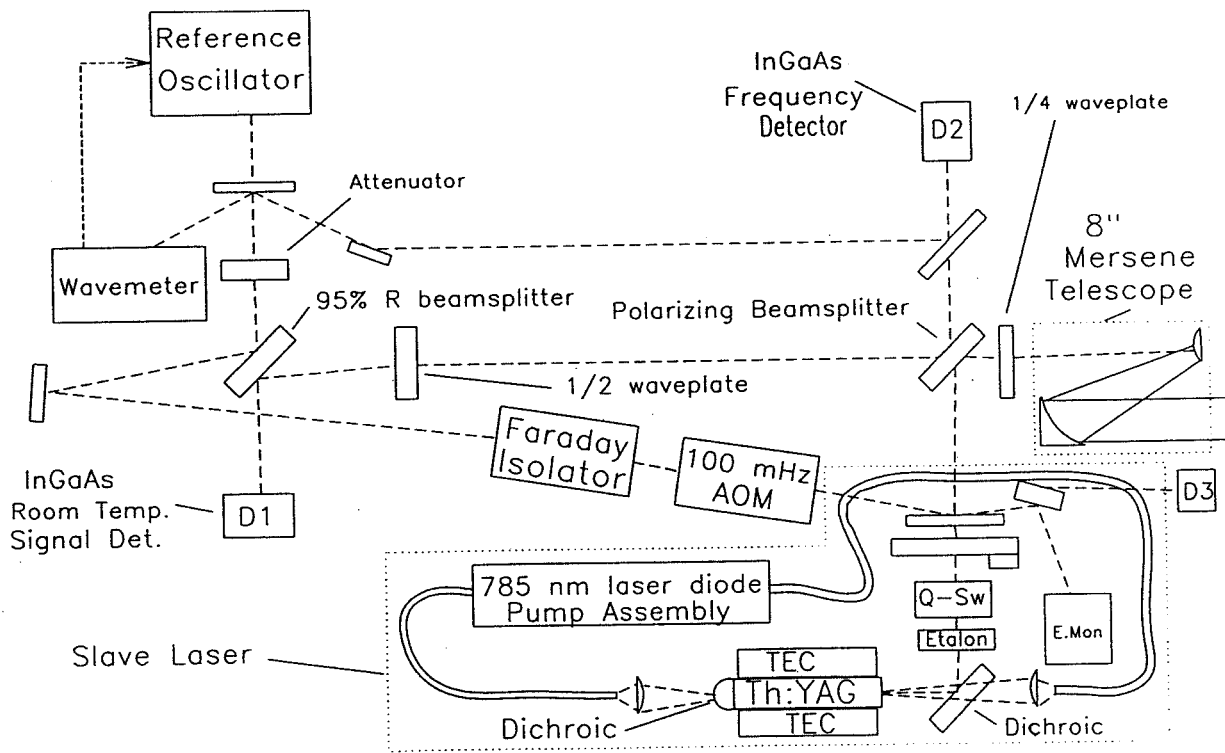


Fig. 3 Preliminary design for the NOAA Th:YAG coherent Doppler lidar system.

A pulsed CO₂ Doppler lidar for boundary layer monitoring

Guy N. Pearson

*Cooperative Institute for Research in Environmental Sciences (CIRES)/NOAA
University of Colorado, Boulder, CO 80302*

Tel: 303 497 6495

Abstract

A monostatic, master oscillator power amplifier (MOPA), CO₂ pulsed Doppler lidar has been constructed and tested. The system is compact (120 x 60 cm), operates at high pulse repetition rates (> 1 kHz) and is intended for simultaneous Doppler/DIAL monitoring of the planetary boundary layer. Details of the system design, hard target calibrations and aerosol returns will be presented.

Summary

A pulsed CO₂ Doppler lidar intended to provide high temporal (< 0.5 sec.), spatial (< 50 m) and Doppler resolution (< 0.5 ms⁻¹) measurements in the boundary layer is described. The instrument operates at low pulse energies (1-10 mJ), has a variable pulse width (0.1-5 μs) and a high pulse repetition frequency (kHz). The system is compact and is capable of running sealed-off with a long lifetime on a rare CO₂ isotope to reduce atmospheric absorption.

The basic elements of the system are an oscillator module containing the synchronously tunable master and local oscillators, a pulsed power amplifier and a compact off-axis telescope. The Q-switched master oscillator produces pulse energies of 100-200 μJ and the two lasers were designed to achieve a high degree of offset frequency stability. The power amplifier is a multi-pass device which exhibits power gains of 10-15 dB and experiments have verified that it induces negligible distortion of the pulse shape, beam profile and frequency stability.

Operation of the system as a lidar was first demonstrated by detecting the return from a calibrated target. The lasers were operating on the P(18) line of the regular CO₂ isotope at 10.571 μm. The target was fabricated from sheets of 400 grit sandpaper and was positioned at a range of 800 m from the lidar. The alignment of the transceiver was optimised using the target return. An example of the transmitted pulse and the target return are shown in Figures 1 and 2 respectively.

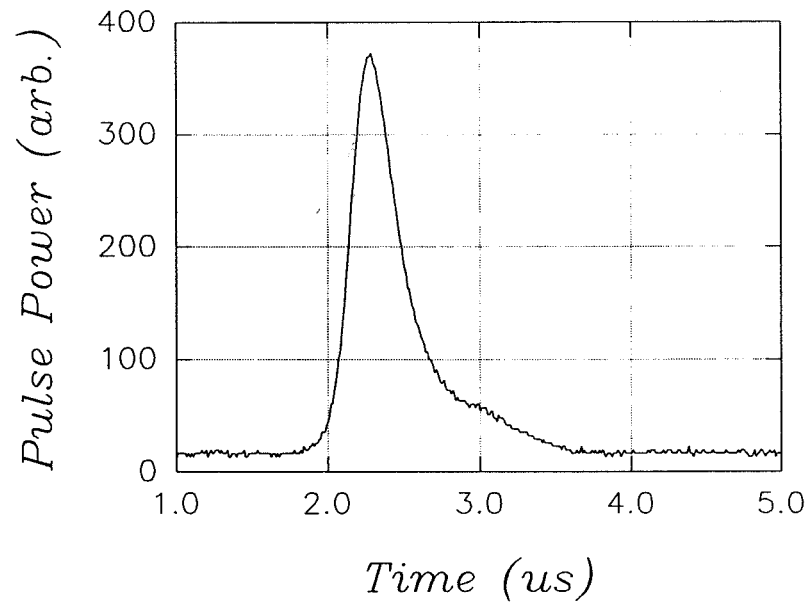


Figure 1. Pulse transmitted to calibration target. For calibration the pulse energy was reduced to $30 \mu\text{J}$ and the laser was run at 1 kHz.

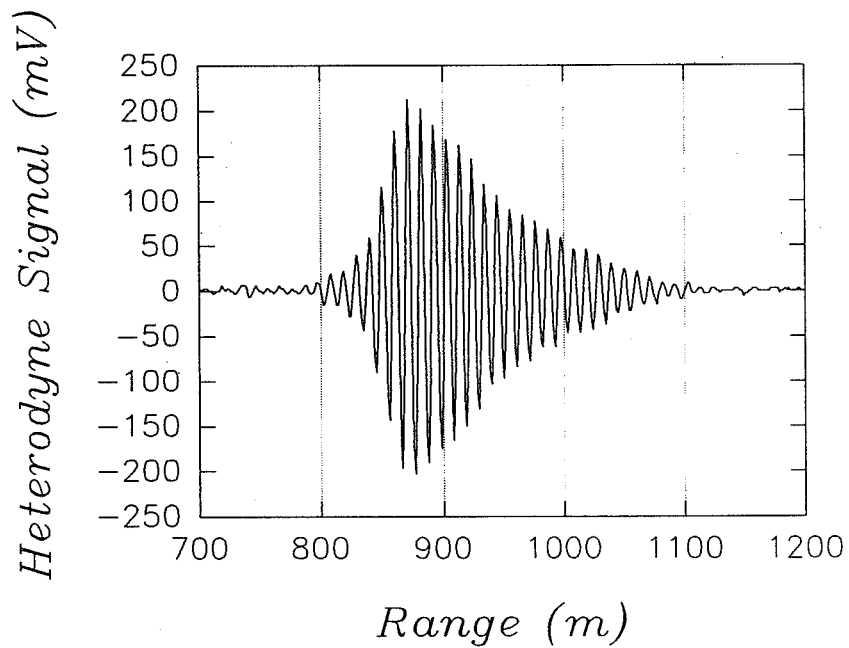


Figure 2. Return signal from a sandpaper target at a range of 800 m.

Analysis of the return signal showed that the system was operating about 1 dB below what was predicted. A single shot aerosol return is shown in Figure 3. The lidar was looking north over the city of Boulder, and independent data taken with the NOAA TEA CO₂ lidar showed that the volume aerosol backscatter cross section was around $10^{-8} \text{ m}^{-1} \text{ str}^{-1}$.

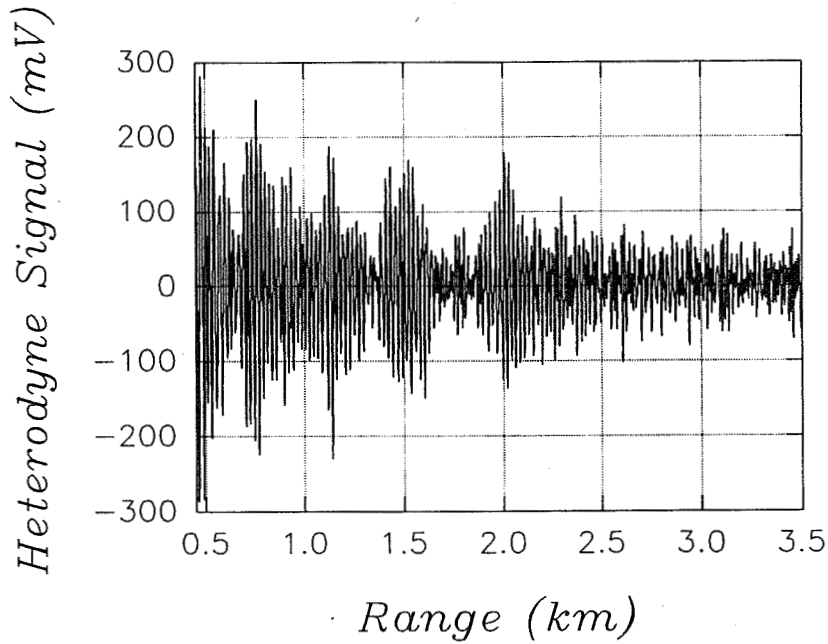


Figure 3. Single shot aerosol return using the pulse shown in Figure 1. The transmitted energy was 1.2 mJ and the 7.0 inch telescope was focused at infinity.

Full details of the system design and characterization experiments will be given as well as further examples of calibration data and aerosol returns.

A COMPACT HIGH REPETITION RATE CO₂ COHERENT DOPPLER LIDAR

S. Alejandro, R. Frelin, B. Dix
Phillips Laboratory, Geophysics Directorate, Optical Environment Division
Hanscom AFB, MA 01731

P. McNicholl
PhotoMetrics, Inc., Woburn, MA 01801

1. INTRODUCTION

As part of its program to develop coherent heterodyne detection lidar technology for space, airborne, and ground based applications, the Optical Environment Division of the USAF's Phillips Laboratory has developed a compact coherent CO₂ TEA lidar system. Although originally conceived as a high altitude balloon borne system, the lidar is presently integrated into a trailer for ground based field measurements of aerosols and wind fields. In this role, it will also serve as a testbed for signal acquisition and processing development for planned future airborne and space based solid state lidar systems. The system has also found significance in new areas of interest to the AF such as cloud studies and coherent DIAL systems.

2. LASER TRANSMITTER

The laser transmitter is a modified Laser Science Inc. PRF-150 CO₂ TEA laser. Building upon a commercial laser design took advantage of the well developed power supply, gas management, control, and interlock systems developed for the series. This reduced both the risk and scope of the laser transmitter development effort. In order to achieve the single mode, frequency stable output of 0.1 J, the discharge cavity region was lengthened and the standard gain cell was replaced by a combined grating/injection locking scheme. The performance parameters of the lidar are given in Table 1. The laser optical cavity is mounted on a three bar super invar mount structure to minimize the effects of temperature. The laser discharge region is contained in a compact hermetically sealed aluminum cylinder which incorporates the discharge electrodes, UV preionizers, heat exchanger, recirculating fans, and gas regenerator. The discharge enclosure is mounted within the super invar cavity support structure. A low pressure cw CO₂ laser acts as the master oscillator (MO) source for both the injection locking of the TEA laser and the local oscillator (LO) energy for the detector photomixing. The output of the cw laser is split by a 90% reflective beam splitter. The reflected portion is frequency shifted by 40 MHz by an acousto-optic modulator and used as the seed for injection locking the TEA laser. The transmitted portion is further split to provide LO's for the receiver and automatic frequency control (AFC) detectors.

Injection of the seed into the TEA cavity is by reflection off a Brewster window. Only a small fraction of the seed power is actually reflected into the cavity, however, this is not a problem since only microwatts are required for locking to occur and the inefficiency of this technique has the added benefit of reducing feedback from the pulsed laser output back into the MO. The frequency match between the seed and a TEA cavity longitudinal TEM₀₀ mode is maintained by the AFC system. This system measures the frequency offset from 40 MHz of a TEA laser pulse and corrects the cavity length proportionately.

TABLE 1
CO₂ Lidar Operating Parameters

Wavelength	10.6 μm (Tunable)
Energy/Pulse	100 mJ
Pulse Length	1 - 2 μsec
PRF	10 - 100 Hz
Spatial Mode	TEM ₀₀
Spectral Width	\approx 1 MHz
Spectral Jitter	\pm 1 MHz
Telescope	30 cm Mersenne

3. LIDAR OPTICAL SYSTEM

The lidar optical system, excluding the scanner, is integrated into a single mechanical unit. It is built on a 10 cm thick, 0.6 m by 2.1 m optical bench with the lasers and the AFC optics mounted on the upper surface and the telescope and a small bench containing the receiver optics suspended beneath (see Figure 1). Holes in the bench allow passage of the TEA laser pulse and cw LO beams to this lower deck. This unit can be floated upon air bearings, although in practice we have found that rubber vibration isolation pads provide sufficient isolation.

A thin film polarizing (TFP) beam splitter and Fresnel quarter wave rhomb act as the transmit/receive optical multiplexer. The transmitter energy is passed through the rhomb where it becomes circularly polarized. The component of the return energy with oppositely sensed polarization passes through the rhomb and is reflected off the TFP into the receiver photomixing optical train. This is then combined with the LO beam and focussed onto a cryogenic HgCdTe photovoltaic diode. Fine adjustment of the LO power is controlled with a double wire grid polarizer. This adjustment is important in being able to set the LO power correctly for optimum shot noise limited heterodyne detection.

The transmit/receive telescope is a 25x, 30 cm diameter, eccentric pupil Mersenne designed to be oriented in any position, although for this application it is set horizontal. The telescope's focus is temperature stabilized by invar metering rods which are contained within the support trusses. A reflective optical flat directs the telescope field of view vertically into a full hemispherical scanner which is mounted on the reinforced ceiling of the trailer and is retractable through a weather-proof hatch. A dual axis, computer interfaced, dc servo-drive system allows for manual or programmed scanner control. Both axes employ 14 bit resolver encoding yielding 380 μrad resolution. The scanner unit also contains a color CCD camera to provide a display and record of the target area. This is particularly useful when the system is being operated manually to track a target.

4. SIGNAL ACQUISITION AND PROCESSING

Two different modes of data acquisition have been employed. In the first, "intensity" mode, the photocurrent power within a bandpass about the carrier frequency is recorded versus time of flight. The one principle advantage of this technique is that it allows for incoherent, pulse-to-pulse signal averaging in standard hardware and hence for operation at the maximum laser repetition rate (100 Hz) while being undemanding on data transfer and CPU speed. However, there are a number of fundamental disadvantages to this technique in addition to it providing no Doppler information. Laser frequency jitter and Doppler shifts result in a signal frequency offset from the carrier so that the passband filtering required to significantly reduce noise levels can lead to reduced signal levels and, more importantly, a velocity bias. In addition, the rf

diode used is not a true square-law detector: it typically rolls off at higher power levels. This requires a non-linear correction of the data and, more fundamentally, can result in a bias due to the intrinsic shot-to-shot fluctuations in signal levels expected in a heterodyne receiver.

In "amplitude" mode, the detector/preamp signal is amplified directly by a pair of broad band amplifiers and reduced to baseband by a conventionally configured IQ demodulator with 10 MHz low pass filtering. A fast GaAs switch before the demodulator is used to gate in the AFC detector/preamp signal for the first 6-7 μ sec after the TEA laser fires. This allows a single data stream to characterize the laser and the backscattered radiation and is similar to a technique used by M.J. Post, et al [1]. The short range data lost is not useful due to scatter from the transmit/receive optics. An integrated, high speed, dual channel ADC and parallel processing system is presently being built to handle this data. We discuss some attributes of this system below. For preliminary measurements as well as testing system performance and data reduction algorithms, we employ two synchronized 12-bit, 20 MHz sampling rate, CAMAC bus, transient recorders to digitize the I and Q component signals and download the results, shot-by-shot, directly to the RAM memory of the host computer--presently, a 386-20 MHz based machine. For range coverage of 15 km, collection rates in excess of 70 Hz are possible. We employ this technique to collect data for off-line processing. At a more modest repetition rate of 10 Hz, hand optimized assembler routines calculate in real time frequency, gain, and phase corrected power spectra in several selectable range gates or true rms and digitally filtered return power versus range. The latter overcomes all of the disadvantages discussed above for the "intensity" mode except possible velocity bias. Typically, it is employed when sampling vertically. Currently, we are testing a prototype floating point parallel processor which should speed up processing (e.g. transforms and digital filters) throughputs by about a factor of 10.

The integrated acquisition/processing system is being developed by Canetics, Inc. It consists of a dual channel 8 bit, >200 MHz sampling rate digitizer with a direct high speed bus to an array (4-8) of floating point processors in addition to a higher level i860 based parallel processor for algorithm development. The high sampling rate was specified to cover the larger bandpasses required for future planned 1-2 μ m solid state systems. At 20 MHz sampling, the design throughputs are sufficient for complete real time processing of the 10.6 μ m system at its maximum repetition rate (100 Hz). In addition, the higher achievable sampling rates will allow for direct sampling of the IF signal without demodulation to test demodulator performance for possible artifacts [2].

5. SYSTEM PERFORMANCE

Initial calibration measurements were made using a blue polystyrene foam target material [3,4]. The results of these measurements will be presented at the meeting. They indicate a system sensitivity about 5 times below that expected for ideal transmitter/LO wavefront matching. A known astigmatism of the telescope primary may have been responsible for some of this deviation. This aberration has since been corrected and future sensitivity tests are planned.

Preliminary Doppler measurements of hard stationary targets show artifactual shifts and shot-to-shot jitter corresponding to velocities on the order of 1 m/s. We believe these effects may be similar to those reported in reference 2 and are presently investigating the origin of them.

The authors acknowledge the scanner control design work of Kevin Sparks.

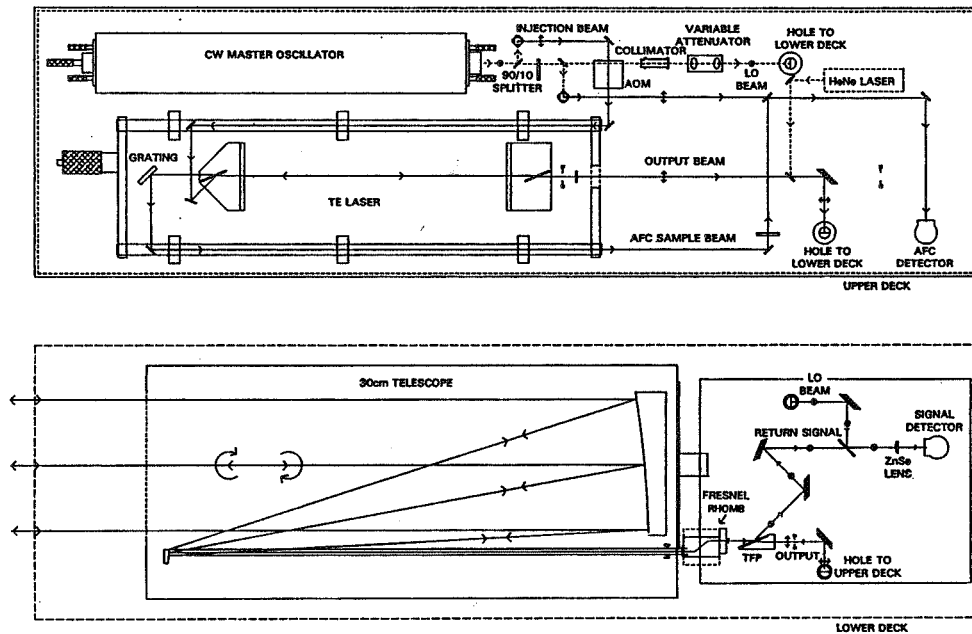


Figure 1.

References:

- [1] M. J. Post and R. E. Cupp, "Optimizing a pulsed Doppler lidar," *Appl. Opt.* **29**, 4145-4158 (1990).
- [2] M.J. Post and R.E. Cupp, "The effects of CO₂ gain-switched spikes on estimating lidar Doppler shifts," in Technical Digest on Coherent Laser Radar: Technology and Applications, 1991 (Optical Society of America, Washington, D.C., 1991), Vol. 12, pp 19-22.
- [3] D. A. Haner and R. T. Menzies, "Reflectance characteristics of reference materials used in lidar hard target calibration," *Appl. Opt.* **28**, 857-864 (1989).
- [4] H. Henshall and J. Cruickshank, "Reflectance characteristics of selected materials for reference targets for 10.6- μ m laser radars," *Appl. Opt.* **27**, 2748-2755 (1988).

SIMPLIFIED SIGNAL PROCESSING FOR AN AIRBORNE CO₂ DOPPLER LIDAR

R. L. Schwiesow and M. P. Spowart

National Center for Atmospheric Research*, ATD/RAF
PO Box 3000, Boulder, CO 80307-3000 USA

1. Context

In the development of the NCAR airborne infrared lidar system (NAILS), we have emphasized a simple, modular design to suit the instrument to its mission of providing measurements of atmospheric structure and dynamics from an aircraft platform. Based on our research to this point, we believe that a significant simplification of the signal processing approach compared with that now used is possible by using high-speed digitization of the signal.

The purpose of this presentation is to place signal processing in the context of the overall system design and to explore the basis of the alternative technique so that the community can comment on the approach.

2. Design features

Resolution. The applications for which NAILS will be used, such as turbulence statistics, cloud entrainment, and flux profiles, emphasize spatial resolution (Schwiesow et al., 1990). Some of the implications for signal processing are that (1) the TEA pulse length is as short as 0.67 μ s (although not yet achieved), (2) a high pulse-repetition frequency is employed, and (3) raw (unprocessed but digitized) signals are recorded. Because of the emphasis on spatial resolution, requirements for velocity resolution (but not accuracy) are relaxed. This means that only the zeroth and first moments of the velocity spectrum contain meaningful atmospheric data.

Two lasers. To reduce cost, weight, and power requirements, NAILS uses an injection-seeded, pulsed TEA laser transmitter and a single CW local oscillator (LO) and seeding source laser. This means that the LO laser seeds the TEA cavity at an offset of 10 MHz from its operating frequency. This appears to select satisfactorily the longitudinal mode of the TEA resonator that is closest to the seed frequency, but raises questions of coupling between the two lasers. The method for stabilizing the frequency offset between the two lasers is part of the signal-processing task.

3. Current signal processing

To put the simplified processing scheme in perspective, we outline the current signal processing approach. More details are given in Schwiesow et al. (1989) and Schwiesow and Spowart (1991).

*The National Center for Atmospheric Research is sponsored by the National Science Foundation.

Signal sources. The frequency offset between the two lasers is measured by mixing a majority of the LO power with a small sample of the transmitter output on a room-temperature HgCdTe detector having a magnetic bias to produce a photovoltaic output. The beat frequency varies about the 10-MHz nominal value by a few MHz on a pulse-to-pulse basis, sometimes falling outside the 8-to-12-MHz band pass for an individual pulse.

The backscattered signal from the atmosphere is mixed with the LO on a sensitive, cooled, HgCdTe photodetector, which uses a current-mode preamplifier. The result of the optical mixing is a radio-frequency signal with a nominal frequency varying between 5 and 15 Mhz.

No changes to the signal sources are contemplated as part of the simplified processing scheme.

Analog processing. The output of the reference detector drives a discriminator to measure the frequency offset of the two lasers. The output of the discriminator is sampled to set a radio-frequency oscillator (called a coherent oscillator or CohO with sine and cosine outputs) to the laser offset frequency on a pulse-by-pulse basis. The output of either the CohO or a stable, 10-MHz oscillator (depending on the particular research project) is mixed with the radio-frequency signal from the cooled detector in a balanced mixer to give in-phase (I) and quadrature (Q) signals over a 0-to-5-MHz frequency band.

The advantage of using a CohO is that correction for pulse-to-pulse variation in the frequency offset between the two lasers is automatic; an I and Q frequency of 0 corresponds to a velocity of 0 m/s. As a result, it is possible to make velocity estimates from averaged autocorrelation functions rather than averaging velocity estimates from individual autocorrelation functions. Although more research on the issue is required, there may be an advantage in accuracy when autocorrelation functions are averaged in a low signal-to-noise environment.

Digital processing. I and Q signals are digitized in two channels at 10 Ms/s with 12-bit resolution to provide the basic data that are recorded. The first 4 μ s of data from each pulse comes from the reference detector to document the laser offset. After that, the inputs to the digitizers are switched to the I and Q signals from the cooled detector. At present, 1024 words of data for each channel (corresponding to a maximum range of 15 km) are written to a buffer.

From the buffer, digital data are written to 8-mm digital tape.

Display. Real-time processing of the I and Q data is done in a DSP32C chip to provide velocity estimates for each 100-m range gate. Either single- or multiple-lag, complex covariances can be programmed into the DSP32C.

We use a height vs. time display to present radial velocity values as color coding in a plane containing the aircraft flight track.

4. Simplified processor

One important reason for the present processing scheme is to be consistent with modern practice in radar signal processing, which uses 10-Ms/s digitizers and I and Q channels. However, newly available computer cards with 100-Ms/s, 8-bit digitizers and resident chips for digital signal processing now allow the design of an alternative approach to processing Doppler lidar signals.

Direct digitization. In principle, the radio-frequency output of the cooled detector can be digitized directly at 30 Ms/s. (If mixed to base band, 0 to 10 MHz, 20 Ms/s would be adequate, but this introduces unwanted complexity.) Note how this one change greatly simplifies the analog elements of the present processor. We have no need for either radio-frequency oscillator, the balanced mixer, or the host of filters associated with the mixing technique in practice. In addition, we eliminate a range gate generator to drive the digitizer chips and the entire Q digital channel.

A similar direct digitization of the output of the reference detector allows simplification of the circuitry for determining the frequency offset between the two lasers. This eliminates the discriminator and the timing necessary to sample its output at the proper time. In practice, the discriminator is sensitive to the pulsed nature of the reference signal, and avoidance of time-dependent output and bias requires significant effort. For the reference channel, direct digitization eliminates three oscillators, a mixer, and various amplifiers and filters in the reference chain.

With a 100-Ms/s digitizer, a number of averaging techniques can be applied to reduce the data rate, because sampling at an effective rate of 30 Ms/s or less suits the Nyquist criterion for reproducing the input signal. To reduce the complexity associated with high-speed switching of inputs, we have chosen to use separate digitizer cards for reference and atmospheric detectors.

Recording. The data rate for recording from the high-speed digitizers is not much faster than two channels of 10-Ms/s, 12-bit data if the 100-Ms/s, 8-bit data are added to become 33-Ms/s, 11-bit data.

The reduced number of effective bits in the high-speed digitization (7 bits at 30 Ms/s) can give adequate dynamic range if the gain of the digitizer input amplifier is properly chosen for the experimental conditions at hand. We plan a linear amplifier with 4 gain ranges to allow selection of the optimum gain for environments with different mean backscatter coefficients and maximum ranges.

Computation. Given digitized signals in a buffer memory, a number of algorithms can be employed to prepare the data for recording. Simple sample averaging eliminates the possibility losing valuable data by overprocessing.

For real-time display, each of the analog components eliminated by direct digitization can be replaced by a suitable algorithm. For example, the reference channel data can be fit to a chirped waveform in a least-squares sense to determine accurately the effective laser offset frequency for each pulse. This frequency, in turn, drives the servo, through a D/A converter, that corrects the length of the TEA resonator to maintain a 10-MHz offset from the stabilized LO on the average.

Autocorrelation. With a direct digital representation of the atmospheric signal, it is possible to simplify calculation of the first moment of the velocity spectrum. The present system uses the phase of the complex covariance at a single lag or a few lags to estimate the velocity. The function of the balanced mixer in the old scheme can be reproduced in the new with a suitable algorithm. The results of fitting a frequency to the reference channel substitutes for the CohO input.

On the other hand, the greater sampling rate of the simplified signal processing system allows other covariance techniques, such as fitting a damped sine function to a real autocovariance function, to be employed.

Summary. High-speed digitization of reference and atmospheric signals from a heterodyne, Doppler lidar allows the use of signal processing schemes that are much simpler to implement in hardware than schemes that depend on digitization at speeds below the Nyquist limit for the direct output from the heterodyne detector. We can use commercially debugged and supported components in place of custom circuitry. The simplified signal processing approach substitutes algorithms for analog components and leads to greater research flexibility.

5. Laser coupling

There is an unavoidable feedback of a small fraction of the TEA pulse along the path of the injection seed from the LO. Heavy attenuation is used to provide decoupling between the lasers. However, when the lasers are aligned so that the TEA energy reaches the reference detector via reflection from the output coupler of the LO, the reference frequency between the lasers is unstable. We attribute this to the influence of the energy from the TEA on the LO during the short time of the pulse rather than to the influence of the attenuated LO output coupler on the TEA.

At present, additional decoupling is provided by introducing a slight difference in the angles from which the LO and TEA beams arrive at the reference detector. In the future, we intend to use an optical isolator, which is just now becoming available commercially for operation at 10 μm .

6. Acknowledgements

Jeff Bogen is active in developing the circuitry for the present processing system and in improving the amplifiers and servos needed for the simplified signal processor. Kim Weaver implemented the recording and display portions of the present signal processor.

7. References

- Schwiesow, R.L., A.J. Weinheimer and V.M. Glover, 1989: Applications and development of a compact, airborne Doppler lidar for atmospheric measurements. SPIE Vol. 1119, 5th Conference on Coherent Laser Radar, 20-24.
- _____, M.P. Spowart, V.M. Glover and P.W. Young, 1990: Design of an airborne heterodyne lidar for atmospheric wind measurements. 15th International Laser Radar Conference, Tomsk, USSR, 23-27 July, 40-43.
- _____, and M.P. Spowart, 1991: A compact, injection-seeded, heterodyne lidar: lessons learned from airborne tests. 6th Conference on Coherent Laser Radar, 8-12 July, 55-57.

PHASE NOISE IN PULSED DOPPLER LIDAR AND LIMITATIONS ON
ACHIEVABLE SINGLE-SHOT VELOCITY ACCURACY

P. McNicholl
PhotoMetrics, Inc., Woburn, MA 01801

S. Alejandro
Phillips Laboratory, Geophysics Directorate, Optical Environment Division
Hanscom AFB, MA 01731

1. INTRODUCTION

The smaller sampling volumes afforded by Doppler lidars compared to radars allows for spatial resolutions at and below some sheer and turbulence wind structure scale sizes. This has brought new emphasis on achieving the optimum product of wind velocity and range resolutions. Several recent studies have considered the effects of amplitude noise, reduction algorithms, and possible hardware related signal artifacts on obtainable velocity accuracy [1,2]. We discuss here the limitation on this accuracy resulting from the incoherent nature and finite temporal extent of backscatter from aerosols.

For a lidar return from a hard (or slab) target, the phase of the intermediate frequency (IF) signal is random and the total return energy fluctuates from shot to shot due to speckle; however, the offset from the transmitted frequency is determinable with an accuracy subject only to instrumental effects and the signal to noise ratio (SNR)--the noise being determined by the LO power in the shot noise limited regime. This is not the case for a return from a media extending over a range on the order of or greater than the spatial extent of the transmitted pulse--such as from atmospheric aerosols. In this case, the phase of the IF signal will exhibit a temporal random walk like behavior. It will be uncorrelated over times greater than the pulse duration as the transmitted pulse samples non-overlapping volumes of scattering centers [3]. Frequency analysis of the IF signal in a window similar to the transmitted pulse envelope will therefore show shot-to-shot frequency deviations on the order of the inverse pulse duration reflecting the random phase rate variations. Like speckle, these deviations arise from the incoherent nature of the scattering process and diminish if the IF signal is averaged over times greater than a single range resolution cell (here the pulse duration).

Apart from limiting the high SNR performance of a Doppler lidar, this shot-to-shot variance in velocity estimates has a practical impact on lidar design parameters. In high SNR operation, for example, a lidar's efficiency in obtaining mean wind measurements is determined by its repetition rate and not pulse energy or average power. In addition, this variance puts a practical limit on the shot-to-shot hard target performance required of a lidar.

2. ANALYTIC MODEL

For a square data window and a chirp-free pulse, reference 4 gives a formula in the context of Doppler radar for the variance in the central moment of the velocity. In the limit of high SNR, the residual term in this expression is the variance under discussion. For application to present lidars, we derived a similar expression with flexible windowing and allowing for pulses which are not Fourier transform limited. We use a mono-disperse, stationary model which leads to an analytic treatment for the simple pulse shapes adopted in this section. In the following section we discuss the more general dependence of this variance.

For the analytic model, the transmitted pulse (E) is taken to be of Gaussian shape with a power temporal variance of σ_T . A linear chirp is included and is characterized by the incremental phase variation (δ) in the transmitted field amplitude

over a time $2\sigma_T$. We also use a Gaussian windowing function (W) which is functionally equivalent to that for the field amplitude with analogous width σ_W and no chirp. The backscattered field amplitude (A) is represented by

$$A(t) = \sum_i a_i E(t-2z_i/c),$$

where E is the transmitted field amplitude, the summation is over aerosol particles, z_i is the radial position and a_i the complex scattering amplitude of the i^{th} aerosol particle. We assume that $\langle a_i a_j^* \rangle = |a|^2 \delta_{ij}$, where the brackets indicate an ensemble average. The windowed spectral amplitude is then

$$A(\omega, t) = (2\pi)^{-1/2} \int d\tau W(t-\tau) A(\tau) e^{i\omega\tau}$$

and the power spectral density is $I(\omega, t) = |A(\omega, t)|^2$. We choose in this analysis to use the central moment, ω_1 , of I as the measurement of the return frequency. Note that ω_1 , through I, is dependent on the random variables a_i . The mean of this expression, $\langle \omega_1 \rangle$, can be shown to yield the central return frequency. After some tedious but straightforward manipulation, the variance ($\Delta\omega_1^2$) of this central moment can be found to be

$$\Delta\omega_1^2 \equiv \langle (\omega_1 - \langle \omega_1 \rangle)^2 \rangle = \sigma_0^2 / 4\sigma_W\sigma_\omega \quad (1)$$

where σ_0 and σ_ω are the spectral widths respectively of the bare and the windowed transmitted pulse. They are given here by

$$\begin{aligned} \sigma_0^2 &= (1 + \delta^2) / 4\sigma_T^2 \\ \sigma_\omega^2 &= \sigma_0^2 + (1/4\sigma_W^2). \end{aligned}$$

As an example if $\sigma_T = \sigma_W = 1 \mu\text{sec}$ (a pulse FWHM of about 2.3 μsec and a matched windowing function), and $\delta = 0$, then the shot to shot deviation in the central moment estimate of the return frequency is about 47kHz. For a CO_2 lidar operating at a wavelength of 10.6 μm , this corresponds to about 0.25 m/sec.

3. DISCUSSION

In Figure 1, we show the results of equation 1 for a laser pulse at 10.6 μm and with $\sigma_T = 0.5 \mu\text{sec}$ (a FWHM of about 1.2 μsec). The solid and dashed curves indicate, respectively, the expected performance with and without a linear chirp which broadens the pulse spectral width (σ_0) from the Fourier transform limit of 160 kHz to 1 MHz. These roughly correspond to the characteristics of the pulse for the Phillips Laboratory (PL) CO_2 Doppler lidar [5]. The range resolution has been taken as that radial spatial period of wind structure for which the system response--as measured by the mean central moment--drops by a factor e^{-2} . For transmitted pulses with Gaussian power envelopes--as used in the last section--this is given by

$$\Delta r^2 = (\pi c/2)^2 (\sigma_T^2 + \sigma_W^2).$$

The extent of the values plotted in figure 1 correspond to a window duration (σ_W) of from 0.5 to 4.5 μsec .

Generally, it can be shown that the variance in the central moment depends only on the power spectrum of the transmitted pulse and not explicitly on its temporal profile. This has the important physical consequence that this variance is explicitly independent of pulse profile features like gain switched spiking and implicitly depends

on them only to the extent that they effect the spectral power distribution. On the other hand, the spatial resolution depends only on the temporal power envelope. As an example of this the dotted curve in figure 1 shows the velocity variance versus range resolution for a chirp free pulse with the same spectral shape but narrower temporal profile as that for the linearly chirped pulse (solid line). With the same windowing function, these exhibit the same amount of velocity estimate variance, but the narrower pulse has a smaller resolution element.

These results were checked with a Monte Carlo simulation the results of which are given by the boxes and triangles in figure 1. The triangles are actually the result for a pulse with a Gaussian envelope and a quadratic chirp (more accurately reflecting the transmitted pulse of the PL lidar) but with a spectral width the same as that for the linearly chirped pulse used for the solid curve. Despite the significant difference in the spectral profiles of the linearly and quadratically chirped pulses (see figure 2), the variance in the velocity estimate shows remarkable agreement.

For the PL lidar, we are presently working on direct numerical integration of recorded laser pulses to determine the expected velocity-range resolution performance. Compared to the preliminary expected performance represented by the solid line in figure 1, we expect the range resolution to be better due to the gain switched spike. In addition, we have noticed indications of saturation during the gain switched spike which may have led to overestimates for the preliminary values of the chirp dominated spectral width. Correction of this could result in somewhat lower expected shot-to-shot velocity variance. Finally, subject to the concurrence of conditions for adequate SNR from a sufficiently quiescent atmospheric volume, we are planning to make measurements to confirm these results.

References:

- [1] R.M. Hardesty and B.J. Rye, "Simulations of discrete spectral peak estimators for single and multiple lidar pulse returns," in Technical Digest on Coherent Laser Radar: Technology and Applications, 1991 (Optical Society of America, Washington, D.C., 1991), Vol. 12, pp 219-222.
- [2] M.J. Post and R.E. Cupp, "The effects of CO₂ gain-switched spikes on estimating lidar Doppler shifts," in Technical Digest on Coherent Laser Radar: Technology and Applications, 1991 (Optical Society of America, Washington, D.C., 1991), Vol. 12, pp 19-22.
- [3] R.T Menzies and R.M Hardesty, "Coherent Doppler lidar for measurements of wind fields," in Proceedings of the IEEE, Vol. 77, pp 449-462 (1989).
- [4] R.J Doviak and D.S. Zrnic, Doppler Radar and Weather Observations, New York, NY: Academic Press, 1984.
- [5] S. Alejandro, R. Frelin, B. Dix, P. McNicholl, "A compact high repetition rate CO₂ coherent Doppler lidar," submitted to the 16th International Laser Radar Conference.

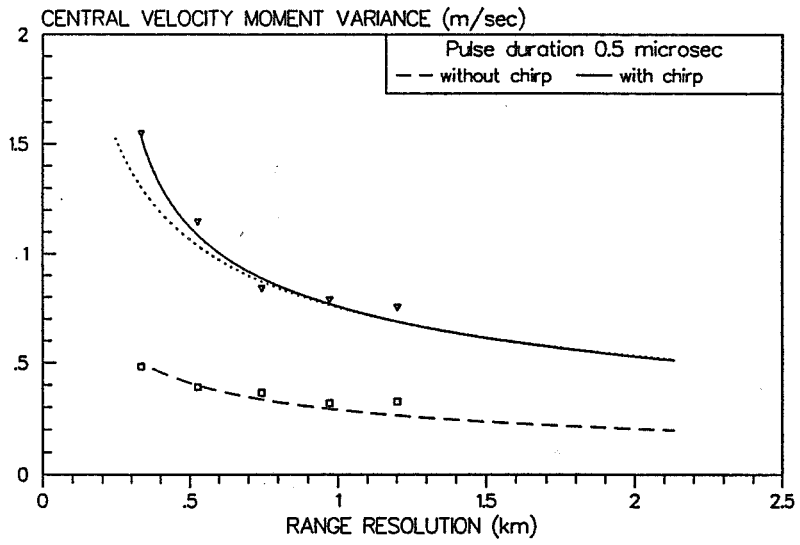


Figure 1.

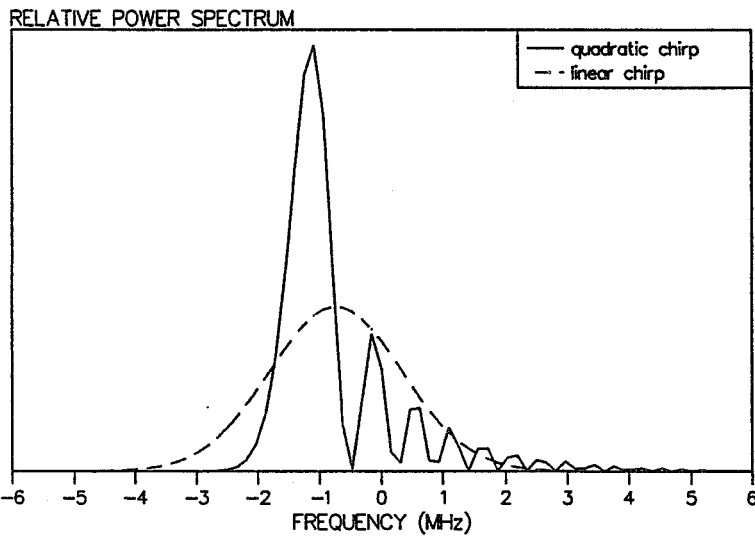


Figure 2.

A Comparison of Ultra-Sensitive Coherent Detection(USCD) and Heterodyne Detection
For A Wind Sensing Application

Sherwin Amimoto, Rolf Gross, Bob Lacy, Lissa Garman-DuValle, and Tom Good

The Aerospace Corporation

P. O. Box 92957

Los Angeles, CA 90009

Ultra-Sensitive Coherent Detection(USCD) and conventional heterodyne detection methods were evaluated for use as a space-borne wind sensing system. For this study we assume that the wind sensing system would become available by the year 2015. Consequently laser systems and detectors more advanced than those under consideration for near term programs could be included. Three laser candidates under evaluation are Nd-YAG at 1.06 μm , Ho-YAG at 2.1 μm , and CO₂ at 9.11 μm . Both heterodyne and USCD detection methods were included. The primary emphasis of this study stresses the optimization of weight and power consumption of the wind sensor portion of the satellite system.

Previous well-known wind sensing system level studies include LAWS(Laser Atmospheric Wind Sounder)¹ and WINDSAT². To reduce the scope of this study, the effects of wind sampling and earth coverage were not addressed. The following Windsat-like assumptions were used. We assume a satellite orbit of 830 km altitude in a polar orbit. A conical scanning pattern on the ground with a 53.6 degree Nadir half-cone angle and a 8 Hz illuminator rep-rate were assumed to provide coverage in a timely manner. Horizontal patches of 300x 300 km broken into 1 km vertical height intervals up to 20 km altitude. The minimum measurement error of wind speed was 1 m/s with a maximum of 100 m/s.

Using the procedure and the expression for the estimate of radial wind velocity error used by Menzies³, the required signal to noise was estimated. This estimate was used to relate the desired accuracy of wind speed to the signal to noise which in turn will be related to the energy of the illuminator laser. For estimating the narrowband signal to noise the bandwidth uncertainty of the laser, $V_{\text{BW}} = 1/2\text{pt}$, was set equal to the atmospheric velocity fluctuations, $V_{\text{atm}} = 0.4$ m/s. The laser pulse duration, t , at 9.11 μm was 2.5 ms. The width of one filter element in the bank of frequency filters was determined by the desired accuracy of 1 m/s which at 9.11 μm is 1.5 MHz. This value was used to derive the corresponding Nyquist sampling frequency of 7 MHz. Both the Nyquist frequency, laser pulse duration, and filter widths were scaled to other wavelengths. From this analysis, a

signal to noise of 0.60 was required of the lidar system to meet the 1 m/s accuracy which is independent of wavelength.

The energy of the illuminating laser was estimated using an expression for detector shot noise limited SNR with a bandwidth matched to the laser pulse duration².

$$\text{SNR} = \frac{p h E b c t D^2 K A}{8 h n [R^2(1+D^2/4r_a^2) + (p D^2/4l)^2(1-R/f)^2]} \quad (1)$$

where h is the overall detector and optical jitter system

efficiency,

E is the transmitter laser energy(J)

b is the atmospheric backscatter coefficient($\text{m}^{-1}\text{sr}^{-1}$)

c is the speed of light(3×10^8 m/s)

t is the laser pulse duration(s)

D is the telescope mirror diameter

K is the beam shape compensation factor with jitter

R is the range(m)

$h n$ is the photon energy(J)

r_a is the turbulence-induced transverse coherence radius(m)

f is the focal length

A is the two way attenuation loss integrated over the transmitted range including optics

The appropriate values for r_a , typically 50 m or more are so large compared to the mirror diameter so that its effect may be ignored in the first term in the denominator. The effects of focussing may also be ignored in the second term in the denominator.

Three lasers at various wavelengths were considered, Nd-YAG at 1.06 μm , Ho-YAG at 2.1 μm , and CO₂ at 9.11 μm . Two types of detection methods were also carried in the calculations, USCD and heterodyne detection. Quantum efficiencies for USCD and heterodyne detectors were 1.0 and 0.4. The spatial overlap factors with jitter were identical for both detectors, 0.25. The values for backscatter coefficients are known to vary over several orders of magnitude. The most stressing cases for the northern and southern

hemisphere are pre-volcanic values^{4,5}. Volcanoes have injected enough mass into the atmosphere to cause a five-fold increase over the pre-volcanic levels. The lowest values as a function of altitude occur at 5-8 km height. These pre-volcanic levels are known to obey a 1^{-2} scaling law which was used in this study. A slant range of 1130 km was used.

The laser energy necessary to meet the SNR requirement and rep rate of 8 Hz may be used with the appropriate algorithms to estimate weight and power. They assume light-weighting of the large mirror by a factor of 0.2 in the absence of light-weighting. Power for the laser illuminator and the USCD laser were included. Laser efficiencies of 0.1 were assumed. The power and weight were calculated as a function of mirror diameter. A set of curves were generated which showed a minimum in weight for an optimized mirror diameter. At smaller diameters, the weight increased due to higher laser powers needed to achieve the SNR. At larger diameters, the weight increased due to a larger component of mirror weight. The optimum diameters and corresponding system weights and power levels are shown in Table 2.

Table 2. Optimized systems weight and power for the Southern Hemisphere(Northern Hemisphere in parenthesis)

Wavelength (μm)	Weight (kg)	Power (kw)	Energy/shot (J)	Mirror Diam (m)
1.06(USCD)	59(38)	192(117)	1.96(1.03)	0.75(0.65)
2.1(USCD)	51(41)	183(144)	1.42(0.93)	0.65(0.60)
9.11(het.)	375(87)	1177(272)	14.7(3.4)	1.50(0.90)

These optimum are specific to each choice of wavelength and detector. The optimum weight of 1.06 μm is 16% the optimum weight at 9.11 μm . The optimum 2.1 μm weight is 14% the optimum 9.11 μm weight. The higher efficiency of the USCD relative to the heterodyne detector leads to lower weight and power for the shorter wavelengths as discussed below. The lower weights for the 1.06 μm and the 2.1 μm system over the 9.11 μm system is caused by a more favorable backscatter coefficient. Sensitivity analysis revealed that the effect of increasing the detector efficiency from 0.1 to 0.25 was to reduce the overall systems weight of either the USCD or CO₂ heterodyne detector systems by a factor of 0.60. We conclude that shorter wavelengths and the use of a USCD could significantly reduce systems weight for a wind sensor.

Technology assessments and laboratory experiments are in progress to further establish a firm technical basis for the use of USCDs in wind sensing and other LIDAR applications.

References

1. LAWS Instrument Panel, LAWS Earth Observing System Instrument Panel Report, vol IIg, NASA, 1987.
2. R. M. Huffaker, T. R. Lawrence, M. J. Post, J. T. Priestly, F. F. Hall, Jr, R. A. Richter, and R. J. Keeler, Appl. Optics, 23, pp 2523-2536, 1984.
3. R. T. Menzies, Appl. Optics, 25, pp2546-2553, 1986.
4. G. S. Kent and G. K. Yue, J. Geophys. Research, 96, pp 5279-5292, 1991.
5. J. L. Gras, C. M. R. Platt, W. D. Jone, R. M. Huffaker, S. A. Young, S. M. Banks, and D. J. Tooth, J. Geophys. Research, 96, pp 5357-5367, 1991.

Diversity Imaging Techniques in Lidar

K. I. Schultz

MIT Lincoln Laboratory
244 Wood Street/L200
Lexington, MA 02173

Abstract

Diversity imaging techniques have been successfully employed in conventional microwave range-Doppler imaging radars to obtain high resolution images of both natural and man-made targets. These techniques allow microwave radars to achieve image resolution which would otherwise require excessively large antennas. Recent advances in coherent laser radar techniques and signal processing have led to the development of range-Doppler imaging laser radars. While much of the theory and signal processing techniques used in microwave radars can be brought to bear on laser radars, the significant difference in wavelength results in issues peculiar to laser radar systems. Both the fundamental concepts and specific applications of diversity imaging techniques applied to laser radar imaging systems will be discussed.

Angle, frequency, and bistatic angle degrees of freedom can be employed in a coherent laser radar imaging system to achieve image resolution which exceeds the traditional Rayleigh criterion associated with the receive aperture. In diversity imaging, angle and frequency degrees of freedom can be used to synthesize an effective aperture providing range and Doppler target information. The ability to vary the bistatic angle provides an additional means of synthesizing an effective aperture. Both simulated and experimentally obtained laser radar images of spinning and/or tumbling objects utilizing both angular and frequency diversity will be presented.

In coherent laser radar systems, image quality can be dominated by laser speckle effects. In particular, the signal-to-noise ratio (SNR) of a coherent laser radar image is at most unity in the presence of fully developed speckle. Diversity techniques can be utilized to improve the image SNR; simple incoherent averaging of images utilizing temporal and polarization degrees of freedom can significantly improve image SNR. Both the SNR and image resolution (as defined by the synthetic aperture) contribute to image quality. The relationship between the available degrees of freedom and image quality will be discussed.

A RANGE-RESOLVED BISTATIC LIDAR USING A HIGH-SENSITIVE CCD CAMERA

K. Yamaguchi^{*,**}, A. Nomura^{*}, Y. Saito^{*} and T. Kano^{*}

^{*}) Faculty of Engineering, Shinshu University, Nagano-shi 380 Japan

^{**}) Meisei Electric Co., Ltd., Moriya-cho, Kitasouma-gun 302-01 Japan

Until now monostatic type lidar systems have been mainly utilized in the field of lidar measurements of atmosphere. We propose here a range-resolved bistatic lidar system using a high-sensitive cooled-CCD camera.

This system has the ability of measuring the three dimensional distributions of aerosol, atmospheric density, and cloud by processing the image data of laser beam trajectory obtained by a CCD camera. Also, this lidar system has the feature of allowing dual utilization of CW lasers and pulse lasers.

The scheme of measurement with this bistatic lidar is shown in Fig. 1. A laser beam is emitted vertically and the image of its trajectory is taken with a remote high-sensitive CCD detector using an interference filter and a camera lens. The specifications of the bistatic lidar system used in the experiments is shown in Table 1.

The receiving power per pixel, P_r , is given by the following bistatic lidar equation:

$$P_r = P_0 \frac{\eta K A T_X T_R \{\beta_M(z, \theta) + \beta_A(z, \theta)\}}{\ell} d\theta \quad (1)$$

where P_0 is transmitting power; η , quantum efficiency; K , optical efficiency; A , receiving area of camera lens; T_X and T_R , transmittance of transmitting laser light and scattering receiving light, respectively; $\beta_M(z, \theta)$ and $\beta_A(z, \theta)$, scattering coefficients of atmospheric molecules and aerosols, respectively; ℓ , distance between transmitter and receiver; $d\theta$, view angle per pixel. Equation (1) indicates the interesting fact that the receiving power per pixel does not depend on range z ; instead, the range resolution increases with range.

The preliminary result of field measurement is shown in Fig. 2. A YAG laser (SHG) was emitted vertically and a CCD camera ($f=55\text{mm}$, $F=2.8$, exposure time=15s) recorded its trajectory at a distance of 215m away from the transmitter with an elevation angle of 86° . The picture shows the trajectory from 1.5km to zenith. The variation of received photoelectrons with height obtained by processing the image data is shown in Fig. 3. The height resolution is also indicated by a dotted line in the same figure. The peak at 2km shows the echo from clouds and the broad peak of 15~27km shows that of aerosols by the Pinatubo eruption.

The preliminary experimental results of our range-resolved bistatic lidar system suggest its potential applications in the field of lidar measurements of atmosphere.

The authors wish to acknowledge the support of Dr. T. Itabe and his colleagues in Communication Research Laboratory.

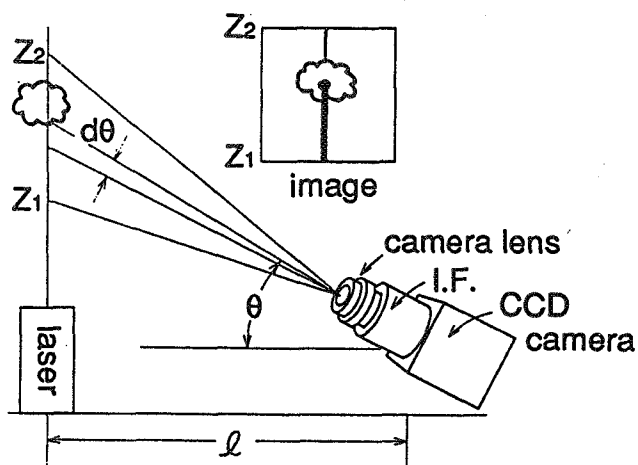


Figure 1. The scheme of measurement with the bistatic lidar.

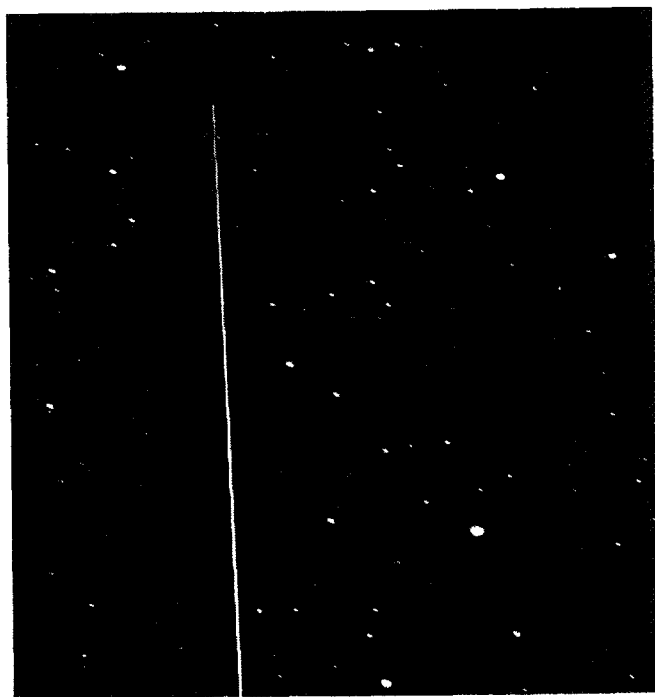


Figure 2. A laser beam trajectory taken with a CCD camera ($f=55\text{mm}$, $F=2.8$). Exposure time is 15s.

Table 1. Specifications of the lidar system.

Transmitter

Ar ion laser	single-line (514.5nm, 1W) multi-line (514.5nm, etc., 300mW)
Nd:YAG laser	SHG (532nm, 600mJ/shots, 20pps)

Receiver

Collector	camera lens — $f=55\text{mm}$, $F=2.8$ (Nikon), $f=28\text{mm}$, $F=2.0$ (Nikon)
Filter	$\lambda=514.5\text{nm}$, $\Delta\lambda=1.5\text{nm}$ (Nihon Shinku Kogaku)
CCD camera	C-3140 (Hamamatsu Photonics) Pixels — 510×492 Quantum efficiency — 8% (near 530nm), 1.6% (at 1064nm) Temperature — -30°C

Processor

Interface	C-3366 (Hamamatsu Photonics)
Computer	PC-9801 DA/U5 (NEC)

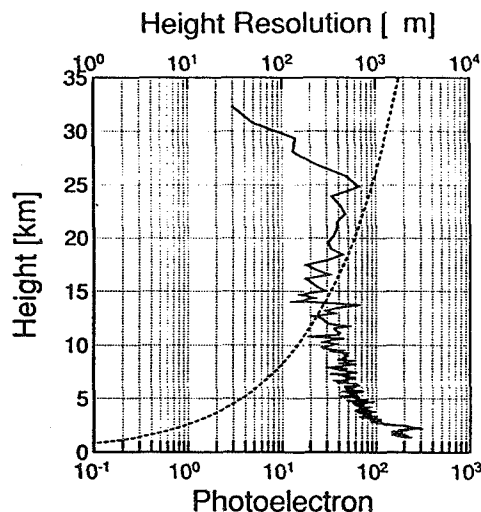


Figure 3. Variation of received photoelectrons with height (solid line) and height resolution (dotted line).

FLUORESCENCE LIDAR MULTI-COLOR IMAGING OF VEGETATION

J. JOHANSSON, E. WALLINDER, H. EDNER, and S. SVANBERG

Department of Physics, Lund Institute of Technology
P.O. Box 118, S-221 00 Lund, Sweden

ABSTRACT

Multi-color imaging of vegetation fluorescence following laser excitation is reported for distances of 50 m. A mobile laser-radar system equipped with a Nd:YAG laser transmitter and a 40 cm diameter telescope was utilized. Image processing allows extraction of information related to the physiological status of the vegetation and might prove useful in forest decline research.

- * -

In many regions of Europe forests are subject to severe damage due to environmental influence. It is of considerable interest to be able to perform early detection and mapping of damaged vegetation. One possibility is to use reflectance spectroscopy, which is readily adaptable to satellite multi-spectral imagery. Active remote sensing using a transmitter can provide additional information. On excitation with laser light in the UV or blue-green region, vegetation exhibits characteristic chlorophyll fluorescence, with two peaks in the red spectral region, at 690 nm and at 740 nm. The relative intensity of these peaks is related to the physiological state of the leaves. In addition, a broadband fluorescence in the 450-600 nm region is also obtained from the surface wax layer and other leaf constituents. The possibility to use this information for vegetation status assessment is now being investigated by several groups (for reviews, see e.g. Ref. [1]).

Following remote spectral point monitoring of vegetation fluorescence [2] using a mobile system intended primarily for atmospheric lidar investigations [3], we have now performed remote fluorescence imaging of vegetation using a multi-color imaging system [4] adopted to the 40 cm diameter optical receiving telescope of the lidar system. A general view of this type of measurements is given in Fig. 1.

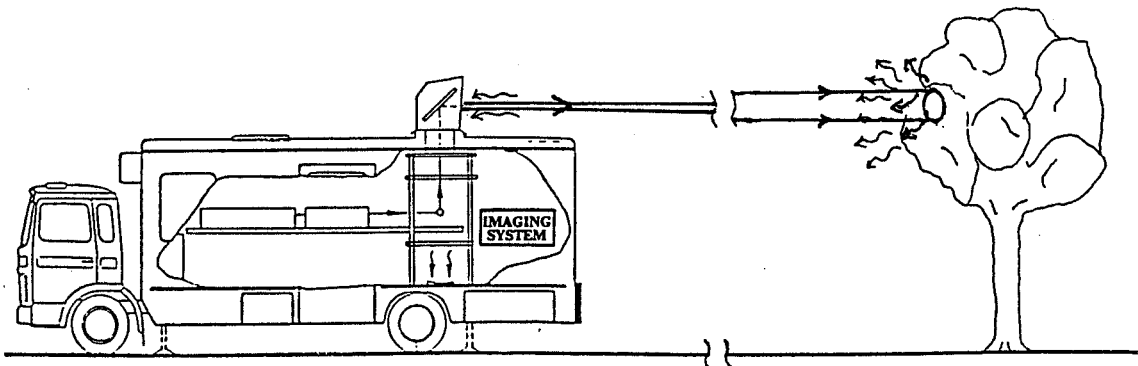


Figure 1. Remote fluorescence imaging of vegetation

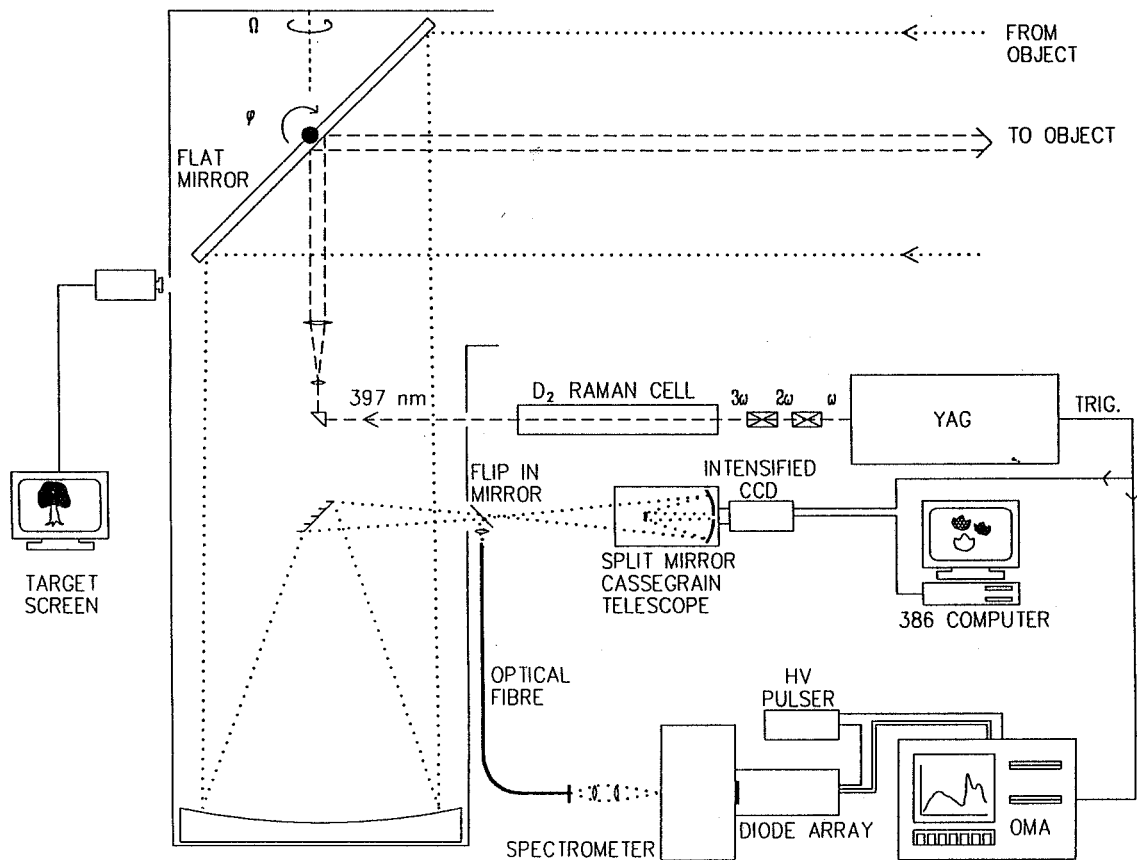


Figure 2. Optical and electronic lay-out of the multi-color fluorescence imaging lidar system

In order to induce chlorophyll fluorescence efficiently while still staying eyesafe we used a frequency-tripled Nd:YAG laser (355 nm, 200 mJ pulse energy) and Raman-shifted the output in a high-pressure deuterium cell to 397 nm. An output pulse energy of 30 mJ was achieved at 20 Hz. The radiation was transmitted in a divergent beam towards the target area. The fluorescence light was collected by the lidar telescope and was divided up into four individually filtered images placed in the four quadrants of a gated image intensifier preceding a ccd array. In this way four images could be recorded simultaneously, later to be subjected to image processing. Alternatively, fluorescence could be collected pointwise and dispersed in an optical multichannel analyzer. In this way remote spectra could be recorded. The optical and electronic lay out of the system is shown in Fig. 2. Spectra from a green and a slightly yellow maple leaf in 50 m distance are included in Fig. 3. It can be clearly seen, that the leaf with impaired photosynthesis exhibits a strong reduction in the 740 nm fluorescence peak in relation to the 690 nm peak. Spatially resolved recordings of the same leaves are shown in the figure. In order to exemplify image processing for extracting environmental information we show an image obtained by dividing the 690 nm image by the 740 nm image, pixel by pixel. In the resulting image the stressed leaf is strongly demarcated against the normal green leaf. Similar measurements were also performed on multiple oak leaves. Experiments were also made on leaves of *Brasica Campestris*. Normal plants were compared to plants subject to enhanced UV radiation (ozone hole simulation). In this case

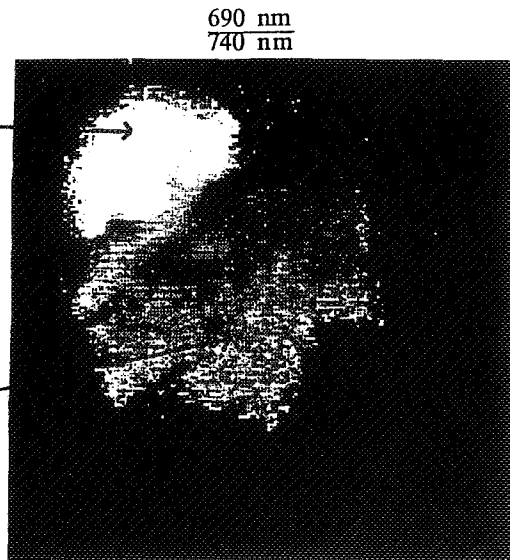
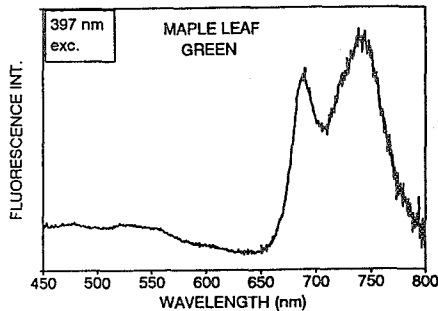
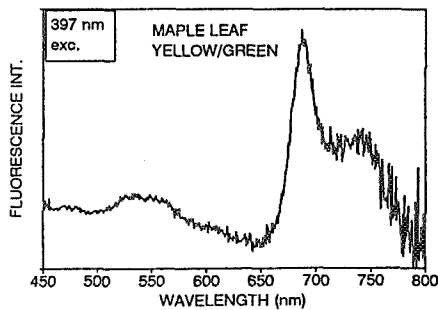
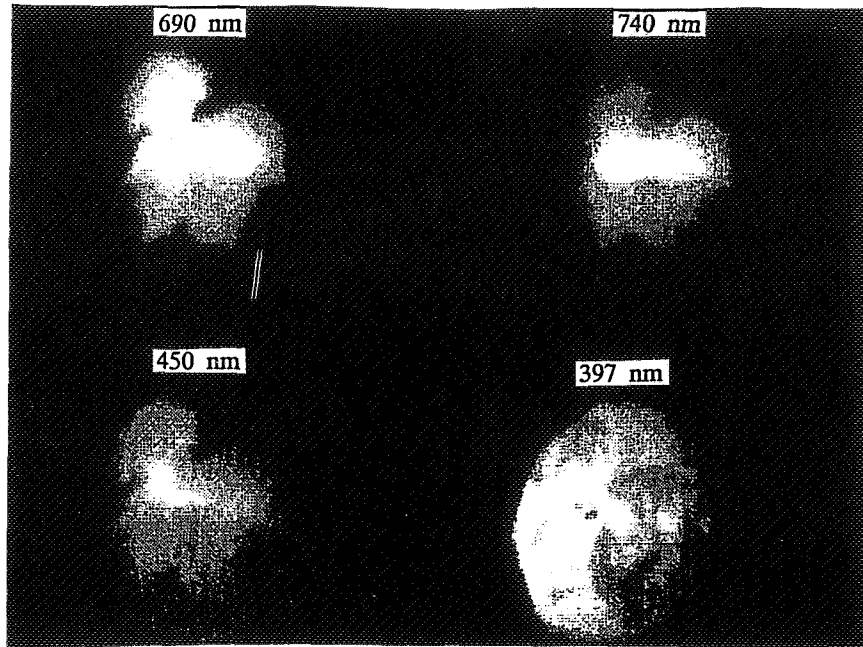


Figure 3. Simultaneous fluorescence images of two maple leaves recorded at 740, 690 and 450 nm. An elastic backscattering image is also seen. A computer processed image obtained by dividing the 690 nm and the 740 nm images is shown, clearly discriminating between a green and a slightly yellow leaf. Fluorescence spectra from green and slightly yellow leaf recorded in 50 m distance are included in the figure, and clearly show the origin of the discrimination.

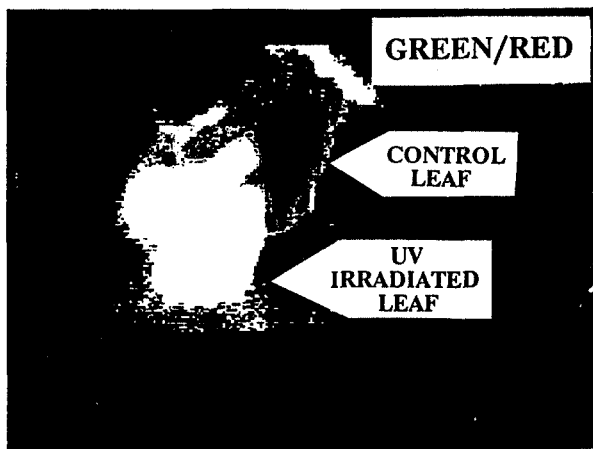
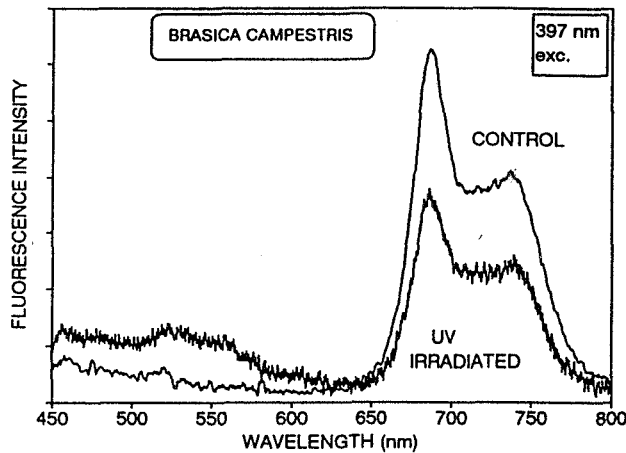


Figure 4. Remotely recorded fluorescence spectra for leaves of *Brasica Campestris* grown in normal light and in the presence of additional UV light. The image of one leaf of each kind was formed dividing the green fluorescence by the red fluorescence pixel by pixel

discrimination was provided in the red-to-green ratio, as shown in the remotely recorded fluorescence spectra in Fig. 4. This figure also includes a processed image dividing the green intensity by the red intensity. Statistical analysis of multi-leaf frames will be performed within the European LASFLEUR project.

ACKNOWLEDGEMENTS

Collaboration with L.O. Björn, Department of Plant Physiology, Lund University, is gratefully acknowledged. This work was supported by the Swedish Natural Science Research Council and the Swedish Space Board.

REFERENCES

1. L. Pantani and R. Reuter (eds), Lidar Remote Sensing of Land and Sea, EARSEL Proceeding (EARSEL, Paris 1992).
2. H. Edner et al., in Ref. 1.
3. H. Edner, K. Fredriksson, A. Sunesson, S. Svanberg, L. Unéus and W. Wendt, Appl. Opt. 26, 4330 (1987)
4. S. Andersson-Engels et al., IEEE J. Quant. Electr. QE-23, 1798 (1987)

A Geodetic Laser Radar Rangefinder
with 10^{-7} Resolution

by

Y.Mizushima, M.Takeichi, Y.Warashima,
A.Takeshima, I.Ogawa, K.Ichie

Hamamatsu Photonics K.K.

1126 Ichino-cho, Hamamatsu 435, Japan

and

N.H.Schiller

Hamamatsu Corporation

360 Foothill Road, Bridgewater, NJ 08807 USA

A novel geodetic laser radar rangefinder unit utilizing a pair of synchronized 10psec streak camera systems has been developed for displacement measurements of the earth's plates. In order to achieve minimum computing error and assure extremely high spatial resolution, an optical pulse registration clock was developed and used to register a fiducial mark on the time scale of the system.

Conventional optical rangefinders have been limited to a relative resolution of 10^{-6} even for short distances.⁽¹⁾⁽²⁾ The system to be reported on today has the capability of measuring a 50km range with an accuracy of 4mm corresponding to a relative resolution of 10^{-7} . With a gain of greater than 3×10^3 , the system has the capability of detecting extremely weak signals on the order of photon counting. This combined with temporal gating makes daytime measurements comparable in SN ratio to nighttime viewing. This is useful for measuring faint signals returning over a range of several tens of kilometers. The present ranging system was designed to observe the mutual displacement of geodetic plates⁽³⁾ and was employed to measure the boundary between the Philippine and Asian geodetic⁽⁴⁾ plates that pass beneath the Suruga Bay near Hamamatsu City, Japan. The system has been in operation for over 3 years.

In addition the system has the ability of producing and detecting optical ranging pulses of several wavelengths simultaneously making this a complete multicolor system.

The basic GLRR system consists of; a frequency stabilizing crystal, optical clock, YAG laser, KDP doubling crystal, KD*P tripling crystal, two matched streak cameras (A and B), a control computer, and an output/input periscope system (see Figure 1).

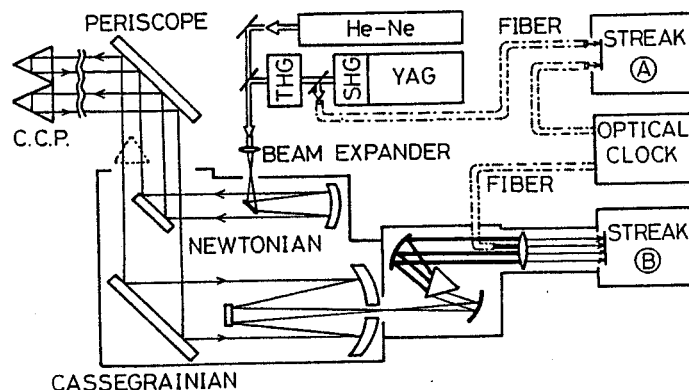


Figure 1. Schematic Diagram of the Geodetic Laser Radar Rangefinder System

Timing of all components of the system are governed by a single frequency stabilized quartz oscillator crystal which serves as a master clock. The signal from the master clock is an electrical signal and acts as a reference to synchronize operation of the optical clock, mode-locked YAG laser and streak cameras A and B.

The "optical clock" system generates a train of optical pulses precisely spaced in time. The optical pulses are generated by regulated pulses from a single master clock quartz oscillator driving a semiconductor gain-switched laser diode. The train of pulses is then directed via fiber cables to the inputs of each of the two streak cameras thereby producing a fiducial marker within the streak sweep output image. Using the optical clock in place of an electronic gate circuit the intrinsic resolution of the overall system is improved. The fiducial register mark produced by the optical clock serves as a sweep timing reference mark to normalize out any inconsistencies between the two streak cameras and to provide a time base for long distance ranging.

The YAG laser/pulse selector system outputs a continuous train of single narrow 1.06um pulses with 2ms spacing. Each pulse is then up-converted to its 2nd (0.53um) and 3rd (0.355um) harmonic resulting in three simultaneous wavelengths to be used for optical ranging.

Just after the second harmonic generator crystal a portion of the combined 1.06um and 0.53um optical pulse is beam split off and delivered to reference streak camera A via an optical fiber. The two-wavelength signal together with the fiducial marker generated by the optical clock is then swept in time and displayed on the output phosphor screen of streak camera A. The time resolved sweep image is then captured and recorded in the streak camera readout system memory for later analysis and comparison with the returning ranging signal.

The remaining majority of the two-wavelength signal is then directed through the third harmonic generator crystal. After emerging from the third harmonic generator, the three-wavelength ranging pulse is directed into a beam expander and launched via the sending telescope toward a target station from the central observatory. The target station is equipped with an array of 19 quartz prism corner-cube reflectors mounted in a housing. The reflector units are used to redirect the ranging pulse back toward the central observatory. A 15mW He-Ne laser is used for the initial alignment of the telescope prior to each sequence of measurements. The returning pulses are captured by the receiving telescope and directed through a prism to the input of measurement streak camera B. The three wavelengths of the ranging pulse are then spacially separated by using a 60°, quartz prism. The prism also serves to disperse background light.

The three wavelength components of the ranging signal are then spacially positioned across the entrance slit of streak camera B along with an identical optical clock signal as incident on streak camera A. The range signal together with the fiducial marker is then swept in time by streak camera B and displayed on its output phosphor screen.

Each streak camera's output sweep image is viewed by the streak camera readout system. A temporal profile is produced for each of the three wavelength components of the ranging pulse and optical clock pulse, and recorded into memory. The averaged profiles (at each wavelength) always very nearly resemble a Gaussian in shape, closely reproducing the outgoing ranging pulse waveform. Therefore, the exact instant, within several picoseconds of the signal peak is easily computed by the principle of the center of gravity of the temporally streaked image. In the present system, the overall resolution is 4mm, which is mostly limited by the streak camera readout distortion.

Ranging to the target is achieved by measuring the time of flight of each optical pulse. For an accurate measurement, the transit time within the telescope

system needs to be subtracted from the range path. This is accomplished by placing a corner cube in front of the periscope (telescope system). The null measurement is made before each sequence of ranging measurements.

Timing of the outgoing and returning ranging pulse is measured with reference to the optical clock pulse. Streak camera A measures the time relation between the optical clock pulse and the outgoing ranging pulse prior to being launched via the sending telescope. Streak camera B measures the time relation between the optical clock pulse and the returning ranging pulse after being captured by the receiving telescope. The time difference is then computed by the control computer. The major portion of the transit time of the ranging pulse is measured by a pulse counter in increments of 1ns. The pulse counter, counts the number of optical clock pulses between the time of launch and the time of return. The total propagation time is the arithmetic sum of these minor and major timing components.

A schematic representation of a typical streak camera readout system monitor image for a 32km range measurement is shown in Figure 2. Displayed in the diagram is a measure of the relative time of arrival of each of the three wavelength components of the ranging pulse after traveling through the atmosphere to the target site. From left to right, 4 analysis windows can be seen showing the 1.06um pulse arriving first, followed by the 0.53um pulse and the 0.35um pulse. The optical clock (fiducial marker) is seen in the third window from left. Also, overlaid on the left of the screen is an intensity profile corresponding (in this case) to the 0.355um region window. For each reading, 100 streak sweeps are overlapped and integrated on the output phosphor screen of the streak camera. An intensity profile as a function of time is then generated for each analysis window by the streak readout system and recorded in memory.

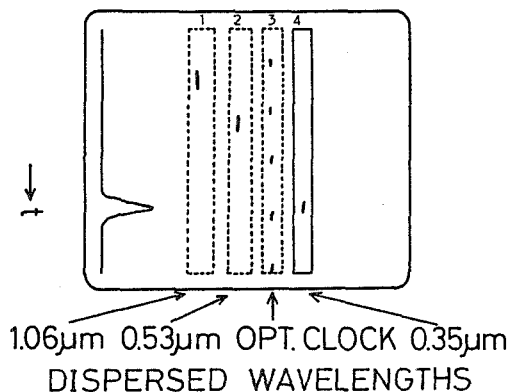


Figure 2. Schematic diagram of the streak camera monitor image. Shown in the diagram are 4 analysis windows, each containing an optical pulse representing the relative time of arrival for each wavelength and an intensity vs. time profile corresponding to the 0.355um pulse in window 4.

Range measurement data is then normalized using refractivity data⁽⁵⁾⁽⁶⁾ taken from the literature for varying atmospheric parameters.

Since the first proposal of the multiwavelength⁽⁷⁾ correction method for optical ranging, there has been no practical test or actual evaluation. The present system allows for the first practical field test of that method. Further, both the multiwavelength and single wavelength correction methods to correct for varying atmospheric conditions were compared. In addition the authors have developed an improved multiwavelength correction⁽⁸⁾ method reducing the influence of atmospheric parameters. Report of the first practical field test and evaluation and comparison

of the multiwavelength and single wavelength methods will be presented. Considering the available device accuracy, the single wavelength method is rather superior if combined with a suitable estimation of the atmospheric parameters.

For single wavelength measurements, the observed temperature lapse rate due to the altitude difference of the launching and target sites proves that the adiabatic lapse rate holds at sunset for fine weather conditions. Also, for correction of the atmospheric boundary layer effect, difference of the diurnal temperature changes at altitudes of 38m and 3m from the ground is continuously monitored. When the potential temperature distribution is vertically equal, the adiabatic lapse rate can be applied. After correction, 3×10^{-7} resolution (1cm for 30km range) was achieved for geodetic observation.

A new proposed system will incorporate a higher temporal resolution streak camera capable of providing better than 1ps resolution. If the new streak camera is carefully calibrated, an instrument resolution better than 0.5mm will be achieved. Then, together with our new improved multiwavelength correction method, 1×10^{-7} relative resolution will be provided. Since this measurement method is considerably independent of atmospheric parameters, measurements can be made at any time, and its use for general applications will become more practical.

Acknowledgments

The Authors are grateful to T. Hiruma, President of Hamamatsu Photonics K.K. for supporting this project, the Japan Key Technology Center for their encouragement and financial loan, and the Shizuoka Prefectural Government for their encouragement and various support in construction of the stations and Prof. J. Kondo of Tohoku University for helpful discussions.

References

- 1) P.L.Bender, Laser Measurement of Long Distances, Proc. IEEE 55, no.6, 1039-45, 1967
- 2) J.B.Abshire, Pulsed Multiwavelength Laser Ranging System for measuring atmospheric delay, Appl.Opt. 19, no.20, 3436-40, 1980
- 3) M.Takeichi et al, A Geodetic Laser Radar Rangefinder with 10^{-7} Resolution, (to be published)
- 4) K.Ishibashi, Earthquake Prediction - An International Review Maurice Ewing Series vol.4, AGU, pp.297-332, 1981
- 5) J.C.Owens, Optical Refractive Index of Air:Dependence on Pressure, Temperature and Composition, Appl.Opt. 6, no.1, 51-58, 1967
- 6) P.Schellenkens et al, Measurement of the Refractive Index of Air Using Interference Refractometer, Metrologia 22,279-87, 1987
- 7) L.E.Slater and G.R.Huggett, A Multiwavelength Distance-Measuring Instrument for Geophysical Experiments, J.Geophys. Res.81, no.35, 6299-6306, 1976
- 8) I.Ogawa et al, Improvement of the multicolor method for optical distance measurement, (to be published)

Altimetry and Lidar Using AlGaAs Lasers
Modulated with Pseudo-Random Codes

James B. Abshire
Jonathan A.R. Rall
NASA-Goddard Space Flight Center
Experimental Instrumentation Branch
Greenbelt MD 20771

Serdar S. Manizade
Science Systems and Applications Inc.
5900 Princess Garden Parkway
Lanham MD 20706

April 14, 1992

Abstract: We have demonstrated a prototype laser altimeter and lidar which uses a low power AlGaAs laser modulated with a pseudorandom noise (PN) code, a 20 cm diameter telescope and a photon counting receiver. Measurements to tree canopies over a 400 m horizontal path show strong signal with 5.3 mW average power and a 6.4 msec averaging time. Computer simulations predict lidar performance for various types of scattering targets.

Summary: AlGaAs lasers offer significant size, weight, and efficiency advantages compared to other laser sources. Their emission wavelengths, between 780 and 860 nm, are well matched both to atmospheric water vapor absorption bands and to photomultiplier and silicon detectors. Due to their limited peak powers, conventional short pulsed measurement techniques are not practical for lidar or altimeters using AlGaAs sources. However, these lasers are well suited for PN code modulation, whose noise-like correlation properties are very useful for ranging measurements [1].

Several prior lidar have used PN code modulation to obtain range resolved signals with lasers of low peak power. In 1983, Takeuchi *et al.* [2] externally modulated the 514.5 nm output from an Argon laser with a PN code to measure the lidar return from a smoke plume at 1 km. In 1986, Takeuchi *et al.* [3] demonstrated a PN code aerosol lidar using a single AlGaAs laser as a transmitter. This system measured lidar returns from falling snow, smoke from a smoke candle, aerosols at night, and cloud structures. In 1988, Norman and Gardner [5] proposed a PN code technique for performing laser ranging measurements to satellites, and presented a signal and error analysis.

We have designed, constructed and tested a prototype PN code lidar and altimeter using AlGaAs lasers emitting near 820 nm. The system is shown in Figure 1 and its characteristics are summarized in Table 1. Although our initial measurements were made using 100 nsec (15 m) range bins, the prototype system is capable of measurements with range bins as short as 5 nsec (75 cm). The receiver system is also capable

of accumulating more than the 2048 sequences in the 6.4 msec averaging time we used for all these initial experiments.

We measured the prototype system's sensitivity in laboratory tests by using a corner reflector to direct highly attenuated signals from the transmitter back into the receiver. Signal correlation peaks twice the height of the noise peaks were observed with a photocathode illumination of 29 fW and a signal photoelectron count rate of 9.8 kHz. We also measured the performance of the prototype system by making measurements to tree canopies at a distance of 200 and 400 m. For trees at 200 m, clear correlation peaks were measured with a transmitted power of 0.53 mW. Strong repeatable correlation peaks, shown in Figure 2, were measured with 5.3 mW power transmitted to tree canopies at a range of 405 m.

We have also developed a Monte Carlo simulator to investigate PN lidar operation and its ability to measure range and detect differences in target reflectivity. The simulator accepts an arbitrary target profile, corresponding to a hard target at a specified range, or a distributed target, such as clouds, defined by variable backscatter and extinction coefficients. We model the lidar or altimeter by parameters including the transmitted power, receiver telescope aperture, and detector background counts and photon detection efficiency. The lidar equation is used to determine the target response function, which is then convolved with the transmitted code to yield the average time-resolved received signal. The simulator generates received signal counts in the histogram by using Poisson statistics on a per bit basis. Background counts, due to background illumination or dark current, are generated independently and added to the histogram.

The simulator mimics the instrument by accumulating a received photon histogram over a specified number of repetitions of the PN code. A cross-correlation performed between the histogram and the transmitted code recovers the detected target response function. For a hard target, this correlation yields the range and reflection coefficient of the target. For distributed targets, the correlation may be inverted to yield estimates of the range-resolved extinction and backscatter coefficients.

Preliminary results of a simulation of a spaceborne aerosol lidar are shown in Table 2 and figures 3 & 4. Figure 3 shows an input backscatter profile representing two atmospheric scattering layers and the earth's surface. The output cross-correlation function (Fig. 4c) shows the instrument's ability to detect the range and strength of the scattering targets. The system parameters may be optimized for the measurement objectives. For example, a measurement of topography can be made with only a 1msec observation time in place of the 5.1 seconds listed in Table 2, but the associated reduction in sensitivity does not allow observation of the aerosols in the output cross-correlation.

The prototype and simulations demonstrate the feasibility of the lidar and altimeter using AlGaAs lasers modulated by a PN code. We are now improving the prototype in a number of ways which will result in improved measurement resolution and sensitivity.

References:

1. R. C. Dixon, *Spread Spectrum Systems* (Wiley, New York, 1976).
2. N. Takeuchi, N. Sugimoto, H. Baba, and K. Sakurai, "Random modulation cw lidar," *Applied Optics* 22, 1382 (1983).
3. N. Takeuchi, H. Baba, K. Sakurai, and T. Ueno, "Diode-laser random-modulation cw lidar," *Applied Optics* 25, 63 (1986).
4. C. Nagasawa, M. Abo, H. Yamamoto, and O. Uchino, "Random modulation cw lidar using new random sequence," *Applied Optics* 29, 1466 (1990).
5. D. M. Norman and C. S. Gardner, "Satellite laser ranging using pseudonoise code modulated laser diodes," *Applied Optics* 27, 3650 (1988).

Table 1 - Prototype AlGaAs Lidar Characteristics

Laser Type	AlGaAs Laser Diode, Mitsubishi ML5702A
Laser Modulator	Positive Drive, Current Steering
Collimating Lens	3 element, NA=0.5
PN Code	31 bit, 10 MHz bit time
Range Resolution	100 nsec \approx 15 meters
Telescope	20 cm diameter, f6.3
Interference filter	820 nm, 10 nm bandpass
Photomultiplier	GaAs photocathode, \approx 3% QE, 20 nsec pulse width
Amplifiers	60 dB gain
Low pass filter	Gaussian, 20 nsec impulse response
Discriminator	Leading edge type
Waveform Digitizer	Digitizing Oscilloscope, 500 elements/scan
Signal Averaging	2048 waveforms/record

AlGaAs Altimeter BreadBoard System

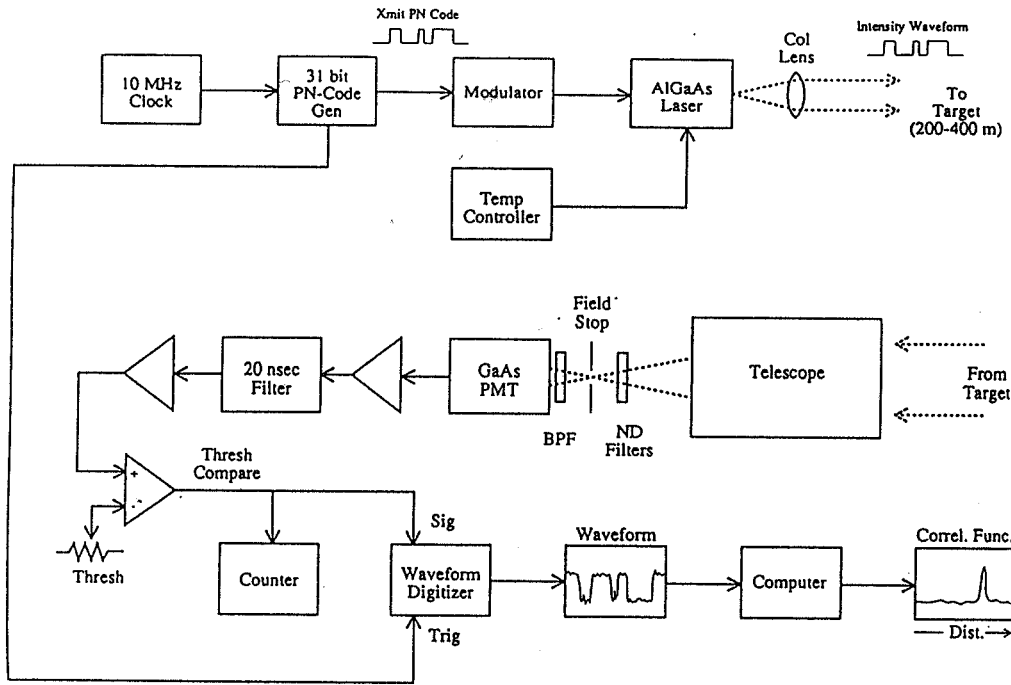
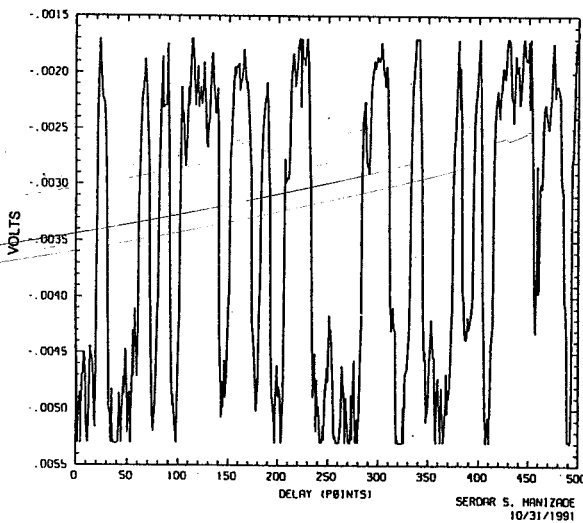


Figure 1

Figure 2
Results from Horizontal Path Tests of Breadboard System
 10/30/91
 5.2 mW Average Transmitted Power Range ~400 m
 31 bit PN Code Varian 192 PMT detector
 15m (100nsec) bit resolution 6.4 msec integration time
 Target: Tree Canopies

Digitizing Oscilloscope Waveform



Correlation Function

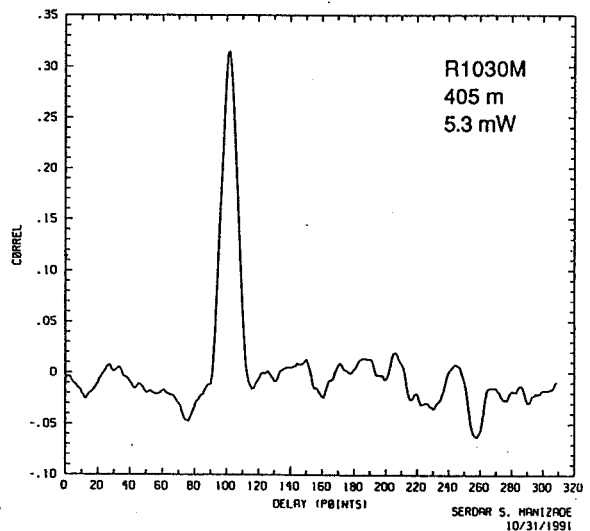
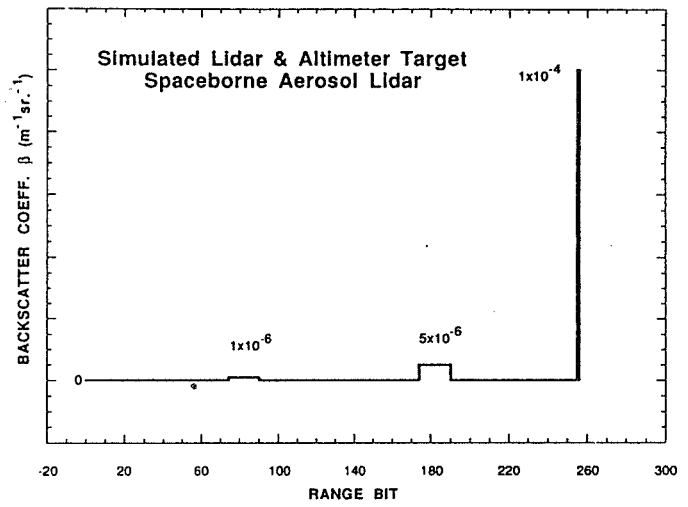


Table 2 - Spaceborne Lidar Simulation Parameters

Modulation Rate	1 Mbit/sec
Range Resolution	150 m/bit (1 μ sec/bit)
PN Code Length	255 bits
Ave. Transmit Power	5 W
Range Span	38.2km
Starting Range	400 km
Telescope Area	0.6 m ² (90cm diam, 15cm c.o.)
Receiver transmission	50%
Detector Quantum Effic.	20% (Geiger mode SiAPD)
False Alarm Probability/bit	10%
Observation Time	5.1 sec

Figure 3



(4a)

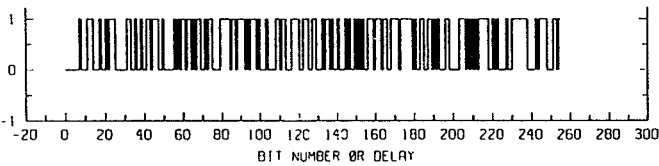
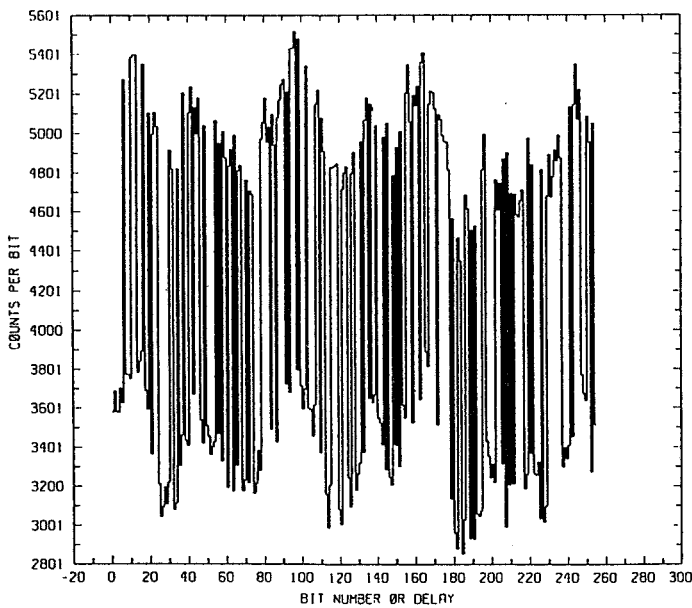
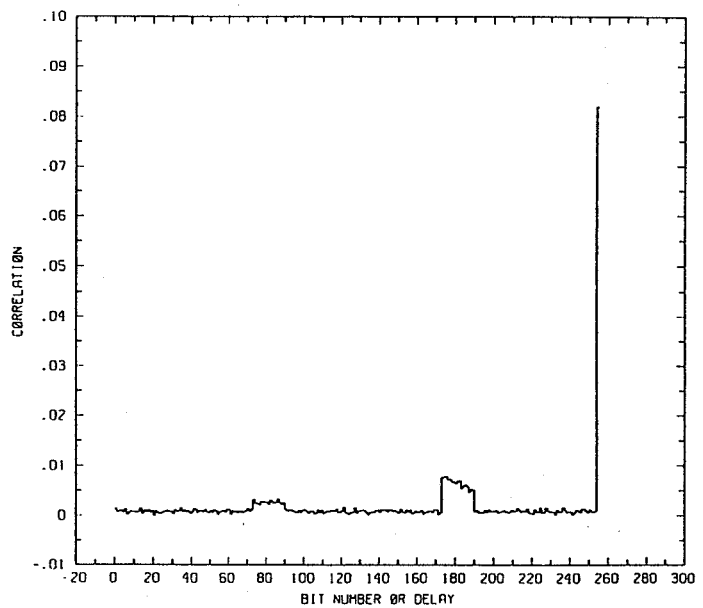


Figure 4
 Simulator Results- Spaceborne Aerosol Lidar
 a) Transmitted PN Code
 b) Received Histogram
 c) Output Cross-Correlation

(4b)



(4c)



Multiple Scattering Technique Lidar

Luc R. Bissonnette

DREV-Defence Research Establishment Valcartier
P.O. Box 8800, Courcellette, Québec, Canada , G0A 1R0

1 Introduction

It is well known that the lidar technique has limitations for the determination of the aerosol extinction coefficient. The single scattering lidar equation depends on two unknowns: the backscatter and extinction coefficients, β and α respectively. Hence, hypotheses or additional measurements are needed to resolve the indeterminacy. In the conventional solution method, one assumes a relation of the form $\beta = \text{const} \alpha^k$, where *const* and *k* are constants, and then differentiates the resulting equation with respect to range. The result is an ordinary differential equation of the Bernoulli-Ricatti type. This equation has a known general solution but the difficulty arises with the boundary value needed to construct a particular solution. Since the Bernoulli-Ricatti equation was arrived at by differentiation of the measured signal, the boundary value cannot be arbitrary. It must be consistent with that measured signal and, in general, it cannot be derived from it. Hence, an independent measurement or guess must be made. This necessarily involves errors and, owing to the nonlinearity of the Bernoulli-Ricatti equation, errors on the boundary value can have disastrous consequences. Klett [1] has shown that integrating backward from a far end boundary value makes the solution stable but the problem of determining that boundary value from lidar-derived information remains unsolved.

The Bernoulli-Ricatti equation is based on the single scattering description of the lidar backscatter return. In practice, especially in low visibility conditions, the effects of multiple scattering can be significant. Instead of considering these multiple scattering effects as a nuisance, we propose here to use them to help resolve the problems of having to assume a backscatter-to-extinction relation and specifying a boundary value for a position far remote from the lidar station. To this end, we have built a four-field-of-view lidar receiver to measure the multiple scattering contributions. The system has been described in a number of publications [2-4] that also discuss preliminary results illustrating the multiple scattering effects for various environmental conditions. This paper reports on recent advances made in the development of a method of inverting the multiple scattering data for the determination of the aerosol scattering coefficient.

2 Multiple Scattering Inversion Method

A multiple scattering lidar equation is derived from a phenomenological and approximate integration of the forward scattering events that contribute to the illumination of the sample volume seen by the lidar receiver, and that also increase the strength of the signal reaching the receiver after reflection by the sample volume. The equation is as follows:

$$\begin{aligned}
 P(z, \theta) = & P_0 \frac{A}{z^2} \frac{ct}{2} \alpha_s(z) p(z, \pi) e^{-2\tau(z)} \\
 & \cdot \left\{ 1 + 2\pi e^{\tau_s(z)} \int_0^z dz' \alpha_s(z') e^{-\tau_s(z')} \int_0^\psi d\phi \sin \phi p(z', \phi) \right\} \\
 & \cdot \left\{ 1 + 2\pi z e^{\tau_s(z)} \int_0^{\pi/2} d\gamma \cos \gamma \frac{p(z, \pi - \gamma)}{p(z, \pi)} \right. \\
 & \left. \cdot \int_0^\theta d\beta e^{-\tau_s(R)} \alpha_s(z'') p(z'', \beta + \gamma) \frac{(\tan \beta + \tan \gamma)}{\sec \beta \sin(\beta + \gamma)} \right\}, \quad (1)
 \end{aligned}$$

with

$$\tan \psi = \frac{z}{z - z'} \tan \theta ; \quad z'' = \frac{z \tan \gamma}{(\tan \beta + \tan \gamma)} ; \quad \text{and } R = \frac{z \tan \beta}{(\tan \beta + \tan \gamma) \cos \gamma},$$

where $P(z, \theta)$ is the lidar return from range z and within a field of view of semi-angle θ ; P_0 is the average power of the laser pulse; c is the speed of light; t is the duration of the laser pulse; α_s is the scattering coefficient; $p(z, \phi)$ is the scattering phase function; $\tau(z) = \int_0^z \alpha(z') dz'$ is the optical depth; and $\tau_s(z) = \int_0^z \alpha_s(z') dz'$ is the scattering optical depth. Equation 1 is the conventional lidar equation multiplied by two correction terms that respectively take into account the multiple scattering effects for the forward and backward propagation legs of the lidar pulse. The correction depends only on the scattering properties of the medium in terms of the scattering coefficient α_s , the scattering phase function $p(z, \phi)$ and the scattering optical depth τ_s .

The proposed inversion method consists in ratioing the lidar returns measured at the four concentric fields of view of our instrument. This factors out the expression for the conventional lidar return and the ratios of the signals at the different fields of view depend on the multiple scattering correction terms only. As it turns out, the integrands in the correction terms are weighted toward values of z' and z'' close to z . Under these conditions, we can work out algebraic approximations to the integrals of eq. 1 in terms of the scattering coefficient α_s , the scattering optical depth τ_s , the amplitude of the forward lobe of the phase function $p(z, 0)$, and the field of view θ . Of these, only two are independent unknowns since θ is a system parameter and τ_s is a function of α_s . Therefore, by measuring $P(z, \theta)$ at three or more fields of view, we have two or more independent ratios to solve for $\alpha_s(z)$ and $p(z, 0)$.

The method does not require an absolute calibration because it is based on ratios of simultaneously measured signals. A boundary value is needed in the form of the scattering optical depth $\bar{\tau}_s$ over the near field range $0 - \bar{z}$ where the multiple scattering contributions are below the noise level. This is not a problem since $\bar{\tau}_s$ is nearly constant for all situation and since the solutions for $\alpha_s(z)$ and $p(z, 0)$ are not very sensitive to errors on $\bar{\tau}_s$.

The solution $p(z, 0)$ can be related to the radius of the large particles. The large particles have a dominant effect on the forward peak of the phase function and, if the particles are large enough, the effect is mostly diffraction. Under these conditions, we have $p(z, 0) \simeq \pi a^2/\lambda^2$, where λ is the lidar wavelength and a , some effective size of the large particles responsible for the forward scattering peak. Therefore, we can derive from the $p(z, 0)$ solution the following estimate:

$$a(z) \simeq \lambda \sqrt{p(z, 0)/\pi}, \quad (2)$$

for the radius a of the large particles that cause most of the lidar multiple scattering effects.

3 Results

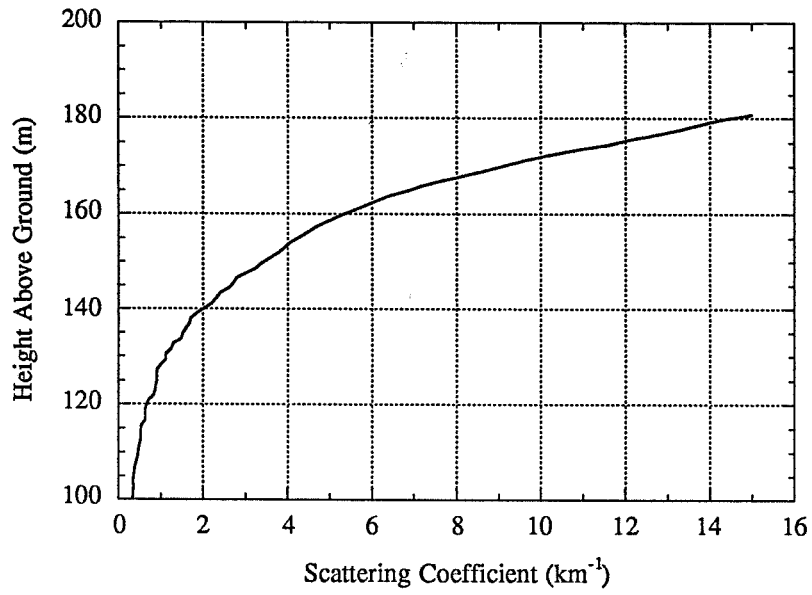
Figure 1 is an example of the results obtained with the proposed method. It shows the vertical profiles of α_s and the particle radius a obtained from low stratus clouds. For this example, a series of lidar returns were recorded at 50-s intervals over a period of 15 minutes. The lidar was fired at an elevation of 13.3° . The inversion was performed for each lidar shot and the resulting solutions averaged to give the curves of Fig. 1a-b.

The scattering coefficient goes through an upward turn at an altitude of about 130–140 m from where it increases monotonically up to a value of $\sim 15 \text{ km}^{-1}$ at 180 m where the inversion is terminated because the signal from the central field of view falls below the instrument noise level. There is no sign that we have attained the maximum cloud concentration. On the contrary, the solution trend clearly indicates a continued increase. Typically, the scattering coefficient in such clouds reaches values on the order of 50 km^{-1} and it is therefore consistent that the solution should still indicate no sign of leveling off at 15 km^{-1} . Hence, it seems that the proposed multiple scattering inversion method continues to give satisfactory results up to the point where it is no longer applicable since the return signal in one field of view has reached the instrument dynamic range limit.

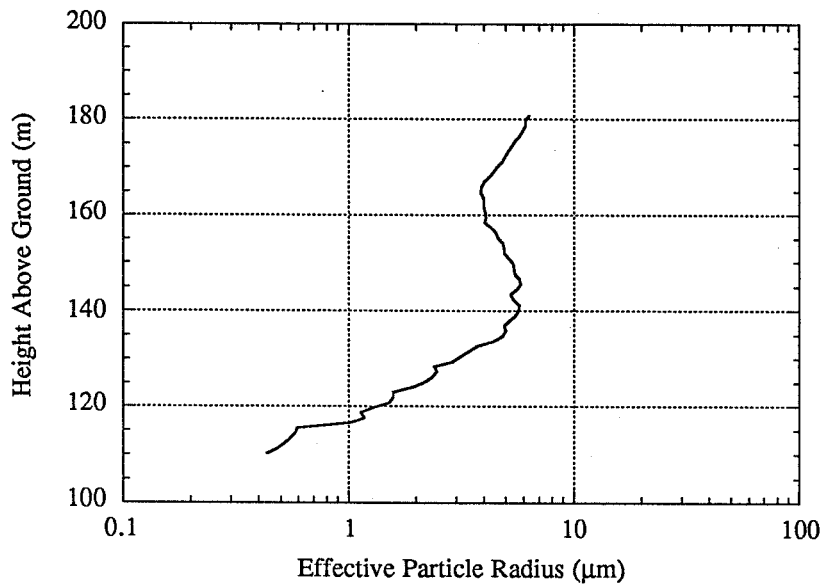
The profile for the effective particle radius shows a rapid increase at the cloud boundary but then settles to a more or less constant level of 4–6 μm . These values are within what is expected for stratus clouds.

References

- [1] J.D. Klett, "Stable Analytical Inversion Solution for Processing Lidar Returns," *Appl. Opt.*, **20**, 211, 1981.
- [2] L.R. Bissonnette and D.L. Hutt, "Multiple Scattering Lidar," *Appl. Opt.*, **29**, 5045, 1990.
- [3] L.R. Bissonnette and D.L. Hutt, "Multiple Scattering Contributions to Lidar Returns Measured with a Four Field of View Receiver," *Proc. 4th Intl. Workshop on Multiple Scattering Lidar Experiments*, University of Florence, pp. 10-21, 1990.
- [4] D.L. Hutt, L.R. Bissonnette and L. Durand, "Multiscattered Lidar Returns from Atmospheric Aerosols," *SPIE Proc. 1487 on Propagation Engineering*, pp. 250-261, 1991.



(a)



(b)

Figure 1: Multiple scattering inversion solutions for low stratus cloud profiles averaged over 20 lidar pulses fired at 50-s intervals. a: for the scattering coefficient; b: for the effective particle radius.

Multiple Scattering Effects on Spaceborne Lidar

DAVID M. WINKER AND LAMONT R. POOLE

Atmospheric Sciences Division
NASA Langley Research Center
Mail Code 475
Hampton, VA, USA 23665-5225

Introduction.

LITE (the Lidar In-space Technology Experiment) is a lidar system being developed by NASA Langley Research Center to be carried on the Space Shuttle. LITE is designed to make measurements from the middle stratosphere down to, and including, the Earth's surface. The system will be operated from the cargo bay of the Shuttle at an altitude of about 300 km and returned to Earth after the mission. Multiple flights are planned. The system is now under construction and scheduled to fly for the first time in early 1994. Among the primary science objectives of LITE are to demonstrate the utility of space-based lidar for mapping and characterizing clouds, and to develop retrieval methods for cloud optical depth and extinction. Further details on LITE are given in Couch et al. (1991). Preliminary results of a study of the significance of multiple scattering effects on lidar measurement of cloud optical properties are given here.

LITE contains a movable wheel located at the focus of the receiving telescope holding three field stop apertures, which may be rotated into place sequentially. A 3.5 mr aperture is used at night to minimize vignetting effects. A 1.1 mr aperture, matched to the divergence of the 1064 nm beam, improves the signal-to-noise ratio during daylight operations by reducing the background illumination at the cost of a small loss in signal. These two apertures were chosen to optimize operation in daytime and nighttime conditions, but also allow observation of the dependence of multiple scattering effects on field of view (FOV). The final aperture is annular with a 3.5 mr outer diameter and a 1.1 mr obscuration in the center. This aperture was designed to block the single-scattered return, permitting detection of the multiply-scattered return only.

Multiple scattering calculations.

A semianalytic Monte Carlo code originally developed for oceanographic calculations (Poole et al., 1981) has been modified for use in studying multiple scattering of space-based lidar. The approach is very similar to that described by Kunkel and Weinman (1976). The trajectory of each photon is followed from the transmitter through multiple scatterings until the photon is either scattered backward out of the atmosphere, scattered forward into the ground and absorbed, or scattered out the sides of the cloud. The probability that the photon will return directly to the detector is computed and summed over all significant scattering events within the field of view of the detector. Multiple scattering of the lidar pulse causes an apparent increase in the transmittance

of the medium. The total-scatter return can be modeled as due to an apparent decrease in optical depth between z_o and z by a factor $\eta(z - z_o)$:

$$P_{TS}(z) = (C/z^2)\beta(z) \exp \left[-2\eta(z - z_o) \int_{z_o}^z dl \sigma(l) \right].$$

The transmittance factor $\eta(z - z_o)$ can then be determined from the ratio of total scatter to single scatter:

$$\eta(z - z_o) = 1 - \frac{1}{2\tau(z)} \ln \left(\frac{P_{TS}(z)}{P_{SS}(z)} \right).$$

Results.

Multiple scattering effects for space-based lidar are more significant than for ground-based lidar due to the much larger beam diameter in the atmosphere. These larger diameters are due not only to the greater range between the lidar and the scattering volume, but also the need to maintain relatively large beam divergences to satisfy eye safety restrictions on the laser irradiance at the Earth's surface. The simulations presented here are for a wavelength of 1064 nm and the Deirmendjian C1 phase function, which yields an extinction coefficient of 17.259/km. We have looked at two cases: a space-based lidar at 296 km observing a C1 cloud 293 km from the lidar and, for comparison purposes, a ground-based lidar looking at a C1 cloud with a base height of either 2 km or 5 km. The C1 size distribution roughly approximates that of stratocumulus or altocumulus clouds (aufm Kampe and Weickmann, 1957).

Figure 1 shows the relative contributions of the various scattering orders for the space-based configuration and 3.5 mr FOV. The first order scatter decreases exponentially into the cloud while the second and higher scattering orders build up with penetration depth and quickly become dominant. Twenty to 30 orders of scattering must be considered for a penetration depth of 600 meters. Figure 2 compares the single scatter return vs. the summation of the first 30 orders of scattering for three fields of view. The contribution of the higher order scattering is so strong that even though the optical depth is 10, the overall return drops only one or two orders of magnitude for the larger FOVs. In contrast, Figure 3 shows the single-scatter and total-scatter returns for a ground-based system with a 2 mr FOV. Only the first few orders of scattering are important, and after a few tens of meters the total-scatter signal decreases exponentially. In the space-based case the lidar profile through the cloud is seen to be quite dependent on the FOV of the receiver. The three field stop apertures available in LITE will be used to aid in characterizing the influence of multiple scattering on observations made with LITE.

Figure 4 shows the transmittance factor, $\eta(z - z_o)$, corresponding to the space-based case simulated above. It can be seen that $\eta(z - z_o)$ is strongly dependent on FOV. $\eta(z - z_o)$ decreases with penetration depth and eventually asymptotes to a low value, meaning the cloud appears to be much more transparent than it is. This transmittance is only apparent, however. In Figure 2 it is seen that the apparent attenuation of the lidar signal 600 meters into the cloud is only about an order of magnitude. In reality, many of the photons which appear to be coming from 600 meters into the cloud are multiply-scattered photons with path lengths equal to a range of 600 meters, but which have been scattered from shallower levels in the cloud.

This pulse stretching effect of multiple scattering is illustrated in Figure 5. When accumulating photon statistics, the code allows returns to be binned either by time of flight or according to the true depth in the cloud at which the scattering occurred. Figure 5 shows the return from a 120 meter deep C1 cloud binned both ways. Beneath the cloud is a Rayleigh atmosphere, providing non-zero returns. When binned by time-of-flight, the base of the cloud appears to be quite diffuse. When binned by depth, it is seen that all the scattering, is in, fact occurring within the cloud, and it is the increased path length of the multiply-scattered photons which makes the scattering appear to be coming from beyond the cloud. This illustrates the necessity of understanding multiple scattering effects even to interpret cloud returns qualitatively.

REFERENCES

- R. H. Couch, and 13 others, 1991: "The Lidar In-space Technology Experiment: NASA's first in-space lidar system for atmospheric research," *Optical Engineering*, 30, 88-95.
- H. J. aufm Kampe and H. K. Weickmann, 1957: "Physics of clouds," *Meteorological Research Reviews*, 3, 182-225.
- K. E. Kunkel and J. A. Weinman, 1976: "Monte Carlo analysis of multiply scattered lidar returns," *J. Atmos. Sci.*, 33, 1772-1781.
- L. R. Poole, D. D. Venable, and J. W. Campbell, 1981: "Semianalytic Monte Carlo radiative transfer model for oceanographic lidar systems," *App. Opt.*, 20, 3653-3656.

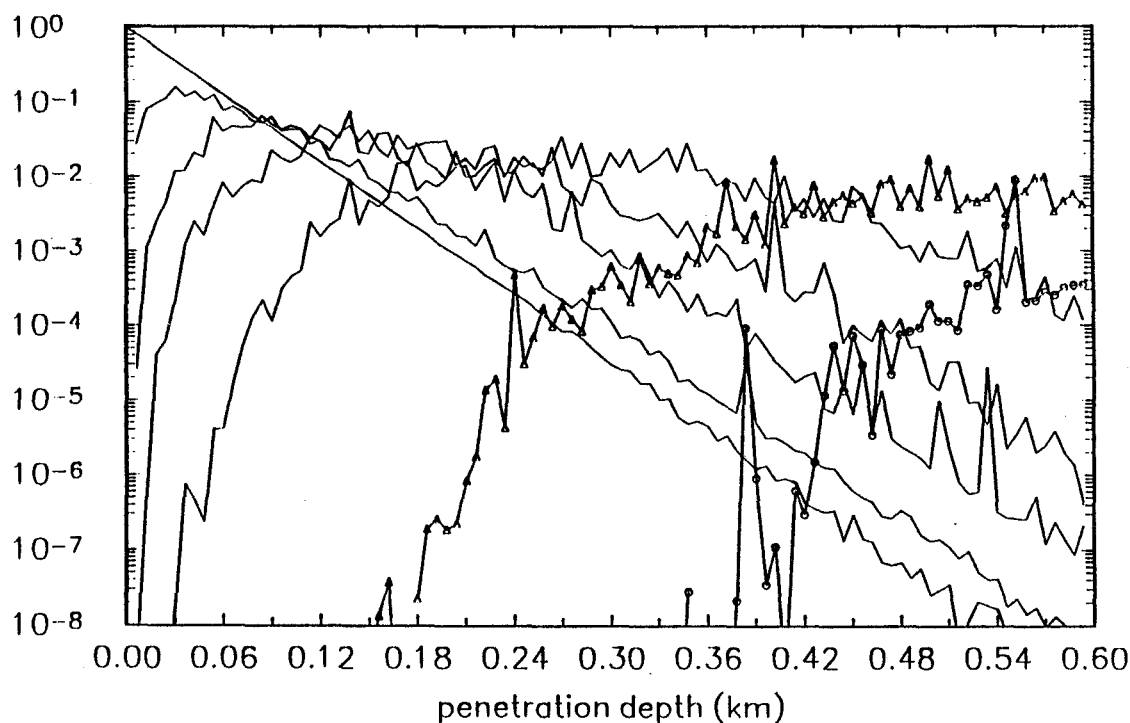


Figure 1. Relative scattering from C1 cloud for 3.5 mr FOV, space-based case. Shown are 1st, 2nd, 4th, 6th, 10th, 20th, and 30th orders of scattering.

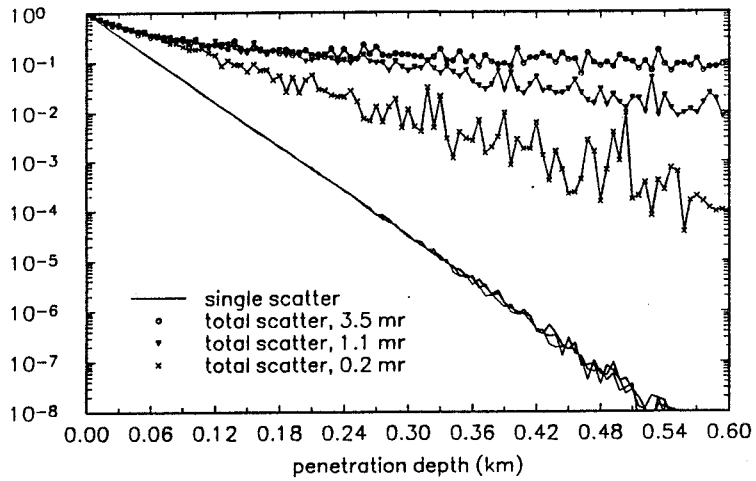


Figure 2. Relative returns from C1 cloud, space-based case. Shown are first-order scatter and summation of first 30 orders for three FOV's.

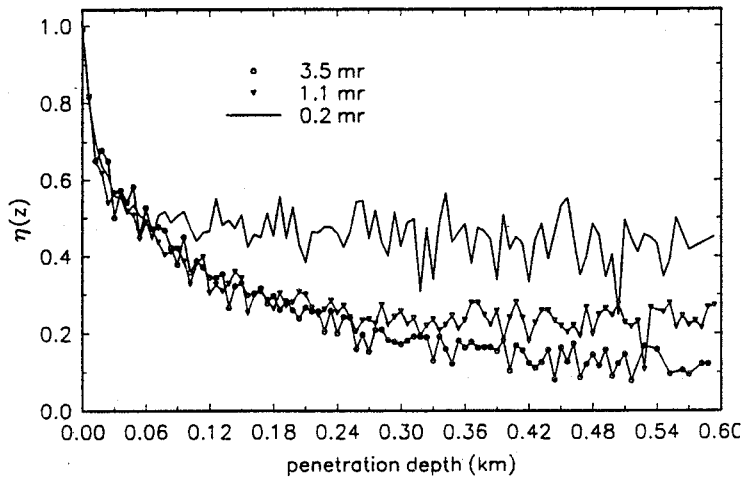


Figure 4. Multiple scattering factor $\eta(z - z_0)$ for cases of Figure 2.

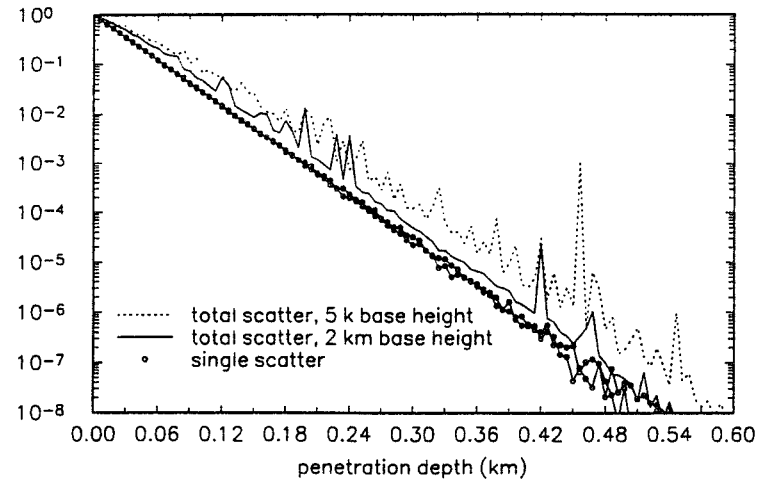


Figure 3. Relative returns from C1 cloud, ground-based case. Shown are first-order scatter and summation of first 30 orders for 2 mr FOV.

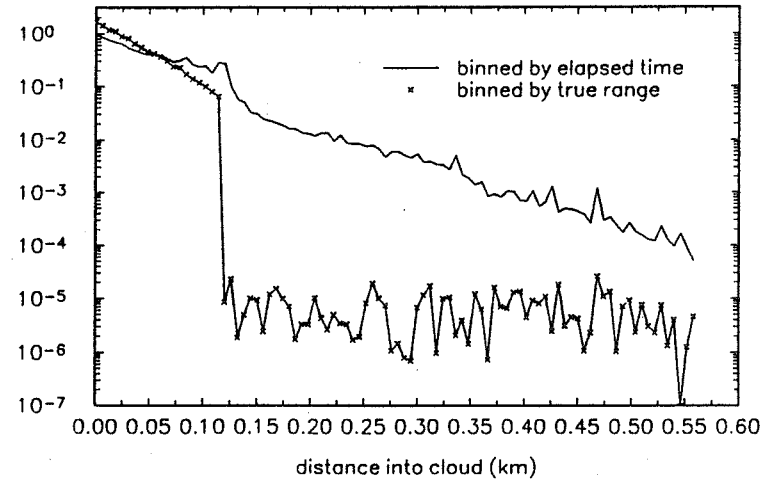


Figure 5. Pulse stretching from a 120 m thick C1 cloud, spacebased case. 3.5 mr FOV.

Measurement of multiple scattering effects with a polarization Raman elastic-backscatter lidar

Ulla Wandinger, Albert Ansmann, Claus Weitkamp, Walfried Michaelis
GKSS-Forschungszentrum, Postfach 1160, W-2054 Geesthacht, Germany

1 Introduction

The GKSS Raman elastic-backscatter lidar has successfully been used to measure water vapor profiles as well as extinction and backscatter coefficient profiles of aerosols independently from each other [1,2,3]. An open question is how multiple scattering influences these measurements, especially the aerosol extinction coefficient and the extinction-to-backscatter ratio. Some investigations have been made to determine multiple scattering effects quantitatively, for example from depolarization measurements [4,5,6], from multi-field-of-view measurements [7], or from a combination of both [8]. The depolarization technique suffers from the fact that both multiple scattering and single scattering from nonspherical particles cause a depolarization of the elastically backscattered light, so that it cannot be applied to measure the multiple scattering effect in ice clouds. The multi-field-of-view technique, on the other hand, has been used only for short measurement ranges until now.

This contribution describes a new method for the determination of multiple scattering effects. A polarization Raman elastic-backscatter lidar is used which allows the measurement of the depolarization of both the elastically backscattered light and the light Raman scattered from nitrogen molecules. With this technique the depolarization effect due to multiple scattering can be separated from single scattering depolarization. The apparatus and the calibration of the system are described in Ref. [9]. Here, a short discussion of the idea and a measurement example are given.

2 Measurement principle

The emitted laser light is linearly polarized. The component of the backscattered radiation with **E** vector parallel (superscript ||) and the component with **E** vector perpendicular (superscript ⊥) to the **E** vector of the emitted light are measured for both the nitrogen Raman signal and the elastic signal.

The elastic backscatter signals

$$\parallel P_{\lambda_0} = \parallel P_{\lambda_0}^{s,aer} + \parallel P_{\lambda_0}^m + \parallel P_{\lambda_0}^{mol} \quad (1)$$

and

$$\perp P_{\lambda_0} = \perp P_{\lambda_0}^{s,aer} + \perp P_{\lambda_0}^m + \perp P_{\lambda_0}^{mol} \quad (2)$$

are caused by single scattering from particles ($\parallel P_{\lambda_0}^{s,aer}, \perp P_{\lambda_0}^{s,aer}$), by multiple scattering ($\parallel P_{\lambda_0}^m, \perp P_{\lambda_0}^m$), and by single scattering from molecules ($\parallel P_{\lambda_0}^{mol}, \perp P_{\lambda_0}^{mol}$).

The magnitude of the depolarization ratio of the Rayleigh scattering process is known to be

$$\delta_{\lambda_0}^{\text{Ray}}(\pi) = \frac{\perp P_{\lambda_0}^{\text{mol}}}{\parallel P_{\lambda_0}^{\text{mol}}} = 0.016 \quad (3)$$

including oxygen and nitrogen rotational Raman scattering.

The nitrogen Raman signals

$$\parallel P_{\lambda_R} = \parallel P_{\lambda_R}^{\text{Ram}} + \parallel P_{\lambda_R}^{\text{m}} \quad (4)$$

and

$$\perp P_{\lambda_R} = \perp P_{\lambda_R}^{\text{Ram}} + \perp P_{\lambda_R}^{\text{m}} \quad (5)$$

contain singly scattered Raman light ($\parallel P_{\lambda_R}^{\text{Ram}}, \perp P_{\lambda_R}^{\text{Ram}}$) and radiation which underwent before or after the Raman scattering process elastic scattering from particles ($\parallel P_{\lambda_R}^{\text{m}}, \perp P_{\lambda_R}^{\text{m}}$).

Since the depolarization ratio of the Raman scattering process for the whole vibration-rotation branch of nitrogen is constant,

$$\delta_{\lambda_R}^{\text{Ram}}(\pi) = \frac{\perp P_{\lambda_R}^{\text{Ram}}}{\parallel P_{\lambda_R}^{\text{Ram}}} = 0.094, \quad (6)$$

any variation of the measured ratio $\delta_{\lambda_R} = \perp P_{\lambda_R} / \parallel P_{\lambda_R}$ with height results only from the multiple scattering effect which can thus be determined.

However, to quantify the influence of multiple scattering on the determination of extinction and backscatter coefficients further studies are necessary. For example, the dependence of the depolarization and of the multiple scattering effect on scattering angle and receiver field of view must be investigated.

3 Measurement example

A very first measurement taken in an optically and geometrically thick cirrostratus cloud is shown in Fig. 1. The measured lidar signals are plotted in Fig. 1a. The backscatter coefficient profile in Fig. 1b is determined using both the Raman and the elastic signals [2]. The height profiles of the depolarization ratios for the elastically and Raman scattered light are given in Fig. 1c.

In the lower part of the cloud between 4.4 and 5.6 km height the depolarization of the Raman scattered light is constant and has values typical for single Raman scattering (cf. Fig. 1c, solid line). Thus, multiple scattering does not play a role and the depolarization of the elastically scattered light (cf. Fig. 1c, dotted line) is caused by single scattering from randomly oriented, nonspherical ice particles. Between 5.4 and 6.2 km height a strong backscatter peak together with a low depolarization of the elastically scattered light is

measured. This is typical for cloud layers containing horizontally oriented ice crystals. Above 5.6 km height the Raman depolarization increases from the single scattering value to about 0.15 indicating that multiple scattering takes place. An extinction coefficient of about 0.6 km^{-1} is found in that region. The depolarization of the elastically scattered light measured above 6.2 km height is hence caused by both multiple scattering and single scattering from nonspherical particles.

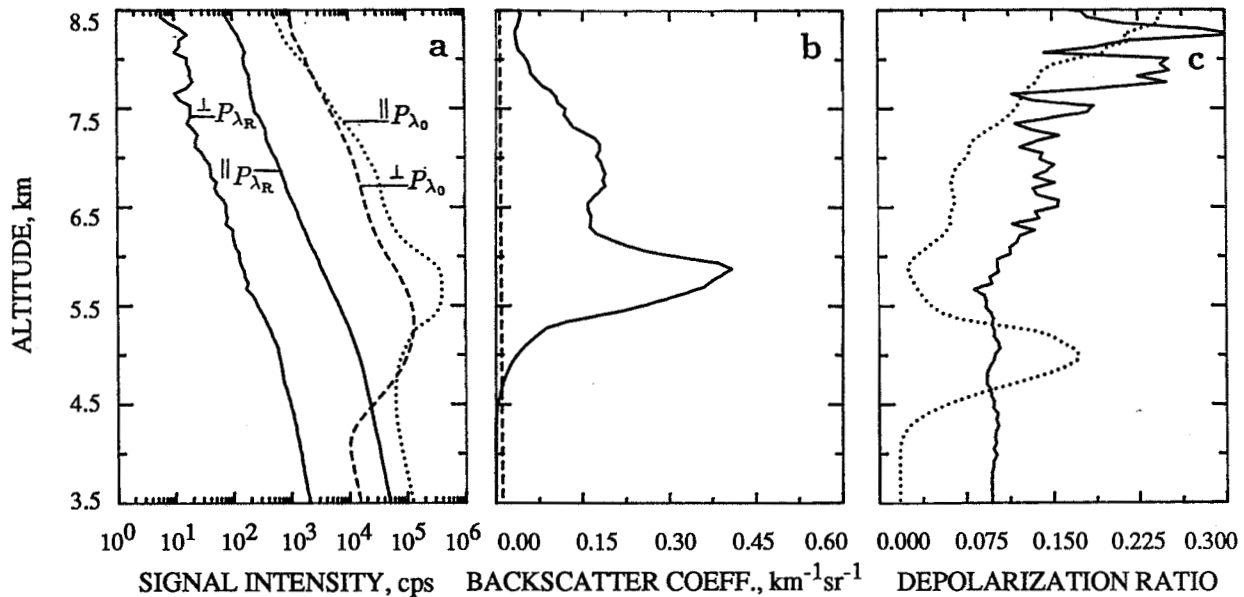


Fig. 1. Cirrostratus cloud measurement: a. Perpendicular and parallel polarized Raman nitrogen signals (solid lines) and elastic backscatter signals (dashed and dotted lines), b. backscatter coefficient, c. depolarization ratio of the Raman scattered light (solid line) and of the elastically scattered light (dotted line). 120,000 laser shots are averaged. Signals are smoothed with a sliding average window of 600 m. The dashed line in (b) is the molecular contribution.

4 Conclusion

The first measurements with the polarization Raman elastic-backscatter lidar show that this system allows to measure the multiple scattering influence on lidar signals. More measurement examples and the correction of multiple scattering effects on optical parameters derived from the lidar measurements will be discussed at the conference.

References

1. A. Ansmann, M. Riebesell, U. Wandinger, C. Weitkamp, E. Voss, W. Lahmann, and W. Michaelis, "Combined Raman elastic-backscatter lidar for vertical profiling of moisture, aerosol extinction, backscatter, and lidar ratio", *Applied Physics B* 54 (1992), in press
2. A. Ansmann, M. Riebesell, U. Wandinger, C. Weitkamp, W. Michaelis, "Independent measurement of extinction and backscatter profiles in cirrus clouds using a combined Raman elastic-backscatter lidar," *Appl. Opt.*, to be published
3. A. Ansmann, U. Wandinger, C. Weitkamp, W. Michaelis, "Stratospheric backscatter, extinction, and lidar ratio profiling after the Mt.-Pinatubo eruptions", this conference
4. S.R. Pal, A.I. Carswell, "Multiple scattering in atmospheric clouds: lidar observations", *Appl. Opt.* 15, 1990-1995 (1976)
5. C.M.R. Platt, "Lidar Observations of a Mixed-Phase Altostratus Cloud", *J. Appl. Met.* 16, 339-345 (1977)
6. K. Sassen, R.L. Petrilla, "Lidar depolarization from multiple scattering in marine stratus clouds", *Appl. Opt.* 25, 1450-1459 (1986)
7. L.R. Bissonnette, D.L. Hutt, "Multiple scattering lidar", *Appl. Opt.* 29, 5045-5046 (1990)
8. C. Werner, P. Hörmann, H.-G. Dahn, H. Herrmann, "Technical problems with respect to the separation of single and multiple scattering by a monostatic lidar" *Proceedings of: 4th International Workshop on Multiple Scattering Experiments, Florence, Italy, 29-31 October 1990, 147-174*
9. C. Schulze, U. Wandinger, A. Ansmann, C. Weitkamp, W. Michaelis, "Verification measurement of a polarization Raman elastic-backscatter lidar", this conference

Determining Water Cloud Particle Sizes from
Lidar Depolarization Measurements and
Time Dependent Multiple Scattering Calculations*

R.C. Garner, PhotoMetrics, Inc., Woburn, MA 01801

G.G. Koenig, Phillips Laboratory/Geophysics Directorate, Hanscom AFB, MA

We present a technique of extracting water cloud particle size information from lidar measurements in conjunction with double scattering calculations. In this presentation, we describe the technique and give examples using data taken with the Air Force Phillips Laboratory's (Geophysics Directorate) low altitude Nd:YAG, elastic backscatter lidar. In a related presentation we describe the double scattering lidar model which we developed for this work.

The technique uses simultaneous measurements of two orthogonal linear polarization components of lidar returns from water clouds, or other media composed of spherical particles. Any depolarization of the incident lidar radiation backscattered by such a media can only be due to multiple scattering. The amount of depolarization is dependent on the extinction coefficient and the single scatter phase matrix, both of which are functions of position in the medium. The phase matrix is dependent on the index of refraction of the particles and the particle size distribution.

Our technique is a modification of a procedure presented in Reference 1. There, particle sizes of water clouds are determined from double scattering calculations together with measurements of radiation scattered from volumes outside the lidar receiver's field of view (which can only be multiply scattered radiation). The methodology of our technique is similar but our "probe" of the scattering phase function (and thus the particle size distribution) is different.

The technique is performed in three parts:

Part 1

In the first part the total lidar return (both polarizations), is used to determine the extinction profile along the lidar beam path using standard methods which assume single scattering.

We use a modification of a procedure proposed by Sassen, et. al. [2] which they use to determine extinction coefficients in cirrus clouds. In that procedure the boundary condition required to solve the single scatter lidar equation is obtained by matching lidar measurements below the cirrus cloud to calculations which assume a model Rayleigh atmosphere

*Work Supported by the Air Force Phillips Laboratory, Geophysics Directorate, Hanscom AFB, MA.

for the given meteorological conditions. We modify this technique for lower altitude water clouds by matching to calculations which assume a model aerosol atmosphere.

The single scatter lidar equation is solved for the backscatter coefficient in the cloud as a function of range in the following way:

$$\beta_{\pi}^c(z) = \frac{G(z_o, z)}{1 - 2\frac{\eta_c}{k_c} \int_{z_o}^z G(z_o, z') dz'} - \beta_{\pi}^a(z) \quad (1)$$

where

$$G(z_o, z) = \beta_{\pi}^a(z_o) \frac{P(z)z^2}{P(z_o)z_o^2} \exp \left[2 \left(\frac{1}{k_a} - \frac{\eta_c}{k_c} \right) \int_{z_o}^z \beta_{\pi}^a(z') dz' \right]. \quad (2)$$

$P(z)$ is the measured backscatter signal, $P(z_o)$ is the measured backscatter signal at some level just below the cloud, β_{π}^a is the molecular plus aerosol (ambient atmosphere) backscatter coefficient and is obtained from the appropriate LOWTRAN aerosol model, k_a and k_c are ratios of extinction to backscatter coefficients for the ambient atmosphere and the cloud, respectively, and $\eta_c(z)$ is a range dependent multiple scattering correction factor for the cloud. The multiple scattering correction factor provides a heuristic way of including multiple scattering effects in the single scatter lidar equation. It can initially be assumed to be unity and updated at the end of Part 3 of this calculation using the double scattering lidar model. Then, the three parts of the calculation can be repeated with the new values of $\eta_c(z)$.

Part 2

In the second part the extinction profile, together with assumptions about the particles comprising the cloud, are used in the double scattering lidar model to determine depolarization as a function of variations in the particle size distribution.

We simplify the problem by making two assumptions about the size distribution:

1. The size distribution shape is independent of position in the cloud. It is a function of distance only through its normalization (i.e., the particle density).
2. The shape of the size distribution is represented by a functional form with one or two free parameters. For example, water cloud size distributions have been represented by [3]

$$f(r) = A \left(\frac{r}{r_m} \right)^{\alpha} e^{-r/r_m} \quad (3)$$

where $f(r)$ is the number of particles with radii between r and $r + dr$, α and r_m are free parameters and A is a normalization constant.

An array, or matrix, of depolarizations profiles are compiled for different values of the free parameters.

Part 3

In the third part the measured depolarization profiles are compared to the calculated depolarization profiles. The “best” calculated depolarization profile is chosen by minimizing a figure of merit such as

$$C(\vec{v}) = \frac{1}{N} \sum_{i=1}^N \left[\frac{D^m(z_i) - D_{\vec{v}}^c(z_i)}{D^m(z_i)} \right]^2 \quad (4)$$

where \vec{v} is the array of free parameters in the size distribution, $D^m(z_i)$ is the measured depolarization corresponding to position z_i , $D_{\vec{v}}^c(z_i)$ is the calculated depolarization at z_i for free parameter values \vec{v} . The quantity C is simply a figure of merit and other figures of merit may exist which have better behavior.

Lidar returns (at 532 nm) of water clouds are obtained with the Air Force Phillips Laboratory's (Geophysics Directorate) mobile, low altitude Nd:YAG lidar system. The lidar has the following characteristics:

- transmitter power: 25 mJ per pulse at 532 nm,
- transmitter divergence: 2.5 mrad,
- telescope aperture diameter: 15 cm,
- telescope field of view: 10 mrad full angle,
- optical filter bandwidth: 10 Å,
- maximum data acquisition rate: 20 MHz (7.5 m range bins).

The lidar is mounted on a steerable trunion on the roof of a trailer.

References

1. Y. Benayahu, S. Fastig, and A. Cohen, “Multiple Scattering by the Side Looking Lidar,” 1991 Technical Digest for Conference on Optical Remote Sensing of the Atmosphere, Williamsburg, VA, 18, 227–229 (1991).
2. K. Sassen, M.K. Griffin, and G.C. Dodd, “Optical Scattering and Microphysical Properties of Subvisual Cirrus Clouds, and Climatic Implications,” *J. Appl. Meteor.* 28, 91–98 (1989).
3. D. Deirmendjian, “Electromagnetic Scattering on Spherical Polydispersions,” American Elsevier, New York (1969).

MULTIPLE SCATTERING LIDAR RETURNS FROM STRATUS CLOUDS

D.L. Hutt* and L. R. Bissonnette

Defence Research Establishment Valcartier
P.O. Box 8800 Courcellette, Québec, Canada, G0A 1R0* Also with: COPL, Equipe laser et optique guidée
Dep. Physique, Université Laval, Ste. Foy, Québec, Canada, G1K 7P4

Multiple scattering lidar returns from stratus clouds have been measured using a multi-field-of-view (MFOV) lidar operating at $1.054 \mu\text{m}$. The detector consists of four concentric silicon photodiodes which define half-angle fields of view (FOV) of 3.8, 12.5, 25 and 37.5 mrad . The central FOV receives the conventional lidar signal, while the outer FOVs receive only multiply scattered contributions. The system is described in detail in Refs. 1 and 2. The ratios of the signals in the outer FOVs to the signal in the central FOV is an indication of the lateral spreading of the scattered component of the laser pulse, as it propagates through the cloud.

MFOV lidar returns from stratus clouds measured between October 1991 and March 1992 can be divided into two distinct types, those with large multiple scattering ratios and those with small ratios. An example of each type of return is shown in Figs. 1 and 2. Both measurements were made at an elevation angle of 45° . The maximum of the central FOV signal (detector 1) is nearly the same in both measurements but the multiscattered signals measured by the outer FOVs (detectors 2, 3 and 4) is much greater in Fig. 1. Simulations using Bissonnette's multiple scattering propagation model³ show that a cloud layer composed of water droplets with a mode radius from 3 to $10 \mu\text{m}$ would give MFOV lidar signals similar to the measurements in Fig. 1. An example simulation is shown in Fig. 3. For that calculation, the droplet size distribution was assumed to be the Shettle and Fenn⁴ advection fog 1. This model is a modified gamma distribution with a mode radius of $10 \mu\text{m}$. Similar distributions have been measured in stratus clouds⁵. The extinction coefficient in the simulation cloud was 25 km^{-1} .

The clouds with small multiple scattering signals probably have a high concentration of much larger particles on the order of hundreds of micrometers in size. This is a typical size range for suspended ice crystals or precipitation. Stratus clouds often have a high concentration of ice crystals even when there is no precipitation⁶. Large ice crystals would give smaller signals in the outer FOVs because much of the scattered intensity is contained in a narrow diffraction peak with an angular width on the order of milliradians. The result is that for a given extinction, many more orders of scattering are required for the laser pulse to spread out. So far we have not been able to

do simulations of MFOV lidar returns from ice crystal clouds because of uncertainties about the phase function of the crystals, particularly the magnitude of the backscatter peak at 180° .

On two occasions, MFOV lidar returns measured just prior to snowfall, showed a striking vertical profile. An example is shown in Fig. 4. From 900 to 1300m the multiply scattered signals are negligible compared to the return in the central FOV. Abruptly, at 1300m strong signals begin in the outer FOVs. These results could be explained by the presence of a cloud layer composed of water droplets at a range of 1300m (or 900m above ground) with snow precipitation forming at the bottom of the cloud. By measuring the polarization ratio of lidar signals, Pal and Carswell⁷ have observed snow precipitating from a cloud layer composed of water droplets.

Based on these results, we believe that analysis of multiple scattering lidar returns can yield important information on the phase of clouds particles.

REFERENCES

1. Bissonnette, L.R. and Hutt, D.L., "Multiple scattering lidar", *Appl. Opt.*, 29, pp. 5045-5046, (1990).
2. Hutt, D.L., Bissonnette, L.R. and Durand, L., "Multiscattered lidar returns from atmospheric aerosols", *Proc. SPIE Propagation Engineering*, Vol. 1487, pp. 250-261 (1991).
3. Bissonnette, L.R., "Multiscattered model for propagation of narrow light beams in aerosol media", *Appl. Opt.*, 27, pp. 2478-2484 (1988).
4. Shettle, E.P. and Fenn, R.W., "Models for the aerosols of the lower atmosphere and the effects of humidity variations on their optical properties", AFGL-TR-79-0214, Air Force Geophysics Laboratory, Hanscom AFB, Mass., USA, 1979.
5. Pruppacher, H. R., "The microstructure of atmospheric clouds and precipitation", in Clouds Their formation, optical properties and effects, P. V. Hobbs and A. Deepak, ed., (Academic Press, New York, 1981), pp. 93-186.
6. Hobbs, P. V. and Rangno, A. L., "Ice particle concentrations in clouds", *J. Atmos. Sci.*, 42, pp. 2523-2549 (1985).
7. Pal, S. R. and Carswell, A. I., "The polarization characteristics of lidar scattering from snow and ice crystals in the atmosphere", *J. Appl. Meteor.*, 16, pp. 70-80 (1977).

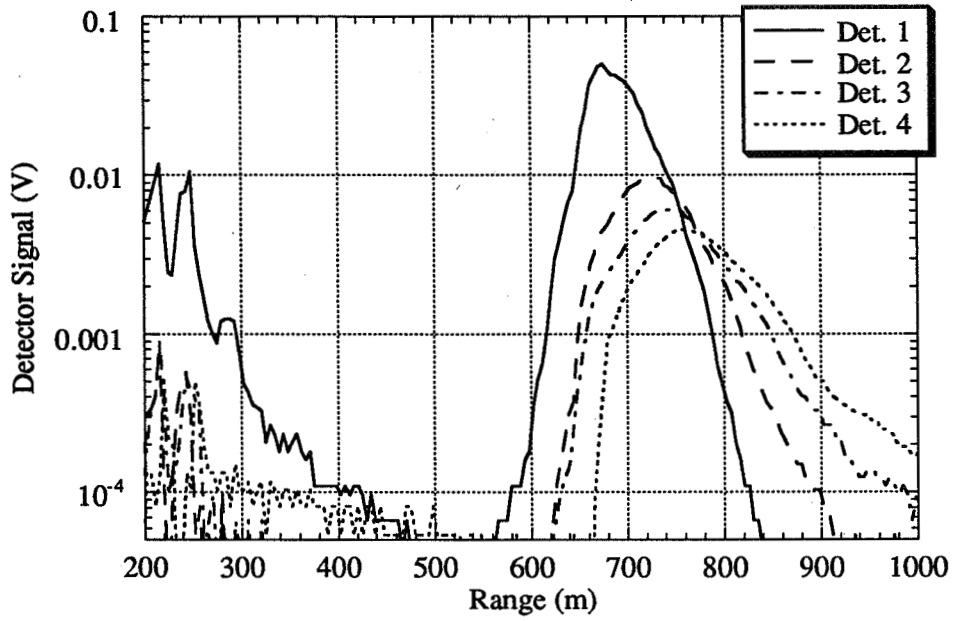


Fig.1 Typical MFOV lidar returns from stratus clouds composed of water droplets. The measurement was made at an elevation angle of 45°.

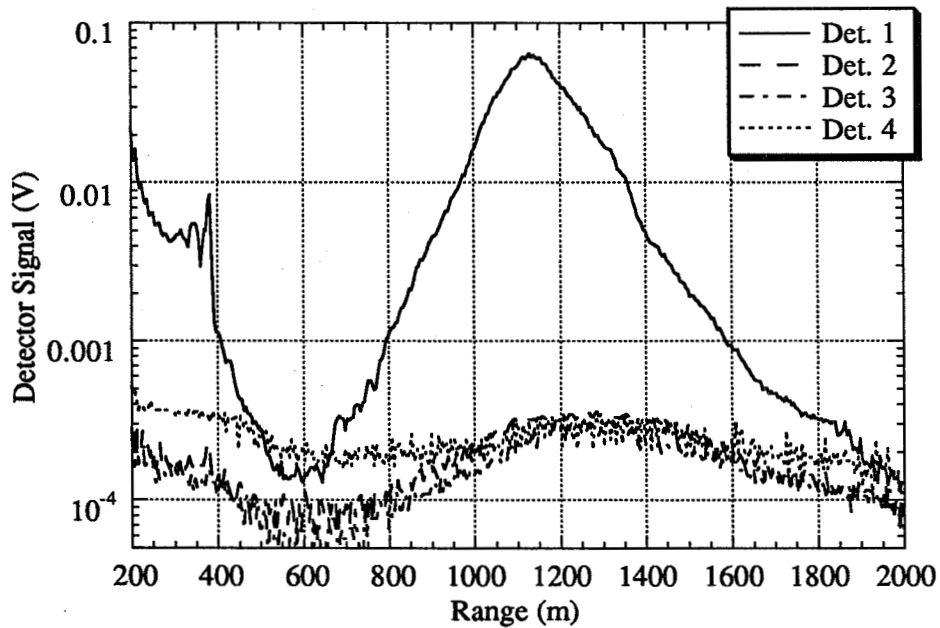


Fig. 2 Typical return from stratus cloud believed to have a high concentration of ice crystals. The measurement was made at an elevation angle of 45°.

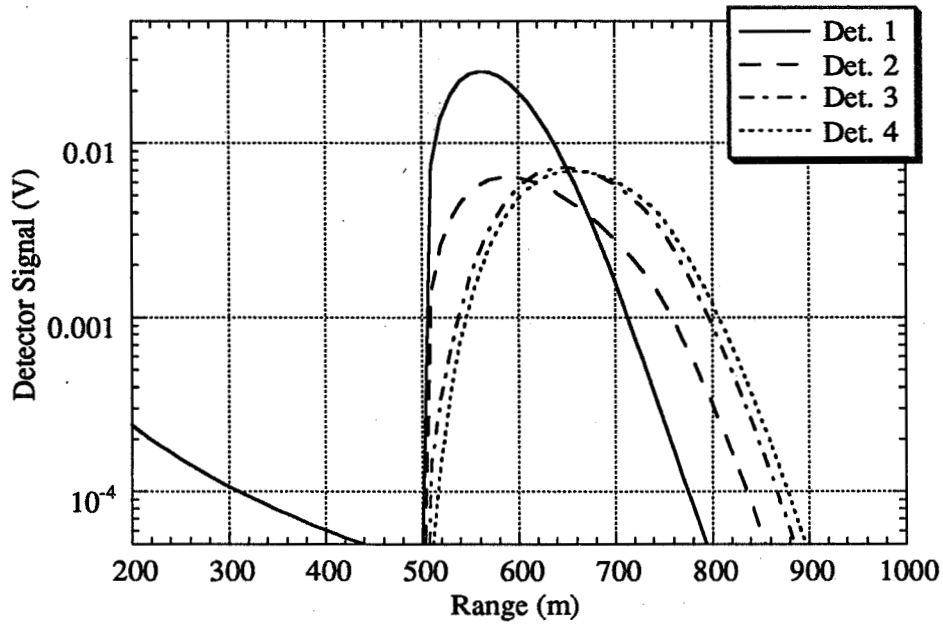


Fig.3 Simulated MFOV lidar return from a cloud layer composed of water droplets with mode radius $10\ \mu\text{m}$ and an extinction coefficient of $25\ \text{km}^{-1}$.

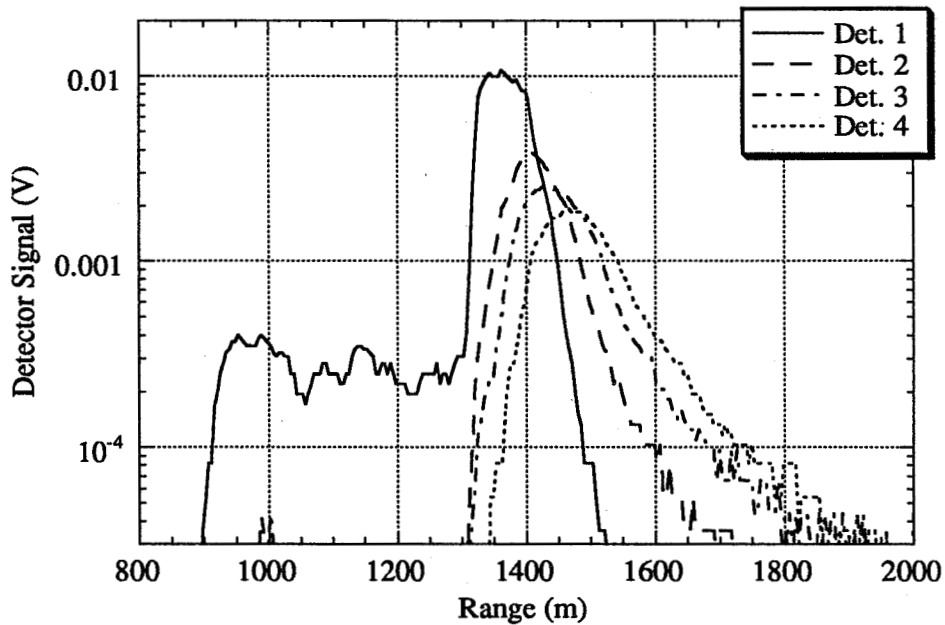


Fig.4 MFOV lidar returns at an elevation angle of 45° , prior to snowfall. From 900 to 1300m the signal is likely due to suspended ice crystals. Beyond 1300m the return is characteristic of water droplet clouds.

**Analytical Multiple Scattering Correction to the Mie Theory:
Application to the Analysis of the Lidar Signal**

C. Flesia

Institute of Atmospheric Physics ETH-Honggerberg, CH-8093, Zurich, Switzerland
and Observatoire Cantonal de Neuchâtel, CH-2000 Neuchâtel, Switzerland

P. Schwendimann

Defence Procurement and Technology Group, System Analysis Division, CH-3000
Bern, Switzerland

- Introduction

The contribution of the multiple scattering to the lidar signal is dependent on the optical depth τ . Therefore, the radar analysis, based on the assumption that the multiple scattering can be neglected is limited to cases characterized by low values of the optical depth ($\tau \leq 0.1$) and hence it excludes scattering from most clouds.

Moreover, all inversion methods relating lidar signal to number densities and particle size must be modified since the multiple scattering affects the direct analysis.

The essential requests of a realistic model for lidar measurements which include the multiple scattering and which can be applied to practical situations are the following:

- a) Not only a correction term or a rough approximation describing results of a certain experiment, but a general theory of multiple scattering tying together the relevant physical parameter we seek to measure.

- b) An analytical generalization of the Lidar equation which can be applied in the case of a realistic aerosol. A pure analytical formulation is important in order to avoid the convergency and stability problems which, in the case of numerical approach, are due to the large number of events that have to be taken into account in the presence of large depth and/or a strong experimental noise.

- Theory

Scattering of light by spherical particles is described within the theory of Mie [1], which leads to analytical expressions for the components of the scattered fields. In general

only single scattering events are calculated in this approach. Some results on multiple scattering are presented, which are obtained by extending the solution of Mie. An analytical expression of the n-fold scattered field leads to a generalization of the lidar equation describing the multiple scattering process without losing the advantage of working in the framework of the Mie theory.

We illustrate our procedure with the following example : consider only two spherical particles at a distance d from each other. In the single scattering regime both particles scatter the impinging field independently and the scattering coefficients $a_\ell^{(1)}$ and $b_\ell^{(1)}$ are given by the standard expressions [2]

Double scattering implies that the light scattered by the first particle is rescattered by the second one and viceversa. Therefore, the scattering coefficients for double scattering, denoted by $a_\ell^{(2)}$ and $b_\ell^{(2)}$, will be obtained from the boundary conditions on the particle using the single scattered field on input. Notice that now the incident wave on the second particle is a spherical wave. After straightforward calculations one obtains:

$$a_\ell^{(2)}(x_1, x_2, d_{1,2}) = a_\ell^{(1)}(x_1)\gamma_\ell(x_2, d_{1,2}) \quad (1)$$

$$b_\ell^{(2)}(x_1, x_2, d_{1,2}) = b_\ell^{(1)}(x_1)\delta_\ell(x_2, d_{1,2}) \quad (2)$$

where (x_1, q_1) and (x_2, q_2) are respectively the size parameters and the positions of the first and the second particle and $d_{1,2} = |\vec{q}_1 - \vec{q}_2|$ is the distance between them normalized to the wavelength. The quantities $a_\ell^{(2)}$ and $b_\ell^{(2)}$ are the corrections to the Mie theory due to the double scattering.

The multiple scattering contributions in a realistic aerosol of N particles, are formed by integrating over all distances i.e. over all scattering paths between the particles.

The explicit expression of the components of the 2- fold scattered field $E^{(2)}$ is constructed as in the Mie theory [2] and depends on the particle positions through the coefficients $a_\ell^{(2)}$ and $b_\ell^{(2)}$. As an example, we report the explicit form of the θ -component of \vec{E} in spherical coordinates. It reads

$$E_\theta^{(2)} = \cos \phi \sum_i \frac{1}{|\vec{q} - \vec{q}_i|} \sum_\ell (\zeta_\ell^{(1)'(|\vec{q} - \vec{q}_i|)} P_\ell^{(1)'(\cos(\theta))} \sin(\theta) a_\ell^{(1)}(x_1) \gamma_\ell(x_2, d_{1,i_2}) + \zeta_\ell^{(1)}(|\vec{q} - \vec{q}_i|) P_\ell^{(1)}(\cos(\theta)) \frac{1}{\sin(\theta)} b_\ell^{(1)}(x_1) \delta_\ell(x_2, d_{1,i_2})) \quad (3)$$

where $P_\ell^{(1)}(\cos(\theta))$ is the Legendre polynomial of order ℓ .

In analogy, we consider the light scattered by the second particle as the incoming field for the scattering on the third particle. The same calculation will give the third order corrections to the scattering coefficients. A simple recurrence relation leads to a generalization of equations (1,2) and to the coefficients for the n^{th} scattering order. The amplitude of the n-fold scattered field will then be

$$E^{(n)} = \sum_{j=1}^n E^{(j)} \quad (4)$$

where $E^{(j)}$ are the contributions of the scattering process of order j to the field.

To determinate the attenuation of light due to the medium, including the effects of multiple scattering, the flow of energy is calculated as usual using the Pointing vector for the incident, the internal and the scattered fields. However, in this case, the scattered field contains the multiple scattering contributions as well. This is the only difference which exists with respect to the expressions for extinction and the backscattering in the single scattering case. In the same way, from the expression of the amplitude of the n-fold scattered field, the analytical formulation of the multiple scattering lidar equation can be derived. Moreover, the knowledge of the analytical form of the n-fold scattered electromagnetic field will allow to generalize this approach including some deviations from the spherical shape of particles.

- Results for ground based and space borne lidars

Following this approach, the multiple scattering contributions to the lidar return have been estimated as a function of the receiver's field of view for a space born and a ground based lidar at different laser emission wavelengths in the case of nighttime and daytime measurements and for different atmospheric models.

In particular, the effect of the multiple scattering contributions to the lidar return from space have been estimated in the case of a low laser energy, high background radiation and integration over a small number of shots. A careful evaluation of the competitive effect between the increase of the intensity of the signal due to the higher scattering order contributions and the increase of the background noise as a function of the field of view have been performed.

From the analysis of the simulations some general features are evident :

- 1) Even with a reduced signal to noise ratio, the values of the multiple scattering contribution are larger in the infrared than in the green.

2) A competitive effect between the increase of the intensity of the signal due to the higher scattering order contributions and the increase of the background noise as a function of the field of view has been shown.

For instance, in the case of a space borne system at 800 km altitude, for a C1 Cumulus (concentration 100 particles / cm^3 , mean particle radius 4 μ) and for a cloud depth of 50 m, the increase of the signal to noise ratio in the green with an energy of 500 mj can reach 33 % for a variation of 0.6 mrad (from 0.1 mrad to 0.7 mrad) of the receiver's field of view during the night, while during the day the increment is around 12 %. For an energy of 50 mj the situation during the day is inverted and the signal to noise ratio decreases as a function of the field of view. In the infrared with an energy of 1000 mj for the same variation of the receiver's field of view the signal to noise ratio double during the day.

Moreover, the error introduced by performing lidar measurements at a single field of view has been evaluated both in the case of a ground based system and a space system for different atmospheric models. This has been done taking into account that in routine measurements it might be complex to perform simultaneous measurements at different field of views. The evaluation of different geometries in order to minimize the error introduced by multiple scattering has been performed.

Part of this work was performed with the support of the European Space Agency

REFERENCES

- [1] G. Mie, Ann. Phys.,25,377,445 (1908)
- [2] M. Kerker :” Scattering of Light and Other Electromagnetic Radiations”, Academic Press, New York (1969).
- [3] C. Flesia, P. Schwendimann, Proceedings of ”4th Int. Workshop on Multiple Scattering Lidar Experiments”, Florence Italy 29-31 October 1990.
- [4] C. Flesia, M. Morandi, L. Stefanutti:” Technical Assistance for the inversion of the Lidar equation” Final Report ESA/ESTEC Contract N. XA/89/171/PK

Airborne lidar & radiometric observations of PBL and low clouds

P.H. Flamant*, R. Valentin*, J. Pelon**

*Laboratoire de Météorologie Dynamique, Ecole Polytechnique, 91128 Palaiseau

**Service d'Aéronomie du CNRS, Université Pierre & Marie Curie, 75005 Paris

Boundary layer- and low altitude clouds over open ocean and continent areas have been studied during several field campaigns since mid-1990 using the french airborne backscatter lidar LEANDRE in conjunction with on-board IR and visible radiometers. LEANDRE is an automatic system and a modification of the instrumental parameters when airborne is computer controlled through an operator keyboard. The vertical range squared lidar signals and instrument status are displayed in real time on two dedicated monitors. The lidar is used either down- or up looking while the aircraft is flying above or below clouds. A switching of the viewing configuration takes about a minute. The lidar measurements provide with a high resolution description of cloud morphology and holes in cloud layers. The flights were conducted during various meteorological conditions on single or multilayers stratocumulus and cumulus decks. Analysis on a single shot basis of cloud top- (or bottom) altitude and a plot of the corresponding histogram allows to determine a probability density function (PDF). The preliminary results show the PDFs for cloud top are not gaussian and symmetric about the mean value. The skewness varies with atmospheric conditions. An example of results recorded over the Atlantic ocean near Biarritz is displayed on figure 1 showing : a) the range squared lidar signals as a function of time, here 100 s corresponds to about 8 km, 60 shots are averaged on horizontal. The PBL - up to 600 m - is observed at the beginning of the leg as well as the surface returns, giving an indication of the porosity; b) the cloud top altitude variation between 2.4 to 2.8 km during the 150 to 320 s section, c) the corresponding PDF. Similar results are obtained on stratocumulus over land. Single shot measurements can be used also to determine an optical porosity at a small scale as well as a fractional cloudiness at a larger scale.

A comparison of cloud top altitude retrieved from lidar and narrowbeam IR radiometer is conducted to study the scale integration problem. A good agreement within less than 100 m relies on spatial uniformity and an optically thick layer. In presence of holes a discrepancy is observed. This is illustrated on figure 2 displaying as a function of time : a) the lidar signals, b) the target temperature (either clouds or sea surface) retrieved from a narrowbeam IR radiometer, 17°C is the sea surface temperature on that day; c) the visible flux - linked to cloud albedo - measured by a pyranometer.

In preparation of ASTEX down- and up looking measurements were conducted on stratocumulus cloud over the Atlantic ocean near Quimper in brittany. Depending on the flight pattern orientation with respect to the wind the top and bottom cloud morphologies are different. Preliminary results on : cloud morphology, cloud top PDFs, optical porosity, fractional cloudiness, comparison of lidar and radiometric measurements will be presented at the conference.

ELAC flight 1 leg 8 14:17:00 October 17 1990

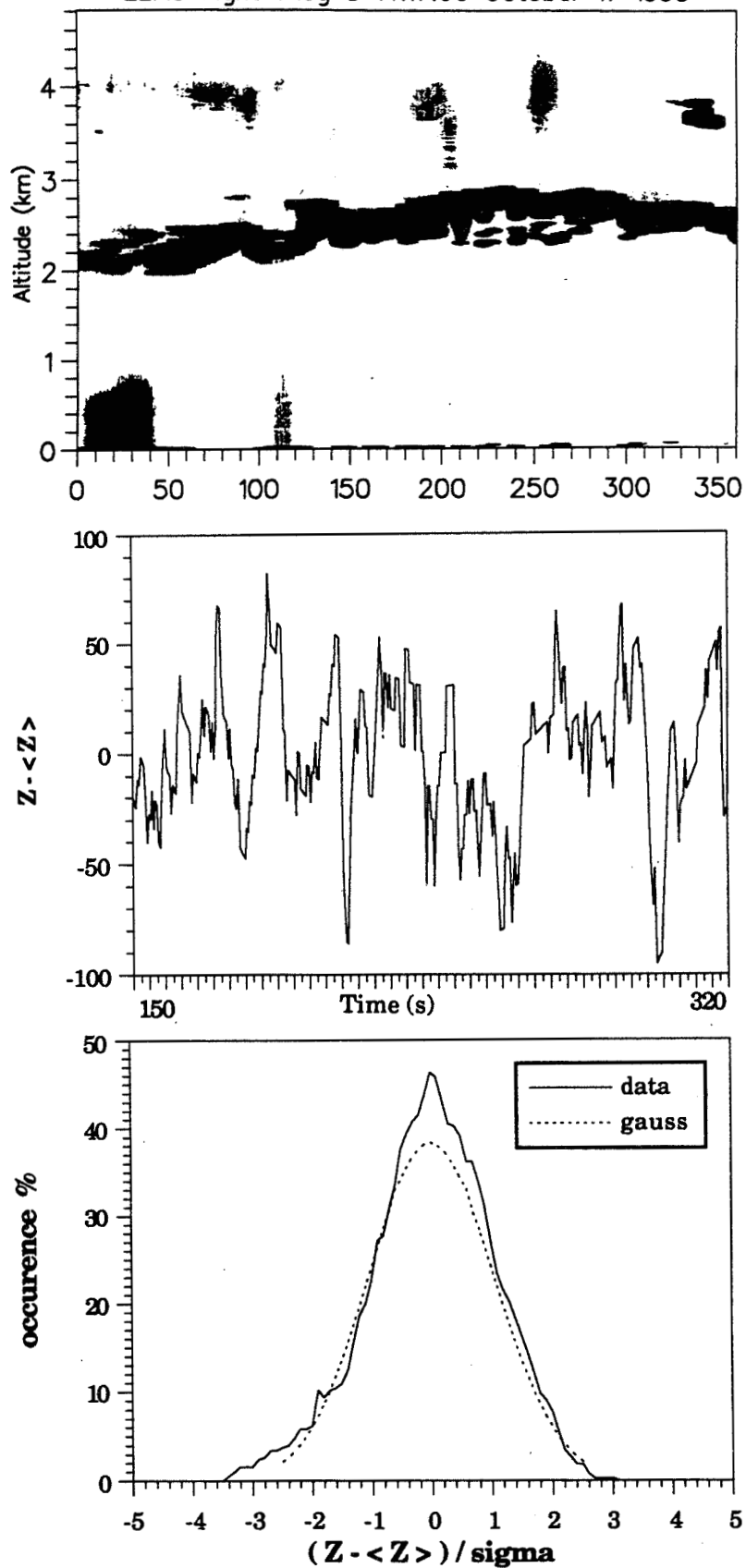


figure 1

ELAC flight 1 leg 9 14:24:00 October 17 1990

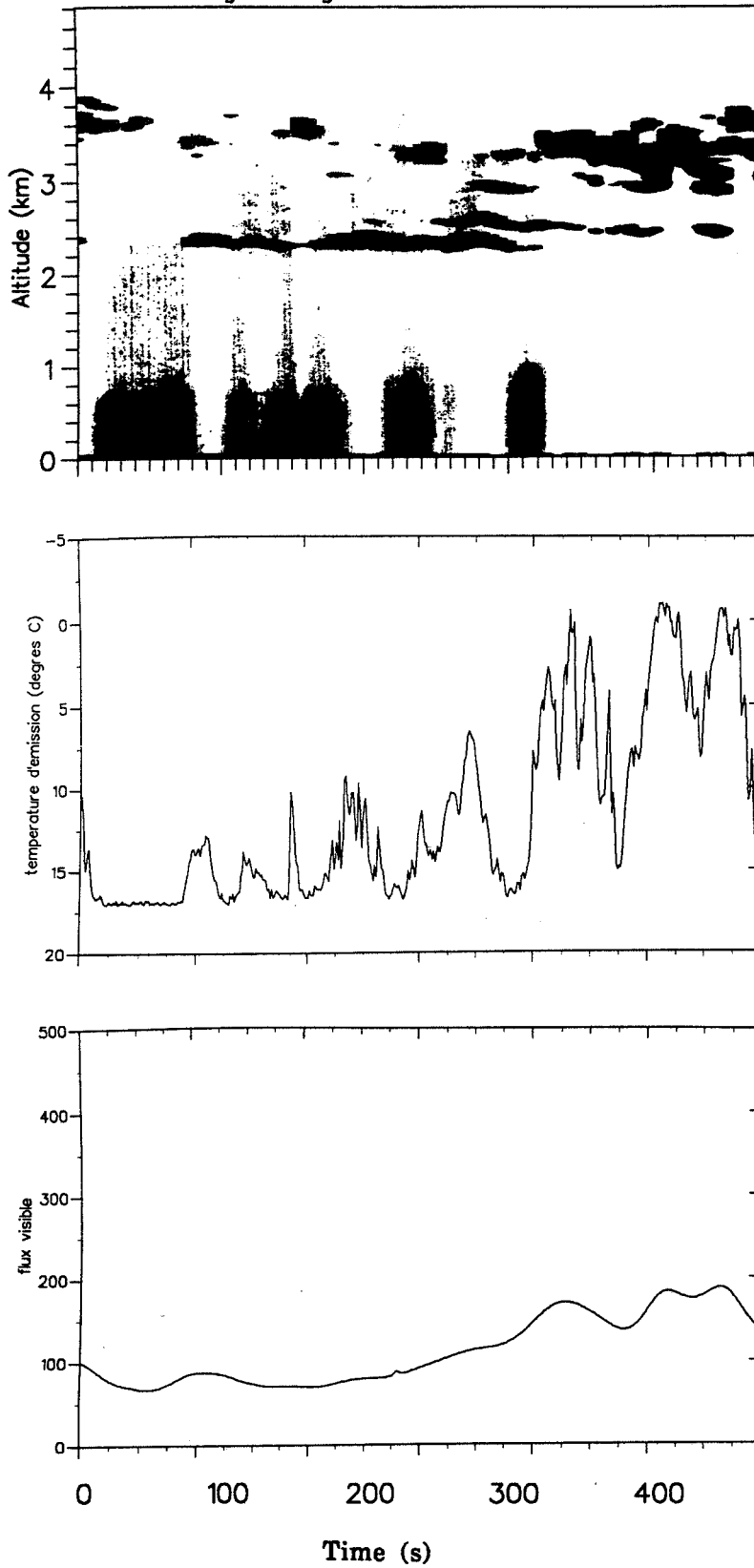


figure 2

ECLIPS at LMD : preliminary results of phase 2.

*R. Valentin, L. Menenger, S. Elouragini, P.H. Flamant, **J. Pelon

**Laboratoire de Météorologie Dynamique, Ecole Polytechnique, 91128 Palaiseau*

** *Service d'Aéronomie, Université Paris 6, 4 place Jussieu, 75252 Paris Cedex*

The LMD ground-based backscatter lidar station (48°4 N, 02°0E) near Paris was operated daily during the ECLIPS phase 2 from May 22 to June 19, 1991 simultaneously with a radiometric equipment recording the downward short wavelength (SW) and long wavelength (LW) fluxes. A day-by-day summary of the field measurement as a function of universal time (UT) is displayed on figure 1. Considering a 5 days week there are only two days of missing data (05/31 and 06/06) in our record. The nearby meteorological station (10 km away) provides with rawindsounding at 00UT and 12UT. During two days the french airborne lidar LEANDRE was flown over the ground-based station. The airborne equipment looked down while the ground based equipment looked up. The two lidars were operated at 532 nm, and the on-board radiometers were identical to the ones on the ground. The measurements were synchronized with AVHRR overpasses as required. We also indicate the Meteosat data corresponding to the period of measurements. Two examples of simultaneous ground-based lidar, pygeometer and pyranometer data are displayed on figure 2 and figure 3.

Figure 2. A single stratus layer is observed on June 3. The cloud base recorded by the lidar (upper curve) varies between 1.4 and 2 km. Holes occur at various time, which are correlated with pyranometer measurement (lower curve) and identified by a peak in the downward visible flux above 600 W m^{-2} . On the contrary when the cloud layer is thick and solid the SW flux ranges from 200 to 400 W m^{-2} . The LW (pyrgeometer) is constant during the experiment at a value of 300 W m^{-2} .

Figure 3. A stratus layer at 2 km and an altostatus layer at about 5 km are observed by lidar (upper curve) on June 6. The mid-cloud is recorded only when a large hole occurs in the stratus deck. It corresponds to a maximum in downward SW flux reaching 500 W m^{-2} (lower curve). The peak value is less than previously due to a second layer. The LW flux is constant at 330 W m^{-2} . The preliminary results for the complete ECLIPS phase 2 field experiment, taken from the ground and airborne will be presented at the conference.

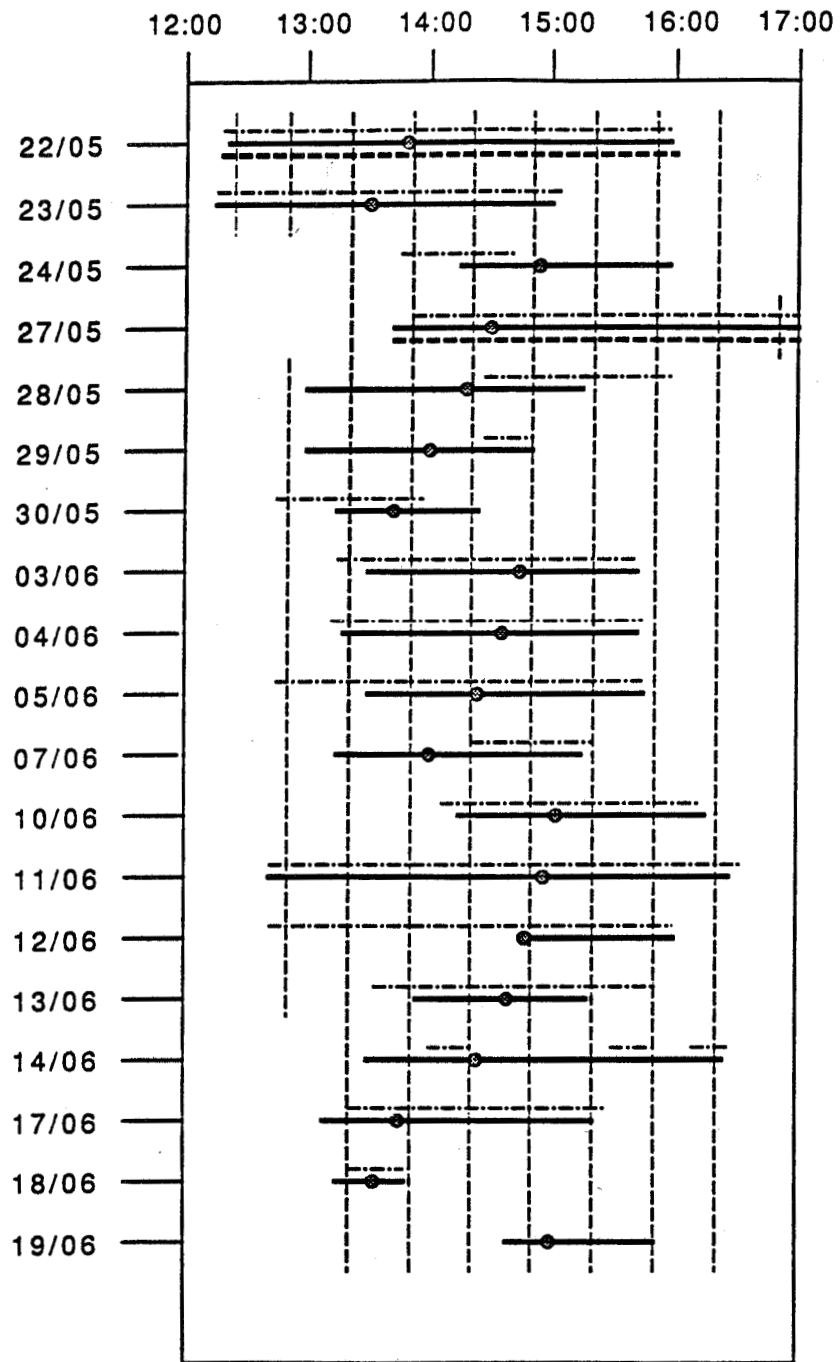


figure 1

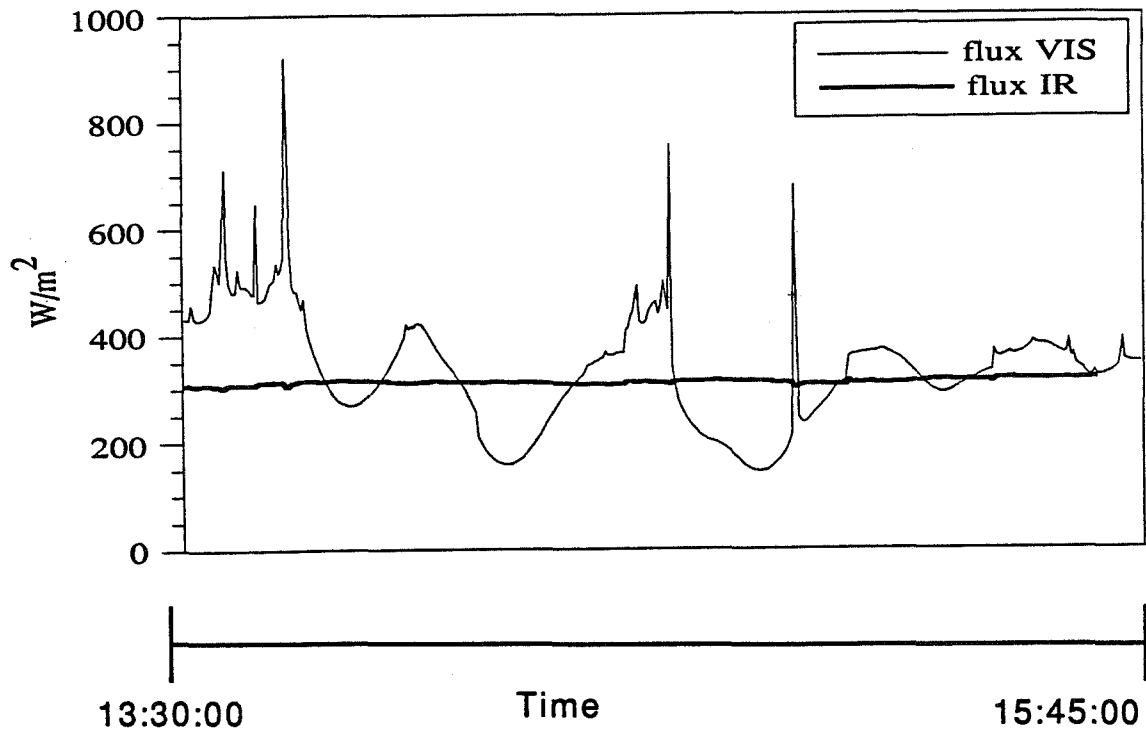
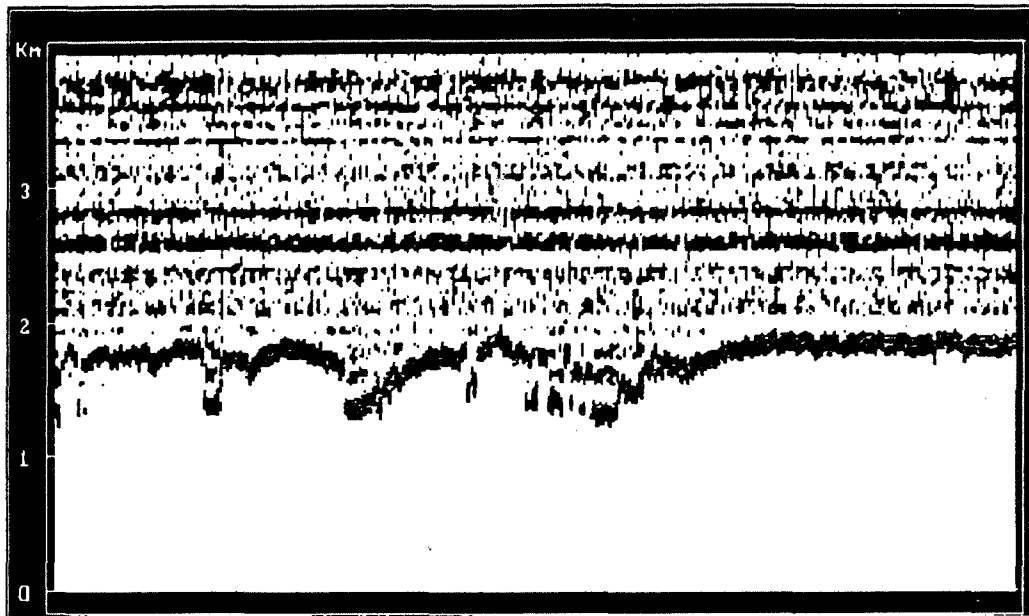


figure 2

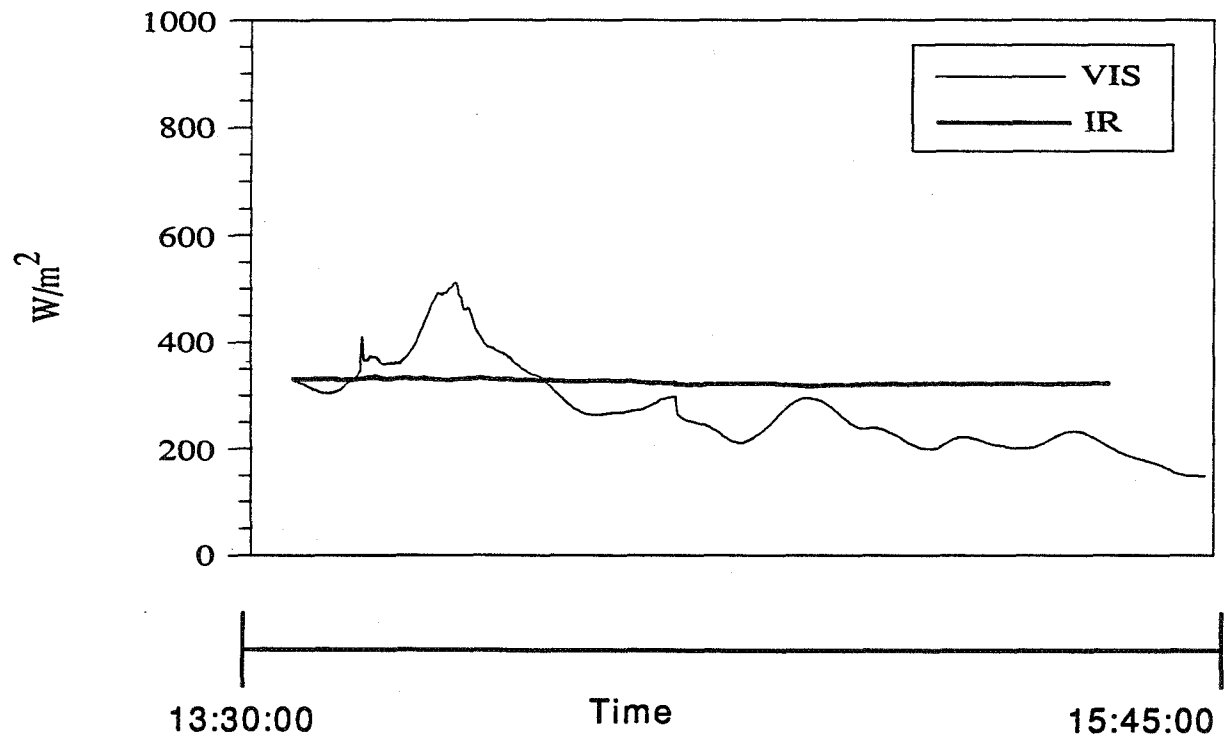
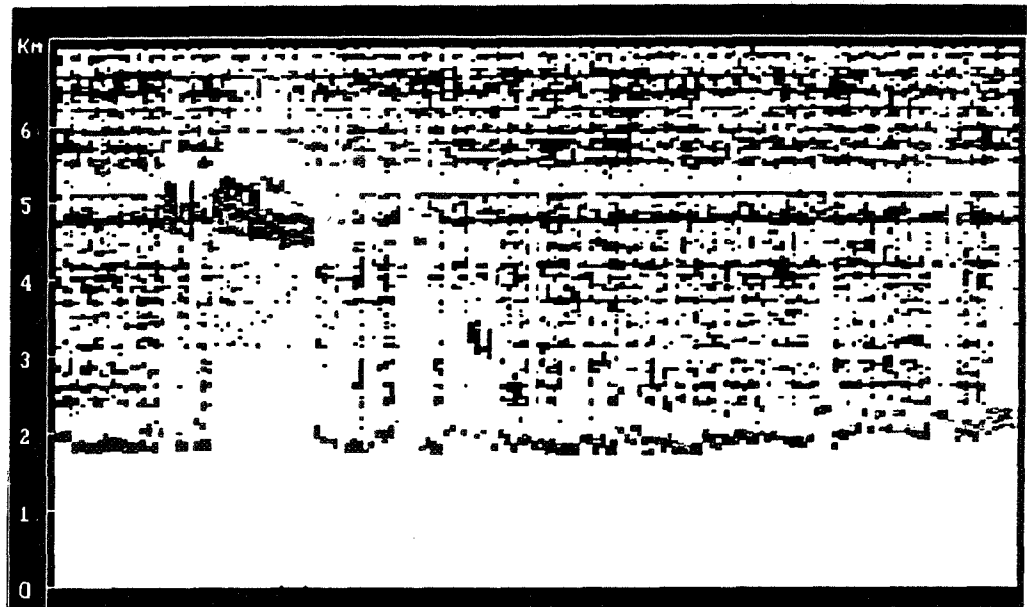


figure 3

**The 2nd phase of the LEANDRE program:
Water-vapor DIAL measurement**

P.Quaglia, D.Bruneau, J.Pelon

Service d'Aéronomie du CNRS, Université Pierre et Marie Curie, 4 place Jussieu, Boite 102,
75230 Paris cédex 05, France

Introduction

As a follow on of the backscattered lidar, a differential absorption lidar (Leandre 2) is now being developed as part of the Leandre program for airborne meteorological studies (ref1,2).

The primary measurement objective of Leandre 2 is water vapor. Pressure and temperature measurements are aimed at a second stage. The goals are to obtain an horizontal resolution of a few hundred meters for a vertical resolution of less than hundred meters, with an absolute accuracy of 10% for humidity measurement. As compatibility is an important feature between the 2 first phases of Leandre, most of the Leandre 1 sub-systems will be used and adapted for Leandre 2 (fig 1). For example, detection electronics, central computer, detectors and telescope will be the same. However, important modifications have to be done on the laser source and spectral control has to be added. Most of the work is thus devoted to those developments, and its status will be presented here.

Laser source

A double-pulse-dual-wavelength-flash-pumped-Alexandrite laser (fig 2) has been developed at Service d'Aéronomie (ref 3). This laser emits two pulses at a repetition rate of 10 Hz; each pulse energy is 50 mJ, with a pulsewidth of about 200 ns. The temporal separation between the two pulses is about 50 μ s, the spectral separation is 442 pm. The water-vapor absorption region near 730 nm is used for humidity measurement. The oxygen absorption region near 760 nm could be used further for pressure and temperature measurement. Spectral and spatial performance have been defined from DIAL measurement requirements (ref 4) and laser source characterization is in progress to check its conformity with requirement.

Spectral purity characterization is determined with a 1 meter long multi-pass White cell filled with water vapor. The cell is heated to avoid water vapor condensation allowing so a higher partial pressure. The experiment is under way and results will be presented.

Spectral linewidth, stability and profile are measured by the Fizeau wavemeter developed at Service d'Aéronomie (ref 5). The last stage of this wavemeter is used to determine shot to shot centroid of the emitted spectrum with an accuracy of 0.06 pm.

Spatial characteristics are determined with a CCD camera coupled with a PC image acquisition system. We then checked the recovery of the on-line and off-line pulse far field, their divergence and spatial profile.

Energy emitted by each pulse is recorded by a photodiode and a PC acquisition system.

First results show a linewidth better than 1 pm, a divergence of 1.3 mrad, an energy stability better than 30% ($\pm 1.5 \sigma/E$). Further results will be presented.

Spectral control

The airborne spectral control will be made by a photoacoustic cell and the Fizeau wavemeter. The spectral tuning and stabilisation of the emitted wavelength on the water vapor absorption line needs to be fully automatized. Coarse tuning is performed by intracavity motorized Lyot filter and thin Fabry-Perot, whereas a piezo electric intracavity Fabry-Perot performs the fine tuning to the center of the line. Algorithm is being developed to optimise the feedback loop between wavemeter, photoacoustic cell and filters motorisation.

The laser spectral control by diode injection seeding of the Alexandrite laser is also under study, for pressure and temperature measurements. In this case a lower resolution airborne wavemeter will be sufficient.

Conclusion

Developments of the laser source and associated spectral controls are under way for H₂O vapor measurement within Leandre phase 2. The Lidar implementation on board the Fokker F27 will benefit from the modular conception of the Leandre system.

References

- 1: "The Leandre project: a french airborne lidar system for meteorological studies". J.Pelon, P.Flamand, G.Megie, M.Messonnier. ILRC 1988 abstracts, p:197. Istituto di ricerca sulle onde elettromagnetiche (IROE), San Candido, Italy.
- 2: "The french airborne backscattered lidar Leandre 1: conception and operation". J.Pelon, P.Flamand, M.Messonnier. ILRC 1990 abstracts part I, p:36. Institute of atmospheric optics publication. Tomsk, USSR.
- 3: "Double-pulse-dual-wavelength-alexandrite laser for atmospheric water vapor measurement". D.Bruneau, H.Cazeneuve, C.Loht, J.Pelon. Appl. Optics, 30, 27, 3930, 1991
- 4: "Water vapor in the atmosphere. DIAL measurement". C.Cahen. Thesis, Université Paris VI, 1981.
- 5: "Conception and characterization of a Fizeau wavemeter for Dial airborne measurements", O.Blanchard. Thesis, Université Paris VI, 1990.

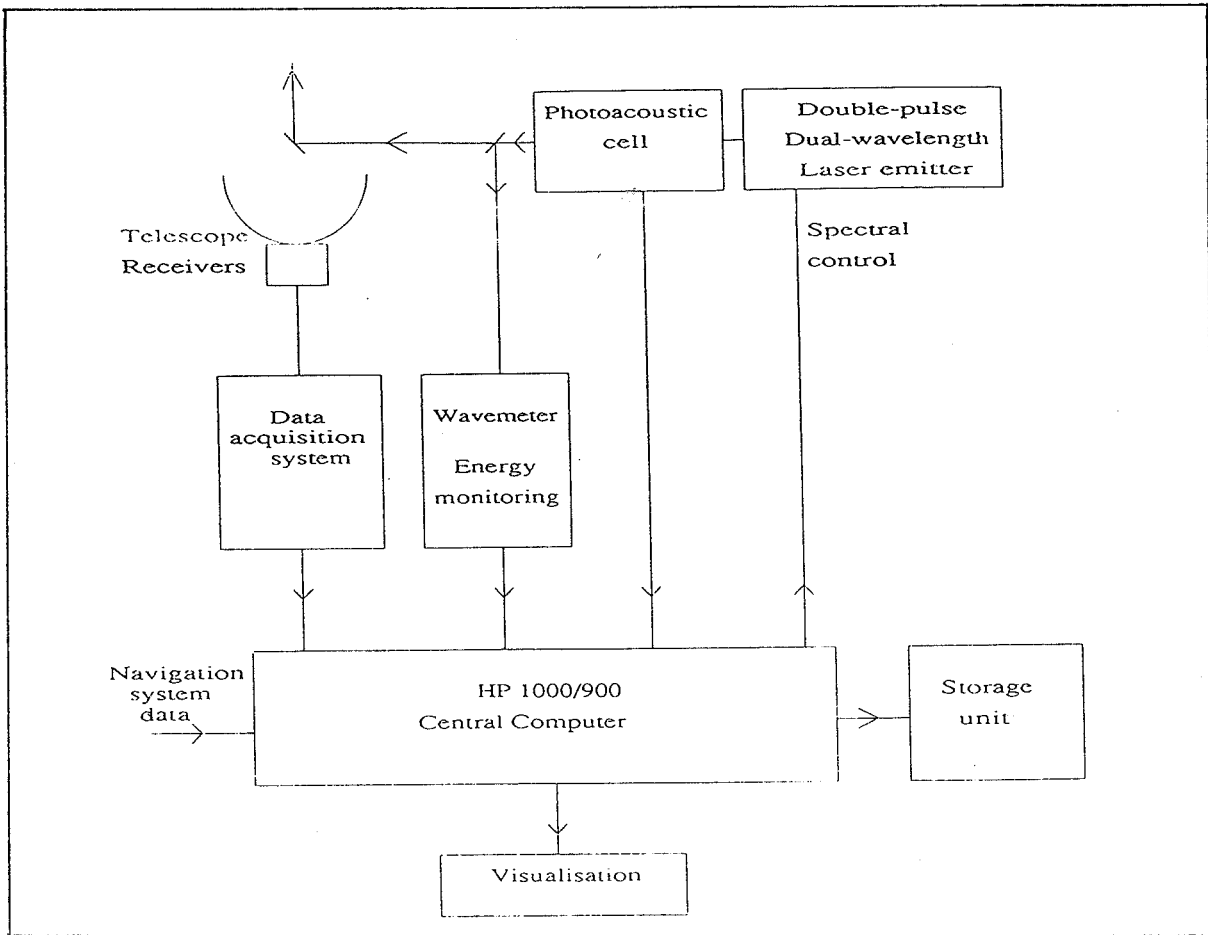


fig 1: Schematic diagram of the Leandre 2 system

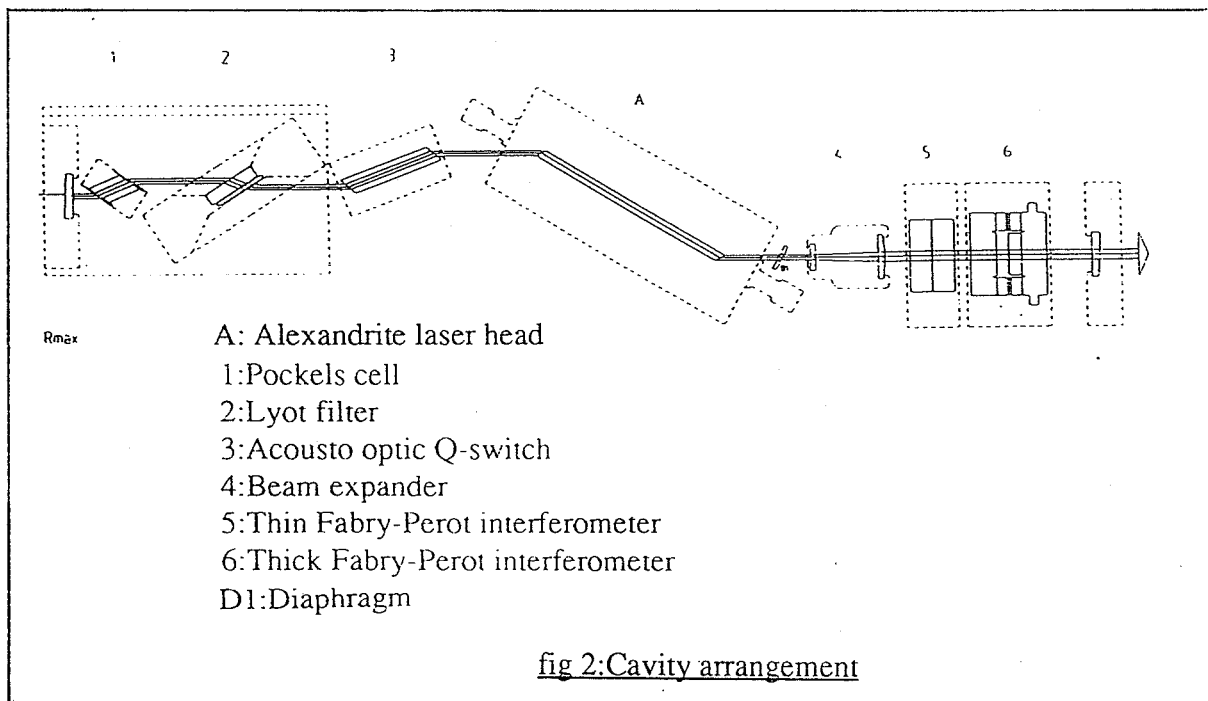


fig 2: Cavity arrangement

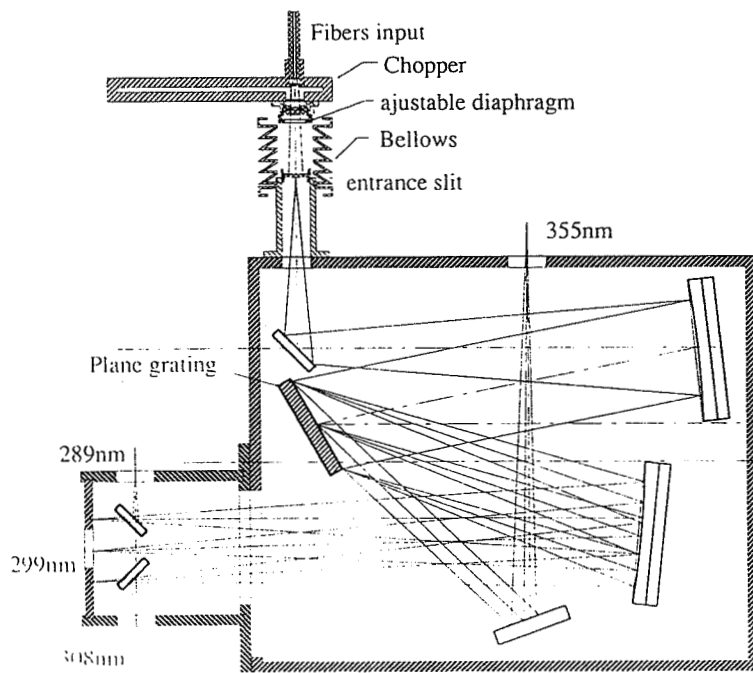


fig 3 : multichannel monochromator

Advanced Raman Water Vapor Lidar

David N. Whiteman¹, S. Harvey Melfi², Richard A. Ferrare³, Keith A. Evans⁴, Luis Ramos-Izquierdo¹, O. Glenn Staley¹, Raymond W. DiSilvestre¹, Inna Gorin¹, Kenneth R. Kirks⁵, William A. Mamakos⁶, Lewis S. Wan⁷, Nita W. Walsh⁵, James M. Marsh, Richard L. Aldridge⁹

¹NASA/Goddard Space Flight Center, Laboratory for Terrestrial Physics, Greenbelt, MD 20771

²NASA/Goddard Space Flight Center, Laboratory for Atmospheres

³Universities Space Research Association

⁴Hughes STX, Corp.

⁵Science Systems Applications Inc.

⁶Fairchild

⁷Ressler Associates

⁸University Research Foundation

⁹Nyma/RMS

Water vapor and aerosols are important atmospheric constituents. Knowledge of the structure of water vapor is important in understanding convective storm development, atmospheric stability, the interaction of the atmosphere with the surface and energy feedback mechanisms and how they relate to global warming calculations.

The Raman Lidar group at NASA/GSFC has developed an advanced Raman Lidar for use in measuring water vapor and aerosols in the earth's atmosphere. Drawing on the experience gained through the development and use of our previous Nd:YAG based system¹⁻³, we have developed a completely new lidar system which uses a XeF excimer laser and a large scanning mirror. The additional power of the excimer and the considerably improved optical throughput of the system have resulted in approximately a factor of 25 improvement in system performance for nighttime measurements.

Every component of the current system has new design concepts incorporated. The lidar system consists of two mobile trailers; the first (13m x 2.4m) houses the lidar instrument, the other (9.75m x 2.4m) is for system control, realtime data display and analysis. The laser transmitter is a Lambda Physik LPX 240 iCC operating at 400 Hz with a XeF gas mixture (351 nm). The telescope is a .75m horizontally mounted Dall-Kirkham system which is bore sighted with a .8m x 1.1m elliptical flat which has a full 180 degree scan capability; horizon to horizon within a plane perpendicular to the long axis of the trailer. The telescope and scan mirror assembly are mounted on a 3.65m x .9m optical table which deploys out the rear of the trailer through the use of a motor driven slide rail system. The Raman returns from water vapor (403 nm), nitrogen (383 nm) and oxygen (372 nm) are measured in addition to the direct Rayleigh/Mie backscatter (351). The signal from each of these is split at about a 5/95 ratio between two photomultiplier detectors. The 5% detector is used for measurements below about 4.0 km, while the 95% detector provides the information above this level.

The data acquisition system operates completely in the photon counting mode. Thus there are eight multichannel scalers used. The multichannel scalers are housed in a standard CAMAC crate. The crate is interfaced to an IBM PS/2 running OS/2 via a GPIB interface. The PS/2 data acquisition computer is on an ethernet-based local area

network. Via the network, the data are made available to a suite of realtime analysis computers.

Certain aspects of the optical system design were driven by the output characteristics of the laser. The XeF excimer laser can lase on three different line groups in the 351 vicinity. Thus there are three Raman return lines for each molecular species being measured. Care must be taken to insure that cross talk between the Raman wavelengths is prevented⁴. In addition, features designed into the system allow for quick system self-calibration. These and other aspects of the system design will be discussed.

In addition, the capability of making measurements during the daytime using the 248 nm output of a KrF excimer laser was designed into the system. Raman scattering has been observed from nitrogen and oxygen to beyond 3 km and from water vapor to beyond 1 km. A progress report on this work will be presented.

The new Raman lidar completed a very successful first deployment as a part the FIRE-II/SPECTRE field campaign in Coffeyville, KS during Nov - Dec 1991. In other papers at this conference data products including time/height imagery of water vapor mixing ratio and aerosol backscattering ratio, atmospheric temperature, spectral analysis of scales of motion, aerosol extinction/backscatter under cirrus cloud conditions and for Mt. Pinatubo aerosols from this field campaign will be presented.⁵⁻⁷

1. Melfi, S. H., and D. Whiteman: "Observation of Lower-Atmospheric Moisture Structure and its Evolution using a Raman Lidar: *Bull. Amer. Meteor. Soc.* 66 1288-1292, 1985
2. Melfi, S. H., D. Whiteman, R. Ferrare, 1989: "Observation of Atmospheric Fronts using Raman Lidar Moisture Measurements", *J. Appl. Meteor.*, **28**, 789
3. Whiteman, D. N., S. H. Melfi, R. A. Ferrare, "Raman Lidar System for Measurement of Water Vapor and Aerosols in the Earth's Atmosphere", to appear in *Appl. Opt.*, May 1992
4. Whiteman, D. N., W. F. Murphy, N. W. Walsh, "XeF Excimer Laser Output Characteristics and Implications for Raman Lidar", sub. to *Optics Letters*
5. Melfi, S. H., D. N. Whiteman, R. A. Ferrare, K. A. Evans, J. E. M. Goldsmith, M. Lapp, S. E. Bisson, "Raman lidar measurements of water vapor and aerosols/clouds during the FIRE/SPECTRE field campaign", to be presented at 16th ILRC July, 1992
6. Ferrare, R. A., S. H. Melfi, D. N. Whiteman, K. A. Evans, "Raman lidar measurements of Pinatubo aerosols over southeastern Kansas during November-December 1991", to be presented at 16th ILRC July, 1992
7. Evans, K. A., S. H. Melfi, R. A. Ferrare, D. N. Whiteman, "Water vapor variance measurements using a Raman Lidar", to be presented at 16th ILRC July, 1992

Water Vapor Variance Measurements Using a Raman Lidar

K. Evans*, S. H. Melfi, R. Ferrare+ , D. Whiteman

NASA/Goddard Space Flight Center
Greenbelt, MD

Water vapor is highly variable in both space and time in the earth's atmosphere. One clear indication of this variability is the distribution and structure of clouds. Clouds form when the air is saturated. Saturation in an air parcel is a function of both the quantity of water vapor in the air parcel and its temperature. As a result, clouds form in regions of high moisture, moisture convergence, and during vertical ascent due to cooling. Moisture variability is also associated with turbulent processes. In a convective planetary boundary layer near the earth's surface, changes in moisture reflect turbulence scales from a few kilometers down to less than a meter. Variance of moisture typically at larger scales is found in the stable free atmosphere. This large-scale variance which primarily is in the vertical and forced by surface orography and synoptic features like meteorological fronts and jet streams is a manifestation of ever present gravity waves. Moisture variance is also associated with the diurnal cycle and large globe circling horizontal Rosby waves.

Knowledge and understanding of moisture variance is important for a number of reasons. The most obvious is the question of measurement representativeness. For example, a single balloon-sonde measurement of water vapor may be quite accurate along the line of ascent but may not provide a representative measure of moisture over larger space and time scales. Representativeness is also of concern for satellite sensors designed to observe atmospheric moisture. They typically observe signals from a relatively large area ("footprint") of the atmosphere. Some of these sensors, especially those which utilize upwelling microwave energy have "footprints" which may be several tens of kilometers. Variability of moisture within these "footprints" may influence the sensor's precision, accuracy and sensitivity and will certainly make calibration with ground-truth balloon-sondes difficult.

Probably the most important reason for knowing and understanding water vapor variance is related to general circulation models (GCM's). These numerical, models which are used to predict weather and to forecast climate attempt to simulate atmospheric dynamics and moisture processes to provide a realistic picture of the state of the earth's atmosphere and its future state. Because of computing costs, the modelled atmosphere is divided into a limited number of grid points. Each grid point generally represents an area of several hundred kilometers on a side. Water vapor variance and moisture processes

*Hughes-STX, Lanham, MD

+Universities Space Research Association, Columbia, MD

such as surface fluxes, cloud formation, convection, and precipitation frequently occur on scales smaller than a typical GCM grid. The important effects of this sub-grid variance must be included in the models through some form of parameterization. Clearly, the success of GCM parameterizations of moisture and moisture processes depend on a good understanding and knowledge of moisture variability on scales equal to and less than the GCM grid size.

Because of the importance of atmospheric water vapor variance, we have analyzed data from the NASA/Goddard Raman lidar to obtain temporal scales of water vapor mixing ratio as a function of altitude over observation periods extending to 12 hours. The ground-based lidar measures water vapor mixing ratio from near the earth's surface to an altitude of 9-10 km. Moisture profiles are acquired once every minute with 75 m vertical resolution. Data at each 75 meter altitude level can be displayed as a function of time from the beginning to the end of an observation period. These time sequences have been spectrally analyzed using a fast Fourier transform technique. An example of such a temporal spectrum obtained between 00:22 and 10:29 UT on December 6, 1991 is shown in the figure. The curve shown on the figure represents the spectral average of data from 11 height levels centered on an altitude of 1 km (1 ± 0.375 km). The spectra shows a decrease in energy density with frequency which generally follows a $-5/3$ power law over the spectral interval 3×10^{-5} to 4×10^{-3} Hz. The flattening of the spectrum for frequencies greater than 6×10^{-3} Hz is most likely a measure of instrumental noise. Spectra like that shown in the figure are calculated for other altitudes and show changes in spectral features with height. Spectral analysis versus height have been performed for several observation periods which demonstrate changes in water vapor mixing ratio spectral character from one observation period to the next. The combination of these temporal spectra with independent measurements of winds aloft provide an opportunity to infer spatial scales of moisture variance.

Examples of other temporal spectra showing changes with altitude and over different observation periods will be presented and discussed.

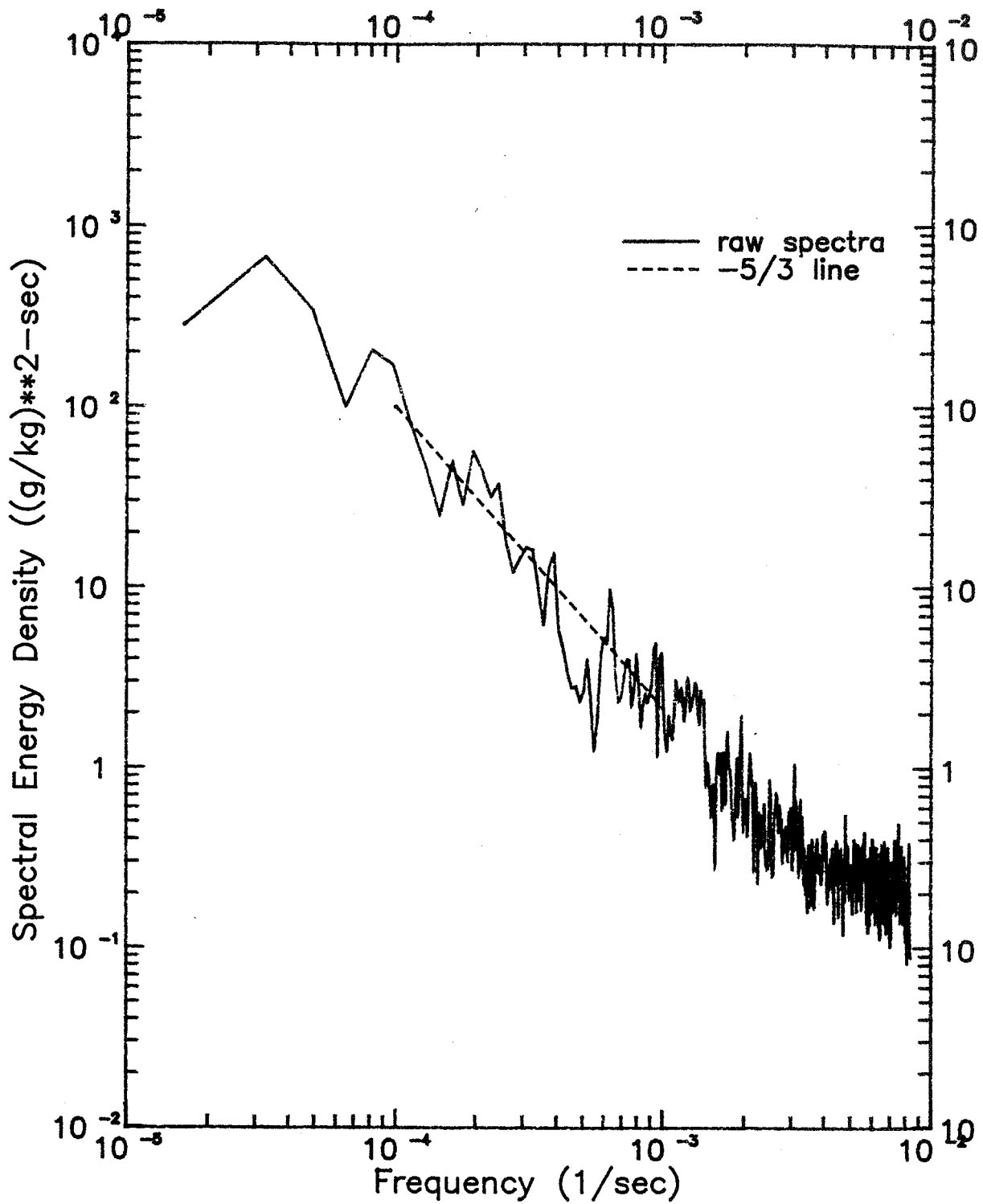


Figure: The average water vapor mixing ratio spectral energy density versus frequency for 11 altitudes at 75 meter intervals centered on a height of 1 kilometer. The data were acquired on Dec. 6, 1991 between 00:22 and 10:29 UT. A $-5/3$ power law distribution is shown as the dashed line.

Airborne Remote Sensing of Tropospheric Water Vapor Using a Near Infrared DIAL System

Ehret G., Kiemle C., Renger W. and Simmet G.

Institute of Atmospheric Physics
German Aerospace Research Establishment (DLR)
D-8031 Oberpfaffenhofen

This paper summarizes the results of airborne water vapor measurements in the lower middle and upper troposphere using the DIAL technique in the near infrared. The measurements were performed in July 1990 in Southern Bavaria between Allersberg and Straubing from 20 to 23 UTC taking advantage of night time conditions. The tropospheric H_2O profiles were range solved investigated both horizontally and vertically. With the used DIAL system water vapor measurements in the upper troposphere have been carried out for the first time. To calibrate the H_2O - retrievals effective absorption cross sections of selected H_2O lines in terms of altitude around 724 nm were calculated using line parameter data from the literature (B. E. Grossmann et al). The frequency of the on-line measurements was adjusted by the spectra of a PAS cell filled with H_2O . We found that the calibration error range between 0.005 and 0.015 cm^{-1} . The systematic errors of the H_2O as a function of altitude were estimated, leading to the result that a 6 % accuracy is achievable for measurements performed below 7 km and 12 % accuracy in the upper troposphere. The vertical H_2O profile agrees well with in situ measurements in the investigated range between the top of PBL up to near the tropopause (Fig.1). Horizontal and vertical H_2O profiles are calculated by means of averaging single lidar returns (Fig.2-4). Typical horizontal resolutions range from 4 km in the lower to 11 km in the upper troposphere with vertical resolutions varying from 0.3 km up to 1 km, respectively, in order to satisfy a 5 - 10 % accuracy in the statistical error. The measurement sensibility of the water vapor mixing ratio in the upper troposphere is 0.01 g/kg.

The experimental setup of the whole DIAL system mounted on board the aircraft Falcon 20 is presented in Fig.5. The laser transmitter consists of a narrow-band tunable dye laser repetitively pumped by a frequency doubled Nd: YAG laser. For wavelength calibration purposes during data recording in the aircraft, the radiation passes the PAS cell and is then emitted into the atmosphere passing the aircraft window on the floor of the aircraft cabin. The photons scattered back from the atmosphere are collected by a Cassegrain type telescope. After traversing the receiver optics these photons are detected either by a photodiode or by a photomultiplier in a dual channel receiver. The amplified current is digitized with a resolution of 12 bits at a sampling frequency of 10 or 20 MHz. By means of a real time micro computer which controls the data acquisition system, these digitized signals are stored on a removable cartridge disc. Together with the spectrum of the dye laser output, which is monitored by a Fizeautype spectrometer, the relative pulse energies of the fundamental at 1064 nm, of the doubled at 532 nm and the dye laser at around 720 nm are recorded and monitored in the aircraft cabin simultaneously for each shot. The transmitter and receiver components of the DIAL system are rigidly fixed together and mounted on a supporting structure on the floor of the Falcon cabin using shock suppressing mounts. The most important parameters of the just described DIAL system are summarized in Tab. 1.

Reference

Grossmann B.E. and Browell E.V.. Water Vapor Line Broadening and Shifting By Air, Nitrogen, Oxygen, and Argon in the 720 nm Wavelength Region. J. Mol. Spectrosc., 138(2), 562-595.

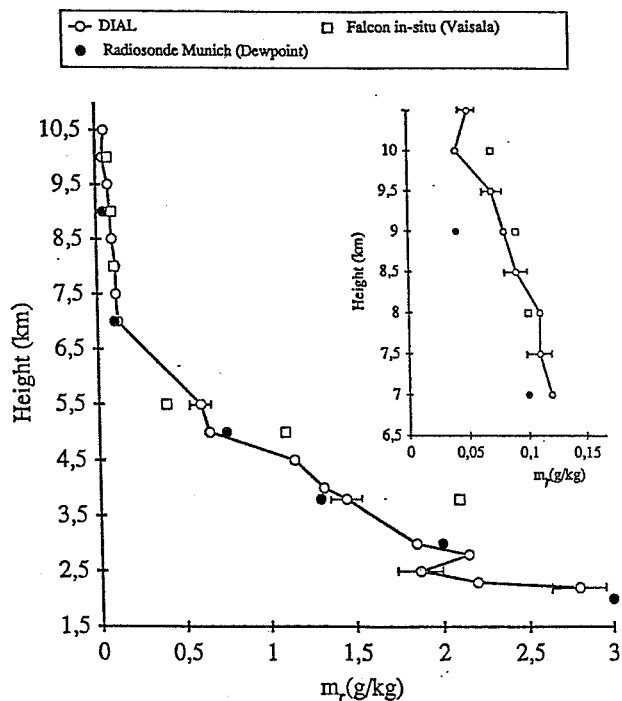


Fig.1: Vertical distribution of the mixing ratio as deduced from DIAL measurements averaged over the flight track Allersberg-Straubing in comparison with in-situ-data.

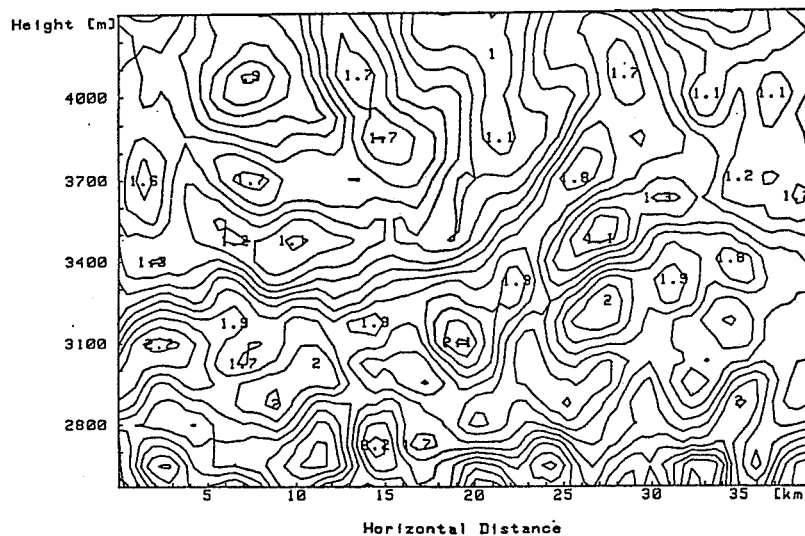


Fig.4: Two-dimensional H_2O mixing ratio plot: Vertical cut through the atmosphere, with a vertical resolution of 300 m and a horizontal one of 4 km. The spacing between two isolines is 0.1 g/kg.

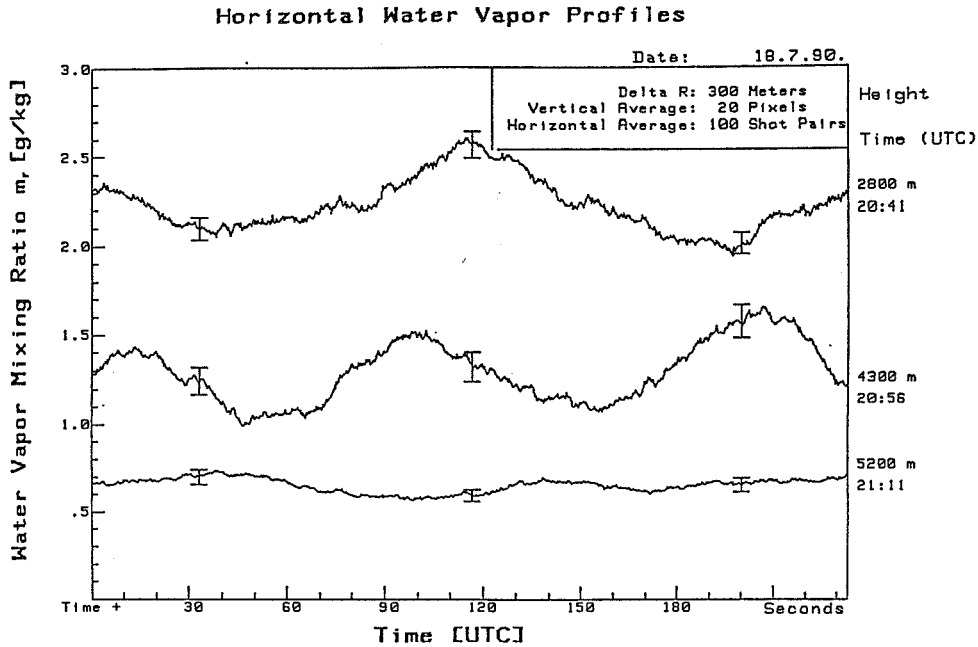


Fig.2: H_2O mixing ratios as function of time and altitude ranges calculated from lidar returns in the lower and middle troposphere. The vertical resolution of these profiles is 300 m while the horizontal resolution ranges between 4 km for the profiles at 2800 m and 5 km for those at 5200 m.

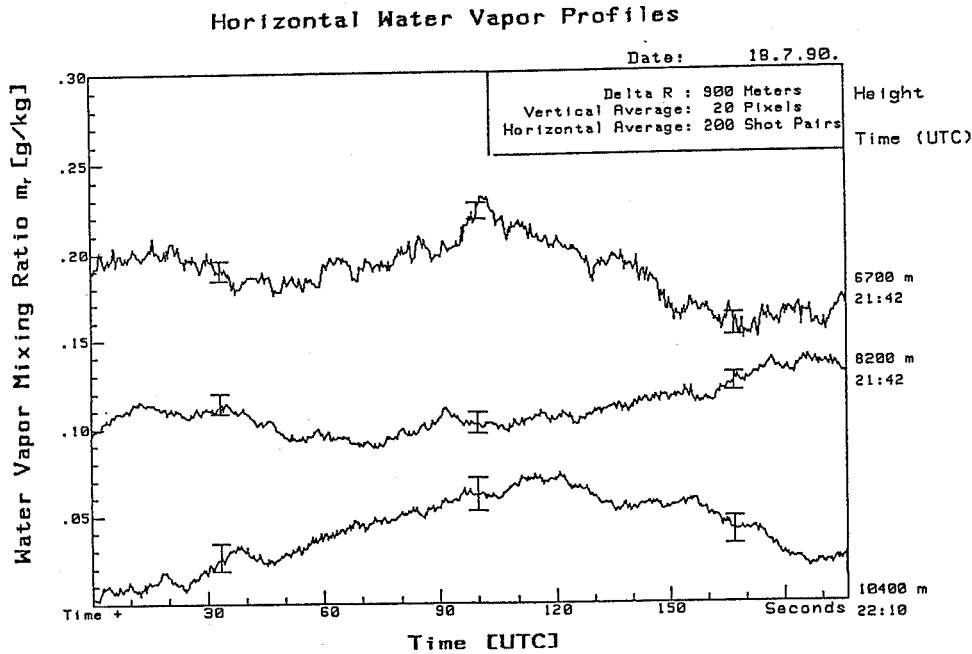


Fig.3: H_2O mixing ratios as function of time and altitude ranges in the upper troposphere. The vertical resolution of these profiles is 900 m while the horizontal resolution lies between 11 and 12 km. The reduced spatial resolution of these profiles as compared to those from Fig.2 results from a 200 shot pair average and an increased flight speed of the aircraft in the upper troposphere of nearly 180 m/s. The flight time of about 200 seconds corresponds here to a horizontal distance of approximately 36 km.

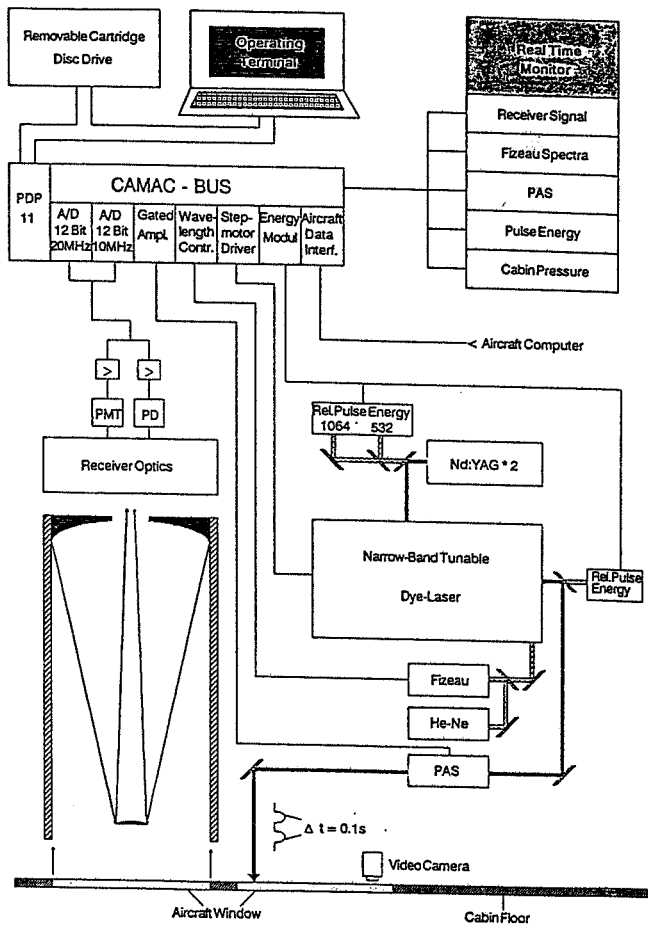


Fig.5: Exp. setup of the DIAL system in the aircraft Falcon 20.

Pump Laser	
Energy per shot	500mJ at 1.06 μm
Simultaneous	200mJ at 0.53 μm
Beam quality	multimode
Beam divergence	1.5 mrad
Rep. rate	single shot to 10 Hz
Power cons.	24 V/50 A max.
Dye Laser	
Dye solution	Pyridin 2 in Methanol
Energy per shot	30-40mJ at 0.72 μm
Beam divergence	0.5 mrad
Bandwidth	0.015 cm^{-1} (FWHM)
Fizeau Spectrometer	
Wedge angle	10°
Free Spectral Range (FSR)	0.56 cm^{-1}
Finesse	80
Frequency resolution	0.02 cm^{-1}
CCD-Array	512 pixel separated by 25 μm /pixel
Pixel resolution	0.002 cm^{-1} /pixel
PAS cell	
Sealed gas mixture	Water vapor ~ 15 Torr Clean nitrogen 50-100 Torr
Telescope	
Type	Cassegrain
Primary diameter	35 cm
Focal length	400 cm
Field of View	typ. 0.8 mrad
Spectral Filter	
Center wavelength	724.5 nm
Bandwidth at center wavelength	0.65 nm (FWHM)
Transmission	50 %
Angle tunable	724 - 722 nm
Detector	
Photomultiplier	Hamamatsu R 928
Photodiode	SI: APD from RCA
Digitizer	
Transiac	12 bit 10 MHz 12 bit 20 MHz
Data Acquisition System	
Computer	PDP 11
Bus-system	Q-Bus, CAMAC
Storage medium	Removable disc 50 Mbyte
Data Processing System	
Computer	HP 9000/360
Storage medium	Optical disc 650 MByte

Table 1: H_2O DIAL system parameter.

Trial of a Slant Visual Range Measuring Device

by

J. Streicher⁺, C. Mönkel^{*} and H. Borchardt[#]

⁺DLR Institute of Optoelectronics, D-3081 Oberpfaffenhofen

^{*}Hagenuk GmbH D-2000 Hamburg

[#]by order of the German Weather Service D-2000 Hamburg

Abstract

Each year, fog at airports renders some landing operations either difficult or impossible. The visibility that a pilot of a landing aircraft can expect is in that case the most important information. It could happen that the visibility versus the altitude is constant decreasing or increasing. However it is not possible to distinguish this with the existing sensors at an airport. If the visibility is decreasing with the altitude one has the worst case, ground fog. The standard visibility sensor, the transmissometer, determines only the horizontal visual range, which will be underestimated in comparison with the real visibility a pilot has on his landing approach.

This paper describes a new technique to measure the slant visual range making use of a slant scanning device; an eye safe laser radar.

A comparison with commercial visibility sensors shows that it is possible to measure visibilities with the slant looking laser radar in the range from 50m up to 2000m and even distinguish inhomogenities like ground fog.

1. The slant visual range sensor

One of the most complicated phases of flying an aircraft is the landing approach. The ground staff therefore provide the pilot with the most important weather parameters near the airport. One of these parameters is the visibility - the runway visual range (RVR).

The RVR is comprised of the meteorological visual range (MOR) measured with ground based visibility sensors (transmissometers), the brightness of the background, and the illumination of the air-strip.

The visibility estimated in this way does not always correspond to the real visual range of the pilot in a landing approach: low-lying clouds deceive with better apparent visibility while ground fog produces smaller apparent visibilities.

The second case may even lead to the worst situation: the closing of the airport.

The problem of measuring the real slant visual range is well known, a technical solution was proposed by the DLR¹ and has been tested in conjunction with the IMPULS Physik GmbH (now Hagenuk GmbH) in practice².

The principle is similar to the measurement of the RVR - the goal is the determination of a transmission, but in this case on a slant path.

The device has to be placed near the air-strip, therefore it is impossible to put the receiver on a tower. It is instead fixed adjacent to the transmitter - a Laser diode.

¹ Werner Ch.:

Determination of the slant range visibility from lidar signatures using the two-point-method. Optics and Laser Technology Vol. 7, pp 27-36 (1981)

² Streicher J., Werner Ch., Berghaus U., Gatz H., Gelbke E., Lisius A., Mönkel C.:

Prototyp eines Meßgeräts zur Erfassung der Schrägsichtweite
DFVLR FB 88-42

This configuration is called a laser radar or short a lidar.
 The atmosphere can then be scanned at different elevation angles to detect vertical layers as shown in figure 1.

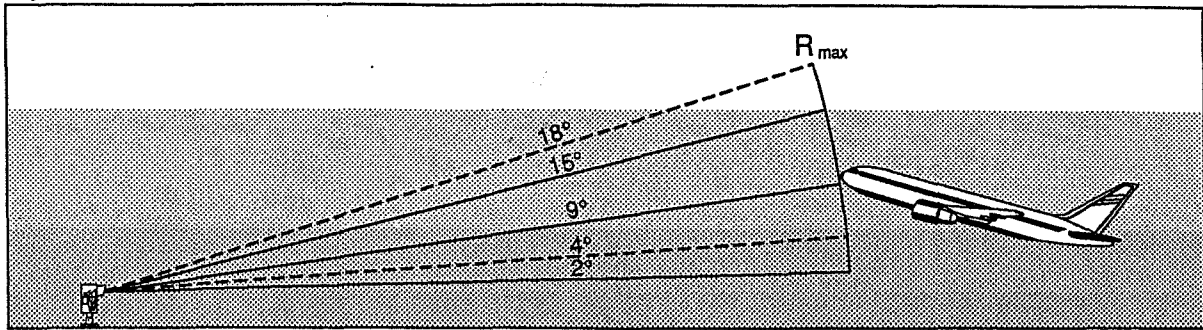


Figure 1. Scanning procedure through a vertical layer

The main requirement of the laser is therefore the eye safety criterion. Such a laser was located in a cloud ceilometer manufactured by the Hagenuk GmbH:

Laser:	GaAs laser diode array
Wavelength:	906nm
Pulse energy:	1.6μWs
Pulse duration:	50ns
Pulse repetition rate:	2.5kHz
Optical diameter:	14cm
Laser safety:	conforms to IEC 825/VDE 0837 class 3A

The very low pulse energy and therefore the small signal to noise ratio is improved by averaging over some hundreds of shots. This can be done very quickly because of the high repetitions rate of 2500 shots per second.

The averaging process has another positive effect besides smoothing; the transient recorder (specially designed for this device) digitises every single shot with an 8bit A/D converter. The shots are then stored in a 17bit sized array. The size of the digitising steps can be reduced from 1/256 (least significant bit of an 8bit converter) to 1/131072 (17bit), if the noise is greater than the least significant bit of the single shot converter, i.e. noise level > 1/256. The total dynamic range of this fast (20MHz) transient recorder is therefore 17bit when averaging over many shots. This digitiser therefore provides an almost ideal lidar signal:

- very small digitising steps, necessary for the range correction of the signal
 $(S(R) = U(R) R^2)$
- and a large dynamic range to follow the $1/R^2$ dependence signal especially for low visibilities i.e. small transmission of the atmosphere.

This technique makes it possible to measure visibilities between 50m and 2000m visual range.

Another modification in comparison to the standard cloud ceilometer is a turnable mirror, which is tilted to the vertical axis of the optics automatically when the cloud altitude becomes less than a suitable altitude. A rough sketch of the SVR sensor is shown in figure 2.

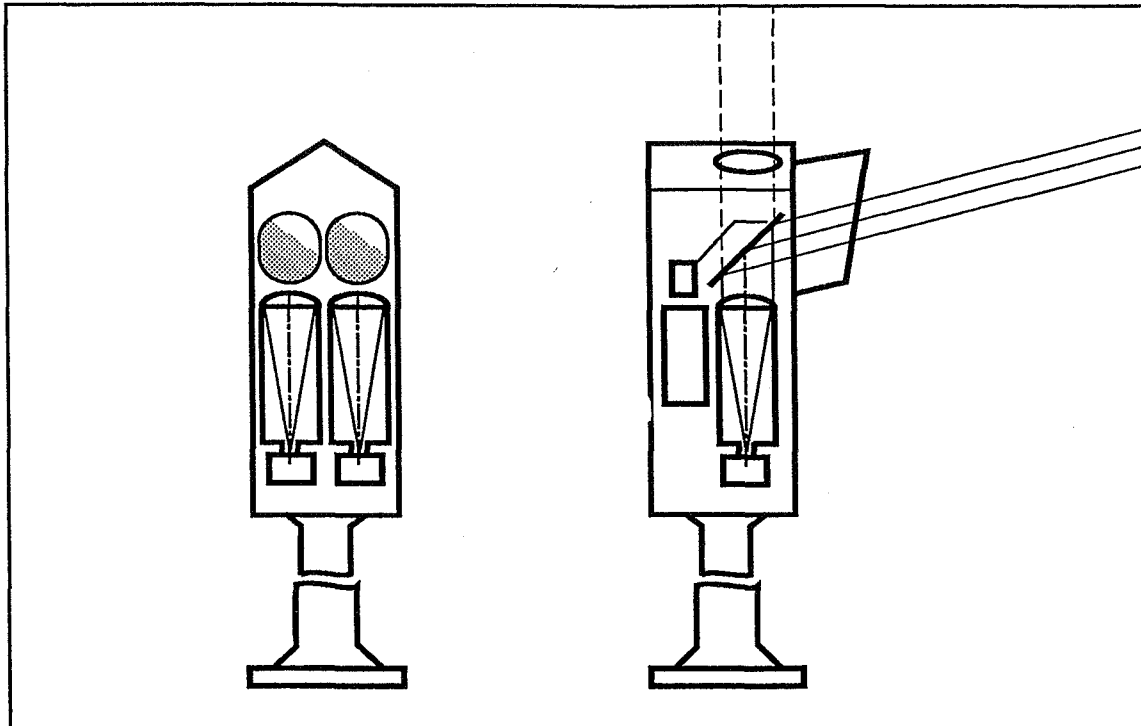


Figure 2. Modified cloud ceilometer for SVR measurements and cloud height

The measuring range for cloud altitudes is up to 5000ft, the typical penetration depth for the slant path is 1500ft or in altitudes between 30ft (2°) and 300ft (18°). The slant measuring path has also an effect on low level cloud monitoring: every lidar has an geometrical overlap function. The consequence of this is the absence of a signal in the range gates up to $30\text{m} \approx 150\text{ft}$. With a standard cloud ceilometer one has not only an upper limit, mainly caused by the output energy, but also a lower limit caused by the geometry of the optics. The monitoring of the slant path overcomes this deficiency: a layer can be distinguished down to zero height with a much better accuracy in height resolution than a standard ceilometer.

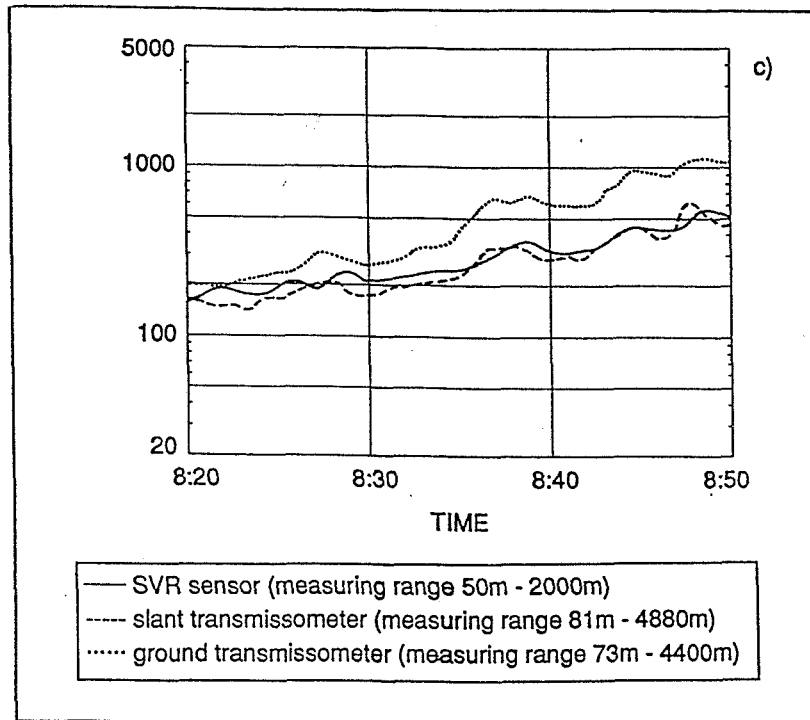
2. Measurements in Quickborn

The slant visibility sensor had been tested by the German Meteorological Service in Quickborn (Germany) over one year.

Additional sensors were placed close to the SVR device to obtain comparable results. One commercial transmissometer was set up in the usual way with a horizontal base to get the horizontal MOR, the other with a slant base of 9° . The receiver of the second transmissometer was fastened at a height of 20m on a tower, on which three forward scattering devices additionally measured the visibilities at different altitudes.

A comparison of the horizontal, the slant transmissometer, and the SVR sensor, for the case of low-lying clouds, is shown in figure 3.

The diagram shows a lifting fog. At the beginning of this measurement all three sensors show the same visibility of about 200m, whereas the horizontal transmissometer shows at the same time about two times better visual range than the slant sensors. The conformity of the slant sensors shows that the horizontally measured RVR may lead to a dangerous situation: the pilot will expect much better visibility conditions than he will really have on the approach.



An additional application for the SVR sensor in this situation is the exact measurement of the cloud base. As mentioned in chapter 2 there is no information in the first 150ft for a vertical measurement with a standard ceilometer.

3. Conclusions

The comparisons with the standard visibility sensor, a horizontal transmissometer, have shown that the lidar produces the same visibilities in the case of a vertical homogeneous atmosphere.

The comparisons with a slant transmissometer (impossible to install at airports) show that the lidar registers both cases of vertical layers: ground fog and low lying clouds.

It is now possible to give the pilot additional information about the visibility at the height level where he has to decide whether to continue the approach or not: at the decision point.

The pilot is kept informed of critical visual situations allowing him to avoid hazardous go-around manoeuvres: a decisive step towards increasing aviation safety. Especially in the case of ground fog the runway can be kept open for a longer period of time because it is possible to determine accurately the slant visual range.

**Lidar Depolarization by Nonspherical Particles :
Potential of Combined Depolarization/Backscattering Measurements
for PSC's Characterization**

C. Flesia*, A. Mugnai⁺, L. de Schoulepnikoff**, L. Stefanutti⁺⁺

* Institute of Atmospheric Physics ETH, CH-8093, Zurich, Switzerland
and Observatoire Cantonal de Neuchâtel, CH-2000, Neuchâtel, Switzerland.

* Observatoire Cantonal de Neuchâtel, CH-2000, Neuchâtel, Switzerland.

⁺ Istituto di Fisica dell'Atmosfera, CNR, CP 27 - 00044 Frascati, Italy

⁺⁺ IROE/CNR, Florence, Italy

Size and concentration of the Polar Stratospheric Clouds (PSC's) particles play an important role in the chemistry of the polar stratosphere. The speed of chemical reactions in the so called heterogeneous chemistry involved in polar stratosphere is related to the active surface of the ice crystals [1]. In addition, crystal size affects the sedimentation velocity and thus the processes of denitrification and dehydration of the polar stratosphere [2]. Moreover, there are indications that crystal size may be related to the chemical nature of the particles themselves since Nitric Acid Trihydrate (NAT) clouds (type I PSC's) are probably formed by particles smaller than those of ice clouds (type II PSC's) [3]. Accordingly, Toon et al. interpret PSC lidar observations and give a classification of this kind of clouds in terms of their characteristic particle sizes and concentrations.

In this study, we analyze the potential of combined backscatter and depolarization information for deriving the optical parameters of PSC clouds together with size and physical phase of the cloud particles. In particular, we investigate the influence of particles shape and orientation on the parallel and perpendicular backscattered intensities and on the depolarization ratio under experimental noise conditions, and how the first three moments of the particle size distribution (i.e., particle concentration, mean radius and standard deviation) may be used to introduce further distinction between type Ia and type Ib PSC's.

The scattering particles have been approximated with NAT prolate spheroids corresponding to equal-volume spheres with radii between 0.1 and 2 μm , having axial ratios (elongations) between 1.05 and 3. The particles are randomly oriented either in space (3-D random orientation) or on a plane perpendicular to the incoming linearly

polarized radiation (2-D random orientation). Their extinction and backscattering coefficients have been computed by means of the Extended Boundary Condition Method [4-7]

Some previous results [8] have shown that as soon as a little deformation from the spherical shape is introduced, the depolarization of the lidar signal may become considerable. In particular, the depolarization ratio $((I_{\perp}/(I_{\perp} + I_{\parallel})) * 100)$ as a function of the deformation parameter ϵ of "Chebyshev" particles [4] shows maxima as high as 40% that depend on particle size. The deformation giving a first depolarization peak is usually rather small and decreases when the particle radius increases. Moreover, the number of depolarization peaks observed in the same range of deformations increases with particle radius while the depolarization ratio tends to show rapid fluctuations as a function of particle deformation. These maxima appear to be systematically higher when the particles are 2-D rather than 3-D randomly oriented.

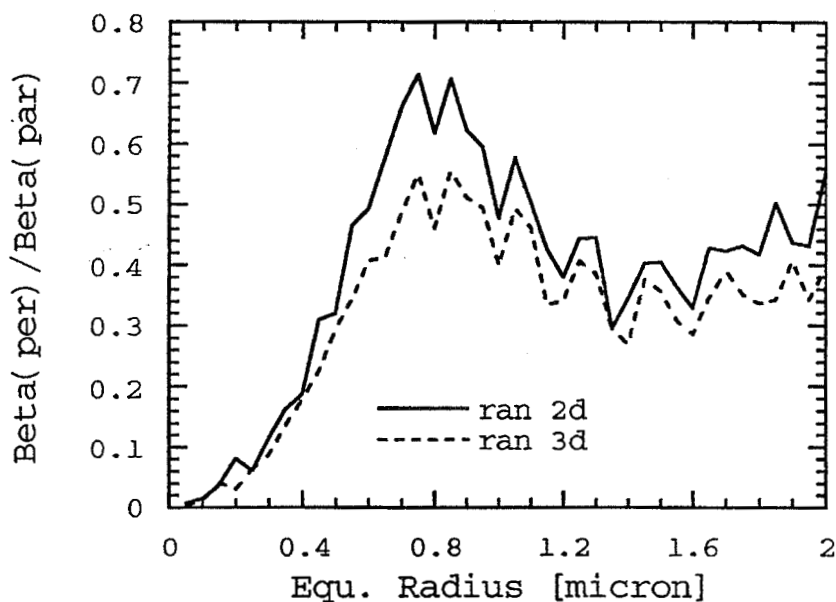


Fig. 1

In this study, in order to consider more physical cases, the lidar depolarization has been computed for various mixtures of elongations and for different mean values and standard deviations of the particle size probability distribution. Fig. 1 shows the ratio β between the perpendicular and parallel backscattering cross sections of a uniform mixture of elongations as a function of the radius of the equivalent volume sphere. The calculated ratio shows fluctuations as a function of particle size

and supports only partially the suggestion of Poole [9] that the depolarization ratio increases significantly with particle size for a given particle shape. Moreover, these results confirm the indication that 2-D randomly oriented particles depolarize more the incident radiation.

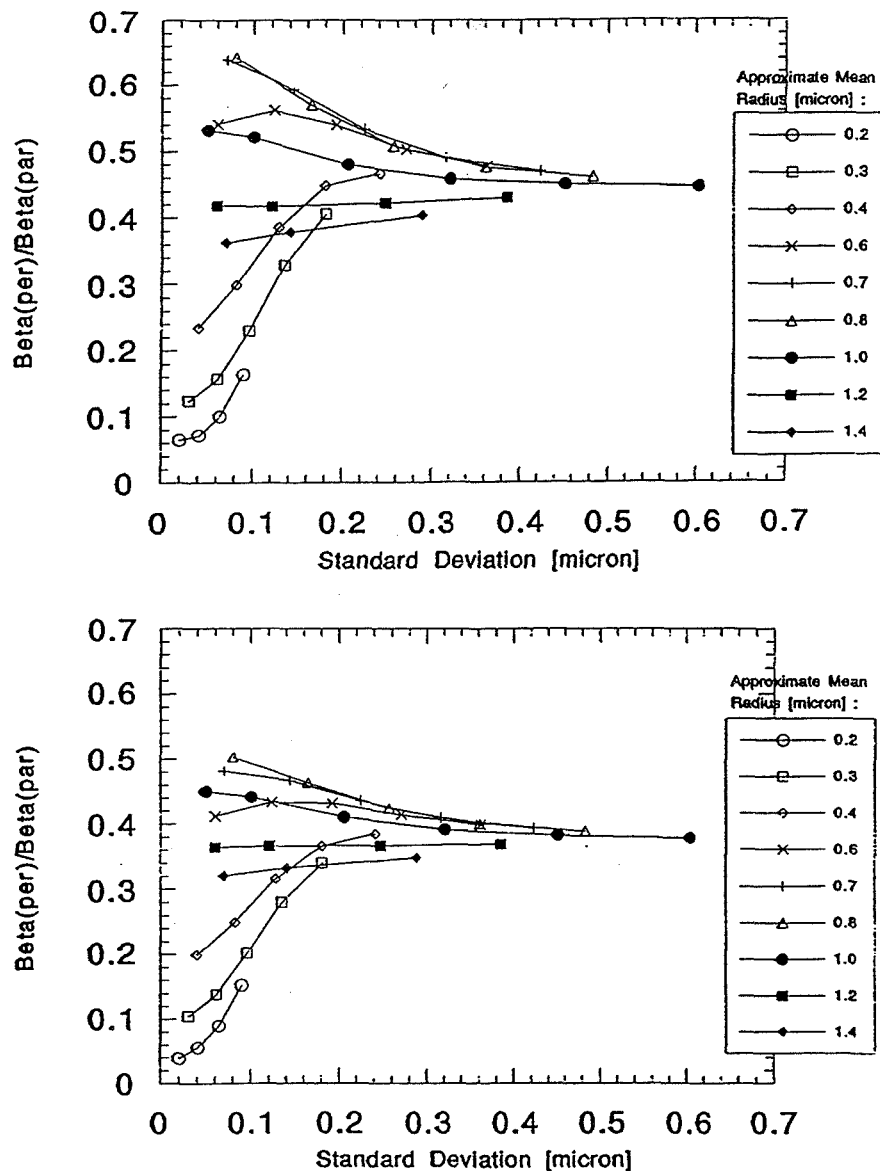


Fig. 2

Fig 2. shows the β ratio as a function of the standard deviation of the lognormal size probability distribution, for different values of the mean radius and for two different orientations of the particles. The results show a very rapid convergence of the β ratio (i.e., the depolarization) as a function of the standard deviation. Moreover, the convergence value appears to be independent of the mean particle size and essentially the same for the two different particle orientations. Nevertheless, the left

side of the curves in this figure underlines the influence of the higher moments of the size probability distribution on the scattering properties and can be used to get an indication about the mean particle radius and its fluctuations.

From the knowledge of the depolarization ratio and of the scattering ratio, β has been calculated for typical values of type Ia and type Ib PSC clouds. This value has been found to be about $\beta=0.5-0.6$ for type Ia PSC's and about $\beta=0.1-0.2$ for type Ib PSC's. This typical values of β can be used in conjunction with fig. 2 to characterize the size of the cloud particles. In fact, they belong to the left region of this figure where β is very sensitive to the mean radius and width of the particle size distribution. Thus, our results indicate that type Ib PSC's are probably composed of very small particles of about $0.1-0.2 \mu m$ with a standard deviation of the same order of magnitude - i.e., a very broad size probability distribution. On the contrary, the type Ia PSC 's appear to be formed of particles of about $0.8-0.9 \mu m$ with a very narrow probability distribution of sizes.

Moreover, even though the orientation of the small particles of the type Ib PSC's is not influent, the crystals in the type Ib PSC's are probably 2-D randomly oriented.

Finally, we have computed the values of the β ratio for a mixture of deformations in two different cases : for very slightly deformed particles, or in presence of big elongations. The results seem to indicate a higher sensitivity of the 2-D randomly oriented particles to degree of deformation of the scatterers themselves. Moreover, the lower value of the depolarization for 3-D randomly oriented particles seems to be confirmed independently on the degree of elongation.

REFERENCES

- [1] M.J. Molina : Proc. of Quadrennial Ozone Symposium 1988, Ed. R.D. Bojkov and P.P. Fabian, 61 Deepak (1989).
- [2] A. Heymsfield : J. Atmos. Sci., 29, 1348 (1972)
- [3] O.B. Toon et al. : Geophys. Res. Lett., 13, 1284 (1986)
- [4] A. Mugnai, W.J. Wiscombe : Appl. Opt. 25, 1235 (1986)
- [5] P.C. Watermann : Proc. IEEE, 53, 805 (1965)
- [6] P.C. Waterman : Phys. Rev. D3, 825 (1971)
- [7] P. Barber, C. Yeh : App. Optics, 14, 2864 (1975)
- [8] C. Flesia, A. Mugnai, L. Stefanutti : Proc. of Topical Meeting on " Atmospheric, Volume and Surface Scattering and Propagation", Firenze 27-30 Aug. (1991).
- [9] L. R. Poole : Geophys. Res. Lett. 15, 867 (1988)

Coherent CO₂ lidar: A superior system for observing clouds?

Wynn L. Eberhard and R. Michael Hardesty
NOAA Wave Propagation Laboratory
Boulder, Colorado

INTRODUCTION

Lidars have long been used to study various parameters of clouds. NOAA's Wave Propagation Laboratory (Post and Cupp, 1990) has operated a coherent CO₂ lidar for over a decade, using Doppler to study wind fields and turbulence, atmospheric absorption for DIAL applications, backscatter to investigate aerosol distributions, and backscatter and extinction measurements on clouds. A system under development for our laboratory (Pearson, this volume) promises to overcome the older system's problems of large size, frequency instability, and need for continual operator attention. We are also thoroughly evaluating the capabilities of CO₂ lidar for observing clouds, including development of some new techniques. CO₂ lidar provides a view of clouds different in many ways from that of lidars at other wavelengths. In this paper we summarize the unique aspects of coherent CO₂ lidar for backscatter and extinction measurements from clouds. (Its excellent potential for Doppler observations are left for another forum.) This discussion argues in support of the proposition: Coherent CO₂ lidar can be a superior lidar system for measuring most cloud properties.

FUNDAMENTAL DIFFERENCES

A CO₂ lidar uses coherent detection to achieve low-noise operation and hence good sensitivity. The coherent optical configuration also affects some practical aspects of a system, as discussed below. A more important factor is that a CO₂ lidar operates at a laser transition in the 9-11 μm wavelength band (commonly at 10.6- μm wavelength), which is in the infrared atmospheric window. Wavelengths for other lidars are near or within the visible part of the spectrum. An important difference is that water drops and ice particles absorb strongly at CO₂ lidar wavelengths, whereas scattering dominates in the interaction of radiation at the shorter wavelengths.

PRACTICAL ASPECTS

Many short-wave lidars operate at wavelengths that permit only very small pulse energies before they are eye-safe. A coherent CO₂ lidar is easily made eye-safe, and can operate with sufficient pulse energy to detect very thin clouds with good sensitivity. WPL's CO₂ lidar beam can even be aimed at aircraft or persons on the ground without danger.

A coherent lidar must use diffraction-limited optics, which is not particularly difficult in the 10- μm wavelength band. However, one problem with any diffraction-limited atmospheric lidar is speckle. Speckle is a statistical fluctuation in the signal, even when signal-to-noise ratio is high, caused by coherent addition of the random phases of the radiation scattered from randomly positioned scatterers. Averaging of backscattered signal power over multiple pulses is the most common method to reduce speckle effects to an acceptable level. The high pulse rate of the mini-MOPA (master oscillator, power amplifier) lidar (Pearson, this volume) will be able to accomplish this quickly.

Multiple scatter in clouds causes serious complications in interpretation of the signal from short-wave lidars. A combination of three factors makes multiple scatter negligible for a coherent CO₂ lidar: 1) the receiver field of view is very narrow (~ 0.1 mr); 2) the angular width of the forward scattering lobe from hydrometeors is an order of magnitude larger than short-wave lidars; and 3) (less important) the large absorption cross section reduces the amount of high order scattering events. In this respect,

quantitative analysis of CO₂ lidar data is much easier than for short-wave lidars.

A short-wave lidar can be designed to use molecular scatter from an altitude free of aerosols for calibration. The other common method, using backscatter from a diffuse hard target of known reflectivity, is used by CO₂ and sometimes short-wave lidars. Although the molecular method is often better for calibration of short-wave lidars observing the cloud-free air, the hard target method is just as efficacious for cloud applications, because both clouds and the hard target give large lidar signals. Correction for attenuation by molecules and aerosol particles can also be important for accuracy in measuring some cloud parameters. For short-wave lidars, correction for molecular scatter is easy, but the highly variable aerosol content of the air can be troublesome. The aerosol effects on propagation of CO₂ lidar radiation are much smaller in comparison. However, a CO₂ laser's radiation suffers substantial molecular absorption, principally from CO₂ and water vapor. The variable concentrations of water vapor and some uncertainty about its absorption cross section can sometimes make accurate correction of CO₂ lidar data difficult. The CO₂ and short-wave lidars are roughly equivalent to each other in regard to these calibration issues.

Because the near field of a coherent lidar may extend to as far as 5 km range, the range sensitivity function $f(R)$ does not have the simple R^2 dependence commonly valid for short-wave lidars. Although more sophisticated methods must be used to determine $f(R)$ for a coherent CO₂ lidar (Zhao et al., 1990), there is also a benefit. The coherent lidar's sensitivity changes much more slowly than R^2 in the near field, so the dynamic range of the coherent lidar's signal is correspondingly less. Also, coherent detection reduces the dynamic range of a coherent lidar's signal by a factor of two (e.g. from 80 db to 40 db), because the electronic signal is proportional to electric vector amplitude rather than power of the received radiation. Therefore, the very large excursions in cloud signal strength are much more easily handled by a coherent lidar.

THEORETICAL CALCULATIONS OF CLOUD SIGNAL

Lidar signals from clouds depend on particle size and shape distributions, the wavelength, and the refractive index of water or ice at that wavelength. The best way to interpret lidar data is by a comparison with the results of scattering calculations. When these are not available, researchers must rely on empirical comparisons with other measurements or on crude assumptions.

We claim that scattering calculations are easier at CO₂ lidar wavelengths than for short-wave lidars. The most obvious advantage is that size parameters are an order of magnitude smaller for the longer wavelength. The strong absorption is also very important. For instance, it prevents wide excursions in backscatter from spherical drops seen at nonabsorbing wavelengths as the size parameters become large. Although scatter from spherical cloud and precipitation drops can be calculated for any wavelength using Mie scatter, the computer resources required for CO₂ lidar wavelengths are much less.

More importantly, we believe that calculation of scatter from nonspherical ice particles is more tractable for CO₂ lidar wavelengths. The discrete dipole method (Purcell and Pennypacker, 1973) can be used for particles with maximum dimensions up to about 10 μm . The e^{-1} penetration depth of 10.6- μm radiation into ice is only 7 μm , so most of the backscatter from thicker particles originates in reflection from the first surface. We believe that a simple model incorporating first-surface reflection and diffraction will be adequate for calculating CO₂ lidar signals from most ice particles. Work is in progress at WPL to develop these nonspherical scattering methods and to evaluate their usefulness for interpreting CO₂ lidar signals from clouds.

MEASURING CLOUD PARAMETERS

In this section are listed cloud parameters observable by a coherent CO₂ lidar. For those parameters also measureable by short-wave lidar, we briefly compare the two types of systems. Other parameters can be measured only with CO₂ lidar. Finally, we state some advantages of coherent CO₂ lidar in multi-sensor measurements.

Geometrical structure -- Base height, multiple layers, top height, brokenness, and other geometrical structures of clouds are important factors in the development and effects of clouds. Both short-wave and CO₂ lidars are excellent approaches to these measurements. Our research has demonstrated that coarser range resolution and averaging for speckle reduction prevent a CO₂ lidar from observing fine structure in clouds with the same exquisite detail as short-wave lidars can. However, quantitative applications rarely require this much detail. The eye-safe nature of CO₂ lidars is a definite advantage when scanning is desired. We anticipate that the high pulse rate of the mini-MOPA lidar will provide excellent spatial and temporal coverage of the sky for studying the effects of inhomogeneous cloud structure on radiative transfer.

Ice/water discrimination -- Depolarization of backscatter from ice particles is a frequently used tool for discriminating between ice and water phase in clouds (Sassen, 1991) using short-wave lidars. Depolarization of CO₂ lidar backscatter from ice clouds is very small (Eberhard, 1992), so it cannot use this method.

We propose an alternative for CO₂ lidar based on differential backscatter at two wavelengths. Our preliminary analysis shows that backscatter from ice clouds increases substantially with wavelength above 10.5 μm, while backscatter from water clouds decreases slightly. One attractive option would be a ¹³C¹⁶O₂ isotope lidar operating simultaneously (or perhaps with alternating pulses) at wavelengths of 10.74 and 11.19 μm. The ratio of backscatter from an ice cloud at the two wavelengths (in the geometrical optics approximation) is 2.83, while the ratio based on Mie scatter calculations for water clouds is $.87 \pm .10$, depending on the drop size distribution. We expect a dual-wavelength CO₂ lidar will easily discriminate between clouds purely in one phase or the other, and will be able to estimate the fraction of ice particles in mixed phase clouds with good accuracy.

Mean or effective radius of water droplets -- A calibrated CO₂ lidar can estimate a characteristic radius (Platt and Takashima, 1987) based on measurement of extinction-to-backscatter ratio averaged over the penetration depth of a pulse. Some enhancements to this method and results of an actual measurement are discussed in another paper (Eberhard, this volume).

Profile of liquid water content -- Platt and Takashima (1987) also proposed a method to obtain the profile of liquid water content. Their method assumes a constant extinction-to-backscatter ratio along the lidar beam, a condition that will often be violated. We agree with their comment that additional information, e.g., constraints on the form of the drop size distribution, can be applied to make the technique useful. We plan to study these alternatives and hope to be able to apply them in future field projects.

Enhanced backscatter from oriented crystals -- Many lidar operators have observed an enhancement in backscatter when viewing ice crystals near the vertical. This is caused by reflection from the faces of oriented plates (Platt et al., 1978) or possibly from a maximum in backscatter from oriented columns or needles. The angular width of this enhancement as observed by a lidar scanning about the vertical depends on crystal flutter motions as they fall at terminal velocity and on imperfections in shape that affect backscatter or orientation. The width also depends on diffraction effects, which increase linearly with wavelength. If diffraction dominates for a CO₂ lidar's enhanced backscatter from plates, the diameter of the flat side can be estimated from the angular width (Eberhard and Post, 1991).

We obtained an excellent data set on enhanced backscatter with the CO₂ lidar at the FIRE II cirrus experiment in late 1991. Theoretical evaluations and comparison with experimental measurements are in progress.

Infrared optical depth -- A lidar can measure the narrow-beam optical depth of a cloud that is not too thick if a target of known reflectivity is available on the other side. The result is affected by multiple scatter. Hall et al. (1988) measured transmittance through cirrus with a surface-based CO₂ lidar using stratospheric aerosol layers from El Chichon as a cooperative target. An airborne or satellite lidar may sometimes be able to use the surface as a cooperative target. It is worth noting that the optical depth of water clouds in the 10-μm wavelength band is considerably less than in the visible if the mean radius

is much less than 10 μm .

Emissivity profile of cirrus -- The long-wave emission from cirrus depends on emissivity and temperature. Mie scatter calculations show that the volumetric emissivity at 10.6- μm wavelength is proportional to the backscatter coefficient at the same wavelength to within 6% for a wide variety of ice particle size distributions. This suggests the potential for determining the emissivity of a cloud from CO₂ lidar backscatter to learn more about its radiative effects than column-integrating instruments can. The extinction coefficient is also proportional to backscatter to good accuracy if spherical ice particles can be assumed. However, the deviations of real ice particles from spheres will have some effect, perhaps major, on these relationships. We are analyzing experimental data to determine how well they hold for real ice clouds. We will also use the theoretical calculations for nonspherical particles to examine the potential for inferring emissivity and extinction of cirrus from CO₂ lidar backscatter.

Multi-sensor observations -- As cloud research advances the need will grow for more sophisticated measurements. Parameters derived from observations by multiple sensors will help fill this need. One example is estimation of effective radius of cirrus particles using simultaneous radar and lidar measurements (Intrieri et al., 1991). We believe CO₂ lidar has an advantage in such quantitative applications, because multiple scatter is negligible and the scattering properties can be calculated with relative ease.

CONCLUSIONS

We believe that coherent CO₂ lidars have inherent advantages for sensing clouds compared to short-wave lidars. These are: high sensitivity with complete eye safety, negligible multiple scatter, relative ease in calculating backscatter from large particles, and an ability to measure important cloud parameters in addition to those observable by short-wave lidar. The development of robust and easily-operated CO₂ lidars is a prerequisite to realization of this potential.

REFERENCES

- Eberhard, W.L., 1992: Ice cloud depolarization of backscatter for CO₂ and other infrared lidars. *Appl. Opt.*, **31** (in press).
- Eberhard, W.L., and M.J. Post, 1991: CO₂ lidar techniques for observing characteristic particle size of selected cloud types. *Extended Abstracts, Lower Tropospheric Profiling: Needs and Technologies*, Sept. 10-13, 1991, Boulder, Colorado, National Center for Atmospheric Research, 7-8.
- Hall, F.F., Jr., R.E. Cupp and S.W. Troxel, 1988: Cirrus cloud transmittance and backscatter in the infrared measured with a CO₂ lidar. *Appl. Opt.*, **27**, 2510-2516.
- Intrieri, J.M., W.L. Eberhard and T. Uttal, 1991: Determination of cirrus cloud particle effective radii using radar and lidar backscattering data. *Preprints, 25th International Conference on Radar Meteorology*, June 24-28, 1991, Paris, France, Amer. Meteor. Soc., 809-812.
- Platt, C.M.R., N.L. Abshire and G.T. McNice, 1978: Some microphysical properties of an ice cloud from lidar observations of horizontally oriented crystals. *J. Appl. Meteor.*, **17**, 1220-1224.
- Platt, C.M.R., and T. Takashima, 1987: Retrieval of water cloud properties from carbon dioxide laser soundings. *Appl. Opt.*, **26**, 1257-1263.
- Post, M.J., and R.E. Cupp, 1990: Optimizing a pulsed Doppler lidar. *Appl. Opt.*, **29**, 4145-4158.
- Purcell, E.M., and C.R. Pennypacker, 1973: Scattering and absorption of light by nonspherical dielectric grains. *Astrophys. J.*, **186**, 705-714.
- Sassen, K., 1991: The polarization lidar technique for cloud research: A review and current assessment. *Bull. Amer. Meteor. Soc.*, **72**, 1848-1866.
- Zhao, Y., M.J. Post and R.M. Hardesty, 1990: Receiving efficiency of monostatic pulsed coherent lidars. 1: Theory. *Appl. Opt.*, **29**, 4111-4119.

Measurement of Aerosol Profiles Using
High-Spectral-Resolution Rayleigh-Mie Lidar

D. A. Krueger, R. J. Alvarez II, L. M. Caldwell, and C. Y. She
Physics Department, Colorado State University
Fort Collins, CO 80523, U. S. A.

High-spectral-resolution Rayleigh-Mie lidar measurements of vertical profiles (1 to 5 km) of atmospheric pressure and density, as well as aerosol profiles, including backscatter ratio and extinction ratio are reported. These require simultaneous measurement of temperature. Use of the technique does not require any assumptions about the aerosol but does require that the pressure at one altitude is known and that the gas law of the air is known (e.g. an ideal gas).

High-spectral-resolution Rayleigh-Mie lidar using a narrowband transmission system (0.1GHz) and a narrowband filter can separate molecular and aerosol scattering.¹ A Fabry-Perot interferometer has been used as the filter to measure backscatter ratios.² An atomic resonance blocking filter can separate more completely the molecular and aerosol scattering components^{3,4,5,6}. The backscattered light is collected in a telescope (0.203 m diameter), is divided into two receiving channels ($i=1,2$) by a plate dielectric beamsplitter, passes through a barium atomic vapor filter and an interference filter and then is photon-counted. Using Doppler-free saturated absorption spectroscopy with a reference barium cell, the transmitting laser frequencies are set on and off the barium resonance at 5537 Å, and the number of photons at each range bin, N_{ion} and N_{ioff} , are recorded. The ratio of the simultaneous lidar returns of the two channels at the two frequencies, yields two power-independent signal ratio profiles, $C_{on} = N_{1on}/N_{2on}$ and $C_{off} = N_{1off}/N_{2off}$. The on-resonance signal ratio contains atmospheric temperature and pressure information, and the off-resonance signal ratio measures the relative efficiencies of the two channels. These lidar signals are then compared with the molecular attenuation factors, $f_{mi} = (f_{Ri} + \gamma f_0) / (1 + \gamma)$ where $\gamma = \beta_{RR}/\beta_R$, the ratio between the rotational (Raman) sidebands and the central (Cabannes) component of the Rayleigh scattering. The Rayleigh (Cabannes) attenuation factor, $f_{Ri}(T,P) = \int R(\nu,T,P) F_i(\nu) d\nu$ can be calculated from the laboratory measured transmission function of the atomic filter, $F_i(\nu)$, and the calculated Rayleigh/Brillouin scattering function, $R(\nu,T,P)$, based on a theoretical model such as the S6 model of Tenti *et al.*⁷ The normalization factor is $f_0(T) = (2/\lambda)\sqrt{2k_B T/m}$, where λ , k_B , and m are wavelength, Boltzmann constant and average molecular mass, respectively. Using

$$\frac{f_{m1}(T,P)}{f_{m2}(T,P)} = \frac{N_{1on}/N_{2on}}{N_{1off}/N_{2off}} = \frac{C_{on}}{C_{off}} \quad (1)$$

the atmospheric temperature at any height can be determined once the atmospheric pressure at that height is provided. To determine atmospheric profiles, we first divide a vertical range into bins. We then input the pressure at a chosen reference height and use Eq. (1) to determine the temperature at that height. The atmospheric pressure at the neighboring range bin may be calculated by assuming hydrostatic equilibrium and ideal gas law; Eq. (1) then yields the temperature of this neighboring bin. Successive iterations in this manner yields vertical atmospheric temperature, pressure, and thus density profiles.

With these measured atmospheric profiles, the lidar equations will permit the calculation of aerosol properties. The backscatter ratio, r_β , is defined⁸ as the ratio of the total backscattering coefficient, $\beta_m + \beta_a$, to the backscatter due to the air molecules, β_m . In terms of the measured signals this becomes

$$r_\beta = \frac{N_{off} P_{on}}{N_{on} P_{off}} \frac{f_m(T,P)}{f_o(T,P)} \quad (2)$$

Note that, due to the f_{mi} and f_o factors, the atmospheric temperature and pressure are required in addition to the ratios of the signals, and the laser powers, P_{on} and P_{off} . The aerosol extinction coefficient profile may be calculated from

$$\alpha_a(z) = \frac{1}{2} \frac{d}{dz} \ln \left\{ \frac{\beta_m(z) f_{mi}(T,P)}{N_{ion} f_o(T)} \right\} - n(z) \sigma \quad (3)$$

where β_m is the molecular backscattering coefficient [$n(z)$ times the Rayleigh cross section for backscattering], $n(z)$ is the air density, and σ is the total Rayleigh cross section. The relative aerosol/molecular importance for extinction is given by the extinction ratio, $\alpha_a(z) / n(z) \sigma$.

On the night of Feb. 4-5, 1991, lidar field measurements were carried out with a nearby balloon sonde at Fort Collins, CO. Temperature profiles with estimated error bars were reported earlier⁹. The reference height was chosen at 1.5 km and the pressure from the balloon-sonde at this level was used for the lidar inversion. Figure 1 shows the atmospheric pressure and density profile from the lidar measurements on three consecutive runs of about 18 minutes each. The pressure profiles are in close agreement (agree with one another within ± 2 and ± 3 % at 3 and 5 km respectively and are within 4 % and 6 % at 3 and 5 km respectively of the

balloon-sonde measurements) as is expected for a quantity that is obtained by integrating from a known reference point. The density profiles show a wavy structure that is not understood. The density is reflecting a variability that is present in the temperature profiles. Figure 2 shows the backscatter ratio and extinction ratio, as determined from the lidar measurements. All of these quantities depend upon the prior temperature determination and thus at least part of the errors in their measurement is due to temperature uncertainty.

The measured temperature uncertainty is

$$\delta T = [\{ \delta \ln \left(\frac{C_1}{C_2} \right) \}^2 + \{ \delta \ln \left(\frac{f_{m1}}{f_{m2}} \right) \}^2]^{0.5} / S_{T12} \quad (4)$$

where we have not included a term due to pressure errors because an incorrect estimate of the atmospheric pressure at the reference height by 20 mb amounts to an error of 0.3 K in our case. The temperature sensitivity coefficient, S_{T12} , which is defined as the fractional change in the ratio (f_{m1}/f_{m2}) for a change in the air temperature of 1 K, depends on the width of the two filters, $(\Delta\nu)_1$ and $(\Delta\nu)_2$. It decreases as the two filter widths approach each other. For typical filters, it is about 0.002 K⁻¹. Since fluctuations in the filter transmission function leads to a measured 1.5% uncertainty in the ratio of f_{m1}/f_{m2} , and photon fluctuations in signal at the power level are 0.3% and 2.2%, respectively, at 1 km and 5 km, the temperature uncertainties assessed at one standard deviation are 8 K and 14 K.

We have presented simultaneous determinations of atmospheric temperature, pressure and density, and aerosol backscatter ratios and extinction ratios from returns of a high-spectral-resolution Rayleigh-Mie lidar. Development of more stable atomic vapor filters with ten-fold reduction in filter fluctuations is expected and will reduce the temperature uncertainty to 2 K at 1 km at the reduced power level. Uncertainties in other quantities will be reduced accordingly. These improvements will make the high-spectral-resolution Rayleigh-Mie lidar a uniquely useful system for atmospheric studies. Since our system has 100 times more available power and a telescope with larger diameter is now available, the measurement time can be further reduced and the measurement range extended to cover the entire troposphere and lower stratosphere.

References

3. H. Shimizu, S. A. Lee, and C. Y. She, *Appl. Opt.*, **22**, 1373 (1983).
4. F. J. Lehmann, S. A. Lee, and C. Y. She, *Opt. Lett.* **11**, 563 (1986).
1. C. Y. She, *Contemporary Physics*, **31**, 247 (1990).
2. Shipley, D. H. Tracy, E. W. Eloranta, J. T. Trauger, J. T. Sroga, F. L. Roesler, and J. A. Weinman, *Appl. Opt.* **22**, 3716 (1983).
5. R. J. Alvarez II, L. M. Caldwell, Y. H. Li, D. A. Krueger, and C. Y. She, *J. Atm. Oceanic Tech.*, **7**, 876 (1990).
6. R. J. Alvarez II, *Measurement of tropospheric temperature and aerosol extinction using high-spectral-resolution lidar*, Ph.D. Thesis, Colorado State University (1991).
7. G. Tenti, C. D. Boley, and C. R. Desai, *Can. J. Phys.*, **52**, 285 (1974).
8. C. Y. She, R. J. Alvarez II, L. M. Caldwell, and D. A. Krueger, *Opt. Lett.* **17** (1992).
8. Kobayashi, T., 1987: Techniques for laser remote sensing of environment. *Remote Sensing Rev.* **3**, 1-56.

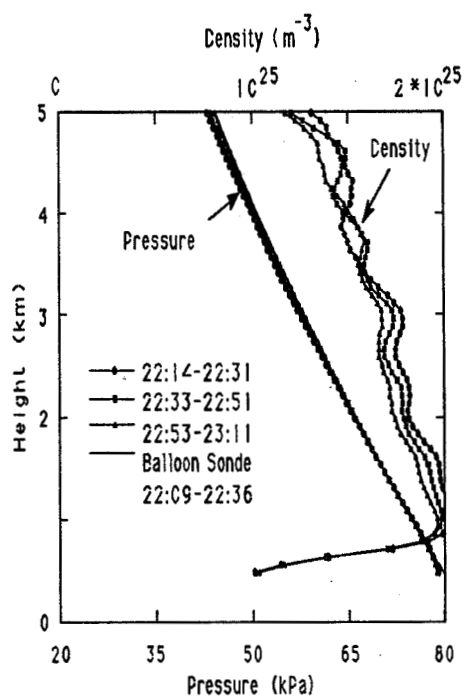


Fig. 1 Pressure and molecular density from lidar and pressure from balloon sonde taken at Fort Collins, CO. on Feb. 4, 1991. Times are MST.

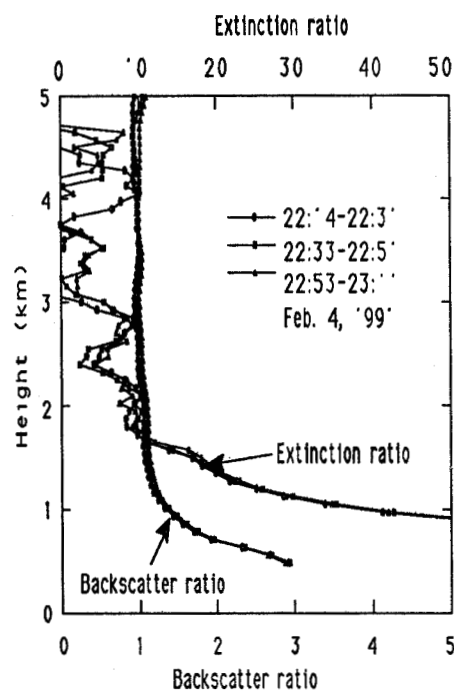


Fig. 2 Profiles of backscatter ratio and extinction ratio calculated from lidar data taken at Fort Collins, CO on February 4-5, 1991.

LABORATORY SCALED SIMULATION OF LIDAR CLOUD SOUNDING EXPERIMENTS

G. Zaccanti*, P. Brusciaglioni*, M. Gurioli** and P. Sansoni*

* University of Florence, Physics Department, Via S. Marta, 3 - 50139 Florence, Italy

** LENS Laboratory, Largo E. Fermi, 2 - 50125 Florence, Italy

Introduction

The results of lidar measurements carried out on laboratory scale models of clouds are presented. Measurements on laboratory scale models are important since one has the knowledge of the relevant parameters of the diffusing medium, such as: scattering and absorption coefficient, phase function, homogeneity, shape and so on. Knowledge of these parameters enables one to use the results to test the reliability of theoretical and numerical investigations.

To obtain a laboratory scaled model of a Lidar system sounding a cloud it is necessary to scale down all the geometrical quantities by the same factor to reduce distances of the order of kilometers to the order of meters, keeping the size and the optical depth of the diffusers unchanged. If a time resolution of the order of nanoseconds is necessary for a lidar sounding actual clouds, the corresponding time resolution for the laboratory model should be of the order of picoseconds. It is possible to obtain this resolution by using picosecond laser systems and fast electrooptical detectors like the streak camera.

The results of the laboratory measurements showed that the multiple scattering effect strongly depends on the size of the diffusers, as well as on the concentration. In the geometrical situation considered, which is similar to that of a ground based lidar system with a field of view $\alpha = 4.6$ mrad (semiaperture) sounding a cloud 300 m deep at a height of 1 km, at least the first part of the lidar echo remained almost linear (in a semilogarithmic scale) even when the optical depth of the cloud was as large as 20. The value of the scattering coefficient obtained from the slope of the lidar echo was significantly smaller than the actual value, especially for large values of optical depth. For the largest spheres used (mean diameter $\phi = 5.4 \mu\text{m}$) a significant percentage error was observed, even when the optical depth inside the scattering cell was smaller than 1. The scattering function for these diffusers is similar to that of a C1 cloud model; so these results show that a significant error (due to multiple scattering) on the scattering coefficient can also be expected for lidar measurements on actual tenuous clouds.

Measurements were carried out by using a linearly polarized laser pulse and both the parallel component ($P_{//}$) and the cross polarized component (P_{\perp}) of the lidar echo were recorded. Experimental results showed that the depolarization effect also strongly depends on the size and concentration of the diffusers. For some of the diffusers used, a significant depolarization of the lidar echo was measured even at very small values of optical depth when the received power was mainly due to single scattering. This fact can be explained assuming a (small) non-sphericity in the diffusers used.

The experimental results were compared with the numerical results of a Monte Carlo code. A general good agreement was obtained.

Experimental setup and examples of results

The measurements were carried out by using the picosecond system of the European Laboratory for Non-Linear Spectroscopy (LENS) at the Physics Department in Florence. The system is summarized in Fig.1. The laser emits pulses of 4 ps with a frequency of 77 MHz and was operated at $\lambda = 765$ nm. The full width half maximum of the detector pulse response (in the configuration used by us) was 25 ps. The laser beam was driven on the diffusing medium by means of mirrors and a 50% beam splitter. The beam divergence was 0.5 mrad (semiaperture) and the beam radius at the input of the scattering cell was 1 mm. The cloud model was a suspension of polystyrene spheres in water in a scattering cell 10 cm long. Four different sizes of spheres were used, with mean diameter $\phi = 0.09, 0.369, 1.020$ and $5.4 \mu\text{m}$. Mie calculations showed that the phase function for $5.4 \mu\text{m}$ spheres slightly differs from the one of a C1 cloud

model at $\lambda = 1.064 \mu\text{m}$.

The optical receiver (input radius 0.1 mm, field of view semiaperture $\alpha = 6.1 \text{ mrad}$) coaxial with the laser beam was placed at 25 cm from the scattering cell. Because of the water-air refraction the optical receiver acts as an equivalent receiver, operating without refraction, placed at a distance $25\text{cm} \times 1.33 = 33.3 \text{ cm}$ and with a field of view of $6.1\text{mrad}/1.33 = 4.6 \text{ mrad}$. The geometrical situation is similar, for instance, to the one of a ground based lidar system sounding a cloud 300 m deep placed at a distance of 1000 m. The corresponding values for the receiver are: radius = 30 cm, field of view = 4.6 mrad; and for the laser beam: beam radius at the cloud base = 3 m, beam divergence = 0.5 mrad. These values are typical for lidar systems sounding a cloud, apart from the value of the beam radius at the cloud base (typical value 0.5 m for a cloud at 1000 m). Monte Carlo simulations however, showed that when the beam radius is changed from 0.5 m to 3 m, only insignificant variations in the lidar echo are observed, so that the experimental results reported can be considered representative for a ground based lidar system sounding a cloud.

Since the main purpose of these measurements was to investigate the effect of multiple scattering, a good accuracy in the knowledge of the scattering coefficient σ_s of the medium inside the scattering cell was necessary. This was measured directly by using a transmissometric apparatus and the procedure fully described in [1,2].

Figure 2 shows some examples of experimental results for the cross and parallel polarized components of the lidar echo. As can be seen the depolarization strongly increases when the optical depth inside the scattering cell increases. However a significant depolarization (~8%) is present even when τ_{stransm} is so small as 0.3; for this small value of τ_{stransm} , both experimental and Monte Carlo results showed that the multiple scattering effect is insignificant. The depolarization measured for these small values of τ_{stransm} can be ascribed to a small non-sphericity of polystyrene spheres used. A direct investigation on the shape of the diffusers, however, was not carried out.

Figure 3 reports the quantity τ_{slidar} versus τ_{stransm} where τ_{stransm} is the optical depth (only due to scattering) measured by transmissometric apparatus ($\tau_{\text{stransm}} = \sigma_s L$ with $L =$ length of the scattering cell) and τ_{slidar} corresponding value obtained by lidar measurement. τ_{slidar} was obtained from the slope (in a semilogarithmic scale) of the parallel polarized component ($P_{//}$) after having subtracted the absorption effect due to water ($\sigma_{\text{aw}} = 2.5 \text{ m}^{-1}$ at $\lambda = 765\text{nm}$), and the effect on the slope due to the different solid angle subtending the receiver from different parts of the scattering cell. Whereas for small values of optical depth τ_{slidar} was obtained by a fitting on the whole lidar echo, for large values it was obtained from the slope in the first part of the echo (where the signal attenuation was not larger than two decades) on which the echo was linear and the noise sufficiently small. Figure 2 pertains to $5.4 \mu\text{m}$ spheres. The marks correspond to the experimental results, whereas the continuous line represents the corresponding Monte Carlo results. We should like to emphasize the fact that all Monte Carlo results showed in the figure were obtained from only one Monte Carlo simulation by using a simple scaling relationship [3]. The differences between τ_{slidar} and τ_{stransm} are due to a multiple scattering effect. As can be seen the differences increase when the optical depth increases. Both experimental and Monte Carlo results showed that τ_{slidar} significantly differs from τ_{stransm} even for the smallest values of τ_{stransm} considered.

Measurements for other types of spheres showed results basically similar to the ones for $\phi = 5.4 \mu\text{m}$. Large differences were obtained for $\phi = 0.09 \mu\text{m}$ (acting as Rayleigh scatterers) for which the multiple scattering effect on τ_{slidar} was very small for $\tau_{\text{stransm}} < 8$ and the depolarization effect was significant only for $\tau_{\text{stransm}} \geq 6$.

Conclusions

The results of measurements of lidar echoes carried out on laboratory scale models

simulating a ground based lidar system operating on clouds were reported. The measurements showed that the multiple scattering effect strongly affects the lidar echo when the concentration of the diffusers increases. For the same value of the scattering coefficient the effect strongly depends on the size of the diffusers. A substantially good agreement between the results of Monte Carlo simulations and the experimental results was found.

The measurements clearly showed that by means of modern electrooptical systems it is possible to carry out lidar measurements on laboratory scale models in well controlled situations. These results can be used to check the reliability of numerical and analytical approximate solutions, and in general this type of measurement can be very useful to understand the features of multiple scattering effect in lidar echoes. For instance it is possible to carry out measurements on laboratory scaled models

- 1) to investigate the effect of the diffusers' characteristics (size, polydispersivity, concentration, homogeneity or dishomogeneity);
- 2) to study different geometrical situations such as: ground based lidar systems operating on fogs or clouds; airborne or space based lidar systems operating on atmosphere or ocean;
- 3) to evaluate the effect of source (divergence), receiver characteristics (area, field of view) and of instrument disalignment.
- 4) to check the reliability of inversion techniques based on lidar multiple scattering measurements.

References

- 1) G. Zaccanti and P. Brusaglioni, "Deviation from the Lambert-Beer law in the transmittance of a light beam through diffusing media: experimental results", J. Mod. Opt., 35, 229-242 (1988).
- 2) G. Zaccanti, P. Brusaglioni and M. Dami, "Simple inexpensive method of measuring the temporal spreading of a light pulse propagating in a turbid medium" Appl. Opt., 29 3938-3944 (1990).
- 3) P. Brusaglioni, A. Ismaelli, P. Sansoni and G. Zaccanti, "A comparison of different Monte Carlo codes for evaluating multiple scattering effects on lidar returns from clouds" Proc. MUSCLE 5 Workshop, Philadelphia 13-15 November 1991.

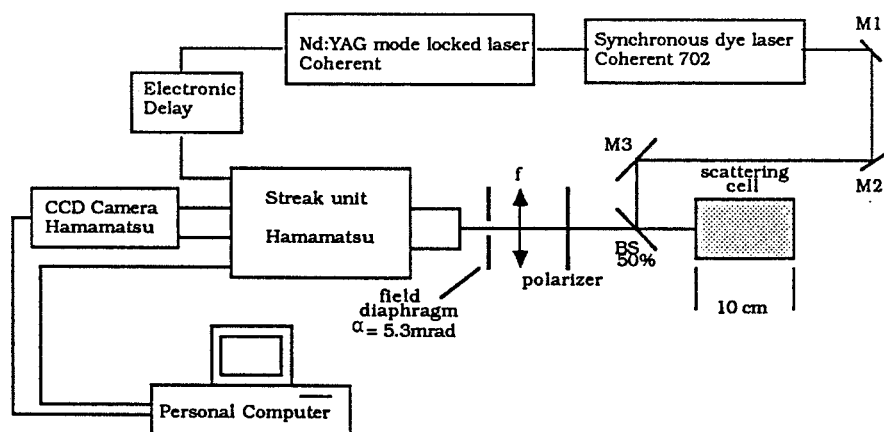


Figure 1 - Experimental setup used for laboratory simulations of lidar experiments.

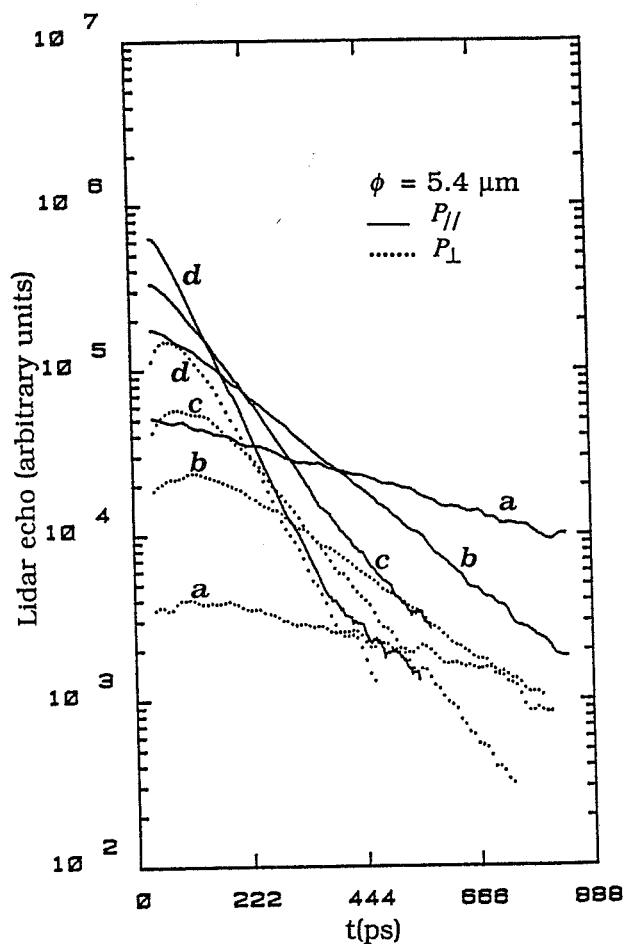


Figure 2- Examples of experimental results. Continuous and dotted curves represent the lidar echo for the parallel and cross polarized components respectively. Curves a,b,c, and d pertain to $\tau_{\text{stransm}} = 0.6, 3.0, 6.3,$ and 13.2 respectively. $\phi = 5.4 \mu\text{m}$.

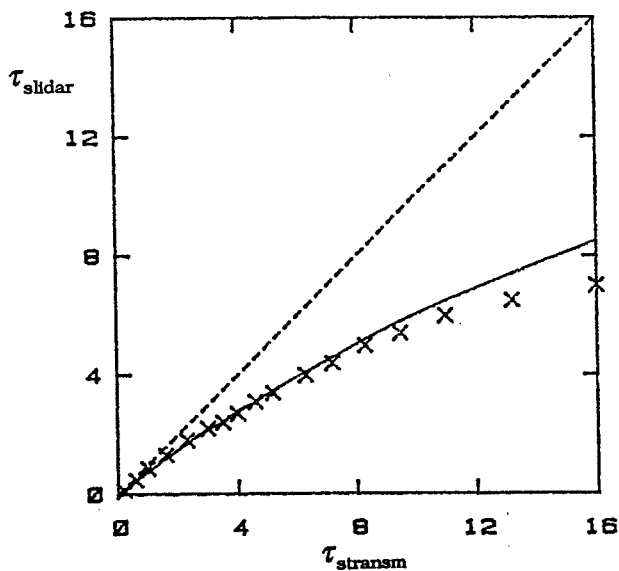


Figure 3 - Optical depth (only due to scattering) obtained from lidar measurements versus the optical depth measured with a transmissometer. Marks: experimental results; continuous curve: Monte Carlo results. $\phi = 5.4 \mu\text{m}$.

An Alexandrite Regenerative Amplifier for Water Vapor and Temperature Measurements

P.-Y. Thro, J. Bösenberg, V. Wulfmeyer
 Max-Planck-Institut für Meteorologie
 Bundesstr. 55, 2000 Hamburg 13, Germany

1 Introduction

The DIAL technique is a powerful method for determining meteorological parameters, but it requires high quality of the laser source : high energy, very narrow bandwidth, high wavelength stability, and spectral purity. Although many efforts have been made to improve the lasers in view of these aspects a satisfactory solution has not been demonstrated up to now. Here we describe a regenerative amplifier, using a Ti:Sapphire laser as master oscillator and an Alexandrite laser as slave amplifier [1], which is expected to meet the requirements for water vapor concentration and temperature measurements.

2 Experimental set-up

The experimental set-up is depicted in Fig.1. A CW Ti:Sapphire ring laser delivers an actively stabilized, single frequency, TEM₀₀ output (≈ 300 mW). The pulse slicer PS produces a horizontally polarized pulse with a duration of 6 ns which corresponds to a Fourier transform limited bandwidth of ≈ 0.13 pm. This pulse is injected through a Glan-Thompson polarizer into the 1.7 m long Alexandrite cavity. It consists of a concave high reflector HR ($R = -40$ cm), the pump chamber (placed so that the cavity is insensitive to small variations of the rod thermal lensing, $\frac{\partial \omega_0}{\partial f} = 0$ for a focal length of 35 cm), a birefringent filter which is necessary if the laser is driven far away from the gain maximum at 752 nm, a beam expander BE (x2) to avoid optical damage at the Pockels cell, the Pockels cell PC2 which provides a static quarter wave retardation and a flat high reflector (Reflectivity = 93%). After passing the Pockels cell twice the pulse which is now vertically polarized is trapped inside the cavity. By switching the Pockels cell to its $\lambda/4$ voltage (in double pass equivalent to a $\lambda/2 + \lambda/2 = \lambda$ wave plate) the pulse stays in the cavity for about 50 round trips. Then PC2 is switched again to its $\lambda/2$ voltage to dump the cavity. The Faraday rotator FR and the $\lambda/2$ wave plate WP rotate the polarization once more and the amplified pulse is then deviated by the extra-cavity polarizer OP as shown on Fig. 1.

3 Results

3.1 The Ti:Sapphire laser

We have modified a commercially available Ti:Sapphire laser in order to adapt it to the DIAL specifications :

- Automatic scanning capability has been added using two step motors which rotate the birefringent filter and the 2 mm thick intracavity etalon PF. So the laser can be scanned

for about 300 pm with a resolution of 0.45 pm (cavity mode spacing) in order to find the suitable absorption line.

- An active wavelength stabilization has been incorporated using two confocal Fabry-Pérot interferometers as wavelength reference, and a piezo-driven mirror correcting the cavity length in the closed loop stabilization. In this mode the wavelength stability is better than ± 0.1 pm.
- To obtain the second wavelength (off-line) which is necessary for the DIAL technique a Pockels cell PC1 has been placed in the resonator between the Ti:Sapphire crystal and the birefringent filter. The additional phase difference between the ordinary and extraordinary waves which depends on the applied voltage shifts the maximum of transmission of the birefringent filter [2]. By applying the suitable voltage on the Pockels cell the wavelength jumps to the next etalon mode. So we obtain alternatively two wavelengths separated by 90 pm by applying a square voltage with a repetition rate of 10 Hz. It is not necessary to stabilize the off-line wavelength.

3.2 The Alexandrite amplifier

Fig. 2 shows the evolution of the pulse in the Alexandrite resonator before the cavity dumping. The gain is ≈ 1.3 per round trip. The extracted pulse reaches energy up to 50 mJ at 730 nm without optical damage. Right now, the energy stability is still unsatisfactory due to pulse to pulse fluctuations of the gain. However, this can be overcome on the one hand by increasing the stability of the Alexandrite laser, and on the other hand by using a fast discriminator triggering the pockels cell when the pulse has reached a selected threshold.

The spectral output has been observed with a 9 mm Fizeau interferometer. No difference between the CW Ti:Sapphire beam and the amplified pulse has been detected. This implies that the linewidth is smaller than 0.2 pm. Spectral purity has not yet been measured. However, it is expected to be very low due to the long lifetime of the upper laser level and the large number of round trips.

4 Conclusion

We have described a promising laser source producing a high energy output with narrow bandwidth and high wavelength stability suiting the specifications for DIAL applications, including fast switching between on- and off-line wavelengths.

Additional experiments will be performed to fully characterize the system parameters and will be presented at the conference.

References

- [1] Harter, D.J. and P. Bado, 1988: Wavelength tunable Alexandrite regenerative amplifier. *Appl. Opt.*, Vol. 27, No. 21, pp 4392-4395.
- [2] Bruneau, D., H. Cazeneuve, C. Loth and J. Pelon, 1991: Double-pulse dual-wavelength Alexandrite laser for atmospheric water vapor measurement. *Appl. Opt.*, Vol. 30, No. 27, pp 3930-3937.

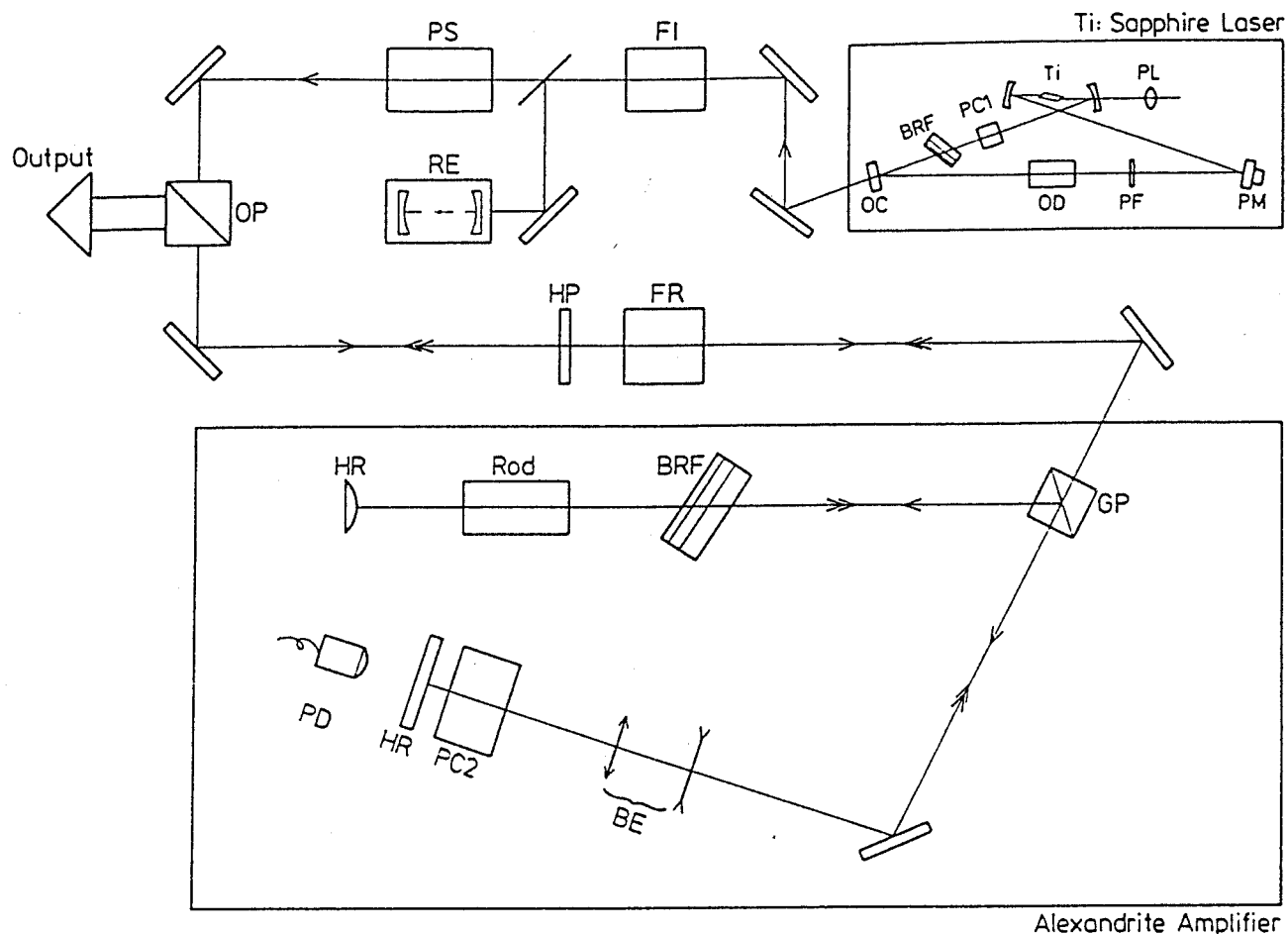


Figure 1: Schematic diagram of the regenerative Alexandrite amplifier :

PL	pump lens	Ti	Ti:Sapphire crystal
PC1	Pockels cell	BRF	birefringent filter
OD	optical diode	PM	mirror mounted on a piezo-electric crystal
PF	Fabry-Pérot etalon	OC	output coupler
RE	reference etalons	FI	Faraday isolator
PS	pulse slicer	OP	output Glan-Thompson polarizer
HP	$\lambda/2$ wave plate	FR	Faraday rotator
HR	high reflector	Rod	Alexandrite rod
GP	Glan-Thompson polarizer	BE	beam expander
PC2	Pockels cell with $\lambda/4$ static retardation	PD	fast photodiode

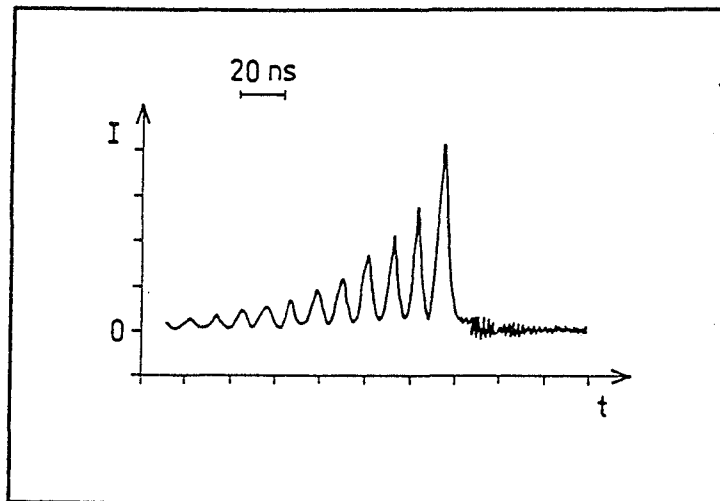


Figure 2: Temporal evolution of the pulse in the Alexandrite cavity measured by a fast photodiode output from the resonator leakage. The pulse has a HWHM width of 6 ns and needs ≈ 12 ns to carry out one round trip.

Wavemeter Measurements of Frequency Stability of an Injection Seeded Alexandrite Laser for Pressure and Temperature Lidar

C. R. Prasad*, G. K. Schwemmer, and C. L. Korb
 Code 917, NASA/Goddard Space Flight Center, Greenbelt, MD 20771
 (*Universities Space Research Association Resident Associate)

The NASA/GSFC pressure-temperature lidar is a differential absorption lidar operating in the oxygen A band absorption region (760 to 770 nm), and utilizes two tunable pulsed alexandrite lasers (Schwemmer, et al, 1987, Korb, et al, 1989). For obtaining temperature measurements with an accuracy of $\leq 1^\circ\text{K}$, it has been determined (Korb and Weng, 1982) that the stability of the on-line laser frequency over a period of time corresponding to a set of measurements, 0.1 to 30 min, has to be better than $\pm 0.002 \text{ cm}^{-1}$. In addition, the requirements on laser spectral bandwidth and spectral purity are $\leq 0.02 \text{ cm}^{-1}$ and $\geq 99.9\%$ respectively. Injection seeding with a stabilized AlGaAs diode laser has been used to achieve the required frequency stability and spectral bandwidth. A high resolution Fizeau wavemeter has been employed to determine the frequency stability of the pulsed alexandrite laser and determine its bandwidth, mode structure. In this paper we present the results of measurements of the frequency stability and the spectrum of the injection seeded alexandrite laser.

INJECTION SEEDED ALEXANDRITE LASER

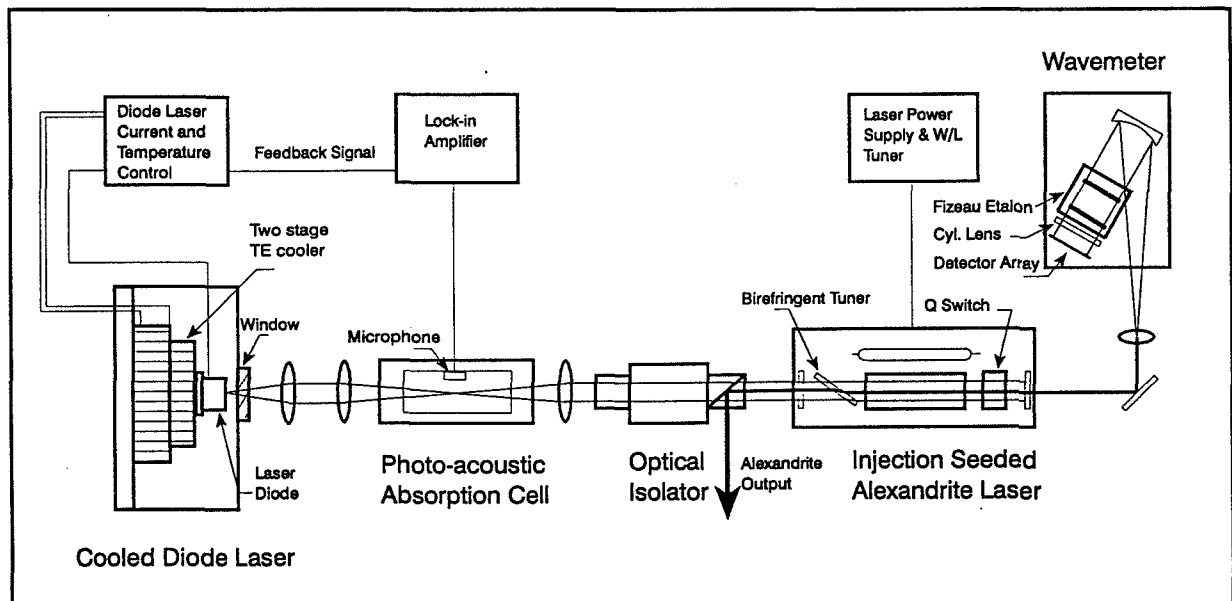


Figure 1. Schematic of the alexandrite laser injection seeded by a frequency stabilized diode laser.

In earlier work (Schwemmer, et al, 1987) frequency tuning and narrow-band operation of the on-line high resolution alexandrite laser was accomplished with a birefringent filter, a tilt tuned thin etalon and a piezoelectric tuned etalon. Measurements of the frequency of this laser showed (Prasad, et al, 1990), however, that its frequency stability was not adequate for temperature measurements. When injection seeding is used for frequency control, instead of the intracavity

etalons advantages such as higher efficiency and better frequency stability can be realized. A cw semiconductor AlGaAs laser operating in the 760 - 770 nm region is utilized currently for injection seeding as shown in Figure 1. Only the birefringent filter tuner is retained in the alexandrite laser, which then yields a bandwidth of about 4.5 cm^{-1} , in normal Q-switched operation. Commercial single longitudinal mode AlGaAs laser diodes (Mitsubishi Model 4402, 3 mW output, and Model 6411, 30 mW), are used to seed the alexandrite laser. The output wavelength of the laser diode is tuned by a combination of temperature and current control. A single diode has been shown to cover a tuning range in excess of 15 nm by cooling the diode from 20 to -65°C (Schwemmer, et al, 1991). We have found that these laser diodes have tuning rates of between -0.1 to -0.3 nm/K , so that a diode with output around 780 nm at 20°C is cooled to between -20 to -40°C to tune its wavelength to the temperature sensitive $^{\text{P}}\text{P27}$ (768.38 nm) or $^{\text{P}}\text{P29}$ (769.22 nm) absorption lines in the oxygen A band. A specially designed vacuum enclosure with multistage thermoelectric Peltier coolers (see Fig 1) was fabricated to house the laser diode. The diode laser frequency is first tuned to the center of the absorption line and is then stabilized by dithering its frequency sinusoidally at 10 Hz and passing the diode beam through a 6 cm long photo-acoustic cell filled with one atmosphere of oxygen. The details of the feedback stabilization scheme are given elsewhere (Schwemmer, et al, 1991). It was found that the diode frequency was held over a period of 15 hours to within 15 MHz ($5 \times 10^{-4} \text{ cm}^{-1}$) of the line center. A trigger pulse is derived from the dither oscillator to synchronize the firing of the alexandrite laser as the diode frequency crosses the line center frequency in its dither cycle.

FIZEAU WAVEMETER

The high resolution spectra of both the diode and the alexandrite laser are obtained with a wavemeter which consists of a coated Fizeau etalon with a 5 cm spacing and a wedge angle of 8 arc seconds, and an EG&G Reticon detector array with 1024 detector elements spaced at $25 \mu\text{m}$ (Prasad et al, 1988). A personal computer is used to control the wavemeter, acquire the fringe data and compute the centroid frequency. An efficient algorithm has been developed to determine the centroid of the laser frequency from the fringe data in real time.

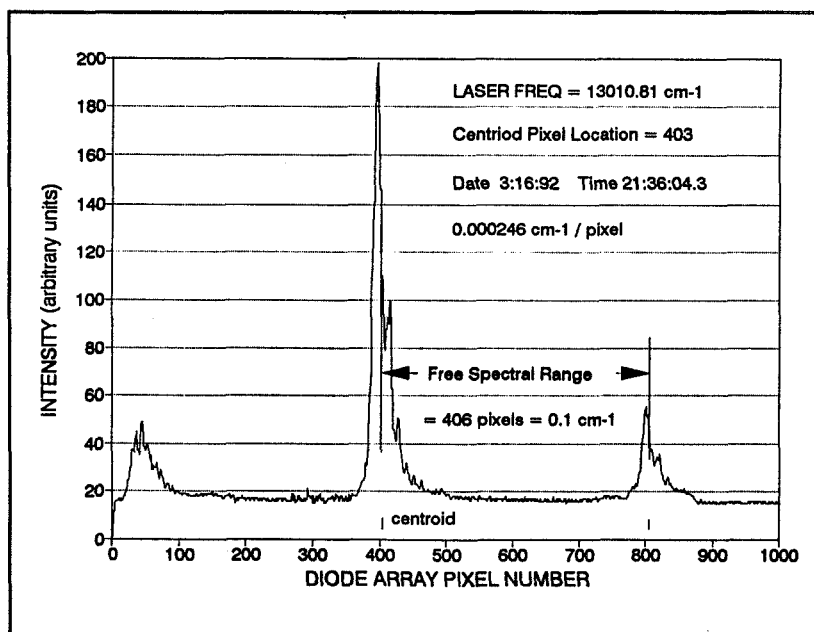


Figure 2. Fizeau wavemeter spectrum of injection seeded alexandrite laser.

The optical resolution of the wavemeter is 0.0033 cm^{-1} (100 MHz), the detector element spacing is $2.5 \times 10^{-4} \text{ cm}^{-1}$ and has a drift of $< 0.004 \text{ cm}^{-1}/\text{hr}$. Figure 2 shows a single shot injection seeded alexandrite laser spectrum taken by the wavemeter. Typically the spectral

bandwidth of the laser diode is about 0.0073 cm^{-1} (220 MHz), and since the longitudinal modes of the on-line alexandrite laser are spaced at about 0.007 cm^{-1} , its output contains two modes on the average. Figures 3 and 4 show the variation of the centroid frequency with time. On examining fig 3, it is seen that when the diode laser is stabilized, the alexandrite laser frequency is held within $\pm 0.002 \text{ cm}^{-1}$ of the line center.

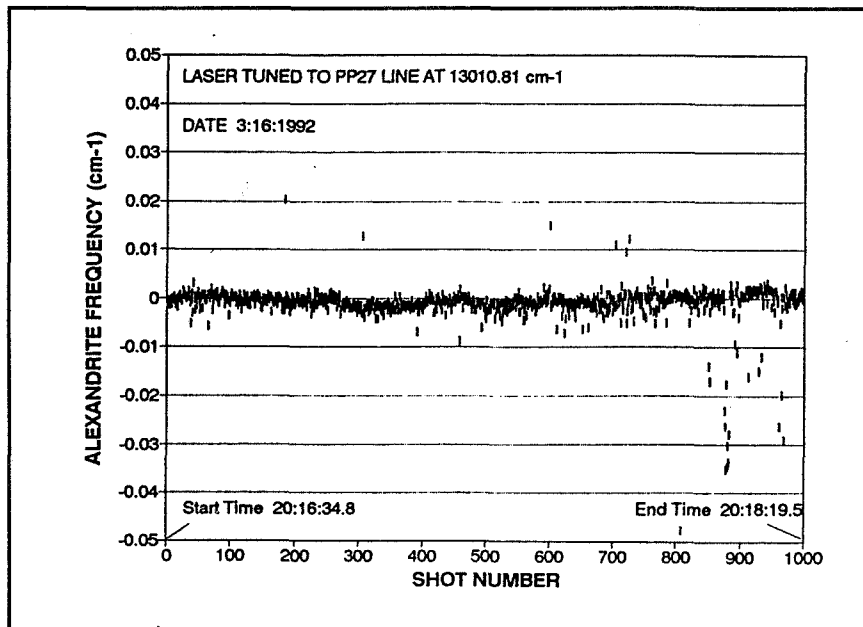


Figure 3. Variation of the centroid frequency of the alexandrite laser injection seeded with feedback stabilized diode laser. Laser pulse repetition rate is 10 Hz.

On the other hand when the diode laser is not feedback stabilized, frequency drift of $\pm 0.005 \text{ cm}^{-1}$ is seen. This drift corresponds to the accuracy of the diode laser current supply and temperature control (0.1°C). It is also observed that there are a number of shots whose frequency is grossly different. These shots correspond to situations where the seed laser has made a mode hop or the seeding is ineffective. During an extended experiment, the wavemeter is used to analyze the spectrum of every shot and this provides an effective means for discriminating against shots which are improperly or imperfectly seeded.

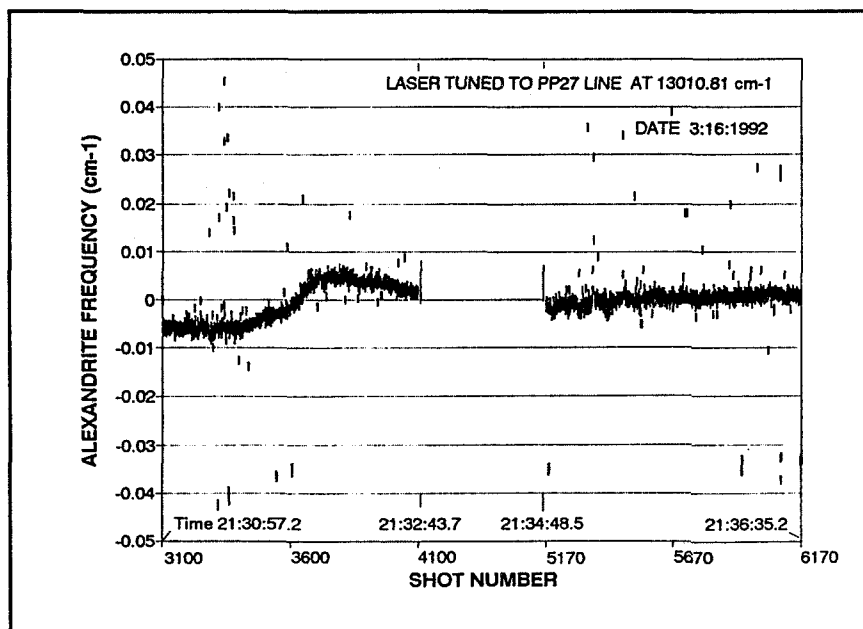


Figure 4. Same as in Fig 3, except that the diode laser is not feedback stabilized.

The spectral purity of the injection seeded laser is under investigation. An examination of the spectrum of the seed laser revealed the presence of weak lines on either side of the principal central mode, at a mode spacing of about 2.88 cm^{-1} . The power in the two modes adjacent to the principal mode was about 0.3% at a diode drive current of 130 mA. The side modes can also

seed the laser and depending on the band pass of the birefringent filter tuner at these frequencies will produce a spectrally impure output. We propose to use an external etalon to suppress the intensity of the diode laser side modes to below 0.05%, before it seeds the alexandrite laser.

REFERENCES

- Korb C.L., and C.Y.Weng, "A theoretical study of a two-wavelength lidar technique for the measurement of atmospheric temperature profiles" *J Appl Meteor*, 21, 1346, 1982.
- Korb C.L., G.K.Schwemmer, M.Dombrowski and C.Y.Weng, "Airborne and ground based lidar measurements of the atmospheric pressure profile", *Appl Opt*, 28, 3015, 1989.
- Prasad C.R., C.L.Korb, and G.K.Schwemmer, "Laser wavelength measurement in presence of speckle", 14 International Laser Radar Conference, San Candido, Italy, Conference Abstracts, p 253, 1988.
- Prasad C.R., C.L.Korb, and G.K.Schwemmer, "Frequency Stabilization of an Alexandrite Laser for Pressure-Temperature Lidar Measurements" Optical Remote Sensing of the Atmosphere, Vol 4, p 344, Optical Society of America, Washington, D.C., 1990.
- Schwemmer G.K., M.Dombrowski, C.L.Korb, J.Milrod, H.Walden and R.H.Kagann, "A lidar system for measuring atmospheric pressure and temperature profiles", *Rev Sci Inst*, 58, 2226, 1987.
- Schwemmer G.K., H.S.Lee and C.R.Prasad, "Narrowband alexandrite laser injection seeded with frequency dithered diode laser" in Earth and Atmospheric Remote Sensing, SPIE Proceedings, Vol 1492, 52, 1991.

Conically Scanned Lidar Telescopes using Holographic Optical Elements

Geary K. Schwemmer
Code 917 NASA Goddard Space Flight Center
Greenbelt, Maryland 20771

Thomas D. Wilkerson
Institute for Physical Science and Technology
University of Maryland
College Park, Maryland 20742-2431

Holographic optical elements (HOE) using volume phase holograms make possible a new class of lightweight scanning telescopes having advantages for lidar remote sensing instruments¹. So far the only application of HOEs to lidar has been a non-scanning receiver for a laser range finder². We introduce here a large aperture, narrow FOV telescope used in a conical scanning configuration, having a much smaller rotating mass than in conventional designs. Typically, lidars employ a large aperture collector and require a narrow FOV to limit the amount of skylight background. Focal plane techniques are not good approaches to scanning because they require a large FOV within which to scan a smaller FOV mirror or detector array. Thus scanning lidar systems have either used a large flat scanning mirror at which the receiver telescope is pointed, or the entire telescope is steered. We present a concept for a conically scanned lidar telescope in which the only moving part is the HOE which serves as the primary collecting optic. Being diffractive, an HOE has spectral dispersion which can also be used to advantage in a lidar system in which only one or a few laser wavelengths are employed. The spectral bandpass of the HOE can be made as narrow as 10 nm, replacing an optical filter in many applications. Unwanted wavelengths pass through the HOE undiffracted to be absorbed by a black backing. This also decreases the scattered light inside the telescope. Thus an HOE can be used to replace three separate lidar components: the scanning mirror, the focusing mirror, and a narrow band interference filter. We also describe methods by which a multiplexed HOE can be used simultaneously as a dichroic beamsplitter.

An HOE is a hologram of a lens or mirror having the ability to focus light³. The hologram consists of an emulsion containing a diffraction pattern either as surface relief, or as index modulation throughout the thickness of the film as in the volume phase hologram⁴ described here. It may be fixed to a planar substrate or to a curved one having optical power⁵.

A reflection HOE is generated when an emulsion of dichromated gelatin or other recording medium is exposed to two mutually coherent laser beams as in Fig. 1a. One beam emanates from a pinhole producing spherical wave fronts and serves as the object beam, while a second plane wave beam serves as the reference to interfere with the object beam in the gelatin. Solubility of the gelatin in water decreases with exposure to light, and interference fringes are registered in the film as variations in hardness or index

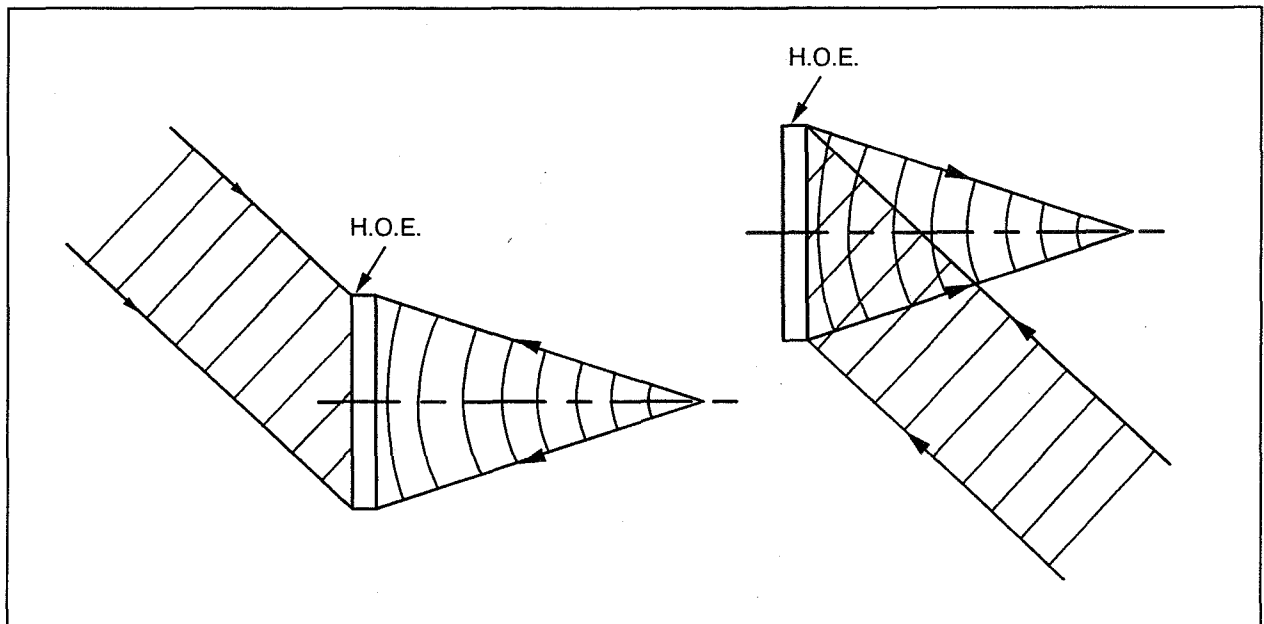


Figure 1 a) Exposure geometry for a reflection HOE, and b) reconstruction geometry.

of refraction. The dichromate is removed from the gelatin during post-exposure chemical processing. The resulting hologram is free of absorption and can have a very high diffraction efficiency. When a completed HOE is illuminated with a monochromatic plane wave source conjugate to the construction reference wave, a conjugate of the original object beam is generated, forming a focus at the position of the original point source (Fig. 1b).

In the lidar application backscattered light acts as the reconstruction beam and is brought to a focus by the HOE. Background light at wavelengths outside the diffraction bandpass of the HOE is transmitted undiffracted to be absorbed behind the HOE. A stop in the focal plane further limits the bandpass of the light reaching the detector as well as light at the laser wavelength that falls outside the FOV. Even without a stop, the HOE will only diffract light incident within a few degrees of the nominal diffraction angle, regardless of wavelength. Thus scattered light in the receiver is minimized by the use of the reflection HOE in place of a conventional reflector.

A 45 cm diameter prototype HOE was recently tested in the Optical Research Section of NASA-GSFC. The actual and design specifications are compared in Table 1. Larger diffraction efficiencies than that obtained should be achieved by using higher laser power during the HOE construction, thereby allowing shorter exposure times.

Fig.2 shows a concept for a scanning lidar telescope in which an HOE turns below a pair of conical baffles. The hologram FOV makes a 45° angle with the normal to the disk. The FOV sweeps out a conical scan as the disk spins about its optic axis. The hologram is the only moving part, allowing a much lighter structure for supporting the detector package and baffles, all of which are stationary. The laser transmission goes through a hole in the baffling, to a turning mirror (positioned above the HOE) which

directs the beam downward along the rotation axis; finally, another mirror (mounted directly on the HOE) sends the beam out coaxially with the telescope FOV. Figure 3 shows the design details for the laser beam directing optics and transmitter beam tubes.

There are two additional baffles (#3,#4) nested between those for the telescope (#2,#5) to enclose the transmitter beam up to the point where it exits the outer baffles. Short lengths of tubing around both the incident and reflected beam on the final beam steering mirror are rotated with the HOE as the system is scanned. Another conical shield (#1) closes the space between the focal plane (top) and the uppermost baffle (#2).

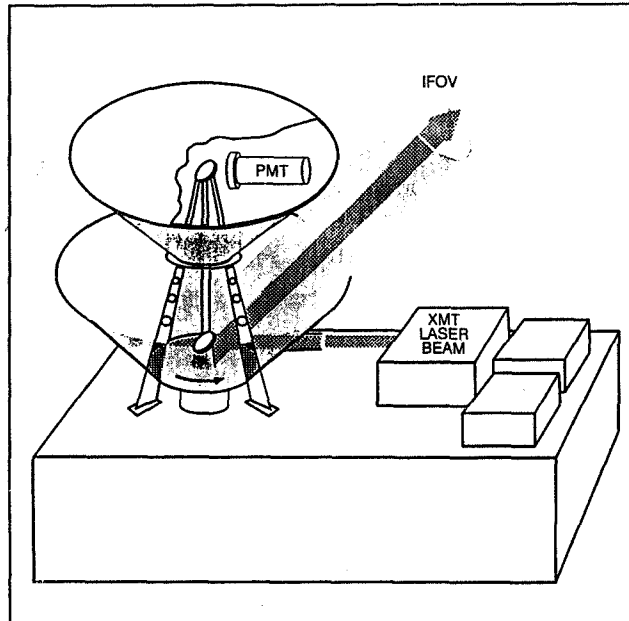


Figure 2 Conceptual design for a conical scanning holographic lidar telescope.

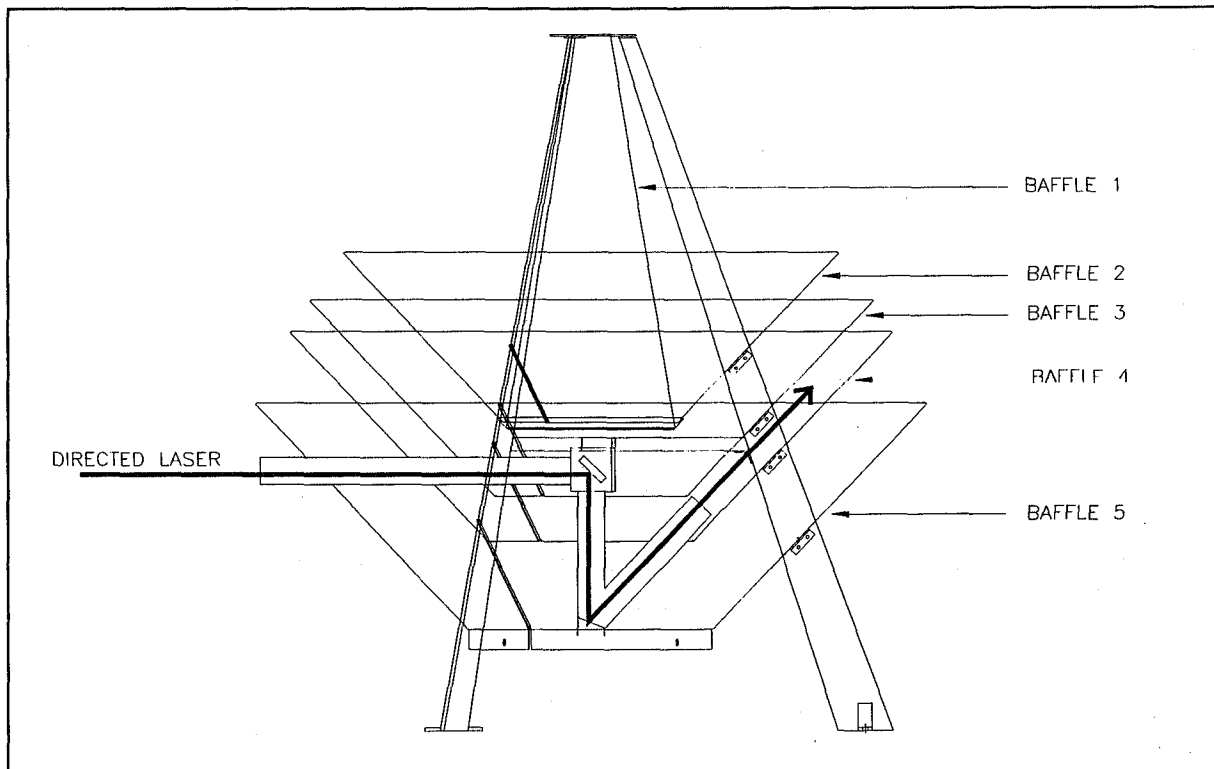


Figure 3 Assembly drawing for the scanning holographic telescope showing additional baffling and laser beam conduits to shield the detector from scattering from the transmitted laser beam.

Table 1

Specification	Design	Acceptance Test Results
Diameter	12 to 16 inches	16 inches
Active (HOE) diameter	> 90 % of substrate diam.	100 %
f #	between f/4 and f/1.2	f/3.2
focal spot (1/e ² diam.)	≤ 1 mrad	0.90 mrad
Diffraction angle	between 40 and 50 degrees	43.25 degrees
Diffraction efficiency	≥ 50 %	73 %
Wavelength (applies to all specifications)	532 nm	532 nm

Multiple wavelength lidars using HOEs can be designed with a number of approaches. One can make a sandwich of individual HOEs, each transparent to the other wavelengths while diffracting its own wavelength, or one may produce several holograms in a single film by means of multiple exposures. To locate different wavelengths at separate detectors, all of which remain fixed as the HOE rotates, the foci may be distributed at various points along the rotation axis where optical fibers can pick off the light to be sent to different detectors located elsewhere.

Development of this technology will allow larger visible and infrared planetary and earth observing lidar telescopes to be deployed while offering significant savings in weight and complexity over existing telescope mirror technology. The lidar application takes advantage of the unique properties of HOEs: spectral selectivity, optical power, and simplified scanning. It is conceivable that these principles will find application in multichannel passive instruments.

Acknowledgements:

The authors gratefully acknowledge the assistance of Dave Content of the Goddard Optics Branch in the use of his optics lab in testing the HOE, and Kirt Medine of Howard University and USRA for the mechanical design of the telescope.

References:

1. "Conically Scanned Holographic Lidar Telescope," patent pending, NASA case No. GSC 13,462-1.
2. Rallison, R.D., "Holographic optical elements (HOES) in dichromated gelatin (DCG): progress," Proceedings, SPIE Vol. 523, 292-295 (1985).
3. Magariños, J.R. and D.J. Coleman, "Holographic mirrors," Proceedings, SPIE Vol. 523, 203-218 (1985).
4. Kogelnick, H., *Bell Syst. Tech. J.*, 48, 2909-2947, (1969).
5. Woodcock, B.H. and A.J. Kirkham, "The analysis and construction of powered reflection holographic optical elements (HOEs)," Proceedings, SPIE Vol. 600, 32-37 (1985).

OPTICS OF THE OZONE LIDAR ELSA.

Service d'Aéronomie du C.N.R.S.

Verrières le Buisson, France

J. Porteneuve

Université Paris 6

Service d'Aéronomie du C.N.R.S.

Verrières le Buisson, France

Introduction

In order to study the ozone layer in Arctic we have to define a new optical concept for a lidar. It was necessary to build a transportable system with a large collecting surface in a minimum of volume.

It was too useful to have a multichannel receptor.

Description

Emission Receptor system.

Emission:

4 wavelength in U V:

289, 299, 308, 355 nm given by 2 lasers:

- Yag laser 3rd harmonic (355nm)

- Xe Cl exciplex laser (308nm)

- 2 Raman cells (H₂ and D₂) with transformation of 4th harmonic of Yag (266nm) to 289 nm and 299 nm.

For the emission we have put a beam expander with lenses for each wavelength

Magnification of 308nm = 3

Output beam diameter = 75mm

Magnification of 289, 299, 355 nm = 2.5

Output beam diameter = 20mm

Collecting system

The optical collector is composed by 4 parabolic mirrors 0,53m of diameter (which is equivalent to a single mirror of 1,06m) and a focal length of 1,5m.

The 4 mirrors are disposed in a square.

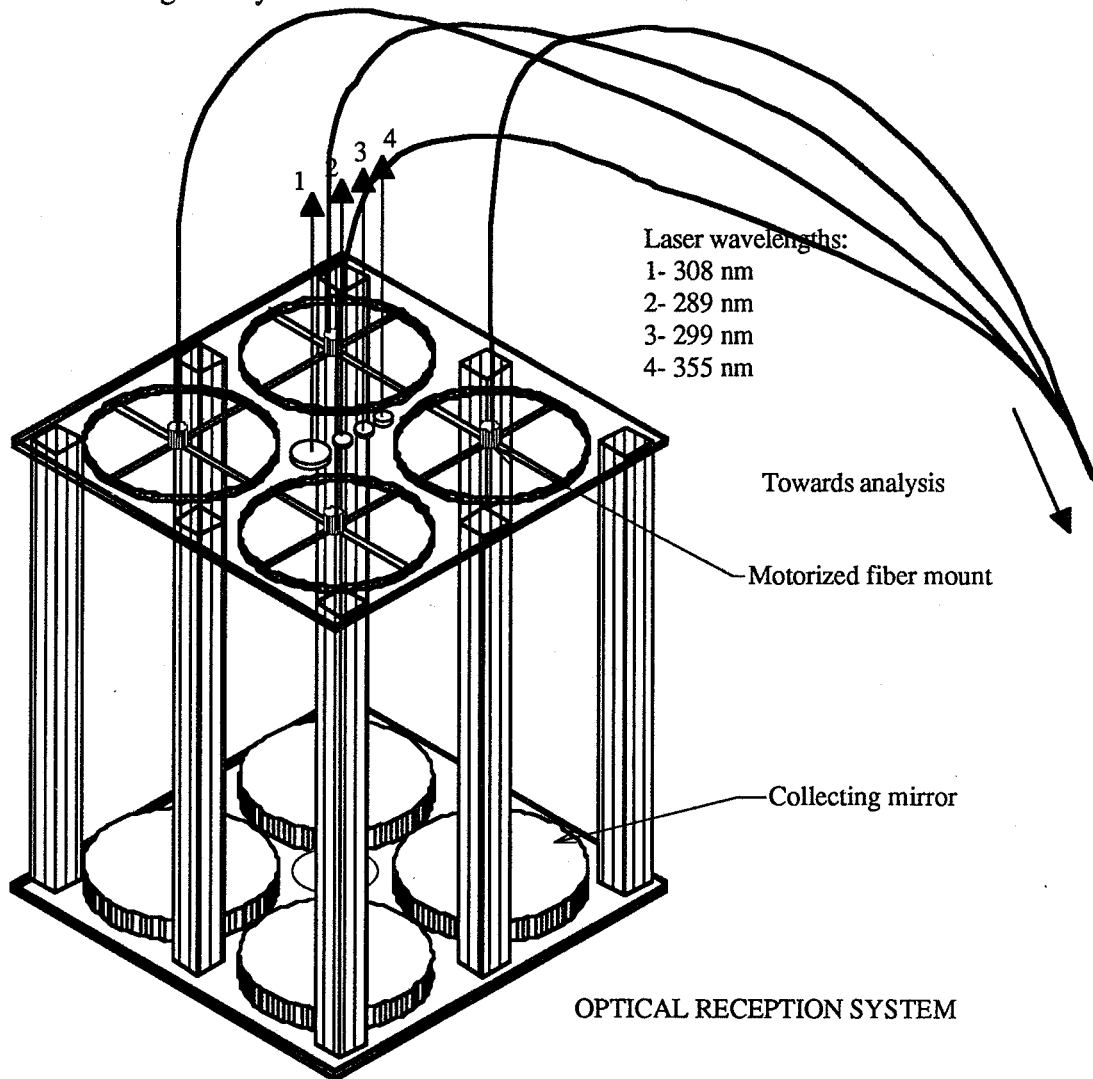
The total size, mounted included is 1.3m x 1.3m.

The emission is disposed in the middle of the square.

At each focus of the mirror we have put an optical fiber in fused silica ($\varnothing=1\text{mm}$)

Each entrance of fiber is hold by a mechanic system for adjusting the position.

The field of view is given by the circular entrance of the fiber.



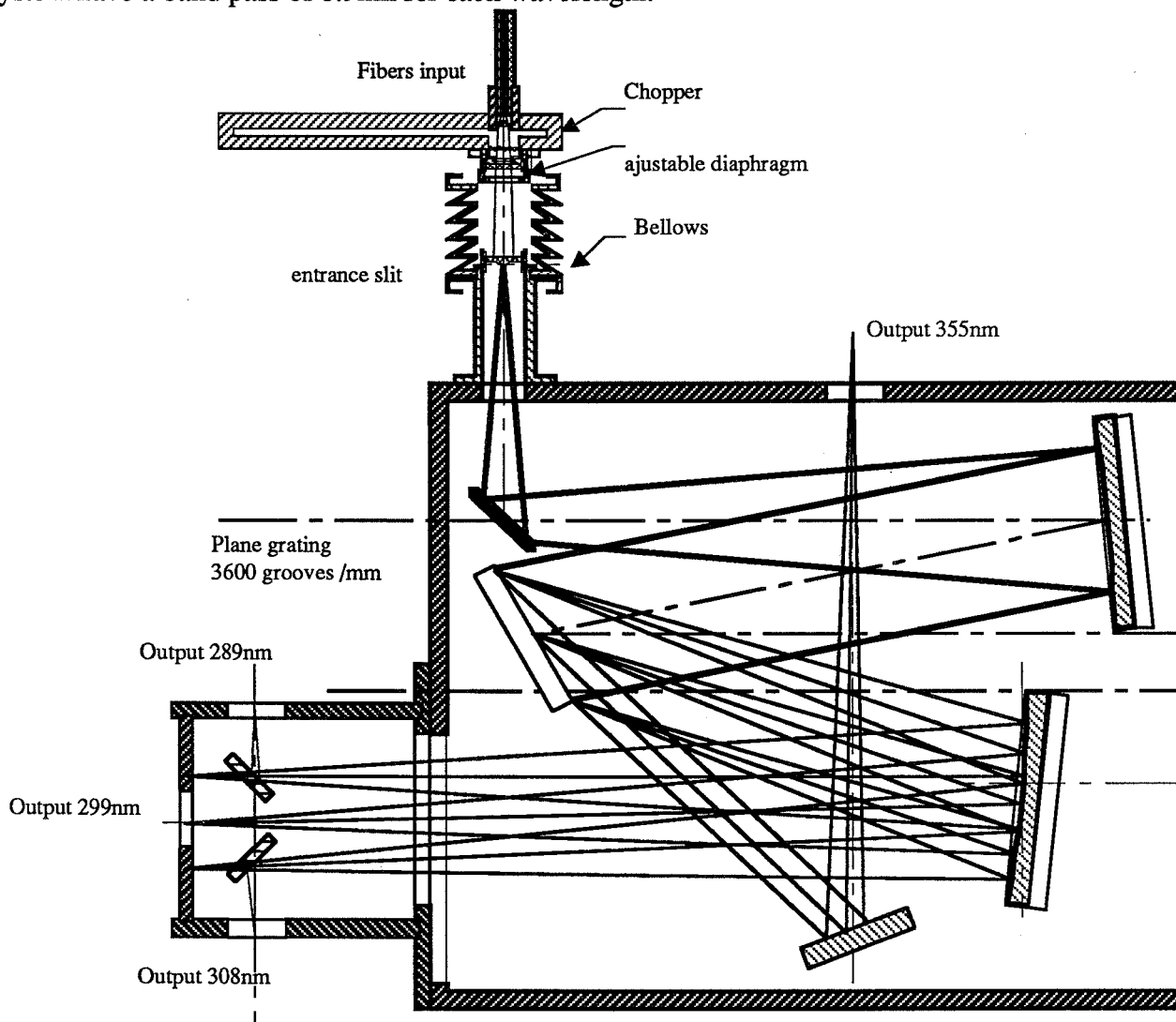
Analysis system

The 4 fibers bring the backscattering light to a system containing a mechanical chopper and a grating spectrometer.

The spectrometer gives the separation of the 4 wavelengths.

The 4 extremities of optical fibers are aligned for the adaptation to the grating system like a slit in a spectrometer.

The system has a band pass of 0.9nm for each wavelength.



GRATING MULTICHANNEL MONOCHROMATOR FOR OZONE LIDAR ELSA

INTERFEROMETERS ADAPTATIONS TO LIDARS

Service d'Aéronomie du C.N.R.S.

Verrières le Buisson, France

J. Porteneuve

Rayleigh lidars

To perform daytime measurements of the density and temperature by Rayleigh Lidar it is necessary to select the wavelength with a very narrow spectral system.

This filter is composed by an interference filter and a Fabry Perot etalon.

The Fabry Perot etalon is the more performant component, and it is necessary to build a specific optic around it.

- Geometrical adaptation

- The optical mounting must be telecentric. The image of the entrance pupil or the field diaphragm is at the infinite and the other diaphragm on the etalon.

The optical quality of the optical system is linked to the spectral resolution of the system for optimized the "étendue géométrique" (reduction of the field of view.).

The resolution is given by the formula

$$R = 8 \left(\frac{x D}{F d} \right)^2$$

$$R = \lambda / \delta \lambda$$

x = diameter of the field diaphragm

D = diameter of the reception mirror

F = focal length of the telescope

d = useful diameter of the etalon

Doppler Rayleigh lidars

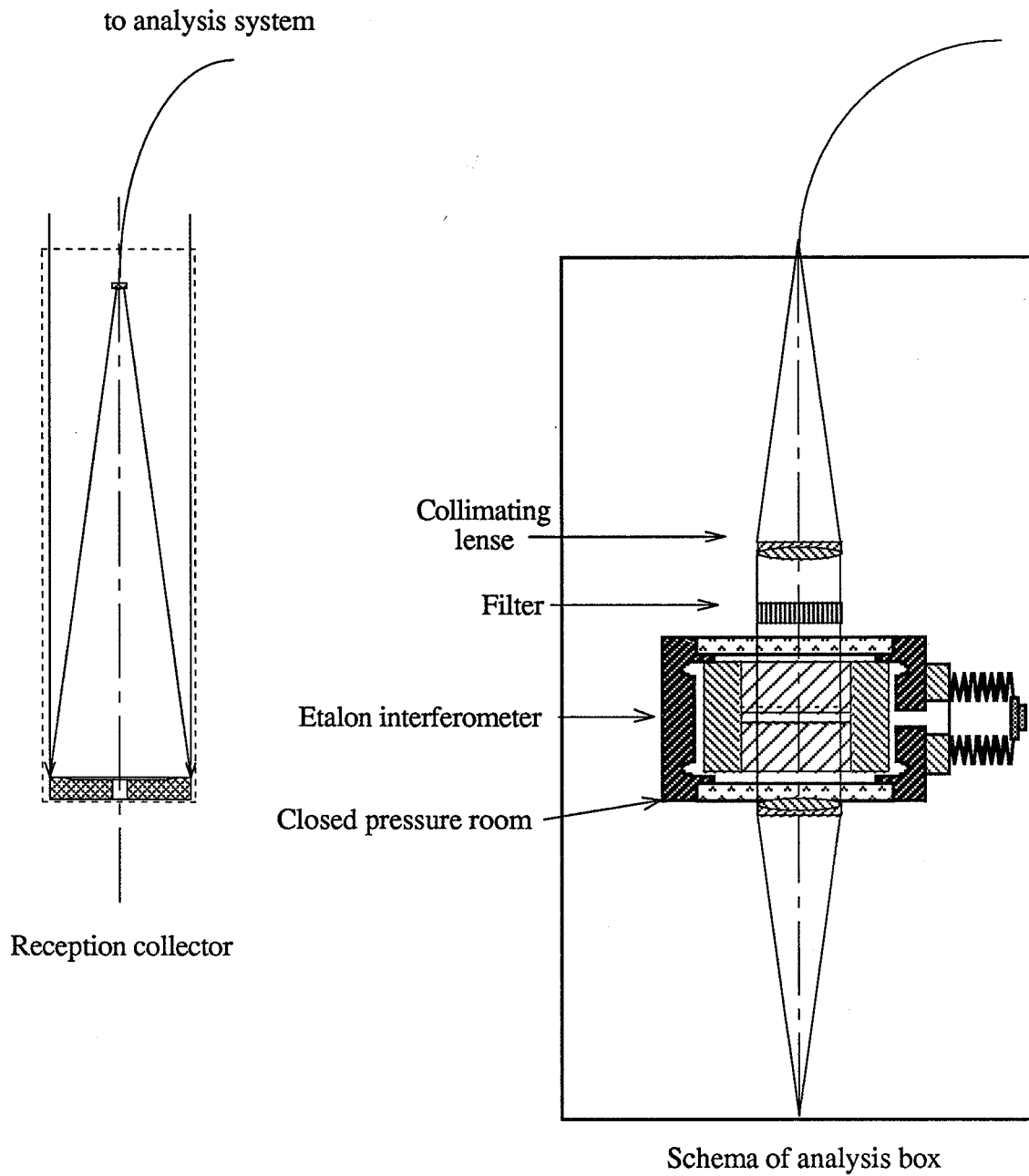
The PF interferometer is the main part of the experiment and the exact spectral adaptation is the most critical problem.

Spectral adaptation of interferometers

The transmittance of the system will be acceptable if the etalon is exactly adjusted to the wavelength of the laser

It is necessary to work with a monomode laser, and adjust the shift to the bandpass of the interferometer.

We are working with an interferometer built with molecular optical contact. This interferometer is put in a special pressure closed chamber



Optical schema of reception and analysis

Optical characteristics of lidars working for the Service d'Aeronomie

Rayleigh lidars

OHP:

Diameter télescope = 800mm
Focal length = 2400 mm
Field = 0,4 mm.
Useful diameter of Fabry Perot = 25 mm
Théoretical resolution = 280 000 as bandwidth = 2pm
Real resolution: : 20 000 (Filter FWHH = 1nm Étalon PF Finesse = 40)
Mesured transmission of spectral system: 0,4

CEL:

Diameter télescope = 1200mm
Focal length = 7200mm
Field = 1 mm.
Useful diameter of Fabry Perot = 25 mm
Théoretical resolution = 180 000 as bandwidth = 3pm
Real resolution: : 20 000 (Filter FWHH = 1nm Étalon PF Finesse = 40)
Mesured transmission of spectral system: 0,4

2- Doppler Rayleigh Lidar

CEL:

Diameter télescope = 445mm
Focal length = 2000mm
Field = 0,4 mm.
Useful diameter of Fabry Perot = 40 mm utile:
Théoretical resolution: 2500 000 as 0.2pm
Mesured transmission of spectral system: 0,4

An Ultra-Sensitive Coherent Detector Capable of Single Photon Detection for LIDAR
Applications

Sherwin Amimoto, Rolf Gross, Bob Lacy, Lissa Garman-DuValle, and Tom Good
The Aerospace Corporation
P. O. Box 92957
Los Angeles, CA 90009

The properties of Ultra-Sensitive Coherent Detectors(USCD) are nearly that of an ideal detector for LIDAR applications. In this paper we will briefly review recent progress in the development of USCDs and demonstrate its imaging capability. These new detectors possess properties with significant improvements over conventional technology. These improvements include a high quantum efficiency of 0.95, gain in excess of 10^{13} , a narrow bandwidth of 180-300 MHz at $1 \mu\text{m}$, imaging capability, and phase conjugation ability.

USCDs were first investigated by Pasmanik and co-workers¹ under single pulse conditions. We have constructed a USCD using two Nd:YAG laser amplifiers and a four-wave Brillouin mirror(FWBM) using SnCl_4 as the Brillouin medium.² Using a 10 Hz repetitively-pulsed single frequency laser, we have shown that the Brillouin medium is free from thermal blooming and from optical breakdown.

Briefly, a USCD functions in the following way.(See Fig. 1.) Signal photons from a collector or telescope are amplified as they pass through the laser amplifiers(gain of 10^4) and enter a FWBM. The FWBM acts as a narrow filter with gains of 10^7 . The return from the FWBM is amplified by a second pass through a single laser amplifier(gain of 10^2) and is detected by conventional photon detectors, i.e. photodiodes, CCD arrays, etc. Experimental details will be discussed.

The gain and noise characteristics of the USCD were investigated as a function of input signal³. Using carefully calibrated absorbing attenuators, signal input energies were varied as the return signal from the USCD were measured. The reflectivity or gain of the USCD were calculated. The results are shown in Fig. 2. The arrows in the lower left corner indicate the noise level and the equivalent input signal level which produces that noise level. The theoretical noise level of a quantum-limited device is 1 photon/(optical mode*QE) where the optical modes are the product of temporal and spatial optical modes and QE is the quantum efficiency of detection. For the experimental configuration used, the total number of modes was 51. The equivalent input energy is 10^{-17} J. Thus the

quantum efficiency is 0.97. At input signal levels near the output noise levels the overall optical gain exceeds 10^{13} . Thus photodetectors of low quantum efficiencies can be used provided that the output from the USCD greatly exceeds the noise of the detector.

Imaging experiments were also performed using a set of 4 relay lenses to image elements of a standard AF resolution chart into the USCD. The number of spatial modes was limited by vignetting of the field of view by one of the laser amplifiers. The estimated number of resolution elements correspond to a field of view of 21 x21 resolution elements. A single resolution element was calculated to be 92 μm for the experimental configuration used. The measured resolution as determined by element 4 of 11 line pairs per mm corresponds to 90 μm in excellent agreement with the calculated.

Results of linewidth and frequency tracking measurements in progress will be presented.

References

1. A. Z. Matveev, and G. A. Pasmanik, *Sov. J. Quantum. Electron.* 14, 187(1984); A. Z. Matveev, *Sov. J. Quantum. Electron.* 17, 466(1987).
2. S. T. Amimoto, R. W. F. Gross, L. Garman-DuValle, T. W. Good, J. D. Piranian, *Optics Lett.*, 16, 1382 (1991).
3. R.W. F. Gross, L. Garman-DuValle, S. T. Amimoto, *Optics Lett.*, 17, 82 (1992).

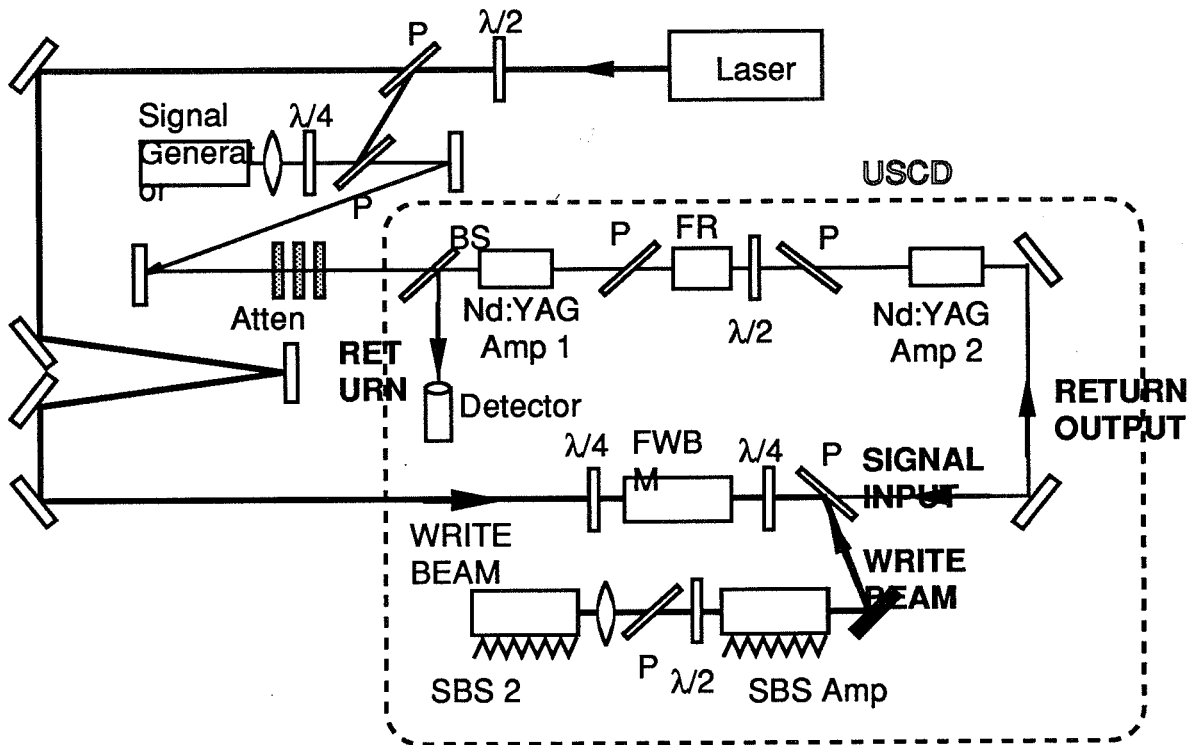


Fig. 1. USCD Experimental Set-up

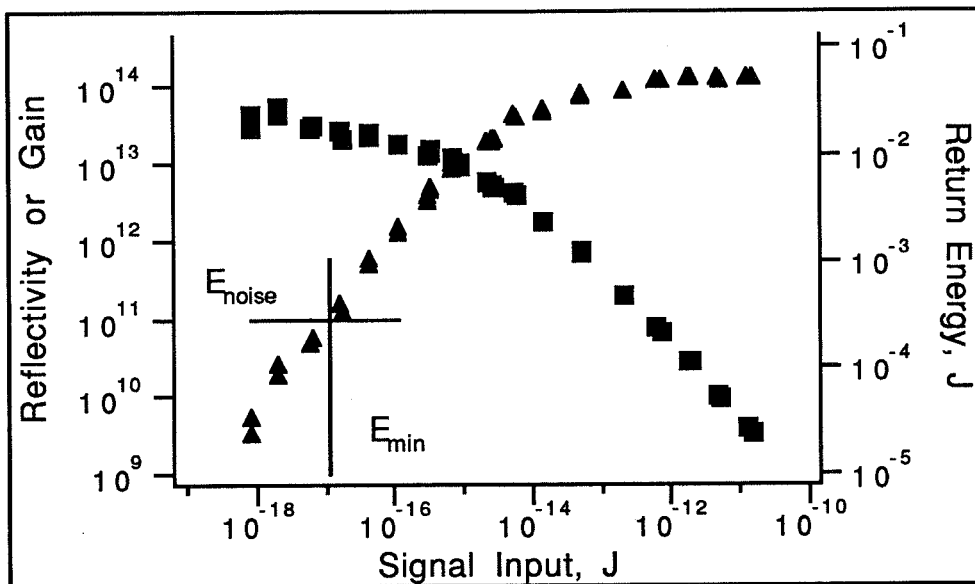


Fig.2 USCD Gain vs. Signal Input

Legend: Squares represents gain and triangles represents return energy (output from USCD).

A High Speed Signal Processing System for a Diode-Pumped YAG Lidar

H. Okumura, T. Sugita, H. Matsumoto, N. Takeuchi and S. Kuwashima*

Remote Sensing and Image Research Center, Chiba University
1-33, Yayoi-cho, Inage-ku, Chiba-city, CHIBA 263, JAPAN

* OKK Inc.

3-26-12, Kitasenzoku, Ohta-ku, TOKYO 145, JAPAN

Introduction

Usually, in acquisition of the lidar echo signal, a transient recorder has been used. However, in a case of using a high-repetitive laser, such as a diode-pumped YAG laser, as a lidar light source, the acquisition speed of a transient recorder is not enough fast. A system using a sampling and direct accumulation in a clock cycle, before transferring a digital data to a computer, is necessary for a fast acquisition, and a new system which equips the necessary functions was developed and reported in this paper.

High speed signal processing unit

The schematic diagram of a specially designed signal processing unit for the lidar echo signal is shown in Fig. 1. The lidar echo signal detected by an APD is amplified and is biased by the gain and offset controls, which are adjustable by variable resistors. Then the signal passes a band-pass filter, and is converted to a 8-bit digital data by a high-speed AD converter. The minimum sampling time is 33 ns (corresponding to 30 MHz sampling frequency). Presently we use a 50 ns sampling time (corresponding to 20 MHz). The 8-bit AD converted signal is summed up by an accumulator and is stored up in a register (32 bits \times 2048 words). The numbers of effective words and accumulation counts can be controlled by commands from a personal computer. The accumulated data is transferred to a personal computer through a parallel interface bus. In the current system, the timing of a processor is given by an external trigger, which is synchronized to the lasing or AO switching. However, it is possible that an internal clock controls both the processing system and the laser timing.

Experiment

As a preliminary test of the system, a return from a building (Fig. 2) was measured and is shown in Fig. 3. The data was accumulated in 5 seconds at 1 kHz repetition frequency. Laser power at this time was 50 mW in average and the pulse width was roughly 25 ns. The noise at the background level is currently governed by the electromagnetic noise from the clock signal of a personal computer. Now the system is under improvement in operational function, and the aerosol profile may be obtained soon.

Conclusion

A diode-pumped solid-state laser is promised to be a suitable light source for a compact and portable lidar as well as space lidar. Usually, it effectively operates at a high repetition frequency. So far there has not been a lidar signal processor which is suitable for a lidar system requiring a fast data acquisition. In this paper, we reported the construction of a lidar system

using a high repetitive diode-pumped YAG laser as a light source, and presented a preliminary lidar echo data from a topographic target.

Reference

1) N.Takeuchi, H.Okumura, T.Sugita, H.Matsumoto, S.Yamaguchi: A portable lidar using a diode-pumped YAG laser, in the Proc. of ILRC16.

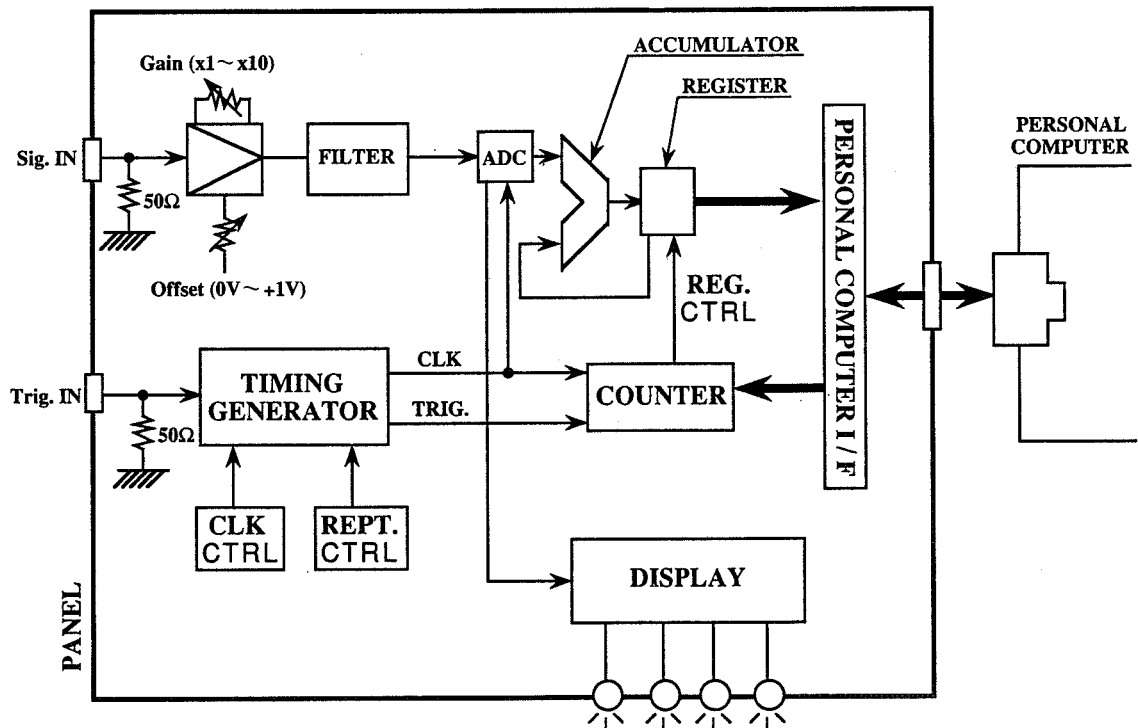


Figure 1 Schematic diagram of the developed high-speed lidar signal processing system.

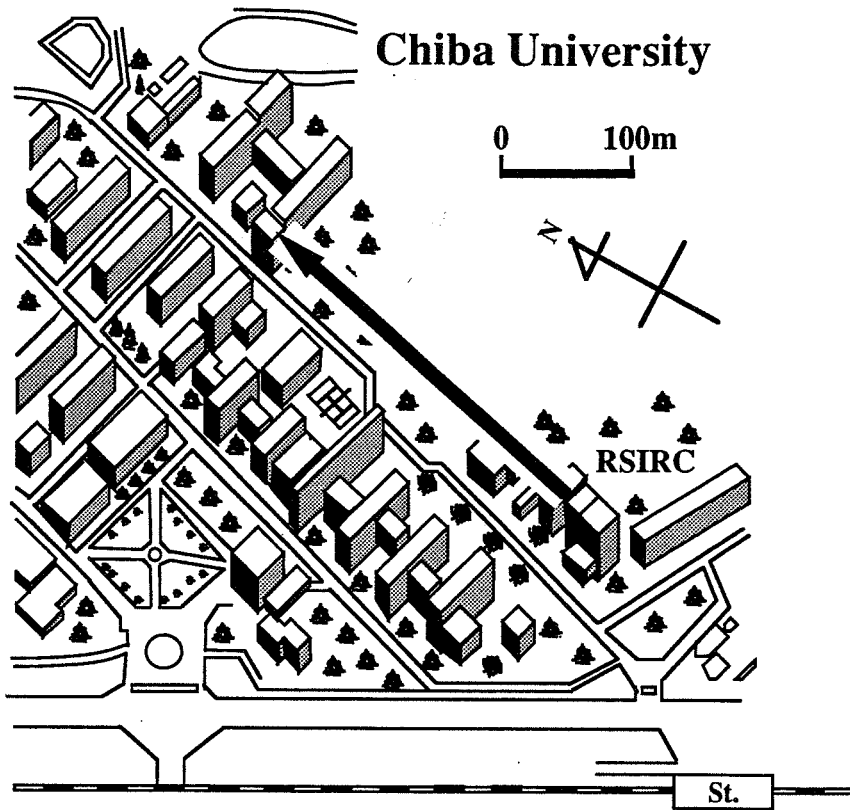


Figure 2 Location of the lidar and the target building.

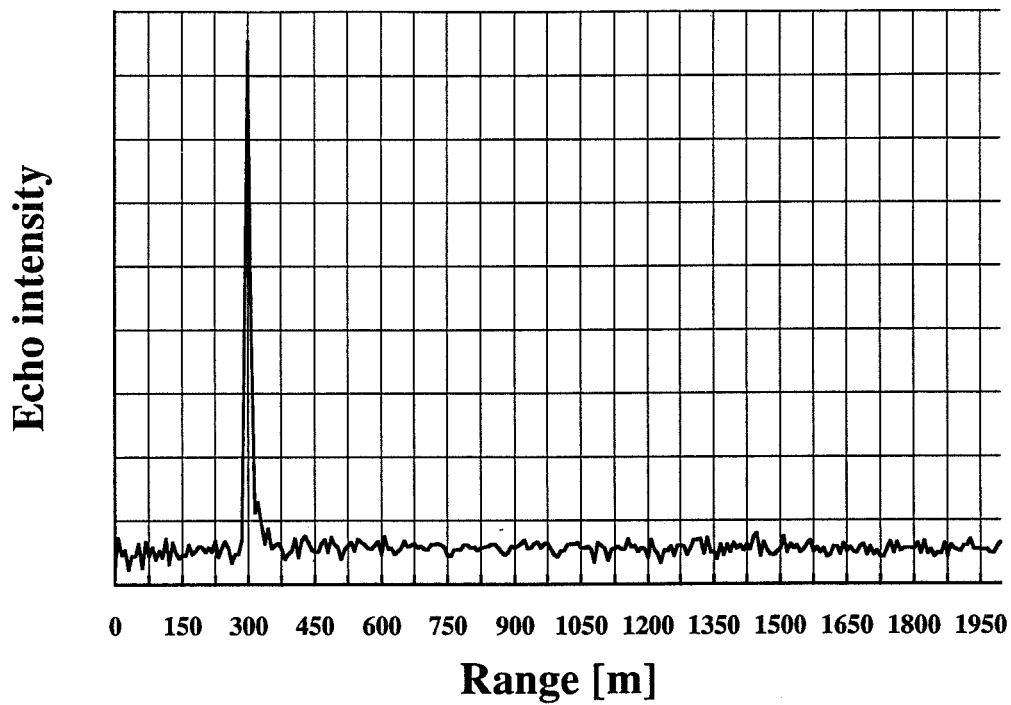


Figure 3 An example of measured lidar echo signal.

Pulsed laser spectral measurement using a Fabry-Perot interferometer: limits to resolution.

Anthony Notari
 Science and Engineering Services, Inc
 4040 Blackburn Ln. Ste. 105, Burtonsville, MD 20866

Bruce M. Gentry
 NASA/Goddard Space Flight Center - Code 917
 Greenbelt, MD 20771

We are developing a Doppler Lidar system using the edge technique to measure atmospheric wind profiles [Korb et al]. The edge technique requires a laser with a narrow spectral bandwidth and a high resolution optical filter. The lidar system will use a Nd:YAG laser operating at 1.064 μm and a high resolution Fabry-Perot interferometer for the edge filter. The Doppler shift measurement is made by locating the laser on the edge of the filter's spectral response function. Due to the steep slope on the edge, large changes in the filter transmission will be observed for small changes in frequency. The Doppler shift can be determined from a measurement of this change in filter transmission if the filter spectral response function in the region of the measurement is well known.

Recently developed injection seeded solid state lasers have made near transform limited laser output readily available for lidar work. Injection-seeded Nd:YAG lasers exhibit single mode output with smooth Gaussian temporal pulse shapes. For a pulse with a temporal width (FWHM) of Δt, the Fourier transform limited spectral profile is also Gaussian with a width of Δν=0.44/Δt. A laser spectral bandwidth of 30-60 Mhz could be used with the edge technique to make high accuracy wind measurements (< 1 m/sec) in the lower atmosphere. When utilizing a short pulse laser with Fabry Perot interferometer (or any spectral device whose spectral response is determined by multiple beam interference) a consideration of the effects of short pulse input on the effective instrument bandwidth is necessary. Here we present results of an experiment we conducted to evaluate the effects of a short Gaussian temporal input pulse on the spectral response of a high resolution Fabry Perot interferometer.

Spectral bandwidth measurements have been a classical use of the Fabry-Perot interferometer. For input radiation from a monochromatic CW source, the output intensity from the interferometer is given by the well-known Airy's formula [Born and Wolf];

$$I(\phi) = \frac{1}{1 + \frac{4R}{(1-R)^2} \sin^2\left(\frac{\phi}{2}\right)} \quad (1)$$

This is the square modulus of the following infinite series, derived by considering the division of amplitude created as an incident ray of polarized light is continually reflected between the two parallel plates of reflectivity R;

$$A(\phi) = T \sum_k R^k \exp(ik\phi) \quad (2)$$

The plates are considered non-absorbing, so the transmission T=1-R. The phase shift between

successive output rays is derived from their optical path difference, which for air-spaced plates is

$$\phi = 2\pi \frac{2d}{\lambda} \cos(\theta) \quad (3)$$

where d is the separation of the plates, θ is the angle of incidence, and λ is the wavelength. In the ideal case, the finesse of the output is determined by the plate reflectivity;

$$F = \frac{\pi\sqrt{R}}{1-R} \quad (4)$$

The analysis of the temporal response of a Fabry Perot interferometer has been considered previously [Roychoudhuri][Kastler][Daussy et al]. The initial assumption in these analyses is that the number of terms, k , summed in Eq. 2 will be limited by the duration of the pulse. Assuming k is equivalent to the finesse, Roychoudhuri showed that for pulse widths, $2d/c < \Delta t < 2dF/c$, the instrument bandwidth is limited to $\Delta\nu \geq 1/\Delta t$. From this analysis it appears that the resolution of the interferometer cannot be improved by increasing the plate separation beyond $d = c\Delta t/2F$.

We have used a Burleigh Fabry-Perot interferometer with high reflectivity plates of $R=97.5\%$, coated for use at $1.064 \mu\text{m}$. A Continuum injection seeded Nd:YAG laser, model YG660 Series modified for long pulse, was operated to produce 125mJ/pulse of output energy. This output was incident on a holographic beam splitter, and the first order containing 1% of the incident energy was deflected towards the interferometer. The beam was further attenuated by neutral density filters, and sent through a 7.5X beam expander before entering the interferometer. The output was focused by a 800mm focal length achromat, and the fringe pattern produced at the focal plane was observed by a CIDTEC camera model CID2250. The camera was synchronized with the laser, and digitized images were recorded into an Intel 80486-based PC. A typical ring pattern is shown in Fig. 1. Clearly the laser produced single longitudinal mode output, and did so very consistently.

With this experimental set-up, we recorded fringe patterns at different plate separations, from $d=3.5 \text{ cm}$ to 8.5 cm . Included in the set-up was a fast photodiode of response $>5\text{GHz}$, measured by a 2GS/sec digital oscilloscope. The photodiode was placed at the other first order output of the holographic beam splitter in order to measure the temporal profile of the laser output. The FWHM pulse width was measured at 14ns (Fig. 2). Assuming the spectral bandwidth is related to the pulse width by $0.44/\Delta t$, the laser spectral width $\Delta\nu \approx 32 \text{ Mhz}$.

The fringe patterns recorded contained one full ring and at least half of a second ring. A computer program was written to find the center of the fringe patterns, and the intensity as a function of the square of the distance from the center was found. Since the square of the distance between the first and second rings is proportional to the interferometer free spectral range, $c/2d$, the intensity can be recast as a function of the relative frequency from the center of the pattern. The bandwidth of the first fringe was then measured using this frequency scale. It was found that with our camera system the horizontal fringes had superimposed a high frequency noise due to image processing electronics built into the camera. This tended to broaden the fringe widths measured from horizontal cross sections of the fringe pattern, and therefore only vertical cross-sections were used to calculate the fringe bandwidth. Five vertical cross sections of a fringe pattern are plotted versus pixel squared values in Fig. 3.

The FWHM of the first fringe was measured for 6 ring patterns obtained when the plate separation was stepped from 3.5 to 8.5 cm in 1 cm intervals. The measured bandwidths are shown in Fig. 4. The expected fringe FWHM is calculated from the following equation and plotted as the solid line in Fig. 4.

$$FW = \sqrt{\left(\frac{c}{2dF}\right)^2 + (LW)^2} \quad (5)$$

The first term is the instrument bandwidth assuming the ideal case where the plate reflectivity determines the finesse, here $F=124$. The second term is the laser bandwidth, $LW=32$ Mhz. The dashed line in Fig. 4 is the expected fringe width in the case where the instrument bandwidth is limited by short temporal duration of the input pulse. Our data reflects more closely the ideal case where the instrument response is determined by the plate reflectivity.

Finally, we add a note of caution before concluding that the short input pulse had no effect on the measurement for the following reasons : 1) Eq. 5 is valid when summing the widths of two Gaussian profiles. Because the Airy function is a Lorentzian, a more accurate representation would be from the convolution of a Gaussian and a Lorentzian. This would result in slightly higher calculated widths, shifting the ideal curve above the measured widths indicating that the data may contain some systematic error. 2) As noted earlier, the processing electronics of the camera contaminated the measurements along rows of pixels with high frequency noise. This leads us to suspect the ability of the camera to give a true representation of the incoming intensity distribution at the pixel level as required in this measurement. A nonlinearity in the pixel-to-pixel response could introduce a systematic error in the fringe width measurement. Therefore, despite the favorable indication that the instrument response is very close to the ideal case, more data will be acquired, perhaps with a different camera array. These results will be presented along with further analysis.

References

Korb C. L., B. M. Gentry, and C. Y. Weng. "The edge technique - theory and application to the lidar measurement of atmospheric winds", accepted for publication in *Appl. Opt.*

Daussy, H., R. Dumanchin, and O. de Witte, (1978). "Fabry-Perot with short pulse lasers: spectral selection and spectral analysis in dye lasers", *Appl. Opt.* **17**, 451-458.

Roychoudhuri, C., (1975). "Response of Fabry-Perot interferometer to light pulses of very short duration", *J. Opt. Soc. Am.* **65**, 1418-1426.

Kastler, A., (1975). "Transmission d'une impulsion lumineuse par un interferometre Fabry-Perot", *Nouv. Rev. Opt.*, **5(3)**, 133-139.

Born, M. and E. Wolf, (1980). *Principles of Optics*, 6th edition, Pergammon Press, New York.

Figures

Fig. 1. Fringe pattern with $d=5.5$ cm.

Fig. 2. Temporal pulse shape of injection seeded Nd:YAG laser.

Fig. 3. Vertical cross sections from one fringe pattern.

Fig. 4. Measured fringe FWHM with ideal case (solid), pulse limited case (dashed).

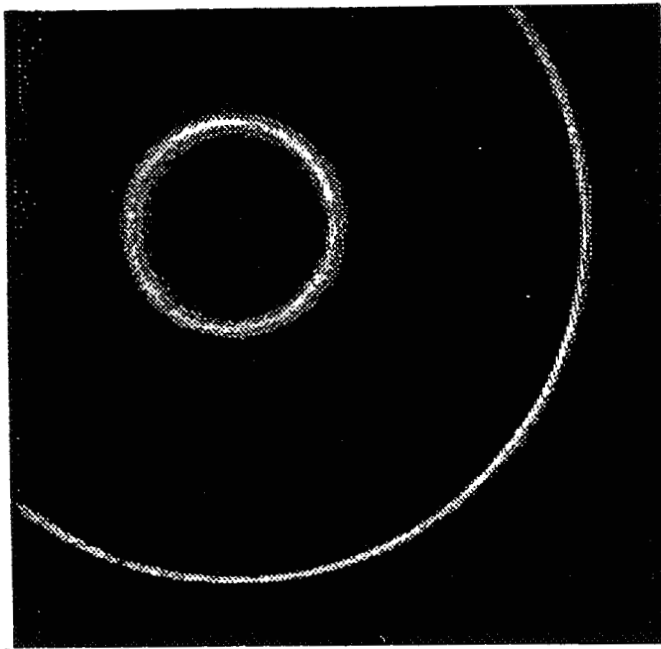


Fig. 1.

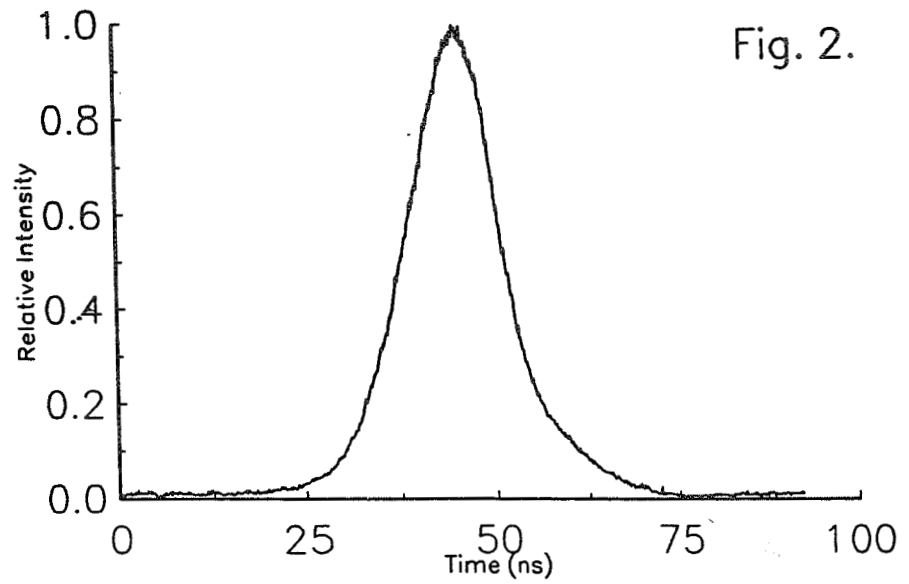


Fig. 2.

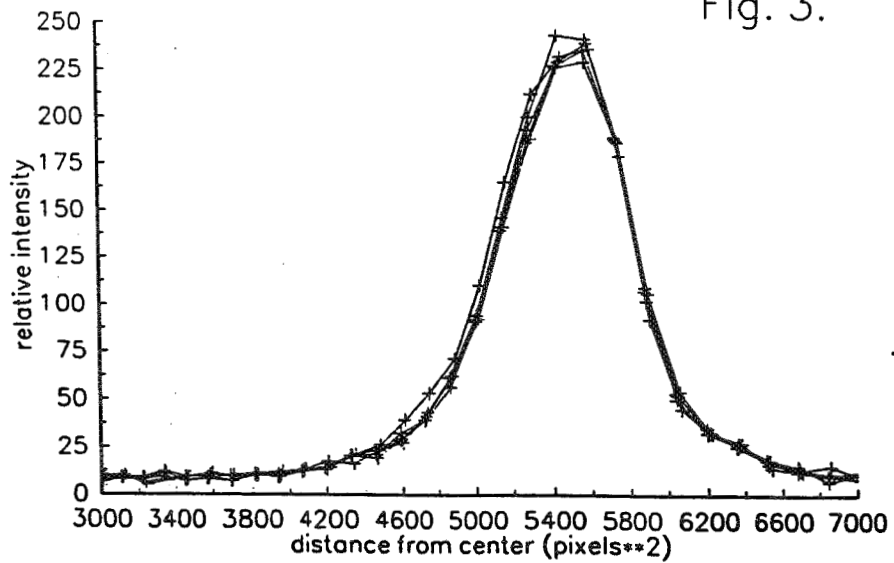


Fig. 3.

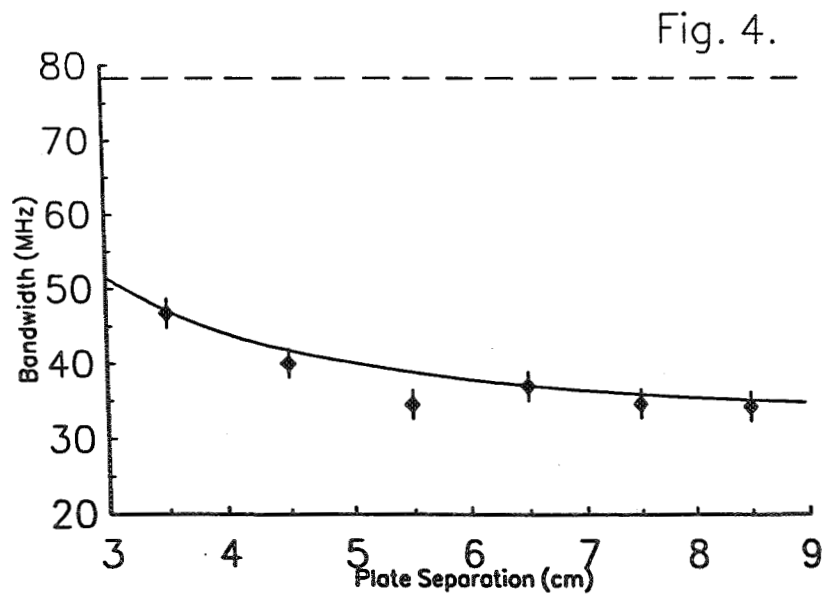


Fig. 4.

Tunable Electro-Optic Modulators for Lidar Systems and Atmospheric Applications *

R. S. Eng, N. W. Harris, and C. L. Summers
Massachusetts Institute of Technology, Lincoln Laboratory,
P. O. Box 73, Lexington, Massachusetts 02173

B. Lax
Physics Department
Massachusetts Institute of Technology
77 Massachusetts Avenue, Cambridge, MA 02139

ABSTRACT

In global sensing applications using different types of lidars, the spectral range and fine frequency coverages are often limited because of the finite tunabilities of molecular lasers and the number of molecular species that are available. To overcome the above obstacle, we have proposed new broadband frequency tunable electro-optic (EO) modulators that can cover a wide spectral range from the mid-infrared to the visible as lidar sources in atmospheric sensing applications such as high resolution atmospheric molecular spectroscopy, DIAL, and laser radar imaging.

The configuration of the proposed new tunable EO modulators includes an electro-optic active crystal element surrounded by a ferrite tuning element which is placed inside a microwave waveguide. The new tunable EO modulator differs from the conventional SSB EO modulator [1] in that the bandwidth of the latter is somewhat limited in virtue of the microwave circuit dispersion characteristics [2]. The tuning is provided by an external magnetic field, which is either longitudinal or transverse. Furthermore, the modulator can be either a single sideband type or a double sideband type depending on the application required for the spectral purity of the modulator output.

Figure 1 shows the single sideband (SSB) version of the tunable EO modulator. It has been designed for operation at the $10\ \mu\text{m}$ CO_2 laser spectral region with microwave modulation at 10 GHz. The square CdTe EO crystal is located at the center and is surrounded by a low-loss calcium-vanadium ferrite with a magnetization of about 1450 Gauss. In operation, the CO_2 laser carrier beam is made to incident on the EO crystal along the magnetic field direction and a sideband is generated at the output end of the modulator just as a SSB EO modulator does [1]. For a 1 cm x 1 cm waveguide cross section, resonant cavity experiments have revealed that the circuit phase velocity is shifted as the applied magnetic field is varied (see Fig. 2 for the splitting and shifting of the resonant frequency as a function of field).

*This research is supported by the Department of the Air Force.

Based on the shifted resonant frequency, we have found that the microwave phase velocity of the composite structure of EO crystal and ferrite can be tuned magnetically to match that of the axially propagating optical beam at the sideband frequency over a microwave frequency range of several GHz. This tunable phase matched bandwidth is plotted in Fig. 3 as a function of the applied magnetic field. It can be seen that the tunable bandwidth is about 3 GHz for a field variation of about 1500 Gauss.

The above phase velocity match condition is satisfied over a broad range of microwave frequency by virtue of the permeability change [3] of the ferrite medium as a function of applied field.

In addition to the magnetically tuned bandwidth, the modulator itself has an instantaneous tunable bandwidth of about 1 GHz depending on the modulator length measured in units of waveguide length [1, 2]. We will also present our calculation results showing much greater tunable widths at optical wavelengths at or shorter than the 1 μm near-IR wavelength using different EO crystals.

Figure 4 shows the double sideband (DSB) version of the tunable EO modulator. Note that the magnetic field is applied transverse to the beam direction. Since the magnetic path is short, the required magnet weight may be much less than that in the SSB EO modulator case. Furthermore, the construction and excitation for the DSB EO modulator are deemed simpler because of its simpler configuration. The calculated results for tunable DSB EO modulator have indicated that a tuning range of several GHz is achievable.

Modulators of these types can be made to cover very wide spectral ranges. For example, the use of a CdTe EO crystal can cover the range 1-20 μm and GaP can cover the 0.6-3 μm range, etc.

We will report the sideband conversion efficiency measurement results on the SSB EO modulators at the meeting. Also reported will be the method of magnetization tuning in which the microwave phase is tuned by the large change in the magnetization in the ferrite caused by a small change in the external applied field. Because the applied field is small, the saving in the magnet weight is convenient for applications in which stringent requirements in both device compactness and low power consumption are present.

REFERENCES

1. N. W. Harris, J. G. Grimm, and R. S. Eng, "Wideband Long Pulse Operation of an Efficient Electro-Optic Modulator at 10.6 μm ," *Opt. Lett.* 15, 1156(1990).
2. B. Lax, R. M. Marino and R. S. Eng, "Broadband Multisection Electro-Optic Modulators," *IEEE J. Quant. Electron.* QE-24, 2101(1988).
3. B. Lax and K. J. Button, Microwave Ferrites and Ferrimagnetics, McGraw-Hill, New York, 1962, chapter 8.

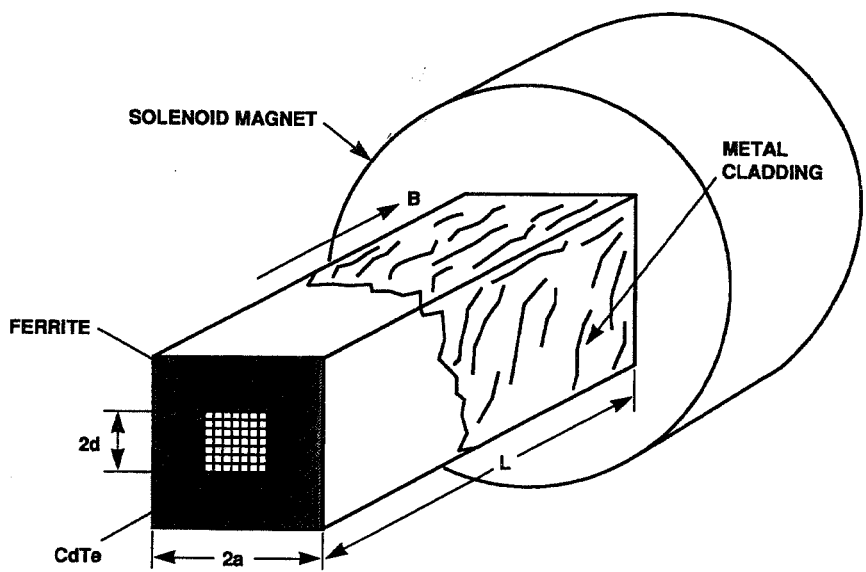


Figure 1: Schematic diagram of a ferrite-loaded waveguide CdTe single sideband electro-optic modulator

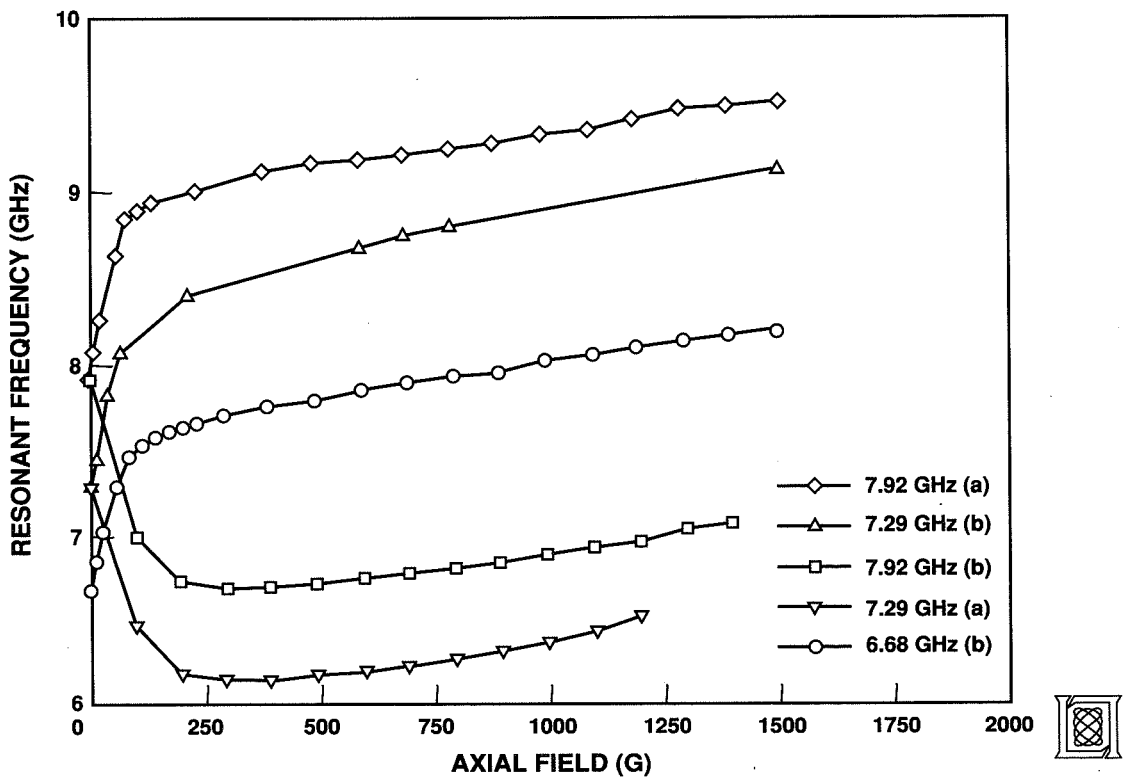


Figure 2: Cavity resonances vs. axial magnetic field for 1 cm² x 5 cm ferrite-filled cavity

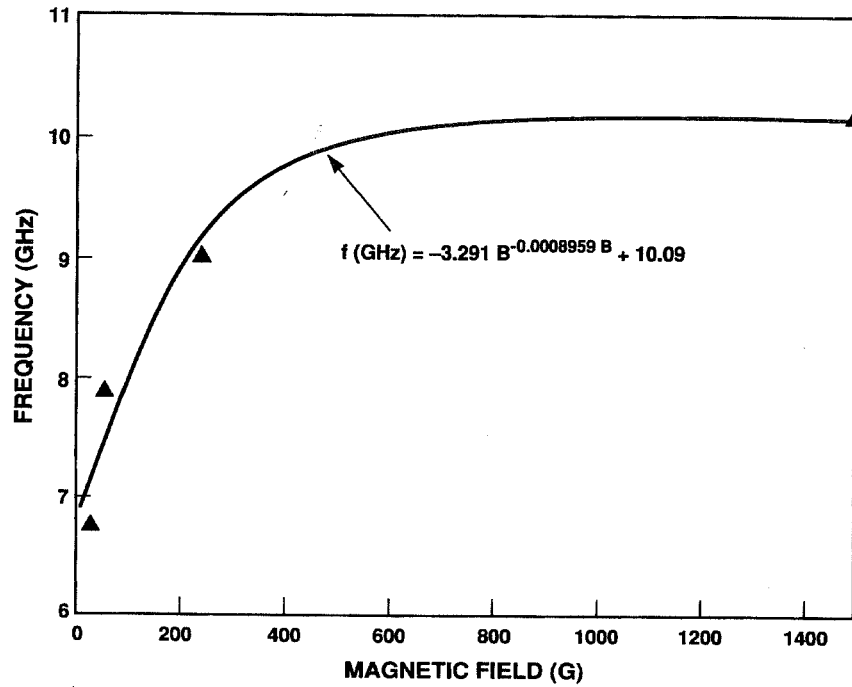


Figure 3: Phase velocity matched frequency vs. magnetic field for a square ferrite-filled waveguide

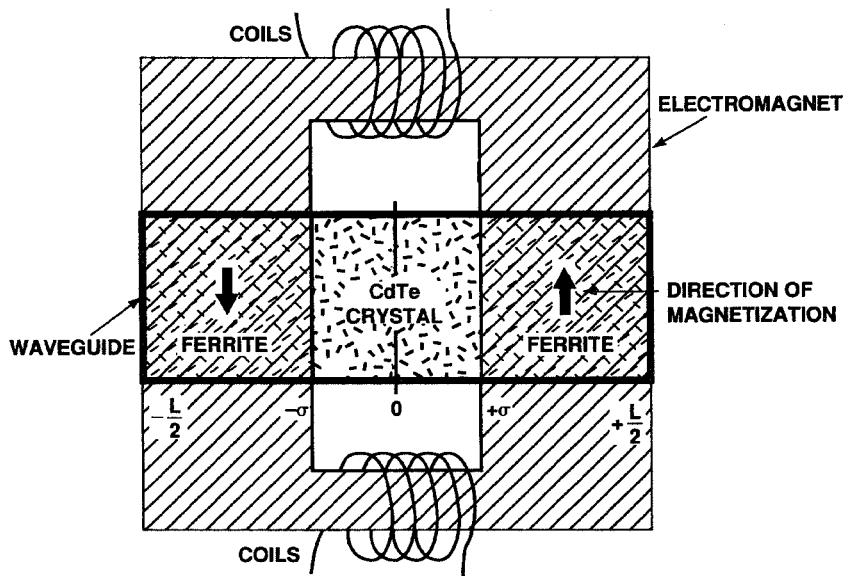


Figure 4: Schematic of a rectangular waveguide DSB EO modulator with external magnet to provide counter magnetization of ferrite slabs

Injection Seeded Single Mode Alexandrite Ring Laser for Lidar Applications

H. Sang Lee and Anthony Notari

Science and Engineering Services, Inc.
4040 Blackburn Ln. Suite 105
Burtonsville, MD 20866

Along with many spectroscopic applications, atmospheric lidar measurements require a tunable, narrow band laser with a very high degree of spectral purity. A standing wave pulsed alexandrite laser tuned by injection seeding with an AlGaAs laser diode has demonstrated high stability ($< 0.005\text{cm}^{-1}/\text{hr}$), with a narrow band output spectrum ($\sim 0.005\text{cm}^{-1}$), and high spectral purity [Schwemmer et al.]. The standing wave cavity, however, poses several difficulties in light of the single mode operation and efficient seeding due partly to the spatial holeburning effect and partly to difficulties in injecting the seeder beam into the cavity. In order to overcome these problems and to operate the high power alexandrite laser in a single axial mode with a high spectral purity, a new ring laser system is being developed. The design features of the ring laser and some measurements of the laser characteristics are presented in this paper.

Figure 1 shows the basic optical configuration of the new ring laser system. The three cavity mirrors are placed to form an isosceles triangular resonator of $\sim 100\text{cm}$ perimeter length. Along with the alexandrite rod, an E-O modulator Q-switch and birefringent filter are placed in the resonator beam path. A diode laser is used for the injection seeding of the slave resonator. A short focal length collimating lens directs the beam through an optical isolator that attenuates the backward traveling wave and prevents the slave laser from damaging the diode. A beam expander achieves mode matching of the diode beam to the slave laser mode [Lee et al.]. The backward traveling intensity is monitored continuously to gauge the efficiency of the injection seeding. The information is then used to adjust the perimeter length of the slave cavity by positioning a mirror mounted on a piezoelectric transducer (PZT) in order to match the slave longitudinal mode to the diode frequency.

A geometrical ray tracing program was used to optimize the ring laser cavity layouts, and to check the stability of the cavity for assigned perturbations in the layout. The stability of a particular resonator was measured in terms of the number of rays that completed 19 transits of the cavity (the number of transits is limited by the capacity of the ray tracing program). For a particular cavity configuration, a goodness parameter was derived by comparing the number of completed rays to the number counted for a reference cavity configuration. The goodness parameter of the reference cavity with a triangular resonator of 70cm length, three plane mirrors aligned, and thermal lensing of 2m focal length is defined to be 100. An uncertainty of up to 5% exists when comparing different cavity configurations.

To estimate the number of rays completing 19 transits, a plane is chosen inside the cavity, normal to the optical axis, from which the rays are initiated. Launch points are chosen along a transverse axis at 0.05cm intervals. From each point, rays are launched inclined in the direction of the transverse axis at $.25\text{mrad}$ intervals. Enough rays are used to obtain a valid statistical sampling of the cavity volume. For aligned cavities, rays sent from the x-transverse (perpendicular to plane of triangle) and y-transverse axes gave nearly the same result, whereas for slight misalignment, the y-axis supports somewhat larger number of rays than the x-axis (implies larger mode volume in y-direction). It was found that as the magnitude of the mirror misalignments was increased, the central ray path diverged away from the optical axis. Since rays launched from the y-transverse axis were used in performing the simulation, the results may underestimate the number of completed rays in highly misaligned cavities.

The simulation was carried out for various resonator configurations including a 3-mirror triangular resonator as well as a 4-mirror rectangular resonator. The effect of thermal lensing of the laser rod [Driedger et al.] was simulated by including a thick lens of 100mm extent, 5mm diameter, at a variety of focal lengths. We find that a triangular resonator performed significantly better than a

rectangular resonator, especially in terms of the tolerance of the mirror alignment. The performance of the triangular resonator generally improves as the resonator length is shortened. The mirror alignment tolerance is somewhat greater for the shorter resonator. The value of the goodness parameter increases as the focal power of the thermal lens increases, reaching a maximum at 25cm focal length for the 70cm resonator, and at 75cm focal length for the 140cm resonator. The shorter cavity maintains the better stability in terms of the thermal lensing power of the alexandrite laser. For example, the 70cm resonator becomes unstable only for a thermal lens focal length of 12cm or less, while the 140cm resonator becomes unstable below 25cm of thermal lens focal length.

The triangular resonators of 70cm length were simulated with different focal length mirrors (plane, 10m, 5m and 2.5m) and various focal lensing. It is observed that higher focal power mirrors give a higher goodness parameter, but also decrease the beam waist size and increase the risk of damage to optical elements. Different mirror configurations of triangular 70cm resonators were compared given three thermal lens focal lengths (5m, 2m, 50cm). These were two curved mirrors of 5m and 10m focal length, and one curved mirror of 5m and 10m focal length. The observation here is much the same as above; the more focal power inside the cavity, the higher the goodness parameter. For the configurations with two curved mirrors, a misalignment of $.01^\circ$ gave a goodness parameter of at least 95% of the aligned resonator. The same conditions for one-curved mirror configurations showed at least 90% of the goodness parameter of the aligned values.

Other 3-mirror resonator configurations were studied, including one right triangular shape, two equilateral triangles, and three isosceles with the longer side 1.5 times the length of the shorter sides. The result shows that the stability of these resonators is not strongly affected by the shape of the configurations or by the position of the flat mirror. It was also noted that the mirror positioned across from the rod had a slightly greater alignment tolerance than the two mirrors adjacent to the rod.

In order to gauge the effect of controlling the cavity length by using a mirror mounted on a PZT in a triangular resonator, the optical path length of the central ray was measured for the aligned case and for a rotation or translation of one mirror. For a 70cm resonator, a rotation of $.01^\circ$ changes the path length 11nm ($\sim 1\%$ of a wavelength), while a translation of $1\mu\text{m}$ gives a $1.67\mu\text{m}$ change in path length. Thus, drift in the rotational alignment of the mirrors can easily be compensated for by the PZT.

The spherical aberrations of the geometrical focal spot were examined to compare the effects between one curved mirror and two curved mirror configurations. These were seen to change with the focal power of the mirrors. In the two mirror configuration, increasing the mirror focal power gave a smaller aberration. Aberrations of one mirror configurations also decreased for higher focal power mirrors. Considering the difference in focal power of the two cases, the aberration due to having two curved mirror is less than that with only one curved mirror.

In order to check conclusions of stability from the ray tracing simulation, Gaussian beam parameters were calculated using the ABCD matrix formulation for a four element (three mirrors and a lens) ring resonator. The thermal lensing effect of the rod was simulated by a thin lens. The resonator studied had a 105cm length with a plane mirror and two curved mirrors. The calculations were performed with different thermal lenses (focal lengths from 10 to 600cm), and for three different focal lengths of the curved mirrors (100, 500, and 1000cm). The result shows the resonator to be stable when $F > P/4$ (F =focal length of the rod thermal lensing, P =cavity length). As an example, the 105cm resonator was seen to be stable when the focal length of the lens was $\geq 30\text{cm}$, confirming the conclusion of stability drawn from the ray tracing simulation.

The radius of the fundamental transverse mode was calculated at the waist and at the position of the mirrors in the resonator. The power density at each optic was calculated assuming a 500mJ, 100ns pulse. For mirror focal lengths of 5m and 10m, the beam radius is $> 350\mu\text{m}$ when the thermal lens has a focal length of greater than 50cm. For shorter thermal lens focal lengths, the power density at the optics approaches $1.5\text{GW}/\text{cm}^2$, which is the damage threshold for many optical coatings [Virgo Optics]. For a mirror focal length of 1m, the power density is $> 1\text{GW}/\text{cm}^2$ on some of the optics regardless of the thermal lens effect.

An optimum cavity design is implemented on a super invar table using high precision optical mounts. A diffuse pump chamber is mounted on the optical table as shown in the layout. The cavity is then tuned initially using an AlGaAs diode laser beam and then fine-tuned by maximizing the output power. Preliminary data for the laser slope efficiency is shown in Fig.2. A relatively low slope efficiency (0.8 %) is due to the reduced clear aperture size (65 % of the rod aperture). In fact without the aperture stops, the slope efficiency of the laser shows close to 2% confirming the results from other flash-lamp pumped alexandrite laser systems. A substantially low lasing threshold power observed in this system indicates a high efficiency of the pump chamber and the laser cavity compared to other systems. The output power is very stable with respect to a tuning of the cavity mirrors indicating high stability of the cavity which was predicted in the simulation study. The high stability of the cavity is also borne out in the measured beam profile as shown in Fig.3. The nearfield beam profile shows a symmetric patterns filling the aperture with a numerous transverse modes. The beam profile pattern repeats fairly well from shot to shot indicating a high cavity stability which is also revealed in the output power measurement. As the output power increases, more modes at higher orders show up filling the aperture more and more uniformly.

In order to optimize the pump period, the fluorescence decay time of the alexandrite is measured at various temperatures. As shown in Fig.4, the fluorescence decay time decreases as a function of the rod temperature. This characteristic of the alexandrite offers a unique possibility of optimizing the pumping by compromising the rod temperature and the pump period at a fixed flash lamp power. At 70°C temperature, the pump period can be as long as 170 μ sec before the fluorescence decay becomes significant. The long pump period at a lower peak power offers several advantages in the laser system design with respect to the mechanical and electrical requirements. The lower peak power pumping causes less stress on the discharge system including the flash lamp. Furthermore, it gives less stress on the alexandrite rod mechanically as well as radiatively providing an optimum condition for the single mode injection seeding where the cavity length is required to be maintained stable during the lasing process. A passive birefringent filter gives an approximately 1 Å FWHM bandwidth output spectrum over a wide tuning range between 740 nm and 770 nm. This bandwidth is considered optimum for the injection seeding and single mode operation of the system for DIAL applications.

References

Driedger, K.P., W. Krouse, and H. Weber, (1986). "Average refractive power of an alexandrite laser rod", *Optics Comm.*, **57**, 6, 403.

Lee H.S., C. Prasad, T. R. Glesne, and G. K. Schwemmer, (1991). "Optimum parameters for injection seeding of a tunable solid-state laser", *Proceedings CLEO Tech. Dig. Series*, **10**, 514, May 12-17, 1991.

Schwemmer G., H.S. Lee, and C. Prasad, (1991). "Narrowband alexandrite laser injection seeded with frequency dithered diode laser", *Proceedings SPIE Earth and Atmospheric Remote Sensing*, **1492**, 52, April 2-4, 1991.

Virgo Optics. "Laser optics general catalog", Port Richey, FL.

Figure Captions

- | | |
|-------|---|
| Fig.1 | Schematic layout of the tunable single mode alexandrite ring laser system |
| Fig.2 | Laser output power as a function of pump power |
| Fig.3 | Fluorescence decay time vs. rod temperature |
| Fig.4 | Near-field laser beam profile |

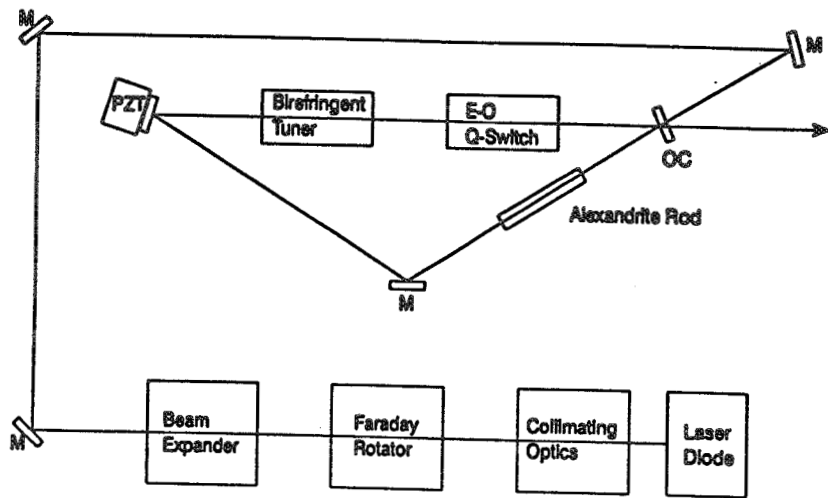


Fig.1

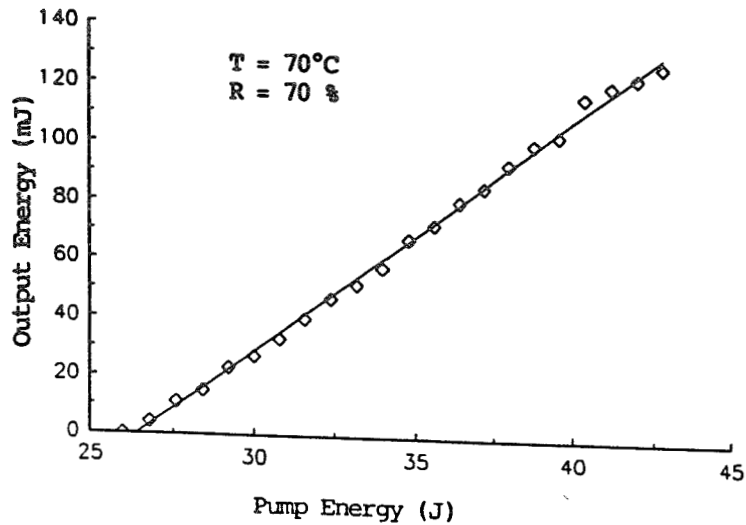


Fig.2

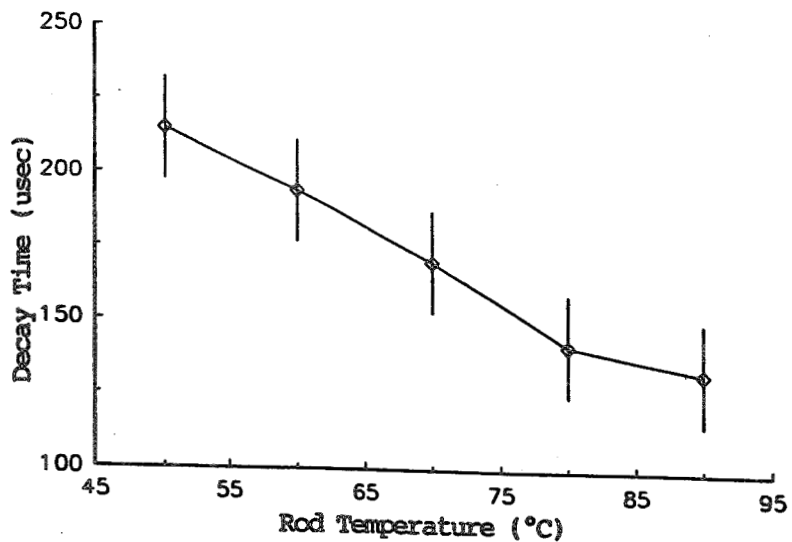


Fig.3

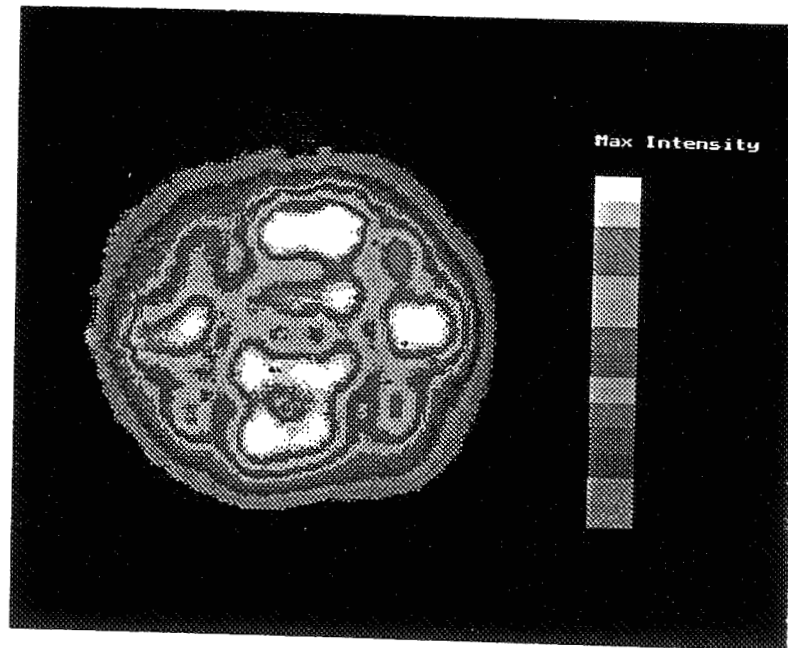


Fig.4

Tm,Ho:YAG LASER WITH TUNABLE RANGE OF 2.08- 2.12 μm AND ITS APPLICATIONS TO SPECTROSCOPY

Kazuhiro Asai

Tohoku Institutes of Technology

Yagiyama Kasumi 35-1, Taihaku-ku, Sendai 982, JAPAN

and

Toshikazu Itabe

Communications Research Laboratories

Ministry of Posts and Telecommunications

Nukui-Kitamachi 4-2-1, Koganei, Tokyo 184, JAPAN

In recent advanced lasers, 2 micron solid-state lasers such as Tm:YAG and Ho:YAG laser are very attractive for laser radar remote sensing technologies, i.e. eye safety, realizations of all solid-state laser pumped by diode laser and smaller dimension, tunability of lasing wavelength, possibility of coherent detection etc. Featuring these advantages, 2 micron lasers have been candidated as laser transmitters for use in water vapor DIAL, laser altimeter, Doppler wind sensor, Mie lidar etc. This paper reports characterization of tunable Cr,Tm,Ho:YAG laser and its applications to spectroscopy concerning with absorption and reflectance.

The Holmium-YAG laser rod, fabricated by Airtron, was 74mm length with a diameter of 6.4mm. Dopant concentrations are Cr,0.85; Tm,5.9 and Ho,0.36, respectively. The Xe flash lamp was connected in series with a 220 μF capacitor. Maximum input energy to the flash lamp yields electrically about 200J. The laser cavity consists in a totally reflecting rear mirror and an output mirror. The cavity length is 80 cm. The output energy, when operated transversely multi-mode, could produce more than 1J with 200J of electrical input energy, while the highest slope efficiency obtained with the 85% reflecting output coupler was 1.3%.

We first studied the tunability of laser. Two uncoated fused quartz etalons as tuning elements were used. One of them has a 0.1 mm thickness for a coarse tuning and the other a 1mm thickness for a fine tuning. The measured tuning spectrum is shown in Fig.1. This figure shows that the laser could be tuned smoothly from 2.083 μm to 2.1 and 2.12-2.13 μm . The linewidth of laser was measured to be approximately less than 0.1 nm.

The spectroscopic measurements are now being made by using this laser with the experiment setup indicated in Fig.2.

Reference

1.N.P.Barnes and D.J.Gettemy,IEEE J.Quantum Electron.,QE-17,1303(1981)

- 2.M.E.Storm,Appl.Opt.,27,4170(1988)
- 3.S.W.Henderson and C.P.Hale,Appl.Opt.,29,1716(1990)
- 4.N.Sugimoto,N,Sims,K.P.Chan and D.K.Killinger,Opt.Lett.,15,302(1990)
- 5.S.W.Henderson,C.P.Hale,J.R.Magee,M.J.Kavaya, and A.V.Huffaker,Opt.Lett.,
- 6.K.Asai and T.Itabe,15th International Laser Radar Conference
(Tomsk,U.S.S.R.,1990)

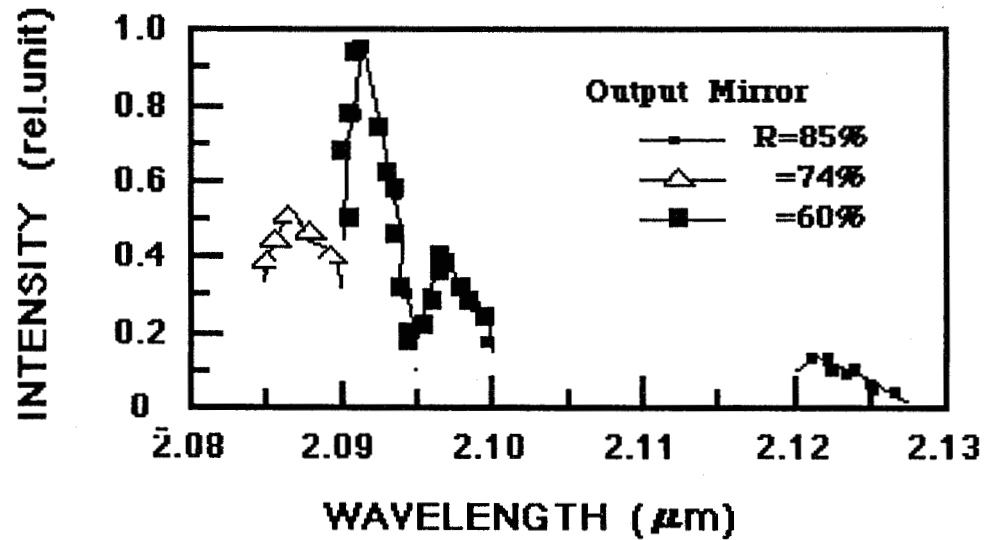


Fig.1 Lasing spectrum at 296 K

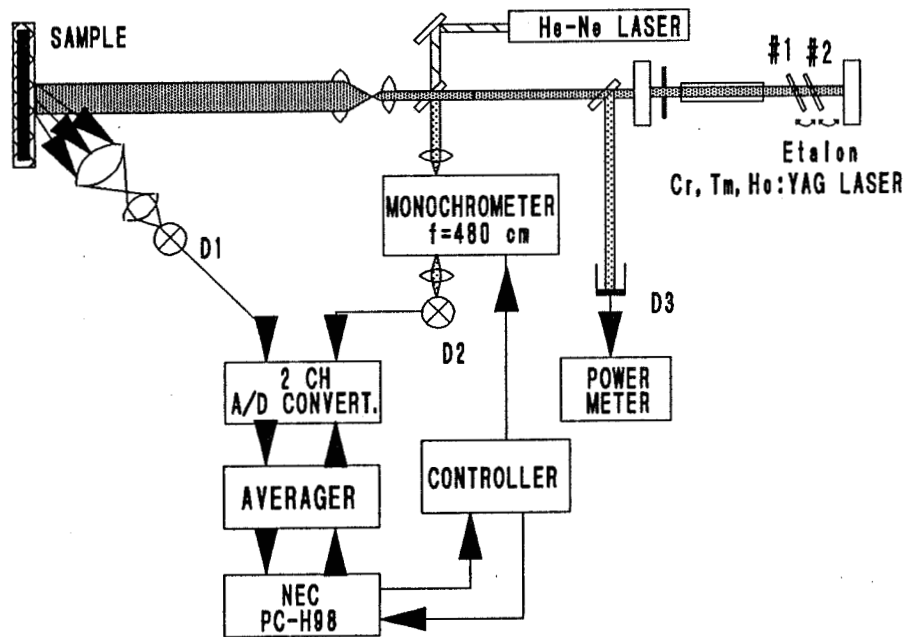


Fig.2 Experimental setup

THEORETICAL SIMULATION OF A 2 μm AIRBORNE SOLID STATE LASER ANEMOMETER.

Béatrice IMBERT - Jean-Pierre CARIOU

ONERA (Office National d'Etudes et de Recherches Aérospatiales) - MEUDON, FRANCE.

1 - Introduction:

In the next future, military aircrafts will need to know precisely their true airspeed in order to optimize their flight conditions. In comparison with classical anemometer probes, an airborne Doppler Lidar allows to measure the air velocity without influence from aircraft aerodynamic disturbance.

While several demonstration systems of heterodyne detection using CO₂ laser have been reported, improvements in the technology of solid state lasers have recently opened up the possibility that these devices can be used as an alternative to CO₂ laser systems. In particular, diode pumped Tm:Ho:YAG laser allows to achieve a reliable compact airborne system working with an eye safe wavelength ($\lambda = 2.09 \mu\text{m}$).

This paper describes the theoretical study of performances of a coherent Lidar using a solid state diode pumped Tm:Ho:YAG laser, called SALSA (Système d'Anémométrie à Laser Solide Aéroporté), for measuring aircraft airspeed relatively to atmosphere aerosols. A computer simulation has been developed in order to modelize the Doppler anemometer in function of atmospheric propagation and optical design. A clever analysis of the power budget on the detector area allows to calculate optical characteristic parameters of the system and can then be used to predict performances of the Doppler system. Estimating SNR and heterodyne efficiency provides the available energy for speed measurement as well as a useful measurement of the alignment of the backscattered and reference fields on the detector.

2 - Coherent detection principle:

The Doppler Lidar measures the aircraft velocity a few tens of meters away in front of the plane (fig 1). A continuous laser wave is transmitted to the atmosphere and is continuously absorbed and scattered by aerosols. Scattered laser light is frequency shifted because of relative motion between scatterers and aircraft (Doppler effect). This Doppler shift $\Delta\nu_D$ is a function of radial plane velocity v and laser wavelength λ :
$$\Delta\nu_D = \frac{2v}{\lambda}$$
. Doppler shift is measured by coherent mixing for optimal detection sensitivity.

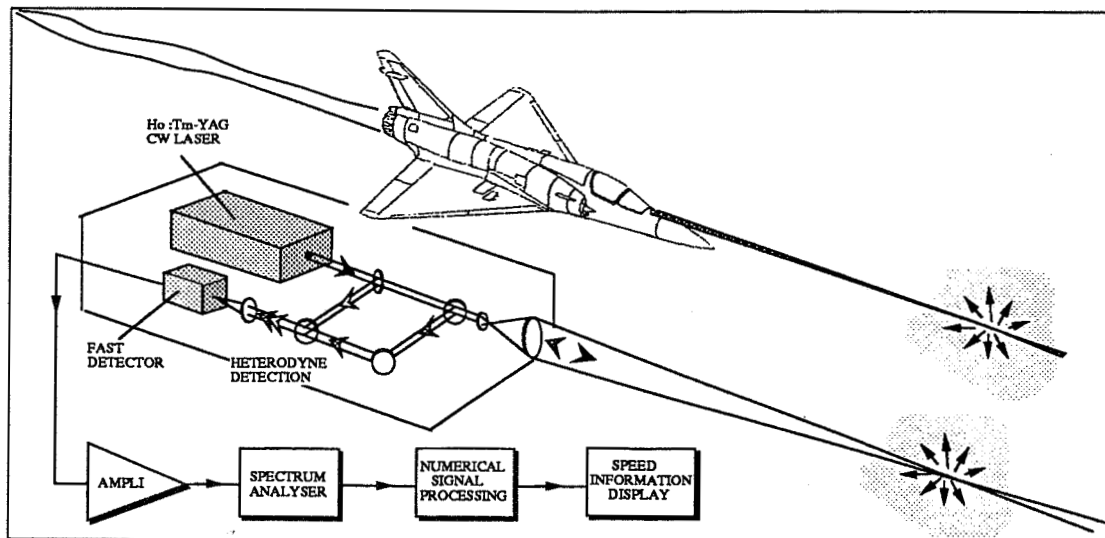


Fig 1 : Schematic of the Ho:Tm:YAG Lidar system

The CW laser beam is splitted into a reference wave called local oscillator (LO) and a signal beam. The signal beam is transmitted to the atmosphere through a focusing lens and is collected back by the receiver aperture. The collected backscattered light is then mixed with the local oscillator on the detector area. The detector integrates over its surface the resultant intensity and produces a current given by:

$$I(t) = I_{OL} + I_S(t) + i_S(t) \quad (1)$$

Where:

— I_{OL} is the direct stationary current caused by the LO:

$$I_{OL} = \frac{\eta e}{h\nu} \iint |E_{OL}(x,L)|^2 dx \quad (2)$$

With :

η : dimensionless detector quantum efficiency.

e (C) = $1,6 \cdot 10^{-19}$: electronic charge.

h (J.s) = $6,62 \cdot 10^{-34}$: Planck's constant.

ν (Hz) = C/λ : optical frequency.

L (m) : detector position

x (m^2) : 2D vector in the detector plane.

E_{OL} ($W \cdot m^{-2}$)^{1/2}: LO field in the detector plane.

— $I_S(t)$ is the direct detection current from the backscattered field E_S ($W \cdot m^{-2}$)^{1/2}:

$$I_S(t) = \frac{\eta e}{h\nu} \iint |E_S(x,L,t)|^2 dx \quad (3)$$

— $i_S(t)$ is the intermediate frequency signal current at frequency $\Delta\omega = \omega_S - \omega_{OL}$:

$$i_S(t) = \frac{2\eta e}{h\nu} \iint E_S(x,L,t) E_{OL}^*(x,L) \cos(\Delta\omega t) dx \quad (4)$$

The power budget of the system is characterized by two important parameters :

$$\eta_h(t) = \frac{\langle i_S^2(t) \rangle}{2I_S I_{OL}} \quad (5)$$

$\eta_h(t)$ is the dimensionless heterodyne efficiency which describes the waves spatial recovery and the waves phase relation on the photodetector.

$$SNR(t) = \frac{\langle i_S^2(t) \rangle}{2 e \Delta f I_{OL}} \quad (6)$$

SNR(t) is the signal to noise ratio defining the coherent detection sensitivity.

The average heterodyne current power, for a deterministic LO field, is :

$$\langle i_S^2(t) \rangle = 2 \left(\frac{\eta e}{h\nu} \right)^2 \iiint_D MsD(x_1, x_2, L, t) E_{OL}^*(x_1, L) E_{OL}(x_2, L) dx_1 dx_2 \quad (7)$$

where $\langle \rangle$ denotes the time average for an ergodic process and where :

$MsD(x_1, x_2, L, t) = \langle E_S(x_1, L) E_S^*(x_2, L) \rangle$ is the mutual coherence function ($W \cdot m^{-2}$) of the total backscattered field in the detector plane ($z = L$).

3 - Modelling the Lidar performances :

The system performances depend on propagation of the transmitted field through random medium. The wave propagation in a turbulent atmosphere is described by the Green's function, obtained from the extended Huygens-Fresnel principle [1]. The turbulence atmosphere propagation model leads to several successive integrations due to dependence of mutual coherence function on the fourth moment of the Green's function [2] ; calculation of heterodyne efficiency and SNR on the detector area is therefore complex. In order to simplify these calculations, the following assumptions are made :

- amplitude transmission of the receiver lens is gaussian.
- transmitted beam and LO are untruncated.
- atmosphere layers are statistically independent.
- backscatter coefficient is constant within the working range.
- atmosphere attenuation is constant and identical for transmitted and backscattered paths.

Taking these assumptions into account, a computer simulation has been developed. Simulation (fig 2) allows numerous input parameters describing the coherent Lidar through optical and atmospheric data. Heterodyne efficiency and SNR values determine the system range and sensitivity. Coherent detection is optimized by tuning diverse optical parameters.

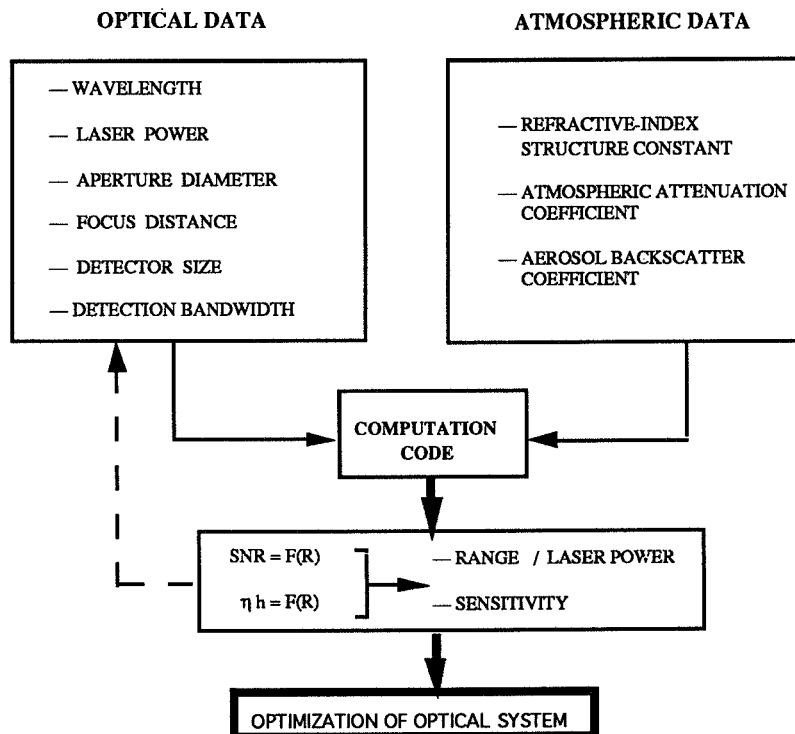


Fig 2 :Computer simulation diagram

4 - Simulation results :

Figure 3 shows examples of SNR and heterodyne efficiency as functions of range for a monostatic homodyne system. Atmospheric data are chosen as follows : aerosol backscatter coefficient β is interpolated versus height (5 km) and wavelength from clear-air tables (Handbook of Optics) ; atmospheric attenuation coefficient Γ is calculated by the 1986 line parameters compilation tape HITRAN and by using the mid-latitude winter model atmosphere.

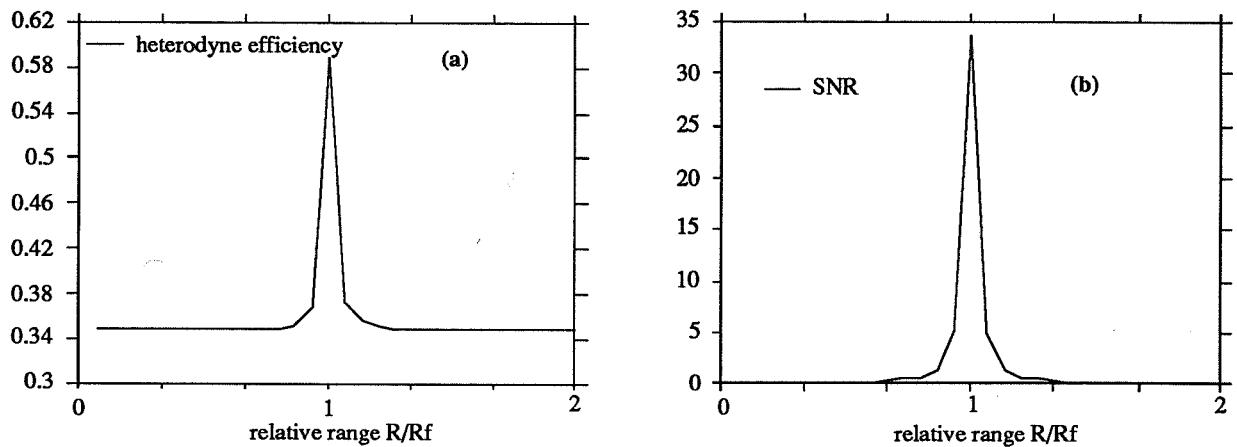


Fig 3 : Performances of a 2.09 μm coherent Lidar system , with a weak turbulence $C_n^2 = 10^{-18} \text{ m}^{-2/3}$
 a) heterodyne efficiency as a function of range.
 b) SNR ($\beta = 8.3 \cdot 10^{-7} \text{ m}^{-1} \cdot \text{sr}^{-1}$; $\Gamma = 8.8 \cdot 10^{-8} \text{ m}^{-1}$).

The maximum of theoretical plots occurs at the focus distance R_f and a narrow depth of focus is observed. Heterodyne efficiency reaches a value of 60 % , where wave front adaptation is optimum (fig 3a). SNR is about 35 in this case at the focus distance by integrating 1000 successive spectra (fig 3b).

5 - Conclusions :

A computer code was developed in order to characterize Doppler anemometry in function of atmospheric propagation (turbulence, aerosol backscatter coefficient, atmospheric attenuation) and optical system design (optics and detector size, mono or biaxial configuration).

Without yet considering possible aero-optical turbulences into the plane boundary layer, nor decorrelation time influence, modelling coherent Doppler Lidar performances can give useful informations about necessary laser power for aircraft speed measurement with a Lidar system using a CW Tm:Ho:YAG laser.

Furthermore, this code will be useful to modelize any other Lidar, whatever optical or atmospheric parameters are.

The work described in this paper was supported by the " Direction des Constructions Aéronautiques" (DCAé-STTE).

References :

- [1] Tatarski V.I, ' The Effect of the Turbulence Atmosphere on Wave propagation', Keter, Jerusalem (1971).
- [2] Frehlich R.G, 'Conditions of Optimal Performance of Monostatic Coherent Laser Radar', Optics Letters 15, 643-645 (1990).
- [3] Chu T.S and Hogg D.C, 'Effects of Precipitation on Propagation at 0.63, 3.5 and 10.6 Microns', Bell Syst.Tech.J.47, 723-759 (1968).

COMPARISON OF EYE-SAFE SOLID STATE LASER DIAL WITH PASSIVE GAS
FILTER CORRELATION MEASUREMENTS FROM AIRCRAFT AND SPACECRAFT

Robert V. Hess, Leo D. Staton, H. Andrew Wallio
NASA Langley Research Center, Hampton, VA 23665
Liang-Guo Wang
William & Mary College, Williamsburg, VA

Differential Absorption Lidar (DIAL) using solid state Ti:Sapphire lasers finds current application in the NASA/LASE project for H₂O vapor measurements in the ≈0.820 μm region for the lower and mid-troposphere and in potential future applications in planned measurements of the ≈0.940 μm region where both strong and weak absorption lines enable measurements throughout the troposphere and lower stratosphere.

The challenge exists to perform measurements in the eye-safe >1.5 μm region. In previous studies by P. Brockman et al., (Ref. 1) we evaluated CO₂ laser DIAL measurements with heterodyne and direct detection of O₃, H₂O vapor and NH₃ in the ≈10 μm region from aircraft and shuttle. In view of their potentially higher efficiency, compactness and lifetime, diode laser pumped eye-safe solid state lasers, with the option of wavelength shifting through Optical Parametric Oscillators in the ≈2 to 5 μm range, are of great interest to DIAL and Doppler lidar. For example, high pulse energy ≈2 μm Tm:Ho:YLF lasers under evaluation for a spacecraft based Laser Atmospheric Wind Sounder (LAWS) can also be made to operate in regions of H₂O vapor absorption lines and may show promise for H₂O vapor DIAL from spacecraft. However, passive Gas Filter Correlation Radiometer measurements have already been performed from spacecraft, for CO and N₂O at 4.6 μm strong absorption lines, and are in the planning stages for CO, CH₄ and N₂O at 2.3 μm and 4.6 μm (Ref. 2). The weaker absorption lines are used in the lower troposphere with ground reflected solar radiation and the stronger absorption lines in the mid/upper troposphere using thermal radiation. Thus, it is important to perform trade-offs with DIAL studies. The comparative study extends the DIAL studies in Ref. 1 through use of the latest (augmented) Hi-TRAN data base. A special effort is made to relate parameters such as concentration measurement error for both systems to physical parameters such as range resolution, signal-to-noise ratio to the performance of lasers and OPOs.. Acknowledgements are given to R. Hardesty for a comparative study of ground-based DIAL humidity profiling with heterodyne/direct detection (Ref. 3) and to N. Menyuk et al., for ground-based DIAL studies of H₂O, HCl, CH₄ (Ref. 4)

The comparison between active DIAL and passive GFCR, benefits from presenting the two approaches in a more or less common form, which facilitates assessment of similarities and differences. As shown in many papers on DIAL (e.g. Ref. 1), the key trace gas concentration measurement error δρ can be written in the form

$$\delta\rho = (1/2\Delta\sigma\Delta r) \left[(1/N) \sum_{i=1}^2 \sum_{j=1}^2 (1/\text{SNR})_{ij}^2 \right]^{1/2}$$

where Δσ is the difference between the "on-line" and "off-line" trace gas absorption line coefficients, Δr is the length of the measurement cell cT/2, with T the integration time and N the number of samples integrated. The δρ error for the passive GFCR will be presented in an analogous form. However, the feasibility of using a similar form has been demonstrated for a discrete case of SNR = 1 by D. Flanigan (Ref. 5) and will be generalized. It is indicated that for both active DIAL and passive GFCR, attainment of a small δρ for a small difference Δσ of

“on” and “off” absorption line coefficients, will require a large Δr and SNR. For the small $\Delta\sigma$ values at 2.3 μm the total column measurements of CH_4 and CO in the lower troposphere will be evaluated using ground reflected laser radiation (DIAL) or using ground reflected solar radiation (GFCR), in addition to range resolved aerosol scattering (DIAL). The latter will also be evaluated for the larger $\Delta\sigma$ mid/upper troposphere DIAL of CH_4 (3.3 μm) & CO (4.6 micrometer) and for a variation in $\Delta\sigma$ values for $\approx 2 \mu\text{m}$ H_2O DIAL, throughout the troposphere. Note that total column measurements are also used to obtain moderate range resolution for passive and DIAL sensors. The passive GFCR uses variation of pressure and temperature in the gas correlation cells to obtain range resolution (Ref. 2). For DIAL, variations with altitude of broadening of atmospheric trace gas absorption lines have been used by R. Seals et al., (Ref. 6) and R. Menzies et al., (Ref. 7).

The essence of the differences in SNR for DIAL and passive GFCR measurements will be examined. For DIAL with heterodyne and direct detection (Ref. 1) and (Ref. 3)

$$(\text{SNR})_{\text{HD}} = P_{ij} (\text{BTM})^{1/2} / (P_{ij} + \text{BT}) ; (\text{SNR})_{\text{DD}} = P_{ij} (\text{BT})^{1/2} / (\text{Noise Terms})^{1/2}$$

In addition to the standard detector, Poisson and background noises, the speckle noise P_{ij}^2/M is also included. The expectation value P of the number of photon per scattering cell at Range R is

$$P = \left[\eta \Gamma E \Delta r A \beta \exp \int_0^R (\sigma_p + \xi) dv \right] / h\nu R^2$$

The bandwidth is taken as the reciprocal of the pulse duration and T is the integration time. The quantity M , the number of coherence areas in the receiver area A can also be expressed as $M = (A \Omega_{\text{FOV}}) / (1.22 \lambda^2)$ where the optical throughput ($A \Omega_{\text{FOV}}$) is also a key quantity for passive sensors. For direct detection an increase in SNR by averaging over M uses a single detector, but for heterodyne detection a detector array is needed. Trade-offs for heterodyne and direct detection will be discussed.

For spacecraft DIAL the characteristic $1/R^2$ signal decay leads to high pulse energy laser requirements. This decrease is not present for passive sensors, but a much weaker signal dependence on the vertical variation in trace gas concentration exists which, however, has to be primarily considered for aircraft based GFCR (an altitude of 6 km will be used). For spacecraft based GFCR even this effect of range can be ignored and only the effect of a larger footprint for a given optical throughput ($A \Omega_{\text{FOV}}$) needs to be considered. The gas correlation filter of the GFCR has other beneficial characteristics. The theoretical radiometric signal at the detector can be expressed as (Ref. 2)

$$\Delta N = \int_{\Delta\nu} L_T(\nu) \left[\tau(\nu)_v - \tau(\nu)_g \right] A \Omega_{\text{FOV}} F T_0 d\nu$$

where $\tau(\nu)_v$ and $\tau(\nu)_g$ represent the monochromatic absorption through the vacuum and trace gas cells. The GFCR thus provides integration over many (1000 for CH_4 , 100 for CO) narrow

bandwidth absorption lines. The multi-wavelength effect also reduces the speckle noise by increasing the number of coherence time intervals within the integration time.

Finally, the state of the art of lasers and OPOs will be discussed. The best developed lasers with potential for spacecraft high pulse energy operation are the Tm:Ho doped lasers in the $\approx 2 \mu\text{m}$ region. While their output is in the region of comparatively weak H₂O vapor absorption lines, their reasonably large gain permits operation with moderately short Q-switched pulses and moderately high DIAL range resolution, without materials damage. The Tm doped ($^3\text{F}_4 - ^3\text{H}_6$) lasers can operate in the shorter $\approx 2 \mu\text{m}$ wavelength region of stronger H₂O vapor absorption lines, however, in view of their lower gain, longer pulses/lower range resolution results. Plans for future development of narrow bandwidth Tm:Ho:YLF lasers (Ref. 9) for feasibility evaluation of a spacecraft based Laser Wind Sounder (LAWS), which also could be used for DIAL will be discussed. In the $2 \mu\text{m}$ region for H₂O vapor DIAL as well as the $2.3 \mu\text{m}$ region for CH₄, CO room temperature Co:MgF₂ lasers which in view of their very low gain operate with longer pulses at higher pulse energies, again to avoid materials damage. Narrow bandwidth long normal mode pulses of 500 mJ at $\approx 2 \mu\text{m}$ and 300 mJ at $2.3 \mu\text{m}$ should be achievable (Ref. 8). Room temperature Tm:YLF ($^3\text{H}_4 - ^3\text{H}_5$) lasers show promise for the $2.3 \mu\text{m}$ region in view of their reasonably high gain, but their efficiency requires further evaluation (Refs. 10, 11). High gain lasing in the $2.3 \mu\text{m}$ region for new U³⁺:YLF lasers has recently been reported (Ref. 12). Studies to achieve high pulse energies with $2 \mu\text{m}$ laser pumped OPOs/OPAs for shifting to longer wavelengths (Ref. 13) will be discussed.

The comparison of laser DIAL and passive GFCR, including new technology developments, is being supported by the Director's Discretionary Fund at NASA Langley Research Center.

REFERENCES

1. P. Brockman, R. Hess, L. Staton, C. Bair: DIAL with Heterodyne Detection Including Speckle Noise: Aircraft/Shuttle Measurements of O₃, H₂O, NH₃ with Pulsed Tunable CO₂ Lasers, NASA Technical Paper 1725, 1980.
2. H. Reichle, H. Wallio, B. Gormsen: Feasibility of Determining Profile of Carbon Monoxide from Space Platform, Appl. Opt., Vol. 28, 1989, p. 2104.
3. R. Hardesty: A Comparison of Heterodyne and Direct Detection CO₂ DIAL Systems for Ground Based Humidity Profiling, NOAA Technical Memo, ERL, WFL-04, 1980.
4. N. Menyuk, D. Killinger: Ground Based Atmospheric Sensing of H₂O Vapor, HCl, CH₄ Using a Continuously Tunable Co:MgF₂ Laser, Appl. Optics, 1987.
5. D. Flanigan: Detection of Organic Vapors with Active and Passive Sensors: A Comparison, Appl. Opt., Vol. 25, 1986, p. 4253.
6. R. Seals, C. Bair: Analysis of Laser Differential Absorption Remote Sensing Using Diffuse Reflection from the Earth; 2nd Joint Conference on Sensing of Environmental Pollutants, 1973.
7. R. Menzies, M. Chahine: Remote Atmospheric Sensing with an Airborne Laser Spectrometer, Appl. Opt., vol. 13, 1974, p. 2840.
8. P. Moulton, Personal Communication.

9. G. Armagan, A. M. Buoncristiani, A. T. Inge, B. DiBartolo: Comparison of Spectroscopic Properties of Tm and Ho in YAG and YLF. Advanced Solid State Lasers Conf., 1991, p. 222.
10. M. D. Thomas, H. H. Zenzie, J. C. McCarthy, E. Chicklis: Tm:YLF at 2.31 μm ; ThJ5, CLEO, 1987.
11. P. C. Stoneman, L. Esterowitz: Tunable 2.3 μm Tm:LiYF₄ Laser. Tunable Solid State Lasers Conf. 1989, p. 154.
12. G. S. Quarles, L. Esterowitz, A. H. Rosenblatt, R. Uhron, R. F. Belt. Crystal Growth and Spectroscopic Properties of U³⁺:LiYF₄. Adv. Solid State Lasers Conf., 1992, WC5.
13. N. P. Barnes: Tunable Mid-Infrared Sources Using Second Order Nonlinearities; to be published in the International JI. of Nonlinear Optics..

Lidar multiple scattering: Dependence on atmospheric parameters**Matthias Wiegner****Meteorologisches Institut der Universität München****Theresienstr. 37, D-8000 München 2, Germany**

Backscatter lidars are very useful tools to gain information on the atmosphere. Inversion of backscatter signals can be used to retrieve the spatial distribution of clouds and aerosols, e.g. vertical extensions of clouds and aerosol layers, detection of 'subvisible' cirrus, etc., very accurately compared to passive radiometers.

To retrieve extinction coefficient profiles, in general, the so-called lidar equation is solved. This equation describes a laser pulse which propagates through an atmosphere with transmission $\exp\{-\int \sigma(z')dz'\}$, which is scattered singly under 180° towards a receiver, and which is attenuated on its way back again by $\exp\{-\int \sigma(z')dz'\}$. For inversion, further information on optical properties of the scatterers are required (extinction to backscatter ratio).

However, it is evident, that at least for optically thick clouds and/or large receiver's field-of-views this approach may be erroneous because of multiply scattered photons. Several studies have been performed to simulate multiple scattering in case of collimated beams or pulses including Monte Carlo, transport and diffusion theory. Unfortunately, most of the approaches require an enormous amount of computer time. Thus, it is meaningful to elaborate approximate methods, one of which is discussed in this paper.

Our model is based on Bissonnette (1988), see Echle (1991). We have improved the numerical simulation of limited field-of-view detectors, and compared the results to Monte Carlo calculations and an exact model of Altmann (1989).

Bissonnette's model is based on the time-independent radiation transfer equation (simulation of a cw laser). Fluxes into the forward and backward hemisphere – in respect to the initial direction of the beam – are calculated by applying the paraxial approximation. The radial flux densities are described analogously to molecular diffusion. The resulting differential equations are solved iteratively, but only the first iteration is considered. The power received by a limited field-of-view, on-axis and off-axis, is calculated by an empirical function. The atmosphere can be inhomogeneous along the direction of the initial beam.

The errors due to neglecting higher order iterations are estimated by checking for energy conservation. It can be shown that the second iteration concerns 'photons' which were backscattered twice or three times, constituting a contribution to the transmitted or backscattered flux density, respectively. In contrast, in the first iteration (used by Bissonnette) multiple backscattering is neglected.

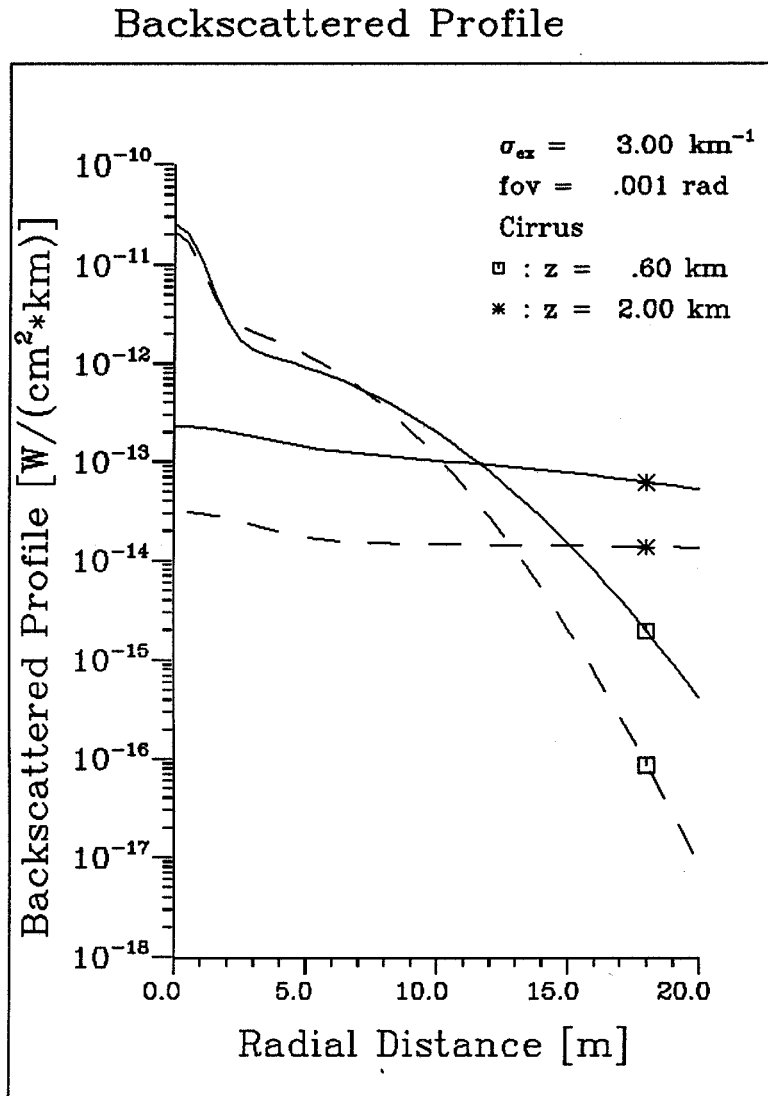


Figure 1: *Backscattered Profiles at $z = 0.6 \text{ km}$ (squares) and 2 km (asterisks) derived from Bissonnette's code (dashed) and the modified one (full line)*

Therefore, a comparison of the radiation budget of a non-absorbing cloud derived from the first and second iteration can be used to determine the accuracy of the numerical method. It was found that the errors increase with increasing optical depth τ and increasing

scattering into the backward direction. However, the errors are rather small: they are below 1 % for cirrus and stratus clouds if $\tau \leq 2.7$, and for a water cloud (C6) if $\tau \leq 7$.

The field-of-view functions are improved by the implementation of a more accurate numerical description of the backscattered flux density. This results in an increase of the backscattered intensity near the optical axis. A typical example of the radial distribution derived from the original and the modified algorithm is given in Fig. 1. In the case shown, a homogeneous 2 km thick cirrus cloud (extinction coefficient 3 km^{-1}), a receiver's field-of-view of 1 mrad, and a beam divergence of 1 mrad were assumed. Note, that a pulsed lidar is approximated by calculating the contribution of certain slabs around z to the total backscattered profile. Here, the backscatter signals from 0.6 km and 2.0 km are plotted.

In this paper the sensitivity of backscattered profiles on variations of different atmospheric and instrumental parameters such as field-of-view, phase function, and optical depth is discussed. Furthermore, comparisons with other models are shown to assess the applicability of the model to pulsed laser systems.

References

- K. Altmann (1989), *Forward scattering formula of Tam and Zardecki evaluated by use of cubic sections of spherical hypersurfaces*, Appl. Opt., **28**, 4077-4087.
- L.R. Bissonnette (1988), *Multiscattering model for propagation of narrow light beams in aerosol media*, Appl. Opt., **27**, 2478-2484.
- G. Echle (1991), *Numerische Modellierung der Mehrfachstreuung eines Laserstrahls*, Diplomarbeit, University of Munich, 101 pp., (unpublished).

Verification measurement of a polarization Raman elastic-backscatter lidar

Christoph Schulze, Ulla Wandinger, Albert Ansmann,
Claus Weitkamp, Walfried Michaelis
GKSS-Forschungszentrum, Postfach 1160, W-2054 Geesthacht, Germany

1 Introduction

By measuring the depolarization of light Raman scattered from a gas of known number density (e.g., nitrogen) it is possible to determine the influence of multiple scattering on lidar signals. In order to realize such measurements linearly polarized laser light is emitted and two components of the nitrogen Raman signals, with \mathbf{E} vectors parallel ($\parallel P_{\lambda_R}$) and perpendicular ($\perp P_{\lambda_R}$) to the plane of polarization of the laser light, are measured. The depolarization ratio $\delta_{\lambda_R} = \perp P_{\lambda_R} / \parallel P_{\lambda_R}$ is constant if only the Raman scattering process contributes to the signal. Any variation of the depolarization is caused by additional elastic, and thus multiple, scattering. If the contribution of multiply scattered light to the lidar signals is known other parameters determined with the system such as extinction, backscattering, and the depolarization of elastically scattered light, can be corrected for this influence.

The present paper describes the lidar system used for the polarization measurements, especially the receiver setup. The calibration of the apparatus and a clear air measurement are discussed. A more detailed description of the underlying idea and an actual cloud measurement are given in Ref. [1].

2 Apparatus

A XeCl excimer laser which emits light at 308 nm is used as the light source. Its beam passes a rotary-mounted polarizer and is then transmitted into the atmosphere with a divergence of 0.1 mrad. A 0.8-m diameter telescope collects the backscattered light and collimates it to a beam of 80 mm diameter which is coupled into a filter polychromator. This optical analyzer is developed to measure five backscatter signals simultaneously: the two polarization components of the elastically scattered light at 308 nm, the two polarization components of the light Raman scattered from nitrogen at 332 nm, and the water vapor Raman signal at 347 nm.

Specially designed beamsplitters and interference filters allow the separation of the different wavelengths and of the two polarization states with high efficiency. The geometric arrangement of the device is shown in Fig. 1.

Two lenses L1 and L2 reduce the beam diameter to 8 mm. With an exchangeable pinhole diaphragm D the receiver field of view can be varied between 0.1 and 0.5 mrad. A dichroic beamsplitter BS1 reflects more than 90 % of the elastically backscattered radiation at 308 nm and the Raman scattered light at 332 nm, while it transmits 86 % of the light Raman scattered by water vapor at 347 nm. The transmitted light is detected with the

photomultiplier tube PMT1 after passing an interference filter. A dielectrically coated polarizing beam splitter cube BS2 separates the two polarization components of both the 308-nm and the 332-nm light. The component polarized parallel to the plane of incidence (the laboratory plane) is transmitted, the component with polarization direction perpendicular to the plane of incidence is reflected. Two wedges of fused silica BS3 and BS4 reflect a small part of the light of the two beams (0.8% and 15%, respectively) to the photomultiplier tubes PMT2 and PMT4 in front of which 308-nm interference filters are mounted. The transmitted part of the light is used to measure the radiation Raman scattered from nitrogen with PMT3 and PMT5 which are equipped with 332-nm interference filters.

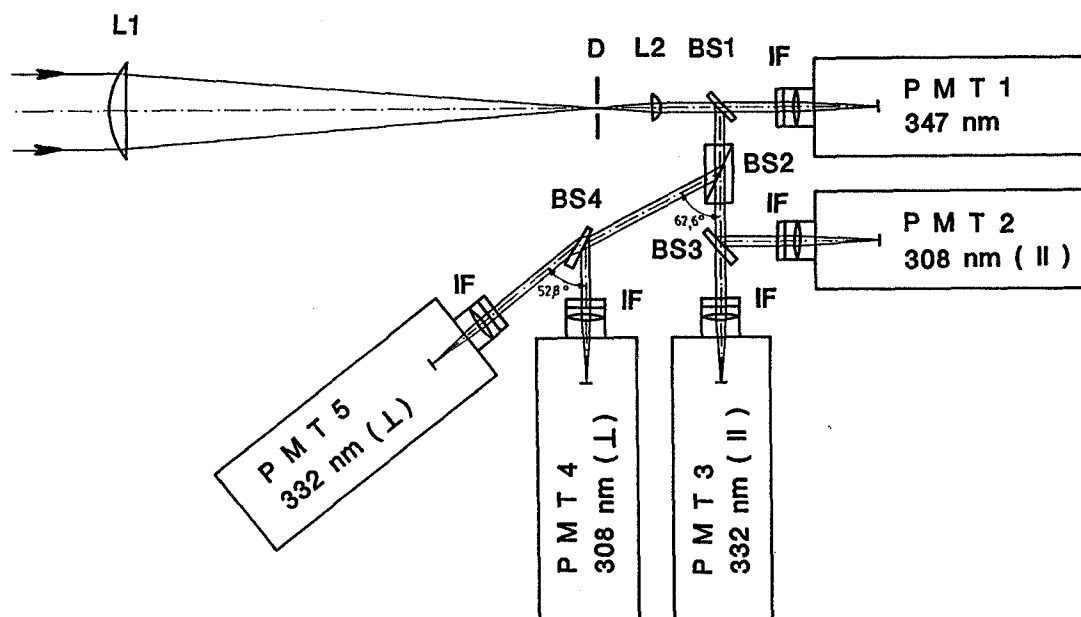


Fig. 1. Setup of the 5-channel filter polychromator. L1, L2 - lenses, D - entrance diaphragm, BS1 - dichroic beamsplitter, BS2 - polarizing beamsplitter, BS3, BS4 - fused silica wedges, IF - interference filters, PMT1-PMT5 photomultiplier tubes

The photomultiplier tubes are operated in the photon counting mode. Their dark currents are below one count per second. The pulses are converted to standard pulses with a discriminator and are registered in a 5-channel photon counting system at a maximum count rate of 300 MHz. Each signal can be recorded in 1024 time bins with a minimum width of 100 ns corresponding to 15 m range resolution. A broader description of the lidar is given, for example, in Ref. [2].

At present, the optical elements of the lidar are investigated in order to quantify the dependence of their transmission, reflection, and depolarization properties on wavelength, angle of incidence, and polarization state of the measured light. Independently, first atmospheric measurements were taken using a calibration measurement to eliminate the transmission properties of the apparatus.

3 Measurements

In order to determine depolarization ratios of the backscattered light at a certain wavelength the ratio of the transmission values of the two measurement channels must be known. A simple way to determine this ratio is to take a calibration measurement with unpolarized laser light. The height-independent calibration factor c_{λ_i} for the measurement wavelength λ_i is then given by the ratio of the two measurement signals

$$c_{\lambda_i} = \frac{\perp P_{\lambda_i}}{\parallel P_{\lambda_i}}. \quad (1)$$

$i=0$ and $i=R$ are used for the 308-nm and the 332-nm light, respectively. If linearly polarized laser light is emitted and the polarizer is rotated such that the plane of polarization of the outgoing radiation is parallel to the laboratory plane, the depolarization ratios of the backscattered light can be determined using calibration factor (1) and the measured signals:

$$\delta_{\lambda_i}(z) = c_{\lambda_i}^{-1} \frac{\perp P_{\lambda_i}(z)}{\parallel P_{\lambda_i}(z)}. \quad (2)$$

An example of a calibration measurement for a clear atmosphere is given in Fig. 2. On the left-hand side the measured lidar signals are shown, on the right-hand side the ratios of the two Raman and of the two elastic signals between ground and 15 km height can be seen. The height-independent calibration factors are $c_0 = 4.3$ and $c_R = 0.57$ except for altitudes below 1.5 km where the overlap between laser beam and receiver field of view is not complete.

Fig. 3a shows the lidar signals measured in a cloud-free atmosphere with linearly polarized laser light. The depolarization ratios calculated after Eq. (2) and shown in Fig. 3b agree very well with the theoretically expected depolarization ratios of 0.094 for pure nitrogen Raman scattering and 0.016 for pure Rayleigh scattering and indicate thus a clean atmosphere and a measurement system free from major systematic errors.

References

1. U. Wandinger, A. Ansmann, C. Weitkamp, W. Michaelis, "Measurement of multiple scattering effects with a polarization Raman elastic-backscatter lidar", this conference
2. A. Ansmann, M. Riebesell, U. Wandinger, C. Weitkamp, E. Voss, W. Lahmann, and W. Michaelis, "Combined Raman elastic-backscatter lidar for vertical profiling of moisture, aerosol extinction, backscatter, and lidar ratio", Applied Physics B 54 (1992), in press

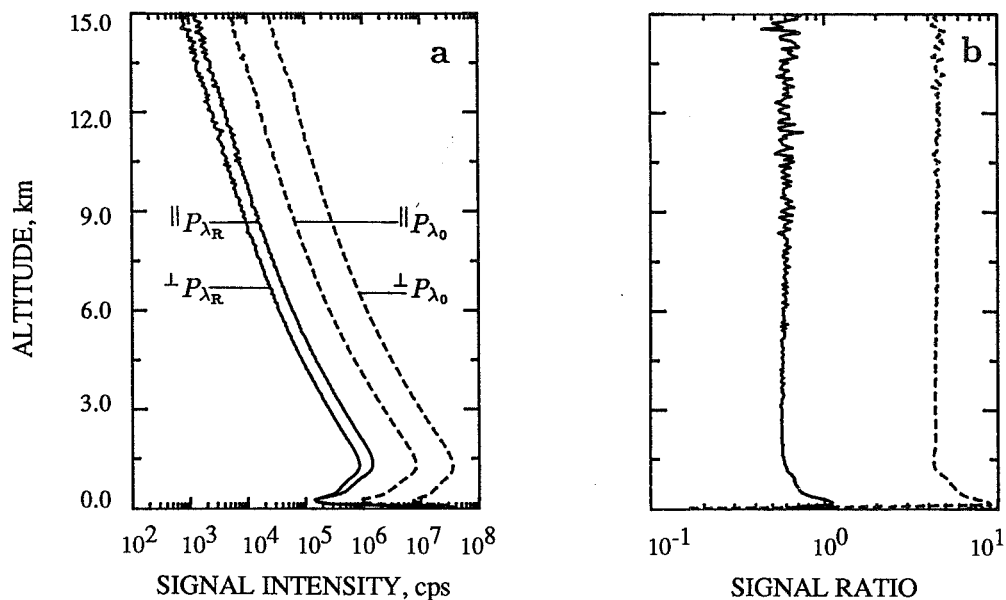


Fig. 2. Calibration measurement: a. Raman nitrogen signals (solid lines) and elastic backscatter signals (dashed lines) for unpolarized emitted laser light, b. ratios of the Raman signals (solid line) and of the elastic backscatter signals (dashed line). 240,000 laser shots are averaged. The range resolution is 60 m.

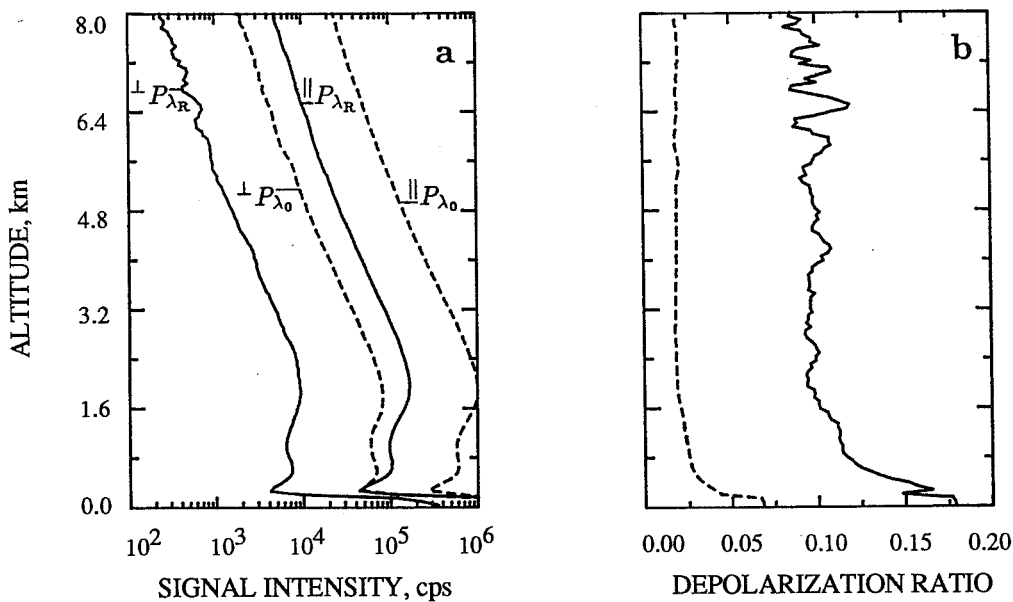


Fig. 3. Clear air measurement: a. Raman nitrogen signals (solid lines) and elastic backscatter signals (dashed lines) for linearly polarized emitted laser light, b. Raman depolarization ratio (solid line) and elastic depolarization ratio (dashed line). 120,000 laser shots are averaged. Signals are smoothed with a sliding average length of 300 m.

Time and Polarization Dependent Double Scattering Calculations of Lidar Returns from Water Clouds*

R.C. Garner, PhotoMetrics, Inc., Woburn, MA 01801

We describe and present results of a double scattering lidar model which we use to calculate lidar returns from water clouds. The model is used in conjunction with the Air Force Phillips Laboratory's (Geophysics Directorate) low altitude Nd:YAG lidar system to determine microphysical properties of water clouds. In a related presentation we discuss and show results of the use of the model with lidar measurements.

The model determines the Stokes parameters of the backscattered lidar radiation, from media composed of spherical particles, as a function of time. The approach is similar to that given in Reference 1, although the method of calculation is different, as we discuss below. The Stokes parameters of the radiation of the lidar return are determined, at each time, by considering all radiation which has traveled the same path length from transmitter to receiver while making two successive single scatters. Each single scatter is considered a Mie scatter. We have also developed a Mie scattering program for use with the double scattering model. Each single scatter takes into account the polarization of the incident and scattered radiation.

Inputs to the double scattering model include the receiver area and field of view, the receiver integration time, the extinction coefficient as a function of distance into the cloud, the particle size distribution (assumed independent of position), and the complex index of refraction of the spherical particles. Unlike Reference 1, the laser radiation is assumed to have zero divergence. This simplification reduces the number of numerical integrations that need to be performed from five to three and allows the calculation to run on an 80386 computer in a reasonable amount of time, which we discuss below. It is a good approximation if the receiver field of view is much greater than the laser divergence.

The degree of polarization, calculated from the Stokes parameters, is a useful concept for characterizing the radiation of the lidar return. When the radiation of the lidar transmitter is completely polarized (i.e., degree of polarization of one) then any particular set of double scatters will leave the radiation in a definite polarization state, although in general different from the transmitter radiation. Depolarization is due to the fact that the return radiation is the incoherent sum of many individual components, all of which are in definite, although different, polarization states. Because of the azimuthal symmetry of the lidar problem, the polarized part of the return radiation has the same polarization state as the transmitter radiation.

Description of Model

The geometry of the situation is shown in Figure 1. At $t = 0$ a laser pulse with zero pulse width is sent out from the origin of the coordinate system along the z axis. The divergence is assumed zero although the radiant intensity (power per steradian) is P_o/Ω_l , where P_o is the power and Ω_l is the true laser divergence. As the pulse propagates its power is diminished by any nonzero extinction coefficient along the path. At position \mathbf{R}_1 the radiation is scattered. The scattering angle is θ_1 and the scattering plane is at an angle ϕ from the x axis.

*Work Supported by the Air Force Phillips Laboratory, Geophysics Directorate, Hanscom AFB, MA.

The scattered radiation propagates in the direction of \mathbf{R}_2 . Its power is again diminished by nonzero extinction along the path. At position $\mathbf{R} = \mathbf{R}_1 + \mathbf{R}_2$ the radiation scatters a second time. The scattering angle is θ_2 . Because we are only interested in radiation that can get back to the receiver, the second scattering plane is the same as the first. Furthermore, we only consider second scattered radiation for which the angle θ is within the receiver's field of view.

The Stokes vector of the (differential amount of) radiation which returns to the receiver after scattering at differential volumes dV_1 and dV_2 is

$$d\mathbf{I}_r = \frac{A_r \alpha_1 \alpha_2 e^{-\tau} dV_1 dV_2}{16\pi^2 R_1^2 R_2^2 R^2 \Omega_l} \bar{\mathbf{L}}(-\phi) \bar{\mathbf{P}}(\theta_2) \bar{\mathbf{P}}(\theta_1) \bar{\mathbf{L}}(-\phi) \mathbf{I}_i \quad (1)$$

where A_r is the receiver area, α_i is the extinction coefficient at differential volume dV_i , τ is the total optical path length, and $\bar{\mathbf{P}}(\theta_i)$ is the phase matrix for scattering angle θ_i . The phase matrix is the scattering matrix with $\sigma_i/4\pi$ factored out, where σ_i is the total scattering cross section. \mathbf{I}_i and \mathbf{I}_r are the initial and final Stokes vectors respectively. The Stokes vectors and scattering matrices are written in the representation $(I_{\parallel}, I_{\perp}, U, V)$. In Equation 1 the Stokes parameters (i.e., the components of the Stokes vector) have units of power. Ω_l is the laser divergence. If we assume $dV_1 = \Omega_l R_1^2 dR_1$ then Ω_l is cancelled out. This is effectively the zero laser divergence assumption. All rays from the laser at all angles are treated as if they travel along the axis.

$\bar{\mathbf{L}}(-\phi)$ is a rotation matrix which describes the transformation of the Stokes vector due to a rotation of the coordinate system by an angle $(-\phi)$ in the clockwise direction (viewed in the direction of propagation) [2]. The matrix $\bar{\mathbf{L}}(-\phi)$ is necessary because the phase matrix is defined in terms of the scattering plane. That is, incident and scattered radiation must be represented by vectors with components perpendicular and parallel to the scattering plane. The rightmost $\bar{\mathbf{L}}$ matrix in Equation 1 represents a rotation of the incident Stokes vector to the scattering plane. The leftmost $\bar{\mathbf{L}}$ matrix represents a rotation of the final Stokes vector of the return radiation back to the original coordinate system. Note that the two rotations have the same angle $(-\phi)$ instead of opposite angles (as might be expected for the two rotations to be in opposite directions). There is an additional sign change of the angle because the radiation scattered from volume dV_2 travels in a direction with a negative z component.

During one detector integration time (Δt) from t to $t + \Delta t$ the total received radiation is the sum of all single and double scattered radiation which travel distances between ct and $c(t + \Delta t)$. The radiation which single scatters does so between distances $ct/2$ and $c(t + \Delta t)/2$. For the double scattered radiation, the set of all second scatters which follow the same first scatter at position \mathbf{R}_1 lie between two ellipses of revolution. Both ellipses have as foci the origin and the first scatter location. The major axis of the inner ellipse is $R + R_2$. The major axis of the outer ellipse is $R + R_2 + c\Delta t/2$.

The total received radiation during one detector integration time is the integral of Equation 1 over R_1 and V_2 (i.e., a quadruple integral), with the proper boundaries on each of the four variables. The four variables that we choose to integrate over are R_1 , θ_1 , R_2 , and ϕ . We note that the choice of variables in Reference 1 are R_1 , θ , R , and ϕ . With our choice of variables there is a nonintegrable singularity at $R = 0$ which is never encountered because the lower boundary of the cloud is always at $R > 0$. For the choice of variables in Reference 1 the nonintegrable singularity occurs for $R_2 = 0$, which is encountered during the course of integration. Of course, this singularity occurs at a point where the two double

scatters coalesce to a single scatter. Therefore, there are physical arguments which can be made to remove it.

The integral in ϕ can be performed analytically. The variable ϕ only appears in the rotation matrices \bar{L} . The other three integrals cannot be performed analytically. If the laser radiation is assumed linearly polarized in the x direction (which we also call the parallel direction), then the integration of Equation 1 over ϕ gives $U = 0$ and $V = 0$. This indicates that the polarized portion of the received radiation is linear and in the same direction as the laser radiation. This we expect from symmetry arguments.

The first two components of the Stokes vector of the radiation received in the time interval between t and $t + \Delta t$ are

$$\begin{bmatrix} I_{\parallel}(t) \\ I_{\perp}(t) \end{bmatrix} = \frac{A_r P_o}{16\pi^2} \int_{z_o}^{ct/2} dR_1 \int_0^{\theta_{1h}(R_1)} \sin \theta_1 d\theta_1 \int_{R_{2l}(\theta_1, R_1)}^{R_{2h}(\theta_1, R_1)} dR_2 \frac{\alpha_1 \alpha_2 e^{-\tau}}{R^2(R_1, \theta_1, R_2)} \times \begin{bmatrix} \frac{3\pi}{4} (K(\theta_1)K(\theta_2) + L(\theta_1)L(\theta_2)) - \frac{\pi}{2} (M(\theta_1)M(\theta_2) - N(\theta_1)N(\theta_2)) \\ \frac{\pi}{4} (K(\theta_1)K(\theta_2) + L(\theta_1)L(\theta_2)) + \frac{\pi}{2} (M(\theta_1)M(\theta_2) - N(\theta_1)N(\theta_2)) \end{bmatrix}. \quad (2)$$

K , L , M , and N are the four nonzero components of the Mie scattering phase matrix written as

$$\begin{bmatrix} K & 0 & 0 & 0 \\ 0 & L & 0 & 0 \\ 0 & 0 & M & N \\ 0 & 0 & -N & M \end{bmatrix}. \quad (3)$$

We numerically integrate Equation 2 on an 80386 based computer (33 MHz and with a coprocessor) using a Romberg integration routine. A calculation of the parallel and perpendicular components of the received radiation for one detector integration time takes approximately five seconds.

Figure 2 shows a sample calculation. For this calculation the lower boundary of the cloud is at 1 km. The extinction coefficient, constant throughout the cloud, is 10 km^{-1} . The particle size distribution is

$$f(x) = A \left(\frac{x}{10} \right) e^{-x/10} \quad (4)$$

where $x = 2\pi r/\lambda$ is the size parameter and A is the normalization constant such that $\int_0^{\infty} f(x) dx = 1$. The index of refraction of the particles is $1.33 + i10^{-6}$. The detector integration time is 100 nsec (15 m of length for the single scatter situation). The receiver aperture diameter is 15 cm and its field of view is 10 mrad (full angle).

References

1. Q. Cai and K. Liou, "Theory of Time-Dependent Multiple Backscattering from Clouds," *J. Atmos. Sci* **38**, 1452-1465, (1981).
2. S. Chandrasekhar, "Radiative Transfer," Oxford University Press, London and New York (1950), and Dover, New York (1960).

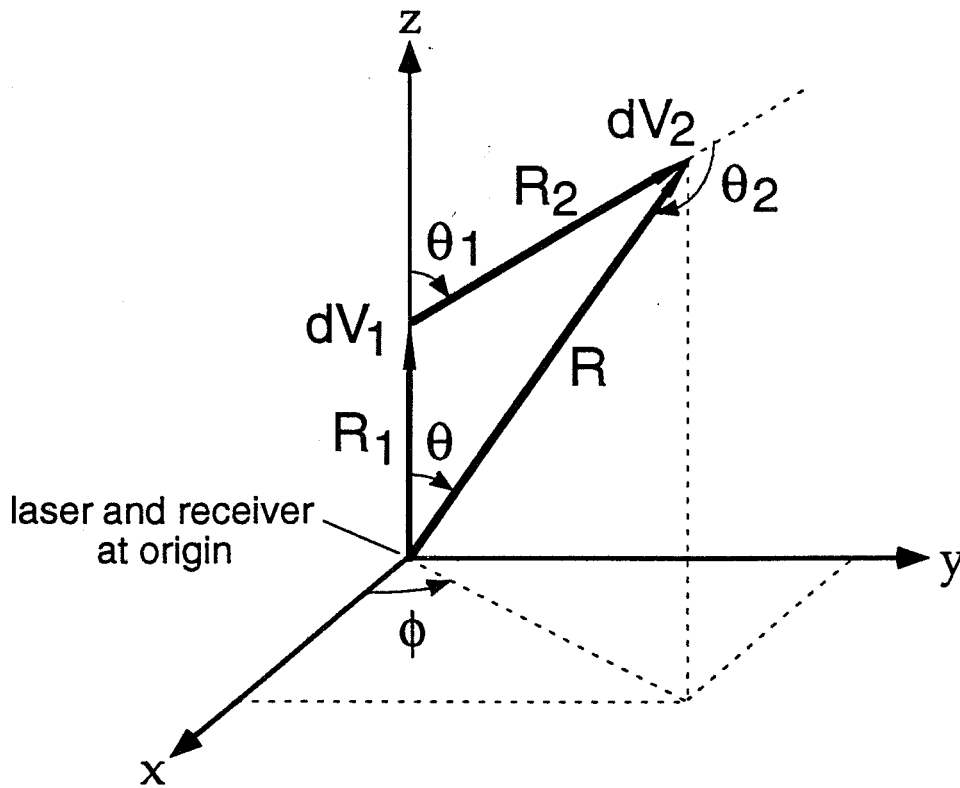


Figure 1: Geometry of double scattering.

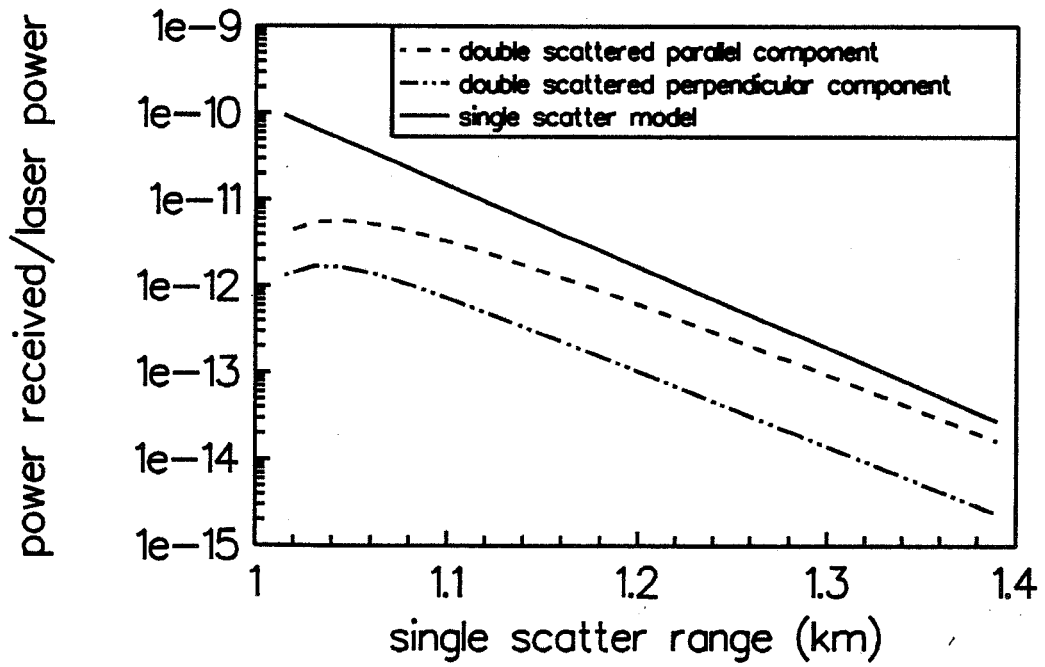


Figure 2: Sample calculation.

Multiple scattering wavelength dependent backscattering of kaolin dust in the I.R. : measurements and theory

Avishai Ben-David

Science and Technology Corporation, Edgewood, Maryland 21040

1. Introduction:

Knowing the optical properties of aerosol dust is important for designing electro-optical systems and for modeling the effect on propagation of light in the atmosphere. As CO₂ lidar technology becomes more advanced and is used for multiwavelength measurements¹, information on the wavelength dependent backscattering of aerosol dust particles is required. The volume backscattering coefficient of aerosols in the I.R. is relatively small. Thus, only a few field measurements of backscattering, usually at only a few wavelengths, are reported in the literature.

In this paper we present spectral field measurements of backscattering of kaolin dust in the 9-11 μm wavelength range. As the quantity of dust increases, multiple scattering contributes more to the measured backscattered signal. The measurements will show the effect of the dust quantity on the spectral backscatter measurements. A simple analytical two stream radiative transfer model² is applied to confirm the measurements and to give insight to the multiple scattering spectra of backscattering.

2. Experiment and theory:

In this experiment the CO₂ lidar system transmitted two groups of wavelengths at a repetition rate of 10 groups per second. Each group contained 10 wavelengths spaced at intervals of 10 ms. The laser beam divergence is 3 mrad, pulse width is 1 μs , detector time constant is 0.4 μs , electronic bandwidth of 5 MHz, sampling rate of 50 MHz, and receiver field of view of 8 mrad. A detailed description of the CO₂ lidar system is given by Ben-David et al.¹ A hard target made of sand blasted aluminum (4m X 4m) was placed at a distance of 1280 m from the lidar and aerosol dust cloud of width (5-10m) was dispersed at a distance 740m from the lidar (i.e. 540 m in front of the target).

Acquisition time for the 20 wavelength measurements, took less than one second. The aerosol cloud was dispersed continuously and with a wind velocity of 1.5 m/s a steady flow of aerosol dust traversed the laser beam. The kaolin dust was pre-analyzed for its size distribution function and all large particles were removed to create a well mixed dust.

For the kaolin dust aerosol size distribution used in this experiment the largest size parameter is less than 4, and most particles have a size parameter less than 0.3. Therefore, Mie theory, which applies to spherical particles, can be used for calculating scattering properties from irregularly shaped dust particles. The wavelength dependent complex refractive indices for the kaolin dust were taken from Powell et al.³

We use a two stream model (van de Hulst², ch. 14) where the scattering is divided into strictly forward and backward scattering (i.e. transforming a 3-D problem to a 1-D problem). This model is for a steady state illumination and not for a time dependent source of incident radiation. A radiative transfer problem is considered to be at a steady state if the source of radiation remains constant in the time required for a photon to transverse the

scattering medium (i.e. there is sufficient time to establish a steady state). In our experiment the cloud depth is 5-10m, thus it takes a photon about 30ns to transverse the medium, while the laser pulse is of a length of 1000ns). Therefore, approximating the time dependent radiative transfer problem with a steady state assumption is reasonable. We use the model to study, qualitatively, the spectral backscattering of a multiple scattering problem.

The parameters of the model are the single scattering albedo $a(\lambda)$, the asymmetry parameter $g(\lambda)$, and the total optical depth $\tau(\lambda)$ of the aerosol size distribution. The probabilities for the scattering process are given by: $p(\lambda)=a(\lambda)[1+g(\lambda)]/2$ for a forward scattering, $q(\lambda)=a(\lambda)[1-g(\lambda)]/2$ for a backward scattering and by $1-a(\lambda)$ for an absorption. Using van de Hulst notations $UR(\tau,a,g)$ is the reflected fraction of flux and $UT(\tau,a,g)$ is the transmitted fraction of flux.

Fig. 1 shows the reflected flux UR computed from the kaolin aerosol dust parameters, for a layer with a spectral optical depth $\tau(\lambda)$ with different values for the maximum value of $\tau(\lambda)$. For a layer with a maximum optical depth larger than 20 the reflected flux is independent of τ (i.e. practically an infinitely thick layer). The figure shows that as the optical depth increases and therefore the multiple scattering contribution to UR increases, the wavelength response of $UR(\lambda)$ changes and is shifted from the $9\ \mu\text{m}$ wavelength region to the $10\ \mu\text{m}$ wavelength region. From the figure we can see two distinct classes of the wavelength dependent backscattered flux. The first for a "thin" layer ($\tau < 5$) and the second for a "thick" layer ($\tau > 5$). The change of the wavelength dependent backscattered flux can be qualitatively explained by noting that the single scattering optical depth peaks at about $9.5\ \mu\text{m}$ but the fractional of absorption ($1-a$) in the $9\ \mu\text{m}$ wavelength range is much larger (factor 2) than the fractional absorption in the $10\ \mu\text{m}$ wavelength region. Therefore, one can expect a multiple scattering and absorption processes to deplete more photons from the $9\ \mu\text{m}$ wavelength region than at the $10\ \mu\text{m}$ wavelength region. As a result the spectral fractional reflected flux will shift its peak to the $10\ \mu\text{m}$ with increasing multiple scattering (i.e. increased optical depth). The effective normalized optical depth $-\ln[UT]=\tau^*$ which can be viewed as the effective optical depth of a layer with an optical depth τ due to the multiple scattering contribution to the transmitted flux is practically independent of wavelength (not shown). It can be explained by the fact that scattering in the forward direction is much less sensitive to the refractive index of the aerosols than scattering in the backward direction.

3. Measurements

Among the 20 wavelengths we chose wavelengths for ozone DIAL detection and water vapor DIAL detection in the $9\ \mu\text{m}$ and the $10\ \mu\text{m}$ wavelength region. These wavelengths were used to check the consistency and accuracy of the lidar measurements. From the reference measurements (before dust dissemination) the partial pressure of the water vapor was computed to be 4.1 mb from (9R14,9R12) wavelength pair, 4.3 mb from (10R20,10R18) pair and 4 mb from (10R20,10R22) pair. A meteorological station located a few hundred meters from the site measured 5.3 mb (Temp= $16^\circ\ \text{C}$). Ozone concentration was computed from the wavelength pair (9P14,9P22) to be 34 ppb. AFGL atmospheric model for a midlatitude summer predicts 33.4 ppb at a height of 1 km. These measurements

show that the lidar system produced reliable measurements throughout the 9-11 μ m wavelength region and serve as reference measurements for calibrating the effect of atmospheric transmission on the kaolin dust backscattering and target reflectance measurements (i.e. a two way path through the aerosol cloud).

Figs. 2 and 3 show the wavelength dependence of the normalized backscattered signal from a "thin" and "thick" kaolin dust cloud respectively, for different cloud optical depth τ^* . The optical depth τ^* was determined from the two way transmission measurements through the cloud (i.e. backscattered from the target which was taken simultaneously with the backscattered from the cloud) and the target reference measurements. In these figures the peak value of the wavelength dependent cloud optical depth $\tau^*(\lambda)$ is given to indicate how "thick" the cloud was during the 20 wavelengths measurements. The theoretical curve (triangle symbol), computed from the radiative transfer model (Fig. 1), is computed for a "thin" layer ($\tau=0.5$) for Fig. 2, and for a "thick" layer ($\tau=20$) for Fig 3.

Fig. 4 shows the backscattered signals for a transition stage between a "thin" and a "thick" cloud. The theoretical curve (triangle symbol), computed from the radiative transfer model, is computed for a layer with optical depth $\tau=5$, which is chosen to represent the transition between "thin" and "thick" layer in the model (Fig. 1). The wavelength dependence of the effective optical depth of the dust cloud measured from the target for all clouds "thin" and "thick" kaolin dust exhibit similar shape (not shown).

It must be noted that the range of available measurements is limited in practice. As the cloud thickness increases the measured signal from the target decreases rapidly (for example for $\tau=1.3$, $\exp[-2\tau]=0.07$) and so does the signal to noise ratio (SNR) of the measurements. For a very "thin" cloud the SNR of the backscatter signal from the dust cloud will be small. Figs. 2-4 show a good qualitative agreement with the simple two stream radiative transfer model and demonstrate the different backscatter spectral response due to multiple scattering.

Acknowledgements:

This work was performed in the U.S. army at the Chemical Research and Development Center (CRDEC) Edgewood MD, and was supported under grant number DAAA15-89-D-0007. The author would like to thank Mr. Fran D'Amico off CRDEC for data acquisition software development; Mr. Bob Knap and Dr. Silvio Emery of CRDEC for their help in designing the lidar pointing mechanism and for Mr. Steve Gotoff and Felix Reyes of CRDEC for their technical support.

References

1. A. Ben-David, S.L. Emery, S.W. Gotoff and F. D'Amico "A high PRF, multiple wavelength, pulsed CO₂ lidar system for atmospheric transmission and target reflectance measurements" was accepted for publication in Appl. Opt. (1992)
2. D. Powell Walter, D. Cooper, J.E. vander Laan and E.R. Murray, " Carbon dioxide laser backscatter signatures from laboratory-generated dust" Appl. Opt. 25, 2506-2513, (1986).
3. H.C van de Hulst " Multiple light scattering tables, formulas and application" ,Academic Press, New-York (1980).

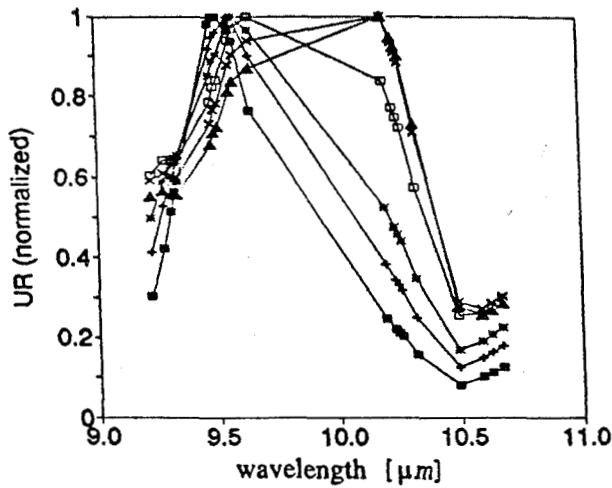


Fig. 1 - Reflected fraction of flux for a layer with spectral optical depth normalized to the following values; 0.1 (filled square symbol), 1 (plus symbol), 2 (astrix symbol), 5 (empty square symbol), 10 (x symbol), 20 (triangle symbol).

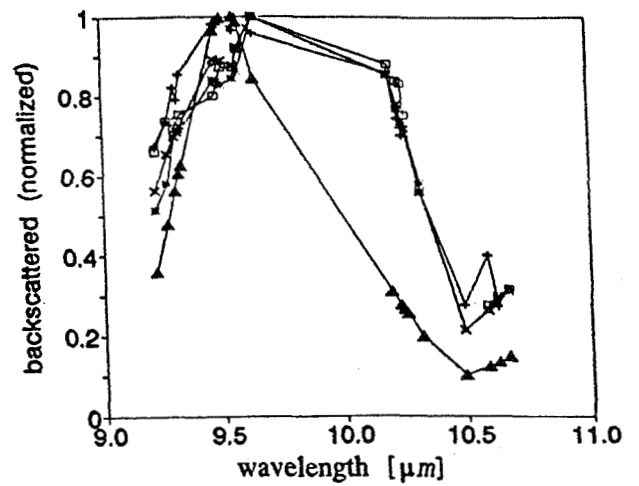


Fig. 2 - Measurements of backscattering from a "thin" kaolin dust cloud with a maximum spectral effective optical depth of the following values; 0.24 (x symbol), 0.43 (plus symbol), 0.44 (astrix symbol), 1.0 (square symbol). Model (triangle symbol).

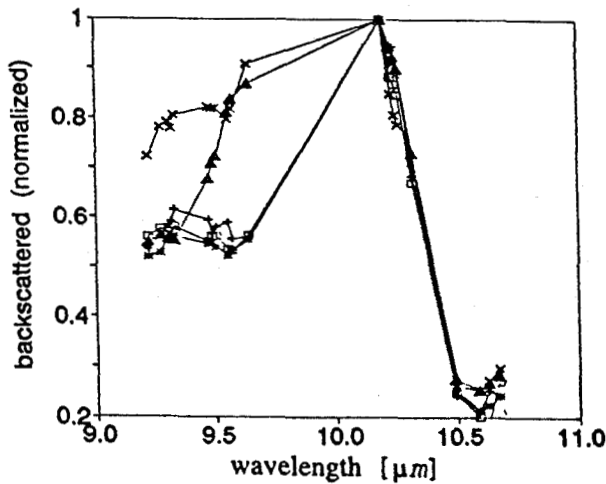


Fig. 3 - Measurements of backscattering from a "thick" kaolin dust cloud with a maximum spectral effective optical depth of the following values; 1.3 (x symbol), 1.8 (plus symbol), 2 (astrix symbol), 2.3 (square symbol). Model (triangle symbol)

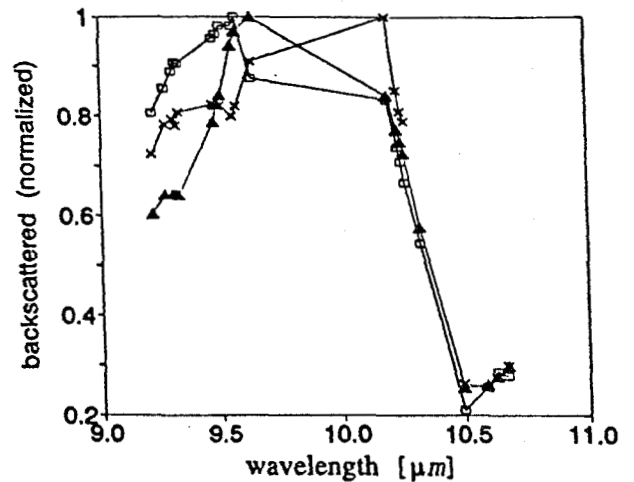


Fig. 4 - Measurements of backscattering for a transition stage between a "thin" to a "thick" kaolin dust cloud with a maximum spectral effective optical depth of the following values; 1.13 (square symbol), 1.27 (x symbol). Model (triangle symbol)

**Aureole Lidar:
Design, Operation, and Comparison with In Situ Measurements**

William P. Hooper
Remote Sensing Division
Naval Research Laboratory
Washington DC 20375-5000
and

D.R. Jensen
Ocean and Atmospheric Sciences Division
Naval Command and Control Ocean Systems Command
San Diego, Ca 92152-5000

In 1986, H. Gerber and one of us (Hooper) examined the signals that could be detected by an airborne lidar flying above the marine boundary layer (mbl). One signal (aureole) formed from laser light returned to the receiver after undergoing a reflect off the ocean and forward scatter off the aerosol particles appeared both be detectable and related to the optical depth of the mbl.^{1 2} Now research has been directed towards developing a practical instrument to measure the aureole and finding mathematical algorithm to use the information.

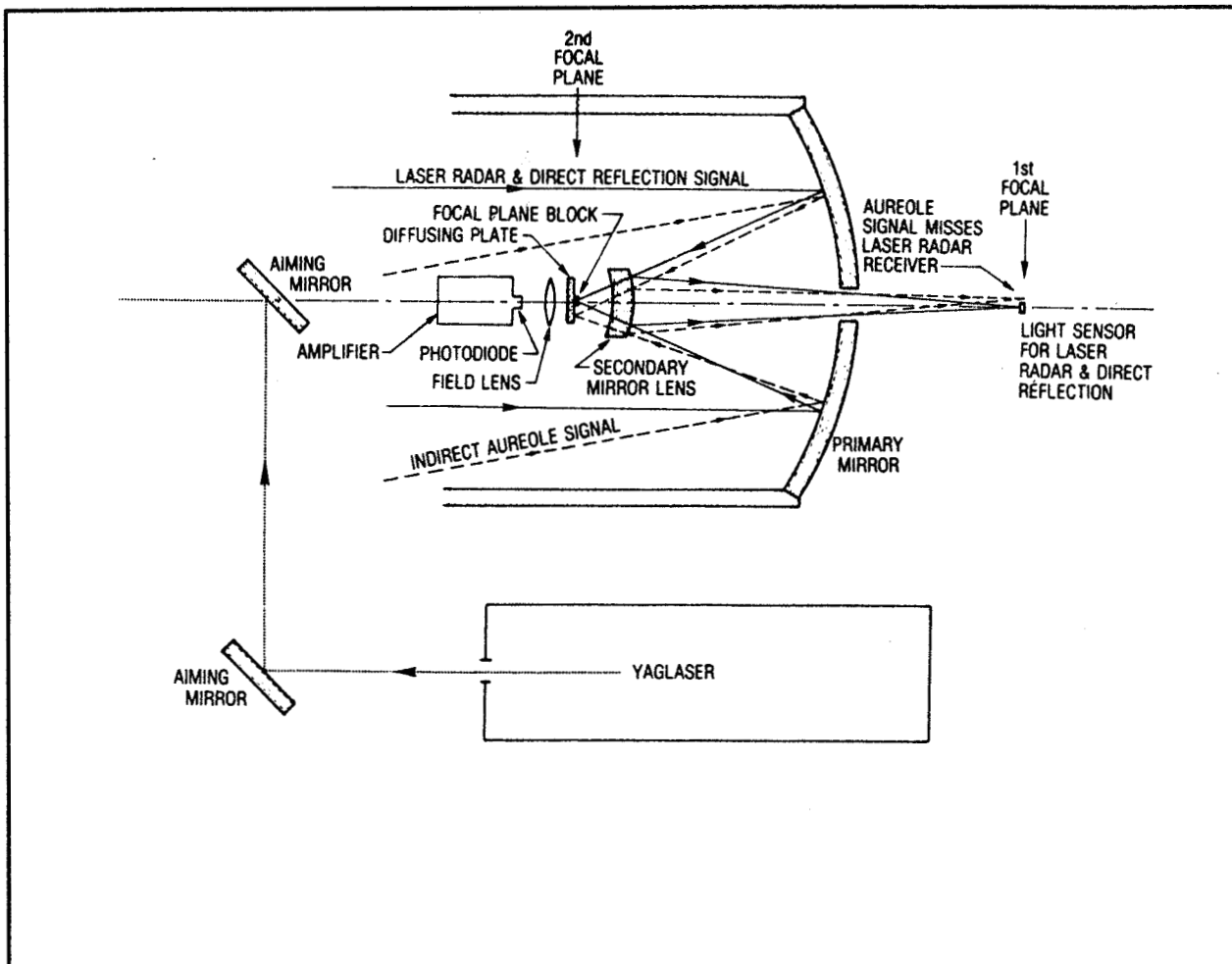
Unlike the lidar backscatter which typically requires a telescope with a narrow field of view (0.5 mrad), the aureole signal occurs over a wide field of view (50 mrad). To accommodate the total different needs, a standard commercial Cassegrainian telescope was modified to yield a telescope with two focal planes (see the figure on the next page). The secondary mirror was replaced by a lens, whose front surface was half silvered and curved to match the replaced mirror. Light reflecting off the lens focused behind the primary mirror. The back lens surface was curved to allow unreflected light to focus at the natural focus of the primary mirror. This focal plane which is behind the lens has a wide field of view.

To calculate an extinction profile, the aureole optical depth estimate is combined with the lidar backscatter profile. Assuming a constant backscatter to extinction ratio, the lidar equation can be converted into a Bernoulli differential equation. Using the logarithm of the range correct lidar signal (S) and an optical depth (τ) constraint, the extinction profile becomes:

$$\sigma(r) = \frac{(1 - e^{-2\tau}) e^{S(r)}}{2 \left[\int_{r'=r_0}^{r_m} e^{S(r')} dr' - (1 - e^{-2\tau}) \int_{r'=r_0}^r e^{S(r')} dr' \right]} \quad (1)$$

where σ is extinction, and r is range with r_0 and r_m being the near and far field range limits.

The aureole lidar (flown in a Navy P-3) and NCCOSC aerosol analysis system (flown in a twin engine Navajo) participated in the Key 90 experiment off the Florida Keys. The Navajo combined straight low level flight segments with profiles, while the P-3



straight low level flight segments with vertical profiles, while the P-3 flew along a race track flight path above the experimental site. Data comparison suggests that the accuracy of the aureole extinction profiles is excellent when the backscatter to extinction ratio is constant and poor when the ratio varies.

Even though both the aureole lidar and inversion appears to work, the sensitivity of this analysis to variation in the backscatter to extinction ratio must be reduced before the aureole lidar can routinely measure extinction profiles. The sky noise detected by the aureole sensor must also be reduced. Despite these problems, the agreement between the lidar and in situ observations is encouraging and suggests that further measurements of mbl should be made.

1. W.P. Hooper and H.Gerber, "Down looking lidar inversion constrained by ocean reflection and forward scatter of laser light, Appl. Opt.25,689-697(1986).

2. W.P. Hooper and H. Gerber, "Monte Carlo simulations of laser-generated sea surface aureole," Appl. Opt.27,5111-5118(1988).

EFFECT OF ATMOSPHERIC EXTINCTION ON LASER RANGEFINDER PERFORMANCE
AT 1.54 AND 10.6 μm

D.L. Hutt*, J.-M. Thériault**, V. Larochelle and D. Bonnier

Defence Research Establishment Valcartier
P.O. Box 8800 Courcellette, Québec, Canada, G0A 1R0

* Also with: COPL, Equipe laser et optique guidée
Dep. Physique, Université Laval, St. Foy, Québec, Canada, G1K 7P4

** Also with: CIMSS, Space Science and Engineering Center,
U. Wisconsin-Madison 1225 West Dayton St., Madison, Wisconsin, 53706

Extinction of laser rangefinder (LRF) pulses by the atmosphere depends on the wavelength, weather conditions and aerosol concentration along the optical path. In the IR, extinction is due to absorption by molecular constituents and scattering and absorption by aerosols. The total atmospheric extinction $\alpha(\lambda)$ is the sum of the molecular and aerosol contributions, $\alpha_m(\lambda)$ and $\alpha_a(\lambda)$. We present simple expressions for $\alpha_m(\lambda)$ and $\alpha_a(\lambda)$ for two LRF sources; Er:Glass and CO₂ which operate at 1.54 and 10.6 μm respectively. The expressions are based on accepted models of atmospheric aerosols and molecular extinction and give an estimate of $\alpha(\lambda)$ as a function of standard meteorological parameters, assuming horizontal beam propagation. Signal-to-noise ratios of LRF returns measured from a reference target under different weather conditions are compared to predictions based on the estimated $\alpha(\lambda)$.

Molecular Extinction

We evaluated the molecular extinction coefficient using the FASCOD2 computer code (Refs. 1-3). $\alpha_m(1.54\mu\text{m})$ was found to be no greater than 0.02 km^{-1} using the mid-latitude summer model at high values of absolute humidity, therefore it can be neglected compared to the aerosol extinction coefficient at 1.54 μm .

Near 10.6 μm , the molecular extinction is due primarily to absorption by the H₂O continuum and is therefore well correlated with the absolute humidity. There is also a small contribution due to CO₂. Using FASCOD2, the molecular extinction coefficient in the spectral range 10.57 to 10.62 μm was calculated for temperatures between -20° and 30° C, relative humidity between 35% and 100% and an altitude of sea level. The mid-latitude winter model was used for temperatures below 0° C while the mid-latitude summer model was used for 0° C and above. The spectral range includes the three primary lines at which a pulsed CO₂ laser operates. These are the P-18, P-20 and P-22 lines at 10.571, 10.591 and 10.611 μm , respectively. It was found that the extinction coefficient was the same for the three lines to within 5% over the full range of temperatures and humidities investigated, therefore we can neglect the effect of the distribution of the laser pulse energy among the three lines and take the extinction for the P-20 line to be representative.

Figure 1 shows the molecular extinction coefficient for the P-20 line plotted as a function of absolute humidity $W(\text{g/m}^3)$, which is given by

$$W(\text{g/m}^3) = HAe^{(18.9766-14.9595A-2.4388A^2)} \quad [1]$$

In Eq. 1, H is the relative humidity expressed as a number between 0 and 1 and $A = 273.15/(273.15+T)$, T being the ambient temperature in degrees centigrade. A least squares fit to the FASCOD2 results shown in Fig. 1 yields:

$$\alpha_m(10.6 \mu\text{m}) = 0.02554 + 0.01058W + 4.856 \times 10^{-4}W^2 \quad [2]$$

The first term in Eq. 2 represents the average contribution of CO_2 while the second and third terms represent contributions of an H_2O line near 944.8 cm^{-1} and the H_2O continuum, respectively. The correlation coefficient of Eq. 2 is 0.998.

Aerosol Extinction

The visibility or meteorological range V , is a good indicator of the visible extinction coefficient due to absorption and scattering by aerosols. The relationship between the visibility and the visible extinction coefficient α_v , is given by Koschmeider's law as $\alpha_v = 3.0/V$, where we have assumed a 5% threshold for visual contrast (Ref. 4). The aerosol extinction coefficient, $\alpha_a(\lambda)$ may be derived from α_v using Mie theory if the size distribution and complex index of refraction of the aerosols is known. We have used the aerosol models of Shettle and Fenn (Ref. 5) to derive approximate relationships between α_v and $\alpha_a(\lambda)$.

Figure 2 shows $\alpha_a(\lambda)$ plotted as a function of α_v for the maritime and rural models of Ref. 5 at eight relative humidities between 10 and 99%. These models represent atmospheric conditions ranging from very clear air to thick haze. The figure shows that there is good correlation between the visible and IR extinction coefficients. A least squares power law fit yields the following relationships:

$$\alpha_a(1.54 \mu\text{m}) = 0.314\alpha_v^{1.11} \quad [3]$$

$$\alpha_a(10.6 \mu\text{m}) = 0.082\alpha_v^{1.01} \quad [4]$$

The correlation coefficients for Eqs. 3 and 4 are better than 0.992.

Equations 3 and 4 are valid for visibilities greater than about two kilometers. For visibilities less than two kilometers, the aerosol may be considered fog. The water droplets in fog are much larger than the aerosols in the maritime and rural models used above. In the visible and IR, the Mie extinction efficiency of these large droplets is a complicated function of wavelength. Therefore, the relationship between $\alpha_a(\lambda)$ and α_v depends greatly on the details of the droplet size distribution and simple generalizations such as Eqs. 3 and 4 are inappropriate. Since molecular extinction can be neglected for $1.54 \mu\text{m}$, the aerosol extinction coefficient given by Eq. 3 may be taken to be the total atmospheric extinction coefficient. For $10.6 \mu\text{m}$, the total extinction is the sum of $\alpha_m(10.6\mu\text{m})$ and $\alpha_a(10.6\mu\text{m})$ given by Eqs. 2 and 4.

Measurements

The voltage signal-to-noise ratio S of a direct detection LRF return is given by (Ref. 6)

$$S = KR^{-2}\rho\gamma e^{-2\alpha R}, \quad [5]$$

where R is the range, ρ the diffuse reflectivity of the target, γ the spillover factor and K a system constant that depends on the characteristics of the LRF source, receiver and detector. Measurements of S were made for LRFs at 1.54 and 10.6 μm over a range of 1.3 km for different weather conditions. K , ρ and γ were known quantities and their determination is discussed in Ref. 6. The values of S that were recorded are plotted as a function of α in Figs. 3 and 4 where α was estimated using Eqs. 2 and 4. The curves in Figs. 3 and 4 are the signal-to-noise ratios calculated with Eq. 5 using the values of K , ρ and γ for each LRF. The agreement between the measured S and that given by Eq. 7 is fairly good, indicating that the estimates of α are reasonable. There are many possible sources of experimental error such as the values of K , ρ and γ used in Eq. 5 and the measurement of the meteorological parameters. Large errors may be assumed in the estimated values of aerosol extinction because the visible extinction coefficients used in Eqs. 3 and 4 were determined from observer estimates of visibility.

Although both Er:Glass and CO₂ LRFs are quite eyesafe, Er:Glass systems are becoming more attractive because the laser is solid-state and a cooled detector is not required. The expressions for atmospheric extinction presented here are useful for predicting the relative performance of 1.54 and 10.6 μm LRFs.

References

1. Clough S.A., Kneizys, F.X., Rothman, L.S. and Gallery, W.O., "Atmospheric spectral transmittance and radiance: FASCOD1B", Proc. SPIE, Vol. 277, pp.152-166 (1981)
2. Ridgway, W.L., Moose, R.A. and Cogley, A.C., "Atmospheric Transmittance/Radiance Computer Code FASCOD2", AFGL-TR-82-0392, (1982).
3. Clough S.A., Kneizys, F.X., Shettle, E.P. and Anderson, G.P. , "Atmospheric transmittance/radiance computer code FASCOD2", Proc. 6th Conference on Atmospheric Radiation, Williamsburg, Va. (American Meteorological Society), 1986.
4. McCartney, E.J., Optics of the Atmosphere, (John Wiley & Sons, New York, 1976),p.42.
5. Shettle, E.P. and Fenn, R.W., "Models for the aerosols of the lower atmosphere and the effects of humidity variations on their optical properties", AFGL-TR-79-0214, (1979).
6. Larochelle, V., Bonnier, D., Hutt, D. L. and Thériault, J-M, "1.54/10.6 μm eyesafe laser rangefinders under adverse weather conditions", submitted to Infrared Physics.

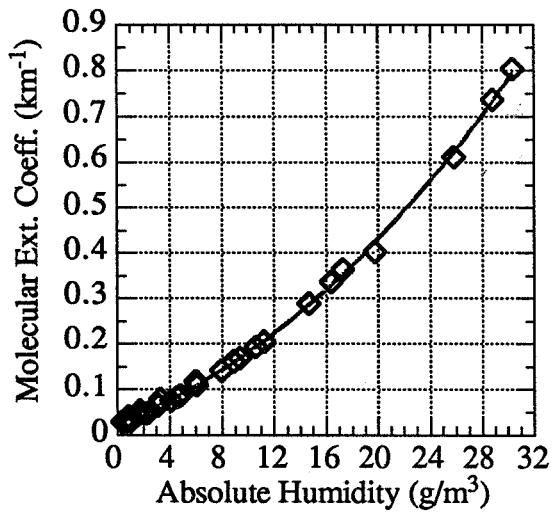


Fig. 1 Molecular extinction at 10.6 μ m from FASCOD2 (Refs. 1-3).

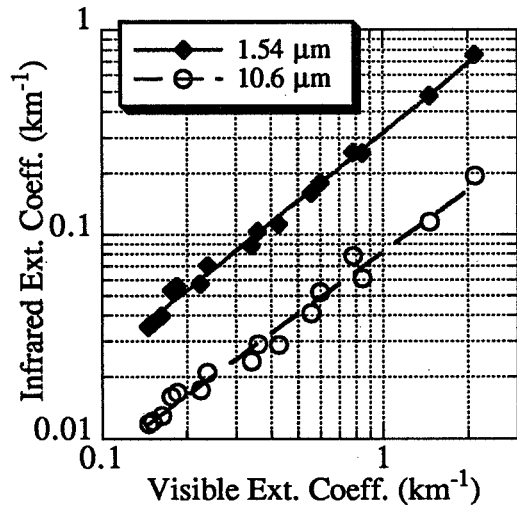


Fig. 2 Aerosol extinction from rural and maritime models of Ref. 5.

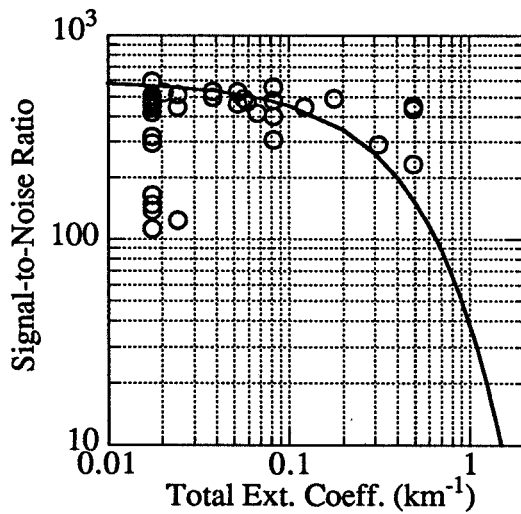


Fig. 3 Measured S/N ratio for Er:glass LRF.

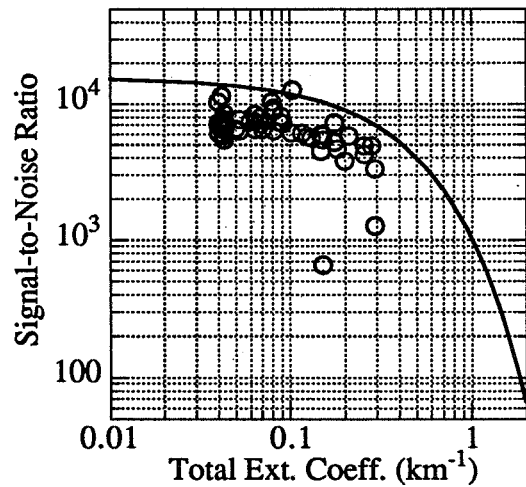


Fig. 4 Measured S/N ratio for CO2 LRF.

A STUDY OF ATMOSPHERIC OPTICAL SCATTERING PARAMETERS AT 1.5 AND 2 MICRON REGION FOR SOLID STATE DOPPLER LIDAR APPLICATIONS

Eli Margalit, Farzin Amzajerdian & Rodney Benoist
Litton Industries, Inc., Aero Products Division
6101 Condor Drive, Moorpark, California 93021, U.S.A.

and

Richard Dubinsky
Sky Council, 689 Indian Road, 3rd Floor
Toronto, Ontario, Canada, M6P 2E1

EXTENDED ABSTRACT

The increasing interest in the development of an eye-safe, solid state, Doppler Lidar for avionic applications has created the need for a quantitative evaluation of atmospheric effects on performance. Theoretical calculations have been completed for optical scattering parameters to be compared with the field measurements. Computer codes have been developed for the required calculations and designed to be interactive and user friendly in order to support comparison with experimental results and thus provide the basis for evaluation of eye-safe Doppler lidar over a wide range of atmospheric conditions and geographical locations. A Holmium Doppler Lidar operating at $2.09 \mu\text{m}$ has been constructed for atmospheric backscattering, attenuation and wind velocity measurements.

Theoretical calculations and field studies have been performed for backscatter coefficients $\beta(\pi)$, attenuation coefficients σ , and the backscatter phase function $P(\pi)/4\pi$, at 1.54, 2.02 and $2.09 \mu\text{m}$ through a midlatitude atmospheric model. The selected wavelengths correspond to Er:glass, Tm:YAG and Tm,Ho:YAG solid state lasers that are suitable for use in an eye-safe Doppler lidar system.

The aerosol models utilize two extreme size distributions [1] for the calculations: Haze L - Continental, and R-H-Stratospheric size distributions. These size distributions are applied to different aerosol models. These models include: Marine - Sea Salt / Coastal Model, Dust - Continental, Urban - Industrial, and Water Soluble Aerosols. Additionally, calculations have been performed for polydisperse cloud, fog, rain, ice crystal and snow models. Based on the estimates of σ and $\beta(\pi)$, relative backscatter strengths at all three laser wavelengths are discussed for most scattering media considered. Sample numerical results are compiled as shown in Table 1 and Figure 1 which represent a small part of many data sets.

Table 1 represents portions of a data set based on the Marshall-Palmer analytical relation [2,3] describing the rain drop size distribution. This relation was adapted for these calculations with the rain rate varying from 5 to 80 mm/hr to cover a range of rain from light shower to heavy rain. The column headings include the scattering parameters σ , $P(\pi)/4\pi$ and $\beta(\pi)$ along with the rain rate R_r , liquid water content C and number density of particles No . The values in table 1 are presented for $1.54 \mu\text{m}$ and $2.09 \mu\text{m}$ [4].

Figure 1 exemplifies the variation of the lidar backscatter functions F_1 and F_2 at $1.54 \mu\text{m}$ and $2.09 \mu\text{m}$ wavelengths respectively for a 100 m laser pulse penetration in rain as a function of the rainfall rate. The lidar backscatter function is equivalent to the range corrected backscatter signal. The curves shown are part of the considerably interesting results in the relative contributions of the backscatter functions for a lidar at near infrared wavelengths. These results have been implemented in the development of a model that predicts the Lidar performance in terms of signal to noise ratios as a function of altitude and range. Figure 2 describes one example of the projected Doppler Lidar performance in clear air as a function of altitude for the $2.02 \mu\text{m}$ and $2.09 \mu\text{m}$ wavelengths.

Figure 3 illustrates the Doppler lidar constructed at Litton Aero Products Division (APD) using a solid state Cr,Tm,Ho:YAG laser. The laser source consists of a diode-pumped continuous wave master oscillator (MO) and a flash-lamp pumped, pulsed, ring slave laser combined in an injection seeding configuration.

A portion of the 30 mw MO output is diverted to be used as the local oscillator (LO) and the remainder is injected into the slave laser. Injection seeding causes the slave laser to generate pulses of approximately 10 mj output energy and 300 ns pulsewidth at the single frequency established by the MO. The transmitted laser output and backscatter return signals utilize a single 15 cm off-axis parabolic telescope for heterodyne detection. The detector output is bandpass filtered, amplified, digitized and processed in real time to determine the Doppler frequency. The frequency spectrum is displayed for each return signal from a transmitted pulse before further processing and analysis.

Preliminary atmospheric measurements using the holmium Doppler lidar have been performed from the roof-top test site at APD. A sandblasted aluminum target has been installed at about 850 meters from the lidar for calibration purposes. To minimize the effect of the atmospheric turbulence, the target has been installed on the side of a hill such that most of the propagation path is tens of meters above the ground. The intent is to gather a substantial amount of atmospheric data at $2.09 \mu\text{m}$ wavelength under various meteorological conditions. This data will be used for comparison with the calculated results of the corresponding aerosol, rain, fog and snow models.

The results of the calculations supported by field measurements provide the means for reliable analytical evaluation of an eye-safe, solid state Doppler Lidar over a wide range of meteorological conditions and geographical locations.

The authors would like to thank Dr. Shiv Pal (York University, Toronto, Canada) for his significant contributions and valuable discussions related to this work.

References:

1. Dubinsky, R.N., and Pal, S.R., (1989), *Determination of Backscatter Coefficients $\beta(\pi)$ at 1.54 and $2.09 \mu\text{m}$ for Atmospheric Aerosol and Molecular Models*, Contract # APC 217598 Report, for Litton Aero Products, by Sky Council, Toronto, Canada.
2. Marshall, J.S., and Palmer, W. McK., (1948), *The Distribution of Raindrops with Size*, J. Met. Amer. Met. Soc., Boston Mass. 5, 165.

3. Zardecki, A., and Tam, W.G., (1982), *Multiple Scattering Corrections to the Beer-Lambert law. 2: Detector with a Variable Field of View*, App. Opt., 21,2413.
4. Pal, S.R., and Dubinsky, R.N., (1991), *Calculation of Atmospheric Optical Scattering Parameters $[\sigma, \beta(\pi), P(\pi)/4\pi]$ at 1.54 μm and 2.09 μm Laser Wavelengths*, Contract # APC 223993, Report for Litton Aero Products, by Sky Council, Toronto, Canada.

Table 1. Scattering parameters at various rainfall rate for 1.54 μm and 2.09 μm wavelengths

R_f mm/hr	C g/m ³	N_0 m ⁻³	σ_s km ⁻¹	σ_p km ⁻¹	$P(\pi)/4\pi$ sr ⁻¹	$\beta(\pi)$ km ⁻¹ sr ⁻¹
$\lambda = 1.54 \mu\text{m}$						
5.	0.3609	.2046E+04	.9551	1.0512	.1051E-01	.1004E-01
10.	0.6460	.2470E+04	1.457	1.626	.8848E-02	.1290E-01
15.	0.9081	.2749E+04	1.865	2.098	.8001E-02	.1492E-01
20.	1.1563	.2963E+04	2.221	2.514	.7451E-02	.1655E-01
25.	1.3947	.3138E+04	2.542	2.893	.7052E-02	.1793E-01
30.	1.6255	.3288E+04	2.8389	3.2440	.6743E-02	.1914E-01
35.	1.8502	.3419E+04	3.1163	3.5743	.6493E-02	.2024E-01
40.	2.0698	.3536E+04	3.3782	3.8875	.6285E-02	.2123E-01
45.	2.2851	.3642E+04	3.6272	4.1865	.6107E-02	.2215E-01
50.	2.4965	.3739E+04	3.8653	4.4734	.5953E-02	.2301E-01
55.	2.7046	.3829E+04	4.0940	4.7499	.5817E-02	.2382E-01
60.	2.9097	.3913E+04	4.3144	5.0171	.5696E-02	.2458E-01
65.	3.1120	.3991E+04	4.5276	5.2762	.5587E-02	.2530E-01
70.	3.3118	.4065E+04	4.7342	5.5281	.5489E-02	.2598E-01
75.	3.5094	.4135E+04	4.9349	5.7733	.5398E-02	.2664E-01
80.	3.7048	.4201E+04	5.1304	6.0126	.5316E-02	.2727E-01
$\lambda = 2.09 \mu\text{m}$						
5.	0.3609	.2046E+04	0.5777	1.051	.1225E-02	.7074E-03
10.	0.6460	.2470E+04	0.8861	1.626	.1225E-02	.1085E-02
15.	0.9081	.2749E+04	1.139	2.099	.1225E-02	.1396E-02
20.	1.1563	.2963E+04	1.362	2.516	.1225E-02	.1668E-02
25.	1.3946	.3138E+04	1.564	2.895	.1226E-02	.1917E-02
30.	1.6254	.3288E+04	1.752	3.247	.1226E-02	.2147E-02
35.	1.8500	.3419E+04	1.928	3.577	.1226E-02	.2364E-02
40.	2.0695	.3536E+04	2.095	3.891	.1226E-02	.2569E-02
45.	2.2845	.3642E+04	2.255	4.190	.1226E-02	.2765E-02
50.	2.4957	.3739E+04	2.408	4.477	.1226E-02	.2952E-02
55.	2.7035	.3829E+04	2.555	4.754	.1226E-02	.3133E-02
60.	2.9082	.3913E+04	2.697	5.021	.1226E-02	.3308E-02
65.	3.1102	.3991E+04	2.835	5.280	.1227E-02	.3478E-02
70.	3.3095	.4065E+04	2.970	5.532	.1227E-02	.3643E-02
75.	3.5066	.4135E+04	3.100	5.777	.1227E-02	.3803E-02
80.	3.7014	.4201E+04	3.228	6.017	.1227E-02	.3960E-02

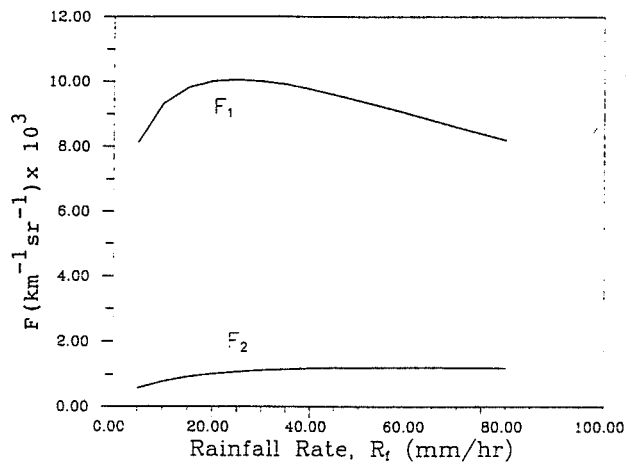


Figure 1. The Backscatter functions F1 and F2 at 1.54 μm and 2.09 μm wavelengths for a 100 m laser pulse penetration in rain at various rainfall rates, R_f .

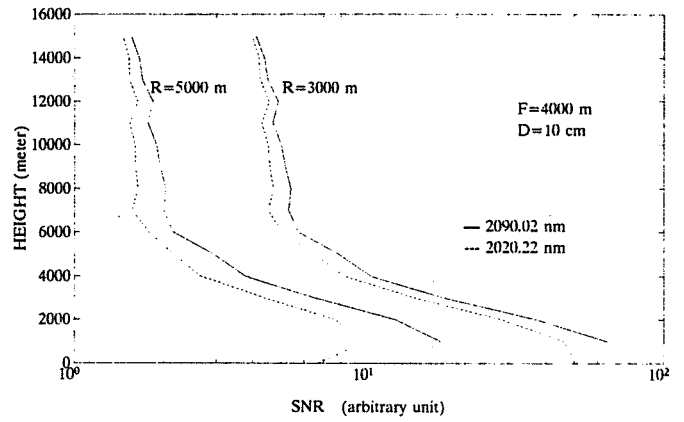


Figure 2. Doppler Lidar performance using Haze I - continental aerosol and midlatitude summer model at 2.02 and 2.09 micron.

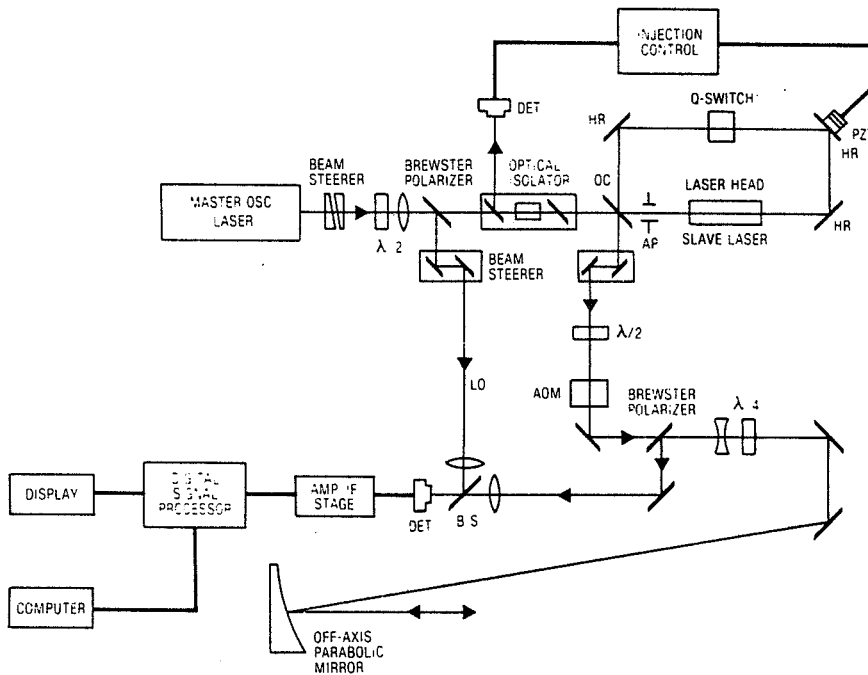


Figure 3. Doppler Lidar schematic

A CABLE DETECTION LIDAR SYSTEM FOR HELICOPTERS

Benoist GROSSMANN, Alain CAPBERN, Martin DEFOUR and Rémi FERTALA

Thomson-TRT Defense
78283 Guyancourt - France

Helicopters in low-level flight are endangered by power lines or telephone wires, especially when flying at night and under poor visibility conditions.

In order to prevent "wire strike", Thomson has developed a lidar system consisting of a pulsed diode laser emitting in the near infrared region ($\lambda=0.9 \mu\text{m}$). The HOWARD (Helicopter Obstacle WARNING and Detection) system utilizes a high repetition rate diode laser (PRF=20 KHz) along with counter-rotating prisms for laser beam deflection with a total field of view of 30° . This system was successfully field tested in 1991. HOWARD can detect one inch wires at ranges up to 200 meters. We are presently in the process of developing a flyable compact lidar system capable of detection ranges in the order of 400 meters.

We first conducted wire reflectance measurements in the $1.06 \mu\text{m}$ wavelength region. Absolute measurements were obtained by using a reference reflectance standard. Investigations were done for a variety of wires and cables at different angles of incidence (up to 50°). We have represented in Fig.1 our measurements. The laser cross section or reflectance is typically seven times lower at 50° incidence angle as compared to normal incidence. Therefore, wires at high incidence angles will lead to a somewhat measurable return signal. No significant differences were observed between wet and dry cables. For comparison, the reflectivity curve will be much narrower for the millimeter wavelength region.

These reflectance measurements were then used to design an obstacle avoidance system. We have used a diode laser (Laser diode, Inc.; model LT-201) with the following specifications: PRF = 20 KHz, energy per pulse = $5 \mu\text{J}$, peak power = 100 W, $\lambda = 904 \text{ nm}$, pulse duration = 50 ns, divergence = 3 mrad. We have made

theoretical computations and found that detection ranges of 200 meters could be obtained for a "standard cable" by using a 50 mm diameter receiver and a silicon avalanche photodiode. The standard cable consists of a wet aluminum cable steel reinforced 25 mm diameter cable oriented at incidence angle of 60°.

We have used counter-rotating prisms to scan the laser beam in a field of view of 30°. The scan pattern is shown in Fig.2. Since the HOWARD targets are long, one-dimensional elements (i.e., wires, antennas, poles), they can be detected with a low density scan geometry. The high PRF of the laser enables us to have a frame time of one second while maintaining a contiguous scan with a large overlap between laser pulses (the angular separation between two laser pulses is 1 mrad to be compared with a laser beam divergence of 3 mrad). The range measurements were then carried out by using a modulation domain analyzer (HP53310A). The data processing was done with an external HP computer. Each return signal above a specified threshold generates a pixel on the display. We have obtained detection ranges of 200 meters for the standard cable.

We have then developed algorithms capable of distinguishing the desired class of "thin" targets from the ground and other massive objects appearing in the image. The target thickness can be inferred through range data information. We have represented in Fig.3 a photography corresponding to the system field of view (30°). One can see a cable across the picture. We have shown in Fig.4 the data points associated with "thin" targets. The ground or other massive objects return signals have been eliminated by the algorithm. The pixels in Fig.4 correspond to the intersection of the cable with the scan pattern shown in Fig.2. The straight line was then obtained with a simple linear least-squares fit.

We have demonstrated that a diode-laser based lidar system could be used for an obstacle avoidance system. The present system can be upgraded by increasing the diode laser average power in order to improve the detection ranges and the frame time. We are currently in the process of developing a flyable compact lidar system capable of detection ranges of 400 meters.

WIRE REFLECTANCE

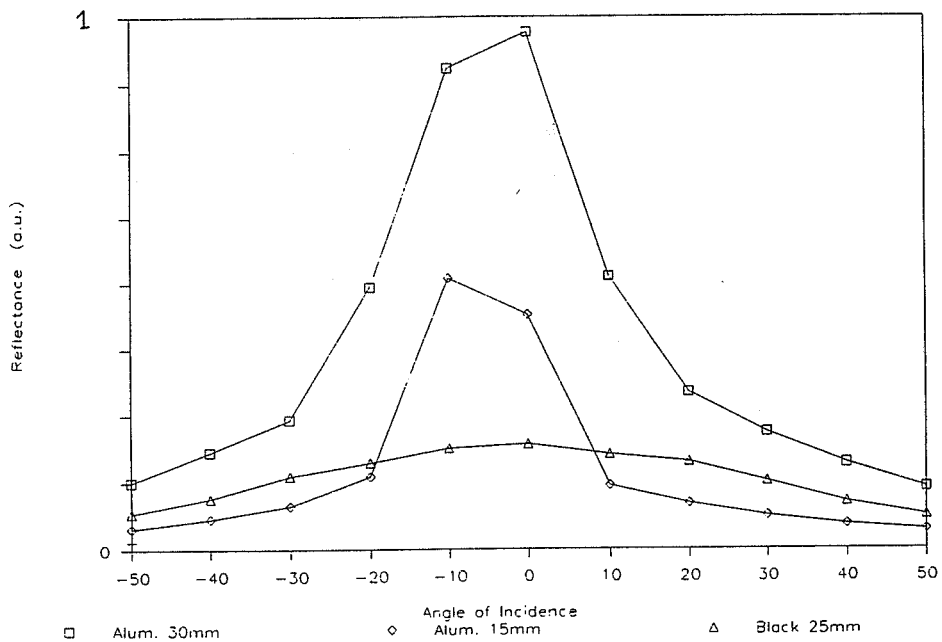


Fig.1: Wire reflectance measurements for a variety of wires at different angles of incidence.

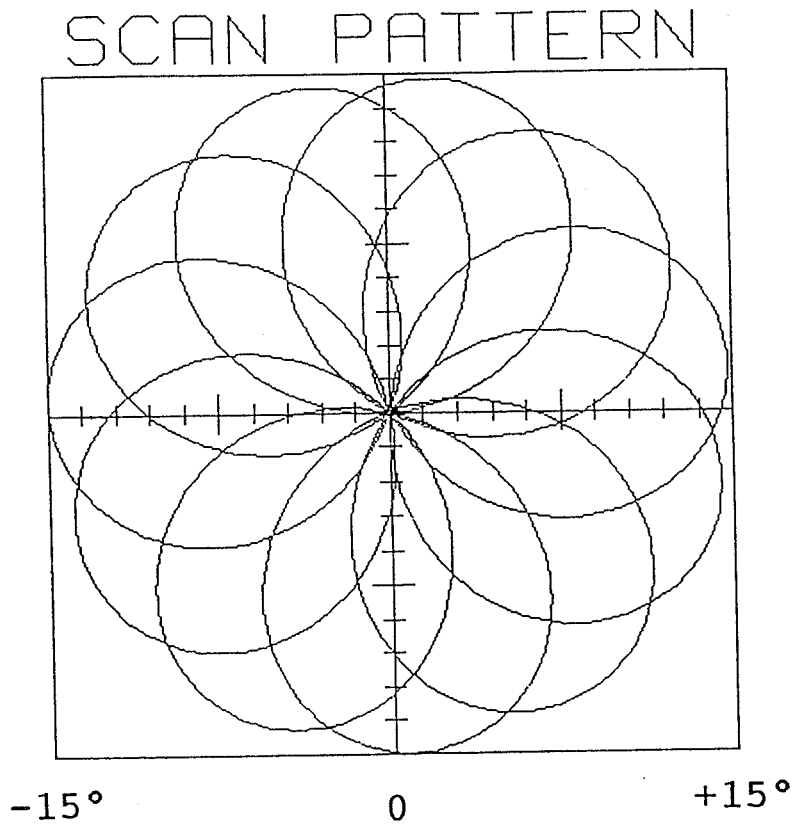


Fig.2: Scan pattern obtained with counter-rotating prisms.



Fig.3: Photography corresponding to the system field of view. One can see a cable across the picture.

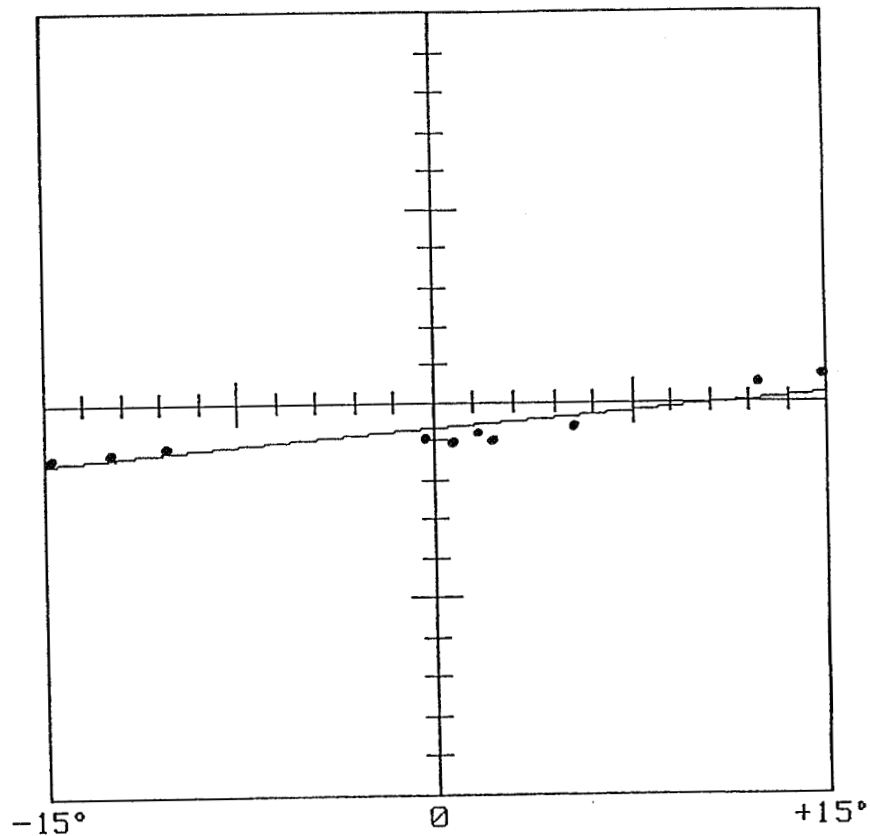


Fig.4: Data points associated with "thin" targets. The straight line is a result of a simple linear least-squares fit.

LIDAR ANALYSIS TECHNIQUES FOR USE IN THE ATMOSPHERIC BOUNDARY LAYER

William E. Eichinger, Daniel I. Cooper, Doug Hof, David Holtkamp,
Robert Quick, Jr., Joe Tjee, and Robert Karl

Los Alamos National Laboratory, MS D449, Los Alamos, NM 87545

There is a growing body of observational and theoretical evidence which suggests that local climate characteristics are associated with variations in the earth's surface [1], [2], [3]. The link between surface variability and local-scale processes must be made if we are to improve our understanding of the feedback mechanisms involved in surface-atmospheric dynamics. However, to understand these interactions, the surface-atmosphere interface must be studied as a large-scale spatial system.

Lidars are ideal tools to study the spatial properties of the atmosphere. The techniques described here were developed for use with the Los Alamos Water Raman-Lidar [4], but are applicable to many other types of lidars. This paper will summarize the methodology for the analysis of lidar data in order to determine meteorological parameters in the atmospheric boundary layer. The techniques are not exhaustive but are intended to show the depth and breadth of the information which can be obtained from lidars.

Two methods for the computation of water-vapor fluxes have been developed. The first uses the fact that the water vapor concentration in the vertical direction follows a logarithmic profile when corrected for atmospheric stability. The slope of the profile is proportional to the water vapor flux [5], [6].

$$\bar{q}_s - \bar{q}(z) = \frac{E}{a_v k u^* \rho} \left[\ln \left(\frac{z-d_0}{z_{0v}} \right) - \Psi_{sv}(\zeta) \right] \quad (1)$$

where k is Von Karman's constant [≈ 0.40], d_0 is the displacement height [m], E is the water vapor flux [$\text{kg}/\text{m}^2 \text{s}$], L is the Monin-Obukhov length [m], \bar{q}_s is the mean water mixing ratio at the surface [kg/kg], $\bar{q}(z)$ is the mean water mixing ratio at height z [kg/kg], u^* is the friction velocity [m/s], (vertical momentum per unit mass), z is the measurement height [m], z_{0m} is the roughness length for momentum [m], z_{0v} is the roughness length for water vapor [m], ρ is the air density [kg/m^3], and $\Psi_{sv}(\zeta)$ is the diabatic correction for water-vapor [5].

Rearranging equation (1) into linear form, one can make a least squares fit with a vertical profile of the water concentration at a given point in space. The flux can then be easily determined from the slope of the fitted line. With an iterative technique, the Monin-Obulkov length, L , can also be determined. Figure 1 is a comparison of "instantaneous" lidar fluxes and those from 30 minute averages from standard instruments over the course of a day.

The second method involves using inertial dissipation techniques in which Lidar-derived spatial and temporal power spectra are used to determine the flux [4]. The spatial power spectral equation for water-vapor has the following form:

$$F_q(\kappa) = \beta_q e^{1/3} e_q \kappa^{-5/3} \quad (2)$$

where β_q is the Kolmogorov constant [≈ 0.80], ϵ is the turbulent energy dissipation rate [m^2/s^3], ϵ_q is the dissipation rate due to molecular diffusion [$1/s$], and κ is the wavenumber [$1/m$]. Two additional relationships are also required to solve for the flux:

$$\epsilon_q = \frac{E^2 \phi_{sv}(\zeta)}{\rho^2 u_* k (z-d_0)} \quad R_m = \frac{k(z-d_0)\epsilon}{u_*^3} \quad (4)$$

where $\phi_{sv}(\zeta)$ is the water vapor diabatic stability gradient [5], R_m is a dimensionless scaling function. Of the many parameterizations for R_m , our studies indicate that the most reliable is $R_m = \phi_m(\zeta) - \zeta$, where ϕ_m is the diabatic stability gradient for momentum [5].

Fluxes can also be derived from temporal data as well as spatial data. By employing Taylor's hypothesis, time series information can be converted into the spatial domain by virtue of the wind velocity, ($\kappa \approx f/u$). This technique is often used to transform time series data obtained from standard point instruments into power spectra. Once a spatial spectrum is derived from the temporal data, then the same analysis is performed as in the regular spatial spectra to obtain fluxes. Figure 2 is a comparison of lidar fluxes from temporal and spatial spectra and those from 30 minute averages from standard instruments over the course of a day. The correlation coefficient, r^2 , between the measurements is 0.98.

The size distribution of the turbulent structures can be evaluated using variogram analysis. The variogram is a plot of the distance or lag, between measurements (x axis) and the average variance of the data minus the covariance at a given lag (y axis) [7]. Thus the plot is a measure of the average variance of measurements separated by a given distance.

A series of variograms derived from the lidar data are shown in Figure 3. The region of constant variability starts between 10 and 20 meters range with fifty percent of the variability occurring at lags of approximately 5-meters. This is in agreement with characteristic lengths calculated from the integral of the autocorrelation function [6] of spatial lidar data which show lengths ranging

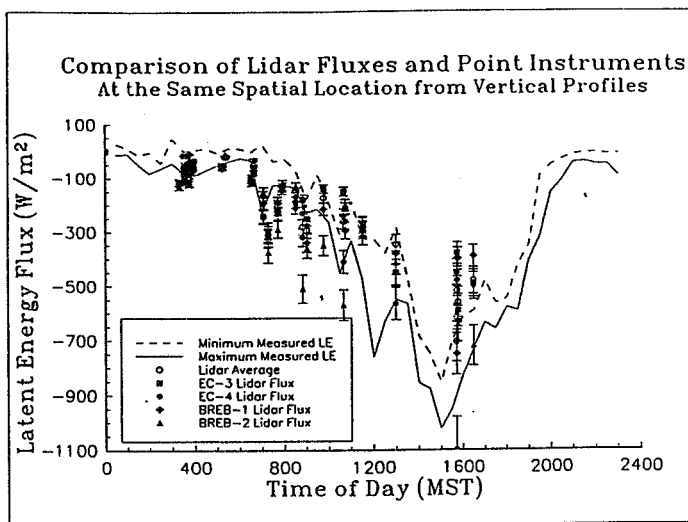


Figure 1

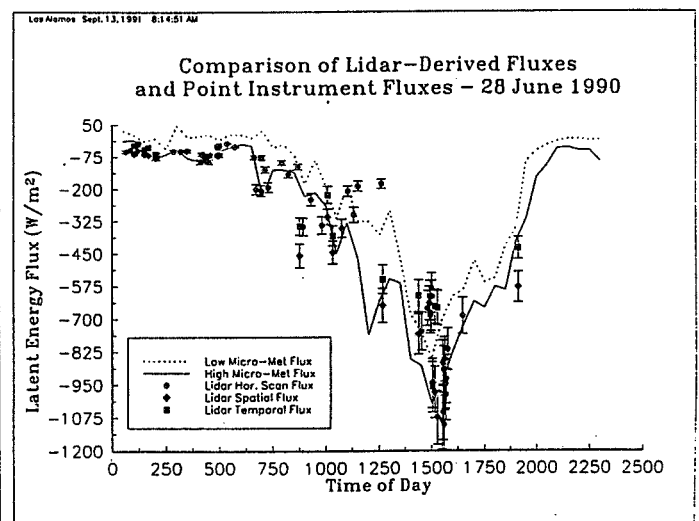


Figure 2

from 3 to 7-m. These distances can be used to describe the regions of relative homogeneity and thus define the characteristic scale of turbulence. The 5 to 10-m size sets the spatial resolution required of lidar systems to do this type of analysis. In practice, oversampling by a factor of two to four is desirable to adequately characterize a signal. Thus a 2.5-m range resolution is the maximum desirable for these conditions with low wind speeds and a stable atmosphere.

The height of the plateau which represents the average variance, is a measure of the natural variations over the entire field where the larger-scale mass and energy transfer processes begin to dominate. The variances and thus the heights of the plateaus, are related through similarity theory to the water-vapor flux.

Taylor's "frozen turbulence" hypothesis is an often-used concept which allows measurements taken by point instruments to be construed as spatial measurements. In this hypothesis, atmospheric structures are considered "frozen" and transported laterally by the wind. The integral of the autocorrelation function is a characteristic time which can be interpreted as the average length of time it takes for a structure to pass by the detector, or in the case of the lidar, one range increment. This time can be used to estimate the sampling time required of a remote sensor to adequately capture a single structure. As one can see from Figure 4, the characteristic time under stable atmospheric conditions and low wind speeds is about 4.9-s. To adequately sample the waveform then, a sampling time of approximately 1-s per record is adequate. For unstable conditions, with moderate wind velocities and small structure sizes, a sampling time of 0.12-s was not adequate.

The integral of the envelope of the correlation peaks in figure 4 is another characteristic time which is interpreted as the lifetime of a structure in the atmosphere. For the case shown, this time is approximately 7.6-s.

There are a series of stability correction functions used in calculations with Monin-Obulkov Similarity theory (equation 4 for example). Measurements of these functions are difficult to make because they require many simultaneous vertical measurements inside the boundary layer. The Businger-Dyer stability

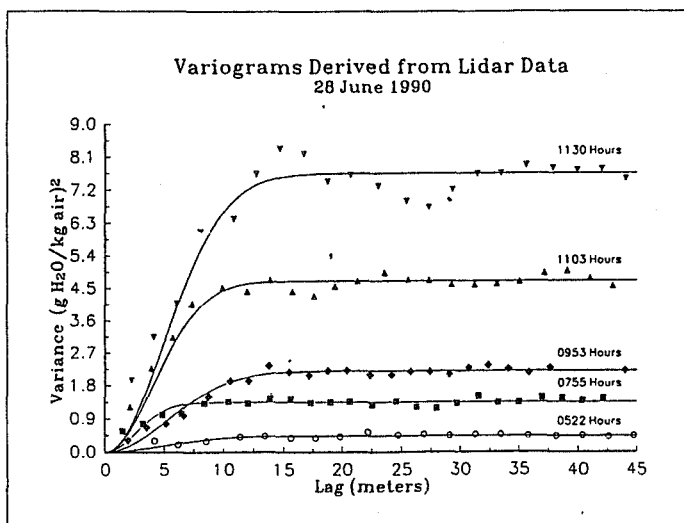


Figure 3

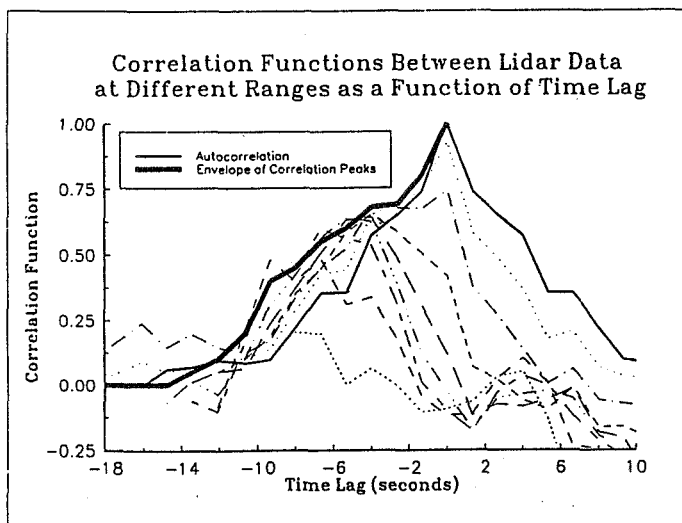


Figure 4

parameterizations for ϕ_m and ϕ_{sv} are normally used [5]. Recently, this parameterization has been challenged for the unstable case [8]. In a single vertical scan, the lidar acquires a large number of vertical measurements which can be used to determine the vertical gradient and thus the stability correction functions from the following equation:

$$\phi_{sv}(\zeta) = -\frac{[ku^*(z-d_0)\rho]}{E} \frac{d\bar{q}}{dz}$$

Lidar measurements of the water-vapor stability function were made and the results averaged over a wide range of values of ζ . The values conform much more closely to the Businger-Dyer formulation than that of Kader and Yaglom for the range of values measured.

Techniques are shown by which lidars can be used to determine many of the fundamental atmospheric parameters used in micrometeorological research. The ability of lidars to take non-intrusive measurements with fine resolution over large areas offers the opportunity to study spatial and temporal variability of many parameters with resolutions never before available. These characteristics are anticipated to be of great value in the study of the surface-atmosphere interface.

REFERENCES

- [1] R.A. Anthes, 'Enhancement of Convective Precipitation by Mesoscale Variations in Vegetative Covering in Semiarid Regions.' *J. Climate and Appl. Meteor.*, vol. 23, pp. 541-554, 1989.
- [2] J.F. Mahfouf, E. Richard, and P. Mascart, 'The Influence of Soil and Vegetation on the Development of Mesoscale Circulations.' *J. Climate Appl. Meteor.*, vol. 26, pp. 1483-1495, 1987.
- [3] R.A. Pielke, and R. Avissar, 'The Influence of Landscape Structure on Local and Regional Climate.' *Landscape Ecology.*, vol. 4(2/3), pp. 133-155, 1990.
- [4] W.E. Eichinger, D.I. Cooper, D.E. Hof, D.B. Holtkamp, R.R. Karl, C.R. Quick, and J.J. Tjee, 'Development and Application of a Scanning, Solar-Blind, Water Raman-Lidar.' Submitted to *Applied Optics*. LA-UR-92-0078, 1992.
- [5] W. Brutsaert, *Evaporation Into the Atmosphere.*, 2nd ed., Reidel Pub. Comp., pp 299, 1984.
- [6] H.A. Panofsky, and J.A. Dutton, *Atmospheric Turbulence*. John Wiley and Sons, New York, 1984.
- [7] J.C. Davis, *Statistics and Data Analysis in Geology*. John Wiley, 2nd Edition 1986.
- [8] B.A. Kader, and M.Y. Yaglom, 'Mean Fields and Fluctuation Moments in Unstably Stratified Turbulent Boundary Layers', *J. Fluid Mech.*, vol. 212, pp. 637-662, 1990.

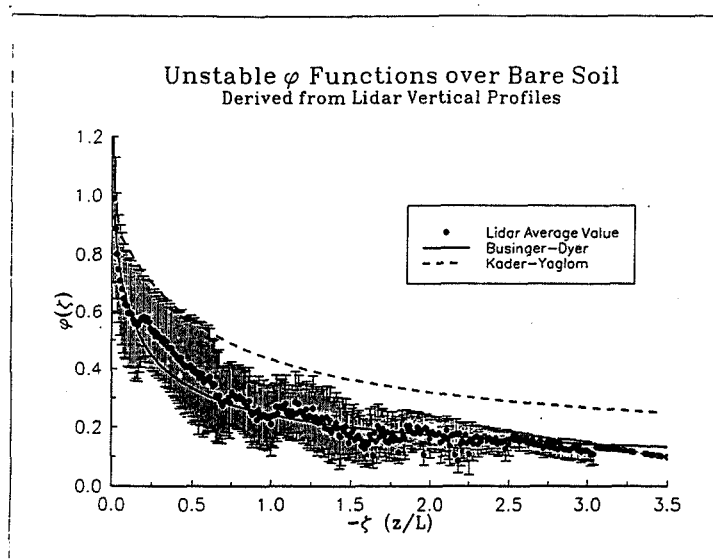


Figure 5

Correction for Nonlinear Photon Counting Effects in Lidar Systems

D.P. Donovan, J.A. Whiteway and A.I. Carswell

Institute for Space and Terrestrial Science and
Department of Physics and Astronomy, York University
4700 Keele Street, North York, Ont., Canada, M3J 1P3
Tel: 416-736-2100 Fax: 416-736-5516

Photomultiplier tubes (PMTs) employed in the photon counting (PC) mode of operation are widely used as detectors in lidar systems. Their use in this mode, however is restricted mainly to conditions where the signal levels are relatively low and the responses of the PMT and the pulse discrimination/counting system are linear. It is well known that in this low light level regime, where the signal-to-noise (S/N) levels approach unity, the inherent S/N for photon counting is better than that obtained from other detection techniques. A problem encountered with such systems however, is that the PC system's response becomes non-linear with increasing incident light flux. That is, at high enough signal levels, the output count rate can no longer be considered proportional to the incident light intensity. In general, assuming the limits of the PMT itself are not being exceeded, non-linearity in a PC system's response is caused by the overlapping of pulses and the finite response time of the electronics. At low count rates one expects the system to register one event for each output pulse from the PMT, however, at higher count rates the limitations of the discrimination/counting system will cause the observed count rate to be non-linear with respect to the true count rate.

In our laboratory we have developed a versatile Nd:YAG lidar which is used for measurements of both the middle atmosphere and the troposphere.[1] With this system we encounter a very wide range of signal levels ranging from the extremely weak signals from the top of the mesosphere to the very strong returns from low level clouds. Although the system is capable of operating the PMTs in either the analog detection or photon counting mode, we find that often when we use photon counting we have portions of our lidar return which contain very useful information but are not within the linear operating regime of the PC system. In this paper we report the results of our efforts to explore the extent to which such high intensity PC signals can be quantitatively analysed (see also [2]). In particular, a useful model relating the mean 'true' count rate and the observed count rate is presented and its application to our system demonstrated. This model takes into account the variation in height of the PMT output pulses and the effect of the pulse height discrimination threshold.

Since our PC system shows the dominant characteristics of a paralyzable system we have chosen to model it as such. The relation between the mean average and mean true count

rates in the case of a paralyzable PC system with uniform pulses, above the discriminator threshold, is well known [3].

$$N = Se^{-S\tau_d}, \quad (1)$$

where N is the observed count rate and S is the true count rate. In this expression $e^{-S\tau_d}$ is just the Poisson probability of no pulse occurring in the time interval τ_d . τ_d is known as the 'dead time'.

In real PC systems, since secondary emission is a statistical process, the PMT pulses will not be uniform, but will vary in size. Thus the situation becomes more complicated than that described by Eq. (1). However, by analogy with Eq. (1) we expect the mean observed and mean true count rates to be related as

$$N = Se^{-\tau_i S} \left[P_{(a)} + P_{(1b \cap 2a)}(\tau_i S) + P_{(2b \cap 3a)} \frac{(\tau_i S)^2}{2} + P_{(3b \cap 4a)} \frac{(\tau_i S)^3}{6} + \dots \right] \quad (2)$$

where: τ_i is a time interval corresponding to the 'mean pulse interaction interval', $P_{(a)}$ is the probability that a individual pulse is above the discriminator threshold, $P_{(1b \cap 2a)}$ corresponds to the probability that given two overlapped pulses, that the amplitude of the first pulse is below the discriminator threshold while the sum of the amplitude of the second pulse plus the amplitude of the first are above the threshold. $P_{(2b \cap 3a)}$ is the probability that given three overlapped pulses, that the sum of the amplitudes of first and second pulses is below the threshold, while the addition of the third pulse causes the voltage to go above the threshold. $P_{(3b \cap 4a)}$ and so on have similar interpretations. The coefficients in Eq. (2) will depend on the discriminator setting, the pulse height distribution and the exact shape of the PMT pulses. However, when dealing with the simplified case of rectangular pulses of a fixed width and a given height distribution one can evaluate the various probabilities. For the case of a uniform height distribution between 0 and 1 we get:

$$N = Se^{-\tau_i S} \left[(1 - T) + (T - \frac{T^2}{2})\tau_i S + \frac{1}{2!}(\frac{T^2}{2} - \frac{T^3}{6})(\tau_i S)^2 + \dots \right] \quad (3)$$

where T is the relative discriminator level, $0 \leq T \leq 1$.

In Fig. 1 we have shown the deviation from linearity predicted using Eq. (3) for a variety of discriminator settings. The deviation from linearity is defined as N/N_l , where N_l corresponds to the what the observed count rate would be if the system's response was linear. The discriminator thresholds labeled on the figure go from a maximum of $T = 0.9$ to $T = 0.1$ in steps of 0.05. The width of the pulses ($\tau_i = 0.015 \mu\text{sec}$) was chosen so that the maximum observed average count rate approximately coincided with that of our lidar's PC system. The results are seen to be similar to the experimental results reported by Darland [4] and others their investigations on the effect of the discriminator setting upon linearity. To investigate the linearity of our PC system the basic method described by [4] was used. That is, a neutral density (ND) filter of high enough optical depth so that the system's response was linear, was inserted in front of the detector. The observed count rate was then compared to the observed count rate obtained without the filter present in the system. The measurements were performed using the lidar return signal from the middle

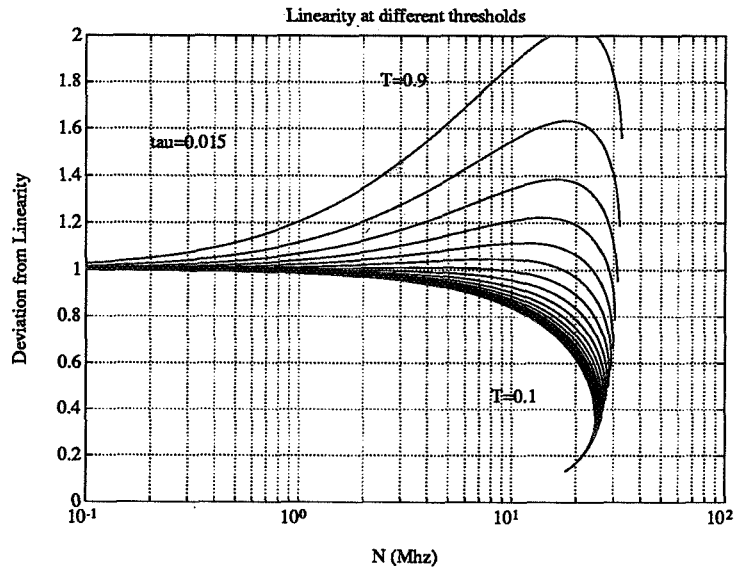


Figure 1: Predicted effect of changing discriminator threshold using Eq.(3).

atmosphere. This method has the advantage of characterizing the system's response under normal operating conditions.

In Fig. 2 we show an example of the deviation from linearity for different discriminator levels that we have measured for one channel of our Lidar's PC system. The discriminator setting labeled on the plot are negative because our PMT pulses are of negative polarity. The measured results compare quite well with the predicted behavior shown in Fig. 1.

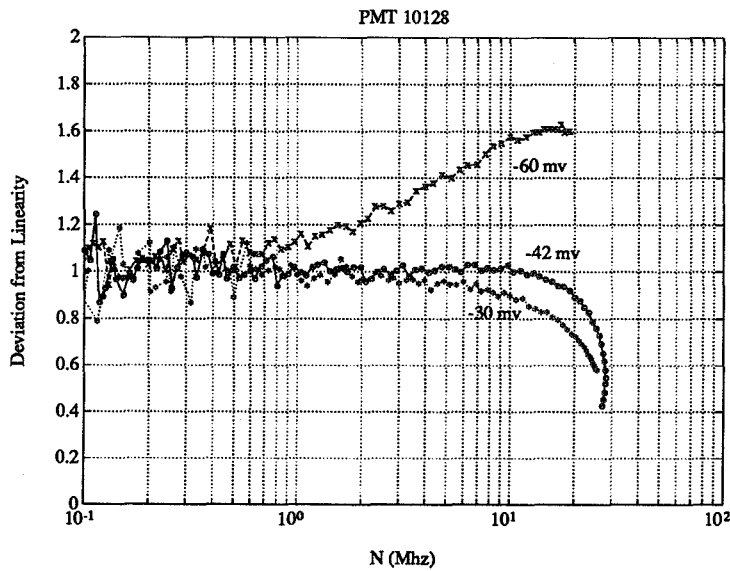


Figure 2: Observed effect of changing discriminator threshold.

Treating τ_i and the various probabilities in Eq.(2) as fitting parameters we can accurately quantified the response of our PC system. In Fig. 3 we show an example of the application of Eq. (2) to the fitting of our measured PC signals. In this figure we see that the modeled behavior described by Eq. (2) gives a very good fit to the data. This information can then be used to accurately correct for nonlinear effects at high count rates.

We have demonstrated the usefulness of our model in explaining the characteristics of our PC system. We have been able to greatly extend our linear PC operating range and, using Eq. (2), we can accurately correct data taken above the linear regime. In this paper we will discuss the details of our model and the methods used to investigate our PC system.

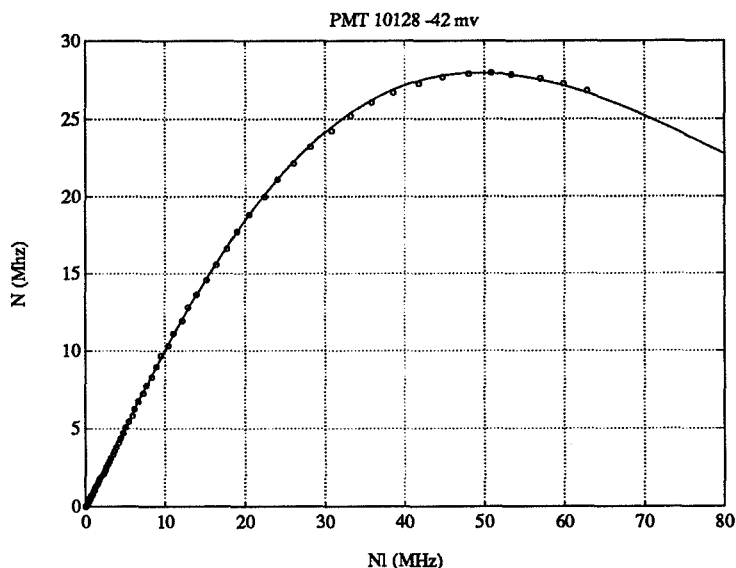


Figure 3: Example of fit of Eq.(2) to lidar calibration data. The points indicate measured values and the solid line is derived from Eq.(2)

References

- [1] A.I. Carswell, S.R. Pal, W.Steinbrecht, J.A. Whiteway, A. Ulitsky and T-Y Wang, "Lidar measurements of the Middle Atmosphere", *Can.J. Phys.* Vol 69, 1076-1086 (1991)
- [2] D.P. Donovan, J.A. Whiteway and A.I. Carswell, "Correction for Non-Linear Photon Counting Effects in Lidar Systems", *Optical Society of America, Technical Digest Series*, Vol 18, 241-243 (1991)
- [3] Jörg W. Müller, "Dead-Time Problems", *Nuclear Instruments and Methods*, Vol. 112 47-57 (1973)
- [4] E.J. Darland, G.E. Leroi and C.G. Enke, "Pulse (Photon) Counting: Determination of Optimum Measurement System Parameters", *Analytical Chemistry*, Vol 51, 240-245 (1979)

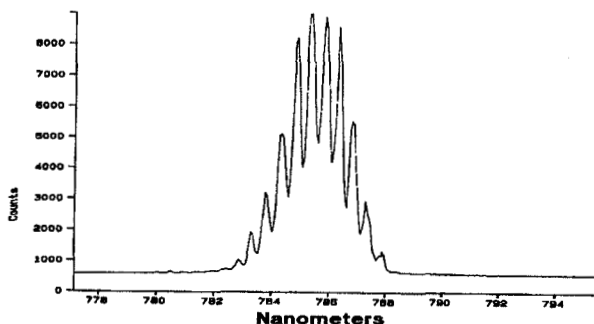
High Background Photon Counting Lidar
W.J. Lentz
Naval Postgraduate School, Monterey, Ca.

Abstract

Photon counting with lidar returns is usually limited to low light levels, while wide dynamic range is achieved by counting for long times. The broad emission spectrum of inexpensive high-power semiconductor lasers makes receiver filters pass too much background light for traditional photon counting in daylight. Very high speed photon counting is possible, however, at more than 500MHz which allows the construction of eyesafe lidar operating in the presence of bright clouds. Detector improvements are possible to count to 20GHz producing a single shot dynamic range of ten decades.

Introduction

Recent advances in near-visible quantum well diode lasers provide an inexpensive, eyesafe, rugged laser source for lidar, but ADP and PIN detectors have great difficulty detecting the small signals in the presence of backgrounds that are a million times larger than the signal.

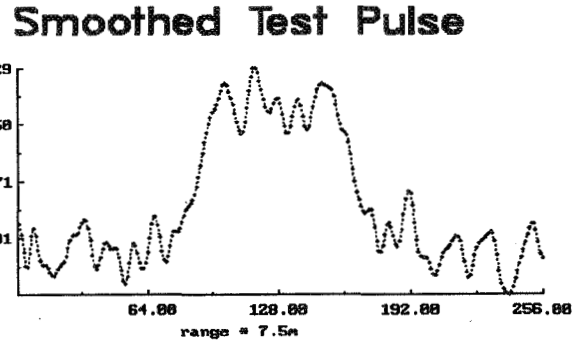
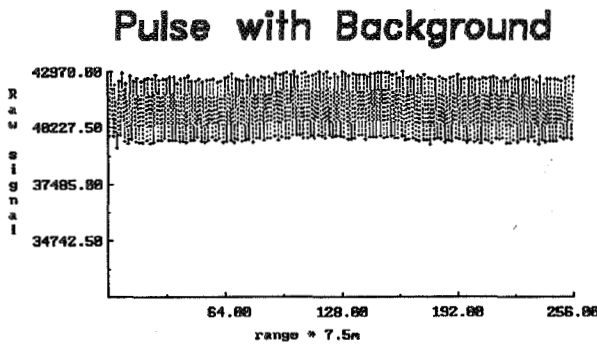


The problem can be illustrated by observing the 4nm emission spectrum of a new 780 nm stacked 100W pulsed laser diode. Although there has been recent progress in selecting a single mode using external laser cavities, selecting a single line is not yet routine. Even narrow wavelength lasers such as doubled Yag can become background limited. An eyesafe lidar was constructed to investigate the feasibility of using photon counting

in natural daylight conditions for cloud ceiling and visibility measurements. The information gathered can be compared favorably to Yag-APD and to Erbium-Pin diode visibility measurements with the Visioceilometer (Ref 1,2).

Photon Counting

Photomultipliers are typically limited to average anode currents of 10 to 100 ua, so the gain of a tube counting at 500 MHz must be no more than a million. For a PMT with 2ns single photon pulse width, this corresponds to 5mv into 50 ohms which is too small for reliable counting. A 2GHz gain of 100 amplifier was used to make up for the PMT gain loss required by the high average anode currents of the background. The following figures show a test pulse generated by a LED in the presence of a high photon-count background followed by the processed signal which was hidden in the background. An additional smear in the raw signal is produced by accumulation of very small differences in count times in the alternating photon counters used to eliminate dead time. The

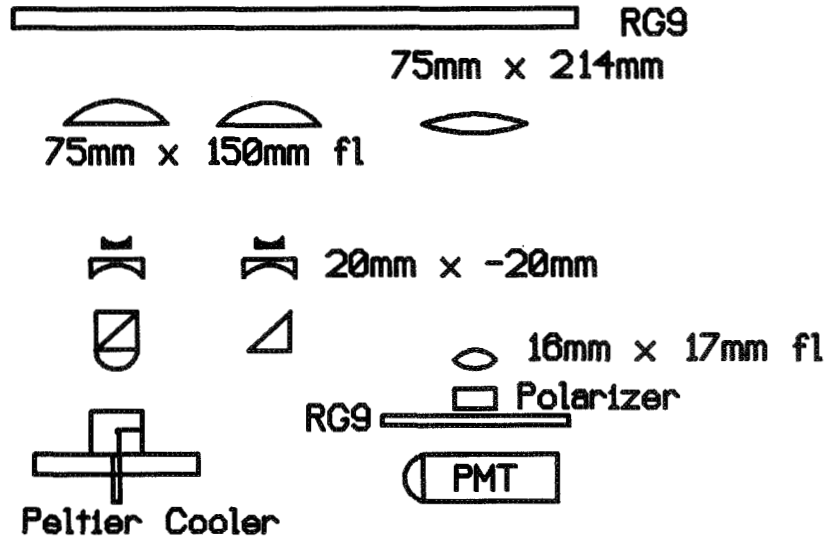
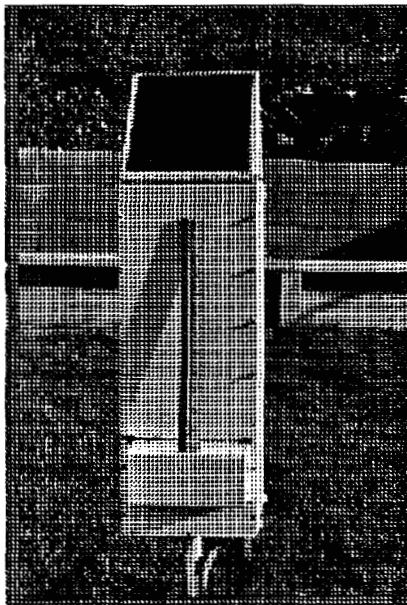


output of one counter is added into a time bin counter while the other counter is counting, and then the process is reversed so that no counts are lost.

Pulse pile-up is reduced by single delay line clipping. In simple terms, the output of the PM anode is shorted to ground through an inch of wire, and the signal is taken across this piece of wire, greatly reducing DC offset and drift. After-pulsing is minimized by the low PMT gain and fast response time.

Lidar System

The transmitted and received lidar energy passes through RG9 filter glass to prevent sunlight from entering the system. A 800 nm laser diode with 75W of peak power is pulsed at 10 KHZ through two 3" lenses by a polarizing beamsplitter to spread the

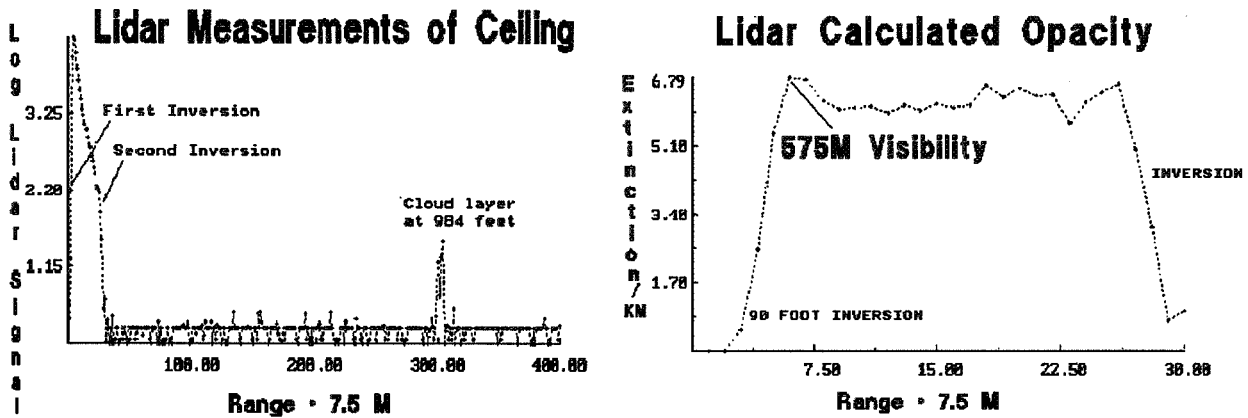


beam to an eyesafe level. The temperature of the laser diode is kept at 0 degrees C so that the emission wavelength always matches the 5nm receiver filter. The backscattered energy is received by a single 3" lens followed by a polarizing filter, RG9 filter, and adjustable field of view and beamstop. The transmitter and receiver compartments are mounted on a common optical table for

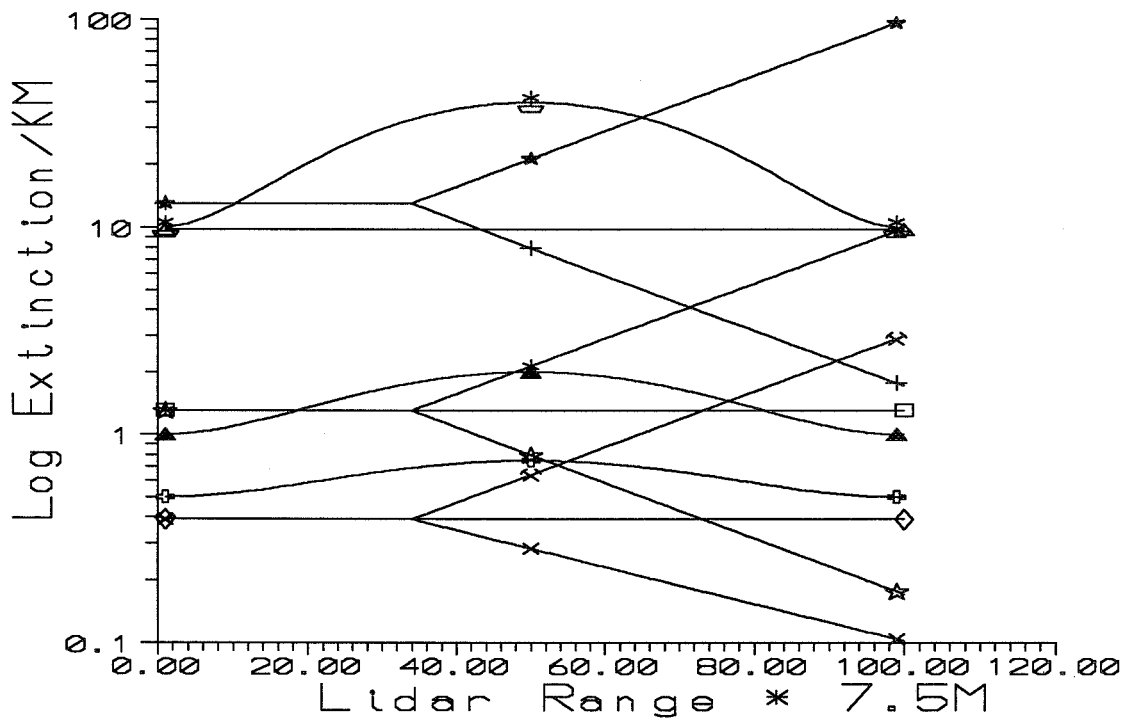
stability. Since the laser output is polarized, the receiver polarization filter can be used to minimize the scattered background sunlight.

Lidar Analysis

The following figures show a processed lidar return obtained with a large background and the resulting extinction calculated with the Klett (Ref 3) method of inversion. Aside from the



manageable problems of pulse pile up, photon statistics, and the asymmetry of alternating counters, the processed photon count signal was superior to the Yag-Visiocyteometer with its log



amplifier and ADP distortions. There were no cases in which the natural background saturated the receiver of the photon counter, and nonlinearities and tilt were completely missing.

The Klett method requires an external boundary value, and the algorithm to deduce extinction can be very unstable in the presence of systematic errors. The previous figure shows twelve standard test extinctions designed to test for instability that have been used with the Visioceilometer for twelve years. The constant extinction cases emphasize noise errors, and allow tests for near-field overlap errors. The exponentially increasing cases are the most stable, and the exponentially decreasing cases often find algorithm weaknesses.

Improvements

A laser tuned with an external cavity to a narrow wavelength of interest would yield lower backgrounds allowing larger collection optics. Further engineering could easily reduce the system to hand-held battery operated size. The backscattered signal could also be split into several detectors in a Digicon-like tube for wavelength discrimination. Digicons are basically Photocathodes with large acceleration voltages that produce gain through the deacceleration of photoelectrons in silicon targets. These tubes can be single detectors or arrays of detectors for imaging or spectroscopic detection. By using different target materials than Silicon and multiple detectors behind a single photocathode, the shift in backscattered wavelength could be measured at count rates exceeding the present system. Detectors of this type are under development and promise improvements that cannot easily be achieved with standard photomultiplier structures.

References

1. W.J. Lentz, "The Visioceilometer: A Portable Visibility and Cloud Ceiling Height Lidar," ASL-TR-0105, January, 1982, U.S. Army Atmospheric Sciences Laboratory, White Sands Missile Range, N.M.
2. Eugene S. Barnes and W.J. Lentz, "The Eyesafe Visioceilometer: A Tactical Visibility and Cloud Height Lidar", ASLTR-0195, January, 1986, U.S. Army Atmospheric Sciences Laboratory, White Sands Missile Range, N.M.
3. J. D. Klett, "Stable Analytical Inversion Solution for Processing Lidar Returns," Appl. Opt. 20, 211 (1981).

DEVELOPMENT OF A RAMAN LIDAR SIMULATION TOOL

R.J. Grasso and J.R. Hummel
SPARTA, Inc.
24 Hartwell Avenue
Lexington, MA 02173

Raman Lidar is a useful and powerful tool for remote probing of the atmosphere. With Raman Lidars, one can accurately determine the identification and concentration of a particular molecular specie present in the atmosphere. We present the results from a program to develop a simulation capability of Raman Lidar systems for the remote detection of atmospheric gases and/or air polluting hydrocarbons. Our model, which integrates remote Raman spectroscopy with SPARTA's BACKSCAT atmospheric lidar simulation package, permits accurate determination of the performance of a Raman Lidar system. The accuracy with which our model operates is due to the accurate calculation, at any given excitation wavelength, of the differential scattering cross section for the molecular specie under investigation. We show excellent correlation of our calculated cross section data with experimental data from the published literature. In addition, the use of our BACKSCAT package, which provides a user friendly environment to define the operating conditions, provides an accurate calculation of the atmospheric extinction at both the excitation and Raman shifted wavelengths. Our code can be used to accurately predict the performance of a Raman Lidar system, the concentration and identification of a specie in the atmosphere, or the feasibility of making Raman measurements.

A Variable Phase Function Approach for the Inversion of Lidar Return Signals

V. A. Kovalev*

U.S. Environmental Protection Agency, P.O. Box 93478, Las Vegas, Nevada 89193

H. Moosmüller

Desert Research Institute, University of Nevada, P. O. Box 19040, Las Vegas, Nevada 89132

The lidar return signal S_0 as a function of distance r is described by the lidar equation as

$$S_0(r) = C \frac{\beta(r)}{r^2} e^{-2 \int_0^r \sigma(x) dx}, \quad (1)$$

where C is the system constant, β the backscattering coefficient, and σ the extinction coefficient. As both $\beta(r)$ and $\sigma(r)$ are unknown, the equation is under-determined and the extinction profile cannot be derived without further assumptions. Traditionally a power law is used to relate β and σ as

$$\beta = a\sigma^k, \quad (2)$$

where a and k are constants. For $k \neq 1$, the phase function P_π , which is defined as the ratio of β and σ , becomes a function of σ

$$P_\pi = \frac{\beta}{\sigma} = a\sigma^{k-1}. \quad (3)$$

Both β and σ are the sum of particulate and molecular contributions, i. e. $\beta = \beta_p + \beta_m$ and $\sigma = \sigma_p + \sigma_m$. When particulate and molecular scattering are comparable, it is instructive to consider their phase functions separately. The molecular phase function is well known,

*Permanent address: Main Geophysical Observatory, Karbysheva St. 7, 194018 St. Petersburg, Russian Federation

$P_{\pi,m} = 3/(8\pi)$, and the particulate phase function may be derived from Eq. 2 as

$$P_{\pi,p} = \frac{\beta_p}{\sigma_p} = \frac{a(\sigma_p + \sigma_m)^k - \beta_m}{\sigma_p} \quad (4)$$

Clearly, this function can only be valid for a certain range of σ_p as $P_{\pi,p}$ diverges for $\sigma_p = 0$. To determine this range, a comparison with experimental data is needed. Kovalev et al.¹ have analyzed a large number of atmospheric measurements of β and σ and subsequently established a set of values of β_p and σ_p , which represent a large number of atmospheric conditions. The particulate phase function $P_{\pi,p}$ in the visible part of the spectrum, resulting from these values, together with a fit of Eq. 4 (dashed line, $a = 0.02 \text{ km}^{-k-1} \text{ sr}^{-1}$, $k = 0.59$) for standard molecular scattering ($\sigma_m = 0.0116 \text{ km}^{-1}$ at 550 nm) is shown in Fig. 1.

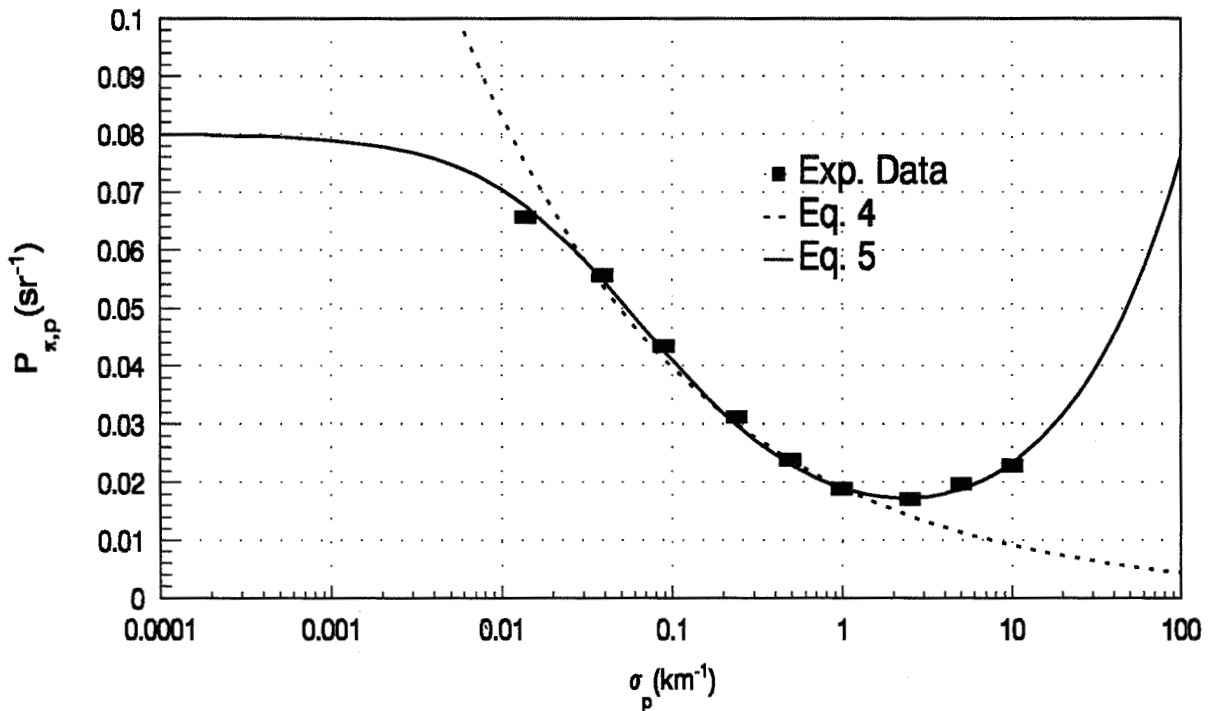


Fig. 1: Particulate Phase Function $P_{\pi,p}$ as a Function of Particulate Extinction σ_p

Equation 4 shows good agreement with the experimental values for σ_p between approximately 0.01 km^{-1} and 1 km^{-1} . Although there are no data below 0.01 km^{-1} , this fit of $P_{\pi,p}$ becomes larger than the molecular phase function, $P_{\pi,m} = 3/(8\pi)$, for $\sigma_p < 0.0012 \text{ km}^{-1}$, which is

unrealistic. Furthermore, the increase of the backscattering coefficient β_p for extinction coefficients σ_p larger than about 1 km^{-1} is not accounted for by this fit.

A simple fitting function for the particulate phase function, which has an improved range of agreement with the experimental values, may be written as

$$P_{\pi,p} = \frac{b}{\sqrt{\sigma_p + \sigma_0}} + c\sigma_p^m \quad (5)$$

With $b = 0.0145 \text{ km}^{-0.5} \text{ sr}^{-1}$, $c = 0.0047 \text{ km}^m \text{ sr}^{-1}$, $m = 0.6$, and $\sigma_0 = 0.033 \text{ km}^{-1}$, this becomes

$$P_{\pi,p}(\sigma_p=0) = \frac{b}{\sqrt{\sigma_0}} = 0.08 \text{ sr}^{-1}. \quad (6)$$

As can be seen in Fig. 1, Eq. 5 gives a good fit over the whole range of experimental values. While it is not easy to judge the extrapolation beyond the data range, the value of the phase function for $\sigma_p = 0$ converges to 0.08 sr^{-1} , which is reasonable. This value may also be easily adjusted by modifying σ_0 according to Eq. 6, to account for new data at lower particulate extinction coefficients.

This variable phase function may be used for the inversion of lidar data in an iterative process:

1. The iteration is started with a constant phase function $P_{\pi,p} = 3/(8\pi)$ and the original lidar return signal $S_0(r)$.
2. A profile of the particulate extinction coefficient $\sigma_p(r)$ is calculated from the lidar return signal $S(r)$ with one of the conventional inversion methods, assuming $k = 1$ in Eq. 2.^{2,3,4}
3. The corresponding profile of the particulate phase function $P_{\pi,p}(r)$ is calculated from $\sigma_p(r)$ with the help of Eq. 5.
4. The original lidar return signal $S_0(r)$ is multiplied with a correction function f_c

$$f_c(r) = \frac{\sigma_p(r) + \sigma_m(r)}{\frac{P_{\pi,p}(r)}{P_{\pi,m}} \sigma_p(r) + \sigma_m(r)}, \quad (7)$$

yielding a modified lidar return signal $S_1(r) = f_c(r) S_0(r)$.

The modified signal $S_1(r)$ is then used as input for the next step of the iteration, and the process is repeated until the profile of the particulate extinction coefficient $\sigma_p(r)$ converges to its final value.

Numerical simulations of this method have been performed successfully, demonstrating fast convergence of the particulate phase function. The method will be used in the future to evaluate extinction and backscattering corrections for a UV-DIAL system measuring tropospheric ozone concentrations.⁵

References:

1. V. A. Kovalev, G. N. Baldenkov, and V. I. Kozintsev, "On the relationship between total- and backscattering in the atmosphere," *Newsletter Acad. Sci. USSR*, **23**, 611 (1987).
2. J. D. Klett, "Stable analytical inversion solution for processing lidar returns," *Appl. Opt.* **20**, 211 (1981).
3. W. Carnuth, R. Reiter, "Cloud extinction profile measurement by lidar using Klett's inversion method," *Appl. Opt.* **25**, 2899 (1986).
4. V. A. Kovalev, E. E. Rybakov, and V. M. Ignatenko, "Determination of the extinction coefficient profile using the one angle lidar measurement data," *Atmospheric Optics* **4**, 830 (Tomsk, 1991).
5. H. Moosmüller, D. Diebel, D. H. Bundy, M. P. Bristow, C. M. Edmonds, R. M. Turner, V. A. Kovalev, R. P. Haas, and J. L. McElroy, "The U.S. EPA airborne UV-DIAL system," *Technical Digest on Optical Remote Sensing of the Atmosphere*, Vol. 18, (Optical Society of America, Washington, D.C., 1991) pp. 253-255.

A comparison of lidar inversion methods for cirrus applications

Salem ELOURAGINI, Pierre H. FLAMANT

*Laboratoire de Météorologie Dynamique du CNRS,
Ecole Polytechnique, 91128 Palaiseau, France*

ABSTRACT

Several methods for inverting the lidar equation were suggested (Platt 1973, Klett 81) to derive the cirrus optical properties (β backscatter and α extinction coefficients, δ optical depth) at one wavelength. The lidar equation can be inverted in a linear or logarithmic form, either solutions assume a linear relationship : $\beta=k\alpha$, where k is the lidar ratio. A number of problems prevent us from calculating α (or β) with a good accuracy. Some of these are :

- the multiple scattering effect (most authors neglect it),
- an absolute calibration of the lidar system (difficult and some times not possible),
- lack of accuracy on the lidar ratio k (taken as constant, but in fact it varies with range and cloud species).
- the determination of boundary condition for logarithmic solution which depends on signal to noise ratio (SNR) at cloud top.

An inversion in a linear form needs an absolute calibration of the system. In practice one uses molecular backscattering below the cloud to calibrate the system. This method is not permanent because the lower atmosphere turbidity is variable.

For a logarithmic solution, a reference extinction coefficient α_f at cloud top is required.

Several methods to determine α_f were suggested. We tested these methods at low SNR. This led us to propose two new methods referenced as S1 and S2.

S1 method

If the optical depth (δ) of a cloud is known (using the slope method for example), this allows to determine the $\alpha(R)$ profile (calculated by Klett's formula) by doing iterations on α_f . The suitable value of α_f corresponds to the equality between the known and calculated optical depths.

S2 method

This method is based on signal numerical simulation and the S1 method. The simulated lidar signal represents a cirrus cloud with a variable optical depth. For each signal, we calculate α_f , (by S1 method) and SNR at the cloud top. Then we plot α_f as a function of SNR. This calibration curve is used to process the experimental signal from which we derive SNR. The corresponding α_f is injected in Klett's formula to calculate $\alpha(R)$.

This method is tested and compared with other methods; results are cheerful until now.

Five inversion methods are selected and tested in a relative and absolute manner. The absolute test uses an atmospheric model with cirrus, aerosols and molecular density. Detection and instrumental noises are included in the model. The input α profile and retrieved profile are compared. The input extinction profile ($\delta=0,3$) and the profile given by S2 method are indistinguishable (Fig. 1). Other methods will be compared to S2.

The relative test uses experimental data (Fig 2). Also extinction profiles have to be compared to S2. S2 profile corresponds to the optical depth derived from the slope method. Note that the linear method is successfully applied on simulated signal but not on the experimental one due to changes in lower atmospheric optical properties. S1 and Gonzalez method give the best results either for simulated or for experimental signals. They are indistinguishable because they use the same reference extinction coefficient (note that Gonzalez method is not based on logarithmic solution). In the table we present the cirrus optical depths δ calculated by the different methods and presented in figures 1 & 2.

	Linear	S1	S2	Gonzalez	Mulders	Slope
numerical	0,30	0,30	0,31	0,32	0,79	0,30
experimental	0,20	0,23	0,23	0,23	0,30	0,23

As a conclusion the best methods are S1, S2 and slope methods while $SNR \geq 5$. For low SNR any method can provide accurate results. Multiple scattering is taken into account by any of these methods in spite of its impact on calculation especially for thick clouds. The S1 and S2 methods and results will be presented and discussed at the conference.

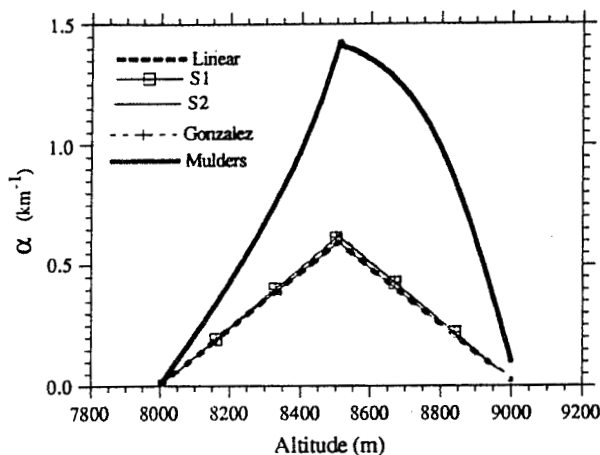


Fig. 1 Absolute comparison of five methods using numerical lidar signal simulation. The true profile is superimposed on S1 profile.

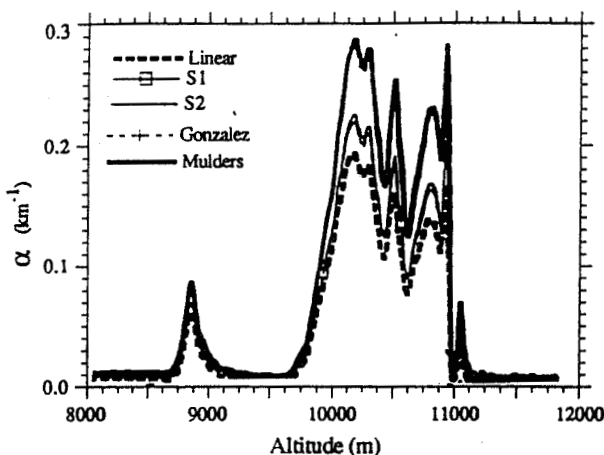


Fig. 2 Same as in figure 1 but using an experimental data. Reference profile is S1.

Time and Wavelength Domain Algorithms for Chemical Analysis by Laser Radar

David L. Rosen and James B. Gillespie
U.S Army Atmospheric Sciences Laboratory
White Sands Missile Range, NM 88002-5501

INTRODUCTION

Laser-induced fluorescence (LIF) is a promising technique for laser radar applications. Laser radar using LIF has already been applied to algae blooms and oil slicks.¹ Laser radar using LIF has great potential for remote chemical analysis because LIF spectra are extremely sensitive to chemical composition. However, most samples in the real world contain mixtures of fluorescing components, not merely individual components. Multicomponent analysis of laser radar returns from mixtures is often difficult because LIF spectra from solids and liquids are very broad and devoid of line structure. Therefore, algorithms for interpreting LIF spectra from laser radar returns must be able to analyze spectra that overlap in multicomponent systems.

Factor analysis-rank annihilation (FARA) is an eigenanalysis technique²⁻⁵ for analyzing two-dimensional data. FARA usually analyzes excitation-emission matrices (EEM). EEM are matrices where the rows (or columns) are emission spectra at fixed excitation wavelengths and the columns (or rows) are excitation spectra at fixed emission wavelengths. FARA is insensitive to the presence of unknown compounds if there is no energy transfer between constituents. This insensitivity would be useful for laser radar applications where not every compound in a natural environment can be known in advance. Although the measurement of EEM requires a wavelength tunable light source, laser sources strong enough for laser radar applications are usually not wavelength tunable. Therefore, scientists have not previously considered FARA a suitable method for analyzing laser radar returns.

This paper analyzes the possibility of using FARA to analyze emission-time matrices (ETM) from laser radar returns instead of EEM. The authors here define ETM as matrices where the rows (or columns) are emission spectra at fixed times and the columns (or rows) are temporal profiles for fixed emission wavelengths. Laser radar usually uses pulsed lasers for ranging purposes, which are suitable for measuring temporal profiles. Laser radar targets are hard instead of diffuse; that is, a definite surface emits the fluorescence instead of an extended volume. A hard target would not broaden the temporal profiles as would a diffuse target. Both fluorescence lifetimes and emission spectra are sensitive to chemical composition. Therefore, temporal profiles can be used instead of excitation spectra in FARA analysis of laser radar returns. The resulting laser radar returns would be ETM instead of EEM.

THEORY

This section describes an FARA algorithm, developed by Ho^{2, 3} for calculating nonzero concentrations. The calculation requires an ETM, D , from an unknown and another ETM, N_k , from a calibrant of known concentration. The subscript k designates the constituent one is looking for in the unknown, that is, the

component of interest. D and N_k are ETM in this paper, but can either be EEM or ETM. The laser radar return could come from an unknown, while the calibrant can be a sample of the component of interest especially prepared in a laboratory. This algorithm calculates the relative concentration, c_k , which is the ratio of the concentration of a constituent in an unknown to the concentration of the constituent in a known laboratory standard. The algorithms discussed in this paper are not valid if c_k is zero. Algorithms for deciding whether c_k is zero are available but will not be discussed in this paper.

The concentration, c_k , can be calculated in four steps. First, calculate the effective rank, r , of the matrix D . The effective rank is the number of fluorescence centers (that is, components with bilinear spectra) in the unknown. Complicated methods of choosing the effective rank are available,⁴ but beyond the scope of this paper. Second, calculate the residual matrix $E(c_k')$, defined as:

$$E(c_k') = D - c_k' N_k \quad (1)$$

where c_k' is a dummy variable that spans over a range of possible concentrations. Note that eq. (1) requires a calibrant only from the component of interest. Third, calculate the eigenvalues, $S_j(c_k')$, of $E(c_k')E(c_k')^t$. The superscript t designates transpose, while the subscript j designates the particular eigenvalue. The subscript j is ordered so that if $j > j'$, then $S_j > S_{j'}$. Finally, find the minimum of $S_r(c_k')$. The value at c_k' where the minimum occurs is the actual relative concentration, c_k , of the component. Another algorithm uses an analytical formula, developed by Lorber,⁵ to find the minimum of $S(c_k')$. However, the authors will show the functional form of $S_r(c_k')$ to clarify the discussion.

One can easily show that the shape of the laser pulse profile cannot affect the calculated values of concentration if the same laser pulse shape with the same time delay generates both the calibrant ETM and the laser radar return. Therefore, FARA also may serve as a type of deconvolution algorithm if both the laser pulse shape and electronic triggering are reproducible.

SIMULATION AND RESULTS

The ETM's of three hypothetical compounds (I, II, and III) were generated. The emission spectra of these compounds are shown in figure 1. Only relative decay times and relative shapes of emission bands affect the calculations. For ease of visualization, this paper will refer to the time units as nano-seconds (nsec) and wavelength units as nanometers (nm). For calculational ease the authors assumed a laser pulse shape to be a double-sided exponential with a decay constant of 0.5 nsec. The fluorescence decay times of the three compounds (I, II, and III) were 2.0 nsec, 6.0 nsec, and 10.0 nsec, respectively. The authors repeated the calculations using a Dirac delta function for the laser pulse profile.

The ETM of compounds I, II, and III were added to create a linear combination with effective concentrations (that is, coefficients) of 1.0, 2.0, and 3.0, respectively. This linear combination was defined as the ETM of the hypothetical mixture.

FARA analyzed both the linear combination and the calibrant EEM to find the nonzero concentrations, c_k . The calculated concentrations for the three compound profiles (I, II, and III) from the ETM are shown in table 1. The values of c_k calculated by FARA were the same as the actual concentrations in the hypothetical mixture. The calculated values were independent of the laser pulse shape, as expected.

The eigenvalue, $S(c_I')$, for the ETM of compound I is plotted in figure 2. The eigenvalue, S , shows a clear minimum at $c_I' = 1.0$, which is the true value of c_I . Note that calculating the value of c_I did not require laboratory standards from compound II or III.

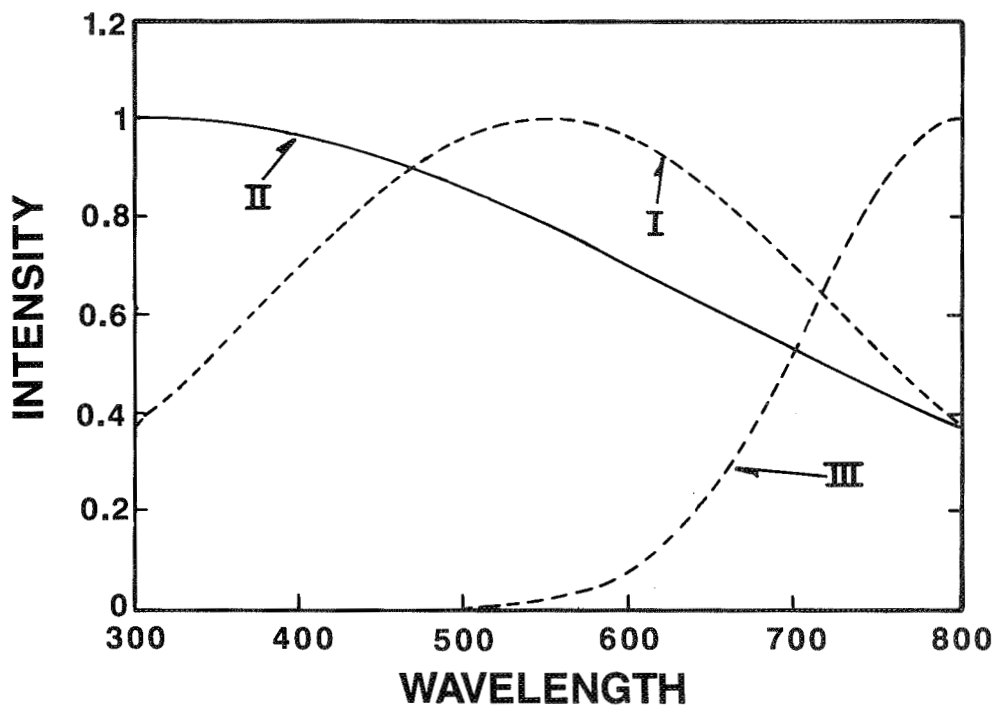


Figure 1. Normalized emission spectra of hypothetical compounds I, II, and III.

TABLE 1. CALCULATIONS FOR CONCENTRATION

Compound	I	II	III
Actual	1.00	2.00	3.00
FARA	1.00	2.00	3.00

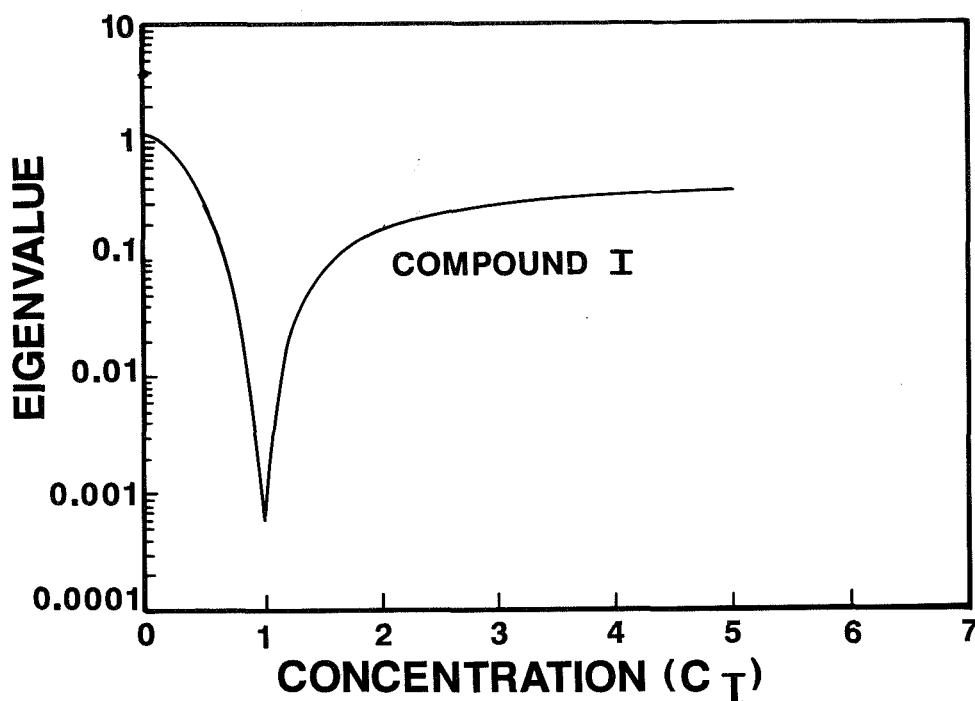


Figure 2. The functional dependence of the appropriate eigenvalue, S , on the hypothetical concentration c_I' for the ETM of compound I.

DISCUSSION AND CONCLUSIONS

FARA has potential as a method for interpreting laser radar returns. FARA can be applied to matrices consisting of fluorescence intensity as a function of emission wavelength and time. The authors have shown that it can calculate the nonzero concentration of a constituent in an unknown without having every laboratory standard from every constituent in the unknown. FARA also can serve as a deconvolution method for laser radar if the temporal profile of the laser pulse is reproducible.

REFERENCES

1. Measures, R., 1984. Laser Remote Sensing, New York: John Wiley and Sons.
2. Ho, C. -N., G. D. Christian, and E. R. Davidson, 1980. Anal. Chem., 52:1071-1078.
3. Ho, C. -N., G. D. Christian, and E. R. Davidson, 1978. Anal. Chem., 50:1108-1113.
4. Malinowski, E. R., and D. G. Howery, 1980. Factor Analysis in Chemistry, New York: John Wiley and Sons.
5. Lorber, A., 1986. Anal. Chem., 58:1167-1172.

LIDAR RECEIVERS FOR PICOSECOND REMOTE SENSING

D.V.STOYANOV, T.N.DREISCHUH

Institute of Electronics, Bulgarian Academy of Sciences

72 Trakia blvd., 1784 Sofia, BULGARIA

Fax (359-2) 757-053, Tlx. 23561 CF BAN BG

1. INTRODUCTION. The lidars of picosecond resolution are an attractive tool for remote probing of some highly dynamic objects as sea subsurface waters, small-scale turbulences in the atmosphere etc. The picosecond lasers are suitable illuminating sources, but the main restrictions are due to the lack of proper receiving methods, combining the both high temporal and amplitude resolution, good sensitivity, short integration time, wide dynamic range. The methods for short pulse measurements are not well suitable for picosecond lidars, operating at low level, highly dynamic signals. The streak-cameras are of high cost, lower sensitivity and dynamic range $\sim 10^3$. Because of the background, the single quantum regime in photo-multipliers (PMT) is ineffective. The sampling of highly dynamic optical signals with resolution ≤ 1 ns is a serious problem, limiting the application of the high speed PMT-MCP [1] in the picosecond lidar systems.

The goal of this work is to describe the use of a new photodetection technique developed in [2-6] at a creation of lidars, combining the picosecond resolution with the high amplitude resolution, dynamic range and sensitivity.

2. BLOCK-SCHEME OF THE PICOSECOND LIDAR SYSTEM. It is shown on Fig.1a,b. The optical scheme (as in Doppler lidars) is applied, because the scattered volumes are usually at relatively short distances, when picosecond resolutions are required. The vertically polarized picosecond pulse of width ≤ 0.1 ns from the laser 1 is passed through the Brewster window 2 and the quarter wave-plate 3 and by the telescope T is directed to the scattering volume. The parallel (after the telescope) backscattered radiation is transformed by the plate 3 into a beam of horizontal polarization, which is reflected by the window 2 and passed through the optical gating block 4 and then by the lenses L1 and L2 is expanded to illuminate uniformly the photocathode of the multianode PMT-MCP. The delay block 5, triggered by the laser pulse, provides the gating pulses of width t_g to control the gating block 4 and the sampling in the receiving block (Fig.1c). According to the method [2-6] each anode is fed to a resonator of frequency ω_0 , $\{\omega_q\}$, $q=1..Q$. The signals on the resonator's outputs, excited by the gated optical flux are amplified and then amplitude detected. Through the multiplexer MP the detected amplitude are sampled by the low speed, high resolution A/D converter (1-10 KHz, 12-16 bits). Finally, using the inverse algorithm, described below, the lidar profile within the gating cell is retrieved with a resolution $\Delta\theta = t_g/Q$, which may be in the picosecond range. Scanning the trigger delay t_d from pulse to pulse, the lidar return from the entire volume may be detected with a picosecond resolution, if the repetition period T_g is longer than to the resonator relaxation time τ_r . In order to avoid some distortion of the lidar profile at short gating cells t_g finally the effect of gating shape function must be taken into account. As a result, volumes of lengths of order of 10-100 m may be sounded with a resolution of 1 - 0,1 ps.

3. DESCRIPTION OF LIDAR SIGNALS. The signals on the resonator outputs are given [6] by

$$S(\omega_q, t) \sim A(\omega_q) \exp(-(\beta - j\omega_q)t); \quad A(\omega_q) = H(\omega_q) \left[\sum_{l=1}^Q N(\vartheta_l) \alpha_{lq} + n_o V(\omega_q) \right], \quad (1)$$

where $A(\omega_q)$ are the amplitudes; $H(\omega_q)$ is the transfer function with bandwidth $\Delta\omega_r$ of the system FMT-resonator [6]; $\alpha_{lq} = \cos(\omega_q l \Delta\vartheta)$; $V(\omega_q) = \sum_{l=1}^Q \alpha_{lq}$; $N_l = N(\vartheta_l) + n_o$ is the lidar profile of resolution $\Delta\vartheta = t_s/Q$, $l = 1 \dots Q$ within the strobe t_s ; $\tau_r = 1/\beta < T_s$. The bandwidth $\delta\omega_q$ of $S(\omega_q, t)$ is of order of $\delta\omega_q \sim 2/\tau_r$. It may be shown, if the frequency differences $\Omega_q = \omega_{q+1} - \omega_q \gg \delta\omega_q$ the signals $S(\omega_q, t)$ form an orthogonal set of eigen-functions and the lidar profile on the resonator outputs may be expressed by a set of equations:

$$B(\omega_q) = \sum_{l=1}^Q \alpha_{lq} N(\vartheta_l), \quad (2)$$

where $B(\omega_q) = A(\omega_q) - n_o V(\omega_q)$, $n_o = N_t/Q$. The mean profile n_o is determined by the resonator of frequency $\omega_o \rightarrow 0$, when $A(\omega_o) \cong N_t$, N_t is the total energy within the gating cell. The centered time-resolved profile is given by

$$N(\vartheta_l) = \sum_{q=1}^Q \left(\frac{D_{q1}}{D} \right) B(\omega_q), \quad (3)$$

where D is the determinant of the matrix α_{lq} , D_{q1} are the co-factors. There are two frequency ranges of interest when a picosecond resolution may be achieved: 1) $\{\omega_q\} = q2\pi/t_s \leq \Delta\omega_r$ (Fourier frequencies) and 2) $\{\omega_q\} \leq \Delta\omega_r < 2\pi/t_s$ - the non-Fourier case, when a specific analysis is required.

3.1. THE USE OF FOURIER RESONATOR FREQUENCIES. This case was analyzed in details in [6]. Here $V(\omega_q) = 0$ and the maximum resolution will be $\Delta\vartheta_F = 2\pi/\Delta\omega_r$. If $t_s = 10$ ns, the resonator frequencies must be chosen by $\omega_q = 100q$ MHz, $Q = 10$, if FMT with $\Delta\omega_r \sim 1$ GHz is used. Therefore the lidar resolution $\Delta R = 15$ cm. The main advantages of this approach for picosecond lidars are [6]: the separation of the time-resolved profile $N(\vartheta_l)$ and the mean profile n_o and their separately sampling, the high amplitude resolution (12-16 bits/1KHz) at 1 ns temporal resolution. As seen, the resolution is of order of the best FMT, but the problems of sampling the highly dynamic lidar signals are essentially avoided.

3.2. THE USE OF NON-FOURIER RESONATOR FREQUENCIES. It is of interest how to provide resolutions, better than in the standard regimes of FMT (0.1 ns or better). The estimate is based on the limiting resolution of the method [4]. The detailed analysis will be published elsewhere. The noises affect on the locality of the coefficients α_{lq} [6] and on the minimum frequency differences Ω_q of the resonators. The effect of sampling noises may be neglected because of the use of high resolution A/D converters. Using the requirement for the statistical distinction of the amplitudes $A(\omega_q)$, the following approximate expression for the frequencies ω_q is obtained:

$$\omega_q \sim q10/(t_s \sqrt{N_t}) \quad (4)$$

There are some problems to solve the Eqs. (3) at $Q \gg 1$ because of the fast

decreasing of the Determinant D at a non-Fourier matrix α_{1q} . In such of cases $D \neq 0$ is not the best criteria. Better estimates may be obtained by an analysis of solutions at different Q and proper choice of $\{\omega_q\} < \Delta\omega_r$ for a given FMT, varying the gating interval t_s . The resolution will depend on t_s and the maximum tolerable number Q_m of resonators. The graph of the resolution $\Delta\theta = t_s/Q_m$ as a function of t_s is given on Fig.2, where the consequent values of Q_m are given too. As seen, Q_m does not exceed 10 at $t_s = 1$ ns ($\Delta\theta = 0.1$ ns). In principle, if $t_s < 1$ ns are available, resolutions better than 0.1 ns may be realized. The minimum pulse energy N_{\min} to hold the frequency differences $\Omega_q < \Delta\omega_r/Q_m$ is $N_{\min} = (10^2 Q_m^2)/(t_s^2 \Delta\omega_r)$.

As a result two approaches, based on the method [2-6] may be proposed to create optical receivers for the picosecond lidars. The main advantages of the non-Fourier eigen-functions are the better resolution and the non-critical choice of resonator frequencies $\{\omega_q\}$. In the Fourier case the equality $\omega_q = q2\pi/t_s$ must be hold in order to reduce the nonstationary background [2,6], which is the main advantage of this case.

4. CALCULATION OF THE LIDAR RECEIVER USING COMMERCIAL FMT. 16-anode FMT-MCP of "Hamamatsu" type R 1712 [7] with a rise time 0.27 ns and $\Delta\omega_r \sim 1.2$ GHz is assumed. The lowest frequency $\omega_0 = 1$ MHz [2] to measure n_0 may be chosen. If $\Delta R = 15$ cm is required, the best choice is the use of Fourier frequencies. In this case, at $t_s = 15$ ns, the frequencies are given by $\omega_q = 66.66q$ MHz, $q = 1 \dots 15$. At higher resolutions, the non-Fourier case must be applied. Here it is better to use the all anodes and to choose the frequencies according to the condition $\omega_q = 80q$ MHz. In this case the frequencies required are chosen using the graph on Fig.2 at a given $t_s < 1$ ns and pulse energy N_t from the previously defined set $\{\omega_q\}$. Determining Q_m the real resolution will be t_s/Q_m . The resonators may be produced using the SAW-technology. An essential simplification is the non-critical value of τ_r (the quality factors of $10^3 - 10^4$ are tolerable).

5. CONCLUSIONS. Lidar receivers, effective at picosecond resolutions, based on the new photodetection method for converting the secondary electron trains into single-frequency decayed oscillations are described. Two variants using Fourier and non-Fourier frequencies are considered. These receivers offer one of the best compromises between the high temporal and amplitude resolution, low cost, sensitivity, the use of low speed A/D converters. They may be applied for remote probing of small-scale scattered objects as subsurface sea sounding, aerodynamic fluxes, atmospheric turbulences, etc.

- REFERENCES:**
1. Hamamatsu, Technical Data, Feb.1989
 2. D.V.Stoyanov, J.mod.Optics, 35, 827 (1988)
 3. D.V.Stoyanov, J.mod.Optics, 36, 1065 (1989)
 4. D.V.Stoyanov, J.mod.Optics, 38, 417 (1991)
 5. D.V.Stoyanov, J.mod.Optics, 38, 2111(1991)
 6. D.V.Stoyanov, Appl. Opt., 30, No31 (1991)
 7. Hamamatsu, Technical Data Sheet No T-111, 1986

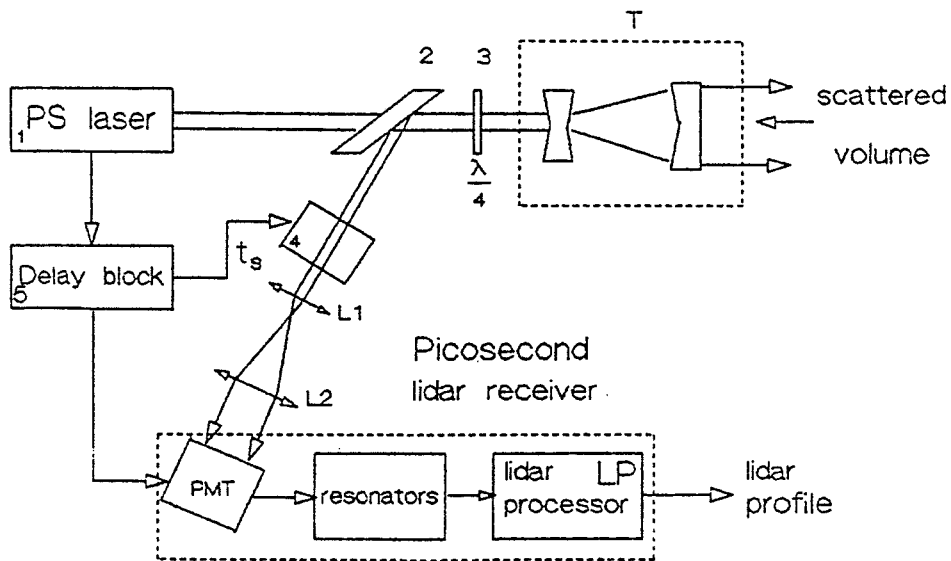


Fig.1a

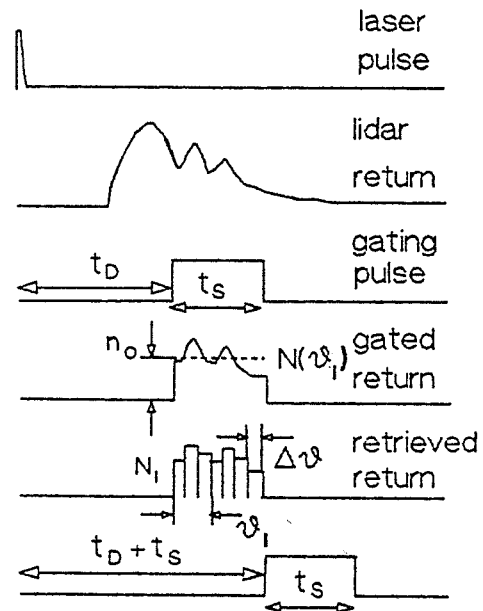


Fig.1b

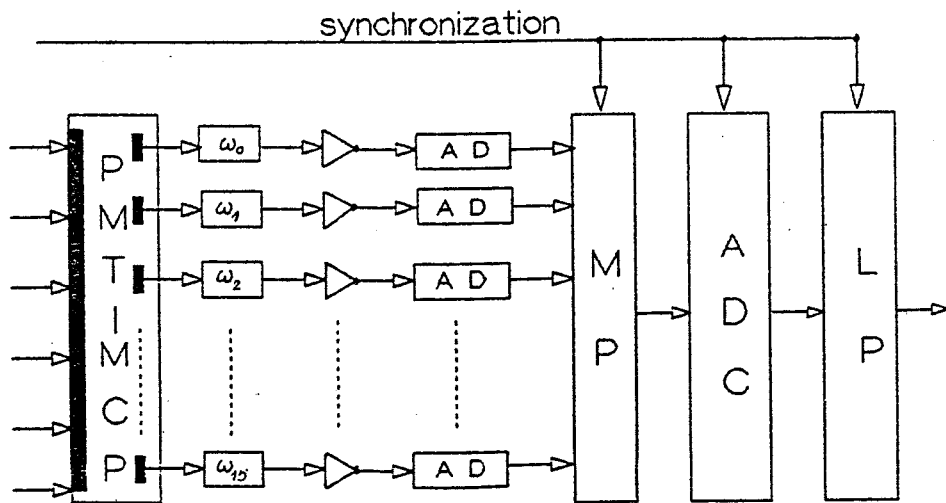


Fig.1c

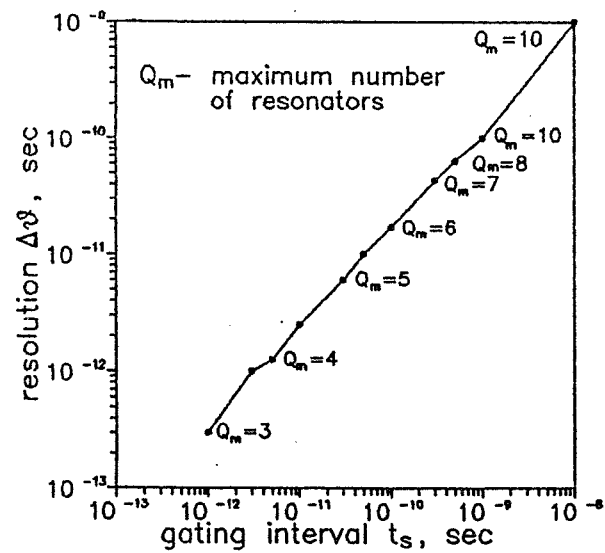


Fig. 2

ACOUSTO-OPTIC FILTERING OF LIDAR SIGNALS

G. Kolarov, A. Deleva, Ts. Mitsev
Institute of Electronics,
Bulgarian Academy of Sciences, Sofia, Bulgaria

The predominant part of the noise in lidar receivers is created by the background radiation; therefore, one of the most important elements of the receiving optics is a spectrally selecting filter placed in front of the photodetector. Interference filters are usually used to transmit a given wavelength. Specific properties of the interference filters, such as simple design, reliability, small size, and large aperture, combined with high transmission coefficient and narrow spectral band, make them the preferred spectral device in many cases. However, problems arise in applications such as the DIAL technique, where fast tuning within a wide spectral region is necessary.

Tunable acousto-optical filters (TAOF), used recently in astrophysical observations [Bates et al., 1984; 1987] to suppress the background radiation, can be employed with success in lidar sounding. They are attractive due to the possibility for fast spectral scanning with a narrow transmission band. The TAOF's advantages are fully evident in DIAL lidars where one must receive simultaneously signals at two laser frequencies; the alternative of implementing a complicated system having two photodetectors is sequential receiving by a single detector with quickly tunable filter. From this point of view, the relevant TAOF properties are: smooth or step wise tuning at an arbitrary wavelength within the $0.35 \mu\text{m} - 5 \mu\text{m}$ range; bandwidth of $0.5 \text{ nm} - 2 \text{ nm}$; switching time between two wavelengths of less than 1 ms ; transmission coefficient approximately equal to 0.4 [Chang, 1981]. Electronic transmission control makes it possible to use TAOF as light switches blocking the high-power signals from the near lidar zone.

In the present paper we discuss the results of laboratory studies of a lidar receiving system using an tunable acousto-optical filter aimed at estimating the its effectiveness in lidar atmospheric sounding applications.

In the laboratory optical set-up (fig.1) we used the receiving system of a high-repetition sounding lidar [Kolarov et al., 1988]. The Cassegrainian telescope was with focal length of 1 m, diameter of 0.2 m, and receiving angle of 1 mrad. Wollaston's prisms were used as TADF polarizer and analyzer. A lens with focal length of 15 mm was used for collimation. The A OF (made of synthetic quartz crystal, with dimensions 7x7x70 mm) was of collinear type (MФ-201Г). A photon-counting photomultiplier (EMI 9863QB100) was used as photodetector.

To determine the laser-light transmission losses for one pass through a lidar optical receiving system with TADF we measured a He-Ne laser power ($\lambda = 632.8$ nm) at the telescope entrance, directly in front of the filter, and at the exit in the first order after the filter. Our estimates for telescope and TADF transmission coefficients were $K_{t_s} = 0.4$ and $K_{AOF} = 0.25$, respectively, at RF supply power of 5 W. The ratio of the first-order power to the indirectly-scattered power in the blocked zero order was > 3500 .

The most important operating characteristic of the filter is its spectral transmission band. It depends on the specific set-up parameters (geometric filter aperture, beam divergence, laser wavelength) and must be determined experimentally. In fact, one measures the relative TADF transmission as a function of the wavelength. We measured a transmission bandwidth of $\Delta\lambda = 0.6$ nm. Two small side maxima were also present shifted at ± 2.2 nm with the ratio to the central maximum being 1 : 50.

The system's characteristics as we measured them, together with the specific TADF properties already mentioned, give us reason to expect that their use will result in further improvements in the lidar systems and will widen the applications of differential absorption, Raman scattering and fluorescence lidar techniques.

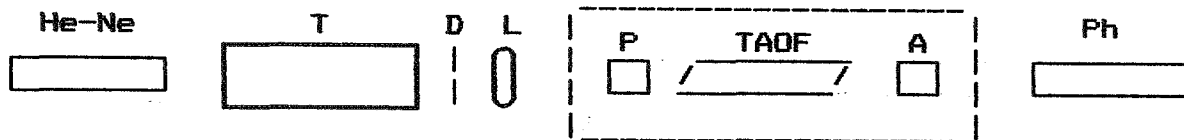


Fig 1. Experimental set-up : He-Ne laser; T- telescope;
 D- diaphragm; L- lens; P- polarizer; TAOF- acousto
 optical filter; A- analyzer; Ph- photo multiplier

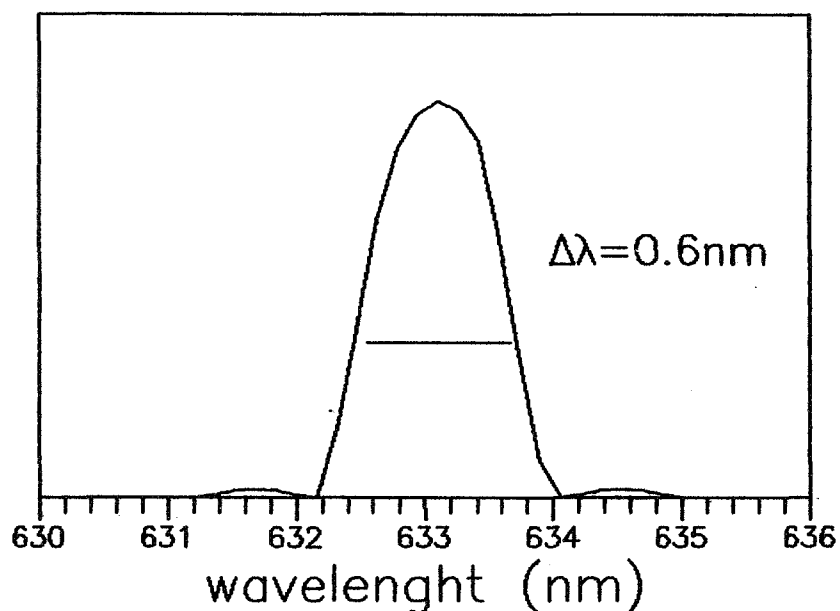


Fig.2. Characteristic filter transmittance profile in
 the region near the center of the passband.

REFERENCES

B.Bates,D.Halliwell at all,(1984),Appl. Opt., 23,no 2, 257
 B.Bates,D.Halliwell at all,(1987),Appl. Opt.,26,no 22, 4783
 I.C.Hang, Optical Engineering,(1981), 20, no.6,.824
 Kolarov,G.V., Stojanov,D.V., Mitsev,Ts.A. Againa,Tz.,(1988),
 Atmosferic Optics, 1, no 2, 125

GROUND-BASED DOPPLER LIDAR OF INCREASED LASER
INSTABILITY: CONCEPTION AND DESIGN

D. V. STOYANOV, B. M. BRATANOV, V. N. NABOKO, M. D. ANGELOVA
Institute of Electronics, Bulgarian Academy of Sciences
72 Trakia blvd., 1784 Sofia, BULGARIA,
Fax 02-757-053, Tlx. 23561 CF BAN BG

1. INTRODUCTION. The pulsed CO_2 Doppler lidars are effective tools for ground-based atmospheric wind sensing, but the high cost of the lidar transceivers mainly due to the required high frequency stability (better than 10^{-9} or 100 KHz) is a restriction factor to their widely use in meteorology. The best approach to overcome this problem is to develop Doppler lidars effective at increased laser instability. This work is based on the results in [1], where a new scheme for Doppler lidar detection by the use of frequency synthesis in wide fluctuation bandwidth of laser instabilities is described. A ground-based system, using this approach is under development in the Institute of Electronics -BAS.

2. BLOCK-SCHEMES OF THE DOPPLER LIDAR. As known, there are two block-schemes of the CO_2 coherent lidars: 1) by an injection seeding TE-laser transmitter [2] and 2) by a hybrid TE-laser [3]. These schemes, adapted to our approach, are represented in fig. 1a and 1b. The local oscillator (LO) in fig. 1a is stabilized around the peak of the gain curve (fig. 2a). The CW injection seeding laser is stabilized at some mean frequency offset $\bar{\omega}_0$ within the bandwidth $\Delta\omega_{\text{CW}}$ in respect to the LO using the reference mixer PD-2 and further the TE-laser cavity is tuned to the CW laser frequency. In the hybrid scheme as shown in fig. 1b, 2b, the CW laser is stabilized within the gain curve, but the LO is further stabilized at some offset $\bar{\omega}_0$ in respect to the CW-frequency. Here the quenching of the CW-lasing during the TE-pulse requires to stabilize the frequency within the intervals after the recovery of the CW lasing. Because of the wide tolerable fluctuation bandwidth, the timeconstant of the stabilization may be essentially short.

As shown in [1] the tolerable laser instability $\Delta\omega_0$ may be reduced to the order of $10^{-7} - 10^{-6}$ (10 - 100 MHz). It is of interest to estimate how to choice the parameters of LO and CW lasers in order to realize the all advantages of the method [1] to operate in wide fluctuation bandwidth. The tolerable instability on the intermediate frequency is $\Delta\omega_0^2 = \Delta\omega_{\text{LO}}^2 + \Delta\omega_{\text{CW}}^2$, where $\Delta\omega_{\text{LO}}$ and $\Delta\omega_{\text{CW}}$ are the insta-

bilities of the CW and LO lasers. We will accept that the frequency fluctuations within the time intervals of 100 - 200 μ s (usually of interest in ground-based lidars) may be neglected. The LO-instability $\Delta\omega_{LO}$ on fig. 2a may be accepted to be of order of 10 MHz and further the LO gain bandwidth $\Delta\omega_{gLO}$ may be chosen to be 100 - 200 MHz thus, the pressure of 20 - 40 Torr is required. The gain bandwidth of the CW laser may be determined by the following conditions: 1) $\omega_L > 3 \omega_{Dm}$ and 2) $\omega_H = \omega_{max} = \bar{\omega}_0 + \frac{1}{2}\Delta\omega_0$, where $\omega_L = \bar{\omega}_0 - \frac{1}{2}\Delta\omega_0$ and ω_H are the lower and higher frequency extrema on the fluctuating intermediate frequency ω_0 , ω_{Dm} is the maximum expected Doppler frequency, ω_{max} - the maximum tolerable intermediate frequency. As an example, if $\omega_{Dm} \lesssim 5$ MHz, $\omega_{max} \lesssim 100$ MHz, $\bar{\omega}_0 \sim 45$ MHz, $\Delta\omega_0 \sim 50$ MHz. Therefore, the CW gain bandwidth must be of order of 300 - 400 MHz (60-90 Torr gas pressure). It must be noted, the above parameters are usually used in Doppler lidars.

In the hybrid lasers the CW-gain bandwidth is usually chosen 50 - 100 MHz (gas pressure 20 Torr), because of the longer resonators (>1 m, ~ 150 MHz mode spacing). It is evident, the parameters of the LO are the same as of the CW-laser in the injection seeding transmitter.

As it is evident, the requirements to the frequency stability of the laser sources, transmitter and LO, are very simple, 10^{-7} - 10^{-6} , which effects on the total price of the lidar.

3. DOPPLER DETECTION ON THE INTERMEDIATE FREQUENCY. The problem of operation at higher instability may be solved using an appropriate technique for signal detection on the intermediate (reference) ω_0 frequency and processing of data. At wideband fluctuations the use of a quadrature detector for an extraction the Doppler signals is a serious problem, because of the effect of frequency dependence of the 90° -phase shifter. The main advantages of the method [1] are due to the nonstrictly tracking of the frequency ω_0 and thus to the use of frequency synthesis without the 90° -phase shifters. The Doppler detector is shown on fig.3. It may be applied to the both block schemes in fig.1. Timing diagrams are given in fig.4 and in [1]. The reference frequency ω_0 by the photomixer PD-2 is fed to the tracking synthesizer, where the frequency ω_0 is measured during the pulse τ_1 and then a decision is made to generate one of the frequencies ω_i of the previously determined set $\{\omega_i\}$, $i = 1..I$

in the synthesizer [1]. The measured frequency ω_0 and ω_1 are recorded in the lidar processor as a reference data at final processing. The signal from the synthesizer is used as a reference in the receiving mixer 1 and then by the low-pass filter the Doppler information may be extracted, as was experimentally tested in [1]. The TE-laser pulse is triggered after the recording the all reference data in the processor. Further by the photomixer PD-3 the entire TE-laser pulse is coherently detected and sampled, including the high peak, which affects essentially on the measurement accuracy. Now, using the sampled data from the receiving photomixer PD-1 the Doppler spectra may be calculated as shown in [1].

4. LIDAR PROCESSOR. The lidar processor consists of two channels A/D converter for both the lidar data and the laser pulse (20 MHz/8 bits), additional channels to record the frequencies ω_0 and ω_1 for each shot and a personal computer with a specialized software.

5. PROCESSING ALGORITHMS. The processing of lidar data is in principle the same as in other Doppler lidars, with some peculiarities due to the new principle of the Doppler detection on the intermediate frequency. The value and the sign of the mean frequency of the Doppler spectra may be determined as shown in [1]. The precisely recorded laser chirp history may be used to increase the accuracy of Doppler measurement. Some new inverse algorithms are tested to improve the temporal resolution, which is important at lower heights for ground based systems.

6. CONCLUSIONS. It is shown here, that using the method of Doppler detection, developed in [1], the low cost ground-based Doppler lidars may be developed. The main effect is due to the application of laser sources of higher instability (10^3 times lower) and a simpler detection technique on the intermediate frequency using the frequency synthesis without phase-shifted coherent oscillators. In the ground-based system, developed in the Institute of Electronics-BAS a TEA-hybrid laser (Edinb.Instr.) is used. The detection block was tested at the frequency fluctuation bandwidth $\Delta\omega > 10$ MHz corresponding to a relative instability of order of 10^{-7} . The frequency step in the synthesizer is 1 MHz. For further comparison two Doppler detectors are incorporated in the system: by the new method and by quadrature detection. It must be noted the very easy tuning of the new detection scheme at operation in the wide frequency range in respect to the case, when quadrature detector is used.

REFERENCE

1. Stoyanov D. V., B. B. Bratanov, M. D. Angelova, Rev. of Sci. Instrum., 1991, v. 62, No. 11.
2. Ch. Werner et al., WIND, Phase O/A-Report, 1989.
3. Post M. J., R. A. Richter, R. M. Hardesty, T. R. Lawrence, F. F. Hall, Jr. *Physics and Technology of Coherent Infrared Radar*, Proc. SPIE 300, 1981, pp. 60-65.

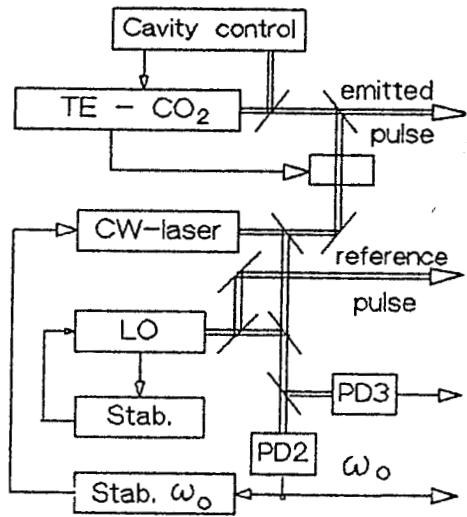


Fig. 1a

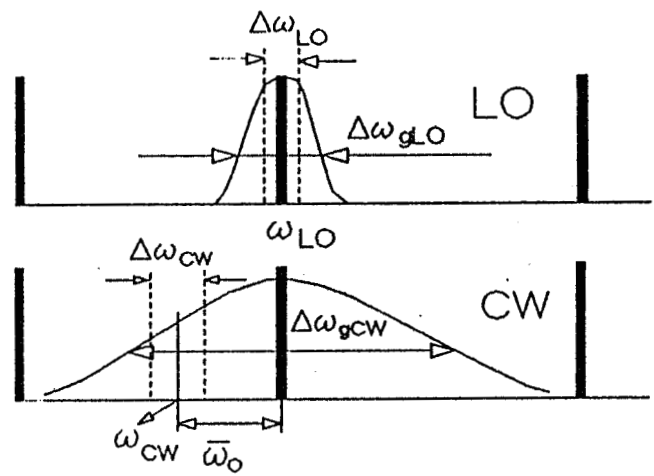


Fig. 2a

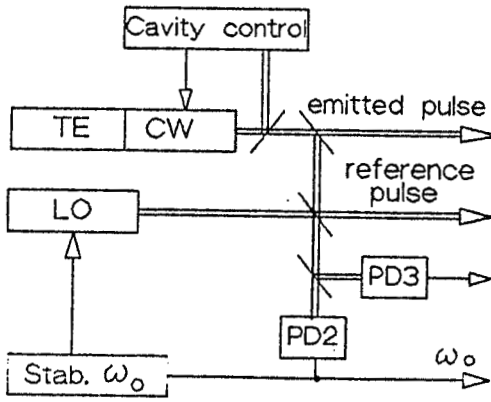


Fig. 1b

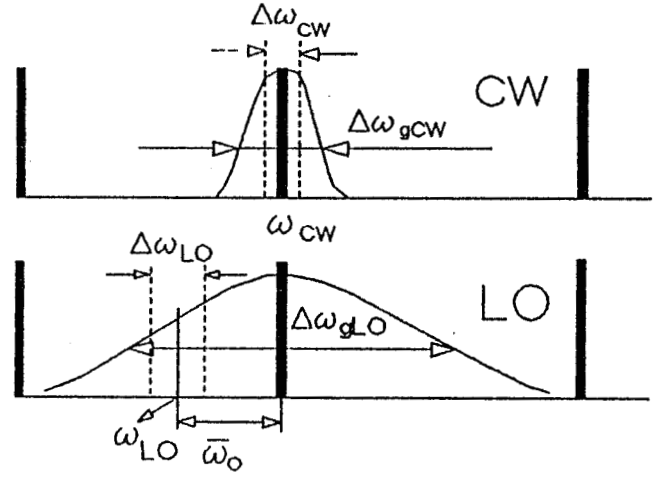


Fig. 2b

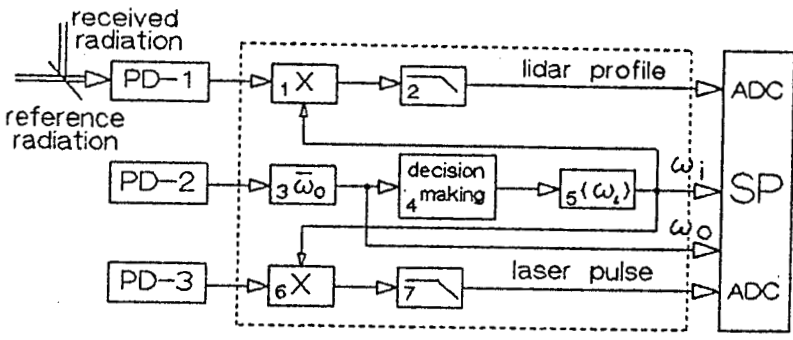


Fig. 3

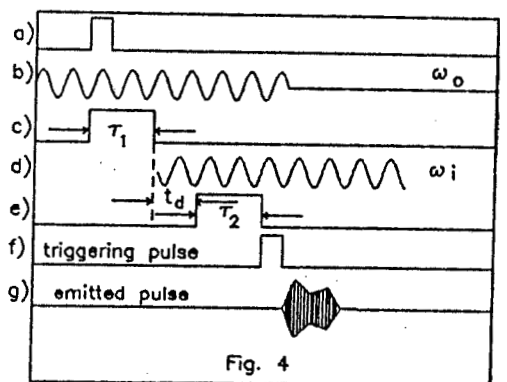


Fig. 4

ANALYTICAL ESTIMATES OF THE PP-ALGORITHM
AT LOW NUMBER OF DOPPLER PERIODS PER PULSE LENGTH

M. D. ANGELOVA, E. V. STOYKOVA, D. V. STOYANOV
Institute of Electronics, Bulgarian Academy of Sciences
72 Trakia blvd., 1784 Sofia, BULGARIA,
Fax 02-757-053, Tlx. 23561 CF BAN BG

1. INTRODUCTION. When discussing the Doppler velocity estimators it is of significant interest to analyze their behavior at low number of Doppler periods $n_D = 2V_r t_s / \lambda \approx 1$ within the resolution cell t_s (V_r is the radial velocity, λ - the wavelength). Obviously, at $n_D \ll 1$ the velocity error is essentially increased. The problem of low n_D arises in PBL, where higher resolutions are usually required but the signal-to-noise ratio (SNR) is relatively high. In this work analytical expression for the relative RMS error of the PP Doppler estimator at low number of periods for a narrowband Doppler signal and arbitrary model of the noise correlation function is obtained. The results are correct at relatively high SNR. The analysis is supported by computer simulations at various SNR's.

2. ANALYTICAL EXPRESSION FOR THE RELATIVE RMS ERROR. The sampled inphase and quadrature signals may be presented by [1]

$$I(i\Delta t) = A_i \cos \theta_i + b_i, \quad Q(i\Delta t) = A_i \sin \theta_i + b'_i; \quad i=1, n \quad (1)$$

where $\Delta t = t_s / n$, A_i and $\theta_i = \omega \cdot i\Delta t + \varphi_i$ are the amplitude and the phase of the signal, which is a stationary narrowband Gaussian process with variance σ^2 , spectral width σ_s and mean Doppler frequency ω_0 ; the independent noise components b_i and b'_i have distribution $N(0, \sigma_b^2)$. If the condition $\sigma_s \ll \omega_0$ is fulfilled, we may assume that the amplitude and the phase of the signal are constant within the resolution cell and fluctuate from shot to shot. We also introduce Gaussian distribution $N(\omega_0, \sigma_\omega^2)$ for the averaged over the range gate frequency ω with $\sigma_\omega \ll \omega_0$. From $n_D \ll 1$ it follows $\omega \Delta t \ll 1$. Then the relative estimate of the Doppler frequency fluctuations can be written in the form [1]:

$$\hat{\mu} = \hat{\omega} / \omega - 1 = \hat{x} / (1 + \hat{y}) \approx \hat{x} (1 - \hat{y} + \dots), \quad (2)$$

where $\hat{x} = \sum_1^n [A\alpha_1 + \beta_1 - \omega \Delta t (A\gamma_1 + \delta_1)] / \omega \Delta t (n-1) A^2$, $\hat{y} = \sum_1^n (A\gamma_1 + \delta_1) / (n-1) A^2$
 $\alpha_1 = b'_{i+1} \cos \theta_i + b_i \sin \theta_{i+1} - b_{i+1} \sin \theta_i - b'_i \cos \theta_{i+1}$; $\beta_1 = b_i b'_{i+1} - b_{i+1} b'_i$

$$\gamma_i = b_{i+1} \cos \theta_i + b_i \cos \theta_{i+1} + b'_{i+1} \sin \theta_i + b'_i \sin \theta_{i+1}; \quad \delta_i = b_i b_{i+1} + b'_i b'_{i+1}.$$

The term \hat{y} in (2) can be neglected if $\text{SNR} \geq 5\text{dB}$. To find the relative RMS error in (2), we average the noise, frequency and amplitude fluctuations, accepting the following approximations:

$$\begin{aligned} \omega &= \omega_0 + \delta\omega, & 1/\omega &\approx 1/\omega_0 (1 - \delta\omega/\omega_0) \\ \cos(s\omega\Delta t) &\approx \cos(s\Omega) - s \cdot \Delta t \cdot \delta\omega \cdot \sin(s\Omega) \\ \sin(s\omega\Delta t) &\approx \sin(s\Omega) + s \cdot \Delta t \cdot \delta\omega \cdot \cos(s\Omega), & \Omega &= \omega_0 \Delta t \\ A &= A_0 + \delta A; & A_0 &= \langle A \rangle; & 1/A &\approx 1/A_0 (1 - \delta A/A_0 + \delta A^2/A_0^2). \end{aligned}$$

Finally, the general expression for the relative RMS error μ becomes:

$$\mu^2 = \frac{2.396\xi}{\Omega^2(n-2)^2} \left\{ M + \sum \left[P(s) \cos(s\Omega) + Q(s) \sin(s\Omega) + 4.168\xi R(s) \right] \right\} \quad (3)$$

$$\begin{aligned} \text{where } P(s) &= 2bH(s) + k_1 U(s) + k_2 V(s)s, & Q(s) &= 4dH(s) + k_3 U(s)s + k_4 V(s), \\ R(s) &= aF(s) + \Omega^2 G(s), & U(s) &= (n-2-s) \cdot [\rho(s+1) + \rho(s-1)], \\ H(s) &= (n-2-s) \cdot \rho(s), & V(s) &= (n-2-s) \cdot [\rho(s+1) - \rho(s-1)], \\ F(s) &= (n-2-s) \cdot [\rho^2(s) - \rho(s+1) \cdot \rho(s-1)], & a &= 1 + \nu^2, & b &= 1 + \nu^2 + \Omega^2, \\ G(s) &= (n-2-s) \cdot [\rho^2(s) + \rho(s+1) \cdot \rho(s-1)], & d &= \nu^2 \Omega, & c &= \Omega^2 - 1, \\ M &= (n-2) \cdot (a+b-\rho(1)) \cdot \cos \Omega + \rho(1) \cdot (2\nu^2+1) \cdot (c \cdot \cos \Omega - 2\Omega \cdot \sin \Omega) + \\ & & & + 2.084\xi \cdot [b \cdot (1-\rho^2(1)) + 2\Omega^2 \rho^2(1) \cdot (n-1)], \\ k_1 &= a \cdot (b \cos \Omega - 2\Omega \sin \Omega) + d \cdot \Omega \cdot \cos \Omega, & k_2 &= d \cdot [b(\Omega \cos \Omega - 2 \sin \Omega) - \Omega(a+1) \cdot \cos \Omega], \\ k_3 &= d \cdot [b(2 \cos \Omega + \Omega \sin \Omega) - \Omega(a+1) \cdot \sin \Omega], & k_4 &= a \cdot (2\Omega \cos \Omega + b \sin \Omega) + d \cdot \Omega \cdot \sin \Omega, \\ \rho(s) &= \text{normalized noise correlation function, } \xi = \sigma_b^2 / \sigma^2. \end{aligned}$$

Using the above expression, we can analyze the behavior of the RMS error μ at different $n_D < 1+2$ for an arbitrary noise model $\rho(s)$, varying the SNR and the number of samples $n = t_s / \Delta t$ within the interval t_s . The graphs of $\mu(n_D)$ at $n=16, 32$ and 64 for the case of white noise and $\text{SNR}=10$ and 20 dB are given in Fig.1. As seen, the RMS error decreases at lower n . It is due to the increase of the phase step $\Omega = \omega t_s / n$ of the Doppler vector, while the white noise variance (or SNR) is not affected by n . There is a strong dependence of μ on SNR at lower n_D (Fig.2). At higher SNR ≈ 30 dB (as in the PBL), the relative error does not exceed 10% when $n_D \approx 0.5$ and 15% at $n_D \approx 0.25$. The graphs of μ on the radial velocity V_r for different resolutions $\Delta R=50, 100, 200$ m ($n=16$) calculated by the above expressions are shown in Fig. 3. As seen, good resolutions may be achieved using PP-algorithm

when $n_D < 1$. At $V_r < 5$ m/s, the errors in the expressions (3) are essentially increased.

3. COMPUTER SIMULATION. At low SNR's and high n_D the neglect of the high-order terms in the estimate $\hat{\mu}$ decomposition would not be correct. In such cases, a computer simulation of the time series (1) has been performed with the number of pairs $N=2000$, 4000 and 6000 for a white noise at SNR ≥ 10 , 0 and -10 dB respectively. Some of the results are shown in Figs. 4-6. In Fig. 4 the percentage of cases when PP technique leads to wrong velocity direction is plotted as a function of n_D for $n=16$. As seen, the probability of wrong velocity direction may be neglected for $n_D > 0.4$ at SNR ≥ 10 dB. The same may be concluded for SNR ≈ 5 dB and $n_D \geq 1$. In Fig. 5 the minimum values of n_D ensuring the relative RMS error of 10% (solid lines) and 20% (dashed lines) are plotted as a function of SNR. At 10 dB, the simulation gives 10%-RMS error at $n_D = 2$ for $n=32$ and $n_D = 1.5$ for $n=16$; $\mu=20\%$ is provided at $n_D = 0.5 \div 0.7$. These values show that SNR=10 dB permits an accurate single-shot velocity measurement for $2V_r t_s / \lambda \approx 1$. At lower SNR's the $n_D > 2$ is required. The fraction of estimates with relative error below 10% vs the SNR at $n_D = 0.5, 1$ and 2 is presented in Fig. 6.

The comparison between the analytical and computer simulation results for $n_D \leq 1$ shows a good agreement at high SNR $> 10 \div 20$ dB. It must be noted that the use of PP-algorithm at lower n_D is limited mainly by the relative error in velocity magnitude but not by the probability for wrong direction determination.

4. CONCLUSIONS. The results of this work show the relatively good performance of the PP-algorithm for Doppler frequency estimation at high SNR when better resolutions are required. The analytical expressions, obtained here may be used with different models of additive noises. The preliminary calculations show that at $n_D \leq 1$ the algorithm is strongly affected by the presence of correlated noises. Our further analysis of the expression (2) will be emphasized mainly on the effect of correlated noises, the presence of which is sometimes not easy to be controlled in the Doppler lidar channels.

REFERENCE 1. E. V. Stoykova, L. L. Gurdev, B. M. Bratanov, M. D. Angelova, D. V. Stoyanov, ILRC15, July 23-27, 1990, Tomsk, USSR, pp. 413-417.

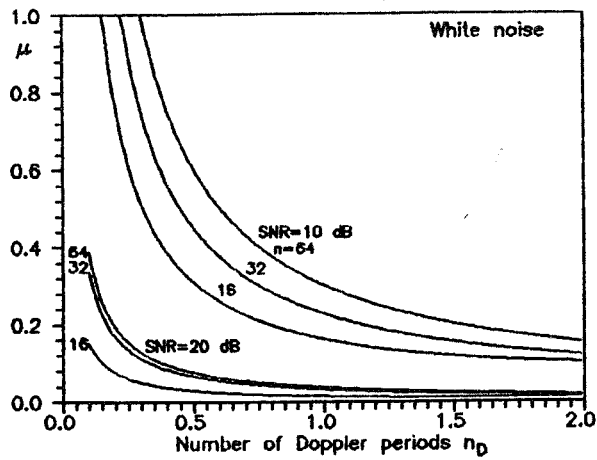


Fig. 1

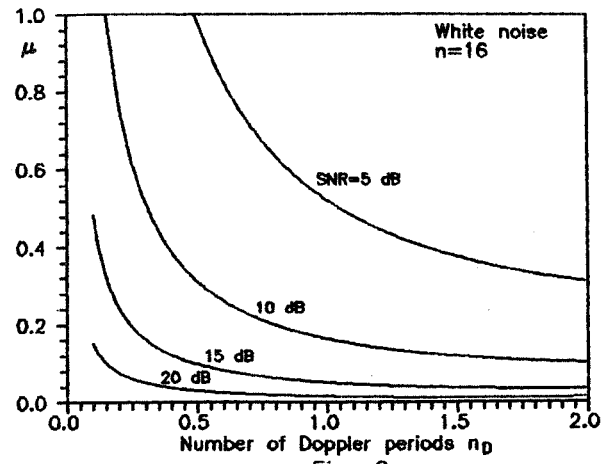


Fig. 2

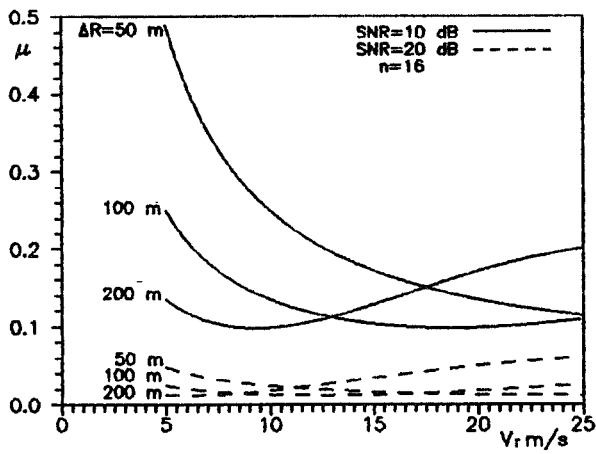


Fig. 3

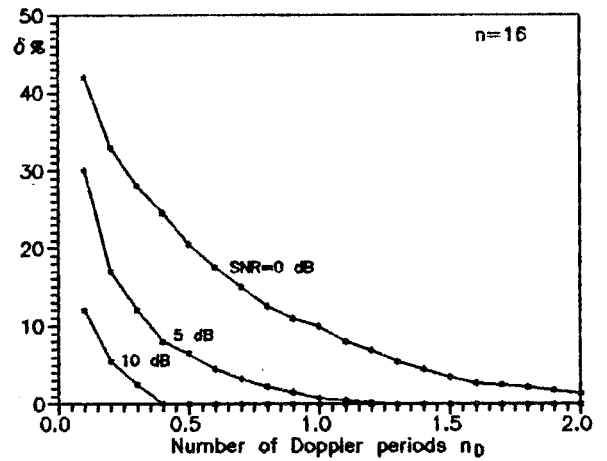


Fig. 4

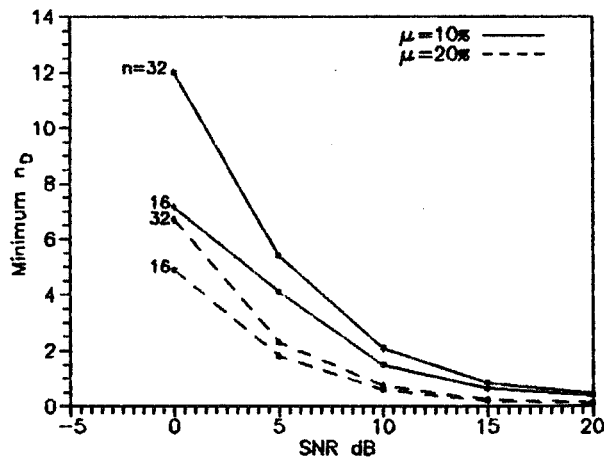


Fig. 5

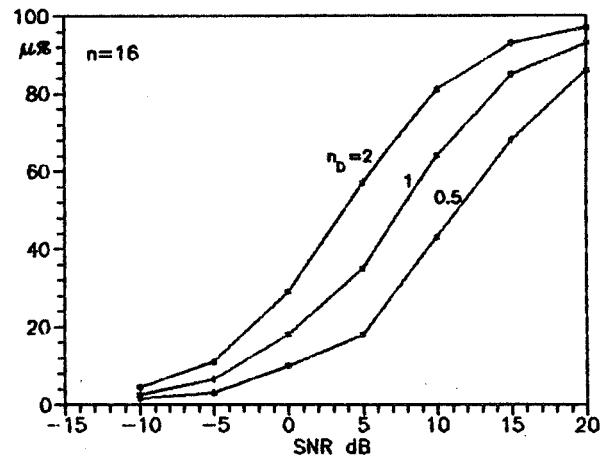


Fig. 6

A CONSIDERABLE EFFECT OF STRATOSPHERIC AEROSOL ON LIDAR-DETECTED OZONE PROFILE AND A THREE-WAVELENGTH INVERSION TECHNIQUE FOR BOTH OZONE AND AEROSOL

Qiu Jinhuan

*Institute of Atmospheric Physics
Chinese Academy of Sciences, Beijing 100029, China*

1. INTRODUCTION

As far as DIAL technique is concerned, it is optimum that the off-line wavelength is very near to the on-line wavelength in order to avoid a difficult consideration of the atmospheric aerosol scattering. However, the two wavelengths of ozone-DIAL is usually considerably different. Usually, Excimer laser of 308nm (on-line) and Raman shifting of 353nm or third harmonic of Nd-YAG laser with 355nm (off-line) are selected for measurements of the stratospheric ozone, and there is a difference of 45nm or 47nm between them. Because of the difference there is a difference in the atmospheric scatterings of the two wavelengths, which can cause some error in the retrieved ozone profile if the aerosol scattering is neglected. This paper is devoted to a study of the effect of the stratospheric aerosol on the ozone solution and proposed a three-wavelength detection technique for obtaining the more exact ozone profile and the aerosol profile in the stratosphere.

2. INVERSION MODELS AND RESULTS

According to lidar equation the mean ozone concentration between heights z_i and z_{i+1} can be determined from detected two-wavelength photon numbers as follows:

$$N(z_i, z_{i+1}) = \frac{\ln[Q(z_{i+1}, \lambda_0) / Q(z_{i+1}, \lambda_1)] - \ln[Q(z_i, \lambda_0) / Q(z_i, \lambda_1)] - \ln[R^*(z_{i+1}) / R^*(z_i)]}{2(\delta_1 - \delta_0)(z_{i+1} - z_i)} - \frac{S^*(z_i) + S^*(z_{i+1})}{2(\delta_1 - \delta_0)} \quad (1)$$

$$\text{with } R^* = [\beta_m(z, \lambda_0) + \beta_a(z, \lambda_0)] / [\beta_m(z, \lambda_1) + \beta_a(z, \lambda_1)],$$

$$S^* = \sigma_m(z, \lambda_0) + \sigma_a(z, \lambda_0) - \sigma_m(z, \lambda_1) - \sigma_a(z, \lambda_1),$$

where λ_1 and λ_0 are the on-line wavelength and the off-line one, which are 308nm and 355nm in this paper, and δ_1 and δ_0 are their ozone absorption sections. $Q(z, \lambda)$ is the photon number at height z , β_m is the molecular backscattering section and β_a the aerosol one, σ_m is the molecular extinction coefficient except for ozone contribution and σ_a the aerosol one. If aerosol scattering needs considering, there is a difficulty in determining R^* and S^* . In order to study the effect of the aerosol of the ozone solution, the following models of determining R^* and S^* are considered, and their corresponding values are marked as R and S .

(A) $R = R^*$, $S = S^*$, considering both aerosol and molecular in backscatter and extinc-

tion.

(B) $R = \beta_m(z, \lambda_0) / \beta_m(z, \lambda_1)$, $S = \sigma_m(z, \lambda_0) - \sigma_m(z, \lambda_1)$, neglecting the aerosol backscattering and extinction.

(C) $R = \frac{\beta_m(z, \lambda_0)}{\beta_m(z, \lambda_1)}$, $S = S^*$, neglecting the aerosol backscattering.

(D) $R = R^*$, $S = \sigma_m(z, \lambda_0) - \sigma_m(z, \lambda_1)$, neglecting the aerosol extinction.

(E) $R = 1$ and $S = 0$, neglecting differences of the aerosol scatterins and the molecular ones at two wavelengths.

In our numerical experiments, the vertical profiles of molecular and ozone are taken from the US standard atmosphere, and Following three aerosol profiles are considered.

a: Aerosol extinction coefficient profile at 694.3nm wave-length presented by McClatchey⁽¹⁾.

b and c: Two profiles (15–35km) of Lidar-measured aerosol backscattering sections at 694.3nm over Mauna Loa on June 25, 1982 and December 28, 1983⁽²⁾. Here for the heights of lower than 15km aerosol data are same with the first case.

Fig.1a,b and c show the backscatter ratios for the three aerosol profiles at 694.3nm (crosses) and 355nm (dotts). Fig.2a,b and c illustrate errors of the ozone solutions by inversion models A (dotts) and B (crosses), corresponding with three aerosol profiles a, b and c, respectively.

Table 1 Inversion Error of Total Ozone Amount and Standard Deviation of Ozone Profile

Inversion Model	Aerosol Profile a		Profile b		Profile c	
	ER(%)	D(%)	ER(%)	D(%)	ER(%)	D(%)
A	0.0	0.0	0.0	0.0	0.0	0.0
B	0.8	3.5	4.7	72.3	1.1	19.2
C	1.3	3.4	0.6	72.2	0.6	19.1
D	0.6	0.2	3.9	5.6	0.3	0.6
E	4.8	9.1	10.3	72.9	6.8	22.0

Table 1 gives percent inversion errors (marked as ER) of total ozone amounts and standard deviations (markd as D) of retrieved ozone profile (0.2km resolution) from 15km to 35km for five inversion models and three aerosol profiles.

It can be found from Figs.1–2 and Table 1:

(1) Among three aerosol profiles, the first one (background model) has the smallest backscatter ratio peak, and the profile b has largest peak because of El. Chichon volcanic cloud, which is up to 8.45 at the 27km height for the 355nm wavelength, implying a dominant contribution of aerosol to total backscatter there.

(2) Model A is corresponding to no error of the ozone solution. If aerosol scattering is

neglected (Model B), a very large error is obtained for profile b and c, even being larger than 100% in some heights and with standard deviation of 72.3% for profile b. For the profile a the standard deviation is 3.5% in the case of Model B.

(3) As shown by a comparison of Model C with Model D, neglect of aerosol backscatter has much stronger effect on the ozone solution than neglecting aerosol extinction.

(4) The error of the ozone profile is much larger than the one of its total amount. For example, in the case of the profile b and Model B the standard deviation of the ozone profile is 19.2%, but the error of its total amount is only 1.1% because of the fact mentioned next.

(5) There is a vibration error in the ozone solution. if backscatter ratio increases with the height the ozone concentration solution deviates large, and if the ratio decreases, the solution is smaller than its exact value (compare Figs.1 and 2).

Furthermore, error of the ozone solution caused by an uncertainty in the aerosol size distribution is studied in this paper with the result that the error is large for the aerosol profile b or c and so the information about aerosol size distribution is important for improving accuracy.

3. THREE-WAVELENGTH INVERSION TECHNIQUE

As mentioned above, the information about aerosol scattering and its size distribution is important for improving accuracy of the ozone solution. In this section a three-wavelengths (532nm, 355nm and 308nm) lidar inversion technique is proposed for the simultaneous determination of ozone concentration, aerosol backscatter section and its size distribution. The inversion technique goes like this:

(1) Derive aerosol backscatter sections at two wavelengths of 532nm and 355nm from lidar return signals. In this paper the signals are simulated according to a ozone-lidar developing in our Institute⁽³⁾ and with 10 laser shots for the 308nm wavelength;

(2) Fit a Junge aerosol size distribution through Mie calculation by using above backscatter data from 16km to 26km, and then determine aerosol backscatter section at the 308 wavelength and the extinction coefficients at three wavelengths of 532nm, 355nm and 308nm with a known aerosol refractive index;

(3) Derive the ozone profile by using inversion Model A. Numerical tests is made with a logarithmic stratospheric aerosol size distribution⁽⁴⁾, and some inversion results will be given here. The result shows that the ozone solution is greatly improved by the present three-wavelength inversion algorithm.

REFERENCES

- (1) R.A. McClatchey et al., 1975: Optical Properties of the Atmosphere, AD-753075.
- (2) J. Deluisi et al., 1985: Lidar observations of stratospheric aerosol over Mauna Loa Observatory, NOAA Data Report ERL ARL-5.
- (3) Sheng Siping et al., 1992: A DEVELOPING multiple-wavelength lidar for detecting ozone and aerosol in the stratosphere, submitted to 16th ILRC.
- (4) Espenscheid, W.F., et al., 1964: Logarithmic functions for colloidal particles, J. Phys. Chem., 68, 3093-3097.

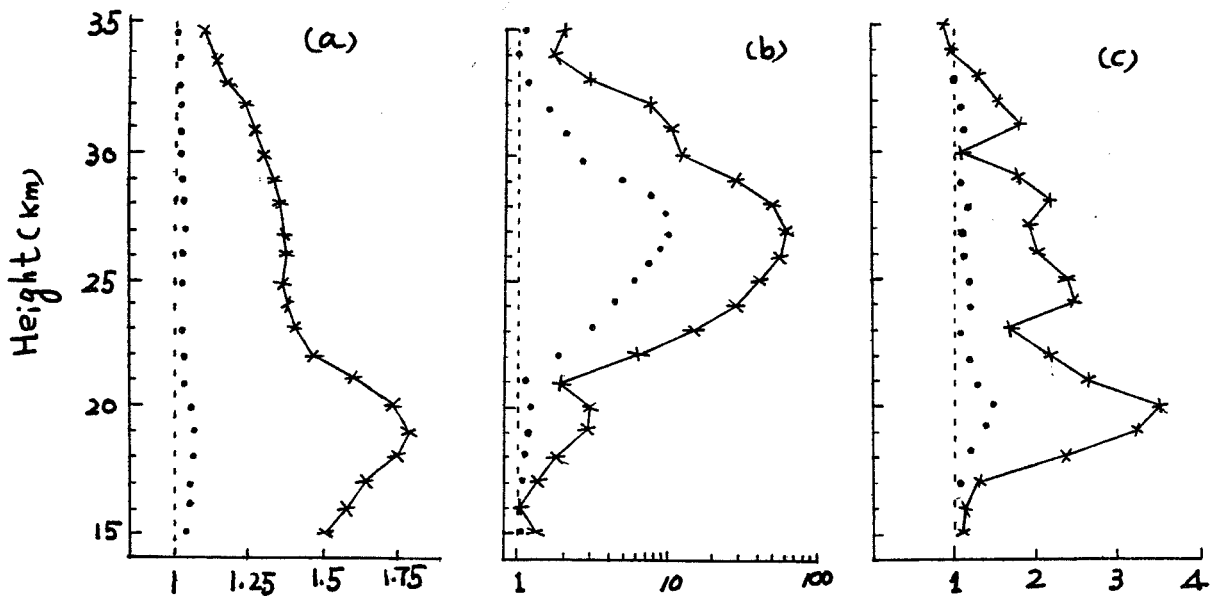


Fig.1 Backscattering Ratio vs Height

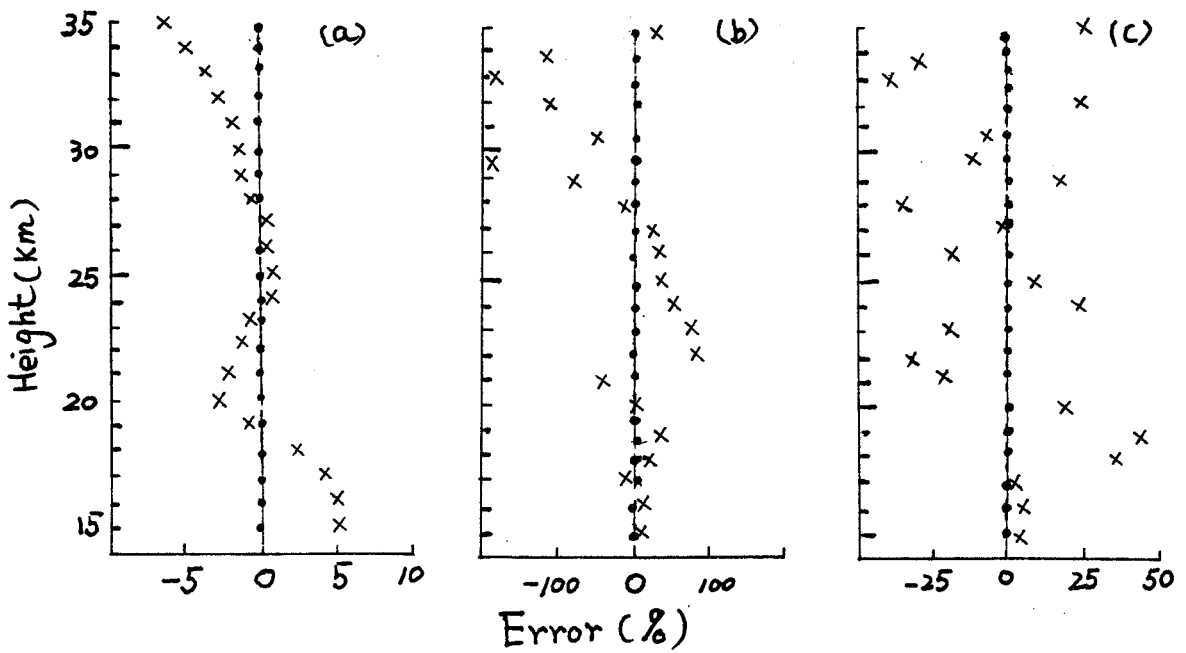


Fig.2 Percent Error of Ozone Solution vs Height

HIGH-RESOLUTION PROCESSING OF LONG-PULSE-LIDAR DATA

L.L.GURDEV, T.N.DREISCHUH, and D.V.STOYANOV

Institute of Electronics, Bulgarian Academy of Sciences
72 Trakia blvd., 1784 Sofia, BULGARIA
Fax (359-2) 757-053, Tlx. 23561 CF BAN BG

1. INTRODUCTION The purpose of this work is to demonstrate the performance of the Fourier-deconvolution technique developed earlier [1,2] for improving the resolution of long-pulse coherent lidar power profile with account of the multiplicative fluctuations. The behaviour of the error due to the power fluctuations as well as a way to reduce it are analysed theoretically and simulated numerically. A processing of real data obtained from the NOAA ground-based Doppler lidar is also presented. Similar problems have been investigated by Zhao and Hardesty [3], using a different approach based on introducing a correction function to the lidar equation.

2. BASIC CONSIDERATIONS AND MODELS A general form of the lidar equation in the case of pulsed lidars is given by

$$F(t) = \int_{c(t-\tau)/2}^{ct/2} f(t-2z/c) \bar{\Phi}(z) dz, \quad (1)$$

where $F(t)$ is the lidar return at the time t after the pulse emission, $f(\vartheta)$ is the normalized pulse shape function, c is the speed of light, z is the distance from the lidar, τ is the pulse duration, $\bar{\Phi}(z)$ is the short-pulse lidar profile ($\tau \rightarrow 0$).

The problem of retrieving $\bar{\Phi}(z)$ on the basis of known $f(\vartheta)$ and measured $F(t)$ has been analysed in detail in [1,2]. As a result, retrieving deconvolution algorithms have been developed based on Fourier-transformation technique, or the solution of a Volterra integral equation, or a recurrence relation between $\bar{\Phi}(ct/2)$, $\bar{\Phi}[c(t-\tau)/2]$, and $F'(t)$ in the case of rectangular pulses. The effect of a stationary additive (to $F(t)$) noise on the algorithm performance has been also investigated [2].

In the case of coherent detection, the function $F(t) = I(t)^2 + Q(t)^2$ describes the signal power profile ($I(t)$ and $Q(t)$ are the inphase and the quadrature components, respectively). In consequence of the incoherent aerosol scattering, the profile $\bar{\Phi}(z \approx ct/2)$ fluctuates very strongly, and the range of the fluctuations is of the order of $\bar{\Phi}(z)$. Their effect on $F(t)$ is equivalent to an additive quasihomogeneous (quasistationary) noise. A decrease of the noise level is achievable by averaging over some number of laser shots. When the pulse duration τ is less than the fine-structure characteristic period T of the mean profile $\bar{\Phi}_m = \langle \bar{\Phi} \rangle$, we obtain practically the short-pulse (maximum-resolved) lidar profile $F(t) = K \bar{\Phi}(z \approx ct/2)$ ($K = (c/2) \int_0^\tau f(t') dt'$). When τ exceeds T , the mean values $F_m(t) = \langle F(t) \rangle$ and $\bar{\Phi}_m(z \approx ct/2)$ are already connected by the convolution (1). Then, in order to improve the lidar resolution, we have to retrieve $\bar{\Phi}_m(z \approx ct/2)$ using the deconvolution techniques developed in [1,2], for $f(\vartheta)$ and $F(t)$ recorded by some minimal sampling interval $\Delta t_0 < \tau$. For extremely short Δt_0 , we would near ideally retrieve $\bar{\Phi}_m(z)$. In this case, the effect of noises is maximum. Consequently, in order to suppress the noises and to retrieve $\bar{\Phi}(z)$ correctly, we must choose some optimum computing step $\Delta t = m \Delta t_0$ (m is integer) so that $\Delta t_0 < \Delta t < T$. In this way the noise level will be decreased $\sim (\Delta t / \Delta t_0)^{1/2}$ times.

The following models are used for simulations. Namely, the complex amplitude $dA(z)=dI(z)+idQ(z)$ per interval of range $\Delta z_0=c\Delta t_0/2$ and $f(\theta)=1$, is assumed to be

$$dA(z) = [\bar{\Phi}_m(z)\Delta z_0]^{1/2} w(z), \quad (2)$$

where $w=w_r+iw_i$, w_r and w_i are independent Gaussian-distributed random functions with mean values equal to 0, variances equal to 1/2, and covariances $C_{r,i}(\Delta z)=\langle w_{r,i}(z)w_{r,i}(z+\Delta z) \rangle=(1/2)\delta(\Delta z)$; δ denote delta function. Formally, we can write $\langle dA(z)dA^*(z') \rangle=\bar{\Phi}_m(z)\delta(z-z')dzdz'$. Obviously, $\langle |A(z)|^2 \rangle=\bar{\Phi}_m(z)\Delta z_0$, and $\bar{\Phi}(z)\Delta z_0=|A(z)|^2=\bar{\Phi}_m(z)\Delta z_0+n_{\bar{\Phi}}(z)$, where $n_{\bar{\Phi}}(z)=\bar{\Phi}_m(z)\Delta z_0(|w(z)|^2-1)$. The variance $Dn_{\bar{\Phi}}(z)=\langle n_{\bar{\Phi}}^2(z) \rangle$ of the equivalent additive noise $n_{\bar{\Phi}}(z)$ is equal to $(\bar{\Phi}_m(z)\Delta z_0)^2$. The model of the pulse-integrated complex amplitude $A_j(t)$ corresponding to the model (2) is the sum

$$A_j(t) = \sum_{j=1}^N [f(t-2z_j/c)]^{1/2} dA(z_j), \quad (3)$$

where $z_j=c(t-\tau)/2+(j-1)\Delta z_0$. The sum (3) is a numerical analog of the integral

$$A_j(t) = \int_{c(t-\tau)/2}^{ct/2} f(t-2z/c)dA(z) \quad (4)$$

The relation (1) between $\bar{\Phi}_m(z)$ and $F_m(t)=\langle |A_j(t)|^2 \rangle$ follows from Eq.(4), and the properties of $dA(z)$. For a single profile $F(t)$ we have $F(t)=|A_j(t)|^2=F_m(t)+n(t)$ where $n(t)$ is a zero-mean noise with variance $D_n(t)=\langle |n(t)|^2 \rangle=F_m^2(t)$, and correlation time $\tau_c=\tau$.

3. SIMULATIONS The model of the mean profile $\bar{\Phi}_m(z)$ used here (Fig.1) is a sum of some smooth profile and a high-resolution component of period T shorter than the laser pulse. The laser pulse shape is shown in Fig.2. It is constructed on the basis of the NOAA Doppler lidar data, and the assumption that the pulse is of gain-switched type. Fig.3 shows a profile $\bar{\Phi}(z)$ which is the average one of 32 single short-pulse profiles $\bar{\Phi}_j(z)=|A_j(z)|/\Delta z_0$ ($j=1\dots 32$) simulated according to the above models (Eq.(2)) using a sample interval $\Delta z_0=15m$. Although the averaging, the profile $\bar{\Phi}(z)$ remains intensively fluctuating. The corresponding 32 long-pulse profiles $F_j(z)$ ($j=1,2\dots 32$) obtained on the basis of Eq.(3) are also averaged, and the mean profile $\bar{F}(z)$ is given in Fig.4. The distortion of $\bar{F}(z)$ with respect to $\bar{\Phi}_m(z)$ is well seen. The processing of the profile $\bar{F}(z)$, using the Fourier-deconvolution algorithm [2] leads to retrieving $\bar{\Phi}_m(z)$ with bias and random errors depending on the computing step $\Delta t=m\Delta t_0$ ($\Delta t_0=2\Delta z_0/c$). In Fig.5 the profile $\bar{\Phi}_m(z)$ is shown retrieved by computing step $\Delta t=\Delta t_0$ on the basis of the profile $\bar{F}(z)$ (Fig.4). A similar result obtained for $\Delta t=8\Delta t_0$ is given in Fig.6. As seen the increase of Δt leads to a decrease of the noise effect. The bias error consist in an elevation, mainly around the maximum area, of the smooth

component of the model in Fig.1, and an amplification of the amplitude of the high-resolution oscillations. The explanation of such behaviour is that the bias error is proportional to the expression $-(d^2\Phi(z)/dz^2)(\Delta z)^2$ [2].

4. REAL LIDAR DATA PROCESSING Here we have used raw data from the NOAA Doppler lidar. An averaged over 32 laser shots profile $\bar{F}(z)$ is given in Fig.7. The estimated laser pulse shape is that given in Fig.2. The restored, by Fourier-deconvolution technique, profile for $\Phi_m(z)$ is shown in Fig.8. A computing step $\Delta t = 8\Delta t_0$ is used. The profile obtained with a resolution interval Δt shorter than the pulse duration has a clear fine structure which is not practically seen in the long-pulse profile $\bar{F}(z)$. We may suppose, by analogy with the preceding computer simulations, that the highest region of the profile in Fig.8 is probably elevated, and the high-resolution variations are amplified with respect to the original short-pulse profile $\Phi(z)$.

5. CONCLUSION Finally, we may conclude that the deconvolution techniques developed in [1,2] for improving the resolution of long-pulse lidars can be used successfully in the case of coherent detection of aerosol-backscattered lidar returns to extract its fine structure. In this case, the computing step defining the resolution scale must be as possibly large to suppress the noise effect, but small enough to avoid essential distortions of the retrieved profile with respect to the original one. Combining the choice of an appropriate step with averaging over some number of laser shots is a way to obtain good results.

6. ACKNOWLEDGEMENT The authors are grateful to Dr. R.M. Hardesty for providing data obtained from the NOAA ground-based Doppler lidar, which have been used in the study.

REFERENCES

1. L.L. Gurdev, D.V. Stoyanov, T.N. Dreischuh, in Technical Digest on Coherent Laser Radar: Technology and Applications, 1991 (OSA), vol.12, p 284.
2. L.L. Gurdev, T.N. Dreischuh, and D.V. Stoyanov, "Deconvolution Techniques for Increasing the Resolution of Long-Pulse Lidars", in preparation
3. Y. Zhao, R.M. Hardesty, Appl. Opt, 27, p.2719 (1988)

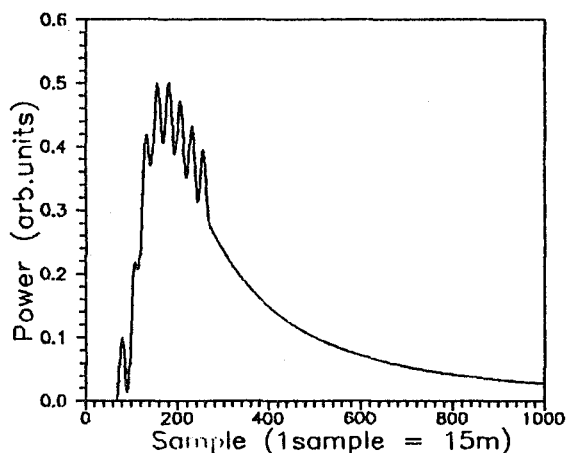


Fig.1

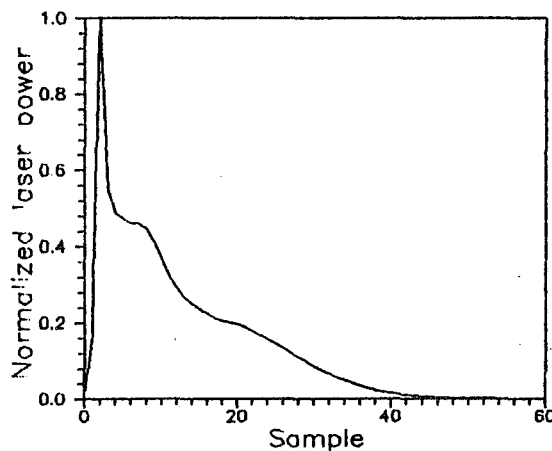


Fig.2

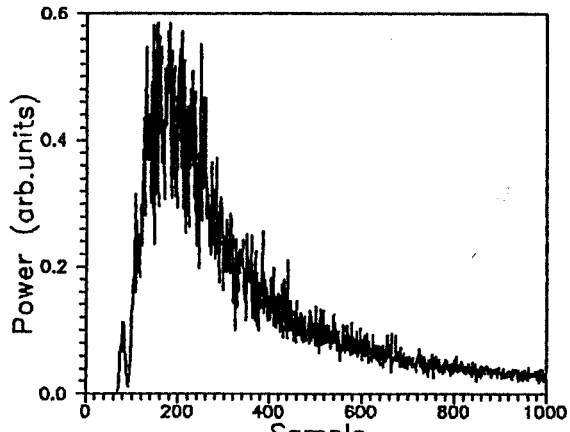


Fig.3

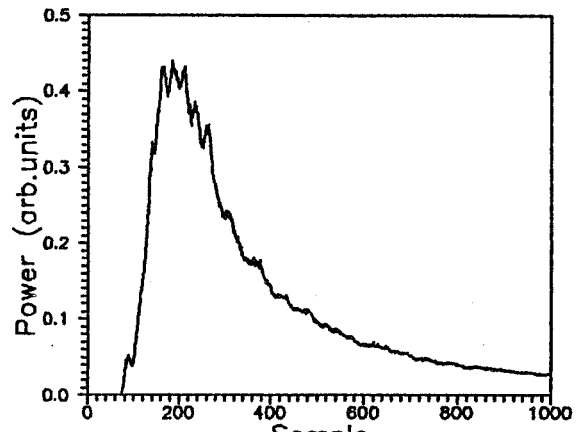


Fig.4

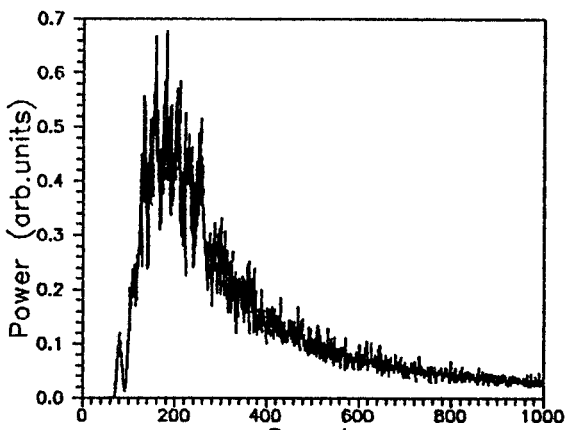


Fig.5

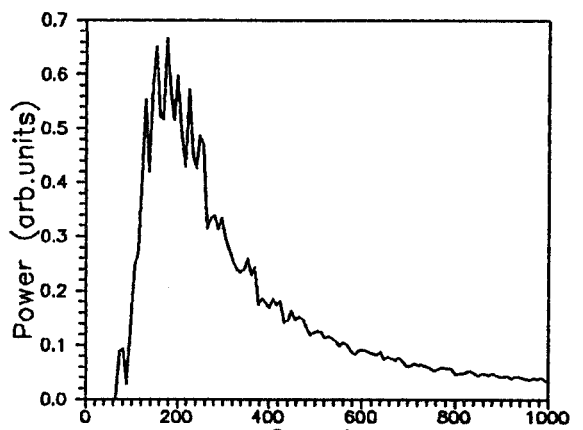


Fig.6

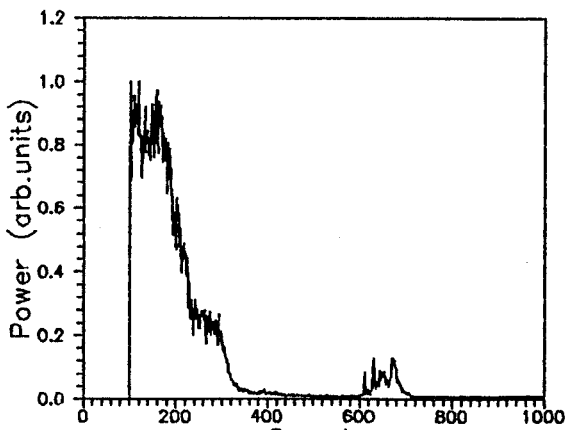


Fig.7

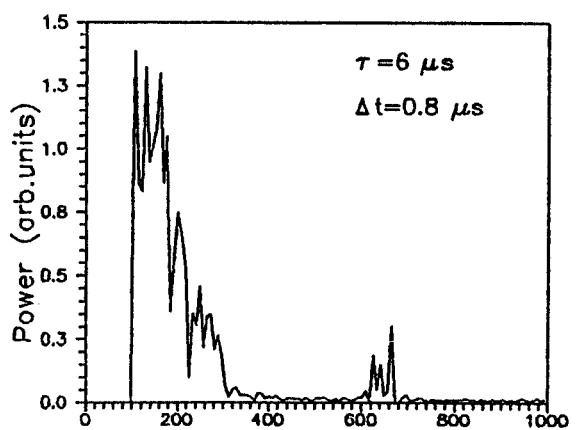


Fig.8

LIDAR MEASUREMENTS OF CLOUD EXTINCTION COEFFICIENT DISTRIBUTION
AND ITS FORWARD SCATTERING PHASE FUNCTION ACCORDING TO MULTIPLY
SCATTERED LIDAR RETURNS

Qiu Jinhuan, Huang Qirong

Institute of Atmospheric Physics
Chinese Academy of Sciences, Beijing 100029, China

1. INTRODUCTION

The study on inversion algorithm to the single-scatter lidar equation for quantitative determination of aerosol or cloud optical property has been being paid to great attention for about thirty years. Some difficulties have not been solved yet. One is that one single scatter lidar equation has two unknowns. Because of the difficulty the determination of the far-end boundary value in the case of the Klett's algorithm will be a problem if the atmosphere is optically inhomogeneous. Another difficulty is the multiple scattering. There is a large error of the extinction distribution solution in many cases if only the single scatter is

considered with neglecting the multiple scattering component^[1,2]. On other hand, there is a promising application of the multiple scattering in remote sensing of aerosol or cloud optical property. For these reasons, in our early study an inversion method for simultaneous determination of cloud (or aerosol) Extinction Coefficient Distribution (ECD) and its Forward Scattering Phase Function (FSPF) is proposed according to multiply scattered lidar returns with two fields of view of the receiver^[2]. The method is based on a parameterized multiple scatter lidar equation deve-

loped by Qiu et al.^[2,3]. This paper is devoted a further numerical tests and an experimental study of lidar measurements of cloud ECD and FSPF by using this method.

Numerical tests are made in two cases of the ground-based lidar and the spaceborne lidar.

Experiments started on March 22, 1992 and will continue to the end of May of this year by using a Nd-YAG lidar with four fields of view, combined a sunphotometer and a hemispheric radiometer with five wavelengths of 450, 550, 650, 750, 850 nm. Table 1 gives specification of the lidar system.

Experiments are made mainly for measurements of cloud optical property. Lidar return data of two fields of view, i.e. 4 mrad and 20 mrad, are used in retrieving cloud ECD and FSPF according to the present inversion method. Lidar-detected cloud optical depth will be compared with the atmospheric columnar Mie optical depth detected by sunphotometer or hemispheric radiometer for testing suitability of our method.

Table 1 Specification of the LIDER System

Transmitter	
Laser	Nd:YAG
Wavelength	1060 nm
Output Energy	80 mJ
Repetition rate	1 Hz
Beam divergence	1.5 mrad
Receiver	
Telescope diameter	80 mm
Field of view(mrad)	4, 9, 15, 20
Signal Processor	
Transient recorder	20MHz, 8bit

References

- [1] H. Quenzel, M. Wiegner and Qiu Jinhuan, 1990: Effects of multiple scattering on lidar remote sensing from space, Abstracts of papers in 15th ILRC, 59-63.
- [2] Qiu Jinhuan and Lu Daren, 1992: Simultaneous determination of cloud (or aerosol) extinction coefficient and its forward phase function from multiple scattering information, In proceeding of MUSCLE6.
- [3] Qiu Jinhuan, H. Quenzel and M. Wiegner, 1990: A parameterized multiple-scatter lidar equation and its application, Abstracts of papers in 15th ILRC.

Measurements of the Backscattering
Phase Matrices of Crystal Clouds
with a Polarization Lidar

B.V.Kaul, A.L.Kuznetsov, E.R.Polovtseva

Institute of Atmospheric Optics,
Siberian Branch, of the Academy
of Sciences of Russia, Tomsk, Russia

A Polarization technique based on measurements of intensities of the polarized I_{\parallel} and crosspolarized I_{\perp} components of scattered radiation is often used in lidar studies of aerosols. The ratio I_{\perp}/I_{\parallel} is related to nonsphericity of scattering particles and it is often called, though unjustified, as depolarization. Correct definition of the term has been introduced earlier [1] as the value $d = 1 - P$, where P is the degree of polarization defined in terms of the Stokes parameters as

$$P = \sqrt{Q^2 + U^2 + V^2} / I$$

In fact, measurements of I_{\parallel} and I_{\perp} enable one to determine the Stokes parameter $Q = I_{\parallel} - I_{\perp}$, and under the condition

$$U = V = 0 \quad (1)$$

the depolarization is determined by the relationship

$$d = 2 \times I_{\perp} / (I_{\parallel} + I_{\perp}) \quad (2)$$

In the case of an ensemble of randomly oriented particles of irregular shapes the condition (1) is always valid. At the same time the situation is quite different in the case of ensembles of crystal particles like, for example, in cirrus clouds. Violation of the condition (1) has been noticed earlier in Ref.2 and 3. In 1988 we have started a new cycle of measuring the Stokes parameters of lidar returns from scattering media irradiated with a linearly polarized light. Basic parameters of our lidar are presented in the catalogue [4]. Based on the lidar data obtained during 1988 to 1990 period a classification of scattering ensembles has been made which reveals five types of the scattering particles ensembles differing by a combination of the Stokes parameters [5,6].

In the 1990 and 1991 we have carried out a cycle of measurements of the lidar returns Stokes parameters using sounding radiation with the following four values of the normalized Stokes vector-parameter

$$\vec{S}^0 = \{ 1, q, u, v \} ;$$

$$\vec{S}_1^0 = \{ 1, 1, 0, 0 \} ; \quad \vec{S}_2^0 = \{ 1, -1, 0, 0 \} ;$$

$$\vec{S}_4^0 = \{ 1, 0, 1, 0 \} ; \quad \vec{S}_4^0 = \{ 1, 0, 0, 1 \} ;$$

Using this approach we managed to measure full matrices of the backscatter for the majority of earlier classified types of scattering ensembles. In this paper we should like to present some preliminary results of this study.

Of 39 events of occurrence of the aerosol layers at altitudes from 7 to 11 km four aerosol layers were referred to the first type and 17 ones to the second type of scattering ensembles. For these types the condition (1) is valid and the use of the relationship (2) is well justified. Other 14 events have been referred to the fourth and fifth types of scattering ensembles, in which cases either the parameter U or V is not equal to zero. It is important to note that the classification made assumed that the Stokes vector-parameter of sounding radiation $S^0 = S^1$. An example of measurement data used for reconstructing the backscattering phase matrices obtained on November 11, 1991 is presented in Fig. 1. A layer of crystal particles observed during this measurement cycle was at altitudes from 7 to 8 km.

Measured values of the scattering ratio $R = (\sigma_R + \sigma_a) / \sigma_R$

are given in the right part of the figure, the mean value of R being equal to 10. In the left part of the figure there are presented the profiles of Stokes parameters normalized by the intensity I ($q = Q/I$; $u = U/I$; $v = V/I$).

According to data presented in Fig. 1a this aerosol layer is of the fourth type ($u = 0, v \neq 0$).

The analysis of data presented in the other figures shows that the difference between the fourth and fifth types of scattering ensembles is to a great extent conventional being dependent on the orientation of the lidar's polarization basis.

The backscattering phase matrix of this aerosol ensemble a_{ij} when normalized by the matrix element A_{11} is as follows

$$a_{ij} = \begin{pmatrix} 1 & -0.12 & -0.01 & 0.06 \\ -0.12 & 0.40 & -0.02 & 0.10 \\ 0.01 & 0.02 & -0.21 & -0.20 \\ 0.06 & 0.10 & 0.20 & -0.20 \end{pmatrix}$$

The elements of the matrix are dimensionless. The absolute value of the matrix elements measurements error we estimate to be ± 0.04 . In order to obtain absolute value of the elements of the backscattering phase matrix each element of the above matrix must be multiplied by the value \bar{A}_{11}

$$\bar{A}_{11} = \sigma_R (\bar{R} - 1),$$

where σ_R is coefficient of the Rayleigh backscatter at the altitude of the aerosol layer; \bar{R} is the mean value of the experimentally measured scattering ratio.

It is characteristic of the example that scattering of a linearly polarized light by this ensemble of particles yields an elliptically polarized scattered radiation, while the scattering

of a circularly polarized sounding radiation yields a totally depolarized light. It is interesting to note that such a situation has been predicted in [7] for the case of the ensemble of partially oriented cylinders of a finite length whose diameters are comparable with the wavelength. It is obvious that prisms of comparable size would produce the same effect.

If so then one obtains a possibility of extracting information on the size and orientation of crystals that in turn bear information on the physical conditions in the aerosol layer. It is pity but a more detailed discussion of this problem as well as of other examples of measured matrices cannot be done within a limited space of this paper.

REFERENCES

1. Born M., Wolf E. Principles of Optics. Pergamon Press. Paris - Frankfurt. 1964.
2. Houston J. P. and Carswell A.I. // Appl. Opt. 1978, v.17, No 4, pp. 614-620.
3. Zuev V.E., Kaul B.V., Kozlov N.V., Samokhvalov I.V. // 9-th International Laser Radar Conf. Abstr., Munich, July 1979, FRG.
4. Second International Lidar Researchers Directory. Comp. by M.P.-Mc.Cormick, Atmospheric Science Division NASA, Langley Research Center, Hampton, Virginia, 23665, 1989, p. 64.
5. Kaul B.V. et al. // Atmospheric Optics, v.4, No 4, pp. 394-403, 1991.
6. Kaul B.V., Krasnov O.A., Kuznetsov A.L., Samokhvalov I.V. // 15-th International Laser Radar Conf. Abst., Tomsk, 1990, USSR.
7. Rakhimov R.F., Romashov D.N., // Atmospheric Optics, v.4, No 10, pp. 1011-1016, 1991.

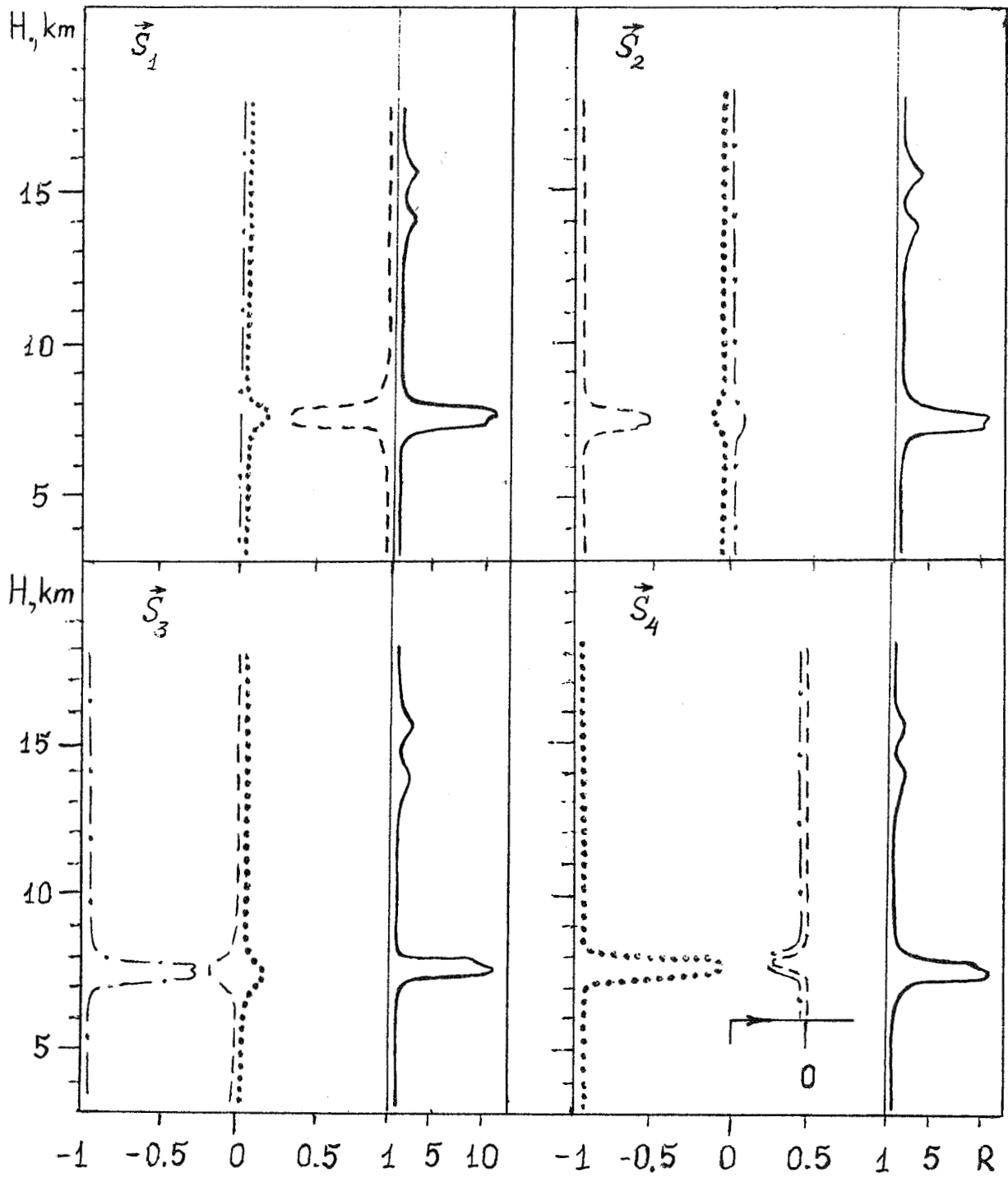


Fig. 1. Vertical profiles of the scattering ratio R and Stokes parameters:

Measurement Capabilities of Giant Lidars for
Middle and Upper Atmospheric Applications

by

Chester S. Gardner
University of Illinois at Urbana-Champaign
Department of Electrical and Computer Engineering
1406 West Green Street, Everitt Laboratory
Urbana, Illinois 61801
(217) 333-4682

Abstract

The development and refinement of sophisticated remote sensing techniques during the past three decades have contributed enormously to our knowledge of the atmosphere. Lidar technologies have developed especially rapidly since the invention of the laser in 1961. Today, sophisticated systems are used to probe composition and structure throughout the atmosphere from the troposphere into the lower thermosphere and are making important contributions to several global change studies. While the recent advances in lidar technology have been impressive, the accuracy, resolution and sensitivity of many systems are still limited by signal levels.

We review the scientific rationale for developing a major new lidar facility to study the chemistry and dynamics of the Earth's atmosphere. The centerpiece of the facility is envisioned to be a 10 meter class telescope which serves as the receiving system for several very large lidar systems. We discuss the observational capabilities of the proposed facility with particular emphasis on measurements of temperature, winds, water vapor and ozone.

LIDAR SOUNDING OF OZONE AND AEROSOLS

V. E. Zuev
 Institute of Atmospheric Optics
 Siberian Branch of the Academy of Sciences of Russia
 Tomsk, Russia

The present report is devoted to the problem of clarifying the mechanism of interaction of ozone molecules with aerosol particles in the atmosphere, taking into account meteorological conditions and the synoptic situation. We have in mind here complex investigations, for which we have built a unique lidar facility providing simultaneous sounding of ozone and aerosols at different heights of the upper troposphere and in the stratosphere. Simultaneous with the retrieval of the standard scattering ratio profiles, data are obtained on the profiles of the microphysical parameters of the aerosols (particle size distribution and particle concentration) using the method of multifrequency lidar sounding developed at the Institute of Atmospheric Optics.

The Lidar facility has the following characteristics:

Transmitter

Wavelength	308	353	413	532	630	771	228	nm
Output Energy	50	30	10	50	30	10	15	mJ/pulse
Pulse Rep.	50-100	50-100	50-100	15	15	15	15	pulses/sec
Beam Divergence	0.1	0.1	0.1	0.1	0.1	0.1	0.1	mrاد

Receiver

Telescope Diameter	220 cm
Field of View	0.5 mrad
Spatial Resolution	15-30 meters

Recording

Detector	PMT-140	-130	-157
Channels	8		
Photon Counting	2		
Number of Gates	512		
Computer	IBM PC/AT		

Along with simultaneous measurements of the vertical profiles of ozone, scattering ratio and microphysical parameters of aerosol, measurements are also made of the ozone and aerosol concentrations, and also many of the gaseous components of the ozone and cycle in the ground layer of the atmosphere in the vicinity of the lidar facility.

The report also discusses results of systematic measurements, carried out in 1991 and 1992, including a series of observations of the volcanic cloud from the eruption of Mount Pinatubo and the results of a statistical analysis of these data.

Atmospheric Measurements Using the LAMP Lidar
during the LADIMAS Campaign

C. R. Philbrick, D. B. Lysak, T. D. Stevens, P. A. T. Haris and Y.-C. Rau
Penn State University, University Park PA 16802

SUMMARY

The results of the Latitudinal Distribution of Middle Atmosphere Structure (LADIMAS) experiment have provided a unique data set to improve our understanding of the middle atmosphere. The project included ship-board and rocket range coordinated measurements between 70N to 65S to study the structure, dynamics and chemistry of the atmosphere. Results on important dynamical processes, such as gravity waves, tidal components, as well as the formation of the layers of meteoric ion and neutral species, have been obtained with lidar, digisonde, microwave radiometer, and spectrometers. The cooperative study of the atmosphere was undertaken by researchers from several laboratories, including Penn State University, University Bonn, University Wuppertal, Lowell University, and others. Several of the parameters studied have never been measured before over such a wide range of latitudes. Instruments were assembled aboard the German research vessel RV POLARSTERN while this vessel was sailing from the Arctic to the Antarctic seas between October 8, 1991 and January 2, 1992. This paper presents an introduction to the data gathered by the PSU investigation with the LAMP lidar.

MEASUREMENTS

The LAMP (Lidar Atmospheric Measurements Program) instrument is an advanced laser remote measurement sensor which has been built-up during 1990-1991. The design follows the progressive development of our two previous lidar designs [1,2]. This instrument extends the measurement range to cover the troposphere as well as the stratosphere and mesosphere, using the molecular and Raman scatter signals at several wavelengths to determine the profile distributions of density, temperature, extinction, particle back-scatter, and water vapor concentration. The instrument uses a high power Nd:YAG laser with an output of 1.5 J/pulse at 20 Hz. The fundamental wavelength is doubled to obtain 600 mJ pulses at 532 nm and mixed to obtain 250 mJ pulses at 355 nm. The transmitter, receiver, detector, and data system combination have been integrated into a standard shipping container, which serves as a field laboratory. The primary receiver is a 41 cm diameter Cassegrain telescope. The measurements of the back-scatter radiation are made at the fundamental wavelengths of 532 and 355 nm with several different detectors in order to cover the dynamic range. Figure 1 shows an example of the raw lidar signal, corrected for R^2 dependance, which is typical of the signals measured on several of the data channels. The low altitude channels for 532 and 355 nm receive about 5% of the collected intensity and the measurement is made in analog mode with an A/D converter at 10 MHz (15 meter altitude steps) with 12 bit resolution. The high altitude channels are mechanically shuttered below 15 km to prevent the PMT's from being saturated. The high altitude channels and the Raman channels for N_2 , at 607 nm, and for H_2O , at 660 nm, use photon counting detectors, with range bins of 500 nanoseconds (75 meter altitude steps). A smaller telescope, 20 cm diameter, was used for independent

measurements, most frequently at the 532 nm wavelength. In Figure 2, the profiles of the low and high altitude channels have been overlapped to provide continuous profiles from 200 meters to 80 km. The back-scatter and extinction associated with the stratospheric aerosols, clouds and the boundary layer can be readily observed in the profiles of these two wavelengths. Notice that the scattering ratio of the 532 nm compared to the 355 nm changes significantly with the changing size of the particle scatterers. When the stratospheric aerosol scattering intensities are compared to those for the tropospheric clouds, the change in extinction and back-scatter cross-section with particle size is obvious.

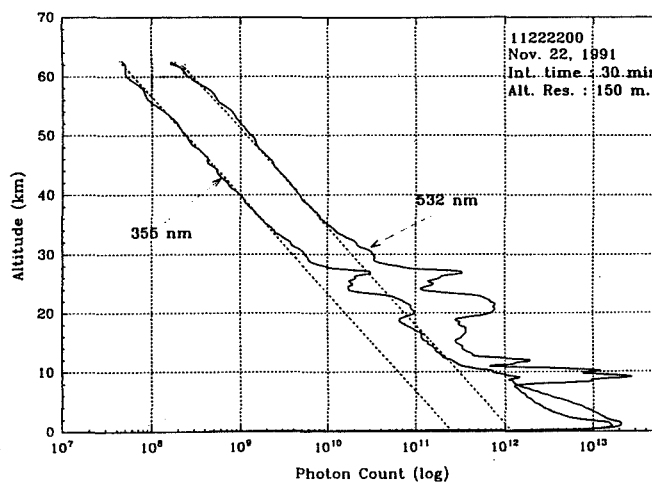
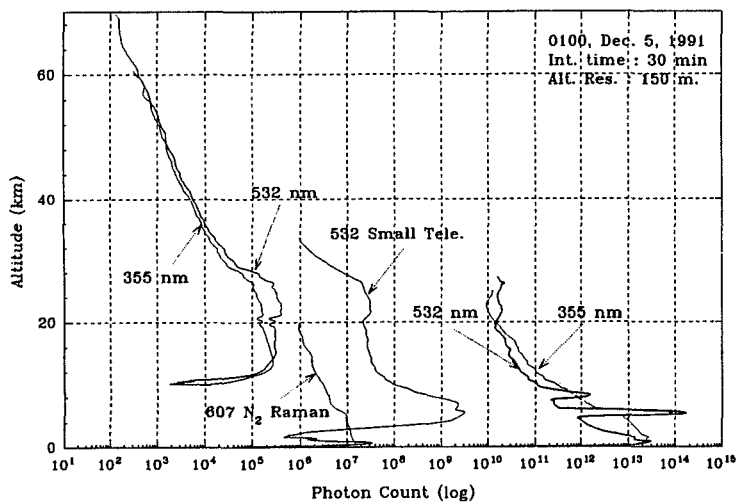


Figure 1. The raw signals, corrected for R^2 , for the low and high altitude channels, small telescope, and N_2 Raman are shown.

Figure 2. Low and high altitude channels are joined to form continuous profiles.

The initial data of LADIMAS, for the LAMP instrument, were gathered at Andoya Rocket Range, Norway. On the leg between Tromso, Norway, and Bremerhaven, Germany, the operational testing of the instrument on the ship was completed. Measurements were made on each clear night, and on some occasions, the measurements were made below and into the clouds. The measurements included high and low altitude channels for the 532 and 355 nm wavelengths, Raman shifted N_2 at 607 nm, Raman shifted H_2O at 660 nm, and 532 nm measurements from a second telescope simultaneously recorded. The variation in the profile, see Figures 1 and 2, near 25 km is due to particle scattering. One of the more striking features observed by the LADIMAS instruments is the lower stratospheric aerosol and particle layer. The high altitude signal, above about 30 km, can be easily analyzed to provide density and temperature profiles [3]. The two-color approach [1, 2] allows the detection of the molecular and particle components. Note that the particle scattering relative intensity is much stronger for the 532 than for the 355 signals. The cross-section for the molecular scatterers is much larger at 355 nm, while the particle cross-section may not differ significantly between the two wavelengths [for example, see 4]. Figure 3 shows the

measured signals of the 355 and 532 nm channels, together with the profiles of the aerosol scattering ratio to the molecular scattering, in this case, unity has been subtracted. Figure 4 shows the latitudinal plot of the scattering ratio for the 355 and 532 nm wavelengths. The strong variation in the scattering ratio as a function of latitude may be a result of the recent Pinatubo volcano eruption which transported dust to stratospheric heights [see 5]. The two color lidar shows a strong difference in relative back-scatter intensity from the stratospheric aerosols. The extinction due to the layers is obvious in the profiles.

532 NM HIGH ALTITUDE SIGNAL - 11/23/91

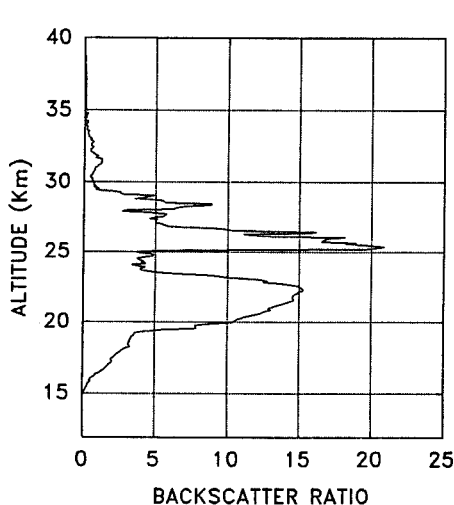


Figure 3. The high altitude channel of the 532 nm signal shows the stratospheric layers enhanced by the Pinatubo volcano.

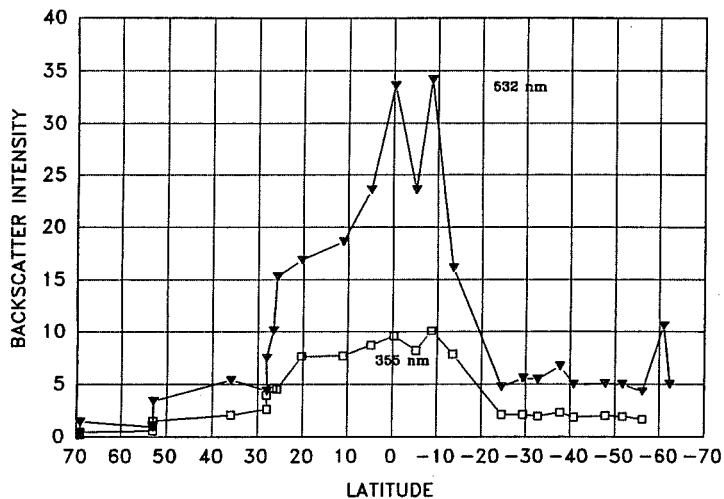


Figure 4. The latitudinal profile of the peak back-scatter intensity at the 532 and 355 nm wavelengths.

At tropospheric altitudes, the Raman N_2 profile together with the two-color back-scatter should allow the separation of the extinction, back-scatter due to particles and the molecular back-scatter signals. The advantage in using the Raman signals in the lower atmosphere is clear from the profiles shown above. Figure 5 shows a representation of the spectral signatures which would be expected from the back-scatter due to the 532 nm laser radiation in an atmospheric volume (after Inaba and Kobayasi [6]). The laser is injection seeded to give a line-width of about 80 MHz and thus the particle back-scatter is of that spectral width, while the molecular peaks are broadened by the thermal Doppler spreading. The vibrational Raman scattering peaks are shown for O_2 , N_2 and H_2O . Each of the peaks is also broadened at their base due to the rotational splitting of each vibrational state. Only the first Stokes vibrational states are indicated. The figure indicates the large cross-section difference in the processes involved. The Raman H_2O signal ratio to the Raman N_2 signal provides a good measure of the water vapor concentration. Figure 6 shows the profiles of the water vapor concentration at two of the times when rawinsonde balloon data were available for comparison. The previous work of Melfi [7] has shown the power of the Raman technique for obtaining water vapor measurements. The results gathered here have provided a data base to study the marine boundary layer.

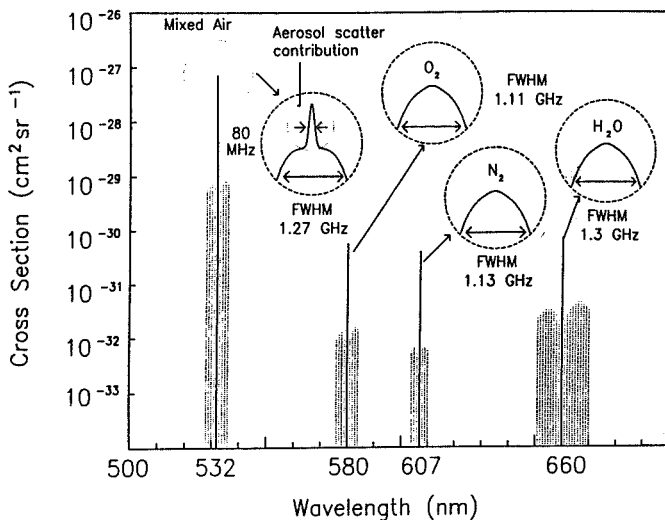


Figure 5. Descriptive representation of the vibrational and rotational Raman signals expected for radiation of an atmospheric volume with 532 nm laser.

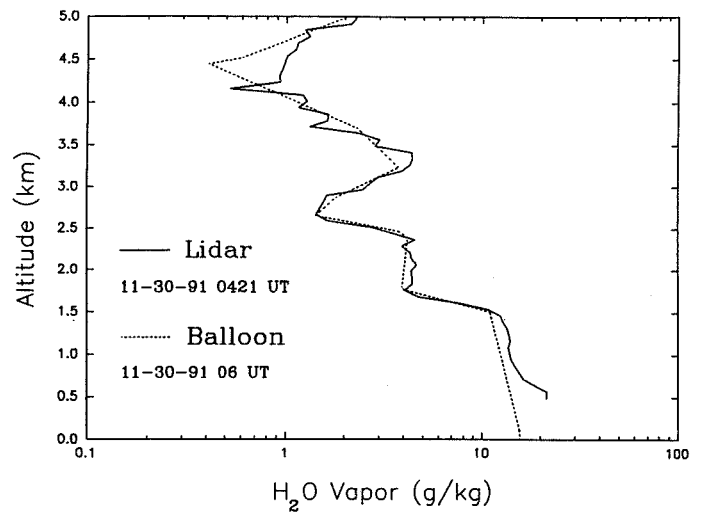


Figure 6. Examples of the water vapor concentration obtained from the Raman signals.

ACKNOWLEDGEMENTS

The effort to prepare the LAMP instrument has been supported by PSU/ARL project initiation funds, PSU College of Engineering, Lidar Atmospheric Profiler program for the US Navy, and the National Science Foundation's CEDAR (Coupling Energetics and Dynamics of Atmospheric Regions) Program. The measurements on the RV POLARSTERN were made possible by invitation of the Alfred-Wegener-Institut which is gratefully acknowledged. The long term collaborative efforts with Professors U. von Zahn and D. Offermann have made these investigations possible. The efforts of D. Sipler, C. Croskey, J.D. Mathews, D.E. Upshaw, D.W. Machuga, S. Maruvada, S. McKinley, G. Evanisko and G. Pancoast have contributed much to the success of the project.

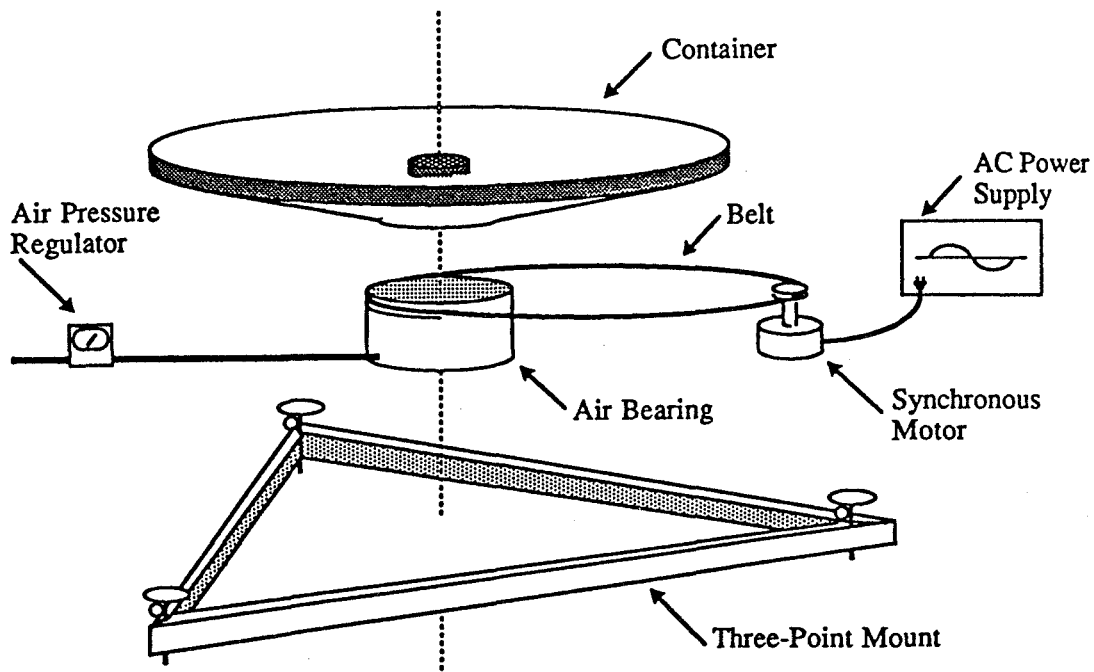
REFERENCES

1. Philbrick, C.R., "Lidar Profiles of Atmospheric Structure Properties," Earth and Atmospheric Remote Sensing, SPIE Vol. 1492, 76-84, 1991.
2. Philbrick, C.R., et.al., "Measurements of the High Latitude Middle Atmosphere Dynamic Structure Using Lidar," AFGL-TR-87-0053, Environmental Research Papers, No. 967, 1987.
3. Chanin, M.L. and A. Hauchecorne, "Lidar Observations of Gravity and Tidal Waves in the Middle Atmosphere," J. Geophys. Res., 86, 9715, 1981.
4. Carswell, A.I., "Lidar Remote Sensing of Atmospheric Aerosols," SPIE Vol. 1312, 206-220, 1990.
5. McCormick, M.P., T.J. Swissler, W.P. Chu, and W.H. Fuller, Jr., "Post Volcanic Stratospheric Aerosol Decay as Measured by Lidar," J. Atmos. Sci., 35, 1296-1303, 1978.
6. Inaba, H. and T. Kobayasi, "Laser-Raman Radar," Opto-electronics, 4, 101-123, 1972.
7. Melfi, S. H., J. D. Lawrence Jr. and M. P. McCormick, "Observation of Raman Scattering by Water Vapor in the Atmosphere," Appl. Phys.Lett., 15, 295-297, 1969.

by the seeded Nd-Yag laser produces 750 mJ/pulse at 532 nm, with a repetition rate of 20 Hz. To measure temperature using the resonance scatter from sodium requires the ability to tune the sodium beam between the fine structure lines of the D₂ doublet as described by *She et al. (Geophys. Res. Lett., 929, 1990)*. Briefly, this tuning over about 2 GHz is accomplished by amplifying the narrow bandwidth (500 kHz) output of a ring dye laser with a pulse dye amplifier pumped by the second output beam of the Nd-Yag laser. The pulse dye amplifier shown in the drawing can handle 15 W of pump beam to generate about 1.5 W of sodium light.

While most lidar systems benefit from the use of laser systems near the limit of available technology, they are often limited by the collecting area of the telescope. The researcher is often forced to make the trade-off of using a poor quality mirror of moderate size or a high quality telescope of small area. A high quality telescope is necessary for operation in the daytime to minimize the sky background, which is desired for our experiment.

The search for a high quality, low cost telescope with a large area led us to consider the use of liquid mirror telescopes (LMTs). An "up to the minute" review of LMTs will appear shortly in *The Astrophysical Journal (Borra et al., 1992)*. Conceptually the set-up of a LMT is very simple. A



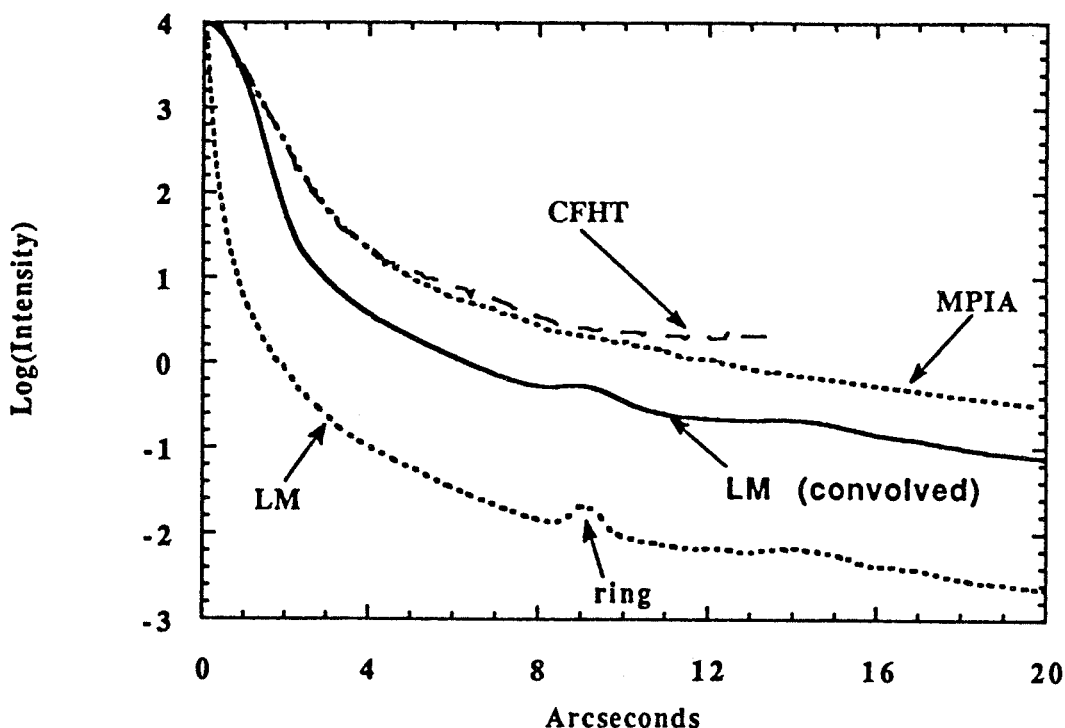
container to hold the mirror surface (mercury) is spun on a commercial air bearing at an angular frequency ω , forming a parabolic surface. The focal length, f , of the mirror is related to ω by the equation

$$f = \frac{g}{2\omega^2} \quad (\text{EQ 1})$$

where g is the acceleration due to gravity. For practical mirrors, the period of rotation varies from 5 - 20 s and the rim velocity of the container from 5 - 20 km/h.

The decision to use a LMT was motivated by the following:

1. The quality of LMTs is near diffraction limited. Detailed interferometric optical shop testing has been performed on a 1.5 m LMT and shown the Strehl ratio to be about 0.8 (i.e. diffraction limited). The following figure shows the measured point spread function (PSF) for a 1.5 m LMT compared to the Canada-France-Hawaii Telescope (CFHT) and the Max Planck Institute of Astronomie (MPIA) telescope. For comparison with the CFHT and MPIAT, the LMT PSF is



also shown convolved with a Gaussian of 1.3 arcsecond full width at half maximum to account for "seeing" (blurring of the image due to atmospheric turbulence). Even when seeing is considered the quality of the LMT is better than conventional large glass mirrors.

2. LMTs allow small research groups to own large mirrors. The UWO lidar is presently receiving its first Rayleigh-scatter returns using a 1 m LMT. We will be replacing this mirror with a 2.7 m LMT in the spring, thus increasing the lidar's performance factor by more than 7. Scaling from 1 m to 2.7 m class LMTs is not simply using a larger container and more mercury, in part because the weight requirements would exceed the capacity of the air bearing. Mercury has a high surface tension and will naturally form a layer approximately 4.5 mm thick. Techniques have been developed at Laval University to reduce this layer to only 1 mm.

3. The use of LMTs allows large mirrors to be used at a much reduced cost compared to glass mirrors. The UWO lidar 1 m LMT was assembled for a small cost compared to a conventional glass telescope. For a fraction of the cost of a conventional glass mirror, we will be replacing this mirror with a 2.7 m LMT in the spring. We envision 4 - 7 m class mirrors to be operational in the next 5 years and affordable for small research projects.
4. LMTs appear to be robust enough for routine field work. Though the UWO lidar mirror has just been commissioned, Laval University has operated LMTs for over 5 years. LMTs have run without stopping in the lab for over 3 months, and been operated outside for two summers and 1 autumn at Laval. Often people are concerned about the safety of having liquid mercury present. Repeated tests have shown that after the no more than 24 hours the mercury vapour levels from large LMTs are essentially undetectable. Mercury LMTs are also very easy to clean, so they keep their high reflectivity in the visible ($\approx 80\%$) and do not have to be routinely recoated.

Our initial observations of stars with the UWO 1 m LMT and the initial Rayleigh-scatter lidar returns suggest that the quality of our LMT is better than 5 arcsecond (the nominal seeing from London, Ontario in the early spring). We will present results from this initial system, and hopefully results from the lidar with the 2.7 m LMT.

Spectroscopic Method for Earth-Satellite-Earth Laser Long-Path
Absorption Measurements Using Retroreflector In Space (RIS)

Nobuo Sugimoto, Atsushi Minato, Yasuhiro Sasano
The National Institute for Environmental Studies
16-2 Onogawa, Tsukuba, Ibaraki 305 Japan

Retroreflector In Space (RIS) is a single element cube-corner retroreflector with a diameter of 0.5 m designed for earth-satellite-earth laser long-path absorption experiments. RIS is to be loaded on the ADEOS satellite which is scheduled for launch in February 1996. The orbit for ADEOS is a sun synchronous subrecurrent polar-orbit with an inclination of 98.6 deg. It has a period of 101 minutes and an altitude of approximately 800 km. The local time at descending node is 10:15-10:45, and the recurrent period is 41 days. The velocity relative to the ground is approximately 7 km/s.

In the RIS experiment, a laser beam transmitted from a ground station is reflected by RIS and received at the ground station. The absorption of the intervening atmosphere is measured in the round-trip optical path. Figure 1 shows the structure of RIS. We use a slightly curved mirror surface for one of three mirrors forming the retroreflector, which diverges the reflected beam to overcome the velocity aberration caused by the satellite movement¹⁾.

We have proposed a simple spectroscopic method which utilizes the Doppler shift of the reflected beam resulting from the satellite movement for measuring the high resolution transmission spectrum of the atmosphere^{2,3)}. We use two single-mode TEA CO₂ lasers. One is tuned to a laser line close to the absorption lines of the target molecule for measuring the absorption spectrum. The other is used for measuring reference signals to correct atmospheric effects. Figure 2 shows the transmission spectrum of the atmosphere generated by the FASCODE program and the CO₂ laser lines for the measurement of ozone. The magnitude of the Doppler shift is 0 - 0.04 cm⁻¹ at 10 μm, which depends on the satellite position relative to the ground station. The spectral region covered by the Doppler shift during a measurement is indicated in Fig.2. We can measure the absorption spectrum of ozone using P(20) or P(24). We can measure the absorption spectrum in the wider spectral region, if we switch the laser lines in turn, for example between P(20) and P(24), during a measurement.

The target species of the RIS experiment using TEA CO₂ lasers with ¹²C¹⁶O₂ and ¹³C¹⁶O₂ isotopes and their second and third harmonics are listed in Table 1. We can retrieve the vertical profiles by inversion using absorption line shape for molecules with large

absorption such as ozone and methane. As for molecules with small or too large absorption, we can measure the column abundance.

We have estimated the signal-to-noise ratio (SNR) of the optical detection with the realistic system parameters listed in Table 2. We also used the result of simulation on the reflected beam intensity, which is a function of the position of RIS relative to the ground station¹⁾. Figure 3 shows the estimated received photon number for a single laser shot measurement at 10 μm . The noise equivalent photon number is also shown in Fig.3. The figure shows that the SNR more than 100 is expected for a single shot measurement. Approximately 10000 shots are supposed to be recorded in a single spectrum measurement. The accuracy of the concentration obtained from the spectrum is being evaluated using a simulator program including the measurement and the data reduction process.

References

- 1) A. Minato, N. Sugimoto and Y. Sasano: Optical Design of Cube-Corner Retroreflectors Having Curved Mirror Surfaces, Submitted to Applied Optics.
- 2) N. Sugimoto, A. Minato and Y. Sasano, 15th ILRC (1990) Tomsk.
- 3) N. Sugimoto, A. Minato and Y. Sasano: Retroreflector In Space for the ADEOS Satellite, CLEO'91 (1991) Baltimore.

Table 1 Target Molecules and CO₂ Laser Lines

Molecule	Laser Line	Isotope	Wavenumber (cm ⁻¹)
O ₃	P(18)	636	1002.4778
	P(20)	636	1000.6473
	P(24)	636	996.9011
	R(34)	636	937.5844 (Reference)
CO ₂	P(26)	626	938.6883
	R(36)	636	938.7776
HNO ₃	P(8)	636	907.0528
CFC12	R(6)~R(14)	636	918.74~924.53
CO	R(24) SH	626	1081.0874 x 2
	R(30) SH	626	1084.6351 x 2
	R(8) SH	626	1070.4623 x 2 (Ref.)
N ₂ O	R(38) SH	626	1089.0011 x 2
	R(40) SH	626	1090.0284 x 2
CH ₄	R(22) TH	626	977.2139 x 3
	R(34) TH	626	984.3832 x 3
	R(26) TH	626	979.7054 x 3 (Ref)

Table 2 System Parameters for RIS Ground System

Laser Pulse Energy	100 mJ (10 μ m)
Laser Beam Divergence	0.1 mrad
Receiver Telescope Diameter	1.5 m
Overall Efficiency of Optics Including the Atmosphere	0.005
Detectivity of Detector	7×10^{10} cmHz ^{1/2} W ⁻¹
Detector Area	0.001 cm ²
Quantum Efficiency	0.6
Gate Time	1 μ s

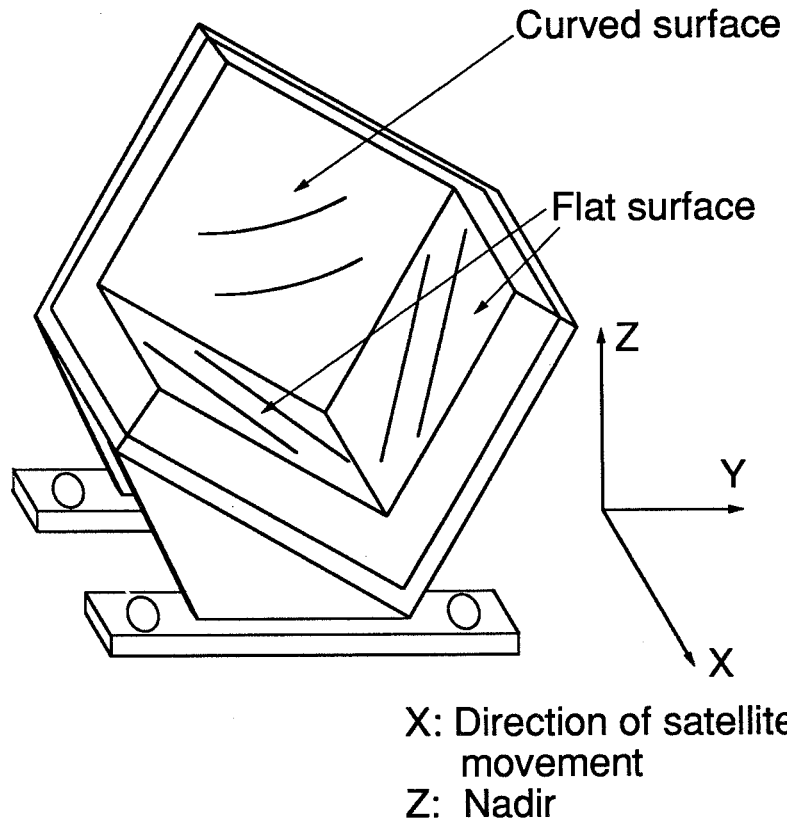


Fig.1 Structure of RIS

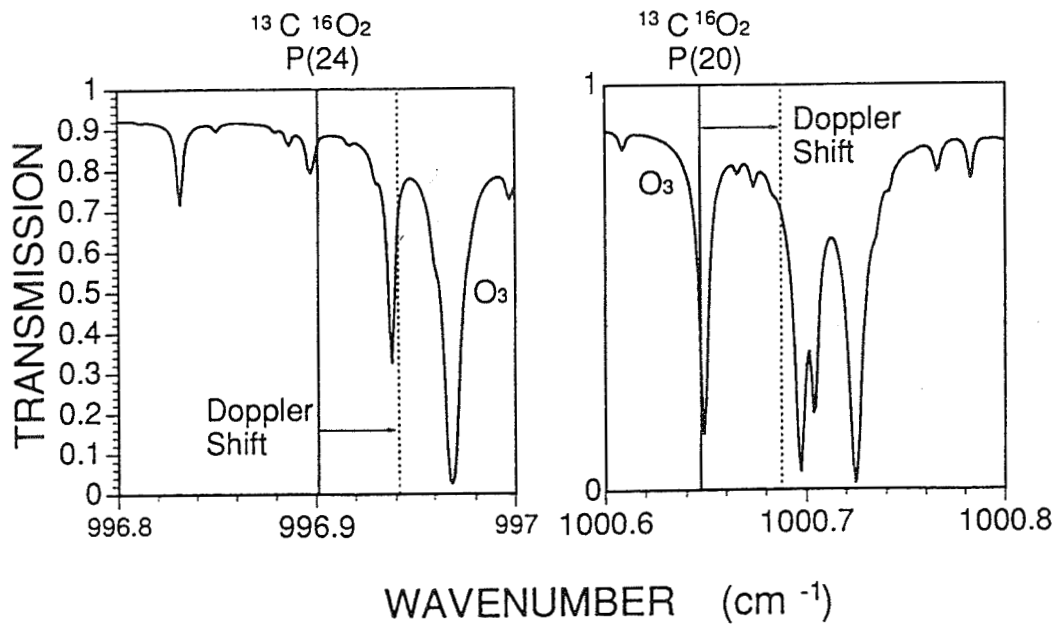


Fig.2 Synthesized atmospheric transmission spectrum (one-way path, elevation angle = 60 deg.) and the CO_2 laser lines for ozone measurement.

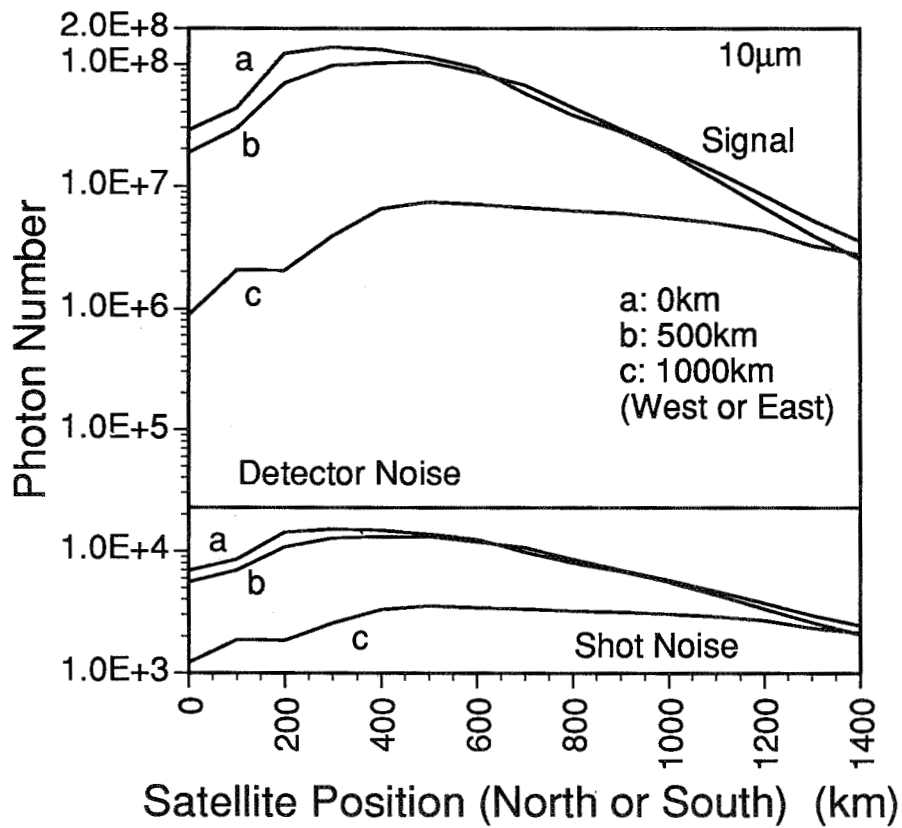


Fig.3 Simulated signal photon number for a single shot measurement at 10 μm .

Raman Lidar Measurements of Water Vapor and Aerosol/Clouds
During the FIRE/SPECTRE Field Campaign

S. H. Melfi, D. Whiteman, R. Ferrare*, and K. Evans⁺
NASA/Goddard Space Flight Center
Greenbelt, MD 20771

J. E. M. Goldsmith, M. Lapp, and S. E. Bisson
Sandia National Laboratories
Livermore, CA 94551

Water vapor is one of the most important constituents of the earth's atmosphere. It has a major impact on both atmospheric dynamics and radiative transfer. From a dynamic standpoint, the distribution of water vapor with height determines convective stability which is the major indicator of destructive storm development. Also, water vapor stored in the planetary boundary layer acts as the fuel to intensify severe weather. In regards to radiative transfer, water vapor is the most active IR molecule in the atmosphere. It is more effective in absorbing and emitting IR radiation than either carbon dioxide or methane, and thus plays an important role in global change.

The FIRE/SPECTRE field campaign was conducted during November-December 1991 in Coffeyville, Kansas. The main objective of FIRE [First ISCCP (International Satellite Cloud Climatology Project) Regional Experiment] was to study the development and radiative characteristics of cirrus clouds. The SPECTRE [Spectral Radiation Experiment] project was designed to acquire the necessary atmospheric observations to compare radiative measurements with radiative transfer theory, with special emphasis on understanding the water vapor spectral continuum. A complete understanding of water vapor, its distribution with height, and its temporal variation was important for both experiments.

A ground-based Raman lidar was deployed at Coffeyville, Kansas from November 12 until December 7, 1991. During the campaign, the lidar operated during 14 observation periods. The periods ranged in length from 3.5 hours to

*Universities Space Research Associates, Columbia, MD

⁺Hughes-STX, Lanham, MD

12 hours for a total operating time of approximately 119 hours. There were two times that the lidar was inoperative due to equipment failure totalling 2.5 hours. As a result, the lidar proved to have a reliability of 98%.

During each of the operational periods the lidar obtained vertical profiles of water vapor mixing ratio and aerosol scattering ratio once every minute with vertical resolution of 75 meters from near the earth's surface to an altitude of 9-10 km for water vapor and higher for aerosols. Several balloon-sondes were launched during each operational period providing an independent measurement of humidity with altitude. Over the entire experiment, there were a total of 48 balloon-sonde intercomparison opportunities. One such comparison of the lidar measurement of water vapor mixing ratio showing excellent agreement with data from a balloon-sonde is given in Fig. 1. The random error of the water vapor measurements are shown as a function of altitude in Fig. 2. The solid curve shows the percent error for a 1-minute measurement. The unusual shape of the curve between 3.5 and 4.5 kilometers is due to a blending of data from low sensitivity detectors used between the surface and 4.5 km and the much higher sensitivity detectors used above 3.5 km. Other curves on Fig. 2 show the reduction in random error when thirty 1-minute profiles and sixty 1-minute profiles are integrated together. The curves of Fig. 2 indicate that the lidar measures water vapor mixing ratio with better than 10% random uncertainty to about 9 km with 1 hour temporal resolution and with better than 10% error at lower altitudes at higher temporal resolution. Additional improvement in the random error of the measurement can be realized by reducing the vertical resolution.

For each operational period, the 1-minute profiles of water vapor mixing ratio and aerosol scattering ratio are composited to give a color-coded time-height display of water vapor and aerosol scattering, respectively. These time-height displays provide a unique opportunity to study the interaction of humidity with aerosols and clouds since both measurements are made in the same scattering volume at the same time using the same laser beam. In addition, the displays show the highly variable nature of the atmosphere and can be used to study dynamical variations over the time period of the observations.

Examples of water vapor and aerosol/cloud time-height displays obtained in Coffeyville will be shown and discussed during the presentation.

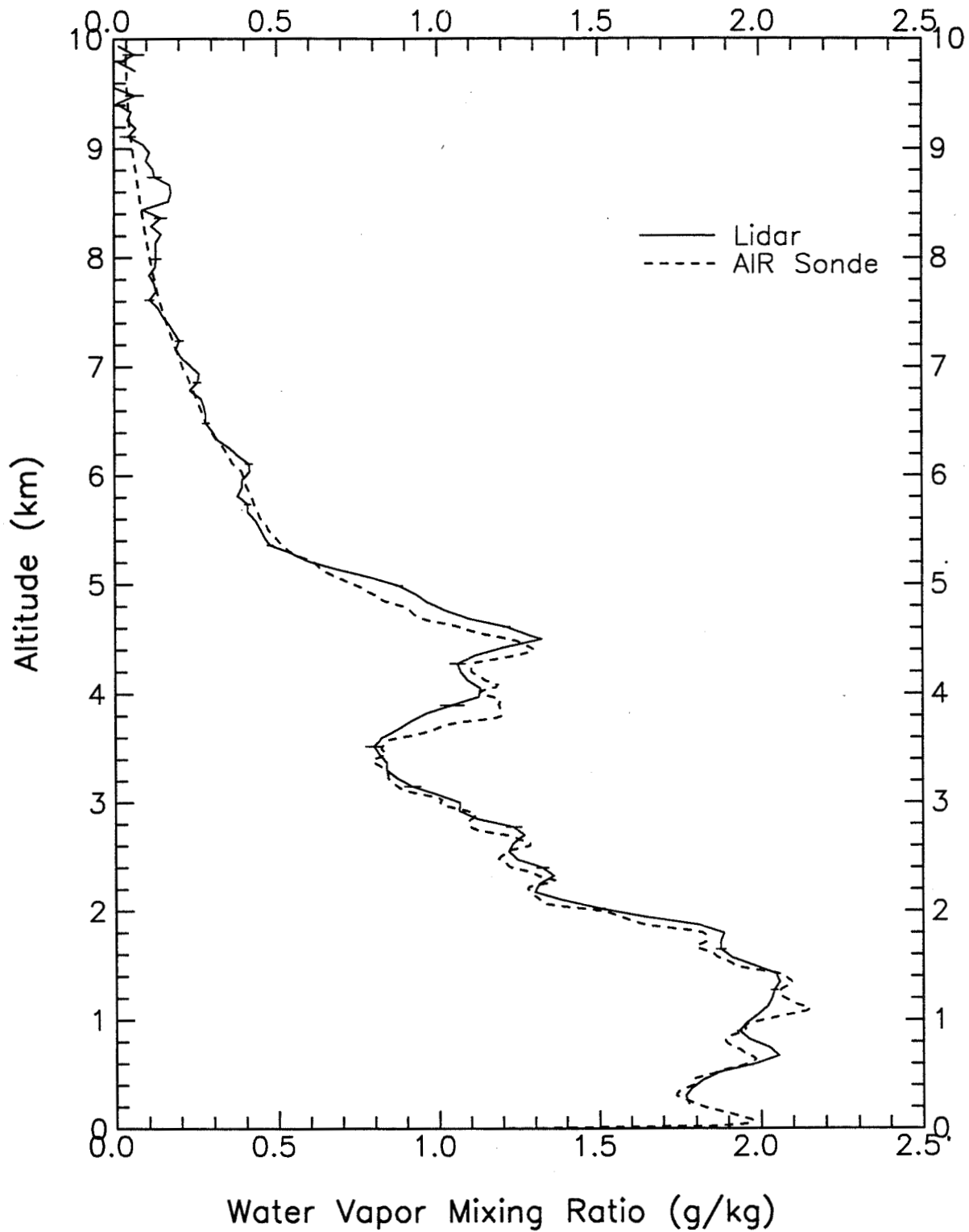


Figure 1. Comparison of water vapor mixing ratio profiles obtained with the ground-based Raman lidar and an independent balloon-sonde. The lidar data represents a 10-minute average acquired at Coffeyville, KA on Dec. 4, 1991 over the time period 01:51-02:07 UT.

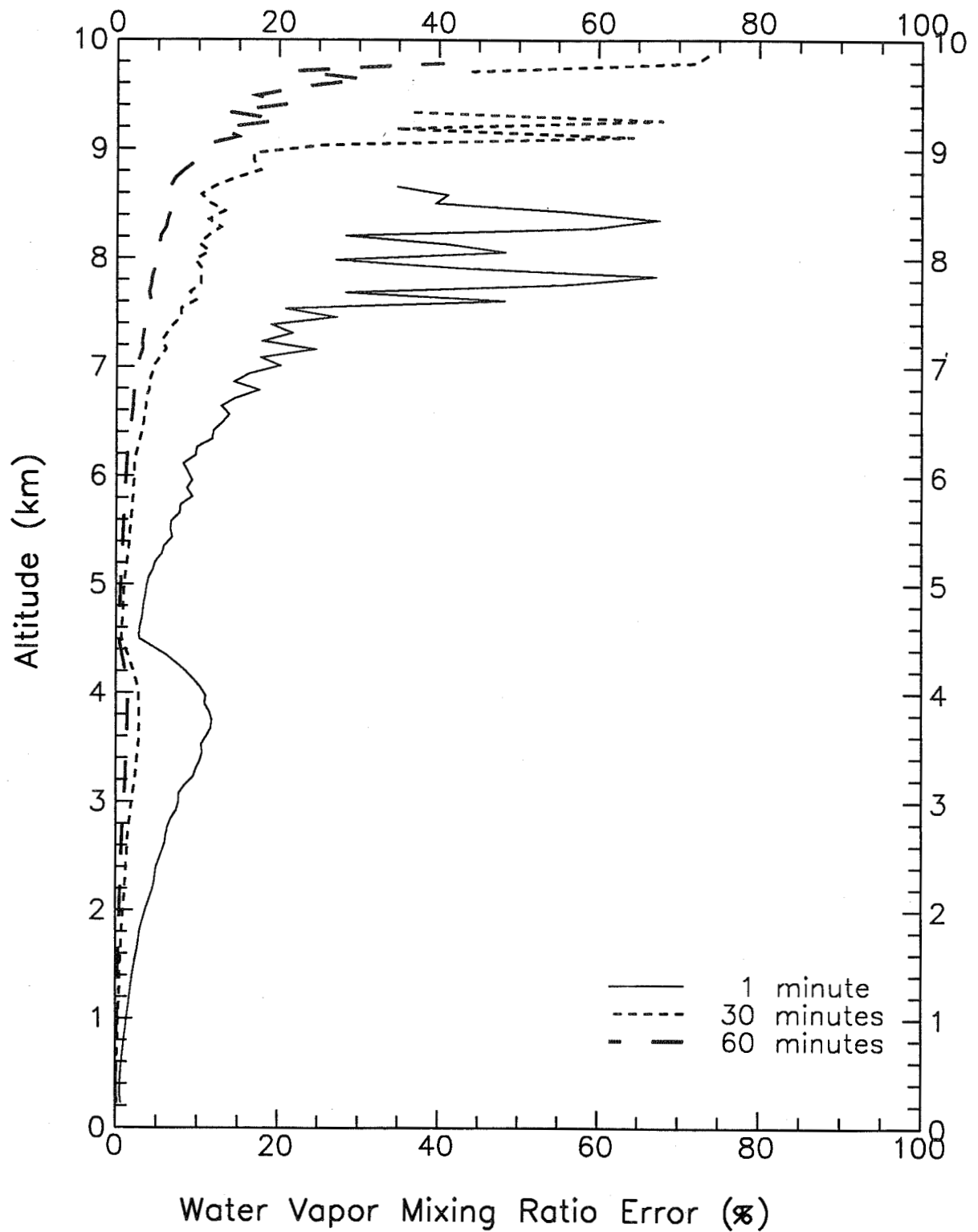


Figure 2. Random error versus altitude for the Raman lidar measurement of water vapor mixing ratio for three averaging times. The data for which the random error was calculated were acquired at Coffeyville, KA on Dec. 4, 1991.

Performance Modeling of Daytime Raman Lidar Systems for Profiling Atmospheric Water Vapor*

J. E. M. Goldsmith
Sandia National Laboratories
Livermore, CA 94551

and

Richard A. Ferrare†
NASA Goddard Space Flight Center
Greenbelt, MD 20771

Introduction

We describe results from a comprehensive computer model developed to guide optimization of an ultraviolet Raman lidar system for measuring *daytime* profiles of atmospheric water vapor. Raman lidar systems detect selected molecular species by monitoring their corresponding wavelength-shifted, backscattered Raman return signals. The Raman lidar technique is a leading candidate for providing the high-resolution profiling of water vapor that is critical to research in global climate change. While Raman lidar is used currently to perform meteorologically important, sustained, reliable nighttime profiling of water vapor, daytime measurements present added challenges because of the difficulties inherent in detecting Raman signals against solar backgrounds.

We are pursuing two concepts for optimizing the daytime performance of a Raman lidar system. The first concept involves operation of the system in the solar blind region of the ultraviolet spectrum. This mode of operation takes advantage of the extremely strong absorption of solar radiation by stratospheric ozone at wavelengths shorter than ~300 nm; thus, the sky appears to be effectively black at these wavelengths. Unfortunately, the use of this region for daytime water vapor detection is a double-edged sword. Attenuation of solar background is accomplished effectively, but tropospheric ozone attenuates both the laser probe beam and the Raman return signal (depending on the local distribution of ozone during the measurement time). Thus the laser wavelength must be selected to balance these competing effects.

The second concept involves operation of the system in a narrowband, narrow field-of-view mode. This mode of operation is more straightforward conceptually, but likely to be more complex experimentally. The concept is to narrow both the spectral bandpass and the angular field-of-view of the instrument in order to reduce the number of detected background solar photons. Narrowband operation will require reducing the bandwidth of both the laser source and the detection system, while also requiring that the excitation and detection wavelengths remain matched at all times. Operation using a narrow field-of-view complicates system alignment, and also makes it difficult to perform measurements at short range. Calculations for lidar systems based on both concepts are presented in this abstract.

* This work is supported by the U.S. Department of Energy Atmospheric Radiation Measurement (ARM) Program, and by the NASA Radiation and Dynamics Program

† Universities Space Research Association Research Associate

Lidar Model

We have developed a detailed Raman lidar instrument model to predict the daytime performance capabilities of Raman lidar systems. The model simulates key characteristics of the lidar system, using realistic atmospheric profiles, estimated background sky radiance, and lidar system parameters based on current instrumental capabilities. The model operates by tracking photons through the atmosphere and the instrument, incorporating atmospheric attenuation (due to Rayleigh and aerosol scattering and absorption by ozone and oxygen) at both the laser and Raman-shifted wavelengths. For the purposes of this abstract, we assume photon-counting operation, with the number of photons observed in the water-vapor channel as the process that limits our sensitivity. Detecting counts from water-vapor signal photons (N_{sig}), background solar photons (N_{back}), and photomultiplier dark counts (N_{dark}) within each range bin integrated over the selected number of laser shots, the S/N (signal-to-noise) ratio is then given by

$$S/N = \frac{N_{\text{sig}}}{\sqrt{N_{\text{sig}} + N_{\text{back}} + N_{\text{dark}}}}$$

Representative Results

The results presented here are representative of a large, trailer-based Raman lidar system operating in the vertically pointing direction with 75-m vertical resolution, and incorporating a high-power excimer laser (capable of producing 500 mJ/pulse at 248 nm or 200 mJ/pulse at 308 nm operating at a 200-Hz repetition rate), a large (0.75-m diameter) telescope, and other commercially available optical and electronic components. Figure 1 illustrates sample calculations for solar-blind operation, presented as the maximum altitude at which measurements can be obtained as a function of excitation wavelength for three assumed integration times if a

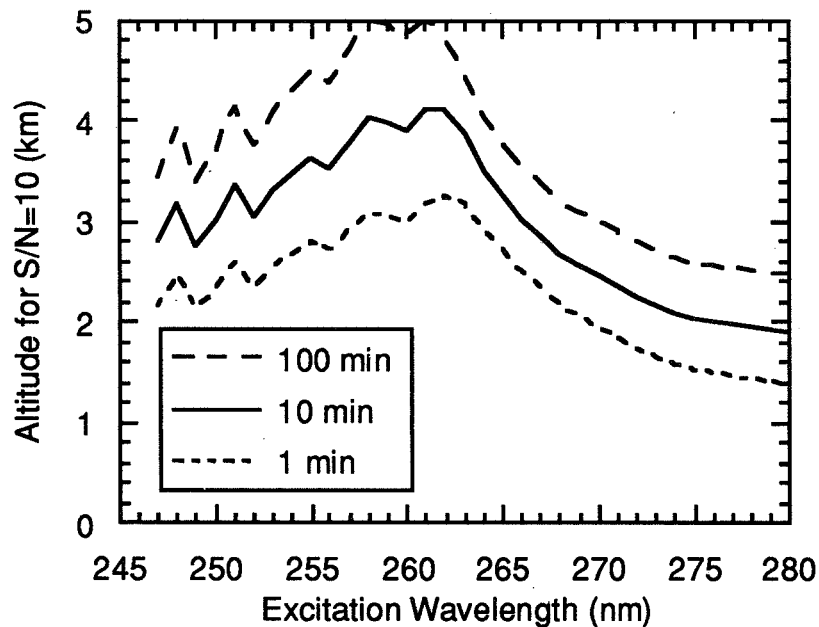


Figure 1. Calculated altitude versus excitation wavelength for the solar-blind concept.

S/N of ten or greater is required (yielding a measurement precision of 10% or better). This calculation makes the (physically unrealistic) assumption that the obtainable laser energy does not change as a function of wavelength (at 500 mJ/pulse, the output energy of the KrF laser at 248 nm). Efficient Raman shifting can be used to reach some wavelengths in this region (in particular, generation of 276-nm radiation by Raman shifting of the 248-nm radiation in molecular hydrogen), but in general the obtainable laser energy, and hence altitude, would be lower than is shown here. This plot nonetheless indicates an optimum excitation wavelength of approximately 260 nm; optical attenuation by tropospheric ozone dominates at shorter wavelengths, and increasing “leakage” of background skylight dominates at longer wavelengths. The general wavelength dependence is very similar to that described by Petri, Salik, and Cooney,¹ but we predict a shorter optimum wavelength, and a weaker dependence at wavelengths shorter than the optimum, than described by Renaut and Capitini.² Attenuation by the weak (“forbidden”) Herzberg I molecular oxygen absorption bands create the structure in the curves for $\lambda < 260$ nm; these bands consist of many narrow lines, and the parameterization used here³ only gives a rough idea of this structure.

Figure 2 illustrates sample calculations for narrowband, narrow-field-of-view operation, presented as the counting time required as a function of altitude for two fields of view and again requiring a S/N of ten. These curves were calculated assuming 308-nm (XeCl) laser operation at 200 mJ/pulse and a filter bandwidth of 0.5 nm. The 0.2-mr curve represents a narrow-field-of-view system. However, one major difficulty with narrow-field-of-view operation is a limitation on how well signals can be obtained at *short* range (as the field of view of the detection system is decreased, the range at which the detector first “sees” the laser increases). For 2.0 mr operation (the other curve shown in Fig. 2), this crossover range is at tens of meters, but it increases to hundreds of meters for 0.2 mr operation. One solution to this difficulty is to implement a dual-field-of-view system; such a system can provide not only enhanced range coverage, but can also provide the equivalent of having separate low- and high-sensitivity channels to enhance the effective dynamic range of the detection system.

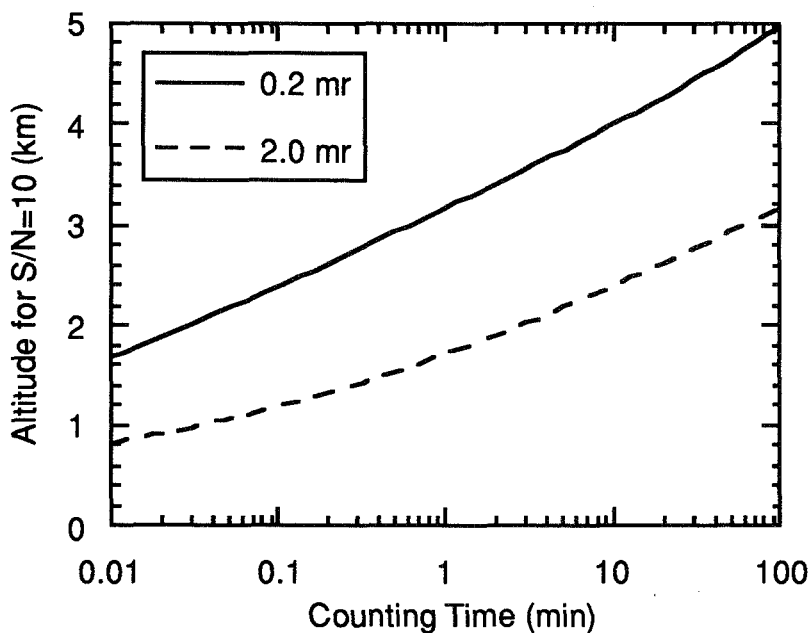


Figure 2. Calculated altitude versus counting time for the narrowband, narrow-field-of view concept.

Conclusion

These calculations represent only signal-to-noise calculations, and do not take into account potential *systematic* effects. One such major effect for solar-blind operation is the strong wavelength dependence of the ozone absorption cross section on the determination of the water-vapor mixing ratio (typically obtained by ratioing the water-vapor Raman signal to the simultaneously measured nitrogen Raman signal). A correction for this effect can be obtained by simultaneously measuring the oxygen Raman signal and calculating an ozone profile from the nitrogen and oxygen Raman signals using a DIAL (differential absorption lidar) approach,² but uncertainties in the ozone measurement will introduce additional uncertainties in the water-vapor mixing ratio.

These results indicate that Raman lidar systems have the potential for measuring *daytime* profiles of atmospheric water vapor to an altitude of several kilometers with reasonable precision (~10%) and reasonable counting times (~10 minutes). Remarkably, and likely fortuitously, the realistic lidar systems we have chosen to model for the two daytime approaches yield almost identical calculated range capabilities (for example, 10-minute counting times required to obtain profiles out to 4 km). Which approach turns out to be "best" may therefore be decided by engineering factors that are critical in the two approaches, such as Raman-shifting efficiencies, filter characteristics, alignment tolerances, dynamic range capabilities, etc. We are currently addressing these and other issues in a joint Sandia/Goddard experimental program that is proceeding parallel to the modeling effort described here.

References

1. K. Petri, A. Salik, and J. Cooney, "Variable-wavelength solar-blind Raman lidar for remote measurement of atmospheric water-vapor concentration and temperature," *Appl. Opt.* **21**, 1212-1218 (1982).
2. D. Renaut and R. Capitini, "Boundary-layer water-vapor probing with a solar-blind Raman lidar: validations, meteorological observations and prospects," *J. Atmos. and Ocean. Tech.* **5**, 585-601 (1988).
3. E. Trakhovsky, A. Ben-Shalom, U. P. Oppenheim, A. D. Devir, L. S. Balfour, and M. Engel, "Contribution of oxygen to attenuation in the solar blind UV spectral region," *Appl. Opt.* **28**, 1588-1591 (1989).

BELINDA: Broadband Emission Lidar with Narrowband Determination of Absorption

A new concept for measuring water vapor and temperature profiles

F.A. Theopold, C. Weitkamp, W. Michaelis

GKSS-Forschungszentrum, Postfach 1160, W-2054 Geesthacht, Germany

Abstract

We present a new concept for differential absorption lidar measurements of water vapor and temperature profiles. The idea is to use one broadband emission laser and a narrowband filter system for the separation of the 'online' and 'offline' return signals. It is shown that BELINDA offers improvements as to laser emission shape and stability requirements, background suppression, and last and most important a significant reduction of the influence of Rayleigh scattering. A suitably designed system based on this concept is presented, capable of measuring water vapor or temperature profiles throughout the planetary boundary layer.

1. Introduction

Moisture and temperature are the most important properties of the atmosphere. The study of dynamical processes both in the planetary boundary layer and in the free troposphere requires the knowledge of these data with high spatial and temporal resolution.

Differential absorption lidar, or DIAL, is a technique that can in principle be used for measurements that meet these demands [1], [2]. The accuracy, however, is restricted by the limited knowledge of the actual laser emission spectrum, i.e. shape and amplified spontaneous emission, and by the backscatter properties of the atmosphere itself. Concerning the latter point, errors of 100% for water vapor [3] and 100 K for temperature measurements [2] can occur. BELINDA is a new measurement scheme which allows the reduction of these errors by at least a factor of four.

2. Theory

The usual scheme for the determination of the absorption coefficient from the return signals $P(\tilde{\nu}_i, Z_i)$ involves the calculation of the expression

$$\mathcal{P}(\bar{Z}) = \ln \frac{P(\tilde{\nu}_1, Z_1)}{P(\tilde{\nu}_2, Z_1)} - \ln \frac{P(\tilde{\nu}_1, Z_2)}{P(\tilde{\nu}_2, Z_2)} \quad (1)$$

in which $\tilde{\nu}_1, \tilde{\nu}_2$ are the 'online' and 'offline' wavenumbers, Z_1, Z_2 are the boundaries of a range cell and $\bar{Z} = (Z_1 + Z_2)/2$. Assuming that the wavelength dependence of the extinction and backscatter coefficients are negligible over the interval $\tilde{\nu}_2 - \tilde{\nu}_1$ we can show that

$$\mathcal{P}(\bar{Z}) = 2 \Delta Z [k(\tilde{\nu}_1, \bar{Z}) - k(\tilde{\nu}_2, \bar{Z})] + f(x, \tilde{\nu}_1, \bar{Z}) - f(x, \tilde{\nu}_2, \bar{Z}) \quad (2)$$

where $\Delta Z = Z_2 - Z_1$ is the depth resolution, k is the absorption coefficient of the species of interest (H_2O for moisture, O_2 for temperature), and

$$f(x, \bar{\nu}_i, \bar{Z}) = \ln \frac{1 - x(Z_1) + x(Z_1) V(\bar{\nu}_i, Z_1)}{1 - x(Z_2) + x(Z_2) V(\bar{\nu}_i, Z_2)} \quad (3)$$

with the backscatter ratio x defined as $x(Z_i) = \beta_M(Z_i)/(\beta_M(Z_i) + \beta_P(Z_i))$ where β_M, β_P are the backscatter coefficients for molecular(Rayleigh) and particle scattering, respectively. V is the normalized backscatter spectrum

$$V(\bar{\nu}_i, Z_i) = \frac{\int_{-\infty}^{+\infty} l(\bar{\nu}', Z_0) \exp(-\int_{Z_0}^{Z_i} k(\bar{\nu}', r) dr) R(\bar{\nu}_i - \bar{\nu}') d\bar{\nu}'}{l(\bar{\nu}_i, Z_0) \exp(-\int_{Z_0}^{Z_i} k(\bar{\nu}_i, r) dr)} \quad (4)$$

where $l(\bar{\nu}, Z_0)$ is the laser emission spectrum and $R(\bar{\nu}, Z)$ is the Rayleigh-Brillouin spectrum.

It can be shown that for homogeneous backscatter, i.e. $x(Z_1) = x(Z_2)$, the maximum error by neglecting f in Eq.(2) is given by

$$f_{hom}(\bar{\nu}_i, \bar{Z}) = \ln \frac{1 + V(\bar{\nu}_i, Z_1)}{1 + V(\bar{\nu}_i, Z_2)}. \quad (5)$$

For the inhomogeneous case, i.e. $x(Z_1) = 0, x(Z_2) = 1$ or vice versa, the maximum error is

$$f_{inh}(\bar{\nu}_i, \bar{Z}) = \ln[V(\bar{\nu}_i, Z_1) V(\bar{\nu}_i, Z_2)]. \quad (6)$$

These two functions are plotted in Fig. 1 for various ranges for the water vapor absorption line at 728.81 nm, calculated with the absorption line parameters given in [4]. Furthermore a standard atmosphere is assumed and the Rayleigh-Brillouin spectrum is approximated by a Gaussian lineshape with a halfwidth (HWHM) of

$$\sigma_R = 2 \frac{\bar{\nu}}{c} \sqrt{2 k_B T \ln 2 / M_{air}} \quad (7)$$

where c is the speed of light, k_B is the Boltzmann constant, T is the temperature and M_{air} is the mean mass of an air molecule. For the laser line shape also a Gaussian distribution is assumed with a halfwidth(HWHM) of 0.2 cm^{-1} which is approximately twice the halfwidth of the absorption line at ground level.

Obviously f_{inh} is by far the main error. Therefore $\bar{\nu}_1$ and $\bar{\nu}_2$ have to be chosen in such a way that

$$\sum_{Z_j=0}^{Z_{max}} [f_{inh}(\bar{\nu}_1, \bar{Z}_j) - f_{inh}(\bar{\nu}_2, \bar{Z}_j)] \stackrel{!}{=} \min. \quad (8)$$

This leads to the selection of $\bar{\nu}_1, \bar{\nu}_2$ as indicated in Fig. 1 by the two vertical lines. The resulting relative error of the absorption coefficient is then

$$\frac{dk}{k}(\bar{Z}) = \frac{f_{inh}(\bar{\nu}_1, \bar{Z}) - f_{inh}(\bar{\nu}_2, \bar{Z})}{2 \Delta Z [k(\bar{\nu}_1, \bar{Z}) - k(\bar{\nu}_2, \bar{Z})]}. \quad (9)$$

As it can be seen from Fig. 1 the maximum deviation occurs at lowest ($\bar{Z} = 100$ m) and greatest height ($\bar{Z} = 1900$ m) corresponding to a relative error in water vapor concentration of $\approx 25\%$. At a height of $\bar{Z}_m \approx 1000$ m $f_{inh}(\bar{\nu}_1, \bar{Z}_m)$ equals $f_{inh}(\bar{\nu}_2, \bar{Z}_m)$ and therefore the error due to inhomogeneous scattering is totally compensated. Here only the contribution of homogeneous scattering remains which corresponds to an error in water vapor concentration of $\approx 2.5\%$.

Similar results are obtained for temperature measurements using the highly temperature-sensitive absorption lines of molecular oxygen in the vicinity of 770 nm with a maximum temperature error of ≈ 25 K for the inhomogeneous case and ≈ 2.5 K for the homogeneous case.

Determination of the backscatter ratio profile $x(Z)$ by the usual inversion technique [5] allows to estimate the contribution of f in Eq.(2). Calculations show that the values of f_{hom} as well as f_{inh} vary approximately linearly with the backscatter ratio. Thus, if $x(Z)$ is known with a relative accuracy of 10%, which seems to be feasible, the errors mentioned above will be reduced by a factor of ten.

3. Receiver system

A possible implementation of the filter system may consist in a grating as a prefilter and four Fabry-Perot interferometers (FPI) working in transmission as well as in reflection. For water vapor measurements FPIs with an effective finesse ≤ 50 and a free spectral range ≤ 0.9 cm $^{-1}$ are required leading to an effective halfwidth(FWHM) of 0.014 cm $^{-1}$. The suppression for all other wavelengths is then $\leq 10^{-3}$. This value is sufficient for practical applications.

Assuming a laser pulse energy of 300 mJ, a repetition rate of 20 Hz, a receiving telescope of diameter 30 cm, an overall system efficiency of 0.05, a depth resolution of 100 m, and pure Rayleigh scattering, i.e. the lowest occurring signal level, the statistical signal error at 2000 m height is less than 0.5% for a 30 s average.

4. Conclusion

Theoretical calculations show that the error in DIAL measurements of water vapor and temperature that originates from Doppler broadened Rayleigh scattering can be reduced by at least a factor of four when using only one 'broadband emission' laser and a receiver filter system with proper choice of the 'online' and 'offline' wavelengths. Due to the very narrow bandwidth of the receiver system the error from amplified spontaneous emission can be neglected, and a low background light level is obtained. Furthermore only two optical axes must be aligned, as compared to three (two laser beams, one receiver) for the usual DIAL systems. Although only a minor part of the backscattered power is transmitted by the filter system, high temporal and spatial resolution can be achieved at least for medium-range measurements. Since a system as the one outlined above can be made light and compact, airborne applications of this novel type of instrument also appear feasible.

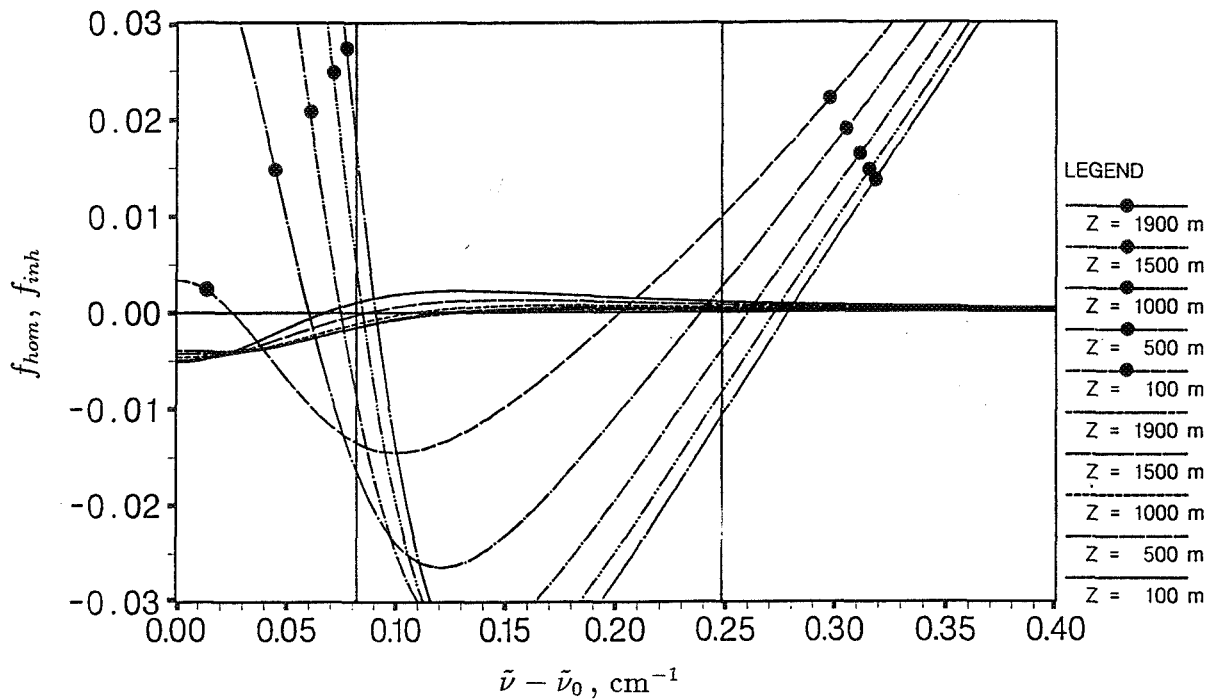


Figure 1: Maximum absolute error in the determination of the absorption coefficient due to Doppler broadening of the backscattered spectrum by Rayleigh scattering for inhomogeneous (graphs marked with dots) and homogeneous (no dots) particle scattering versus wavenumber difference from line center ($\tilde{\nu}_0$). The laser emission spectrum is assumed to be a Gaussian with a halfwidth of 0.2 cm^{-1} . Depth resolution is 100 m.

References

- [1] E.V. Browell, T.D. Wilkerson and T.J. McIlrath, 1979: Water Vapor Differential Absorption Lidar Development and Evaluation. A.O. 18, 3474
- [2] F.A. Theopold and J. Bösenberg, 1992: Differential Absorption Lidar Measurements of Atmospheric Temperature Profiles: Theory and Experiment. J. Atm. Oc. Tech. (to be published)
- [3] A. Ansmann, 1985: Errors in Ground-Based Water-Vapor DIAL-Measurements due to Doppler-Broadened Rayleigh Backscattering. A.O. 24, 3476
- [4] T.D. Wilkerson, G. Schwemmer and B. Gentry, 1979: Intensities and N_2 Collision-broadening Coefficients Measured for Selected H_2O Absorption Lines between 715 and 732 nm. JQSRT 22, 315
- [5] F.G. Fernald, 1984: Analysis of Atmospheric Lidar Observations: Some Comments. A.O. 23, 652

DIAL simulations for satellite water vapor profile measurements
within the BEST Project

P. CHAZETTE, J. PELON, G. MEGIE

Service d'Aéronomie du CNRS, Université Paris VI, T15 E5 B102, 4place Jussieu, 75252
Paris cedex 05, FRANCE

The project BEST has been proposed by several CNRS laboratories to the French Space Agency (CNES) in 1989, as part of the GEWEX programme. Its objective is the study of the Energy Budget of the Tropical System, and aims at measuring different components of the water cycle by coupling several observing systems. As part of it Service d'Aéronomie (SA) proposed to study a Differential Absorption Lidar system (DIAL) to measure tropical water vapor profiles and to determine humidity convergence fields, when coupled with the Doppler wind lidar proposed by the Laboratoire de Météorologie Dynamique.

The differential absorption lidar technique has been chosen as the only one adapted to long distance measurements in daytime condition. To optimize DIAL system parameters, realistic inputs were considered on the basis of present state of the art laser sources and detection systems. A Nd-Yag pumped titanium-sapphire laser was thus selected, with emission in the 820 nm water vapor absorption band. Studies on the laser source and on platform accomodation were performed by BMI and Matra Marconi Space in the frame of a CNES contract.

We have performed at SA simulation analyses for water vapor measurement from the selected orbite of 400 km. For these simulations we have adapted an atmospheric model developed at SA. We have optimized, by a Monte Carlo statistical method, the system parameters and evaluated bias and standard deviation of the retrieved water vapor mixing ratio. We have optimized energy values as a compromise to keep the power demand as low as possible (less than 400 W in total), horizontal resolution compatible with General Circulation Models, while keeping high vertical resolution (better than 500 m) in the first two kilometers.

1. Model

The atmospheric model has been used for the performance simulation of DIAL includes backscatter by the planetary boundary layer (PBL), the free troposphere, the cirrus layer and stratospheric layer. In this model, the earth surface is considered as a Lambertian diffuser. Radiance values for the solar background reflection are taken from 5S model (Simulation of the Satellite Signal in the Solar Spectrum) developed by Tanré et al (1986). As tropical water vapor mixing ratio is highly variable, we have considered three different water vapor profile for the tropical regions :

- dry condition (3 g/cm²),
- moist condition (5 g/cm²),
- very moist condition (7.5 g/cm²).

These profiles are calculated from the TIGR data bank developed at LMD (Chedin et al., 1985)

2. Calculation description

In the near infrared for the lower atmosphere, the absorption linewidth is mainly due to collision broadening. The spectral variation of the absorption cross section of an absorption line, as a function of temperature T and pressure, can be expressed as a Lorentzian shape. Energy level of the lower state must be chosen around 350 cm^{-1} . In this case the parameter deduced from DIAL sounding is the water vapor mixing ratio (Cahen et al, 1982). To optimize lidar measurement it is necessary to minimize the statistical and systematic errors. This last error source is minimized by laser performance, which we supposed meeting requirements. To minimize the statistical error term, the optical thickness should be around one for short noise limitation (Mégie and Menzie, 1980). This can only be reached for a given altitude domain, and for one water vapor profile. As we kept only one wavelength pair, we made the choice between several lines centered at 790, 814, 815, and 817 nm with cross section values respectively equal to 0.8, 1.5, 1.7, $1.1 \cdot 10^{-23} \text{ cm}^2$, at ground level. We have used these different lines to calculate the average bias and standard deviation on the whole TIGR profile bank for final choice.

3. results

The system parameters, given in the table below, have been deduced from Monte Carlo statistical study, for the above mentioned measurement performance.

Emitted energy ON :	: 300 mJ	repetition rate 5 Hz
Emitted energy OFF	: 100 mJ	repetition rate 5 Hz
Telescope diameter	: 1 m	
Field of view	: $2.5 \cdot 10^{-4}$ rad	
Detection optical bandwidth	: 1.5 nm (ocean)	0.5 nm (land)
Optical efficiency	: 45 %	
Detection efficiency	: 75 %	

Several simulations on different ground (forest, sand...) have been performed to determine bias and standard deviation on the retrieval water vapor profile. As the oceans represent most of the surface for the tropical latitudes, energy parameters were optimized for this case. The mixing ratio bias and standard deviation for the moist tropical situation is given on figure 1 for daytime using the 817 nm line. The error is always smaller 10% between 0.5 km and 4 km altitude for a vertical resolution decreasing from 0.3 km to 1.2 km. The bias is smaller than 5% below 5 km altitude, it is mainly due to cross section temperature sensitivity.

For the continental ground, the table below shows the mean mixing ratio error between 0 and 4 km altitude.

Mixing ratio error	ocean	forets	savannas	sand
night	6%	6%	6%	6%
morning/evening	8%	20%	15%	12%
midday	10%	40%	20%	20%

4. Sampling

Taking into account the BEST orbitography and simulation results, we have performed a sampling study on 2D and 3D tropical water vapor fields from the ARPEGE GCM. The results on figure 2 give the mixing ratio relative error due to sampling for a stationary 2D humidity field. This study is achieved for both the 6 days cycle and an altitude orbite of 420 km. The intertropical zone is entirely covered with an horizontal resolution of 300x300 km² and the mean error is smaller than 5%.

Further results will be presented.

References

- E.E. Remsberg and L.L. Gortley
Analysis of differential absorption lidar from space shuttle
Appl. opt. 17, 624, 1978
- C. Cahen, G. Mégie, P.H. Flamant
Lidar monitoring of the water vapor cycle in the troposphere
J. Appl. Meteor. 21, 1506-1512, 1982
- A. Chedin, N.A. Scott, C. Wahiche, P. Moulinier
The improved initialization inversion method : a high resolution physical method for temperature retrievals from satellites of TIROS-N serie
J. of Climat. and Appl. Meteor. 24, 2, 1985
- D. Tanré, C. Deroo, P. Duhaut, M. Herman, J.J. Morcrette, J. Perbos, P.Y. Deschamps
Simulated of the satellite signal in the solar spectrum (5S)
1986

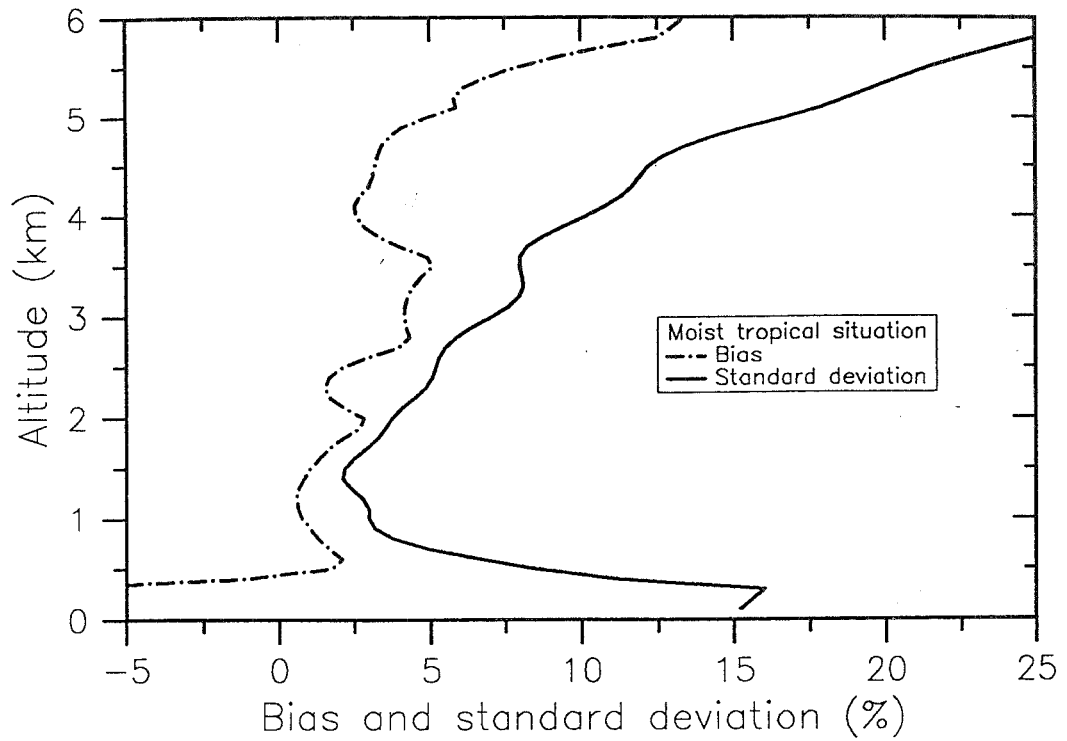


Figure 1 : bias and standard deviation of the water vapor mixing ratio for the moist tropical situation in daytime

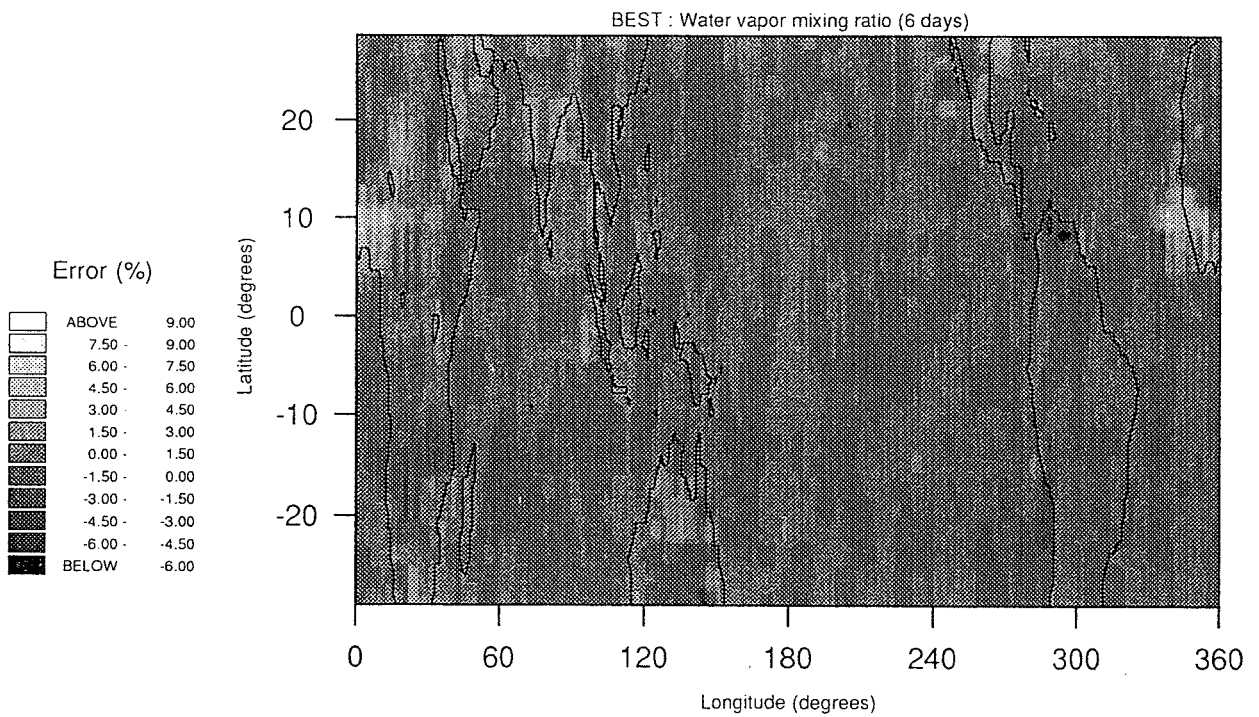


Figure 2 : relative error of the water vapor mixing ratio due to sampling in a 2D humidity field for a 6 days cycle

AIRBORNE WATER VAPOR DIAL RESEARCH: SYSTEM DEVELOPMENT
AND FIELD MEASUREMENTS

Noah S. Higdon, Edward V. Browell, Patrick Ponsardin¹, Thomas H. Chyba²,
Benoist E. Grossmann³, Carolyn F. Butler¹, Marta A. Fenn¹,
Shane D. Mayor¹, Syed Ismail, William B. Grant

NASA Langley Research Center
Atmospheric Sciences Division
Hampton, VA 23665-5225

This paper describes the airborne differential absorption lidar (DIAL) system developed at the NASA Langley Research Center for remote measurements of water vapor (H₂O) and aerosols in the lower troposphere. The airborne H₂O DIAL system was flight tested aboard the NASA Wallops Flight Facility (WFF) Electra aircraft in three separate field deployments between 1989 and 1991. Atmospheric measurements were made under a variety of atmospheric conditions during the flight tests, and several modifications were implemented during this development period to improve system operation. A brief description of the system and the major modifications will be presented, and the most significant atmospheric observations will be described.

A schematic of the current airborne H₂O DIAL system in the NASA WFF Electra aircraft is shown in Figure 1. A tunable, narrowband alexandrite laser is used as the on-line transmitter to provide the required linewidth, stability, and spectral purity for DIAL H₂O measurements (Ismail and Browell, 1989). In the alexandrite laser, a birefringent tuner and two actively stabilized Fabry-Perot etalons are used together to produce the requisite spectral characteristics. Since spectral requirements for the off-line laser are less stringent than for the on-line laser, an Nd:YAG laser-pumped dye laser is used, which has a grating in the oscillator cavity to provide an output linewidth of approximately 15 pm. The spectral performance of the alexandrite laser has been evaluated in the laboratory with a multipass absorption cell using strong oxygen and water vapor absorption features (Ponsardin et al., 1991). A 1-meter spectrometer and a multipass absorption cell are incorporated in the system to accurately position the on-line laser to the center of the H₂O line and to monitor the spectral output during flight operations. The receiver system has a 14-inch

¹Hughes-ST Systems Corporation, 28 Research Drive, Hampton, Virginia 23666

²National Research Council-NASA Research Associate, MS 401A, Hampton, Virginia 23665

³Thomson-CSF, Rue Gynemer - BP 55, 78283 Guyancourt, Cedex, France

diameter Celestron telescope to collect the backscattered laser light and focus it onto the detector optics. The detector optics consist of a collimating lens, a beamsplitter, and an interference filter. The interference filter used during the 1989 and 1990 field experiments had a relatively low transmission of 32% (Higdon et al., 1990). However, a new filter with a transmission of 48% and a bandwidth of 0.4 nm was incorporated prior to the 1991 field deployment. This represents a receiver system efficiency increase of 45% and a resulting measurement signal-to-noise ratio increase of 20%. After transmission through the filter, the return signals are directed onto the detector, which can be either a photomultiplier tube (PMT) or an avalanche photodiode (APD). After the return signals are converted to electrical signals by the optical detector, they are digitized and stored on magnetic tape by the data acquisition system (DAS). The DAS has computers and monitors for signal processing and data display, and the aerosol and water vapor distributions derived by the DAS can be plotted in real time with color printers.

Preliminary engineering flights of the airborne H₂O DIAL system were performed in July 1989. The first extensive observations of lower tropospheric H₂O and aerosols with this system were made during test flights in March and April 1990 with the lidar operating in a nadir mode from the NASA WFF Electra aircraft. Daytime aerosol and H₂O distributions obtained by the airborne DIAL system as it crossed over the coast of Virginia clearly showed the decrease in the mixed layer depth from about 1.7 km over land to less than 1 km over water. The mixed layer had enhanced aerosol loading and elevated H₂O mixing ratios compared to the clean and dry conditions above it. Absolute agreement within 10% between the DIAL H₂O profile and the in situ H₂O measurements from a dew point hygrometer was obtained over Emporia, Virginia, as the Electra spiraled down to the surface from its 4-km flight altitude (Browell et al., 1991). The airborne DIAL measurements made during these field experiments showed the detailed H₂O and aerosol structure that occurs in the free troposphere and in the mixed layer over different land and marine regimes. The first high-spatial resolution distribution of H₂O and aerosols was obtained across a cold front during a flight in March 1990. The transition from the very dry conditions behind the front to the very moist conditions ahead of the front was seen in detail, and the DIAL measurements again compared well with balloonsonde in situ measurements conducted on both sides of the front. In 1991, the DIAL system was deployed in a flight test in which the aircraft overflew a storm cloud. The distribution of moisture above and to the sides of the clouds was clearly evident in the data, and the H₂O distribution was very similar to the aerosol distribution near the clouds. During a nighttime flight the detector was changed from a PMT to an APD and a direct comparison of measurement signal-to-noise ratio was performed. The comparison was accomplished by conducting measurements on a specific flight path with the PMT and, after changing detectors during the turn, retracing the same path for measurements with the APD. The measured H₂O mixing ratios (m), measurement standard deviations (s'), and measurement signal-

to-noise ratios (m/s') are presented in Figure 2. As predicted by Kenimer (1988), the signal-to-noise ratio plots clearly indicate the superior performance of the APD over the entire altitude range. It was found that the APD performed even better during the day compared to the PMT, since the APD is more dark-current limited than the PMT. These experiments have provided new insights into atmospheric processes involving H₂O, and they will serve as a basis for future H₂O investigations, including meteorological observations and studies of H₂O in the Earth's climate system.

Acknowledgments

The authors would like to thank R. J. Allen, A. F. Carter, A. C. Heuser, M. L. Jones, M. N. Mayo, W. J. McCabe, B. L. Meadows, and J. A. Williams of the Lidar Applications Group in the Atmospheric Sciences Division at the NASA Langley Research Center for their assistance in developing the airborne H₂O DIAL system and operating the system in the flight tests.

References

- Browell, E.V., N.S. Higdon, C.F. Butler, M.A. Fenn, B.E. Grossmann, P.Ponsardin, W.B. Grant, and A.S. Bachmeier, "Tropospheric water vapor measurements with an airborne lidar system," in Preprints, Seventh AMS Symposium on Meteorological Observations and Instrumentation, New Orleans, Louisiana, January 14-18, 1991.
- Higdon, N.S., E.V. Browell, P.Ponsardin, and B.E. Grossmann, "Airborne water vapor DIAL system development," Proc. SPIE, 1222, 183-185, 1990.
- Ismail, S. and E.V. Browell, "Airborne and spaceborne lidar measurements of water vapor profiles: A sensitivity analysis," Appl. Opt., 28, 3603-3615, 1989.
- Kenimer, R.L., "Predictions of silicon avalanche photodiode performance in water vapor differential absorption lidar," Proc. SPIE, 889, 126-135, 1988.
- Ponsardin, P., N.S. Higdon, B.E. Grossmann, and E.V. Browell, "Stabilization and spectral characterization of an alexandrite laser for water vapor lidar measurements," Advanced Solid-State Lasers 1991, Technical Digest Series, Optical Society of America, Washington, D.C., pp. 76-78, 1991.

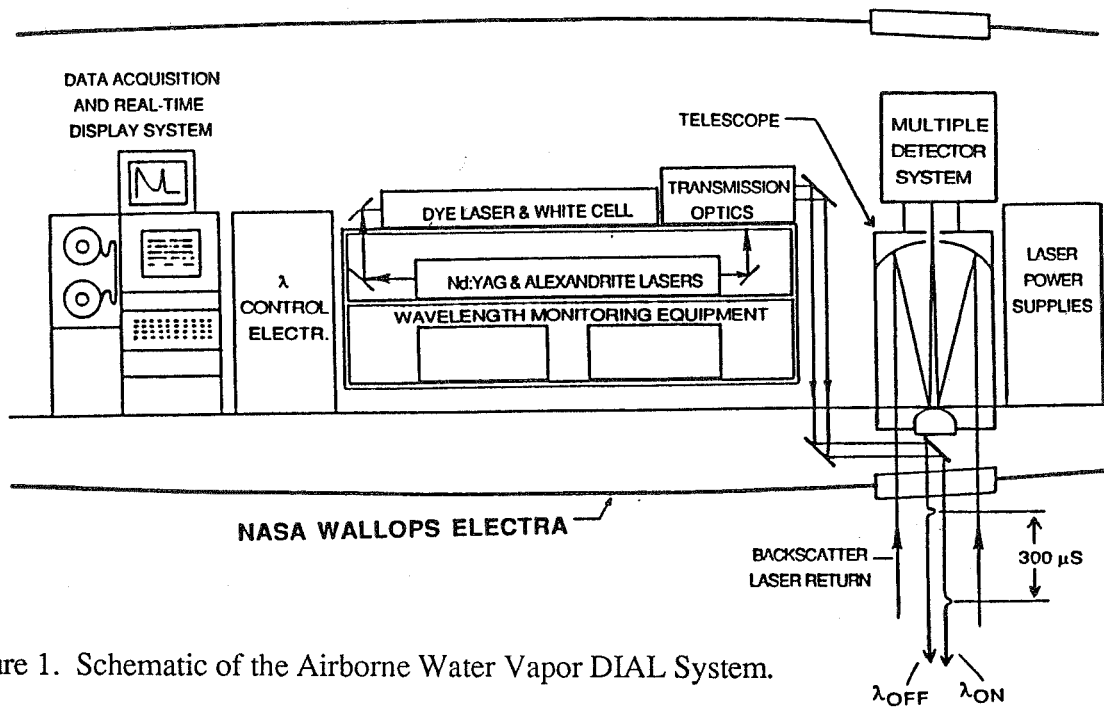


Figure 1. Schematic of the Airborne Water Vapor DIAL System.

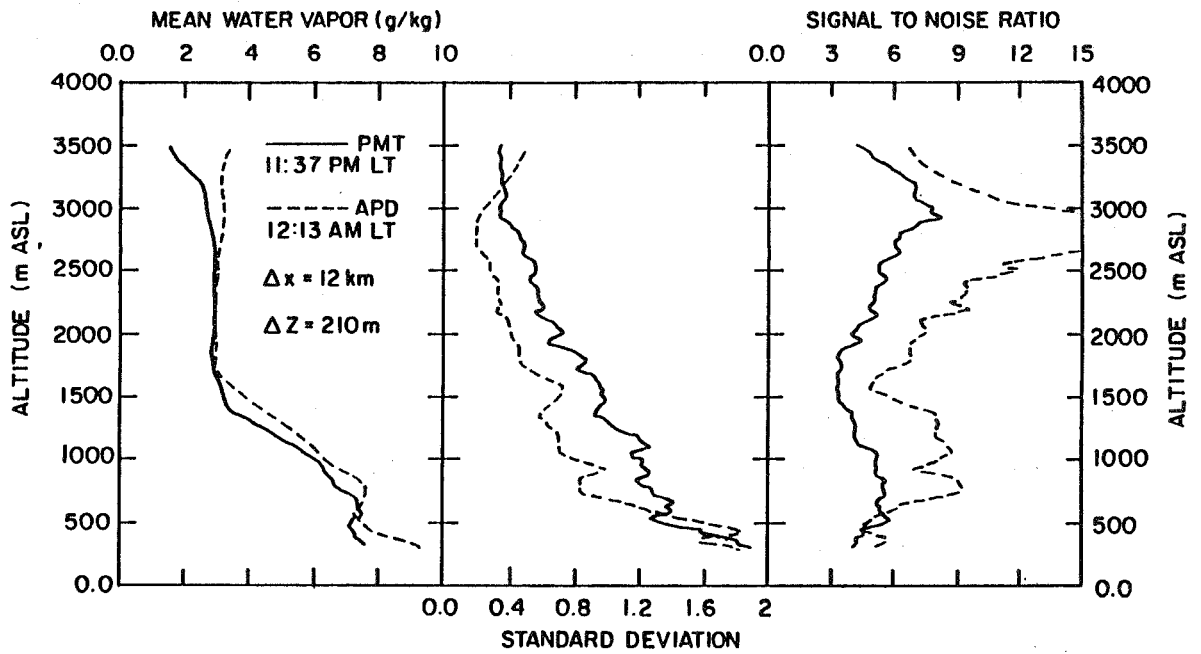


Figure 2. A comparison of data recorded using the APD (dashed line) and the PMT (solid line).

Alexandrite lidar for the atmospheric water vapor detection and development of powerful tunable sources in IR

M. Uchiumi, M. Maeda, K. Muraoka¹ and O. Uchino²

Dep. Electrical Engineering, Kyushu University,
Hakozaki 6-10-1, Higashi-ku, Fukuoka 812, Japan

1 Introduction

New tunable solid-state lasers, such as alexandrite and Ti-sapphire lasers, provide a powerful technique to detect various molecules in the atmosphere whose absorption bands are in the IR region. The DIAL to measure the tropospheric water vapor has been investigated by many authors ^{1)~8)}, in an early stage, by dye and ruby lasers ^{1) 2) 3)}. Using the α band of water vapor, the longest detection range can be obtained with the high accuracy ⁴⁾, and the alexandrite laser is the most suitable laser for this purpose ⁵⁾. In this paper, we describe the detection of water vapor in the atmosphere by an alexandrite lidar, and the development of powerful tunable sources base on Raman lasers in the IR region.

2 Detection of water vapor

The Q-switched alexandrite laser (Light Age, Model PAL 101) has an output energy 200 mJ/pulse (TEM_{00}) at 755nm, and a pulse width of 70 ns. The repetition rate is 20 Hz. Inserting a birefringent filter and a solid etalon with a thickness of 0.4 mm, the linewidth is narrowed to 5 pm. Using a multipass reference absorption cell, the laser is tuned to the absorption line of water vapor.

¹Dep. Energy Conversion, Kyushu University, Kasuga, Fukuoka 816, Japan

²Meteorological Research Institute, 1-1 Nagamine, Tsukuba, Ibaraki 305, Japan

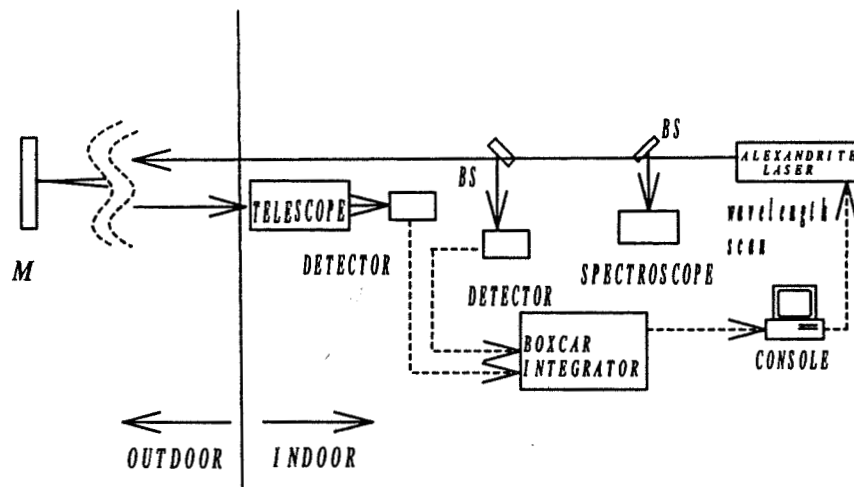


Fig. 1: Setup of the long-path experiment

The long-path absorption measurements were performed in the field by the setup shown in Fig. 1. A reflector M located on a building 125 m apart from the lidar system. The diameter of the telescope (Celestron C8-EX) is 203mm. The laser wavelength was scanned around the 727.7388 nm. The atmospheric temperature was 8 ° C and the humidity was 88 %. The curve simulated for this condition is shown in Fig. 2 (solid curve). The error is within 10 %.

The characteristic parameters of DIAL are shown in the Table 1. The receiver telescope is steerable for all direction.

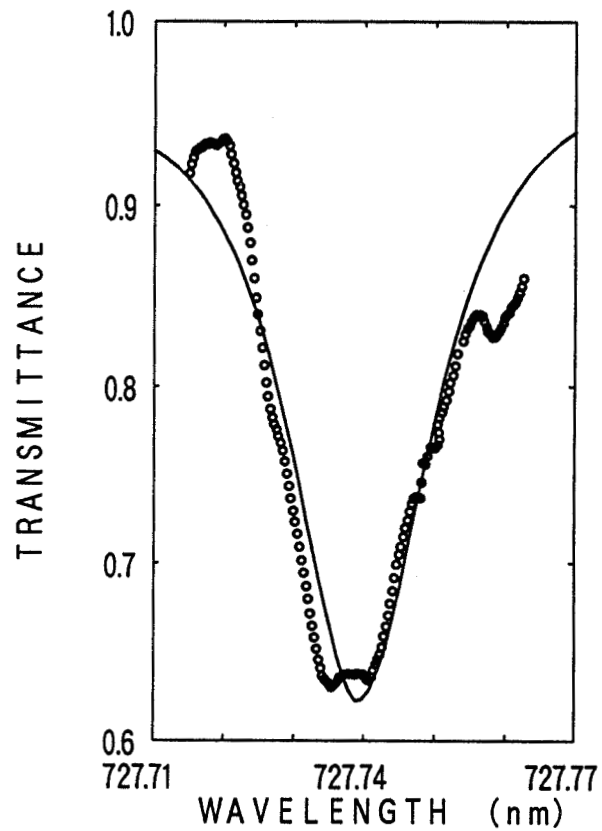


Fig.2: The long-pass absorption measurement of water vapor (open circles). The solid line indicates the simulated transmittance.

Two wavelengths of DIAL on and off line are generated alternately by an alexandrite laser.

Table 1: Specification of the alexandrite lidar developed

Transmitter		Receiver	
Laser	Alexandrite Laser	Telescope type	Coude
Wavelength	727 nm	Diameter	50 cm
Energy	50 mJ/pulse at 727 nm	Focal length	5250mm
Pulse width	70 ns	F	10.5
Repetition rate	20 Hz	Field of view	1 mrad
Beam divergence	0.4 mrad	IF Filter	1nm FWHM

3 Development of tunable IR sources

The tunable range of the alexandrite laser is limited from 720 to 800 nm. The stimulated Raman scattering in high pressure gases H_2 , CH_4 or D_2 is useful to expand the tunable range to the IR region. Fig. 3 shows an example of the tuning curves of the Raman laser pumped by the

alexandrite laser. Especially 32 % conversion efficiency is obtained around 1.1 μm .

On the other hand, we have already developed a Ti:sapphire laser pumped by a frequency-doubled Nd:YAG laser, whose output energy is more than 70 mJ in TEM₀₀ mode. The tunable range of 690-950 nm was obtained with linewidth less than 10pm. Using this laser as the pumping source of H_2 Raman laser, continuous tunable region up to 3 μm will be obtained. These sources are useful for the detection of various molecules in the atmosphere.

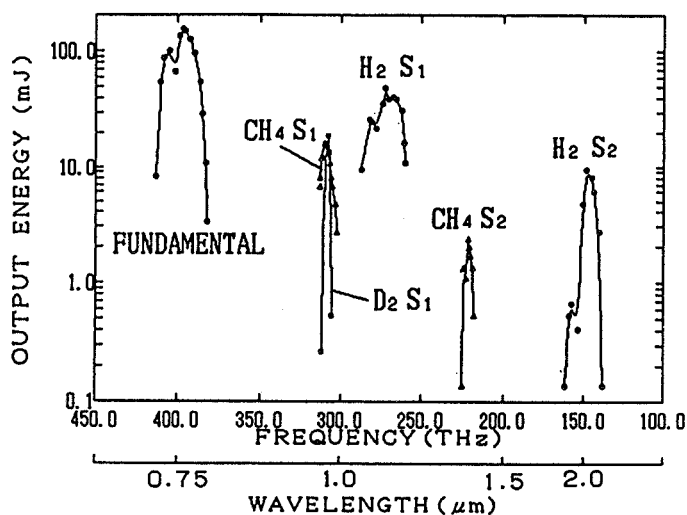


Fig.3: Tuning curves of the Raman laser. S₁ and S₂ stand for the 1st and 2nd Stokes, respectively.

The line strengths in α band of water vapor are so weak to measure the stratospheric water vapor by DIAL. Absorption lines with a strength of $\sim 10^{-20} \text{ cm}^{-1}/(\text{molec. cm}^{-2})$ are suitable to measure gas of the mixing ratio of 1ppm (the stratospheric water vapor). The lines with such suitable strength can be obtained in the $1.1 \mu\text{m}$ band ^{4) 9)}. If the Raman shifted alexandrite laser

is used for airborne DIAL measurements of the stratospheric water vapor, the expected errors are calculated as shown in Fig. 4.

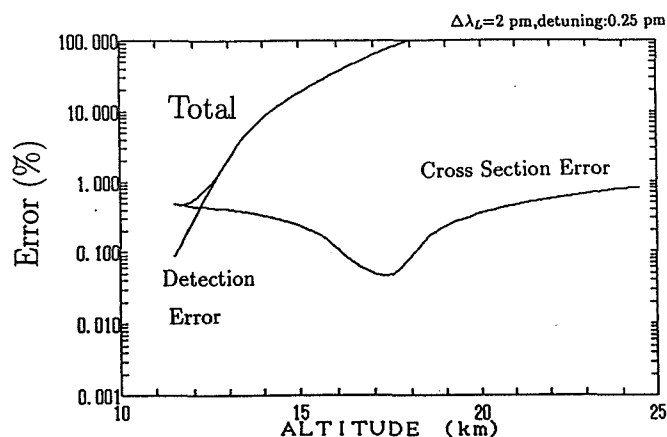


Fig.4: Simulated errors of the measurement of atmospheric water vapor by airborne lidar at the altitude of 10 km using $1.1 \mu\text{m}$ band ($\Delta Z=1\text{km}$, 10 shots, 40mJ, $\Delta\lambda_{Pshift}=1\text{pm/atm}$).

References

- (1) E. V. Browell, T. D. Wilkerson, and T. J. McIlrath, *Appl. Opt.*, 18, 3474-3483, 1979.
- (2) C. Cahen, G. Megie and P. Flamant, *J. Appl. Meteorology.*, 21, 1506-1515, 1982
- (3) V. V. Zuev, V. E. Zuev, Yu. S. Makushkin, V. N. Marichev, and A. A. Mitsel, *Appl. Opt.*, 22, 3742-3746, 1983.
- (4) S. Ismail and E. V. Browell, *Appl. Opt.*, 28, 3603-3615, 1989.
- (5) D. Bruneau, H. Cazeneuve, C. Loth, and J. Pelon, *Appl. Opt.*, 30, 3930-3937, 1991,
- (6) S. Cha, K. P. Chan, and D. K. Killinger, *Appl. Opt.*, 30, 3938-3943, 1991.
- (7) E. V. Browell, S. Ismail, and B. E. Grossmann, *Appl. Opt.*, 1517-1524, 1991.
- (8) N. S. Higdon and E. V. Browell, *SPIE*, 1222, *Laser Radar V*, 183-185, 1990.
- (9) U. N. Singh, Z. Chu, R. Mahon, and T. D. Wilkerson, *Appl. Opt.*, 29, 1730-1735, 1990.

**EMERGING SOLID-STATE LASER TECHNOLOGY
for LIDAR/DIAL REMOTE SENSING**

by

**DENNIS KILLINGER
Department of Physics
University of South Florida
Tampa, FL 33620
Ph (813) 974-3995**

Significant progress has been made in recent years in the development of new, solid-state laser sources. This talk will present an overview of some of the new developments in solid-state lasers, and their application toward LIDAR/DIAL measurements of the atmosphere. Newly emerging lasers such as Ho:YAG, Tm:YAG, OPO, and Ti:Sapphire will be covered, along with the spectroscopic parameters required for different operational modes of atmospheric remote sensing including Doppler-Windshear LIDAR, Tunable laser detection of water/CO₂, and broad linewidth OPO's for open path detection of pollutant hydrocarbon gases.

As an example and as a starting point of discussion, Table 1 is a partial list of some of the recently developed solid-state lasers being investigated for the remote sensing of the atmosphere. As one can see, a wide range of wavelength's and output powers are listed, but each laser source has to be evaluated individually as far as its utility for LIDAR/DIAL is concerned.

A specific example of just one such consideration is given in Fig. 1, which is a plot of the transmission of the atmosphere over a 1000 m path, showing the overlay of the Ho:YAG, Ho:YSGG, and Ho:YLF laser lines. As can be seen, the choice of the Ho laser crystal can significantly influence the transmission properties of the atmosphere and the detection range of the system.

Additional considerations of emerging laser technology for LIDAR/DIAL will be covered.

Table 1: Emerging Solid-State Lasers

Nd:YAG 1 - 10 J, 10 ns - 1 μ s, $\Delta\nu = 1$ MHz
 Tunable 20 cm^{-1} , 1.06, .94, 1.44 μm , etc.

Co:MgF2 10 - 50 mJ (QSW), .5 J Normal Mode,
 1.7 - 2.5 μm , $\Delta\nu = .1$ to .5 cm^{-1}

Ti:Al2O3 : 100mJ, $\Delta\nu = 1$ MHz, Mode Hops

Tm:YAG CW operation / Q-SW, low gain, 1.9 μm

Er:GSGG 2.8 - 2.9 μm
 Er:YAG

OPO 250 mJ (1 cm^{-1}) ; 10 mJ (0.1 cm^{-1})
 - Ho Pumped, 3-5 μm
 - Injection Seeded Idler, Nd/2x/Ti Pumped 2-5 μm

D2 Raman Shifted Nd:YAG 1.55 μm , 200 mJ, 10 ns

Ho : YAG vs YLF vs GSGG 2.1 μm , pulsed ,
 100 mJ Q-switched, 1 J Normal Mode

Tunable GainAsSb Diode Lasers: Room Temperature
 2 - 5 μm , 10 mW

Transmission

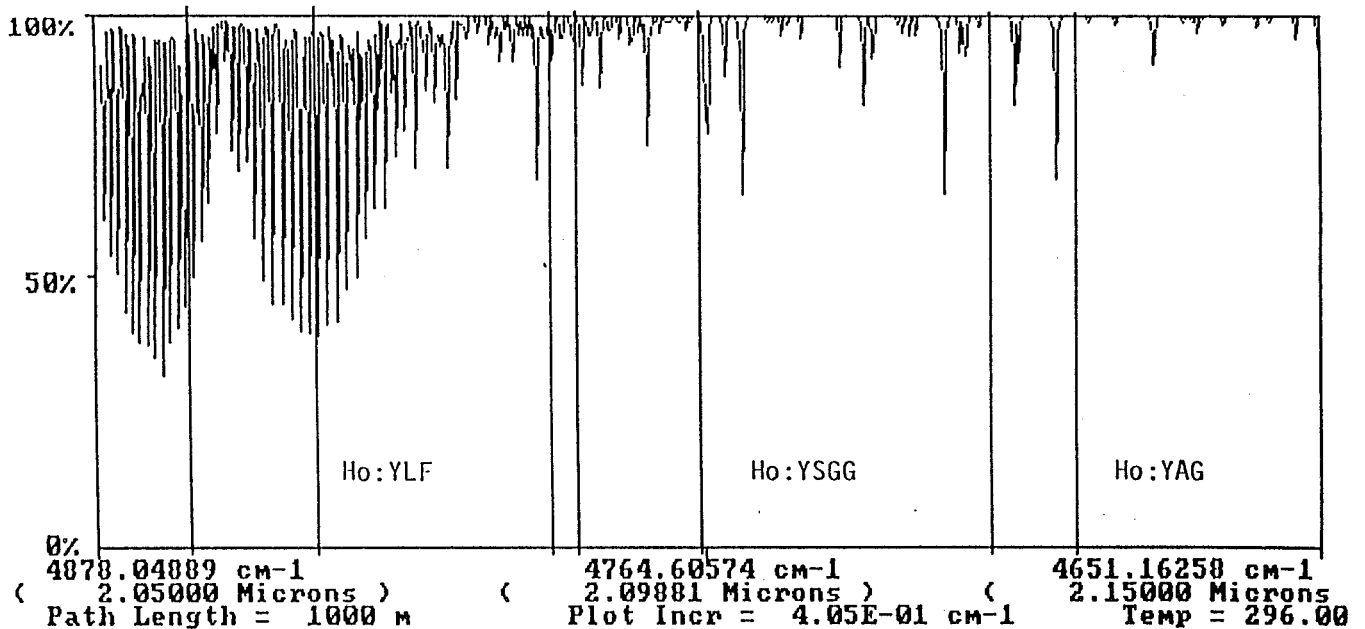


Figure 1: Transmission of Atmosphere and Overlay of Ho Laser Lines

Coherent Summation of Spatially Distorted Doppler Lidar Signals Using a Two-Dimensional Heterodyne Detector Array

Kin Pui Chan and Dennis K. Killinger
Department of Physics
University of South Florida
Tampa, FL 33620
Tel (813) 974-3995

We have investigated the improvement in the signal-to-noise ratio for a coherent Doppler lidar through the use of a multielement heterodyne detector array. Such an array enables the spatial summation of atmospheric refractive turbulence induced speckles, and time-varying target speckles. Our recent experiments have shown that the Non-Coherent summation of the lidar signals from a heterodyne detector array can enhance the heterodyne mixing efficiency and thus the S/N ratio.¹ In this paper, we expand this work to include the Coherent summation of the array signals.

Figure 1 shows a schematic of our experimental setup. A diode-laser pumped, CW, 1-W single-frequency laser was used in a laboratory lidar test-bed. The laser was divided into a local oscillator and transmitted beam. The L.O. was off-set in frequency by 26 MHz, and directed toward the InGaAs detector array. The slowly rotating target produced speckles at the receiver aperture plane which could easily be observed using an IR card. The individual detector signals were recorded by a 4-channel digitizing oscilloscope, and sent to a computer. Figure 2 shows the signals from the 2x2 detector array, and displays the 26 MHz intermediate frequency and the time-varying signal amplitude that was modulated by the speckles.

The digitized heterodyne signals were stored in a personal computer. Fast Fourier transforms were performed on both the non-coherent and coherent summations of the detector array signals. For coherent summation, the four digitized signals were shifted in phase to maximize the Fourier component at the intermediate frequency. It was found that the coherent summation significantly enhanced the accuracy in the Doppler frequency estimate. A theoretical analysis was performed and indicated good agreement with our experimental results. We have also applied these results to the more general lidar applications including atmospheric wind sensing, and have found that in most lidar applications the Doppler frequency estimate is increased through the use of the heterodyne detector array.

Reference:

1. K.P. Chan and D. K. Killinger, "Enhanced detection of atmospheric turbulence distorted 1 μm coherent lidar returns using a two-dimensional heterodyne detector array", *Optics Letters* 16, 1219 (1991).

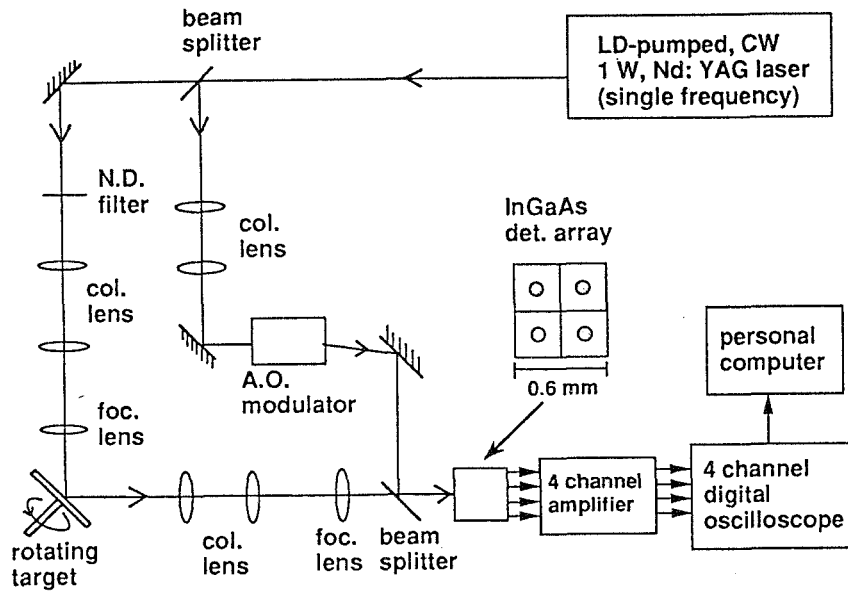


Fig. 1 Schematic of a 1- μm Nd:YAG laser Doppler measurement setup.

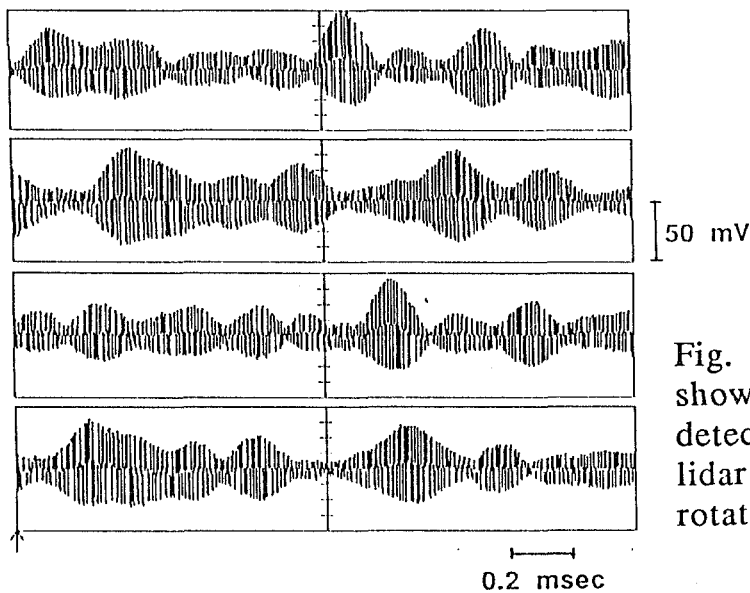


Fig. 2 Oscilloscope displays showing the 2x2 heterodyne detector array outputs for the lidar signal scattered from a rotating disk.

The Role of Laser Coherence in Long-Range Vibration Measurements *

R. S. Eng, C. Freed, R. H. Kingston, K. I. Schultz
A. L. Kachelmyer, and W. E. Keicher
Massachusetts Institute of Technology, Lincoln Laboratory
P. O. Box 73, Lexington, Massachusetts 02173

ABSTRACT

In measurements of vibrating objects by using laser heterodyne techniques, the temporal coherence of the laser oscillator limits the dynamic range of the measurements. This limitation of the optical radar dynamic range has its analog in microwave Doppler radar in which the subclutter visibility level is determined by the phase noise of the microwave oscillator.

In microwave Doppler radar, the oscillator frequency stability is in general characterized in the frequency domain by the single-sideband phase noise expressed as noise power per hertz with respect to the carrier as a function of the frequency offset from the carrier. A phase-noise floor can be calculated which limits the detection of faint radar returns in range or Doppler bins adjacent to the clutter or other large object returns.

In the laser community, the characterization of laser frequency stability, unfortunately, has been done mainly in the time domain by measuring the root Allan variance, in fractional frequency deviation vs. measurement time in seconds. This comes about because there are two different groups of research workers in the laser frequency stability areas with distinctly different objectives. The first group works in the time-frequency standards area where achieving a very high long-term laser frequency stability is the primary goal. This requires that in the Allan variance plot the measurement time be extended out to the tens or hundreds of seconds. On the other hand, the second group works in the coherent laser radar or Doppler velocimeter area where only the short-term laser frequency stability in the range of about 1-100 μ s is of interest. The reason is that most of existing coherent laser radars are tactical laser radars in that their ranges are relatively short and long-range coherent laser radars, such as the Firepond CO₂ coherent laser radar, are not common.

The result in this historical development in the coherent laser radar area is that the effect of laser phase noise has not been critically examined in laser radar measurements because the short range, or short time delay, has a beneficial effect of reducing the phase noise of an average laser oscillator used in either phase-locked heterodyne or homodyne operation so that the low phase noise requirement is usually not a problem to the laser radar designer.

In this paper, the temporal coherence effect of a laser oscillator will be critically examined using existing laser frequency stability data in the time domain by first converting them to

*This research is supported by the Department of the Navy.

the frequency domain. We will limit our discussion to CO₂ lasers. To be more specific, our presentation will include the following items:

- We will review the definitions and representations of laser oscillator frequency stability;
- A methodology will be developed for determining the dynamic range of vibration measurements; the method can also be extended to other Doppler measurements in laser radar applications;
- The methodology will show that the conversion of the laser frequency stability from the time domain to the frequency domain can be performed effectively in the optical region;
- Because of a finite time delay, the phase noise is reduced for offset frequencies close to the carrier frequency; the reduction in laser oscillator frequency stability requirement is especially beneficial for short ranges, i.e., small time delays.

For illustration purposes, the case of a CO₂ waveguide laser and the case of a Fabry-Perot cavity ultrastable CO₂ laser will be discussed.

Figure 1 shows the Allan variance plot of a frequency stabilized Hughes CO₂ waveguide laser, Model EN-6, [1] where the data points are given in stars. This time domain plot is then converted to the frequency domain plot shown in Fig 2 where the effect of time delay on the (single sideband) spectral density is parametrically shown. For a small delay of about 2/30 ms, the phase noise for offset frequency close to the carrier is reduced by several orders of magnitude in comparison with that for a delay 10 times longer. Because of the fact that the phase noise is finite, the integrated phase noise with respect to the carrier level can be considerable for broadband operation. Integration of the phase noise carried out for Fig. 2 shows that the noise floor is as high as 10 dB below the carrier level for a bandwidth of few tens of kHz. This means that the dynamic range is limited to about 10 dB so that low-amplitude target vibrations (relative to a strong amplitude vibration in an adjacent range or Doppler bin) may not be detected.

Figure 3 shows an Allan variance plot similar to Fig. 1 for a Fabry-Perot cavity ultrastable CO₂ laser developed at Lincoln Laboratory [2]. The data denoted by the open and solid circles represent frequency-locked laser data points using the saturated fluorescence techniques, while the (two) cross-filled circles represent short-term frequency stability experimentally observed while the laser was free running. In comparison with Fig. 1, the short-term data for the free-running case are about an order of magnitude better. They may represent the best short-term frequency stability ever recorded. We will discuss in detail using these two lasers as examples the performance and limitations in laser radar vibration measurements using an FM discriminator and other demodulation techniques. We will extend our discussion to other laser wavelengths such as the Nd:YAG laser where very rapid advances have recently been made in the frequency stability of diode pumped CW Nd:YAG lasers.

REFERENCES

1. R. Nordstrom, L. Berg, A. DeSimone, D. Connor, A. Javan, C. K. Bullock, and R. Hintz, "Calibration of the Remote Oscillator/Clocks," paper presented in Active IRIS Conference, Silver Spring, MD, Oct. 29-31(1991).
2. C. Freed, "Ultrastable CO₂ Lasers," The Lincoln Laboratory Journal 3, 479(1990).

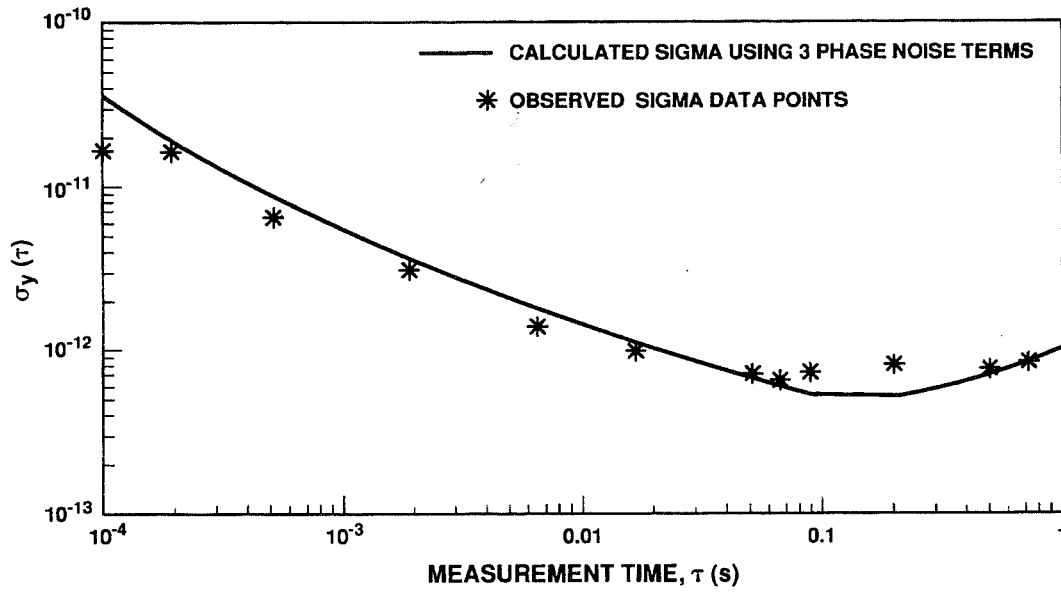


Figure 1: Root Allan variance of frequency stabilized Hughes CO₂ lasers

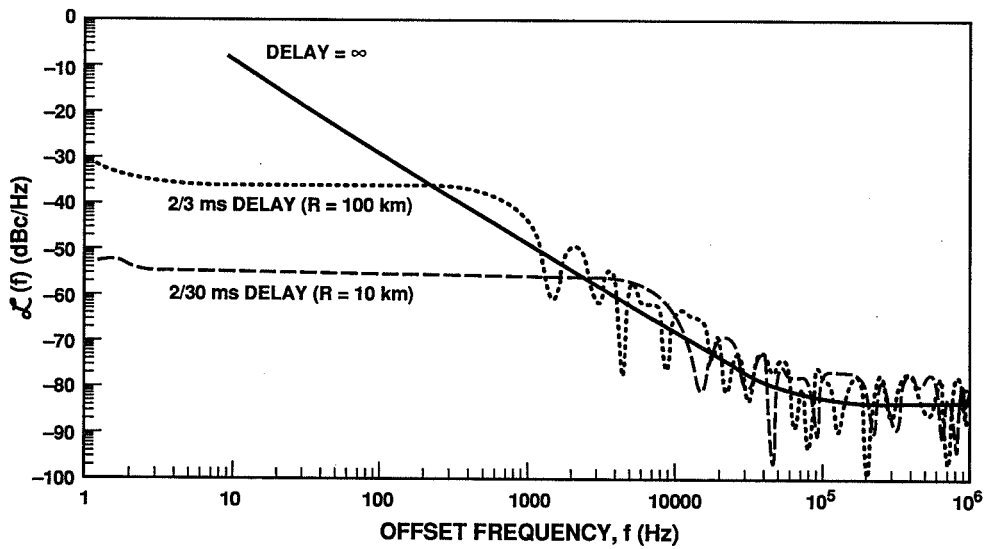


Figure 2: Effective SSB phase noise for two time delays

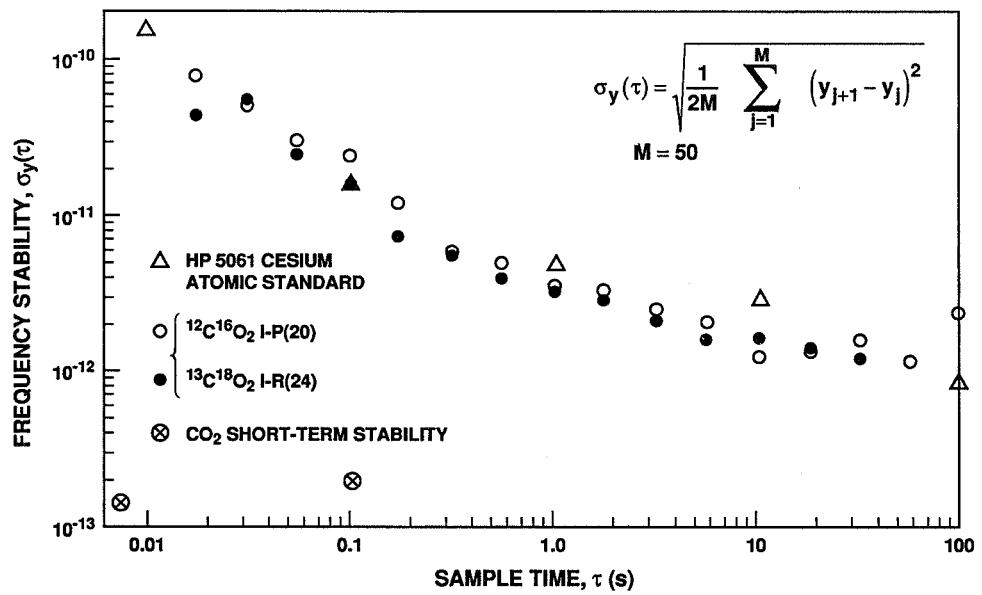


Figure 3: Time-domain frequency stability of a Fabry-Perot cavity CO_2 laser

A Portable Lidar Using a Diode-Pumped YAG Laser

N. Takeuchi, H. Okumura, T. Sugita, H. Matsumoto and S. Yamaguchi*

Remote Sensing and Image Research Center, Chiba University
1-33, Yayoi-cho, Inage-ku, Chiba-city, CHIBA 263, JAPAN

* *Electronics Research Laboratory, Nippon Steel Corp.*
5-10-1, Fuchinobe, Sagamihara-city, KANAGAWA 229, JAPAN

Introduction

A Mie lidar system is technically established and is used for monitoring of air pollution, stratospheric and boundary layer aerosol distribution, plume dispersion, visibility, and the study of atmospheric structure and cloud physics. However, a lidar system is not widely used because of its cumbersome handling and unwieldy portability. Although the author developed a laser diode lidar system based on RM-CW technique¹⁾, it has a limit of measurement distance. Here we report the development of an all solid Mie lidar system using a diode-pumped Nd:YAG laser²⁾ and a Si-APD detector. This was constructed as a prototype of a handy lidar system.

Summary of the system

The block diagram is shown in Fig. 1. The pumping laser diode shows a power level of 930 mW at cw operation with 1.5 A feeding. A Nd:YAG laser can be operated at the power of 250 mW (cw operation) and 70 mW in average (pulse operation by AO modulator at 1 kHz). In a pulse operation, the width is about 25 ns. The output beam has a beam divergence of 10 mrad, which is reduced to 0.5 mrad by a 20-time beam expander. The direction of expanded 25 mm beam is adjusted by rotating a pair of wedge prisms.

Scattered signal is collected by a 20cm diameter telescope. The signal light is introduced to a Si-APD with 0.5 mm aperture, which limits the field-of-view (FOV) of the receiving system. An APD has the amplification factor of 300 times, which is followed by a low noise amplifier with the gain of 300. The detected signal is AD converted by a high speed 8-bit AD converter with the maximum repetition frequency of 30 MHz. The AD converted signal is summed up by a specially designed accumulator (the detail is described in another paper³⁾), and is transferred to a personal computer. The specification of the system is shown in Table 1.

YAG laser performance

A diode pumped YAG laser system is constructed in a cylinder of 5 cm diameter with a length of 15 cm. An AO modulator is used to obtain the pulse operation. The lasing power is built up in the pulse repetition range over 200 Hz. The averaged pulse energy is gradually increased and reached to the level of 270 mW. The pulse energy for an individual pulse is decreasing with the repetition frequency. The signal-to-noise (SN) ratio is effected by the individual pulse energy multiplied by the square root of repetition frequency. The lasing intensity is shown in Fig. 2, with the result of the square root of repetition frequency multiplied by the pulse energy.

High speed signal processing unit

This is the most important part in the current system. The system is controlled by the

command from a host personal computer. The diagram and some performance of the constructed system is described in an different paper³⁾.

Si-APD detector

Another feature of this system is the use of a Si-APD solid-state detector unit C4777, manufactured by Hamamatsu Corp. This unit was constructed in a compact package with a succeeding amplifier with the amplification factor of 100. The band width was adjusted to 10 MHz in order to be consistent to the present system. This unit is directly mounted on the back-fringe of telescope.

SN ratio of system

The SN ratio at range R is expressed as

$$SN(R) = \frac{\sqrt{N} \cdot I_S(R)}{\sqrt{i_S^2(R) + i_B^2 + i_D^2 + i_{nA_i}^2 + i_{fn}^2}} \quad (1),$$

where N : repetition frequency,

$I_S(R)$: electric current caused by an echo signal from range R ,

$i_S(R)$: shot noise caused by $I_S(R)$,

i_B : shot noise caused by the background radiation,

i_D : shot noise caused by the dark current of APD,

i_{nA_i} : noise caused by amplifier,

i_{fn} : thermal noise caused by the resistor in amplifier.

Eq.(1) shows the behavior of measurement ability determined by the square root of the repetition frequency.

Estimation of a lidar ability

The SN estimation of the system is given in Fig. 3 for both cases of the daytime and night time measurement. Here the energy of an individual pulse, visibility and the accumulation time are assumed to be 70.0 μ J at the repetition frequency of 1 kHz, 10 km and 1 sec, respectively. Other conditions are assumed to be the same as the one shown in Table 1.

Conclusion

A portable lidar consisting of all solid-state components, such as a diode-pumped YAG laser and an APD detector, was constructed and the preliminary data was obtained, which is presented in another paper describing the signal processor.

The authors thank Hamamatsu Corp. for providing a C4777 APD unit.

Reference

- 1) N.Takeuchi, H.Baba, K.Sakurai, T.Ueno: Diode laser random modulation cw lidar. Appl. Opt. **25**(1) 63-67.
- 2) S.Yamaguchi, H.Imai: Efficient Nd:YAG laser end-pumped by a 1cm aperture laser-diode bar with a GRIN lens array coupling, IEEE J. Quantum Electron., in print.
- 3) H.Okumura, T.Sugita, H.Matsumoto, N.Takeuchi, S.Kuwashima: A high speed signal processing system for a diode-pumped YAG lidar, in the Proc. of ILRC16.

Table 1 Specification of the developed lidar system.

<u>Laser :</u>	Diode-pumped YAG laser	<u>Signal Processing :</u>	Continuous sampling
	Pulse power 70 mW		Data length 2048 channels
	Pulse width 25 ns		Data size 8 bits
	Repetition 1 kHz		Sampling time 50 ns
<u>Telescope :</u>	Cassegrain-type		Averaging up to 32 bits
	Aperture 20 cm	<u>Control System :</u>	Portable personal computer
	Focal length 2 m		
<u>Detector :</u>	Si-APD 0.5 mm ϕ		
	Sensitivity 5 A/W		
	(with Amplifier)		
	Band width 10 MHz		

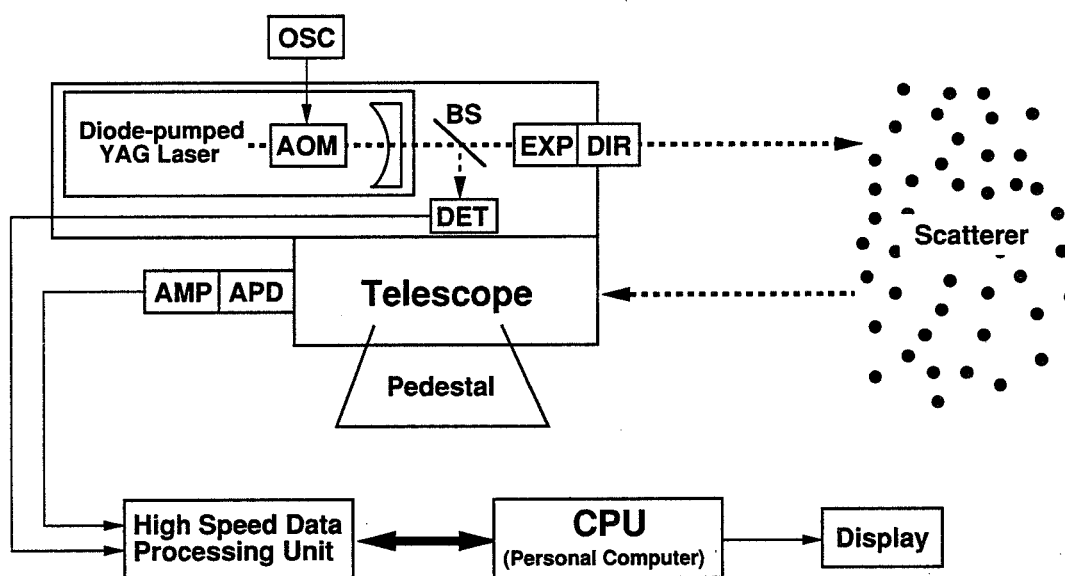


Figure 1 Schematic diagram of the system.

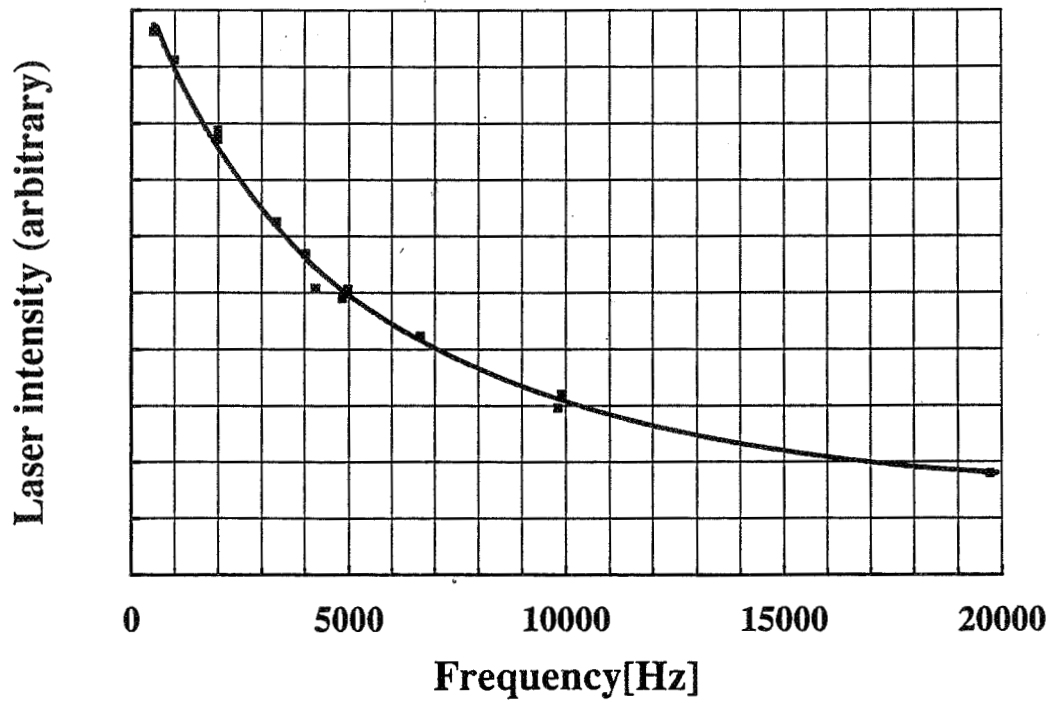


Figure 2 Laser intensity of a diode-pumped YAG laser used in the system.
 (The laser power at 1 kHz repetition frequency corresponds to 70 μ J)

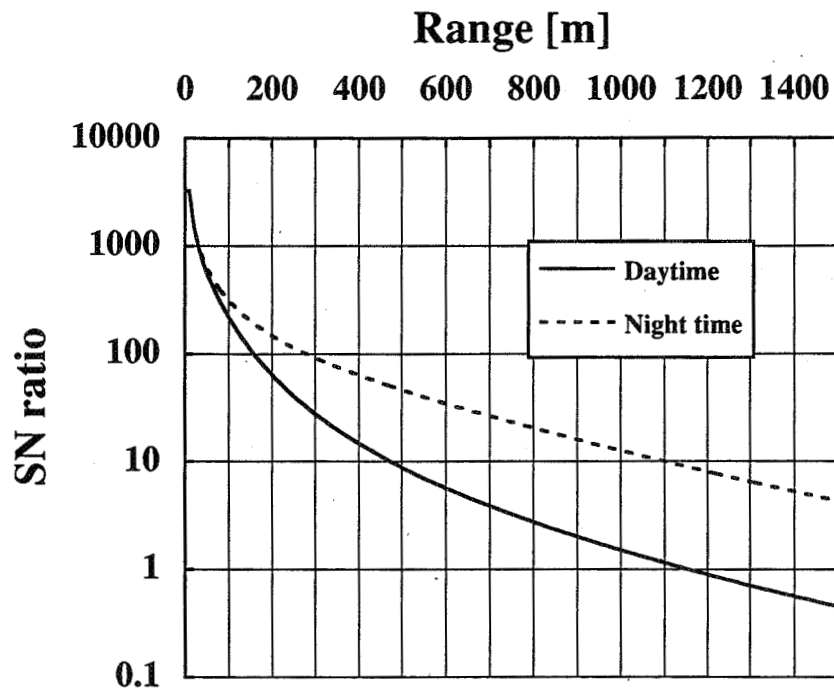


Figure 3 SN estimation of the system.
 (Visibility : 10 km, accumulation time : 1 sec)

INVESTIGATIONS ON ATOMIC-VAPOR-FILTER
HIGH-SPECTRAL-RESOLUTION LIDAR FOR
TEMPERATURE MEASUREMENTS

E. Voss, C. Weitkamp

Institut für Physik, GKSS Forschungszentrum
W-2054 Geesthacht, Federal Republik of Germany

The temperature measurement by the analysis of Rayleigh-scattered laser radiation with atomic vapor filters is investigated in both theory and laboratory experiments. Synthetic air is irradiated with a cw dye laser at 283 nm, and the backscattered spectrum is analyzed with two lead vapor cells in one oven. Temperature measurements are carried out, and the effect of different parameters on the accuracy is investigated. Important aspects for the realization of a lidar are given.

Introduction

Height profiles of atmospheric temperature belong to the important input data in weather and climate research. Measurement systems for the determination of temperature profiles should combine an accuracy of about 1 K with high spatial and temporal resolution, and should be independent of the time of day. High-spectral-resolution lidar (HSRL) with atomic vapor filters was proposed as a technique for this kind of measurement.^{1,2} A few aspects of the principle have been discussed theoretical,^{3,4} but only one laboratory temperature measurement using a cw laser has so far been published.⁵ First attempts with the use of a pulsed laser system for in-situ measurements in the laboratory⁶ and a very first atmospheric night-time temperature measurement⁷ have been reported. Fluctuations of the atomic vapor filter temperature were identified as the major problem. No systematic investigations of the limitations and the nature of the most important error sources for HSRL temperature measurements have been published.

This paper presents a simple solution of the major problem and shows results of both theoretical and experimental investigations of systematic effects in HSRL.⁸

Experimental setup

The light source used is an Ar⁺-laser-pumped single-frequency cw dye laser with intracavity frequency doubling. A scattering chamber allows the observation of backscattered radiation under defined conditions. The backscattered light is coupled into the analyzing unit through an entrance slit and is split into a measuring and a reference beam which pass the atomic absorption cells, the exit slits and two solar blind filters to reach the photomultipliers. Both tubes are operated in the photon counting mode with a 100-MHz two-channel photon counter.

Pb with its transition $6p^2 \ ^3P_0 \rightarrow 6p7s \ ^3P_1$ at 283.306 nm was taken as the absorbing material in the atomic filters. This choice was made after a comparison of nearly all chemical elements with respect to several criteria for use in a daytime lidar. The operating parameters of both cells including their length, temperature and isotopic composition were optimized theoretically to reduce the effect of oven temperature variations on the broad-filter-channel to narrow-filter-channel signal ratio S . These calculations show that by the use of only one oven for both cells, cell parameters can be found for which the influence of cell temperature

variations on S is zero for one value of the air temperature and of tolerable magnitude for other air temperatures. For a given set of cell parameters near optimum this point can be found simply by varying the oven temperature. To confirm these theoretical predictions an experiment was made in which both atomic vapor cells were heated in the same three-zone oven.

Results

The signal ratio S is given experimentally by the darkcount-corrected signals from the measuring (broad filter) and the reference channel (narrow filter). The ratio S has been modeled taking into account the polarization of the light source, the depolarization and backscatter coefficients of Rayleigh and rotational-Raman scattering, and the polarisation-dependent transmittance parameters of the apparatus. A few experimental results and the corresponding theoretical predictions are shown in Fig. 1 and will be discussed briefly.

The theoretically predicted existence of an optimum cell temperature for which S is unaffected by cell temperature variations was proved experimentally (Fig. 1a). Other measurements at cell temperatures of 831 and 860 K show no measurable effect of cell temperature variations on S for periods of 3 to 4 hours.

Measurements of the signal ratio without any cell heating result in a relative standard deviation from the half-year mean value of 2.3 %. This drift is attributed to different electrical and optical instabilities in the two-channel system. Rotational Raman lines which are very close in wavelength also contribute to the signals in the two channels and thus reduce the sensitivity of HSRL air temperature measurements. In addition they complicate the correction of optical and electrical drift. Their elimination is therefore desirable from both points of view.

The sensitivity of the signal ratio on the polarizing angle of the linear polarized laser light was also measured and amounts to about 2.0 % per degree.

The measured transmission at peak absorption is about 3×10^{-5} . This residual transmission which is caused by spontaneous resonance fluorescence from the Pb cells limits the maximum suppression of particle scattering by the atomic vapor filters. As was shown in the experiments, however, S was not affected by particle backscattering up to a ratio of particle-to-Rayleigh backscatter of 4.

The sensitivity of S to a laser detuning or laser jitter (Fig. 1b) is about $-0.008 \text{ \%}/\text{MHz}$. This can be translated into a sensitivity to longitudinal wind of $0.056 \text{ \%}/(\text{m/s})$.

The sensitivity of S to variations in the $\text{O}_2 - \text{N}_2$ gas mixing ratio of the sample volume (shown in Fig. 1c) is about $8.6 \text{ \%}/(\text{kg/kmol})$.

In Fig. 1d measurements of S dependent on air temperature are shown including one curve at 860 K (solid line) measured with particle-to-Rayleigh ratios decreasing from 4 at about 300 K to 1.5 at about 315 K. The absolute accuracy reached with the simple theoretical models is better than 8 %. For practical application a better theory and better input data and a calibration run are necessary. With the knowledge of only two calibration points, a mean temperature resolution of 1.2 K at a mean sensitivity of S to air temperature of $0.24 \text{ \%}/\text{K}$ was measured. This resolution is caused only by statistical errors. It can be improved by using higher laser power, larger measuring times and better readout accuracy of the photon counter which was only three digits in our experiments.

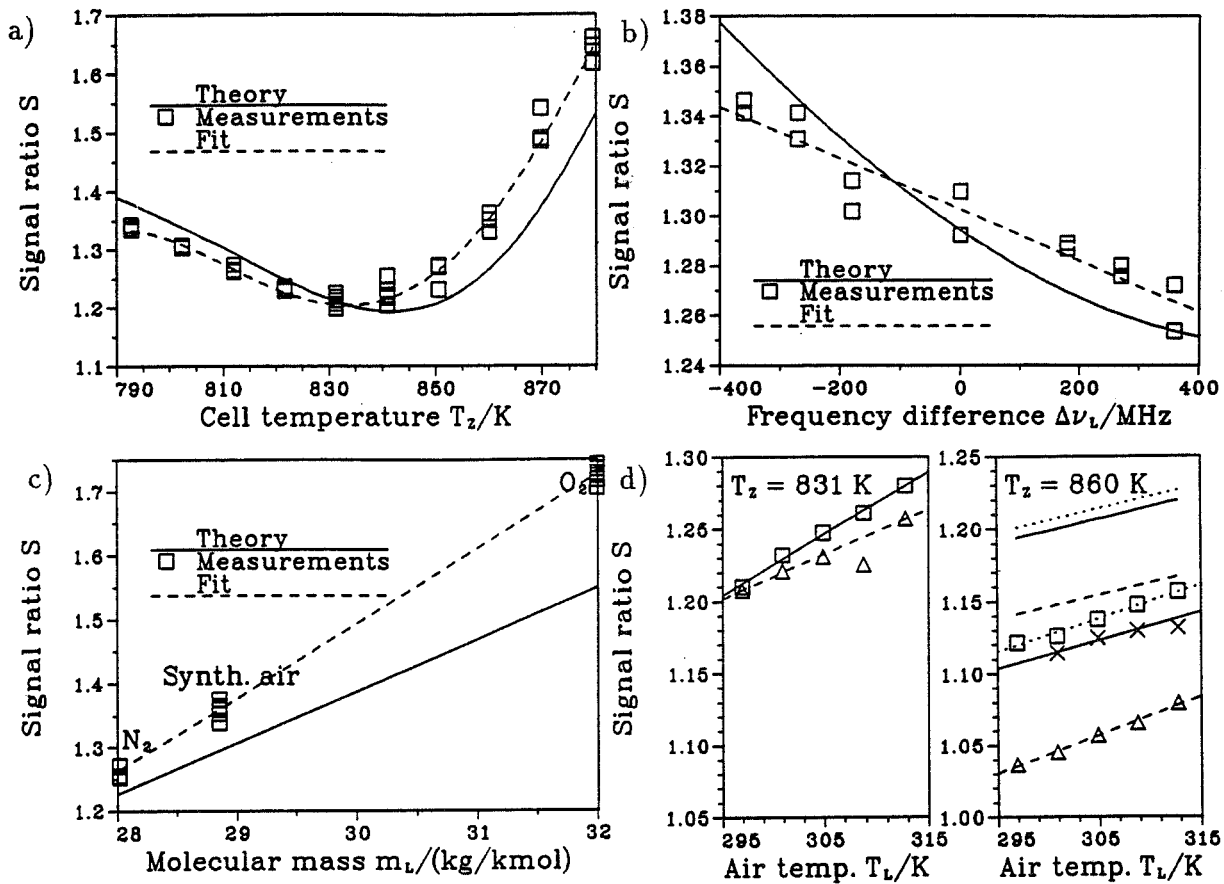


Fig. 1. Signal ratio S as a function of several parameters.

- a) S as a function of cell temperature T_z . Measurements over 300 s (squares), fitted with a polynome of 4th degree (dashed line), and theory (solid line).
- b) S as a function of the frequency difference $\Delta\nu_L$ between laser emission and filter absorption line center. Measurements over 300 s (squares), linear regression (dashed line), and theory (solid line).
- c) S as a function of molecular mass m_L of an N_2 - O_2 gas mixture. Measurements over 300 s (squares), linear regression (dashed line), and theory (solid line).
- d) S as a function of air temperature T_L for cell temperatures of 831 and 860 K. Measurements on different days (squares, triangles and crosses) as mean values of 3 single measurements over 300 s each, with linear regression (dashed, dotted and solid lines), and theory (dashed, dotted and solid lines without measuring points).

Extrapolation to Lidar

Because of the quite good agreement between measurements and theory, results of calculations were used for a rough estimation of the behavior of a HSRL for the troposphere. The results show that the effect of cell temperature variations can be made negligible. Longitudinal wind and variations in water vapor content are the largest error sources. An accuracy of 1 K may under certain conditions be hard to attain. The suppression of particle-scattered radiation is limited by the rejection of spontaneous resonance fluorescence. Spectral suppression of Raman-scattered radiation is advantageous. Care should be taken to avoid frequency and polarization variations of the transmitter as well as sensitivity drifts in the two detection channels.

References

1. H. Shimizu, and C. Y. She, "Atomic and Molecular Blocking Filters for High-Resolution Lidar," Eleventh International Laser Radar Conference, June 1982, NASA Conference Publication 2228, 117-119.
2. H. Shimizu, S. A. Lee, and C. Y. She, "High spectral resolution lidar system with atomic blocking filters for measuring atmospheric parameters," *Appl. Opt.* **22**, 1373-1381 (1983).
3. K. Noguchi, H. Shimizu, and C.-Y. She, "Optimization of the High Spectral Resolution Lidar for Measuring Atmospheric Temperature," *Oyo Buturi* **54**, 972-978 (1985).
4. H. Shimizu, K. Noguchi, and C.-Y. She, "Atmospheric temperature measurement by a high spectral resolution lidar," *Appl. Opt.* **25**, 1460-1466 (1986).
5. F. J. Lehmann, S. A. Lee, and C. Y. She, "Laboratory measurements of atmospheric temperature and backscatter ratio using high-spectral-resolution lidar technique," *Opt. Lett.* **11**, 563-565 (1986).
6. C. Y. She, R. J. Alvarez, H. Sun, H. Moosmüller, and D. A. Krueger, "High-Spectral-Resolution Lidar Technique For Backscatter And Atmospheric Temperature Profiling," 14th International Laser Radar Conference, June 20-24, 1988, Innichen-San Candido, Italy, Conference Abstracts, 339-342.
7. C. Y. She, R. J. Alvarez, L. M. Cardwell, D. A. Krueger, "High-Spectral-Resolution Rayleigh-Mie Lidar Measurements of Vertical Tropospheric Temperature and Aerosol Extinction Coefficient Profiles," Conference on Optical Remote Sensing of the Atmosphere, November 18-21, 1991, Williamsburg, Virginia, USA, Addendum and Post-deadline Papers, PD 2-1/PD 2-3.
8. E. Voss, "Untersuchungen zur Temperaturfernmessung durch Analyse der Rayleigh-Streuung mit Atomdampffiltern," Doctoral Thesis, University Hamburg, 1992, 197 p.

HgCdTe PHOTOMIXERS FOR CO₂ LASER RADAR SYSTEMS

Peter R. Bratt

Santa Barbara Research Center
A Subsidiary of Hughes Aircraft Company
Goleta, California

INTRODUCTION

The Santa Barbara Research Center has developed a variety of high speed HgCdTe photodetectors for use in CO₂ laser radar systems. These detectors have outstanding performance and can be made available in production quantities. Many of them have been employed in a variety of systems applications over the past ten years. In this paper, we briefly describe the detector technology, summarize the state-of-the-art, and indicate some practical applications.

DETECTOR TECHNOLOGY

In response to various system operating requirements, three different detector technologies have been developed. Table 1 lists these technologies, the necessary operating temperature, achievable bandwidth, and range of sensitivities attainable. The photoconductive (PC) mode of operation has been found to work best when higher operating temperatures are required, specifically, those that can be achieved with thermoelectric cooling (190-200K). PC HgCdTe detectors for CO₂ wavelengths can also be made to work at 300K but with greatly reduced sensitivity. HgCdTe photodiodes (PD) are used when the very best sensitivity is required, but these must be operated at 77K. A p-i-n type HgCdTe drift photodiode is employed where very high bandwidth is required (>1 GHz).

Table 1. High Speed HgCdTe Detector Technologies for 10.6 μ m System Applications

	PHOTO- CONDUCTOR	PHOTO- DIODE	PHOTO- DIODE
Maximum Frequency	200-300 MHz	300-400 MHz	2-4 GHz
Operating Temperature	195K	77K	77K
Heterodyne NEP	1-4x10 ⁻¹⁹ W/Hz	3-4x10 ⁻²⁰ W/Hz	4-5x10 ⁻²⁰ W/Hz
Heterodyne Q E	5-15 %	50-65 %	35-50 %
Structure	pc	p-n Heterojunction	p ⁺ -n-n ⁺ (simulates p-i-n)

Figures 1 to 3 show diagrams to illustrate the structural details for each detector technology. The PC HgCdTe detector, shown in Figure 1, is a thin layer of p-type HgCdTe (typically 5 μ m thick) epoxy bonded to a sapphire substrate. Evaporated metals form ohmic contacts to the HgCdTe material and provide bonding points for lead attachment. An evaporated metal layer placed underneath the sensitive area (but insulated from the HgCdTe) provides a reflecting surface which redirects IR radiation not absorbed in the first pass back through the HgCdTe for a second pass. This feature allows use of a thin HgCdTe layer to increase device resistance and lower bias power while still maintaining high quantum efficiency. An antireflection coating (ARC) on top of the HgCdTe additionally enhances quantum efficiency by minimizing the surface reflectance.

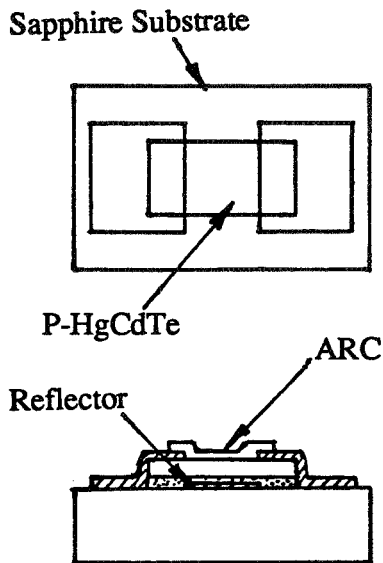


Figure 1. Photoconductor Structure.

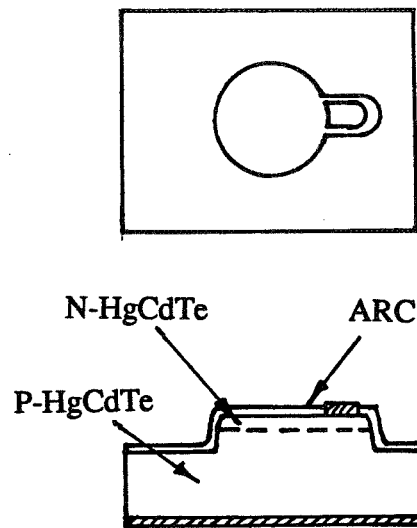


Figure 2. Photodiode Structure.

The PD HgCdTe detector shown in Figure 2 is a heterojunction device made by epitaxially growing a $2\mu\text{m}$ thick layer of n-type $\text{Hg}_{1-y}\text{Cd}_y\text{Te}$ onto a p-type $\text{Hg}_{1-x}\text{Cd}_x\text{Te}$ substrate wafer. The alloy composition factor (y) of the n-layer is typically 0.35 while the composition factor (x) of the p-substrate is 0.21. This makes the n-layer transparent to IR wavelengths beyond $3\mu\text{m}$. Thus incoming $10.6\mu\text{m}$ radiation is absorbed only in the p-material very close to the p-n junction where photogenerated electrons can be quickly and efficiently collected. The photodiode has a mesa structure formed by standard photetching techniques. Metals for electrical contacts are vapor deposited on the p- and n- HgCdTe as shown. An AR coating over the top of the mesa minimizes front surface reflectance. This coating, coupled with the heterojunction design, provides very high quantum efficiency, on the order of 90%.

Figure 3 shows the p-i-n drift PD structure employed to get bandwidths of 2 to 4 GHz. We simulate the textbook p-i-n device with an $n^+n^-p^+$ structure where $n=1 \times 10^{14} \text{ cm}^{-3}$ which is near intrinsic for HgCdTe at 77K. The n-layer thickness is 4 to $5\mu\text{m}$. With reverse bias voltage applied, a very high electric field strength is established within this region. Absorption of IR photons creates electron-hole pairs which are rapidly swept out to the p^+ and n^+ regions. This produces the rapid electrical response time necessary to achieve GHz bandwidths. Note that our design is a backside illuminated structure with incident radiation entering the HgCdTe material opposite the p^+n^- junction. This novel design approach offers several advantages: (1) no obscuration of the sensitive area by contact metals; (2) the p^+ -side contact metal acts as a reflector to redirect radiation back through the absorbing region, enhancing quantum efficiency; (3) low

PERFORMANCE

Figure 3 shows the present state-of-the-art performance versus frequency for the various detector types. For consistency, all data shown is for a detector having sensitive area of $1 \times 10^{-4} \text{ cm}^2$. With photodiodes the p-n junction capacitance influences bandwidth; devices with larger sensitive area will have higher capacitance and less bandwidth. In photoconductors the bandwidth is controlled by p-type Hg vacancy defects in the HgCdTe material and is not limited by device capacitance so larger devices do not suffer in bandwidth. Other factors such as bias power heating effects and material non-uniformities control the practical size limitations of a photoconductor.

APPLICATIONS

For system applications HgCdTe photomixers have been fabricated in various configurations. Single element PC HgCdTe detectors have been made in sizes from $50 \times 50 \mu\text{m}$ to $1 \times 1 \text{ mm}$. We have also made linear arrays up to 10 elements long as well as 2×2 quadrantal arrays. For operation at 190K, detectors are assembled on a 5- or 6-stage thermoelectric cooler in a permanently evacuated metal housing with suitable IR transmitting window. A dc power supply providing 1A at 5V will produce the 190K cold side operating temperature.

Single element PD HgCdTe detectors have been made from $100 \mu\text{m}$ square or round up to 1mm. Also, small linear arrays 5 to 10 elements in length have been made as well as 2×2 quadrantal arrays. The necessary

operating temperature of 77K or lower can be achieved either with LN_2 in a suitable dewar housing or with a mechanical refrigeration cryocooler. The LN_2 cooled dewar is popular for laboratory use while most detectors deployed in the field or in flight equipment use the cryocooler. Present day split Stirling type cryocoolers provide less than 5 minute cool down and continuous operation at a controlled temperature setting, typically around 70K. Cooler power required is 1A at 18V dc. Our Hughes split Stirling cooler configuration provides a detector assembly virtually free from EMI and microphonics noise.

To operate these detectors, a low voltage bias current source is required along with a suitable low noise amplifier. Our preferred approach is to provide to the customer a complete detector/cooler/amplifier assembly which has been specially designed to meet the system

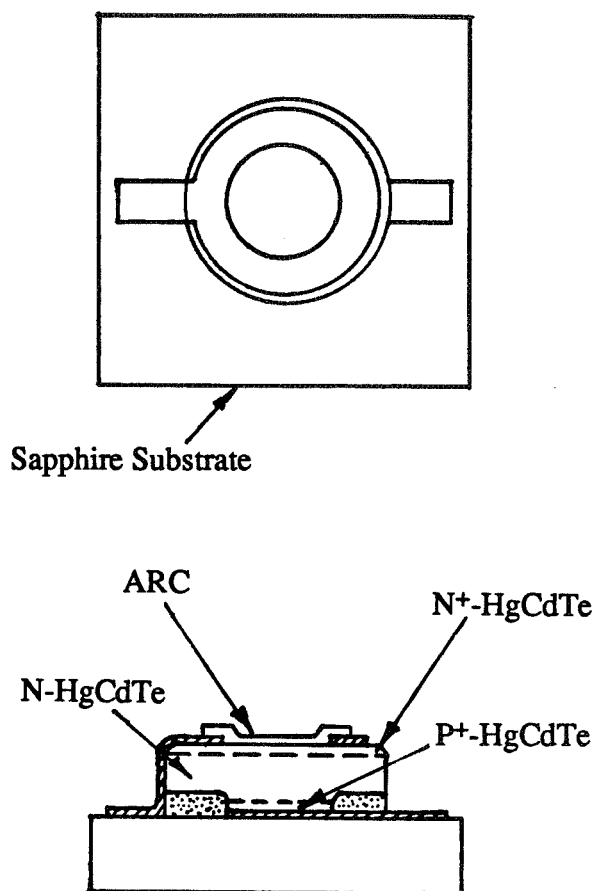


Figure 3. P-I-N Photodiode Structure.

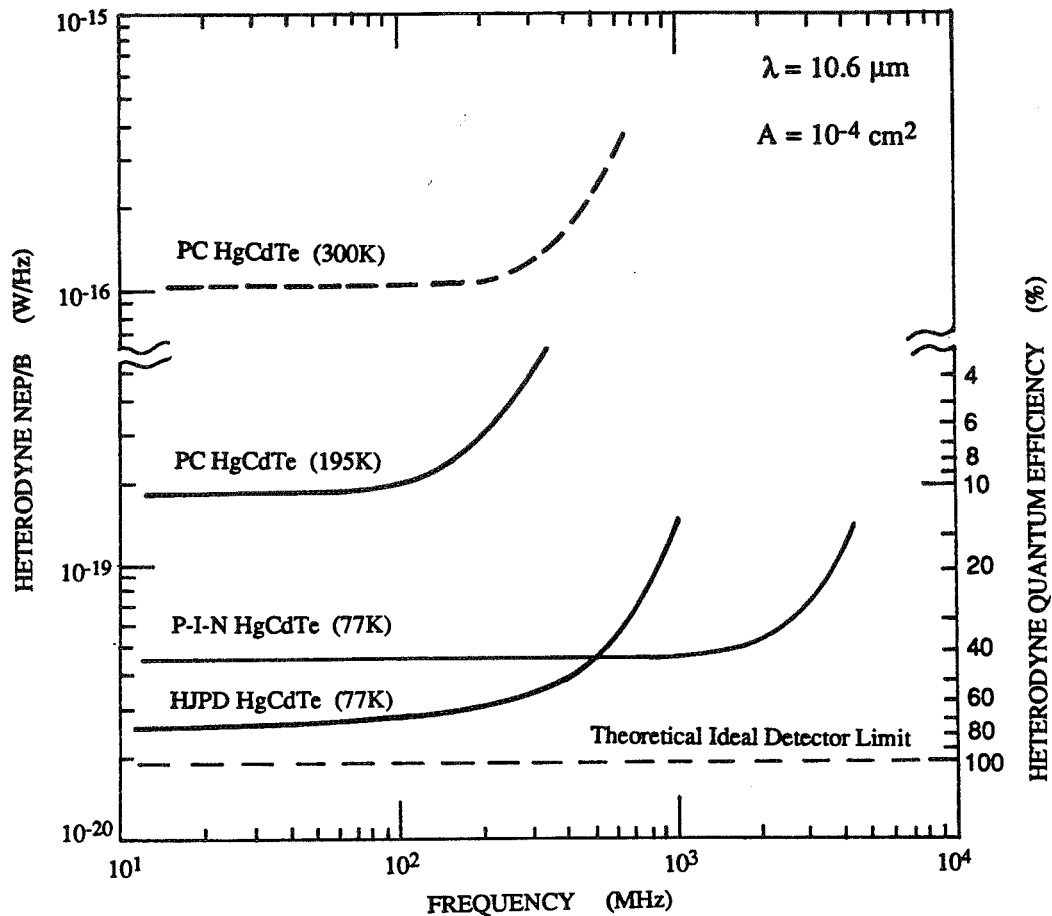


Figure 4. Heterodyne NEP versus Frequency for Various HgCdTe Photomixer Detectors. Operating Temperature Given in Parentheses.

requirements. This fully functional assembly can be thoroughly tested to verify performance specifications and then supplied ready to "plug in" to the customer's laser system.

In past work SBRC has supplied such detector/cooler/amplifier assemblies for a wide variety of laser system applications including: laser range finding; laser doppler velocimetry; pulse doppler imaging laser radar; laser heterodyne spectroscopy; laser threat warning; and DIAL chemical pollution detection.

AIRBORNE LIDAR MAPPING OF VERTICAL OZONE DISTRIBUTIONS IN SUPPORT OF THE 1990 CLEAN AIR ACT AMENDMENTS

Edward E. Uthe, Norman B. Nielsen, and John M. Livingston
Geoscience and Engineering Center, SRI International
333 Ravenswood Avenue, Menlo Park, California 94025

The 1990 Clean Air Act Amendments mandated attainment of the ozone standard established by the U.S. Environmental Protection Agency. Improved photochemical models validated by experimental data are needed to develop strategies for reducing near-surface ozone concentrations downwind of urban and industrial centers. For more than 10 years, lidar has been used on large aircraft to provide unique information on ozone distributions in the atmosphere (Browell et al., 1983). However, compact airborne lidar systems are needed for operation on small aircraft of the type typically used on regional air-quality investigations to collect data with which to develop and validate air-quality models.

Since 1979, SRI International has applied airborne lidar to air-quality studies using elastic scattering, fluorescent scattering, and differential absorption lidar (DIAL) systems operated from a relatively small Queen Air aircraft (Uthe, 1991). SRI recently developed an ultraviolet DIAL (UV-DIAL), suitable for installation on the Queen Air, using an excimer laser and stimulated Raman generation of energy at proper wavelengths for airborne tropospheric ozone measurement as suggested by Shibata et al. (1987). This approach is ideal for air-quality investigations,

because of the high spatial resolutions that can be obtained by the relatively high transmit energies and high pulse rates of excimer lasers. A Questek 2050 v β excimer laser operating with KrF (248.5-nm emission wavelength) was modified to operate on its side with beam exit directed vertically upward through an enclosed optical table attached to the laser, as shown in Figure 1. The beam is directed through a 1-m Raman cell containing H₂ gas and the Raman wavelength-converted energy is transmitted vertically downward from the aircraft. The DIAL receiver consists of a 14-inch telescope and two photomultiplier detectors; the wavelength response of each receiver channel is determined by dichroic and interference optical filters. The detectors are gated off for signal return at short ranges to prevent detector saturation. Signal output from each detector is input to 10-bit, 20-MHz (7.5-m range resolution) transient digitizers with internal memories used to average a number of backscatter returns

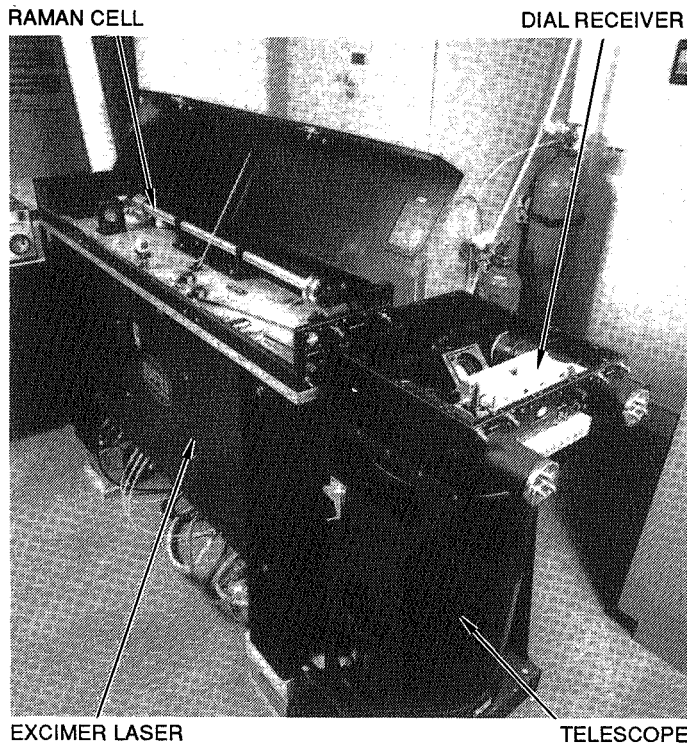


Figure 1 Compact Airborne Ozone DIAL
Transmitter/Receiver System

before the records are transferred to a MicroVax II computer to control data processing, display, and optical disk recording. Details of the UV-DIAL and aircraft installation are given by Nielsen et al. (1991).

The Lake Michigan Air Directors Consortium (the states of Illinois, Indiana, Michigan, and Wisconsin) is conducting a major measurement and modeling study of ozone concentrations over the Lake Michigan regional area. As part of the Lake Michigan Ozone Study, the airborne UV-DIAL was used to measure ozone concentrations across Lake Michigan with higher spatial and temporal resolution than could be obtained by the *in-situ* aircraft used on the program (Uthe et al., 1992).

Figure 2 is a contour analysis of ozone distributions derived from DIAL data collected on 18 July 1991 during the period 1708-1754 CDT as the DIAL aircraft was flown west-to-east along the southern part of the DIAL flight track (Figure 3). As shown by ozone concentrations greater than 80 ppb (the shaded areas of Figure 2), a large-scale ozone plume has developed over Lake Michigan with the highest concentrations (>110 ppb) at altitudes below 300 m. The position of the large-scale ozone plume is consistent with transport by southwesterly winds of effluents from the Chicago area. An interesting ozone minimum (50 ppb) is embedded within the large-scale ozone plume at an altitude of 650 m. The ozone minimum may result from subsidence of clean air aloft or from industrial plumes rich in reactive gases that destroy ozone. The high concentrations located just west of the ozone minimum suggest that the ozone minimum results from subsiding air with compensating high concentration (>100 ppb) air from lower altitudes penetrating above 500 m.

A contour analysis of ozone concentrations derived from data collected on 18 July 1991 (1810-1848 CDT) during the return east-to-west flight on the northern part of the DIAL flight track is presented in Figure 4. Relatively uniform ozone concentrations are observed west of the 87°W midlake location, with an elevated, 90-ppb ozone plume at an altitude above 500 m. The ozone concentrations east of 87°W are substantially greater than those west of 87°W. The ozone concentrations >80 ppb (shaded area) are probably part of the Chicago urban ozone plume identified by data collected along the southern flight leg (Figure 4), being consistent with the southwesterly winds. An ozone concentration minimum located at 86.5°W and 250 m altitude is embedded in the high ozone concentration urban plume resulting in complex ozone distributions with

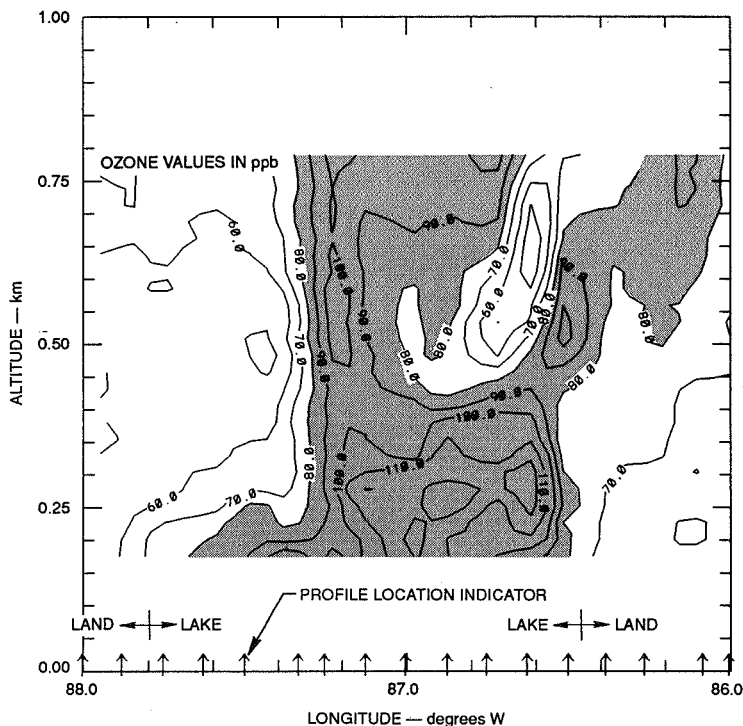


Figure 2 Contour Analysis of Ozone Distributions Derived from Airborne DIAL Observations Made on 18 July 1991, 1708 – 1754 CDT, During a West-to-East Flight Along the Southern Flight Track

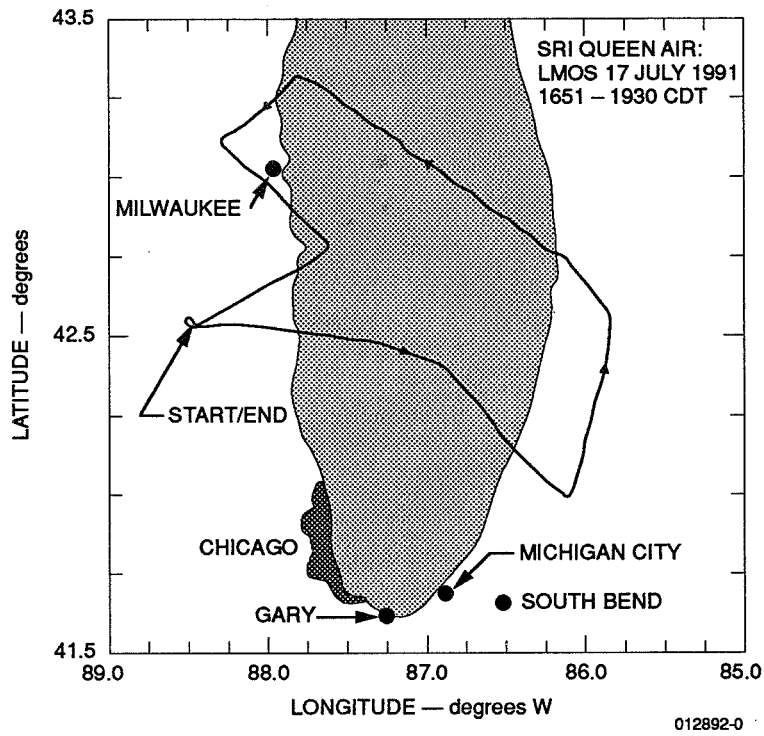


Figure 3 Typical Ozone DIAL Aircraft Flight Track Superimposed on Outline of Lake Michigan

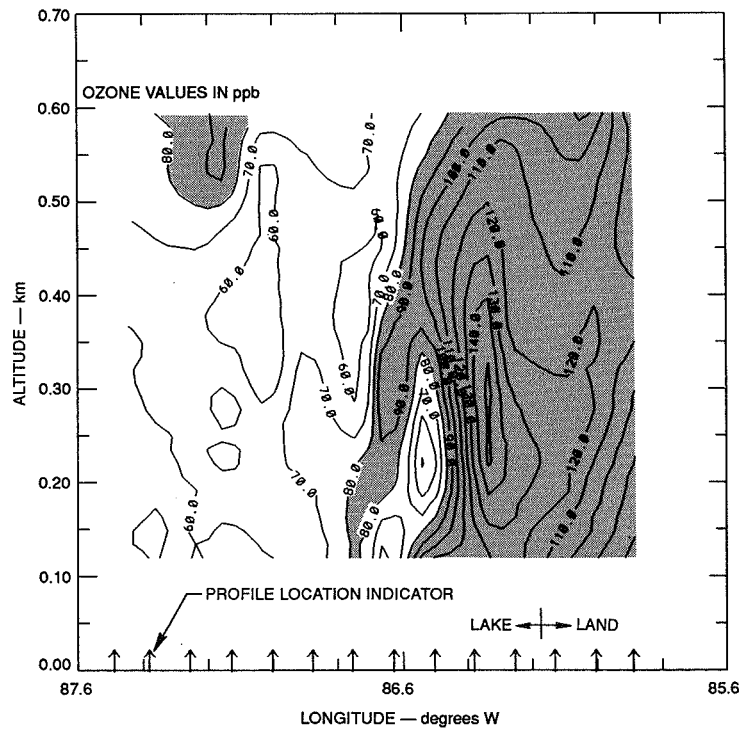


Figure 4 Contour Analysis of Ozone Distributions Derived from Airborne DIAL Observations Made on 18 July 1991, 1806 - 1848 CDT, During a East-to-West Flight Along the Northern Flight Track

concentrations ranging from 50 to 150 ppb over a relatively short distance. The ozone minimum is probably a result of an industrial plume of reactive gas destroying ozone. A search of the *in-situ* data records from one of the *in-situ* measurement aircraft confirmed that sharp ozone minima were associated with sharp NO_x maxima, indicating the effects of reactive gas plumes on ozone concentrations.

Other data examples—including a comparison of airborne DIAL and airborne *in-situ* ozone measurements—will be shown and discussed. Also discussed are future plans to improve the airborne UV-DIAL for ozone and other gas observations and the addition of an FTIR emission spectrometer to investigate the effects of other gas species on vertical ozone distributions.

REFERENCES

- Browell, E.V., A.F. Carter, S.T. Shipley, R.J. Allen, C.F. Butler, N.N. Mayo, J.H. Siviter, Jr., and W.M. Hall, 1983: "NASA Multipurpose Airborne DIAL System and Measurement of Ozone and Aerosol Profiles," *Appl. Opt.*, Vol. 22, No. 4, pp. 522-534.
- Nielsen, N.B., E.E. Uthe, J.M. Livingston, and E. Scribner, 1991: "Compact Airborne Lidar Mapping of Lower Atmospheric Ozone Distributions," *Proc. Int. Conf. Lasers 91* (Society for Optical and Quantum Electronics, McLean, Virginia).
- Shibata, T., T. Fukuda, T. Narikiyo, and M. Maeda, 1987: "Evaluation of the Solar-Blind Effect in Ultraviolet Ozone Lidar with Raman Lasers," *Appl. Opt.*, Vol. 26, No. 13, pp. 2604-2608.
- Uthe, E.E., 1991: "Elastic Scattering, Fluorescent Scattering, and Differential Absorption Airborne Lidar Observations of Atmospheric Tracers," *Opt. Eng.*, Vol. 30, No. 1, pp. 66-71.
- Uthe, E.E., J.M. Livingston, and N.B. Nielsen, 1992: "Airborne Lidar Mapping of Ozone Concentrations During the Lake Michigan Ozone Study," submitted to *Journal of the Air and Waste Management Association*.

ACKNOWLEDGMENTS

The work described here was sponsored by the Lake Michigan Air Directors Consortium. Conclusions relating to causes of the variations in ozone level are those of the authors and not necessarily those of the Lake Michigan Air Directors Consortium.

Measurements of Fugitive Hydrocarbon Emissions with a Tunable Infrared DIAL

M.J.T.Milton, P.T.Woods, B.W.Jolliffe, N.R.W.Swann and R.A.Robinson.

National Physical Laboratory,
Teddington,
Middlesex,
TW11 0LW, UK.

A tunable infrared DIAL system has been designed and developed at NPL which is capable of making measurements throughout the spectral region 3.0 to 4.2 μm . It is ideally suited to measuring a range of organic and inorganic species including methane, propane and butane. The system also has an ultraviolet channel that is capable of making simultaneous measurements of aromatic hydrocarbons such as toluene and benzene [1]. This paper describes the source and detection system, together with some measurements of fugitive hydrocarbon emissions performed at various petrochemical plant.

Source

There are two intrinsic disadvantages of operating a DIAL system in the infrared rather than the ultraviolet or visible spectral regions. These are that the aerosol backscatter coefficients are smaller and that the spectroscopy is significantly more complicated because of atmospheric interference caused by carbon dioxide and water vapour. These two problems, together with the comparatively poor performance of detectors in the infrared demand that an energy of at least 10 mJ per pulse is required to perform effective DIAL measurements. In addition, the complexity of the spectra of the light hydrocarbons ($<C_3$) and atmospheric gases in the 3.3 to 3.5 μm region imposes a maximum linewidth of 0.1 cm^{-1} and the necessity for the source to be continuously tunable.

The source in the NPL infrared DIAL system is based on a pulsed Q-switched Nd:YAG laser (Quantel International YG682) which is frequency doubled and used to pump a tunable dye laser (Quantel International TDL60). The dye laser is tunable over the region 785-851 nm with a linewidth of 0.1 cm^{-1} . The output from the dye laser is difference-frequency mixed with the Nd:YAG laser in lithium niobate to generate wavelengths in the region 3.0 to 4.2 μm [2]. This radiation is then amplified in a pulsed optical parametric amplifier which is also pumped by the Nd:YAG laser. The OPA also generates an idler that covers the wavelength region 1.4 to 1.7 μm . Figure 1 shows the energy available from the OPA at the signal and idler wavelengths as a function of the energy generated by from the difference-frequency mixing. The Nd:YAG laser has an injection-seeded linewidth of 0.002 cm^{-1} so the linewidth of the difference-frequency radiation is dominated by that of the dye laser. The source has a pulselength of 8 nsec and operates at a repetition rate of 10 Hz. The on- and off-resonant wavelengths are generated by switching the wavelength of the dye laser between shots. The phase-matched angles of the subsequent non-linear optical stages are switched in synchronism.

Detection System

The scattered light is collected with a 0.5 m diameter Dall-Kirkham telescope which eventually focuses the light onto a 1 mm detector. The system has been designed to operate with InSb photovoltaic detectors cooled to 77K. The exact detector used depends upon a trade off between the response time and the sensitivity required. Typical measurements are performed with a 1 mm detector with an NEP of 3.5×10^{-12} W/ $\sqrt{\text{Hz}}$ and a bandwidth of 3.1 MHz.

Measurements

The effective range of the system is strongly dependant on atmospheric conditions. Under conditions of low aerosol density, the backscatter is very weak and the range is less than 500 m. In conditions of higher backscatter, such as haze or sea mist, the range extends to greater than 1 km. High concentrations of strongly absorbing species (such as methane) can only be measured on very weak absorption lines.

Figure 2 is an example of the column content measured at a gas processing terminal. The measurement is the average of 1024 pulses and is presented here without any additional smoothing. The measured column shows two steps that correspond to point sources of methane. Between these steps the gradient of the column corresponds to the atmospheric background concentration of methane (1.7 ppm) with a small enhancement caused by fugitive emissions from the plant. The range-resolved concentration has been derived by differentiating and smoothing over 5 adjacent range bins. By recording the wind with an array of anemometers along the path of the DIAL measurement, the information from the column content can be used to estimate the total flux of methane.

Measurements of total fugitive losses from oil refineries, including those emitted by gasoline and crude storage facilities have also been carried out. These require careful calibration using gravimetrically-prepared gas samples in order to obtain accurate figures for the mass loss rate.

References

[1] M.J.T.Milton, P.T.Woods, B.W.Jolliffe, N.R.W.Swann and T.J.McIlveen, to be published Applied Physics B (1992).

[2] M.J.T.Milton, T.J.McIlveen, D.C.Hanna and P.T.Woods, Optics Communications 87 (1992) 273.

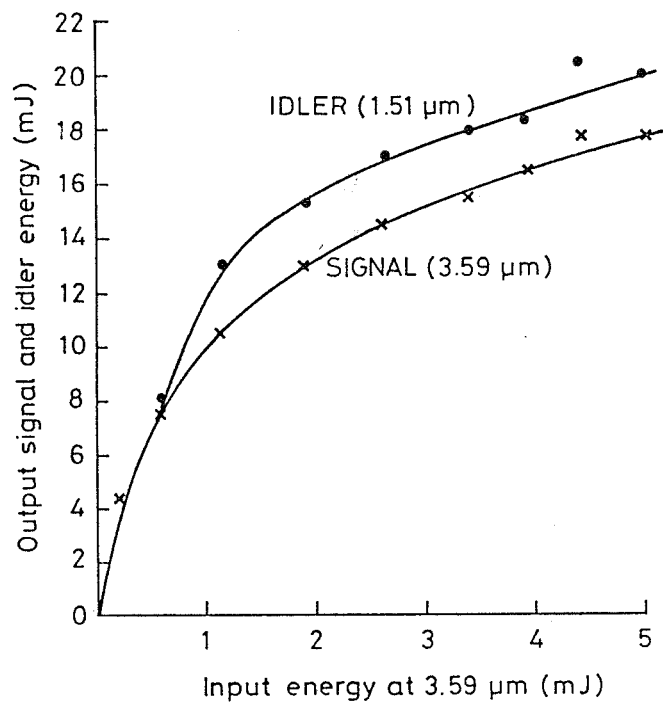


Figure 1 Energy generated at signal and idler wavelengths by optical parametric amplifier

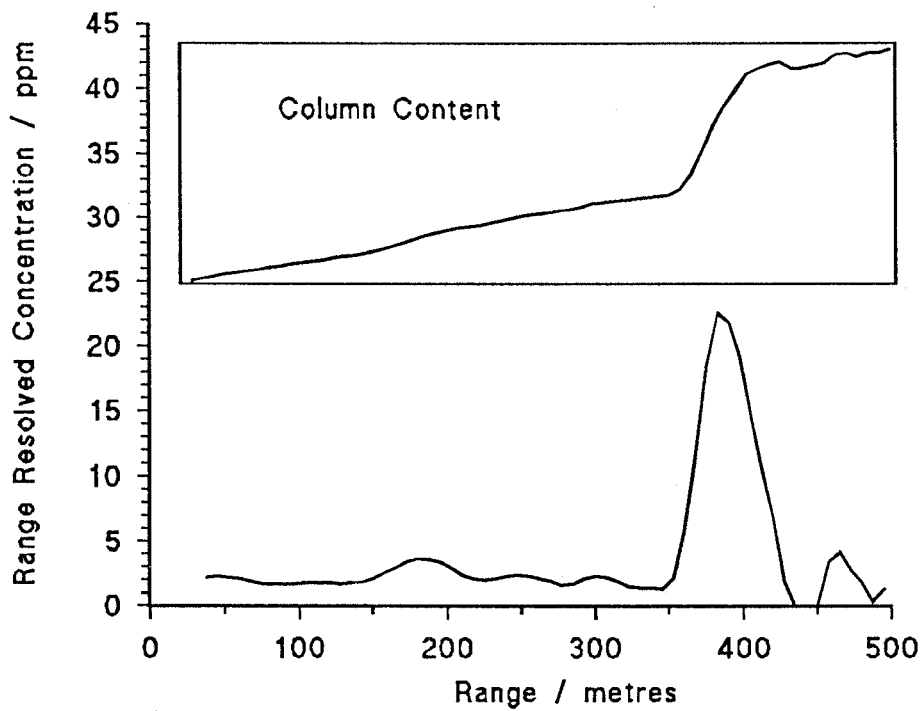


Figure 2 Range resolved measurements of methane

THE ENEA CO₂ LIDAR/DIAL STATION ACTIVITY
IN A TROPOSPHERIC REMOTE SENSING PROGRAM

R.Barbini, F.Colao, A.Palucci, S.Ribezzo.

ENEA, INN.SVIL, P.O. Box 65, 00044 Frascati (RM), ITALY

(Phone No. +39 6 94001)

ABSTRACT

The ENEA CO₂ Lidar/DIAL apparatus has become operational by detecting atmospheric components such as water vapour and ozone, with an useful range of $R \approx 6$ Km. Range resolved concentrations of the investigated molecules are presented together with a discussion upon the techniques adopted for the data analysis.

SUMMARY

A CO₂ Lidar system, designed to monitor minor gaseous components and pollutants in the troposphere, has been put into operation at the ENEA Centre of Frascati [1]. The ground based Lidar station, is composed by a 50 m² container allocating a couple of twin TEA CO₂ laser transmitters and electronics (fig.1) and by a 5 m high tower, dome covered, sustaining a rotateble Newtonian send-receive telescope (fig.2).

Unabsorbed backscattered signals (fig.3) span an useful range of ≈ 6 Km, which allows our system to investigate most part of the troposphere from ground. Range resolved profiles of water vapour and ozone have been obtained using the Differential Absorption Lidar (DIAL) technique and direct detection [2]. Some examples of the retrieved profiles are given in fig.4 and 5.

Ancillary meteorological parameters, as received via an ETHERNET link both from a local station and from remote installations (Ciampino and Pratica di Mare airports), have been stored during the Lidar measurements campaign for later use in the data reduction. A ballon-borne radio-sound is launched every six hours in Pratica di Mare, transmitting meteo and relative humidity data at different quotes up to 6 Km. These informations are now being processed for calibrating the vertical DIAL water vapour profiles.

Extinction coefficients for different laser lines have been obtained both from the backscattered lidar signals by

using Klett-like algorithms, and by running the high resolution computer code FASCOD2 fed with our local meteorological data in the frame of a rural mid-latitude-summer atmospheric model. Preliminary results show a fairly good agreement between the two sets of data, although some refinements are still needed both on lidar inversion techniques and on the use of simulation computer models.

Examples of horizontal and vertical profiles will be presented at the Conference together with a discussion upon the various techniques we adopted for DIAL data analysis and correction and for compressing the received signal dynamic range.

REFERENCES

- [1] - R.Barbini, F.Colao, A.Palucci, S.Ribezzo "Lidar/DIAL measurements of atmospheric components" Int. Conf. on Laser and Electro-Optics, April 1991, Baltimora (USA).
- [2] - R.Barbini, F.Colao, T.Hermsen, A.Palucci, S.Ribezzo "Atmospheric water vapour measurements with the ENEA Lidar station", ENEA Internal Report RT/INN/90/53. "Preliminary measurements of vertical Ozone profiles with the ENEA Lidar station", ENEA Internal Report RTI/INN /91/21.

ORIGINAL PAGE BLACK AND WHITE PHOTOGRAPH

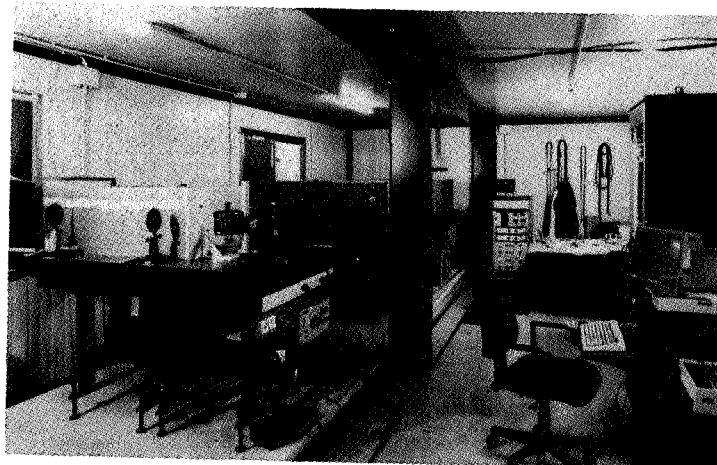


Fig. 1 - Internal view of the Lidar station. Laser transmitters, optics and electronics are in the forefront.

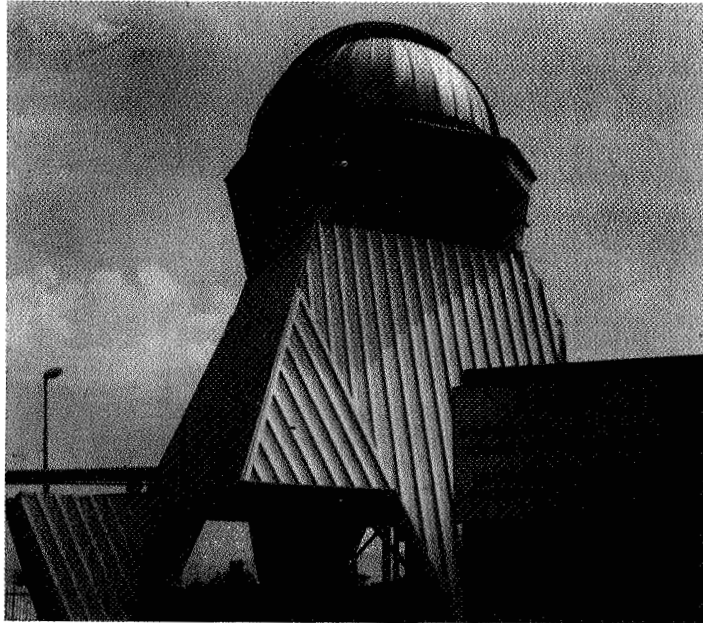


Fig. 2 - The dome covered tower sustaining the send-receive telescope.

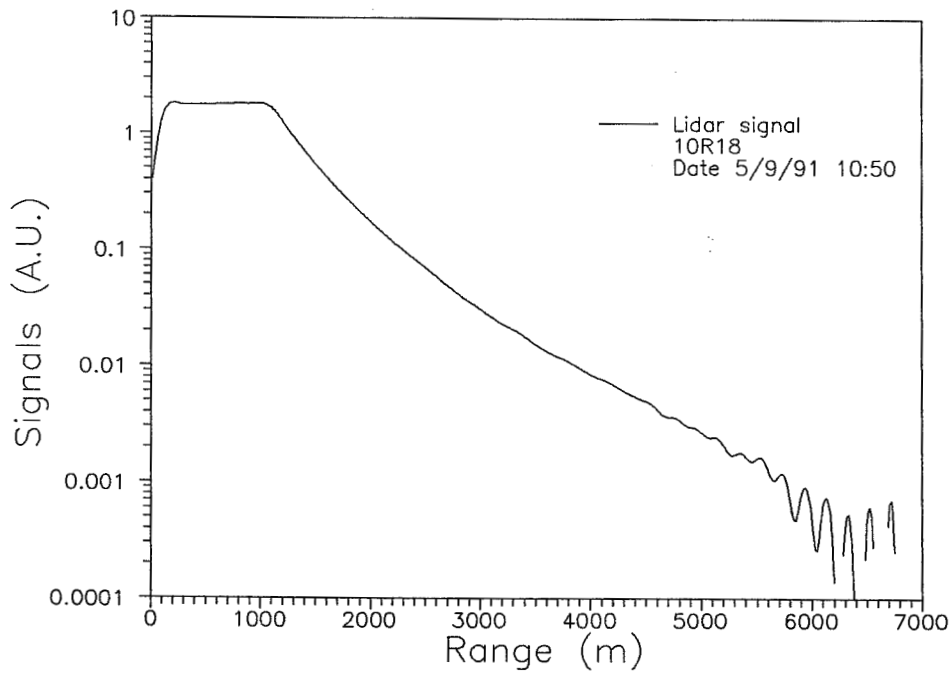


Fig. 3 - Horizontal range resolved lidar signal obtained using the 10R18 CO₂ laser line (not absorbed by water vapour) [Date 5/9/91 Time 10:50].

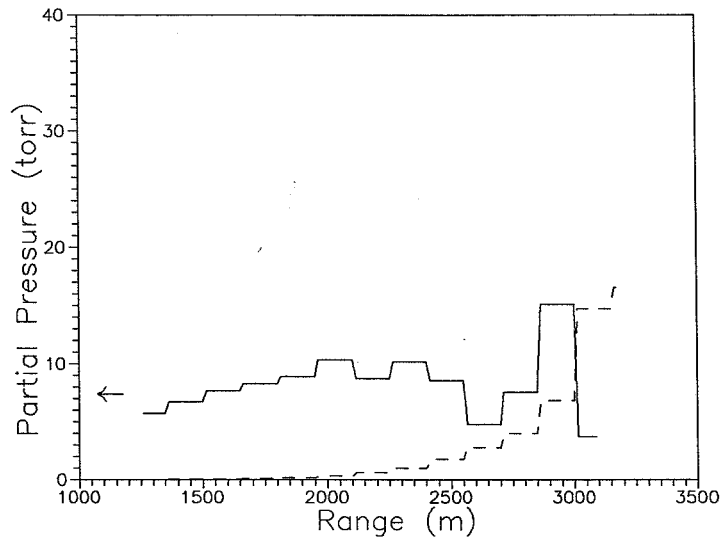


Fig. 4 - Dial horizontal water vapour concentration (solid line) and calculated standard deviation (dashed line) vs. range. Transmitted lines: 10R20 (on) and 10R18 (off); differential absorption coeff. $\Delta\alpha = 1.05E-4 \text{ m}^{-1} \text{ torr}^{-1}$; integration range = 150 m. Arrow indicates the ground concentration value as measured by a local hygrometer [Date 5/9/91 Time 10:50].

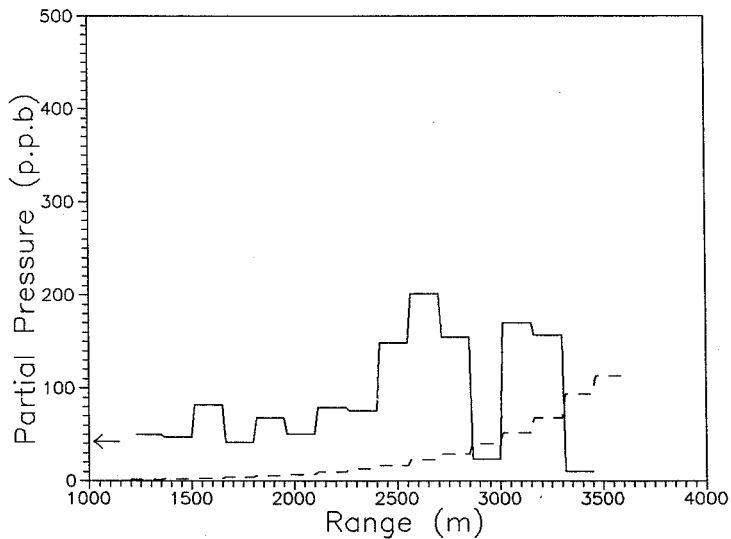


Fig. 5 - Dial horizontal ozone concentration (solid line) and calculated standard deviation (dashed line) vs. range. Transmitted lines: 9P14 (on) and 9P24 (off); differential absorption coeff. $\Delta\alpha = 1.17E-6 \text{ m}^{-1} \text{ ppb}^{-1}$; integration range = 150 m. Arrow indicates the ground concentration value as measured by a local ECC Philips UV photometer [Date 10/9/91 Time 11:25].

Lidar Observation of Marine Mixed Layer

Susumu Yamagishi, Hiroshi Yamanouchi, and Masayuki Tsuchiya

Ship Equipment and Marine Environment Division
Ship Research Institute, Ministry of Transport
6-38-1, Shinkawa, Mitaka, Tokyo, 181 JAPAN

1. Introduction

Marine mixed layer is known to play an important role in the transportation of pollution exiting ship-funnels. The application of a diffusion model is critically dependent upon a reliable estimate of lid. However, the processes that form lids are not well understood, though considerable progress toward marine boundary layer has been achieved.^(1,2)

This report describes observations of the marine mixed layer from the course Ise-wan to Nii-jima with the intention of gaining a better understanding of their structures by a shipboard lidar. The observations were made in summer of 1991. One interesting feature of the observations was that the multiple layers of aerosol, which is rarely numerically modeled, was encountered. No attempt is yet made to present a systematic analysis of all the data collected. Instead we focus on observations that seem to be directly relevant to the structure of mixed layer.

2. Observations

The lidar system is housed in a container with size of L4.7 x W2.2 x H2.3m. The laser is a 140mj YAG SHG laser with a 10 Hz repetition rate. Beam is transmitted into the atmosphere coaxially through the center of the receiver mirror. The returned signal from the 30 cm cassegrainian receiver telescope is coupled to the photomultiplier. The system is so designed that the intensity of the background illumination is obtained after each returned signal and the saturation of the photomultiplier is avoided by reducing the gain during start up period. Data acquisition is done by a transient digitizer coupled to a CAMAC data bus operated through a personal computer. The measurements were performed with the spacial resolution of 6m. Real time processing of A scope was attempted and other treatments were carried out separately by EWS system. Scanning was accomplished by stepping the azimuth and the elevation angle of the receiver mirror. The rolling and pitching motions of the ship were corrected according to the digital memory of 2-axis gyroscope.

3. Data Processing

The operation can be described by the following general lidar equation:

$$P(R) = \frac{C \cdot P_0 \cdot \beta(R) \cdot T^2(R)}{R^2} + P_b \dots \dots \dots (1)$$

where $P(R)$ is the power incident on the optical receiver due to the atmospheric backscattering of the laser pulse P_0 , from a distance R , $\beta(R)$ is the volume backscattering coefficient, $T^2(R)$ is the two-way transmissivity from the lidar to the scattering volume. C is the constant of the system, P_b is the power of the background illumination.

After arranged Eq.(1), we define the quantity, $f(R)$ used in the following discussion

$$f(R) = \{P(R) - P_b\} \cdot R^2 = C \cdot P_0 \cdot \beta(R) \cdot T^2(R) \dots \dots \dots (2)$$

The authors have set the $T(R)$ term equal to one. Since the atmospheric visibility in all cases during the study was greater than 30km, this assumption seems reasonable.⁽³⁾ So the $f(R)$ is directly depend on $\beta(R)$ which mostly depend on aerosol backscattering in the mixed layer.

Assuming that the aerosol size distribution is not greatly changed in the mixed layer, $f(R)$ shows the concentration of the aerosol. For looking out the faint structural changes of the mixed layer, it may be better to watch the gradient of $f(R)$. (Fig.1) Here the normalized concentration gradients, $NCG(R)$ is defined as:⁽⁴⁾

$$NCG(R) = \frac{\{f(R - \frac{\Delta R}{2}) - f(R + \frac{\Delta R}{2})\}}{f(R) \cdot \Delta R} \times 100 \left(\frac{\%}{100m} \right) \dots \dots \dots (3)$$

where ΔR is an interval. The minimum interval is a twice of spacial resolution of the lidar.

4. Results and Discussion

The ship weighed anchor Ise-wan at 8:00 and went ahead Nii-jima. During the cruise, the weather was fine, and the wind of about 16m/sec was blowing from the west. The maximum rolling angle was 3 degrees. In the evening the ship reached Nii-jima, the wind went down. During a typical lidar measurement, meteorological data were obtained from the ship.

The vertical observations of lidar were conducted every half hour with cloud free conditions. Data were the average of 600 corrected returned signals. Figure 2 shows the development of $NCG(R)$ processed according to Eq.(3). The NCG value of 100%/100m corresponds to the abscissa of one hour in the right direction in the figure. The hatched zone indicates the start-up periods where the gain of the photomultiplier has been reduced. We picked up major peaks from each observation and traced by lines. Three discontinuities indicated by "A", "B", and "C" are appeared. "A" is the primary discontinuity at Ise-wan, whose height is about 1.6km. This discontinuity corresponds to the discontinuity of water vapor measured by the rawinsonde at Shiono misaki, the nearest Weather Station. This discontinuity seems to be the top of mixed layer developed in the land, since it disappeared after the ship went out of the bay. "B" is the secondary discontinuity at Ise-wan but after out of the bay it become the primary one and exist during the observation. This seems to be the top of marine mixed layer, whose height is 700m to 900m. When evening came, the other discontinuity, "C" appeared under "B". From the

meteorological data ,Fig.3 it is supposed that the atmospheric temperature goes down and becomes lower than the water temperature, the vaporization becomes buoyantly. "C" seems to be the top of this convective layer.

Vertical scanning operations were performed several times. During the cruise, no significant discontinuity was obtained under above mentioned discontinuities. But in the evening very clear discontinuity of about 170m in depth was observed near the surface, this may be the surface layer which refers to the layer that is well mixed by surface buoyancy and shear.

5. Summary

Observations of marine mixed layer in the east coast of Japan were made by the shipboard lidar in the summer of 1991. Examples are shown of how developing the discontinuities in the marine mixed layer by tracing normalized concentration gradients. Some method will have to be found to describe the structure of the marine mixed layer and to improve the accuracy of the lid altitude.

Acknowledgment: This work was supported by SHIP & OCEAN FOUNDATION. The authors also thank Institute for Sea Training for the cooperation.

References:

- (1) Deardorff, J.W., and Peterson, E.W., 1980, J. Atmos. Sci., 37, 1405
- (2) Chang, S.S. and Prahm, Tr., R.R., 1991, J. Atmos. Sci., 48, 2265
- (3) Hoff, R.M. and Froude, F.A., 1978, Atmos. Envi., 13, 35
- (4) Sasano, Y, Shimizu, H. and Takeuchi, H., 1982, Appl. Opt., 21, 3166

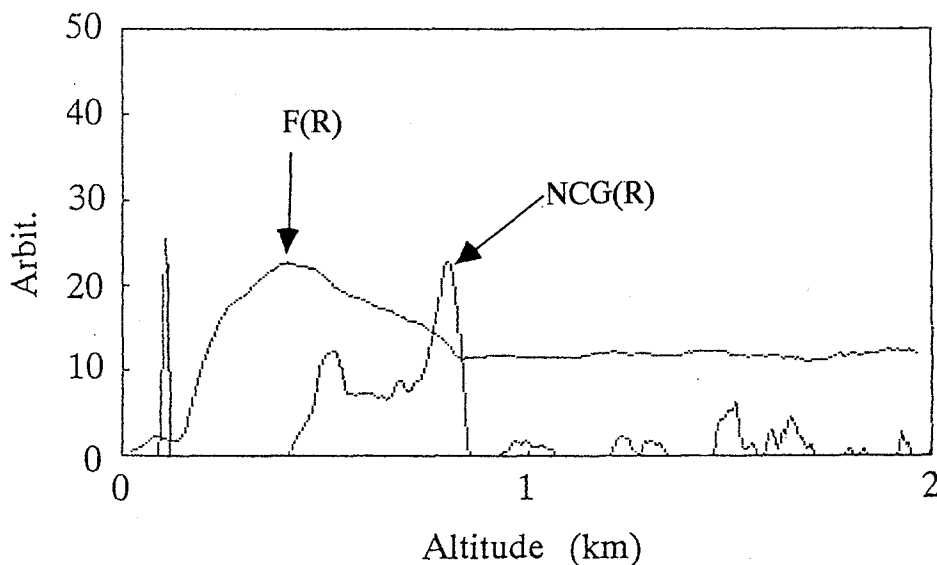


Fig. 1 Example of the vertical profile of aerosol.
from Ise-wan to Nii-jima, 1991 Aug. 8 ,14:00

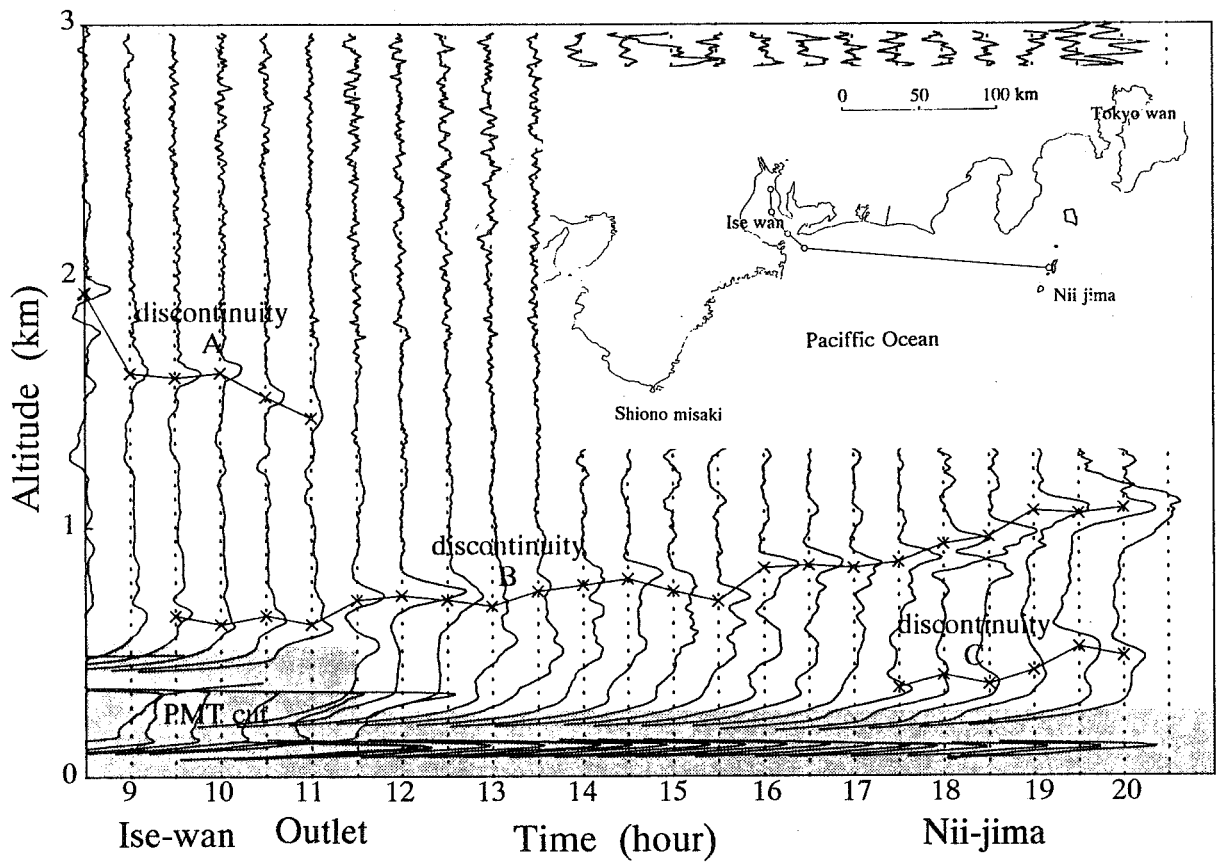


Fig. 2 Development of discontinuity in marine mixed layer.
 Profiles show the normalized concentration gradient.
 from Ise-wan to Nii-jima, 1991 Aug. 8

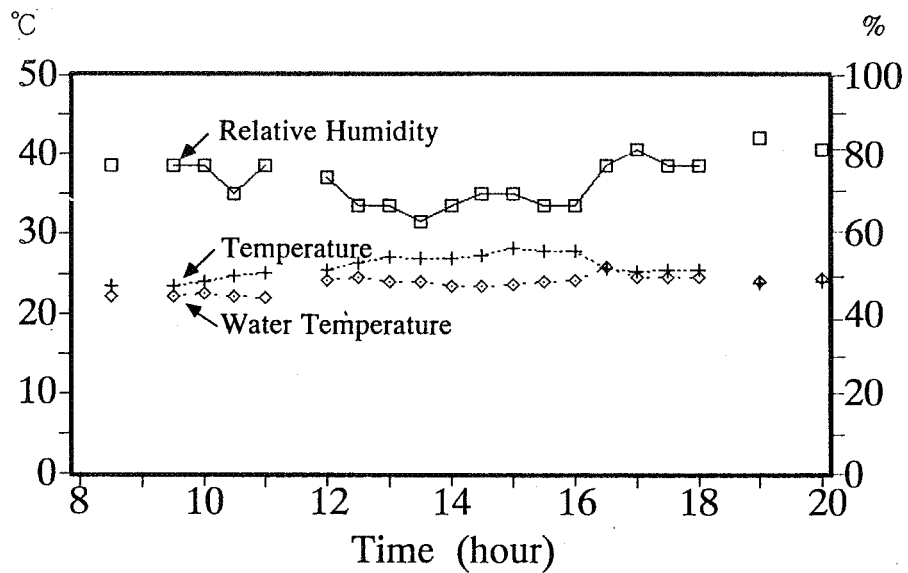


Fig. 3 Meteorological data measured on the ship.

AEROSOL EXTINCTION MEASUREMENTS WITH CO₂-LIDAR

Arne Hågård and Rolf Persson
National Defence Research Establishment
Dep. of Information Technology
P.O.Box 1165, S-58111 Linköping , Sweden

With the aim to develop a model for IR-extinction due to aerosols in slant paths in the lower atmosphere we perform measurements with a CO₂-lidar. Earlier measurements with a transmissometer along horizontal paths have been used to develop relations between aerosol extinction and meteorological parameters. Ref. Nilsson (1986). With the lidar measurements we hope to develop corresponding relations for altitude profiles of the aerosol extinction in the IR. An important application is prediction of detection range for IR-imaging systems.

The basic parts of the lidar system is a TEA CO₂-laser and an incoherent receiver with a nitrogen cooled CdHgTe-detector. The laser pulse energy is 200 mJ, the pulse length is 170 ns plus a tail (< 1μs), the beam divergence is < 1 mrad and the rep. rate is max 150 Hz. Normally the P20 line with the wavelength 10.6 μm is used. The receiver aperture diameter is 30 cm. For processing of the detector signal it is fed through a linear amplifier and digitized to 8 bit words at 100 Mhz. To improve the signal to noise ratio and increase the dynamic range, more than 100 single pulse returns are added before further processing.

In order to determine the extinction profile we perform lidar measurements in three directions. One measurement is done with the lidar pointed horizontally against a target, which is a fiber net. The atmospheric return and the target return together is used to calculate a ground value of the extinction coefficient α . Another measurement is done in a path with high elevation to obtain an estimate of the α -profile. Calculation is done by forward inversion using the ground α as boundary value. Finally a measurement is done along a slant path with lower elevation. The extinction profile along that path is calculated by backward (Klett) inversion with a far end boundary value, which is obtained from the estimated profile above assuming horizontal homogeneity. The reason for this procedure is to reduce the error due to the boundary value. A constant backscattering / extinction ratio β/α is used so far. If a nonlinear relation can be established by measurements in the future, the accuracy may be improved.

For the inversion of a lidar return we correct for geometrical factors (the system function) and for water vapour absorption to get the normalized return $Q(r)$. The extinction coefficient $\alpha(r)$ is then computed by the Klett method as

$$\alpha(r) = \alpha_m q(r) / (1 + 2\alpha_m \int_r^{r_m} q(x) dx)$$

where $q(r) = Q(r)/Q(r_m)$; $\alpha_m = \alpha(r_m)$ is the boundary value at range r_m .

The TEA laser pulse has a long tail, which causes distortion of the return signal as compared to the ideal return from a δ -pulse. This has been discussed by Zhao and Hardesty (1988). We have so far only accounted for the pulse width by shifting the range scale. Our intention is to correct for the distortion in future measurements.

Examples of obtained results are shown in the figures below. Figure 1 shows the return P from a path with 0.8° elevation when the visibility was 9 km. The lidar system function P_0 or a return from a homogeneous path with low extinction is also shown. The ratio $Q = P/P_0$ is the normalized return and α the extinction coefficient. The target return which was used to determine α at the ground is not shown. Figure 2 shows calculated α -profiles for three paths with different elevation angles Θ , including the 0.8° -profile from figure 1. In this case the 25° -profile is used to get the altitude profile. The elevation was limited by site conditions. The 5° - profile was calculated by backward inversion. An indication of the validity of our method is that we obtain nearly the start value of α at range 0.

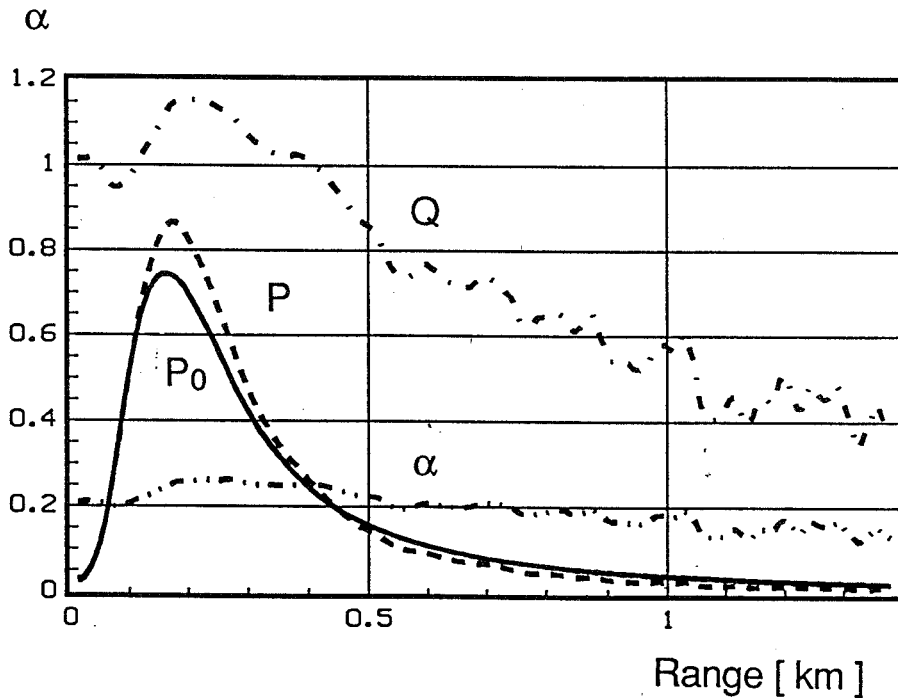


Figure 1. Lidar returns P, P_0 , Q and ext. coeff. α . Visibility 9 km, elevation 0.8° .

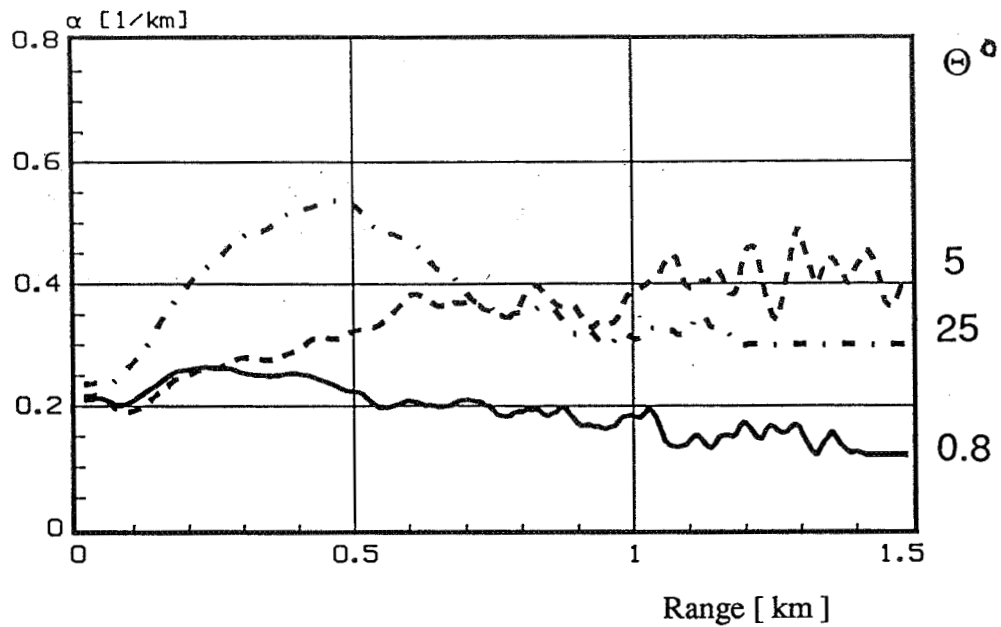


Figure 2. Extinction profiles for three elevation angles θ .

By further measurements we intend to relate parameters of the extinction coefficient profile to weather parameters.

References.

B. Nilsson FOA report C 30396 - E1, E3, April 1986.

Y. Zhao and M. Hardesty; Appl. Opt. Vol. 27, No13, 1 July 1988, p. 2719.

Dense Fog on the Highway Visual Range Monitoring in Cars?

W. Hahn¹, W. Krichbaumer², J. Streicher², and Ch. Werner²

¹: BMW - AG, EW-13, Petuelring, D - 8000 München-40
P.O.Box 40 02 40

²: German Aerospace Research Establishment (DLR),
Institute of Optoelectronics, D - 8031 Oberpfaffenhofen
Federal Republic of Germany

Every year between fall and spring fog endangers the traffic on highways; serious accidents occur with a lot of cars involved. Government authorities regulate speed limits in relation to visibility, but nobody can determine the local visibility exactly.

A similar situation is well known from airport operation. Fog drastically reduces the landing capacity of the airports. Visibility at airports is measured continuously with transmissometers. A new sensor to get the slant visual range for the pilot is being introduced now at Hamburg airport. The basic element of this device is a modified laser cloud ceilometer (Impulsphysik).

It has been the intention of the authors to transfer the knowledge on the slant range visibility sensor to the highway situation. There are two approaches possible:

- 1) installation of visibility sensors on highways, which is already done at a few places;
- 2) installation in cars for control by the driver himself.

This paper reports on the development of a new sensor. Laser range-finders are currently installed in cars and trucks to measure the distance to a proceeding car (LEICA). A modification of such a sensor to measure visibility was made. A few problems had to be solved:

- 1) choice of wavelength with relation to the human eye for visibility measurements,
- 2) dependency of the wavelength on atmospheric turbidity,
- 3) laser eye-safety,
- 4) influence of multiple scattering at visibilities smaller than 200 m.

The wavelength used for the lidar sensor in the near infrared presents no real problem because the object to be sensed is fog appearing white which means that scattering from fog is wavelength-independent.

There are differences in the backscatter-to-extinction ratio for different fog situations. Advective fog and radiation fog are two different fog classes where simple backscatter sensors give different visual ranges, although the same visibility is measured by a transmissometer. It is also possible that other weather conditions (fog containing ice particles, snow etc.) may occur. The sensor must distinguish between

these situations first. Polarisation sensitivity is one solution, multiple scattering is the other.

The sensor is applied to small visibilities below 100 meters, where

- a) the signal is large and the eye-safety problem can be solved, and
- b) multiple scattering is dominant.

As known from airport operations of the laser ceilometer, one can use this multiple scattering contribution to determine the visibility.

Figure 1 shows a simulation of the sensor based on the DLR Lidar Simulation Programme (Werner et al. (1992); Streicher (1992)).

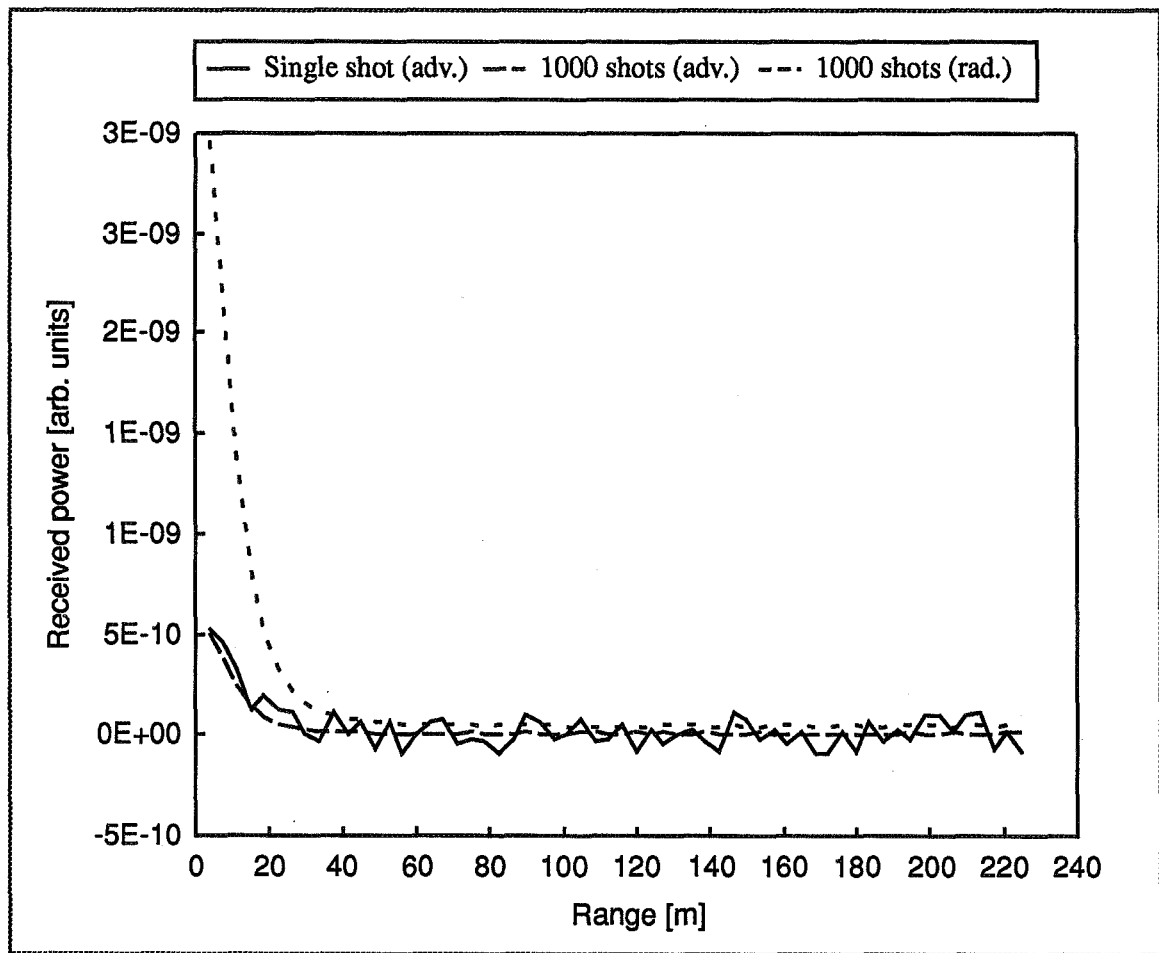


Fig. 1.: Simulated lidar signals for two fog situations with visibilities of 100 m

The solid curve shows a single shot with an eye-safe lidar system (output power about 0.8 μ J). The dashed curve is simulated under the same conditions as the solid one - advective fog with a homogeneous visibility of 100 m - but this time averaged over 1000 shots. The third plot (dotted) shows a lidar signal, again for 100 m visibility, but for radiative fog. A comparison of dotted curve and dashed curve shows that

it is only possible to estimate visibility from backscatter if additional information on the atmospheric condition (fog type) is available because of the variable backscatter-to-extinction ratios for different types of fog: As is well known since Koschmieder's times, visibility is governed by extinction, not by backscatter.

The required additional information on the fog under consideration may be given by a sophisticated analysis of higher orders of scattering, i.e. if the assumption of single scattering as a basis of the evaluation of data is dropped (it is obvious from the high optical depths in fog situations that this assumption is wrong anyway) and if the lidar equipment is suitably modified to enable separate measurement of multiple scattering.

Figure 2 clearly indicates that multiple scattering in this case is indeed an additional source of information if analyzed properly. The picture shows the result of a simulation using our stochastic model of multiple scattering (Krichbaumer and Oppel (1988); Oppel et al. (1989)). A monostatic coaxial lidar is assumed to measure in a fog atmosphere consisting of four homogeneous layers of different monodispersions of spherical particles ($x=20, 15, 10, 5$) but all with the same visibility (the same extinction). We have plotted the ratio double scattering signal/single scattering signal vs. distance from lidar. This ratio for each of these slabs is given approximately by (G is the field of view of the receiver; cf. Oppel et al.(1989), Ch. 7 and also Brusciaglioni et al. (1980))

$$\frac{\mu_2(r,\Gamma)}{\mu_1(r)} \approx A(\Gamma) \cdot \sigma$$

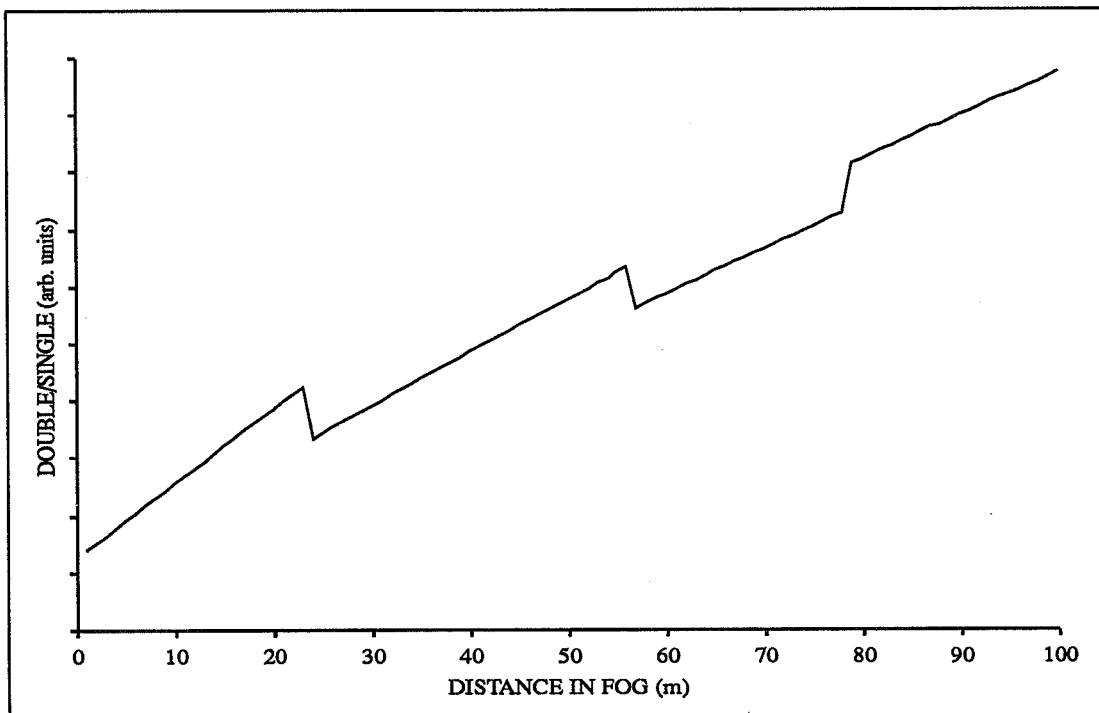


Fig.2.: Double scattering signal/single scattering signal vs. distance (simulated) from four homogeneous slabs of fog using different size distributions

Therefore we should get for each slab a piecewise linear function of range for all four slabs. This is confirmed by the simulation in Fig. 2. Therefore, if multiple scattering information can be extracted properly, then the extinction coefficient (the visibility) can be estimated from the slope of the line plus additional information although different types of fog are present.

The car-specific parts of the sensor and tests will be reported.

Literature:

Bruscaglioni, P.; G. Milloni; and G. Zaccanti (1980): On the contribution of multiple scattering to Lidar returns from homogeneous fogs and its dependence on the Lidar range and on the receiver angular aperture, *Opt. Acta* **27**, 1229-1242.

Krichbaumer, W.; Oppel, U.G. (1988): A general stochastic model for simulation and calculation of multiple LIDAR backscattering and some reconstructions of scattering distributions from double scattering return signals. Proc 14th ILRC, Innichen-San Candido, Italy, June 20-24, 1988.

Oppel, U.G.; A. Findling; W. Krichbaumer; S. Krieglmeier; M. Noormohammadian (1989): "A Stochastic Model for the Calculation of Multiply Scattered LIDAR Returns", DLR-Report DLR-FB 89-36.

Streicher, J. (1992): Simulation of a Lidar to improve Visibility in Dense Fogs, paper accepted for presentation at SPIE conference "Lidar for Remote Sensing", Berlin, June 24-26, 1992.

Werner, Ch.; J. Streicher; H. Herrmann; H.-G. Dahn (1992): Multiple Scattering Lidar Experiments, accepted for publication in *Opt. Eng.*

**KEY TO AUTHORS,
SESSION CHAIRS, AND
PAPERS**

- Abo, Makoto—A4, G5
 Abreu, Vincent J.—D34, I5
 Abshire, James B.—J5
 Adriani, Alberto—D4
 Aldridge, Richard L.—L4
 Alejandro, Steven.—I, I9, I11
 Alvarez, II, R. J.—D8, L10
 Amimoto, Sherwin—II2, L17
 Amzajerdian, Farzin—L31
- Ancellet, G.—B6, B10, D13
 Anderson, Kent—D15
 Angelova, M. D.—L42, L43
 Ansmann, Albert—A3, K3, L26
 Antill, Charles W.—D17
 Apituley, A.—B10
 Archuleta, F. L.—D28
 Arshinov, Yu. F.—D46
 Asai, Kazuhiro—L22
 Avramova, R. P.—D44
- Baker, Wayman E.—E1
 Banta, Robert M.—I2
 Barbini, R.—P3
 Barnes, John E.—D34, I5
 Baulin, E. V.—D48
 Bedo, Donald—E
 Beekmann, M.—B6
 Ben-David, Avishai—L28
 Benoist, Rodney—L31
 Bergwerff, J. B.—B10
 Bisson, S. E.—N1
 Bissonnette, Luc R.—K1, K5
 Blythe, Michael P.—D17
 Bobrovnikov, S. M.—D46
 Bonnier, D.—L30
 Borchardt, H.—L7
 Borghese, A.—D29
 Borra, E.—M4
 Bösenberg, J.—B10, L12
 Bowdle, David A.—C1
 Bowers, Mark S.—E3
 Bowman, Kenneth P.—F4
 Brackett, Vincent G.—B2
 Bratanov, B. M.—L42
 Bratt, Peter R.—O6
 Bristow, M. P.—D8
 Browell, Edward V.—B2, D14, F1, H6, N5
 Brown, M. J.—E5
 Bruneau, D.—L3
 Brusciaglioni, P.—L11
 Bundy, D. H.—D8
 Bunkin, A. F.—D43
 Burka, Michael—G11
 Butler, Carolyn F.—B2, D14, F1, N5
- Cacciani, M.—B9
 Caldwell, L. M.—L10
 Capbern, Alain—L32
 Cariou, Jean-Pierre—L23
 Carswell, Allan I.—A, B3, D6, D38, H2, L34
 Carter, A. F.—F1
 Centurioni, Sante—D4
- Chan, Kin Pui—O2
 Chang, John—D18
 Chanin, Marie-Lise—G, G12, G13
 Chazette, P.—N4
 Chernyavskay, E. A.—D48
 Chudamani, S.—C2, C3, D19
 Chyba, Thomas H.—N5
 Cimolino, Marc C.—D18, E7
 Claude, H.—D12
 Cleis, R. A.—G2
 Colao, F.—P3
 Collins, Richard L.—F4
 Congeduti, Fernando—D4
 Cooley, T. W.—H8
 Cooper, Daniel I.—D32, L33
 Couch, Richard H.—D17
 Courtier, Ph.—D21
 Cousins, Ananda—E3
 Cros, B.—B2
- Dabas, A.—D20, D21
 Dao, Phan D.—G, G10, G11
 David, C.—D13, F3
 Davidson, Gilbert—G10, G11
 de Jonge, C. N.—B10
 de Schoulepniko, L.—L8
 DeCoursey, Robert J.—D1, D7
 Defour, Martin—L32
 DeGloria, D. P.—D35
 DeHart, Terence E.—E3
 Deleva, A.—L41
 DeLorme, Joseph F.—E8
 Demidov, A. A.—D48
 DePiero, N. L.—D35
 Di Girolamo, P.—B9
 di Sarra, A.—B9
 Diebel, D.—D8
 DiSilvestre, Raymond W.—L4
 Dix, B.—I9
 Donovan, D. P.—D6, L34
 Dreischuh, T. N.—L40, L45
 Dubinsky, Richard—L31
 Durand, P.—I1
- Eberhard, Wynn L.—D27, H5, L9
 Edmonds, C. M.—D8
 Edner, H.—B10, D26, J3
 Egert, S.—D33
 Ehret, Gerhard—D11, F2, L6
 Eichinger, William E.—D28, D32, L33
 Eloranta, E. W.—D24, D25, H3
 Elouragini, Salem—L2, L38
 Emery, Y.—D13
 Emmitt, G. D.—D23
 Eng, R. S.—L20, O3
 Evans, Keith A.—A5, L4, L5, N1
- Farley, Robert—G10, G11
 Fenn, Marta A.—A5, B2, D14, F1, H6, N5
 Ferrare, Richard A.—A5, B4, D10, L4, L5, N1, N2
 Fertala, Rémi—L32
 Fiedler, J.—B10
 Fiocco, G.—A, B9
- Fischer, Ken W.—D34, I5
 Fishman, Jack—B2
 Flamant, C.—I1
 Flamant, Pierre H.—D20, D21, II, L1, L2, L38
 Flatt, S.—M4
 Flesia, C.—D13, K6, L8
 Flood, Martin—B7
 Fong, A. Y.—H2
 Freed, C.—O3
 Frelin, R.—I9
 Fuà, D.—B9
 Fugate, R. Q.—G2
 Fujimoto, Toshifumi—A6
 Fujiwara, Motow—A1
- Galle, B.—B10
 Gardner, Chester S.—F4, G4, G6, G8, G9, M1
 Garman-DuValle, Lissa—II2, L17
 Garner, R. C.—K4, L27
 Garnier, A.—G13
 Gentry, Bruce M.—D22, I4, L19
 Gillespie, James B.—L39
 Girard, L.—M4
 Gobbi, Gian Paolo—D4
 Godin, S.—B6, D13, F3
 Goldsmith, J. E. M.—N1, N2
 Goltz, S. M.—D35
 Good, Tom—II2, L17
 Gorin, Inna—L4
 Grant, William B.—B2, F1, N5
 Grasso, R. J.—L36
 Grassotti, C.—H9
 Griffin, J.—D9
 Grigorov, I. V.—D39, D40
 Gross, Rolf—II2, L17
 Gross, Michael—B4, D10
 Grossmann, Benoist E.—L32, N5
 Grund, Christian J.—I7
 Grundev, L. L.—D41, L45
 Guriolo, M.—L11
- Hägård, Arne—P5
 Häring, R.—H7
 Hahn, W.—P6
 Halldorsson, Th.—H7
 Haner, D.—F3
 Hansen, G. M.—D2
 Hardesty, R. Michael—K, D31, I2, L9
 Haris, P. A. T.—M3
 Harris, N. W.—L20
 Harris, M. R.—E5
 Hayashida, S.—B8, D3
 Heaps, William S.—B4, D10
 Heinrichs, R. M.—G3
 Henderson, Sammy W.—I6
 Herrmann, H.—H7
 Hess, Robert V.—L24
 Higdon, Noah S.—N5
 Hof, Doug E.—D28, D32, L33
 Hoffman, R. N.—H9
 Holman, W.—E5
 Holtkamp, D. B.—D28, D32, L33
- Hooper, William P.—L29
 Hori, Akihiro—D37
 Hostetter, Chris A.—G9
 Hotaling, T. C.—G3
 Howell, James N.—D31
 Hu, Huanling—D5
 Huffaker, R. Milton—I6
 Hummel, J. R.—D35, L36
 Hutt, D. L.—K5, L30
- Ichie, K.—J4
 Imbert, Béatrice—L23
 Isaacs, R. G.—H9
 Ismail, Syed—D14, H6, N5
 Itabe, Toshikazu—L22
 Ivanova, I. D.—D41
- Jelonek, M. P.—G2
 Jensen, D. R.—L29
 Jeys, T. H.—G1, G3
 Jinding, Zhang—D47
 Jinhuan, Qiu—D45, D47, L44, L46
 Jinhui, Sun—D47
 Joe, Edmond—D18
 Joergensen, T. S.—B9
 Johansson, J.—J3
 Jolliffe, B. W.—P2
- Kachelmyer, A. L.—O3
 Kane, Timothy J.—G4
 Kano, T.—J2
 Kaprilov, B.—D39
 Karl, Jr., R. R.—D28, D32, L33
 Kaul, B. V.—L47
 Keicher, W. E.—O3
 Kelley, Paul—B
 Kent, G. S.—D2
 Kenyon, David L.—D15, E2
 Kiemle, C.—L6
 Kiernan, S. C.—E4
 Killinger, Dennis K.—F, O1, O2
- Kingston, R. H.—O3
 Kirks, Kenneth R.—L4
 Kist, Edward H.—D17
 Kitada, Toshinobu—D37
 Kitchen, Wayne L.—D17
 Knudsen, B.—B9
 Kobayashi, Takao—D37
 Koch, Michael R.—D17
 Koenig, G. G.—H, K4
 Kolarov, G.—D42, L41
 Kolev, I.—D39
 Korb, C. Laurence—D22, I4, L13
- Korn, J.—G3
 Kovalev, V. A.—D8, L37
 Krichbaumer, W.—H7, P6
 Krueger, D. A.—L10
 Kurzius, S. C.—E5
 Kuwashima, S.—L18
 Kuznetsov, A. L.—L47
- Lacoste, A. M.—B6
 Lacy, Bob—II2, L17
 Lange, W. J.—G2
 Lapp, M.—D9, N1
 Laroche, V.—L30
 Larsen, N.—B9

- Lawrence, T. Rhidian—E2, E3
Lax, B.—L20
Lee, H. Sang—L21
Lentz, W. J.—L35
Leroy, C.—D13
Lieutaud, F.—D20, D21
Livingston, John M.—P1
Loth, C.—D20
Louis, J. -F.—H9
Lysak, D. B.—M3
- Maeda, M.—N6
Mamakos, William A.—L4
Manizade, Serdar S.—J5
Manson, Peter J.—A2
Margalit, Eli—L31
Marsh, James M.—L4
Martinez, R. J.—D32
Matsui, I.—B8, D3
Matsumoto, H.—L18, O4
Mayor, Shane D.—B2, N5
McCormick, M. Patrick—E6
McDermid, I. Stuart—B5
McDonald, Kenneth F.—E3
McElroy, J. L.—D8
McGee, Thomas J.—B4, D10
McGill, Matt J.—I5
McNicholl, P.—I9, I11
McNutt, Ross—G10
Mégie, G.—B6, F3, N4
Mehnert, A.—H7
Melfi, S. Harvey—A5, I3,
L4, L5, N1, P
Mellquist, J.—B10
Menenger, L.—L2
Menyuk, Norman—O
Menzies, Robert T.—C3
Meriwether, John W.—G10,
G11
Michaelis, Walfried—A3, K3,
L26, N3
Mickelson, M.—H9
Milton, M. J. T.—P2
Minato, Atsuchi—B8, D30,
M5
Minga, A.—B2
Mitev, V. M.—B10, D13,
D39, D40, D41, F3
Mitsev, Ts.—D42, L41
Mizushima, Y.—J4
Moerl, Peter—F2
Moody, Stephen E.—E3
Moosmüller, H.—D8, L37
Moskowitz, Warren P.—G10
Mugnai, A.—L8
Münkel, C.—L7
Muraoka, K.—N6
- Naboko, V. N.—L42
Nagai, Tomohiro—A6
Nagasawa, Chikao—A4, G5
Nakane, H.—B8
Nehrkorn, T.—H9
Neilsen, Norman B.—P1
Nganga, D.—B2
Nielsen, Norman B.—
Nomura, A.—J2
Notari, Anthony—L19, L21
Nowicki, Greg D.—H6
Ogawa, I.—J4
- Oh, D.—D20
Okumura, H.—L18, O4
Olivier, Lisa D.—I2
Osborn, Mary T.—D1, D7
- Pagliughi, F. M.—D35
Pal, S. R.—H2
Palm, Stephen P.—I3
Palucci, A.—
Papen, George C.—G4, G6,
G7
Parvanov, O.D39
Patterson, Graeme R.—A2
Pearson, Guy N.—I8
Pelon, J.—I1, L1, L2, L3, N4
Persson, Rolf—P5
Petheram, John C.—E2, E4
Petros, Mulgeta—D18, E7
Pfenninger, W. Matthew—G4,
G6, G7
Philbrick, C. R.—M3
Piironen, A. K.—D24
Piironen, P. K.—H3
Pindroh, Albert L.—E3
Platt, C. M. R.—H, H1
Polovtseva, E. R.—L47
Ponsardin, Patrick—N5
Poole, Lamont R.—K2
Popov, A. G.—D46
Porteneuve, J.—L15, L16
Post, Madison J.—I7
Prasad, C. R.—L13
Pribluda, I.—H2
Prinn, Ronald G.—A7, B, B1
- Qian, Jun—G4
Qilin, Xia—D47
Qirong, Huang—D45, L46
Quaglia, P.—L3
Quick, Jr., C. R.—D28, D32,
L33
- Ragnarson, P.—D26
Rall, Jonathan A. R. —J5
Ramos-Izquierdo, Luis—L4
Rau, Y. -C.—M3
Reagan, J. A.—H8
Regan, Curtis P.—D17
Reithmaier, Karl—D18
Remus, Ruben W.—D17
Renger, Wolfgang—D11, F2,
L6, N
Ribezzo, S.—P3
Rizi, V.—D13
Robinson, R. A.—P2
Robinson, R. J.—E5
Rollins, Courtney H.—D17
Rosen, David L.—L39
Rosenbaum, David M.—D17
Rowland, Carroll W.—D17
Ruane, R. E.—G2
- Sèze, G.—D21
Saito, Y.—J2
Sansoni, P.—L11
Sargoytchev, S.—M4
Sasano, Yasuhiro—D3, D30,
M5
Sassen, Kenneth—H4
Schaberl, T.—B10
Scherrer, Daniel R.—G4, G6,
- G8
Schönenborn, F.—D12
Schotland, Richard—M
Schultz, K. I.—J1, O3
Schulze, Christoph—A3, L26
Schwarzenberger, P. M.—E5
Schwemmer, Geary K.—L13,
L14
Schwendimann, P.—K6
Schwiesow, R. L.—I10
Scott, J. W.—E4
Senft, Daniel C.—G4, G6, G8
Serikov, I. B.—D46
Shaoming, Wu—D45
She, C. Y.—L10
Shufang, Wang—D45
Shumskii, V. K.—D46
Sica, R. J.—M4
Simeonov, V. B.—D39, D40
Simmet, G.—L6
Singh, Upendra N.—B4, D10
Siping, Zheng—D45
Skinner, Wilbert R.—D34, I5
Slavin, A. C.—G3
Smith, Brent—B7
Smith, Duane—J
Smith, I. M.—E5
Snow, William—I
Sonnemann, G.—B10
Spakman, J.—B10
Spinhirne, James D.—C2, C3,
D19
Spowart, M. P.—I10
Sroga, J. T.—E4
Staley, O. Glenn—L4
Staton, Leo D.—L24
Stefanutti, L.—D13, L8
Steinbrecht, W.—B3, D6, H2
Stevens, T. D.—M3
Stevens, K. M.—D2
Stevens, William T.—D17
Stow, Larry L.—B2
Stoyanov, D. V.—L40, L42,
L43, L45
Stoykova, E. V.—L43
Streicher, J.—H7, L7, P6
Sugimoto, Nobuo—D30, M5
Sugita, T.—L18, O4
Summers, C. L.—L20
Surovegina, A. I.—D43
Svanberg, S.—D26, J3
Swann, N. R. W.—P2
Swart, D. P. J.—B10
- Taira, Takunori—D37
Takeichi, M.—J4
Takeshima, A.—J4
Takeuchi, Nobuo—C, L18,
O4
Tellier, L.—D28
Thériault, J. -M.—L30
Thayer, J. P.—D36
Theopold, F. A.—N3
Thompson, Ray—D18
Thro, P. -Y.—L12
Tiee, J. J.—D28, D32, L33
Tratt, David M.—C2, C3
Trotta, J. E.—E4
Tsuchiya, Masayuki—P4
Turner, Clayton P.—D17
Turner, R. M.—D8
- Uchino, Osamu—A6, N6
Uchiumi, M.—N6
Ulitsky, Arkady—B7
Uthe, Edward E.—P1
- Valentin, R.—L1, L2
Vandersee, W.—D12
Veiga, Robert E.—B2
Vickery, William—E
Villane, Ron—D18
Visconti, G.—D13
von Cossart, G.—B10
Voss, E.—O5
- Wall, K. F.—G3
Wallace, S.—E5
Wallinder, E.—B10, D26, J3
Wallio, H. Andrew—L24
Walsh, Nita W.—L4
Wan, Lewis S.—L4
Wandering, Ulla—A3, K3,
L26
Wang, Liang-Gu—L24
Wang, Tin-Yu—B7
Warashima, Y.—J4
Weaver, F. J.—E4
Weigner, Matthias—L25
Weitkamp, Claus—A3, K3,
L26, N3, O5
Wenming, Wang—D45
Werner, Ch.—H7, P6
Whiteman, David N.—A5, L4,
L5, N1
Whiteway, James A.—D38,
L34
Wilkerson, Thomas D.—L14
Willets, D. V.—E5
Willis, Ron J.—D27
Wilson, Alex—G11
Winker, David M.—D1, D7,
K2
Wirth, Martin—D11, F2
Wissinger, Alan B.—D16, E2
Wood, S. A.—D23
Woods, D. C.—D7
Woods, P. T.—P2
Wulfmeyer, V.—L12
- Yamagishi, Susumu—P4
Yamaguchi, K.—J2, O4
Yamaguchi, S.—O4
Yamamoto, Takanobu—D37
Yamanouchi, Hiroshi—P4
Young, P. W.—D25
Young, Stuart A.—A2
- Zaccanti, G.—L11
Zhao, Hongjie—H4
Zhao, Yangzeng—D31
Zhou, Jun—D5
Zuev, V. E.—M2

REPORT DOCUMENTATION PAGE			Form Approved OMB No. 0704-0188											
Public reporting burden for this collection of information is estimated to average 1 hour per response, including the time for reviewing instructions, searching existing data sources, gathering and maintaining the data needed, and completing and reviewing the collection of information. Send comments regarding this burden estimate or any other aspect of this collection of information, including suggestions for reducing this burden, to Washington Headquarters Services, Directorate for Information Operations and Reports, 1215 Jefferson Davis Highway, Suite 1204, Arlington, VA 22202-4302, and to the Office of Management and Budget, Paperwork Reduction Project (0704-0188), Washington, DC 20503.														
1. AGENCY USE ONLY (Leave blank)	2. REPORT DATE July 1992	3. REPORT TYPE AND DATES COVERED Conference Publication												
4. TITLE AND SUBTITLE Sixteenth International Laser Radar Conference			5. FUNDING NUMBERS WU 665-45-20-21											
6. AUTHOR(S) M. P. McCormick, Editor														
7. PERFORMING ORGANIZATION NAME(S) AND ADDRESS(ES) NASA Langley Research Center Hampton, VA 23665-5225			8. PERFORMING ORGANIZATION REPORT NUMBER L-17126											
9. SPONSORING/MONITORING AGENCY NAME(S) AND ADDRESS(ES) U.S. Air Force Office of Scientific Research, Washington, DC, 20035; NASA Langley Research Center, Hampton, VA 23665; the U.S. Air Force Phillips Laboratory, Hanscomb, MA 02106; the American Meteorological Society, Boston, MA 02108; and the Optical Society of America, Washington, DC, 20036.			10. SPONSORING/MONITORING AGENCY REPORT NUMBER NASA CP-3158, Part 2											
11. SUPPLEMENTARY NOTES Abstracts of conference held at Cambridge, Massachusetts, July 20-24, 1992.														
12a. DISTRIBUTION/AVAILABILITY STATEMENT Unclassified-Unlimited Subject Category 35			12b. DISTRIBUTION CODE											
13. ABSTRACT (Maximum 200 words) This publication contains extended abstracts of papers presented at the 16th International Laser Radar Conference, held in Cambridge, Massachusetts, July 20-24, 1992. One hundred ninety-five papers were presented in both oral and poster sessions. The topics of the conference sessions were: <table border="0"> <tr> <td>1. Mt. Pinatubo Volcanic Dust Layers Observations</td> <td>6. Wind Measurements and Measurement Systems</td> </tr> <tr> <td>2. Global Change/Ozone Measurements</td> <td>7. Imaging and Ranging</td> </tr> <tr> <td>3. GLOBE/LAWS/LITE</td> <td>8. Water Vapor Measurements</td> </tr> <tr> <td>4. Mesospheric Measurements and Measurement Systems</td> <td>9. Systems and Facilities</td> </tr> <tr> <td>5. Middle Atmosphere</td> <td>10. Laser Devices and Technology</td> </tr> </table> This conference reflects the breadth of research activities being conducted in the lidar field. These abstracts address subjects from lidar-based atmospheric investigations relating to global change to the development of new lidar systems and technology.					1. Mt. Pinatubo Volcanic Dust Layers Observations	6. Wind Measurements and Measurement Systems	2. Global Change/Ozone Measurements	7. Imaging and Ranging	3. GLOBE/LAWS/LITE	8. Water Vapor Measurements	4. Mesospheric Measurements and Measurement Systems	9. Systems and Facilities	5. Middle Atmosphere	10. Laser Devices and Technology
1. Mt. Pinatubo Volcanic Dust Layers Observations	6. Wind Measurements and Measurement Systems													
2. Global Change/Ozone Measurements	7. Imaging and Ranging													
3. GLOBE/LAWS/LITE	8. Water Vapor Measurements													
4. Mesospheric Measurements and Measurement Systems	9. Systems and Facilities													
5. Middle Atmosphere	10. Laser Devices and Technology													
14. SUBJECT TERMS Lidar, Laser radar, Remote sensing, Atmospheric measurements			15. NUMBER OF PAGES 381											
			16. PRICE CODE A17											
17. SECURITY CLASSIFICATION OF REPORT Unclassified	18. SECURITY CLASSIFICATION OF THIS PAGE Unclassified	19. SECURITY CLASSIFICATION OF ABSTRACT	20. LIMITATION OF ABSTRACT											

National Aeronautics and
Space Administration
Code JTT
Washington, D.C.
20546-0001
Official Business
Penalty for Private Use, \$300

SPECIAL FOURTH-CLASS RATE
POSTAGE & FEES PAID
NASA
PERMIT No. G27



POSTMASTER: If Undeliverable (Section 158
Postal Manual) Do Not Return
